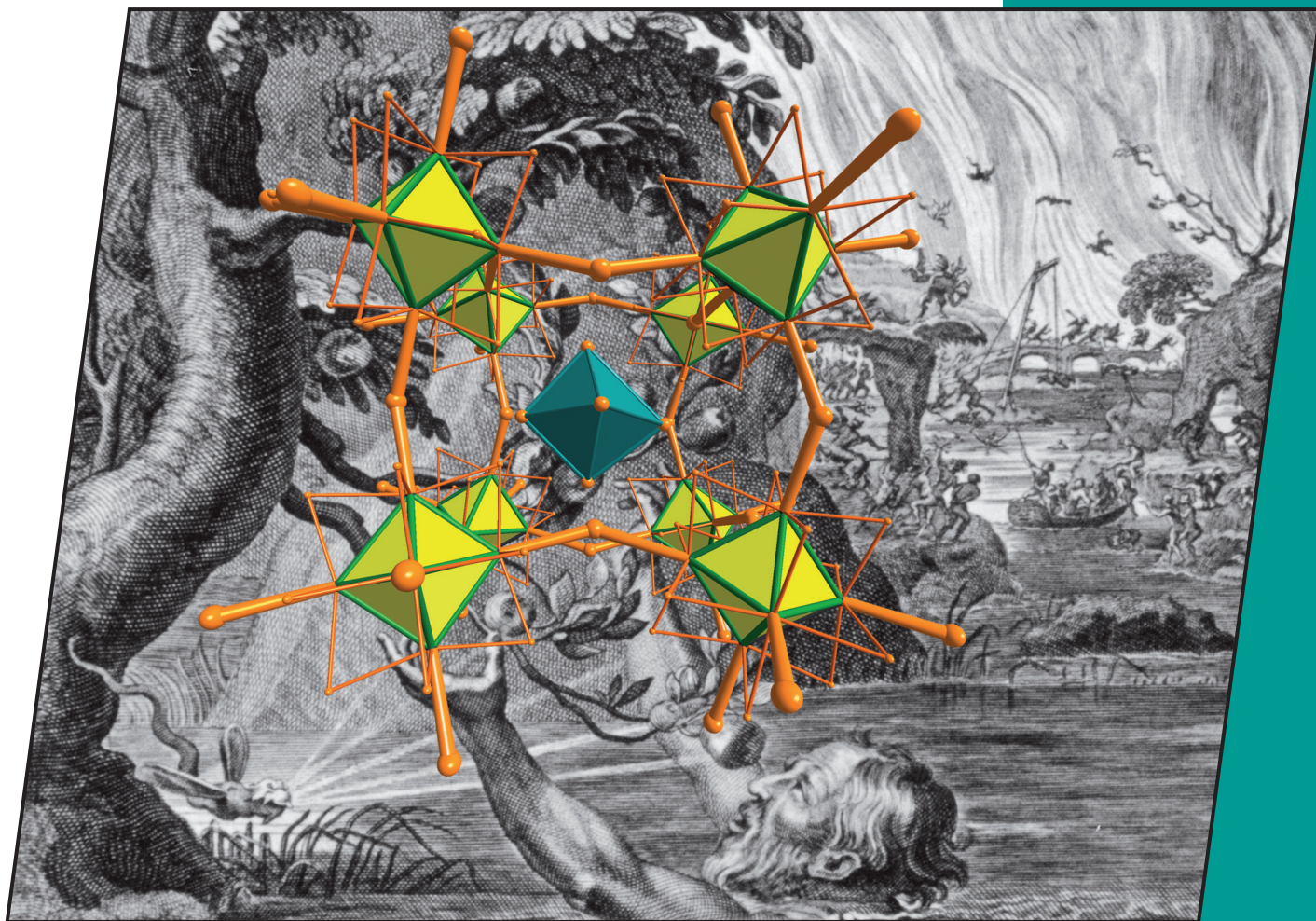


26/2010
2nd September Issue

[26]

EurJIC
European Journal of
Inorganic Chemistry

Eur. J. Inorg. Chem. 2010, 4049–4216



Cover Picture

Katja Habermehl, Anja-Verena Mudring, and Gerd Meyer

The Elusive "Tantalum(III) Bromide": A Perovskite-Related Salt, $[\text{Ta}_6\text{Br}_{12}]\text{Br}_3[\text{TaBr}_6]_{0.86}$

Microreview

Bond Activation with Low-Valent Nickel in Homogeneous Systems

Alma Arévalo and Juventino J. García

 **WILEY-VCH**

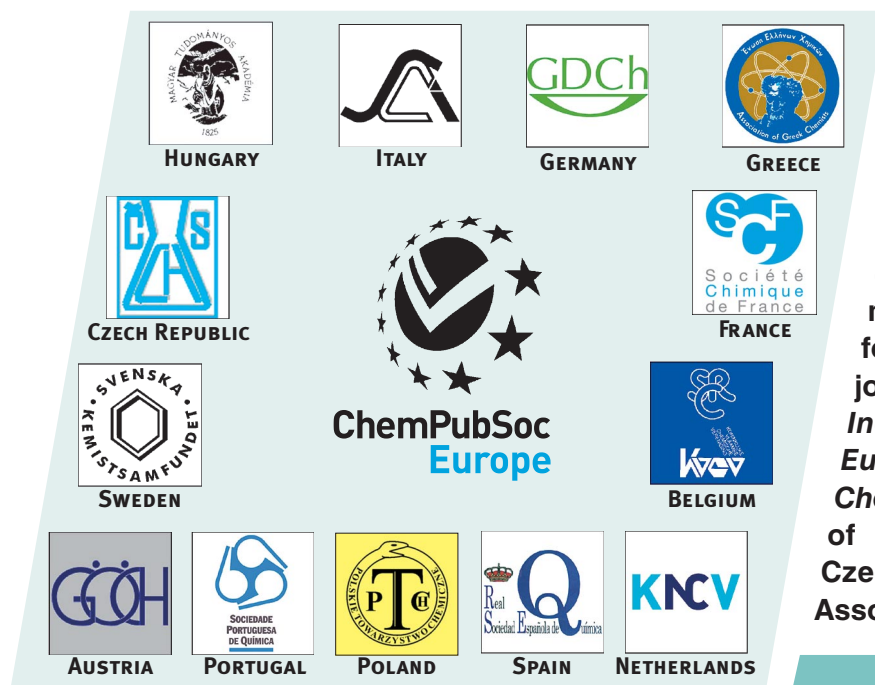
www.eurjic.org

EJICFK (26) 4049–4216 (2010) · ISSN 1434-1948 · No. 26/2010

A Journal of



ChemPubSoc
Europe

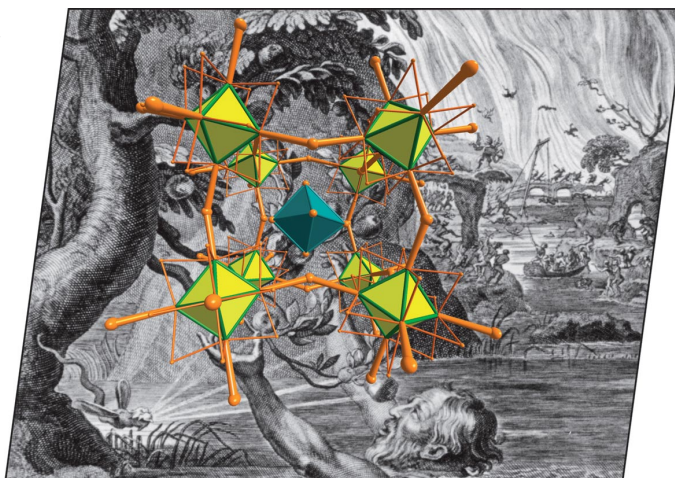


EurJIC is co-owned by 11 societies of ChemPubSoc Europe, a union of European chemical societies for the purpose of publishing high-quality science. All owners merged their national journals to form two leading chemistry journals, the *European Journal of Inorganic Chemistry* and the *European Journal of Organic Chemistry*. Three further members of ChemPubSoc Europe (Austria, Czech Republic and Sweden) are Associates of the two journals.

Other ChemPubSoc Europe journals are *Chemistry – A European Journal*, *ChemBioChem*, *ChemPhysChem*, *ChemMedChem*, *ChemSusChem* and *ChemCatChem*.

COVER PICTURE

The cover picture shows the crystal structure of “tantalum tribromide”, which is, in fact, a perovskite-related salt, $[\{Ta_6\}Br_{12}]Br_3[TaBr_6]_{0.86}$. Unlike the mythical King Tantalos who was not allowed to grasp the fruits above his head, Habermehl et al. (page 4075ff.) were blessed to pick this magnificent fruit that had to ripen for 45 years. Copyright permission for the background picture (The Punishment of Tantalus) was obtained from Photo © maicar.com



CONTENTS

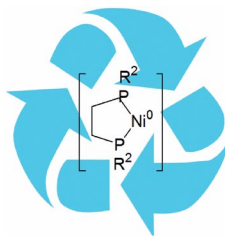
MICROREVIEW

Homogeneous Catalysis

A. Arévalo, J. J. García* 4063–4074

Bond Activation with Low-Valent Nickel in Homogeneous Systems

Keywords: Homogeneous catalysis / Nickel / Isomerization / Desulfurization / Hydration / Bond activation / Nitriles / Alkynes



Recent advances using low-valent-nickel compounds for the catalytic activation of multiple bonds.

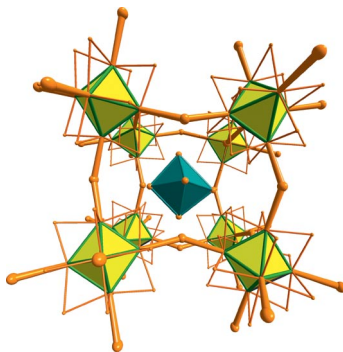
SHORT COMMUNICATIONS

Cluster Halides

K. Habermehl, A.-V. Mudring, G. Meyer* 4075–4078

The Last of the Five: the Elusive “Tantalum(III) Bromide”, a Perovskite-Related Salt, $[\{Ta_6\}Br_{12}]Br_3[TaBr_6]_{0.86}$

Keywords: Bromides / Cluster complexes / Tantalum



The elusive $TaBr_3$, in fact $TaBr_{2.94}$, is a perovskite-related salt, $[\{Ta_6\}Br_{12}]Br_3[TaBr_6]_{0.862(13)} = [Ti]O_3[Ca]$, and thereby a stuffed derivative of its neighbour $\{Ta_6\}Br_{15} = TaBr_{2.5}$.

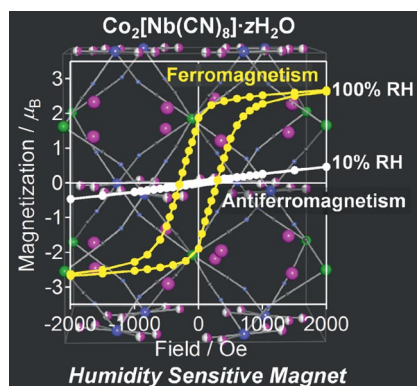
Porous Magnets

K. Imoto, D. Takahashi, Y. Tsunobuchi, W. Kosaka, M. Arai, H. Tokoro, S.-i. Ohkoshi* 4079–4082



Humidity-Sensitive Magnet Composed of a Cyano-Bridged Co^{II} – Nb^{IV} Dimetallic Assembly

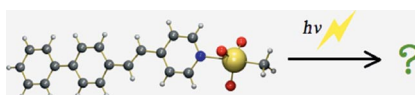
Keywords: Cyano-bridged assembly / Humidity response / Cobalt / Niobium / Magnetic properties



A humidity-induced reversible change between ferromagnetism and antiferromagnetism was observed in a cobalt octacyanoanionobate based magnet. This humidity response is caused by the adsorption and desorption of non-coordinated water (so-called zeolitic water) molecules in the interstitial site. Such a phenomenon is achieved by the structural flexibility of an octacyanometalate-based magnet.

FULL PAPERS

The coordination of a series of chromophoric pyridine derivatives to methyltrioxorhenium was studied. The stability constants of the complexes in dichloromethane were determined and the catalytic performance in the epoxidation of 1-octene was tested. Moreover, the behaviour of the compounds towards irradiation with UV light was examined.



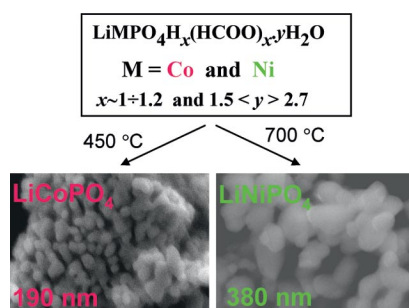
Methyltrioxorhenium Chemistry

S. A. Hauser, V. Korinth, E. Herdtweck,
M. Cokoja, W. A. Herrmann,
F. E. Kühn* 4083–4090

Chromophoric Lewis Base Adducts of Methyltrioxorhenium: Synthesis, Catalysis and Photochemistry

Keywords: Rhenium / Homogeneous catalysis / Photochemistry / Epoxidation / Stability constants

Olivine-type LiCoPO_4 and LiNiPO_4 phases without any Li–M disorder (between the 4a and 4c positions) and Li deficiency were prepared from homogeneous Li–Co(Ni)–phosphate–formate precursors.



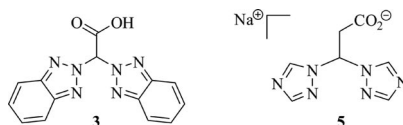
Ordered Lithium–Metal Phosphates

V. Koleva,* E. Zhecheva,
R. Stoyanova 4091–4099

Ordered Olivine-Type Lithium–Cobalt and Lithium–Nickel Phosphates Prepared by a New Precursor Method

Keywords: Lithium / Cobalt / Nickel / Organic-inorganic hybrid composites / X-ray diffraction

Syntheses of bis(2*H*-benzotriazol-2-yl)acetic acid Hbbta (**3**) and sodium 3,3-bis(1*H*-1,2,4-triazol-1-yl)propionate Na[btp] (**5**) are reported. Ligand **3** is a poor electron-donating ligand and forms κ^3 complexes. The 1*H*-1,2,4-triazole-based ligand **5** forms coordination polymers $[\text{Zn}(\text{btp})_2]_\infty$ (**8**) and $[\text{Mn}(\text{btp})_2]_\infty$ (**9**). Deposition of one-dimensional polymer strands of **8** on HOPG was successful and was analysed by STM.



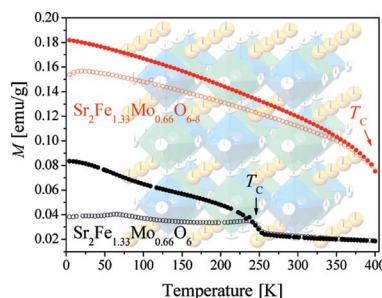
Ligand Design

E. Hübner, N. V. Fischer,
F. W. Heinemann, U. Mitra, V. Dremov,
P. Müller*, N. Burzlaff* 4100–4109

N,N,O Ligands Based on Triazoles and Transition Metal Complexes Thereof

Keywords: Scorpionate ligands / Tripod ligands / Coordination polymers / Zinc / Manganese / Ruthenium

The double perovskite $\text{Sr}_2\text{Fe}_{1.33}\text{Mo}_{0.66}\text{O}_6$ shows a substantial change upon controlled H_2 reduction evidenced in its magnetic properties, which leads to the induction of non-negligible *MR* properties at room temperature.



Magnetic Double Perovskites

C. A. López, M. C. Viola,
J. C. Pedregosa,* J. A. Alonso,
M. T. Fernández-Díaz 4110–4120

Enhancing Magnetic and Magnetotransport Properties by Topotactic Reduction of the $\text{Sr}_2\text{Fe}_{1.33}\text{Mo}_{0.66}\text{O}_6$ Double Perovskite

Keywords: Double perovskites / Magnetic properties / Hydrogen reduction

CONTENTS

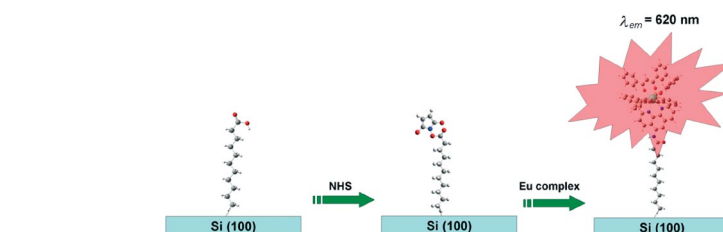
Functionalized Inorganic Surfaces

G. G. Condorelli,* C. Tudisco, A. Motta,
A. Di Mauro, F. Lupo, A. Gulino,
I. L. Fragalà 4121–4129



Multistep Anchoring Route of Luminescent (5-Amino-1,10-phenanthroline)-tris(dibenzoylmethane)europium(III) on Si(100)

Keywords: Monolayers / Luminescence / Surface chemistry / Silicon / Metal complexes



A luminescent Eu^{III} complex has been covalently anchored on Si via surface prefunctionalization with NHS ester followed by the nucleophilic substitution to the NHS activated carboxylic group. The comparison

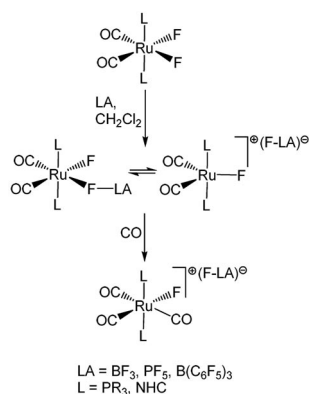
with different silicon prefunctionalization proved the crucial role of NHS activation to maintain intact the Eu coordination environment.

Organometallic Fluorides

K. S. Coleman, J. Fawcett,
D. A. J. Harding, E. G. Hope,* K. Singh,
G. A. Solan* 4130–4138

Routes to Ruthenium–Fluoro Cations of the Type [RuL₂(CO)_nF]⁺ (*n* = 2,3; L = PR₃, NHC): A Play-Off between Solvent, L and Weakly Coordinating Anion

Keywords: Ruthenium / Fluorides / Cations / Lewis acids / Phosphane ligands / Carbene ligands / *N*-Heterocyclic carbenes / Weakly coordinating anions (WCAs)



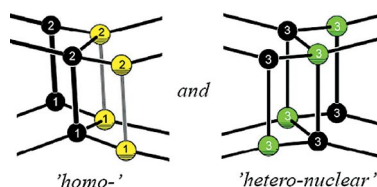
The reactivity of the difluororuthenium complexes [RuF₂(CO)₂(L)₂] (L = PR₃, NHC) towards a range of Lewis acids (LA) has been examined in coordinating and noncoordinating solvents. In a noncoordinating solvent monofluoro cations can be obtained. Addition of donor ligands (e.g., CO) generates the corresponding coordinatively saturated cation–anion pair.

Intermetallic Superstructures

S. Ponou* 4139–4147

On a TiNiSi-Type Superstructure: Synthesis, Crystal and Electronic Structures of CaAgGe and Its Mn-Substituted Derivative

Keywords: Solid-state structures / Intermetallic phases / Zintl phases / TiNiSi-type superstructure



CaAgGe and its Mn-substituted derivative have been structurally characterized in a superstructure of the TiNiSi type. According to the DFT band structure calculations, the mixing of homo- and hetero-nuclear interactions in the featuring atomic square ladders are driven by the electron shortage, and ascribe more electronic flexibility to the system.

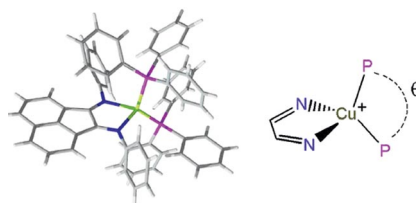
Copper Diimine Photosensitizers

T. Kern, U. Monkowius,* M. Zabel,
G. Knör* 4148–4156

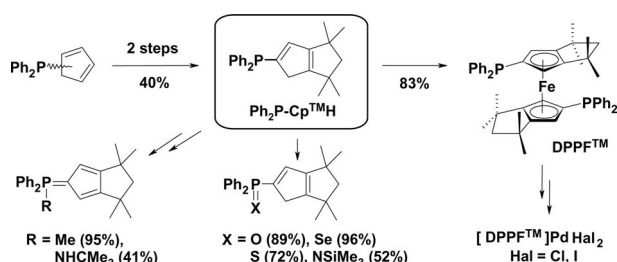


Mononuclear Copper(I) Complexes Containing Redox-Active 1,2-Bis(aryl-imino)-acenaphthene Acceptor Ligands: Synthesis, Crystal Structures and Tuneable Electronic Properties

Keywords: Copper / Electronic spectra / Solvatochromism / Charge transfer



Copper(I) complexes carrying bis(imino)-acenaphthene ligands are introduced as versatile new photocatalysts with low-lying MLCT-excited states suitable for the visible-light driven accumulation of multiple reduction equivalents at the 1,2-diimine ligand. Therefore, such Cu-based systems may become an attractive alternative to classical photosensitizers such as ruthenium polypyridine complexes.



An efficient two-step protocol towards a novel highly crowded Cp-phosphane has been developed, further reactions of which gave a series of bisfunctional phosphoranyl-functionalized ligands. Further-

more, the title compound can be transformed into a new chelating, electron-rich, sterically demanding ferrocenyl-diphosphane dppf^{TM} and its Pd complexes.

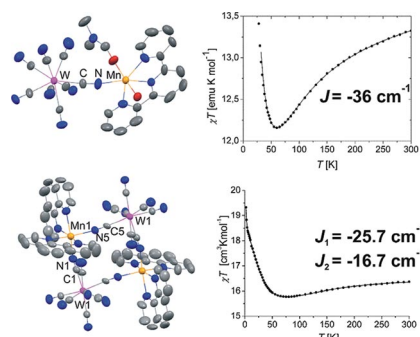
A. R. Petrov, M. Elfferding, J. Möbus, K. Harms, K. A. Rufanov, J. Sundermeyer* 4157–4165

Discovery and Synthetic Value of a Novel, Highly Crowded Cyclopentadienylphosphane $\text{Ph}_2\text{P-Cp}^{\text{TMH}}$ and Its Ferrocenyl-Bisphosphane dppf^{TM}

Keywords: Phosphane ligands / Cyclopentadienyl ligands / Sandwich complexes / Phosphanes / Ferrocenes / Palladium complexes

Polynuclear Complexes

Cyano-bridged dinuclear $\{\text{MnW}\}^-$ and tetranuclear square $\{\text{Mn}_2\text{W}_2\}^{2-}$ motifs reveal intermetallic magnetic coupling constants J_{MnW} ascribed to W-CN-Mn linkages arising from b or m vertices of the octacyanotungstate moiety of the trigonal prism square-face bicapped geometry (TPRS-8).



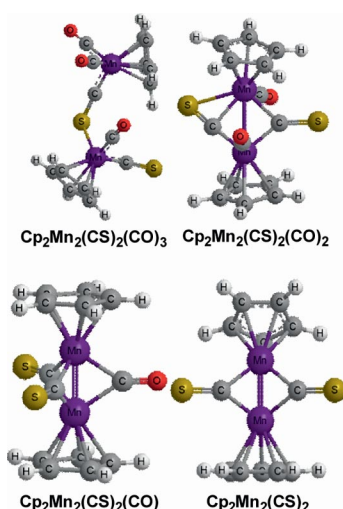
R. Podgajny,* T. Korzeniak, P. Przychodzeń, C. Gimenez-Saiz, M. Rams, M. Kwaśniak, B. Sieklucka 4166–4174

Magneto–Structural Correlations in Discrete $\text{Mn}^{\text{II}}\text{-W}^{\text{V}}$ Cyano-Bridged Assemblies with Polyimine Ligands

Keywords: Manganese / Tungsten / Cyanides / Molecular squares / Magnetic properties / Structure elucidation

Cp-Manganese Thiocarbonyls

Density functional theory predicts end-on four-electron donor CE ($\text{E} = \text{O}, \text{S}$) bridged structures to be preferred over the normal two-electron donor CE bridged structures for $[\text{Cp}_2\text{Mn}_2(\text{CS})_2(\text{CO})_3]$. The lowest energy structure for $[\text{Cp}_2\text{Mn}_2(\text{CS})_2(\text{CO})_2]$ has one four-electron donor bridging $\eta^2\text{-}\mu\text{-CS}$ group, but is predicted to be unstable with respect towards disproportionation. The global minima of $[\text{Cp}_2\text{Mn}_2(\text{CS})_2(\text{CO})]$ and $[\text{Cp}_2\text{Mn}_2(\text{CS})_2]$ are triply bridged singlet and doubly bridged triplet structures, respectively, predicted to contain formal $\text{Mn}\equiv\text{Mn}$ triple bonds. Higher energy $[\text{Cp}_2\text{Mn}_2(\text{CS})_2]$ structures with bridging acetylenedithiolate ligands are also found.



Z. Zhang, Q.-s. Li,* Y. Xie, R. B. King,* H. F. Schaefer III 4175–4186

Binuclear Cyclopentadienylmanganese Carbonyl Thiocarbonyls: Four-Electron Donor Bridging Thiocarbonyl Groups of Two Types and a Bridging Acetylenedithiolate Ligand

Keywords: Manganese / Cyclopentadienyl ligands / Density functional calculations / Metal-metal interactions / Metal thiocarbonyls

CONTENTS

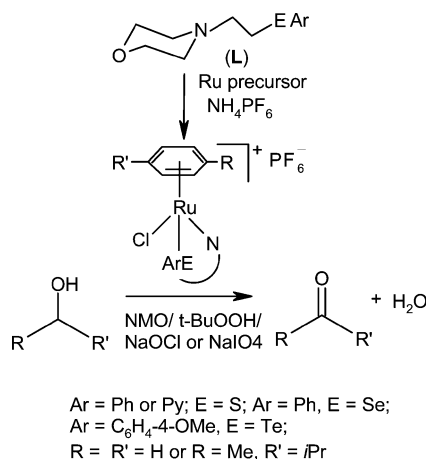
“Piano-Stool” Ruthenium Complexes

P. Singh, A. K. Singh* 4187–4195



“Piano-Stool” Complexes of Ruthenium (II) Designed with Arenes and *N*-[2-(Aryl-chalcogeno)ethyl]morpholines: Highly Active Catalysts for the Oxidation of Alcohols with *N*-Methylmorpholine *N*-Oxide, *tert*-Butyl Hydroperoxide and Sodium Periodate and Oxychloride

Keywords: Alcohols / Chalcogens / Homogeneous catalysis / Oxidation / Ruthenium



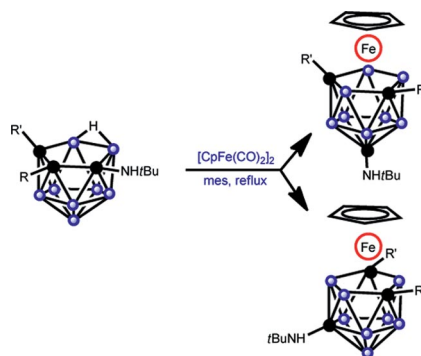
“Piano-stool” ruthenium complexes [RuCl(η⁶-C₆H₆/η⁶-*p*-cymene)(L)][PF₆] have been synthesized, characterized by X-ray crystallography, NMR and IR spectroscopy, and CV, and tested in the catalytic oxidation of primary/secondary alcohols with *N*-methylmorpholine *N*-oxide (NMO), *t*BuOOH, NaOCl, and NaIO₄ (TON upto 9.8 × 10⁴). Ru^{IV}=O appears to be the intermediate. The catalytic efficiency of the ligands is Te > Se > S.

Iron-Containing Cages

J. Holub, M. Bakardjiev, B. Štíbr,*
P. Štěpnička, I. Císařová 4196–4200

Synthesis and Electrochemistry of Cyclopentadienyl Ferratricarbollides Substituted by Me and Ph Groups on the Cage Carbon Atoms

Keywords: Iron / Boron / Carboranes / Cage compounds / Electrochemistry



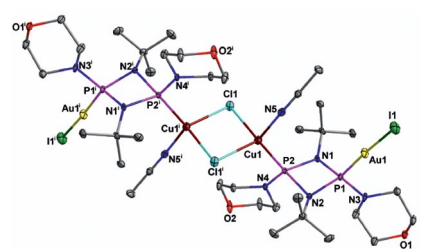
Neutral tricarbollide tautomers 7-*t*BuNH-8,9-*R,R'*-*nido*-7,8,9-C₃B₈H₉ (*R/R'* = Me/H, Ph/H, Me₂, and Ph₂) reacted with [CpFe(CO)₂]₂ to yield the corresponding cage-isomeric, twelve-vertex *closo* ferratricarbollides [1-Cp-12-*t*BuNH-2,4-*R,R'*-1,2,4,12-FeC₃B₈H₈] (**2**) and [1-Cp-10-*t*BuNH-2,4-*R,R'*-1,2,4,10-FeC₃B₈H₈] (**3**), whose Fe^{II}/Fe^{III} redox potentials are primarily affected by the type of the ferratricarbaborane cage.

Cyclodiphosphazanes

M. S. Balakrishna,* D. Suresh,
J. T. Mague 4201–4210

Mono-, Bi-, Tri- and Tetranuclear Palladium(II), Copper(I), and Gold(I) Complexes of Morpholine- and *N*-Methylpiperazine-Functionalized Cyclodiphosph(III)azanes, *cis*-[(*t*BuN-μ)₂-(PNC₄H₈X)₂] (X = O, NMe)

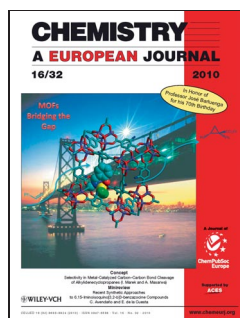
Keywords: Heterometallic complexes / Cyclodiphosphazanes / Palladium / Copper / Gold





On these pages, we feature a selection of the excellent work that has recently been published in our sister journals. If you are reading these pages on a

computer, click on any of the items to read the full article. Otherwise please see the DOIs for easy online access through Wiley Online Library.

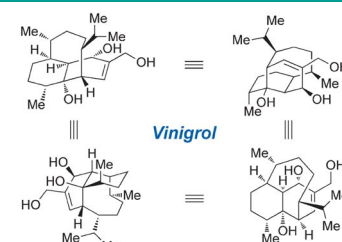


Total Synthesis

A. D. Hutters, N. K. Garg*

Synthetic Studies Inspired by Vinigrol

Vinigrol, a diterpene natural product, has been a fascinating target for total synthesis for over two decades. This minireview describes recent synthetic studies that have ultimately allowed access to the coveted vinigrol scaffold, including the approaches reported by Barriault, Njardarson, and Hanna, as well as the first total synthesis of vinigrol, reported by Baran in 2009.



Chem. Eur. J.

DOI: [10.1002/chem.201000916](https://doi.org/10.1002/chem.201000916)

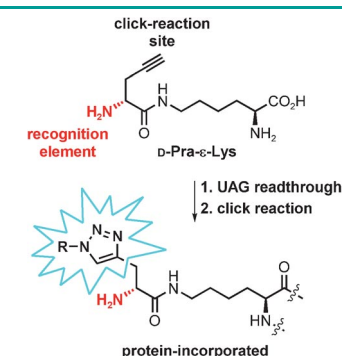


Pyrrolysine

X. Li, T. Fekner, M. K. Chan*

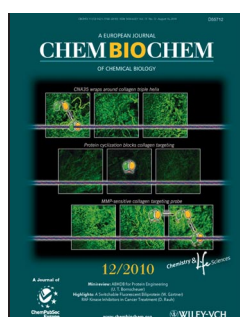
N⁶-(2-(R)-Propargylglycyl)lysine as a Clickable Pyrrolysine Mimic

Clickable copycat! Readily available dipeptide D-Pra-ε-Lys is identified using a modified fluorescence protein assay as a highly efficient clickable pyrrolysine mimic. It is shown to incorporate into calmodulin in high yield to provide a handle for labeling with an azide-containing coumarin.



Chem. Asian J.

DOI: [10.1002/asia.201000205](https://doi.org/10.1002/asia.201000205)

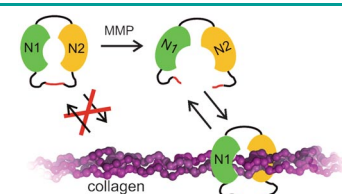


Protein Engineering

M. Breurken, E. H. M. Lempens, M. Merckx*

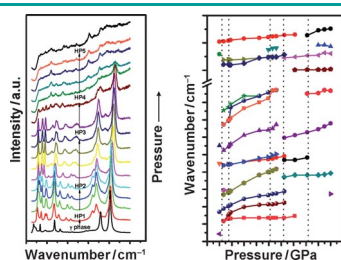
Protease-Activatable Collagen Targeting Based on Protein Cyclization

Threading collagen through a protein needle: The collagen-binding protein CNA35 operates by wrapping itself around the collagen triple helix. By connecting the N and C termini through an MMP recognition sequence, a dual-specific MMP-sensitive collagen-targeting ligand is obtained that can be used for imaging extracellular matrix turnover.



ChemBioChem

DOI: [10.1002/cbic.201000223](https://doi.org/10.1002/cbic.201000223)



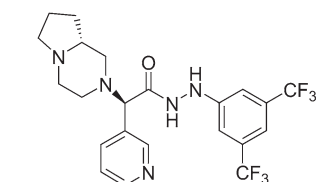
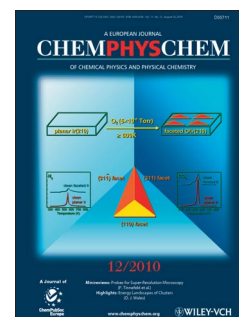
ChemPhysChem
DOI: 10.1002/cphc.201000341

Nanowires

J. Chen,* S. H. Chen, D. Y. Lu, W. H. Zhang, F. Y. Xie, W. G. Xie, L. Gong, C. X. Wang*

Pressure-Induced Structural Transition in WO₃ Nanowires

Pressure-induced structural transition in WO₃ nanowires is followed by Raman spectroscopic analysis (see picture). Upon increasing the applied pressure, WO₃ nanowires undergo four phase transitions at pressures around 1.7, 4.6, 21.5, and 26.2 GPa, which are all less than those reported for bulk WO₃. At a pressure of 42.5 GPa, a new high-pressure phase appears, which has never been reported and is not reversible while unloading pressure.



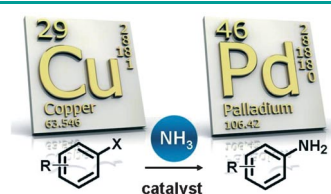
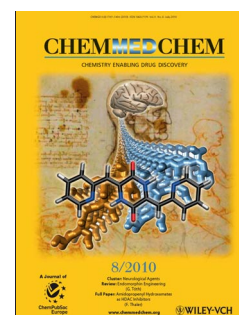
ChemMedChem
DOI: 10.1002/cmdc.201000185

Drug Discovery

F. M. Sabbatini,* R. Di Fabio,* M. Corsi, P. Cavanni, S. M. Bromidge, Y. St-Denis, L. D'Adamo, S. Contini, M. Rinaldi, S. Guery, C. Savoia, C. Mundi, B. Perini, A. J. Carpenter, G. Dal Forno, F. Faggioni, M. Tessari, F. Pavone, C. Di Francesco, A. Buson, M. Mattioli, E. Perdonà, S. Melotto

Discovery Process and Characterization of Novel Carbohydrazone Derivatives as Potent and Selective GHSR1a Antagonists

Ghrelin: don't feed them after dark! A novel class of highly potent and selective growth hormone secretagogue receptor 1a (GHSR1a) antagonists has been identified. The synthesis and preliminary biological investigation, both in vitro and in vivo is described. This compound series is a useful tool for further understanding the role of GHSR1a and may provide new approaches for the treatment of a number of pathological conditions associated with eating disorders.



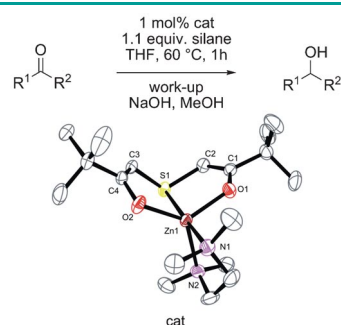
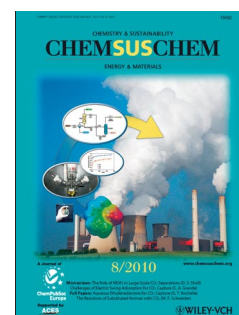
ChemSusChem
DOI: 10.1002/cssc.201000145

Organic Synthesis

S. Enthaler*

Ammonia: An Environmentally Friendly Nitrogen Source for Primary Aniline Synthesis

Got ammo? In the search for sustainable and environmentally benign primary aniline synthesis, the application of ammonia instead of currently applied ammonia surrogates is one major challenge in catalysis. Recent efforts in palladium- and copper-catalyzed transformations of ammonia to anilines are discussed in this Highlight.



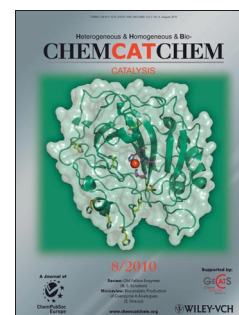
ChemCatChem
DOI: 10.1002/cctc.201000036

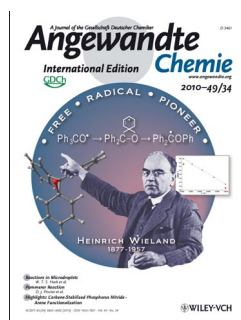
Homogeneous Catalysis

N. A. Marinós, S. Enthaler, M. Driess*

High Efficiency in Catalytic Hydrosilylation of Ketones with Zinc-Based Precatalysts Featuring Hard and Soft Tridentate O,S,O-Ligands

That zinc-ing feeling: A new type of hard and soft tridentate O,S,O-ligands in combination with auxiliary amines have been successfully employed in zinc-catalyzed hydrosilylation of various ketones. Good catalytic activity is obtained with low catalyst loading for several silanes. Variation of the amines indicates a potential catalytic mechanism.



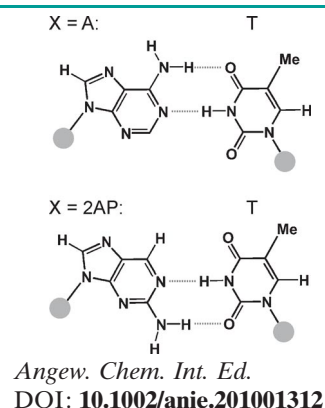


Nonnatural Nucleobases

A. Dallmann, L. Dehmel, T. Peters, C. Mügge, C. Griesinger, J. Tuma,* N. P. Ernsting*

2-Aminopurine Incorporation Perturbs the Dynamics and Structure of DNA

Vive la petite différence: 2-Aminopurine (2AP) induces small but detectable perturbations of the DNA helix. More significant are changes in the base-pair dynamics in the vicinity of 2AP. The differences have been characterized in NMR and UV spectroscopic studies on a 13-mer DNA double strand with either adenine (A) or 2AP in a central position.



Fullerene Chirality

A. Kraszewska, P. Rivera-Fuentes, G. Rapenne, J. Crassous, A. G. Petrovic, J. L. Alonso-Gómez, E. Huerta, F. Diederich, C. Thilgen*

Regioselectivity in Tether-Directed Remote Functionalization – The Addition of a Cyclotrimeratrylene-Based Trimalonate to C₆₀ Revisited

Triple Bingel addition of enantiomerically pure cyclotrimeratrylene-tethered trimalonates to C₆₀ was reinvestigated with regard to the regio- and diastereoselectivity. Electronic and vibrational circular dichroism studies showed that the addition proceeds regioselectively, yielding *trans*-3,*trans*-3,*trans*-3 tris-adducts, contrary to earlier reports.



New Journal

Heterogeneous, Homogeneous and BioCatalysis

www.chemcatchem.org

FREE ONLINE ACCESS

In 2010 for all users from institutions that have registered

Ask your librarian to register for complimentary online access TODAY

www.interscience.wiley.com/newjournals

Founding Societies:

A journal of

Bond Activation with Low-Valent Nickel in Homogeneous Systems

Alma Arévalo^[a] and Juventino J. García^{*[a]}

Keywords: Homogeneous catalysis / Nickel / Isomerization / Desulfurization / Hydration / Bond activation / Nitriles / Alkynes

The use of low-valent nickel complexes in homogeneous catalytic reactions of some industrially relevant trans-

formations that employ low reactive substrates are presented.

Introduction

The activation of unreactive bonds has been a topical issue for a number of years and still represents a challenge in organometallic chemistry and catalysis, particularly in research areas dealing with the functionalization of C–C, C–H, C–S, C–N, C–F, C–Cl and C–O bonds.^[1] The refractory, pseudo-halogen C–CN bonds are also considered among these. As an example, the C–CN bond in CH₃CN is stronger than the related C–F bond in CH₃F (122 vs. 108 kcal/mol).^[2] With the use of the right metal moiety however, the C–CN bond in several organic substrates can be cleaved and functionalized or isomerized effectively. Their activation is of major relevance in both industry and in laboratory scale, allowing the preparation of bulk chemicals, as well as fundamentally important organic and organometallic intermediates.

In industry, adiponitrile (AN) is synthesized by the catalytic double hydrocyanation of butadiene. As discussed below (vide infra) one of the key steps in the process consists on the isomerization of the branched 2-methyl-3-buten-

nitrile (2M3BN) to the linear 3-pentenitrile (3PN), a process that involves the cleavage and formation of a C–CN bond (Scheme 1). The AN is considered relevant for the industry being the precursor of 1,6-hexamethylenediamine, which is then used to obtain Nylon 6,6.^[3]

Despite the relevance of this reaction, there are still many mechanistic details to be determined and fully understood, several of which remain buried in patents. Inspired on these facts, our group has been involved in the study of the isomerization reaction of nitriles. The latter study has been undertaken concertedly with other related useful transformations that involve alkyl and aromatic nitriles, as is the case of their catalytic hydration. The coordination mode of nitriles to low-valent nickel has been an invaluable tool to understand their reactivity and this been exhaustively examined. Finally, additional studies by the group concerning the reactivity of the nickel moieties assisting the catalytic desulfurization of refractory organic substrates is also addressed in the current review in the context of related studies by other research groups.

1) Nitrile Isomerization

As mentioned above, the process for AN production involves the catalytic hydrocyanation of butadiene, a process

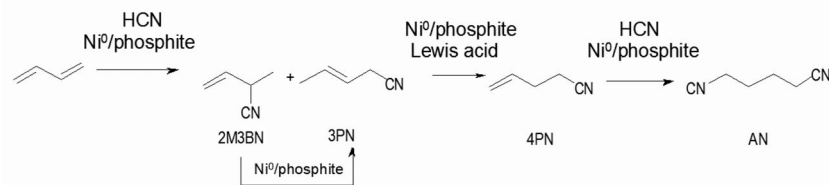
[a] Facultad de Química, Universidad Nacional Autónoma de México, México, D.F. 04510, México
E-mail: juvent@servidor.unam.mx



Alma Arévalo was born in Mexico City in 1962. She obtained her B.Sc. in chemistry at the National University of Mexico (UNAM). She received her Ph. D. under the supervision of Prof. Juventino J. García at UNAM in 2001 and is currently working as a Senior Technician in the Inorganic Chemistry Department at Facultad de Química (Chemistry Faculty), UNAM.



Juventino J. García was born in Mexico City in 1962. He undertook his Ph. D. studies at the National University of Mexico (UNAM) under the supervision of Prof. H. Torrens in 1991 and continued as a Postdoctoral Fellow at The University of Sheffield, U. K., wherein he worked under the supervision of Prof. Peter M. Maitlis from 1992 to 1993. He obtained a permanent position at Facultad de Química, UNAM in 1994. In 1999, he performed a Sabbatical Leave as a visiting Professor at the University of Rochester, USA, working at Prof. William D. Jones' lab. In 2000 he was appointed Full Professor at Facultad de Química, UNAM. His main research interests are in the field of homogeneous catalysis, nano catalysts and mechanistic inorganic chemistry.

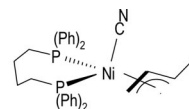


Scheme 1.

that makes use of low-valent nickel complexes and a triaryl phosphite as ancillary ligand. In it, the first HCN addition typically yields a mixture of 3PN and 2M3BN, the latter of which is an undesirable branched product. Isomerization *in situ* of 2M3BN to 3PN by the Ni⁰ catalyst yields the product cleanly. The mechanistic details of such transformation have been studied by different research groups. Sabo-Etienne and coworkers proposed a catalytic cycle for the isomerization of 2M3BN to 3PN based on DFT calculations (Scheme 2).^[4]

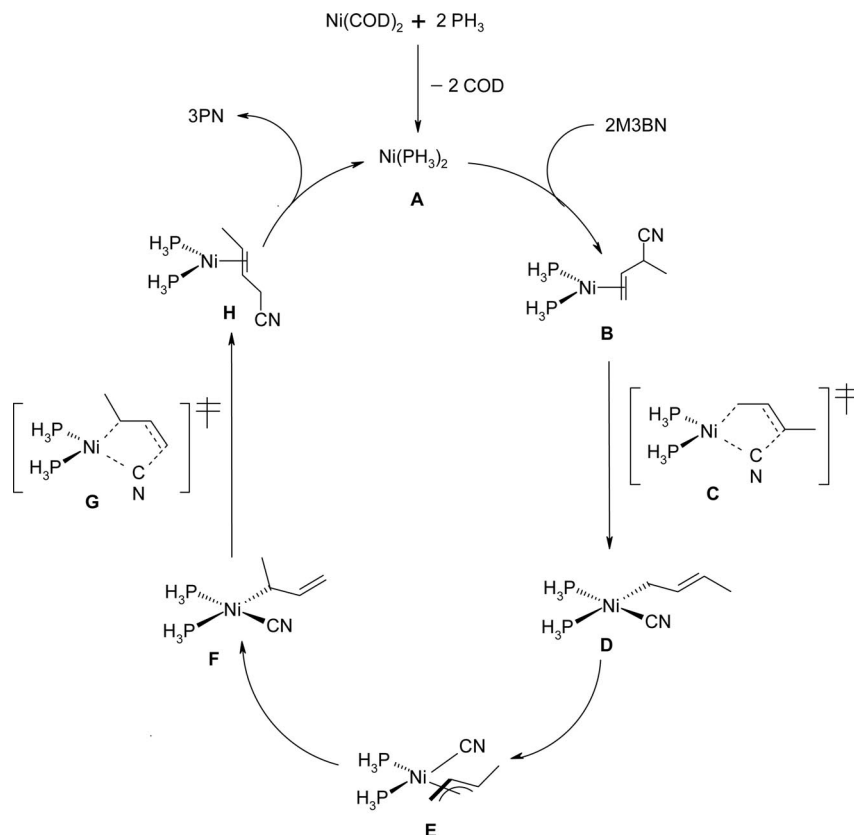
The same report includes experimental results where the isomerization reaction took place in 100% conversion after 3 h, at 100 °C when using [Ni(COD)₂] as catalyst precursor and triphenylphosphane as ancillary ligand. 3PN was obtained in 81% yield. The allyl complex, [Ni(PPh₃)₂(η³-1-MeC₃H₄)(CN)], analogous to E in Scheme 2 was detected in solution in the actual experiment. A derivative of such compound bearing the diphosphane, dppb, was expressly

prepared thus allowing to fully confirm the C–CN bond cleavage by nickel, using single-crystal X-ray crystallography.

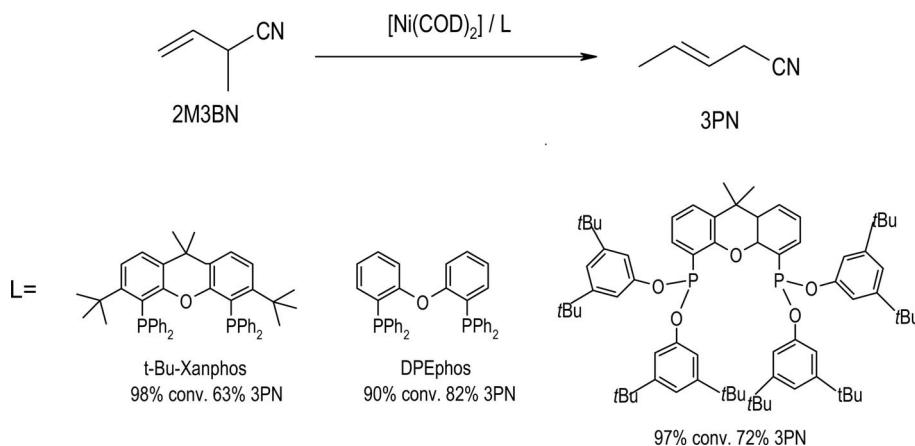


Vogt's group has also made relevant contributions in this field using low-valent nickel compounds with diphosphanes or diphosponites,^[5,6] which result in high conversions above 90% and selectivities in the range of 63–82% to the linear 3PN (Scheme 3).

The use of DPEphos, 2-(diphenylphosphanyl)phenyl ether, and ZnCl₂ allowed to crystallize and fully characterize the complex [Ni(DPEphos)(η³-1-MeC₃H₄)(CN–ZnCl₂)], which is similar to the complex depicted above. In this case, the Lewis acid moiety appears coordinated to the terminal



Scheme 2.



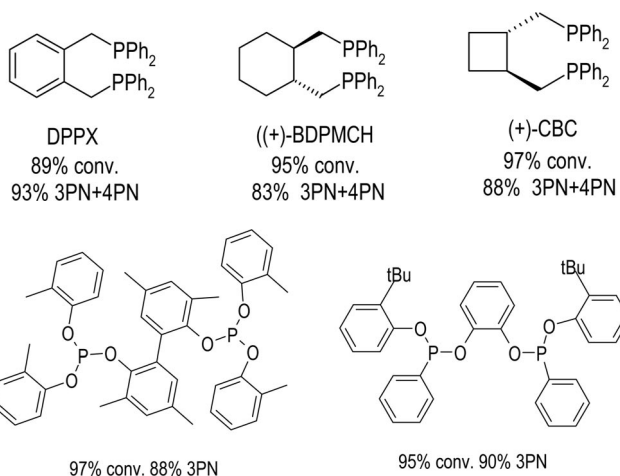
Scheme 3.

CN ligand. Kinetic determinations allowed this group to propose that the isomerization reaction (branched to linear) is zero order in substrate, contrary to the observations by Santini et al.,^[7] while studying the reaction in a variety of ionic liquids and in the presence of various low-valent nickel-phosphanyl compounds. The group also reported the isomerization process to be first order in substrate, thereof suggesting an associative mechanism for the reductive elimination.

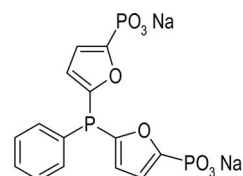
Recently Vogt et al. documented the use of Ni^0 catalysts in the selective hydrocyanation of butadiene toward pentenenitrile using a triptycene-based diphosphane ligand which resulted in extremely high selectivities to 3PN (up to 98%).^[8] In the absence of HCN the same system allowed the isomerization of 2M3BN to 3PN with both high conversions and selectivities (Scheme 4). A recent review devoted to mechanistic studies on hydrocyanation reactions has been recently published by the same group.^[9]

There are several patents where the use of $[\text{Ni}(\text{COD})_2]$ and phosphorus-based ligands have been reported for the same isomerization reaction. Chamard et al. patented the use of bis(diarylphosphanes) with yields over 80% of 3PN and 4PN.^[10] Some of the phosphanes used in this study are depicted below.

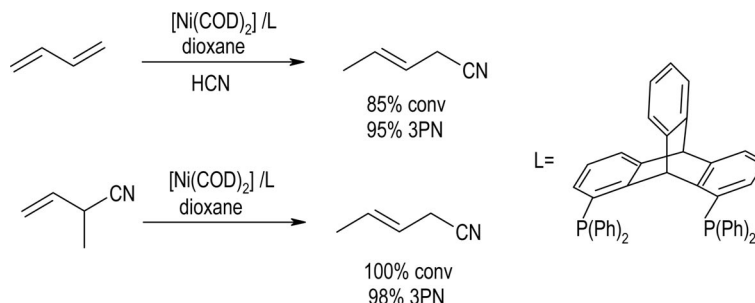
Also, the use of bis(triaryl phosphites)^[11] and bis(diaryl arylphosphonites)^[12] in the production of 3PN from 2M3PN has been patented by Bartsch and coworkers.



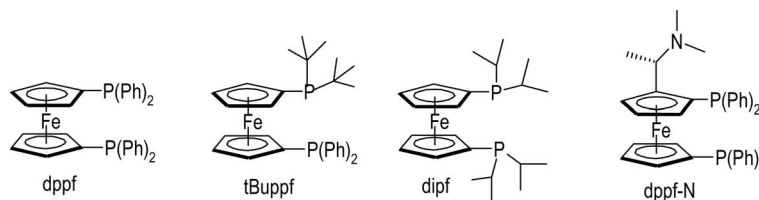
A water soluble version of this reaction has been registered by Mathey and collaborators, which also gives 3PN in good yields.^[13]



The C–CN activation in closely related cyano olefins of shorter chain length such as allyl cyanide has been reported



Scheme 4.

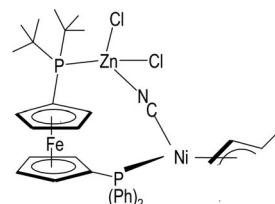


by Jones et al.,^[14,15] using the nickel(I) dimer $[\text{Ni}(\text{dippe})(\mu\text{-H})_2]$ (dippe = 1,2-bis(diisopropylphosphanyl)ethane). The products of C–H and C–CN activation were observed during such studies, summarized in Scheme 5, the latter studies demonstrated that the C–CN activation step is thermodynamically less favorable than the C–H activation, but becomes rate competitive when the temperature is increased.

The C–CN bond cleavage/formation involved in the isomerization of 2M3BN to 3PN has also been studied by our group, using Ni^0 complexes or Ni^{I} catalyst precursors and a variety of ligands. We first reported the catalytic isomerization of 2M3BN using $[\text{Ni}(\text{COD})_2]$ and 1,2-bis(diphenylphosphanyl)ferrocene (dppf)^[16] in the absence and presence of Lewis acids. Detailed VT-NMR studies revealed the intermediacy of Ni^{II} allyl complexes and the use of Lewis acids (Scheme 6), particularly BEt_3 , allowed the crystallization and complete characterization of $[\text{Ni}(\text{dppf})(\eta^3\text{-1Me-C}_3\text{H}_4)(\text{CN-BEt}_3)]$. The best results for the isomerization reaction were however obtained in the absence of Lewis acids and up to 100% conversion, with a selectivity of 83% to 3PN.

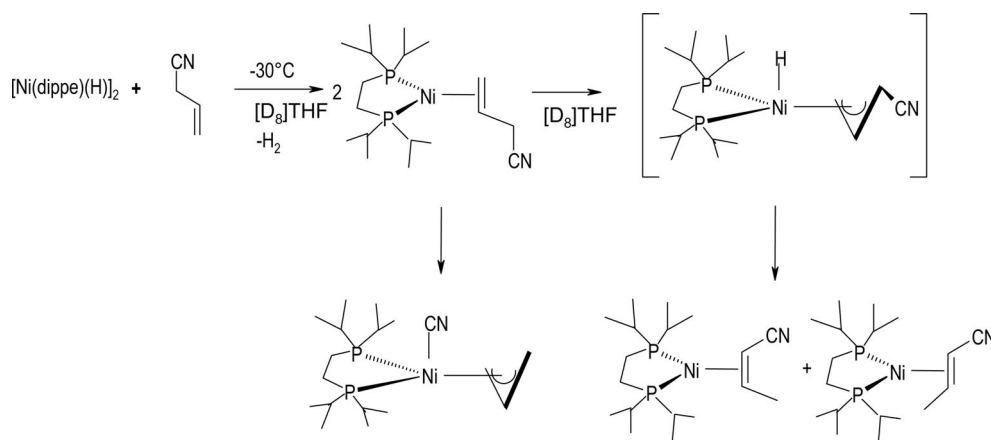
The use of other bis(diphenylphosphanyl)ferrocene ligands also gave very good conversions and selectivities to

3PN.^[17] Noteworthy, the combined use of *t*Buppf and ZnCl_2 allowed the crystallization of a novel hemilabile intermediate, likely involved in the isomerization reaction leading to 3PN.

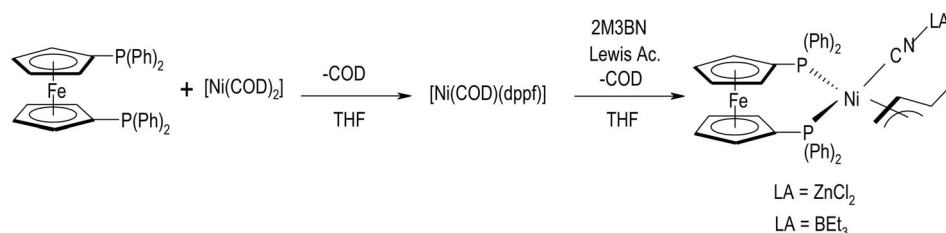


We then extended that study to the use of $[\text{Ni}(\text{COD})_2]$ and a variety of N-heterocyclic carbene (NHC) ligands for the same isomerization reaction.^[18]

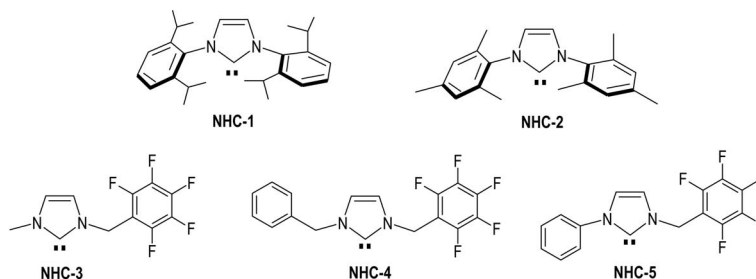
The use of the bulky *N*-aryl NHC ligands, **NHC-1** and **NHC-2**, generally afforded very active catalytic systems which led to the formation of the branched isomers of 2M3BN and with almost zero selectivity toward linear 3PN. Their formation stems from the competing C–H bond activation process. The fluorinated ligands (**NHC-3** to **NHC-5**) yielded very unstable Ni^0 species that ultimately resulted in rapid decomposition.



Scheme 5.



Scheme 6.



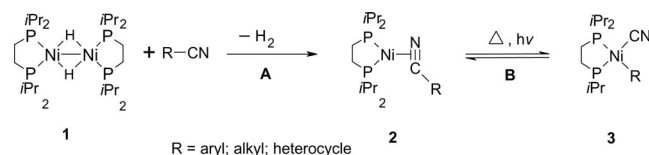
On using other P-donor polydentate ligands we explored the reactivity of Ni^0 complexes with triphos, bis[2-(diphenylphosphanyl)ethyl](phenyl)phosphane, for the isomerization of 2M3BN.^[19] The C–H bond activation was also favored for this system, mainly to yield the branched isomers *E*- and *Z*-2M2BN. To our surprise, a C–P bond cleavage reaction took place over the triphos ligand under relatively mild conditions. The latter activation results in formation of a very stable Ni^{II} complex that halts all catalytic activity.

The isomerization reaction of 2M3BN using the nickel(I) dimer $[\text{Ni}(\text{dippe})(\mu\text{-H})]_2$ was studied using different solvents.^[20] On increasing the solvent polarity, the ratio of C–H activated branched products to C–CN activated linear products increased. The latter was attributed to a better solvation of the C–H activation transition state.

Similar experimental methodologies employing Ni^0 , allyl cyanides and alkynes have been applied to the production of antibacterial natural products^[21] via carbocyanation reactions,^[22] which have recently been reviewed.^[23] Additional examples consist on the cyanoesterification of 1,2-dienes^[24] and the asymmetric arylocyanation of unactivated olefins via C–CN bond activation.^[25]

2) Nitrile Functionalization

Due to the fact that nitriles are useful building blocks for a wide number of organic derivatives,^[26] we decided to explore the reactivity of a variety of nitriles in the presence of Ni^{I} complexes, aiming to produce Ni^0 intermediates that could be useful for the functionalization of such substrates. A general reaction that summarizes this reactivity is depicted in Scheme 7.



Scheme 7.

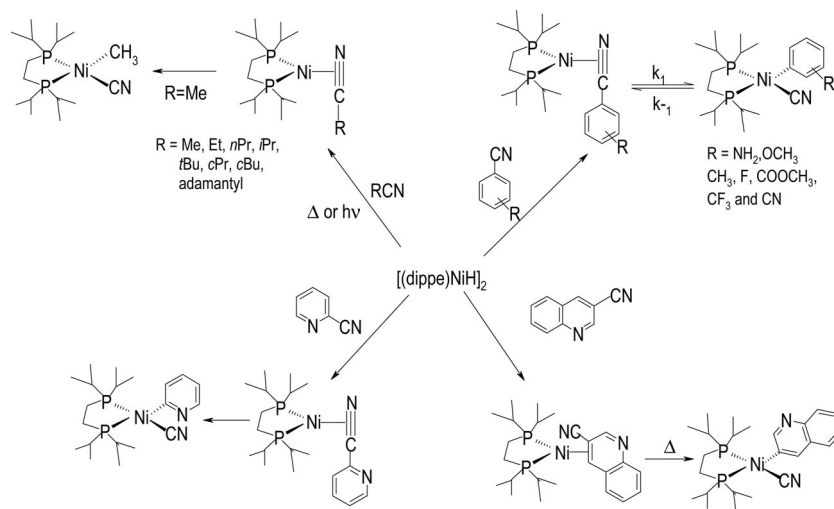
Step A was confirmed to proceed for all nitriles used, i.e., the reductive elimination of H_2 and the formation of Ni^0 complexes was always observed. Following this one, the re-

activity leading to the nitrile oxidative addition, step B, was thermally or photochemically induced for aryl-, heterocyclic and small alkyl-substituted nitriles.

Indeed, our first discovery in this field was the reaction of complex 1 with benzonitrile to yield the Ni^0 complex $[\text{Ni}(\text{dippe})(\eta^2\text{-NCPh})]$ (2), then followed by the oxidative addition product $[\text{Ni}(\text{dippe})(\text{CN})(\text{Ph})]$ (3).^[27] Both were isolated and characterized by single-crystal X-ray diffraction. Worthy to note is that a key difference of this system with other closely related, was the reversibility showed by the oxidative addition process,^[28] which permits to generate complex 2 when starting from complex 3.^[29] Kinetic studies performed for the oxidative addition reaction further allowed to corroborate the polar character of the Ni–C bond. We extended the scope of this reaction to other substituted aromatic nitriles, aromatic dinitriles and to nitrile substituted aromatic heterocycles.^[30] The η^2 -coordination of alkyl nitriles to the low-valent nickel center was also demonstrated (see Scheme 8).^[31] The oxidative addition of the C–CN bond was dependent on chain length and ramification of the alkyl substituent of the alkyl nitrile and was found to proceed irreversibly either under thermal or photochemical conditions. For larger nitriles such as adamantyl-substituted nitrile, the oxidative addition was completely inhibited. Interestingly, the use of Lewis acids also inhibited the C–CN bond activation, probably due to stabilization of the nickel(0) intermediates.

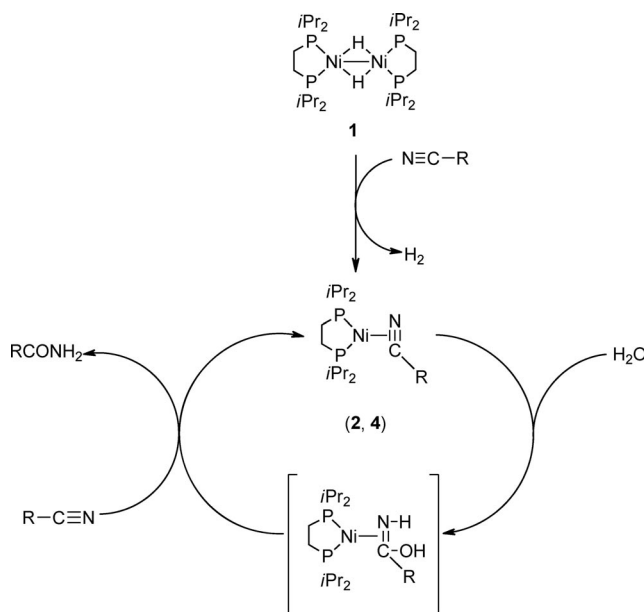
DFT calculations on the cleavage of either the C–H bond or the C–CN bonds in acetonitrile allowed to corroborate that the C–CN bond activation route is both kinetically and thermodynamically more favorable in the presence of nickel(0).^[32] The calculated activation route predicts formation of a weakly bound η^3 -nitrile intermediate that involves the vicinal carbon atoms of the C–CN moiety, following the initial η^2 -coordination step. Similarly, recent experimental and theoretical evidences for the C–CN bond activation of benzonitrile^[33] and other aromatic nitriles^[34] point out to a slip of the η^2 -coordinated CN bond to an adjacent double bond of the aryl substituent, which results in formation of an η^2 -arene intermediate. Migration of the nickel(0) moiety around the ring constitute a series of crucial steps that precede cleavage of the C–CN. Closely related reactions that make use of the NHC carbene nickel complexes have been reported by Radius and coworkers.^[35]

Inspired in the formation of η^2 -nitrile compounds of nickel(0) we decided to explore the reactivity of these com-



Scheme 8.

plexes in reactions of synthetic interest both in the laboratory scale and in industry, starting with the catalytic hydration of benzonitrile and acetonitrile.^[36] The use of complexes of the type $[(\text{diphosphane})\text{Ni}(\eta^2\text{-NC-R})]$ (R = phenyl or methyl; diphosphane = dippe, dtbpe, dcype) as catalysts for the latter reactions, permitted the preparation of benzamide or acetamide in good yields. A mechanistic proposal for this process includes a N,N -dihydro- C -oxo-biaddition step, see Scheme 9.



Scheme 9.

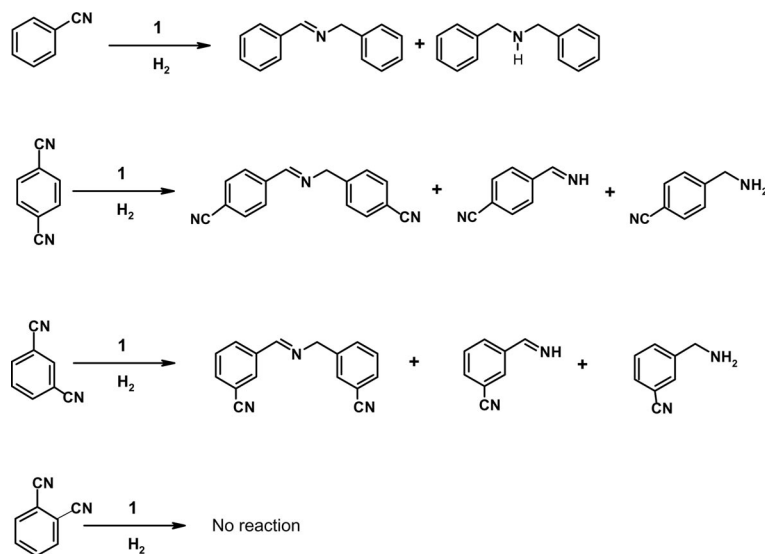
This nitrile hydration methodology developed for the benzonitrile and acetonitrile was further extended to closely related substrates. In the case of aryl-substituted nitriles, the former was also established for 1,2-, 1,3- and 1,4-dicyanobenzenes. Formation of the 1,3- and 1,4-cyanobenzamides was demonstrated at 120 °C. Heating to more a ele-

vated temperature (180 °C) resulted in quantitative production of the corresponding 1,3- and 1,4-dicarboxylic acids and free ammonia. In the case of 1,2-dicyanobenzene, only 1,2-phthalimide was obtained at either temperature limit.^[37]

The catalytic hydration methodology was further optimized for alkyl-nitriles and dinitriles of variable chain length making use of *p*-toluenesulfonic acid (PTSA) as co-catalyst of the hydration reaction, in addition to nickel(0). Additional proofs for the relevance of the latter oxidation state for catalysis were provided by comparing its reactivity with those of related nickel(II) catalyst precursors. The corresponding diamides were obtained selectively, yet strongly dependent on the length of the internal carbon chain of the starting dinitrile. The best catalytic results were obtained on using nickel(0) compared with the use of Ni^{II} precursors.^[38]

According to the lower part of Scheme 8, N -heterocycles containing nitrile substituents produced the corresponding η^2 -nitrile compounds of Ni^0 . We successfully applied the catalytic hydration methodology to the formation of 2- and 3-quinolinecarboxamides derived from the corresponding 2- and 3-cyanoquinolines.^[39] Similar results were also demonstrated for the 2-, 3-, 4-cyanopyridines and the 2,6-cyanopyridine. From these, selective entries to the mixed cyano/amide in addition to the corresponding dicarboxamide, which are derived from the 2,6-dicyanopyridine were established.^[40]

The hydrogenation of η^2 -coordinated nitriles to nickel(0) was also studied as a relevant proof of their functionalization, catalyzed by this metal. Benzonitrile was completely hydrogenated in THF solution under relative mild conditions, resulting in formation of benzyl-benzylimine in 97% yield. The hydrogenation of the related dicyanobenzenes required more forceful conditions in order to yield the corresponding imines, as was the case of the 1,4- and 1,3-dicyanobenzenes. Surprisingly, the 1,2-dicyanobenzene did not elicit any reactivity at all under similar conditions (Scheme 10).^[41]

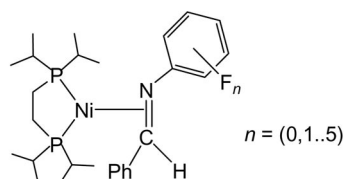


Scheme 10.

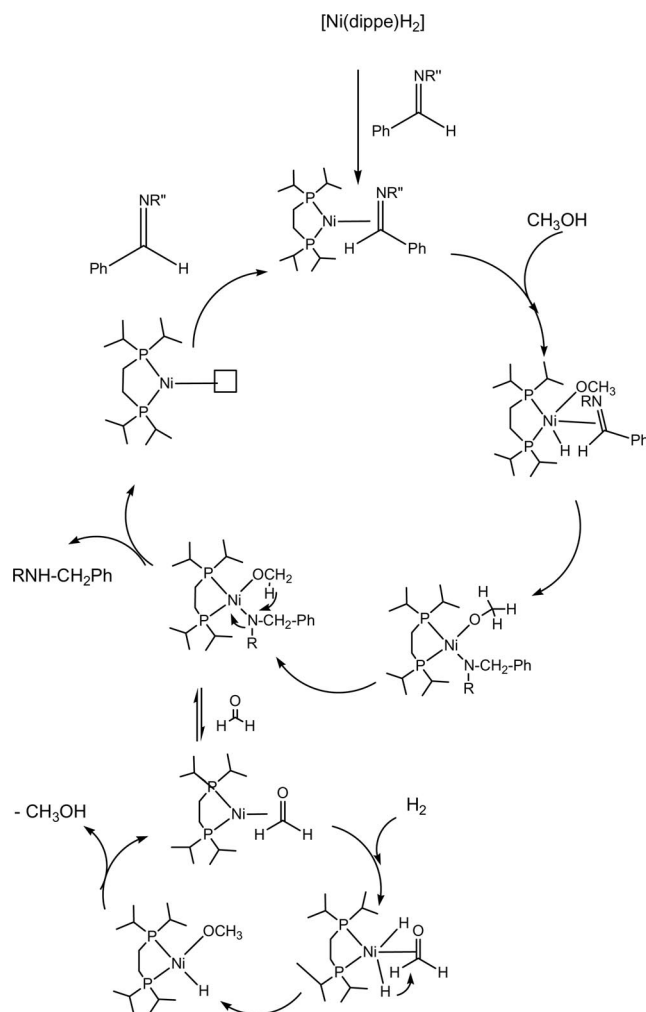
3) Hydrogenation and Activation of Related Multiple Bonds

The hydrogenation of imines to produce amines was undertaken inspired on the success of the hydration and hydrogenation methodologies developed for mono- and dinitriles, discussed above. Since amines are important building blocks in the pharmaceuticals and fine chemicals industry^[42] the demonstration of novel, efficient, atom-efficient synthetic routes continues to be of widespread interest. As a first approach we focused on the preparation of fluorinated amines, due to the distinctive advantage that the fluoro groups offer for the follow-up of the reactions, in addition to the characterization of the products themselves. Incidentally, the preparation of pure fluoro-substituted arylamines finds added value in pharmacology, due to their potential use in novel therapies.^[43]

We initially explored the coordination of fluoro imines to nickel, to yield the expected nickel(0) complexes of the type, $[(\text{dippe})\text{Ni}\{\eta^2-(N,C)\text{-PhHC=NR}^n\}]$, wherein Ar^n refers to the increasing degree of fluorination exhibited by the *N*-aryl moiety ($n = 0, 1, 2, 3, 4, 5$), see below.^[44]



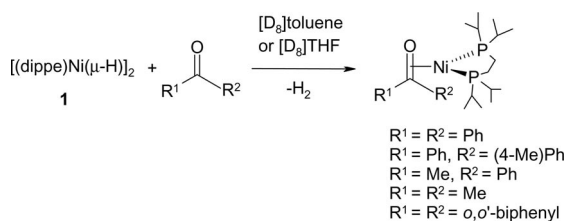
The use of such compounds in catalysis, under low hydrogen pressure and in the presence of excess fluorinated imines resulted in high conversions of the latter into their corresponding amines. The compounds were prepared from **1** in situ, and required very small thermal energy input to drive the catalysis. The best yields were obtained on using a coupled hydrogen transfer system in methanol in addition



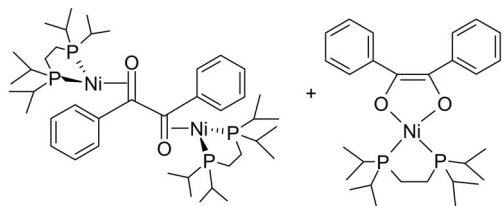
Scheme 11.

to the use of H_2 pressure, which enabled methanol regeneration (Scheme 11).^[45]

Indicated in Scheme 11, the reduction of formaldehyde occurs under the reaction conditions wherein the κ^2 -coordination of the carbonyl to nickel(0) mimics the η^2 -coordination of the imine. Interested by the generality by which π -systems react with the low-valent nickel, we also examined the coordination of carbonyl moieties to nickel(0) and their reduction using a series of ketones and 1,2-diketones. That the partial and total reductions of carbonyl groups are relevant transformations for the preparation of alcohols or alkanes, further add value to the study. It's worthy noting that the use of nickel in this type of reductions is relatively scarce.^[46] As found, a variety of ketones react spontaneously in the presence of **1**, forming the corresponding nickel(0) complexes with a η^2 -coordinated C=O bond (Scheme 12). The results coincide with the structural feature indicated in Scheme 11 for the coordination of formaldehyde.^[47] When benzyl was used as the starting material the double η^2 -coordination of the carbonyl moieties to two independent nickel(0) centers was observed. In addition to this, a κ^2 -O-coordinated oxidative addition product was formed. Both complex were fully characterized in solution and in the solid state, by single-crystal X-ray diffraction.

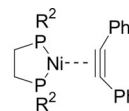


Scheme 12.

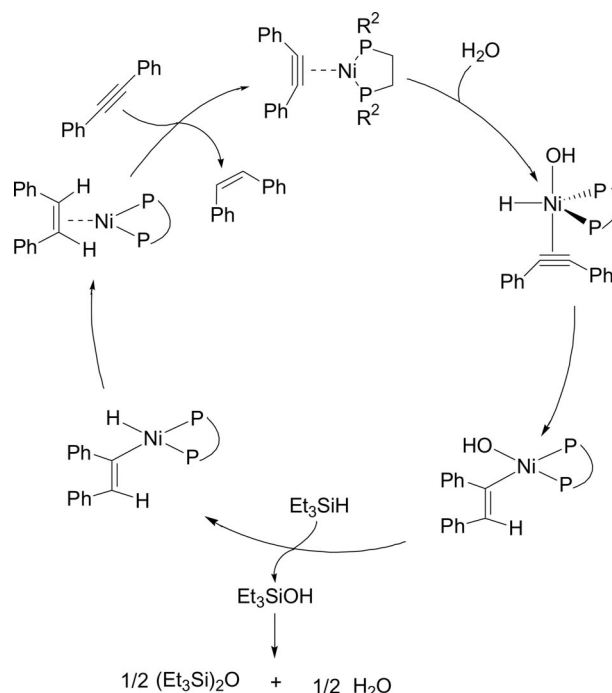


Reactivity studies performed over these complexes towards H_2 reduction revealed the ketones could be converted selectively to the corresponding alcohols or even more strikingly, to the related alkanes. For diketones like benzyl, a β -H elimination process was found to play an important role competing with the hydrogenation route, thereby rendering the benzyl hydrogenation a product-inhibited process.

In the aim of extending the applicability of the reduction methodologies described above for η^2 -coordinated π -systems, we then turned to the use of CC multiple bonds as targets for such reactions. We envisioned the use of alkynes to behave similarly to nitriles (vide supra) and indeed, the analogous nickel(0) compounds with formula $[(P-P)Ni(\eta^2-C,C\text{-alkyne})]$ ($P-P$ = dippe, dtbpe) were prepared from the parent dimeric nickel(I) compounds, $[(P-P)Ni(\mu-H)]_2$.^[48]



We explored the reactivity of the former compounds in the presence of a) water, b) triethylsilane/water and c) methanol, as hydrogen sources. The results showed that the selective production of the corresponding *cis*- or *trans*-alkene from the corresponding alkyne is feasible under such conditions, in high yields. On using water, a metal-mediated process was found. In the case of the mixture of triethylsilane/water or when using methanol only, the reduction of the alkyne occurred catalytically (see Scheme 13).^[49]



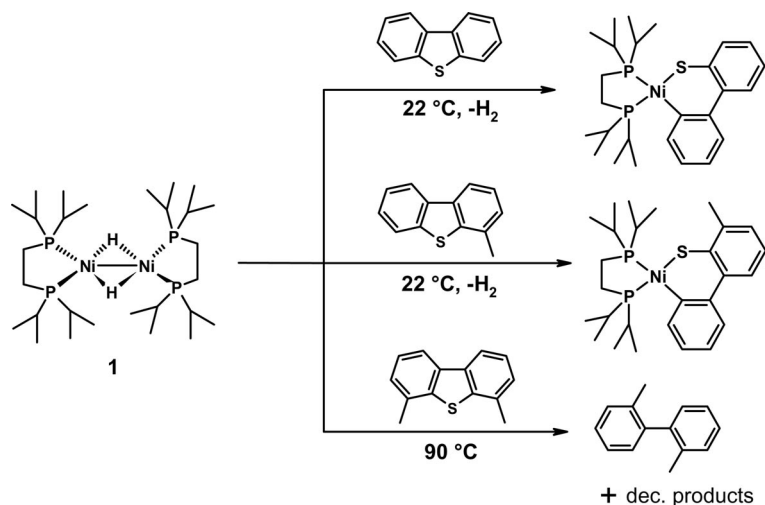
Scheme 13.

4) Use of Low-Valent Nickel Compounds in Desulfurization Reactions

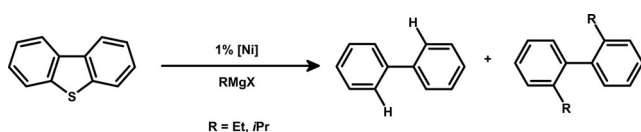
Following the interest of our group on the modeling of hydroprocessing reactions such as the hydrodesulfurization (HDS) reaction, we recently addressed the use of Ni^0 , Ni^I and Ni^{II} complexes as catalyst precursors for reactions leading to the desulfurization of dibenzothiophenes (DBTs), methyl dibenzothiophenes (MeDBTs) and of their derivatized sulfones, via cross-coupling reactions.

Initially, the reactivity of $[(dippe)Ni(\mu-H)]_2$ in the presence of dibenzothiophenes was explored by Vicic and Jones,^[50] who at the time were able to isolate thia-nickelacycles resulting from the C–S bond cleavage of dibenzothiophene and 4-methyldibenzothiophene. In all cases, the latter complexes led to desulfurization products under stoichiometric conditions albeit in low yield (Scheme 14).

Inspired in these results and considering the use of Ni^0 catalysts and Grignard reagents for the production of chiral 1,1'-binaphthyls driven by the asymmetric cross-coupling of

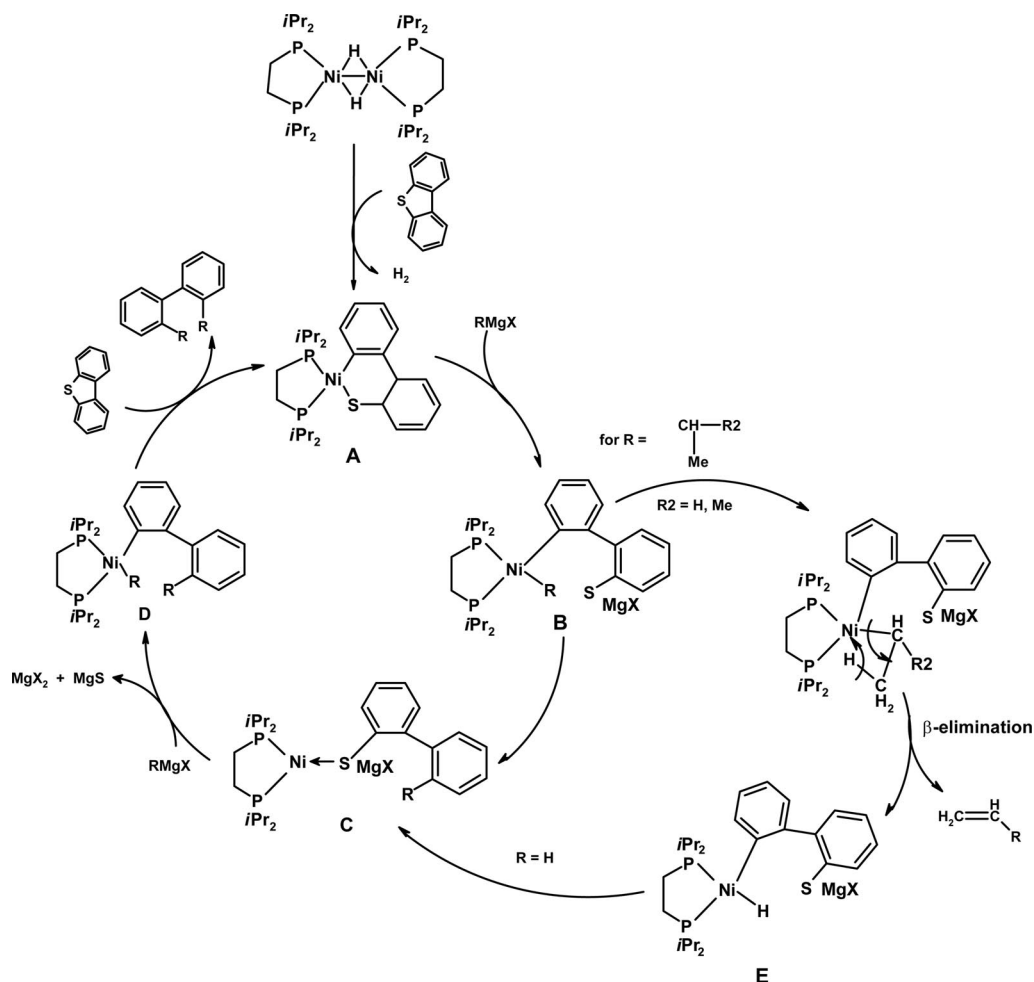


Scheme 14.



Scheme 15.

dinaphtho[2,1-*b*:1',2'-*d*]thiophene and in 1,9-disubstituted DBTs reported by Hayashi and coworkers,^[51] we investigated the reactivity of **1** and of [Ni(PEt₃)₄] in the presence of DBTs and Grignards. In all cases the reactions yielded substituted biphenyls via homogeneous catalytic desulfurization (Scheme 15).^[52] The desulfurization yields for DBT



Scheme 16.

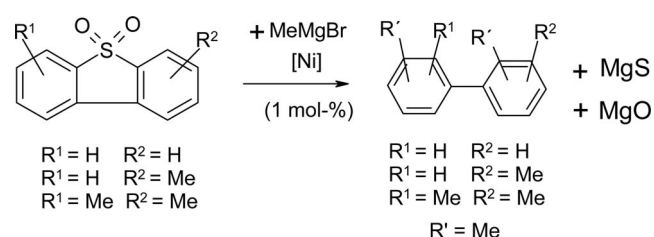
and 4-MeDBT were in most of the cases very high, up to 100% in toluene. Noteworthy, when alkyl Grignards with hydrogen in the β -position were used, formation of biphenyl was favored over the C–C cross-coupling that yields the di-alkyl-biphenyl.

In the case of 4,6-Me₂DBT, the catalytic turnover of the process was in general low, being the most encumbered system of the three addressed. The latter is explained on the basis of the large steric hindrance that the substrate, the Grignard reagent and the ancillary ligand oppose to each other. A proof of this conclusion, the best desulfurization result was obtained using [Ni(PEt₃)₄] as catalyst precursor instead of the diphosphane–nickel systems, additionally using MeMgBr in toluene. For all the desulfurization experiments performed, the formation of MgS yields the driving force of reaction. The isolation and characterization of the latter sulfide was ensured during the study, confirmed to be formed in every experiment. A comprehensive mechanistic proposal that illustrates the C–C cross coupling reaction along with and the β -elimination of hydrogen that leads to the formation of biphenyl, using low-valent nickel is included in Scheme 16.^[53]

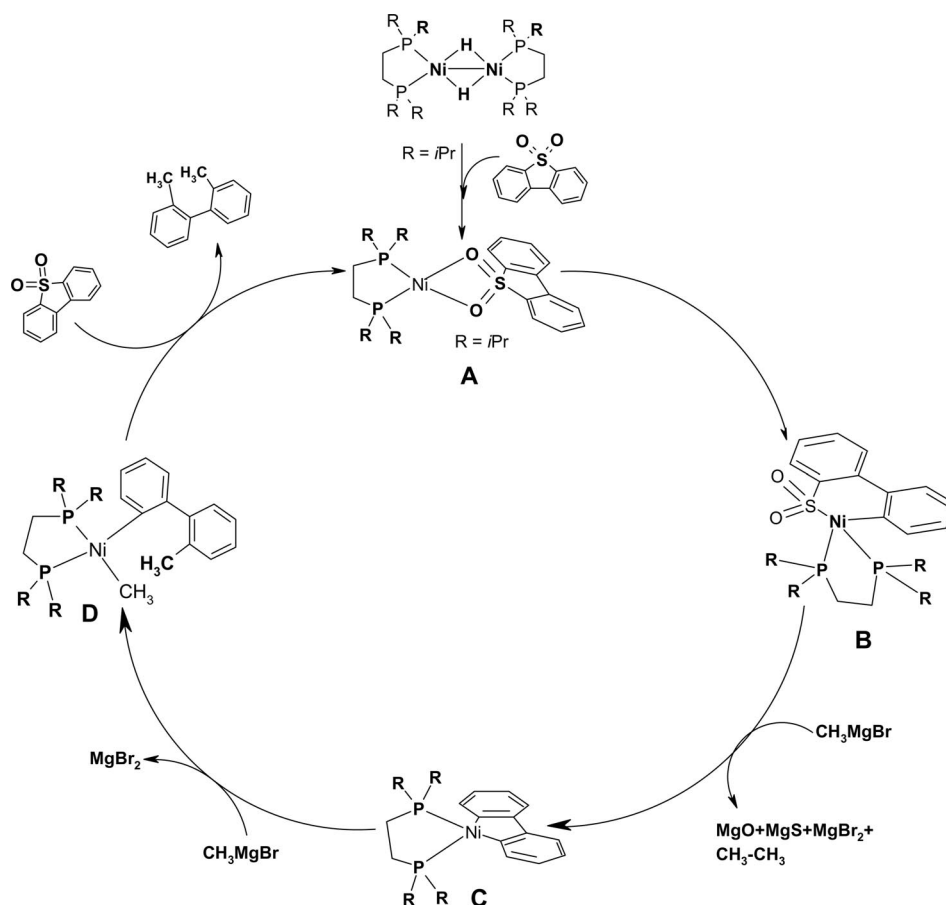
From the intermediates proposed in the two cycles, the thia-nickela-cycle **A** and others were recently prepared independently, isolated and characterized. Furthermore, the participation of the thiolate-dinuclear complexes (species **B**,

C and **E**) as true intermediates was unequivocally established. As encountered, the simultaneous formation of all of these species takes place in solution, prior to the final desulfurization step and thus suggesting bimetallic assistance of metal centers during HDS.^[54]

Closely related to the previous systems, the desulfurization reaction of the DBT-sulfones using low-valent nickel is currently being undertaken by our group, the oxidation of DBTs to their respective sulfones being a method employed by the industry to facilitate their separation from the main petroleum feedstock. As a result of the above, to this date we have only partially disclosed our findings on this chemistry, having found that the sulfones can also be desulfurized via C–C cross coupling reactions which produce sulfur-free biphenyls. The reactions are also run using Grignard re-

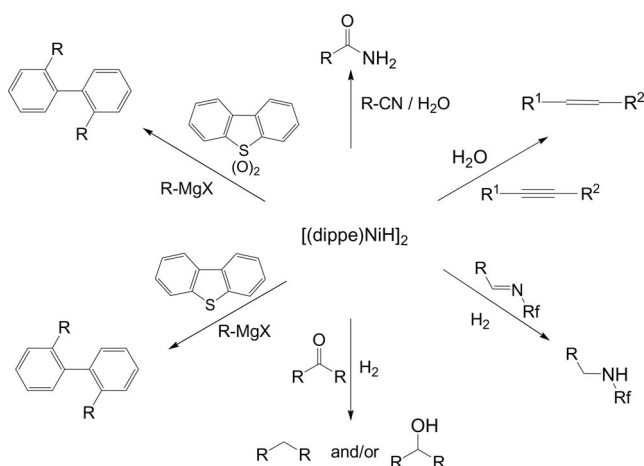


Scheme 17.



Scheme 18.

Scheme 19 summarizes the findings outlined in the current review, on the use of Ni(I) and Ni(0) complexes as active species for catalysis. Their use allows entry to novel and convenient methodologies for the preparation of a wide variety of organic compounds, relevant for both industry and academia.



Conclusions

Acknowledgments

the funding Mexican agencies Consejo Nacional de Ciencia y Tecnología (CONACyT) and Dirección General de Apoyo al Personal Académico – Universidad Nacional Autónoma de México (DGAPA-UNAM) for their financial support.

- [1] S. Murai, *Topics in Organometallic Chemistry: Activation of Unreactive Bonds and Organic Synthesis*, Springer-Verlag, **1999**, Berlin, Germany, pp. 1–5.
- [2] A. J. Gordon, R. A. Ford, *The Chemist's Companion. A handbook of Practical Data, Techniques and References*, John Wiley & Sons, **1972**, USA, pp. 113.
- [3] P. W. N. M. Van Leeuwen, *Homogeneous Catalysis*, Academic Publisher, London, **2004**, pp. 229–233.
- [4] A. Chaumonnot, F. Lamy, S. Sabo-Etienne, B. Donnadieu, B. Chaudret, J. C. Barthelat, J. C. Galland, *Organometallics* **2004**, *23*, 3363.
- [5] J. I. Van der Vlugt, A. C. Hewat, S. Neto, R. Sablong, A. M. Mills, M. Lutz, A. L. Spek, C. Müller, D. Vogt, *Adv. Synth. Catal.* **2004**, *346*, 993.
- [6] J. Wilting, C. Müller, A. C. Hewat, D. D. Ellis, D. M. Tooke, A. L. Spek, D. Vogt, *Organometallics* **2005**, *24*, 13.
- [7] C. Vallé, C. Valério, Y. Chauvin, G. P. Niccolai, J. M. Basset, C. C. Sautini, J. C. Galland, B. Didillon, *J. Mol. Catal. A* **2004**, *214*, 71.
- [8] L. Bini, C. Müller, J. Wilting, L. von Chzanowski, A. L. Spek, D. Vogt, *J. Am. Chem. Soc.* **2007**, *129*, 12662.
- [9] L. Bini, C. Müller, D. Vogt, *Chem. Cat. Chem.* DOI: 10.1002/cctc.201000034.
- [10] A. Chamard, J. C. Galland, B. Didillon, *Method for transforming ethylenically unsaturated compounds into nitriles and branched nitriles into linear nitriles*, PAT. WO 03/031392, France, **2002**.
- [11] M. Bartsch, R. Bauman, D. P. Kunsmann-Keietel, G. Haderlein, T. Junkamp, M. Altmayer, W. Seigel, *Catalysis system containing Ni^0 for hydrocyanation*, US/2004 0176622, USA, **2004**.
- [12] M. Bartsch, D. P. Kunsmann-Keietel, R. Bauman, G. Haderlein, W. Seigel, *Zur Herstellung von Nitrilen. Geeigneter Katalysator und Verfahren zur Herstellung von Nitrilen*, 10038037, **2002**.
- [13] F. Mathey, P. Savignac, F. Ymery, P. Burattin, *Nouvelles furylphosphines et complexes organometalliques les comprenant*, PAT W9960003, France, **1999**.
- [14] N. M. Brunkan, D. M. Brestensky, W. D. Jones, *J. Am. Chem. Soc.* **2004**, *126*, 3627.
- [15] N. M. Brunkan, W. D. Jones, *J. Organomet. Chem.* **2003**, *683*, 77.
- [16] A. Acosta-Ramírez, M. Muñoz-Hernández, W. D. Jones, J. J. García, *J. Organomet. Chem.* **2006**, *691*, 3895.
- [17] A. Acosta-Ramírez, M. Muñoz-Hernández, W. D. Jones, J. J. García, *Organometallics* **2007**, *26*, 5766.
- [18] A. Acosta-Ramírez, D. Morales-Morales, J. M. Serrano-Becerra, A. Arevalo, W. D. Jones, J. J. García, *J. Mol. Catal. A* **2008**, *288*, 14.
- [19] A. Acosta-Ramírez, M. Flores-Alamo, W. D. Jones, J. J. García, *Organometallics* **2008**, *27*, 1834.
- [20] B. D. Swartz, N. M. Reinartz, W. W. Brenessel, J. J. Garcia, W. D. Jones, *J. Am. Chem. Soc.* **2008**, *130*, 8548.
- [21] Y. Hirata, T. Yukawa, N. Kashiwara, Y. Nakao, T. Hiyama, *J. Am. Chem. Soc.* **2009**, *131*, 10964.
- [22] a) Y. Hirata, M. Tanaka, A. Yada, Y. Nakao, T. Hiyama, *Tetrahedron* **2009**, *65*, 5037; b) Y. Nakao, S. Ebata, A. Yada, T. Hiyama, M. Ikawa, S. Ogoshi, *J. Am. Chem. Soc.* **2008**, *130*, 12874.
- [23] a) Y. Nakao, T. Hiyama, *Pure Appl. Chem.* **2008**, *80*, 1097; b) M. Tobisu, N. Chatani, *Chem. Soc. Rev.* **2008**, *37*, 300.
- [24] Y. Hirata, T. Inui, Y. Nakao, T. Hiyama, *J. Am. Chem. Soc.* **2009**, *131*, 6624.
- [25] M. P. Watson, E. N. Jacobsen, *J. Am. Chem. Soc.* **2008**, *130*, 12594.

- [26] P. Pollak, G. Romeder, F. Hagedorn, H. Gelbke, in: *Ullman's Encyclopedia of Industrial Chemistry*, vol. A17, 5th ed., Wiley-VCH, Weinheim, **1985**, p. 363.
- [27] J. J. García, W. D. Jones, *Organometallics* **2000**, *19*, 5544.
- [28] a) M. Abba, T. Yamamoto, *J. Organomet. Chem.* **1997**, *532*, 267; b) G. Favero, A. Morvillo, A. Turco, *J. Organomet. Chem.* **1983**, *241*, 251; c) A. Morvillo, A. Turco, *J. Organomet. Chem.* **1981**, *208*, 103; d) G. W. Parshall, *J. Am. Chem. Soc.* **1974**, *96*, 2360; e) D. Churchill, J. H. Shin, T. Hascall, J. M. Hahn, B. M. Bridgewater, G. Parkin, *Organometallics* **1999**, *18*, 2403; f) D. H. Gerlach, A. R. Kane, G. W. Parshall, J. P. Jesson, E. L. Muetterties, *J. Am. Chem. Soc.* **1971**, *93*, 3543; g) J. L. Burmeister, L. M. Edwards, *J. Chem. Soc. A* **1971**, 1663.
- [29] For closely related formation of C–CN bonds, see: a) G. Favero, M. Gaddi, A. Morvillo, A. Turco, *J. Organomet. Chem.* **1978**, *149*, 395; b) L. Cassar, *J. Organomet. Chem.* **1973**, *54*, C57; c) Y. Tsuji, T. Kusui, T. Kojima, Y. Sugiura, N. Yamada, S. Tanaka, M. Ebihara, T. Kawamura, *Organometallics* **1998**, *17*, 4835; d) F.-H. Luo, C.-I. Chu, C.-H. Cheng, *Organometallics* **1998**, *17*, 1025; e) J. Huang, C. M. Haar, S. P. Nolan, J. E. Marcone, K. G. Moloy, *Organometallics* **1999**, *18*, 297; f) J. E. Marcone, K. G. Moloy, *J. Am. Chem. Soc.* **1998**, *120*, 8527.
- [30] J. J. García, N. M. Brunkan, W. D. Jones, *J. Am. Chem. Soc.* **2002**, *124*, 9545.
- [31] J. J. García, A. Arévalo, N. M. Brunkan, W. D. Jones, *Organometallics* **2004**, *23*, 3997.
- [32] T. A. Ateşin, T. Li, S. Lachaize, W. W. Brennessel, J. J. García, W. D. Jones, *J. Am. Chem. Soc.* **2007**, *129*, 7562.
- [33] T. A. Ateşin, T. Li, S. Lachaize, J. J. García, W. D. Jones, *Organometallics* **2008**, *27*, 3811.
- [34] T. Li, J. J. García, W. W. Brennessel, W. D. Jones, *Organometallics* **2010**, DOI: 10.1021/om100001m.
- [35] T. Schaub, C. Doring, U. Radius, *Dalton Trans.* **2007**, 1993.
- [36] M. G. Crestani, A. Arévalo, J. J. García, *Adv. Synth. Catal.* **2006**, *348*, 732.
- [37] C. Crisóstomo, M. G. Crestani, J. J. García, *J. Mol. Catal. A* **2007**, *266*, 139.
- [38] M. G. Crestani, J. J. García, *J. Mol. Catal. A* **2009**, *299*, 26.
- [39] C. Crisóstomo, M. G. Crestani, J. J. García, *Chem. Today* **2009**, *27*, 15.
- [40] C. Crisóstomo, M. G. Crestani, J. J. García, *Inorg. Chim. Acta* **2010**, *363*, 1092.
- [41] P. Zerecero-Silva, I. Jimenez-Solar, M. G. Crestani, A. Arévalo, R. Barrios-Francisco, J. J. García, *Appl. Catal. A: General* **2009**, *363*, 230.
- [42] a) J. Samec, S. M. Mony, L. Backvall, *Can. J. Chem.* **2005**, *83*, 909; b) X. Liu, S. Zhu, S. Wang, *Synthesis* **2004**, *5*, 683; c) A. Toti, P. Frediani, A. Salvani, C. Giannelli, C. Giolli, C. R. Chim. **2004**, *7*, 769; d) C. Baar, M. C. Jennings, J. J. Vittal, R. J. Puddephatt, *Organometallics* **2004**, *19*, 4150–4158.
- [43] S. Purser, P. R. Moore, S. Swallow, V. Gouverneur, *Chem. Soc. Rev.* **2008**, *37*, 320.
- [44] A. L. Iglesias, M. Muñoz-Hernández, J. J. García, *J. Organomet. Chem.* **2007**, *692*, 3498.
- [45] A. L. Iglesias, J. J. García, *J. Mol. Catal. A J. Mol. Catal.* **2009**, *298*, 51.
- [46] See, for instance: a) S. Fujishige, Y. Nakao, *Chem. Lett.* **1980**, 673; b) N. S. Chang, S. Aldrett, M. T. Holtzapple, R. R. Davison, *Chem. Eng. Sci.* **2000**, *55*, 5721; c) H. Tsai, S. Sato, R. Takahashi, T. Sodesawa, S. Takenaka, *Phys. Chem. Chem. Phys.* **2002**, *4*, 3537; d) D. Q. Zhou, D. J. Zhou, X. H. Cui, F. M. Wang, M. Y. Huang, Y. Y. Jiang, *Polym. Adv. Technol.* **2004**, *15*, 350; e) K. Molvinger, M. Lopez, J. Court, *J. Mol. Catal. A* **1999**, *150*, 267; f) P. Cividino, J. Masson, K. Molvinger, J. Court, *Tetrahedron: Asymmetry* **2000**, *11*, 3049.
- [47] A. Flores-Gaspar, P. Pinedo-González, M. G. Crestani, M. Muñoz-Hernández, D. Morales-Morales, B. A. Warsop, W. D. Jones, J. J. García, *J. Mol. Catal. A* **2009**, *309*, 1.
- [48] a) B. L. Edelbach, R. J. Lachicotte, W. D. Jones, *Organometallics* **1999**, *18*, 4040; b) R. Waterman, G. L. Hillhouse, *Organometallics* **2003**, *22*, 5182.
- [49] R. Barrios-Francisco, J. J. García, *Inorg. Chem.* **2009**, *48*, 230.
- [50] a) D. A. Vicić, W. D. Jones, *J. Am. Chem. Soc.* **1999**, *121*, 7606; b) D. A. Vicić, W. D. Jones, *Organometallics* **1998**, *17*, 3411; c) D. A. Vicić, W. D. Jones, *J. Am. Chem. Soc.* **1997**, *119*, 10855.
- [51] a) T. Shimada, Y.-H. Cho, T. Hayashi, *J. Am. Chem. Soc.* **2002**, *124*, 13396; b) Y.-H. Cho, A. Kina, T. Shimada, T. Hayashi, *J. Org. Chem.* **2004**, *69*, 3811.
- [52] J. Torres-Nieto, A. Arévalo, P. García-Gutiérrez, A. Acosta-Ramírez, J. J. García, *Organometallics* **2004**, *23*, 4534.
- [53] J. Torres-Nieto, A. Arévalo, J. J. García, *Organometallics* **2007**, *26*, 2228.
- [54] J. Torres-Nieto, W. W. Brennessel, W. D. Jones, J. J. García, *J. Am. Chem. Soc.* **2009**, *131*, 4120.
- [55] A. Oviedo, J. Torres-Nieto, A. Arévalo, J. J. García, *J. Mol. Catal. A* **2008**, *293*, 65.
- [56] A. Oviedo, A. Arévalo, J. J. García, manuscript in preparation.
- [57] T. Schaub, M. Backes, O. Plietzsch, U. Radius, *Dalton Trans.* **2009**, 7071.

Received: June 4, 2010

Published Online: August 16, 2010

The Last of the Five: the Elusive “Tantalum(III) Bromide”, a Perovskite-Related Salt, $[\{\text{Ta}_6\}\text{Br}_{12}]\text{Br}_3[\text{TaBr}_6]_{0.86}$

Katja Habermehl,^[a] Anja-Verena Mudring,^[b] and Gerd Meyer*^[a]

Keywords: Bromides / Cluster complexes / Tantalum

The system Ta/Br contains, according to a phase diagram determination of 1965, five compounds. The crystal structures of TaBr_5 , TaBr_4 as well as of $\text{Ta}_6\text{Br}_{15}$ and $\text{Ta}_6\text{Br}_{14}$ are known. The elusive “ TaBr_3 ” was now obtained as single crystals from the reduction of TaBr_5 at the wall of the tantalum reaction container in the presence of a NaBr or RbBr flux. Its structure is that of a stuffed derivative of the structure of $\text{Ta}_6\text{Br}_{15}$. As

this is related to the ReO_3 -type of structure, “ TaBr_3 ” is related to the perovskite-type of structure, in accord with the formulation $[\{\text{Ta}_6\}\text{Br}_{12}]\text{Br}_3[\text{TaBr}_6]_{0.862(13)} = [\text{Ti}]\text{O}_3[\text{Ca}]$, with an under-occupation of the cuboctahedral site. With the composition $\text{TaBr}_{2.94}$ it represents the lower end of a homogeneity range TaBr_{3-x} once reported.

Freshmen textbooks suggest that the chemistry of niobium and tantalum is very similar if not identical, subject to lanthanide contraction. For the highest oxidation state, +5, this is approximately true. For lower oxidation states there are many dissimilarities as Table 1 shows for the halides. Most of the phases known from phase diagram determinations have been analyzed by single-crystal X-ray diffraction. Although the general picture is already known since the 1960's,^[1] there are many open questions.

Table 1. Oxidation states and compounds in the Nb/Ta–Cl/Br/I systems (symbols printed in **bold** indicate structure determinations from single crystal data).

| | Nb–Cl | Ta–Cl | Nb–Br | Ta–Br | Nb–I | Ta–I |
|-------|--------------------------------------|--------------------------------------|-------------------------------------|--------------------------------------|------------------------------------|-------------------------------------|
| +1.83 | | | | | NbI₁₁ | |
| +2.33 | Nb₆Cl₁₄ | | | Ta₆Br₁₄ | | Ta₆I₁₄ |
| +2.5 | | Ta₆Cl₁₅ | | Ta₆Br₁₅ | | |
| +2.67 | Nb₃Cl₈ | | Nb₃Br₈ | | Nb₃I₈ | |
| +3 | | | | TaBr_{3-x} | | |
| +4 | NbCl₄ | TaCl₄ | NbBr₄ | TaBr₄ | NbI₄ | TaI₄ |
| +5 | NbCl₅ | TaCl₅ | NbBr₅ | TaBr₅ | NbI₅ | TaI₅ |

All pentahalides MX_5 ($\text{M} = \text{Nb}, \text{Ta}$; $\text{X} = \text{Br}, \text{I}$) contain dimers consisting of edge-connected octahedra, $^0[\text{MX}_{4/1}\text{X}_{2/2}]_2$. As they may be understood as closest packings of halide spheres with 20% of the octahedral voids filled, al-

though, with the constraints that they are adjacent and share a common edge, there are many possible structures. Theoretical considerations concerning the possible structures have been undertaken by Müller quite a while ago.^[2] We have recently obtained untwinned crystals of TaI_5 ,^[3] it has a crystal structure which had been determined earlier from data obtained from a disordered crystal.^[4] The crystal structure of TaBr_5 was also recently determined.^[5] Hitherto there were only powder data^[6] which led to the wrong assumption that TaBr_5 would be isostructural with NbBr_5 .

Tetrahalides MX_4 appear to be known in all M-X systems. Except for TaI_4 , they seem to all contain chains of *trans*-edge-connected octahedra, $[\text{MX}_{4/2}\text{X}_{2/1}]_\infty$. This has now been confirmed for TaBr_4 .^[5] Surprisingly, TaI_4 consists of face-sharing octahedral dimers which are connected by one edge to tetramers, $[\text{I}_{3/1}\text{Ta}_2(\text{I}_{3/2})_2\text{TaI}_{1/1}(\text{I}_{2/2})_2\text{I}_{1/1}\text{TaI}-(\text{I}_{3/2})_2\text{TaI}_{3/1}] = \text{Ta}_4\text{I}_{16}$.^[7] In all of these, M-M single bonds can be allocated, both by distance considerations and by theoretical calculations.

Tri- and dihalides do not exist, except for “ TaBr_3 ” (see below). The lower oxidation states are characterized by trigonal and octahedral clusters, respectively. Trigonal clusters are known only for the niobium halides Nb_3X_8 , the niobium triangle held together by three single bonds. These have been well characterized by crystal structure determinations and other measurements.^[8] All of the M_6X_{14} - and M_6X_{15} -type halides contain octahedral clusters of the $\{\text{M}_6\}\text{X}_{12}$ -type with connections via halide bridges according to $\{\text{M}_6\}\text{X}_{10}^i\text{X}^{i-a}_{2/2}\text{X}^{a-i}_{2/2}\text{X}^{a-a}_{4/2}$ and $\{\text{M}_6\}\text{X}_{12}^i\text{X}^{a-a}_{6/2}$, respectively. Nb_6I_{11} appears to be one of a kind, with $\{\text{Nb}_6\}\text{I}_8\text{I}^a_6$ cluster complexes connected according to $\{\text{Nb}_6\}\text{I}_8\text{I}^{a-a}_{6/2}$.^[9] Both the M_6X_{15} - and Nb_6I_{11} -types of structure can be identified with a ReO_3 -type arrangement according to $[\{\text{M}_6\}\text{X}_{12}]\text{X}^{a-a}_{6/2}$ or $[\{\text{Nb}_6\}\text{I}_8]\text{I}^{a-a}_{6/2} = [\text{Re}]\text{O}_{6/2}$.

[a] Department für Chemie, Institut für Anorganische Chemie, Universität zu Köln, Greinstraße 6, 50939 Köln, Germany
Fax: +49-221-470-5083
E-mail: gerd.meyer@uni-koeln.de
<http://www.gerdmeyer.de>

[b] Fakultät für Chemie, Anorganische Chemie I – Festkörperchemie und Materialien, Ruhr-Universität Bochum, 44780 Bochum, Germany
Fax: +49-234-32-14951
E-mail: anja.mudring@rub.de

The System Tantalum–Bromine

The system tantalum–bromine is surprisingly rich of compounds. The phase diagram^[10] exhibits five compounds: TaBr₅ (melting point 272 °C), TaBr₄ (m.p. 392 °C, i), TaBr_{2.83} (m.p. 450 °C, i), TaBr_{2.5} (m.p. 675 °C, i) TaBr_{2.33} (dec. >750 °C) where i indicates incongruently melting; dec. denotes decomposition. The crystal structures of both Ta₆Br₁₄^[11] (isostructural with Nb₆Cl₁₄ and Ta₆I₁₄)^[12] and Ta₆Br₁₅^[13] have been determined and are as just mentioned above, as well as the structures of TaBr₄ and TaBr₅.^[5] Elusive is the confirmation of the existence and then the crystal structure of “TaBr₃”. It is the only phase for which a homogeneity range has been reported, $2.9 \leq x \leq 3.1$.^[14] The phase diagram states $x = 2.83$ for TaBr_{*x*} with a decomposition temperature of 450 ± 5 °C.^[10]

Single crystals of “TaBr₃” were now obtained by reduction of TaBr₅ with the wall of the tantalum reaction container at 500 °C with NaBr or RbBr as a flux.^[15] The reaction temperature is similar to that used in equilibration experiments previously (426 °C) and above the incongruent melting point of pure TaBr_{2.83}.^[10]

The present crystal refined to a composition of TaBr_{2.94}.^[16] Its structure corresponds to a stuffed derivative of that of {Ta₆}Br₁₅. This has a ReO₃-type arrangement, according to [{Ta₆}Br₁₂]Br₃ = [Re]O₃ with large (distorted) cuboctahedral holes. These voids are filled with [TaBr₆] octahedra; for the composition TaBr₃ = Ta₇Br₂₁ = {Ta₆}Br₁₅[TaBr₆] the holes would be fully occupied, and the structure would be a perovskite-related arrangement, [{Ta₆}Br₁₂]Br₃[TaBr₆] = [Ti]O₃[Ca], see Figure 1. In TaBr_{2.94}, the holes are only occupied to 86.2(13) %. A superstructure with occupied and empty holes was not detected such that a statistical distribution must be assumed. Nonetheless, the true unit cell is hexagonal, space group *R* $\bar{3}c$, *a* = 1298.60(11), *c* = 3328.5(4) pm, *Z* = 6 × [{Ta₆}Br₁₅][TaBr₆]_{0.862(13)}, see Figure 2.^[16]

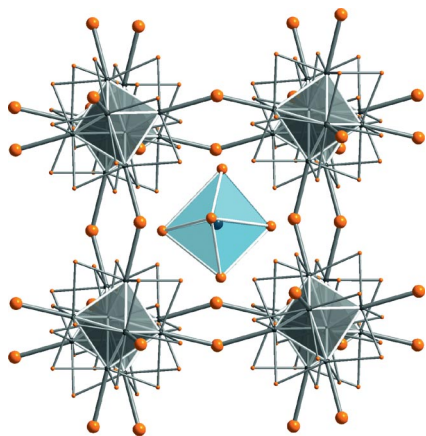


Figure 1. Projection of part of the crystal structure of TaBr_{2.94} = [{Ta₆}Br₁₅][TaBr₆]_{0.86} exhibiting a perovskite-related arrangement with the [{Ta₆}Br₁₂]Br₃ framework encapsulating a [TaBr₆] octahedron (blue).

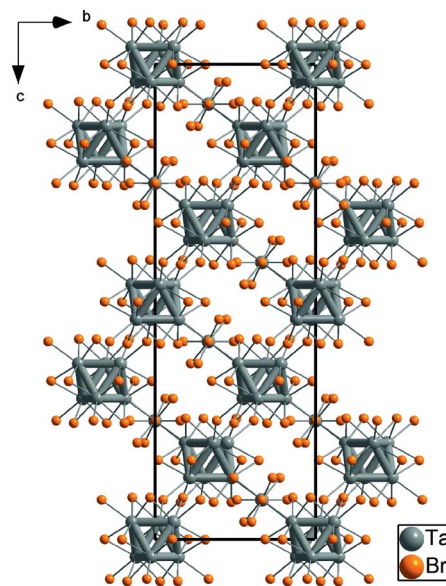


Figure 2. Crystal structure of TaBr_{2.94} = [{Ta₆}Br₁₅][TaBr₆]_{0.86}; projection onto the (100) plane of the hexagonal setting.

The composition TaBr_{2.94} is in good agreement with the lower end of the homogeneity range ($x = 2.9$) once reported^[14] and is only slightly higher than $x = 2.83$ as derived from equilibration studies.^[10] Our synthetic procedure with a large excess of reducing tantalum as the wall of the reaction container, should indeed lead to the lower end of the homogeneity range. With the present structure, a homogeneity range above 3.0 (all voids occupied by [TaBr₆] octahedra), does not make chemical sense, unless the {Ta₆}Br₁₅ network became under-occupied.

Ta...Ta and Ta...Br distances in the {Ta₆}Br₁₅ network of TaBr_{2.94} are identical with those in Ta₆Br₁₅ (= TaBr_{2.5})^[13] with 296.2(1) vs. 295.8(2) for Ta–Ta, and 257.9(2) vs. 257.6(8) pm for Ta–Brⁱ and 280.9(1) vs. 280.4 pm for Ta–Br^{a-a} distances (all averaged). Ta–Br distances in the [TaBr₆] octahedron are 253.0(5) pm, with a rather large standard deviation subject to the large temperature factors of the atoms in the under-occupied large hole. These Ta–Br distances compare very well with those in TaBr₅ where the terminal distances in the Ta₂Br₁₀ double octahedron are, on the average, 243.4 pm and the bridging ones 271.0 pm, which leads to an overall average of 252.6 pm.^[5] Thus, tantalum in the [TaBr₆] octahedron can be considered as pentavalent, such that TaBr_{2.94} may be understood as a salt according to [{Ta₆}Br₁₅]^{0.86+} [TaBr₆]^{0.86-}.

If the cuboctahedral voids were fully occupied, the network would have one positive charge, [{Ta₆}Br₁₅]⁺, or the cluster complexes would be [{Ta₆}Br₁₂]⁴⁺, if only inner ligands were considered. For niobium, a cluster of this formal charge does not exist, it “decomposes” to [{Nb₃}-Br₆]²⁺, incorporated in the binary bromide {Nb₃}Br₈ whose structure was refined recently.^[5,8d] Analogous triangular clusters are not known for binary tantalum halides, but for mixed-halide chalcogenides such as {Ta₃}SBr₇.^[18] On the

other hand, the 14-electron cluster $[\{\text{Ta}_6\}\text{Br}_{12}]^{4+}$, although not known in a binary compound such as $\{\text{Ta}_6\}\text{Br}_{12}\text{Br}_4$, is, for example as $[\{\text{Ta}_6\}\text{Br}_{12}\text{Br}_6]^{2-}$, the species which is responsible for the red solutions observed decades ago.^[19] They have just now been observed in complex salts, for example in $[\text{K}(\text{crypt-2.2.2})]_2[\{\text{Ta}_6\}\text{Cl}_{12}\text{Cl}_6]$.^[20] This is surprising because 14-electron clusters are electron-deficient and are normally unknown for octahedral tantalum clusters. The molecular orbital energy Scheme as obtained from an Extended Hückel Molecular Orbital (EHMO)^[21,22] treatment reveals that the gap between the a_{1u} and the t_{2u} orbitals, see Figure 3, is obviously large enough that it is favourable to form such an anion, especially when it is secured in a salt with a large counter cation, or in an extended cation such as in $[\{\text{Ta}_6\}\text{Br}_{15}]_{0.86}^+[\text{TaBr}_6]_{0.86}^-$. The reason why the a_{1u} orbital is (statistically) only partially occupied in the present case and, thus, an explanation for the unexpected Daltonide composition of $\text{TaBr}_{2.94}$, cannot be answered on the present simple level of theory.

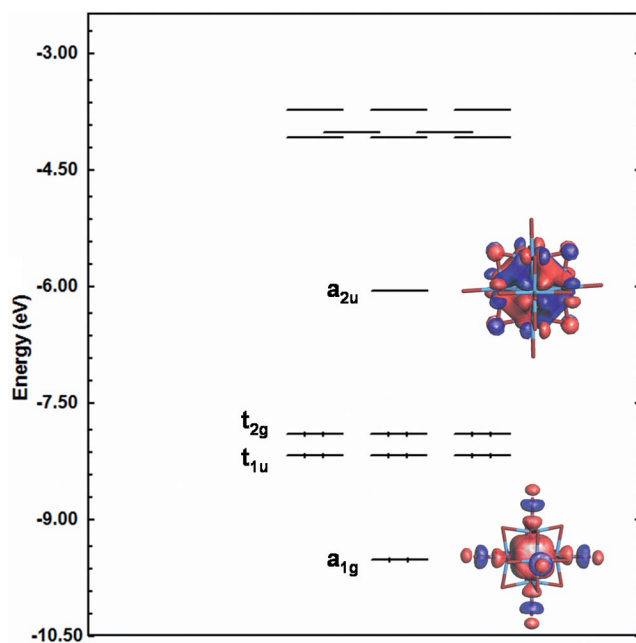


Figure 3. EHMO scheme for $[\{\text{Ta}_6\}\text{Br}_{18}]^{2-}$, representing the 14-electron tantalum cluster in $\text{TaBr}_{2.94}$; the a_{2u} orbital is the highest bonding orbital.

Conclusions

The last of the five compounds known for the Ta/Br system, has now been established structurally, $\text{TaBr}_{2.94} = [\{\text{Ta}_6\}\text{Br}_{15}][\text{TaBr}_6]_{0.86}$. Thus, the structural chemistry of the binary tantalum halides is characterized by $[\text{TaBr}_6]$ octahedra as in TaBr_5 (dimer of two edge-sharing octahedra), TaBr_4 (chain of edge-connected octahedra), and $\text{TaBr}_{2.94}$ (isolated anion), as well as by octahedral clusters $\{\text{Ta}_6\}\text{Br}_{12}$ as in $\text{Ta}_6\text{Br}_{14}$ and $\text{Ta}_6\text{Br}_{15}$ and $\text{TaBr}_{2.94}$. This non-stoichiometric phase, therefore, merges both structural motifs.

- [1] H. Schäfer, H. G. Schnering, *Angew. Chem.* **1964**, 76, 833.
- [2] U. Müller, *Acta Crystallogr., Sect. A* **1978**, 34, 256.
- [3] K. Habermehl, I. Pantenburg, P. Held, G. Meyer, *Z. Anorg. Allg. Chem.* **2008**, 634, 829–831.
- [4] U. Müller, *Acta Crystallogr., Sect. B* **1979**, 35, 2502.
- [5] K. Habermehl, Dissertation, University of Cologne, Germany, **2010**.
- [6] U. Rolsten, *J. Am. Chem. Soc.* **1958**, 80, 2952.
- [7] G. Meyer, R. Wiglusz, I. Pantenburg, A.-V. Mudring, *Z. Anorg. Allg. Chem.* **2008**, 634, 825.
- [8] a) A. Simon, H. G. von Schnering, *J. Less-Common Met.* **1966**, 11, 31–46; b) H.-G. von Schnering, H. Wöhrle, H. Schäfer, *Naturwissenschaften* **1961**, 48, 159; c) M. Ströbele, J. Glaser, A. Lachgar, H.-J. Meyer, *Z. Anorg. Allg. Chem.* **2001**, 627, 2002–2004; d) K. Habermehl, G. Meyer, *Z. Naturforsch. B* **2010**, 65, 770–772.
- [9] A. Simon, H. G. von Schnering, H. Schäfer, *Z. Anorg. Allg. Chem.* **1967**, 355, 295–310.
- [10] R. E. McCarley, J. C. Boatman, *Inorg. Chem.* **1965**, 4, 1486–1491.
- [11] B. Bajan, H.-J. Meyer, *Z. Kristallogr.* **1995**, 210, 607.
- [12] A. Simon, H. G. von Schnering, A. Wöhrle, H. Schäfer, *Z. Anorg. Allg. Chem.* **1965**, 339, 155; H. M. Artelt, G. Meyer, *Z. Kristallogr.* **1993**, 206, 306–307.
- [13] D. Bauer, H. G. von Schnering, *Z. Anorg. Allg. Chem.* **1968**, 362, 259–276; H. G. von Schnering, D. Vu, S.-L. Jin, K. Peters, *Z. Kristallogr. NCS* **1999**, 214, 15–16.
- [14] H. Schäfer, R. Gerken, H. Scholz, *Z. Anorg. Allg. Chem.* **1965**, 335, 96–103.
- [15] Synthesis: 200 mg of resublimed TaBr_5 together with 40 mg NaBr or 20 mg RbBr were sealed by He-arc-welding in tantalum containers which were jacketed in silica ampoules. The temperature program was as follows: heat with 50 °C/h to 500 °C, further heating at constant temp. (500 °C) for five days, cooling with 1 °C/h to 180 °C and then to ambient temperature with 20 °C/h. Black cube-like crystals of “ TaBr_3 ” as well as a grey powder was obtained which consisted of “ TaBr_3 ” and the flux materials, NaBr and RbBr , respectively. EDX measurements (27.2% Ta, 72.8% Br) yield the composition $\text{TaBr}_{2.68}$ which appears to be rather far from $\text{TaBr}_{2.94}$ (25.4% Ta and 74.6% Br) as derived from single-crystal X-ray structure analysis, but is perhaps the best result that can be obtained by this method, given the fact that “ TaBr_3 ” is moisture-sensitive.
- [16] Single crystals of $\text{TaBr}_{2.94}$ suitable for X-ray diffraction were selected under a microscope in a nitrogen dry box. They were inspected by Laue photographs (Mo- K_α radiation, image plate). The best specimen was transferred to a Stoe “Image Plate Diffraction System” (IPDS-II diffractometer, Stoe, Darmstadt, Germany). The data were corrected for Lorentz and polarization effects. A numerical absorption correction based on crystal-shape optimization was applied for all data. The programs used in this work are Stoe’s X-Area as well as SHELXS-97 and SHELXL-97 for structure solution and refinement.^[17] The last cycles of refinement included atomic positions and anisotropic thermal parameters for all atoms. Crystal data for $\text{TaBr}_{2.94} = [\{\text{Ta}_6\}\text{Br}_{15}][\text{TaBr}_6]_{0.862(13)}$: 2944.8 g mol⁻¹; diffractometer Stoe IPDS II, $T = 293(2)$ K; $2\theta_{\text{max}} = 54.8^\circ$; $0^\circ \leq \omega \leq 180^\circ$, $\phi = 0^\circ$, $0^\circ \leq \omega \leq 180^\circ$, $\phi = 90^\circ$, $\Delta\omega = 2^\circ$, 180 images; $-16 \leq h \leq 16$, $-16 \leq k \leq 14$, $-42 \leq l \leq 42$; $\rho_{\text{calc}} = 6.04$ g cm⁻³; 15722 measured reflections of which 1217 were symmetrically independent; $R_{\text{int}} = 0.1075$; $F(000) = 7476$; $\mu = 49.42$ mm⁻¹. Trigon, $R3c$ (no. 167), $a = 1298.60(11)$, $c = 3328.5(4)$ pm, $V = 4861.1(8)$ 10⁶ pm³, $Z = 6$; R values: R_1/wR_2 for 951 reflections with $[I_0 > 2\sigma(I_0)]$: 0.051/0.134, for all data: 0.068/0.146; $S_{\text{all}} = 1.055$. Further details on the crystal structure investigation may be obtained from the Fachinformationszentrum Karlsruhe, 76344 Eggenstein-Leopoldshafen, Germany (Fax: +49-7247-808-666; E-mail: crysdata@fiz-karlsruhe.de), on quoting the depository number CSD-421831.

- [17] X-Shape 1.06, Crystal Optimisation for Numerical Absorption Correction (C), Stoe & Cie GmbH, Darmstadt, **1999**; X-Area 1.16, Stoe & Cie GmbH, Darmstadt, **2003**; X-RED 1.22, Stoe Data Reduction Program (C), Stoe & Cie GmbH, Darmstadt, **2001**; X-STEP32, Revision 1.06f, STOE & Cie GmbH, Darmstadt, **2000**; Sheldrick, G. M. *SHELXL-97*, Programs for Crystal Structure Analysis, University of Göttingen, **1997**.
- [18] M. Smith, G. J. Miller, *J. Solid State Chem.* **1998**, *140*, 226–232.
- [19] R. E. McCarley, B. G. Hughes, F. A. Cotton, R. Zimmerman, *Inorg. Chem.* **1965**, *4*, 1491.
- [20] K. Dücker, G. Meyer, unpublished results, **2010**.
- [21] Semi-empirical extended Hückel calculations (EH) were performed with the program package CAESAR (ref.^[22]) using the following parameters: Ta 6s: $H_{ii} = -8.73$, $\zeta_1 = 2$, $c_1 = 0.5705$, $\zeta_2 = 1.1$, $c_2 = 0.5664$; 6p: $H_{ii} = -3.3$, $\zeta_1 = 1.64$, $c_1 = 1.0$, 5d: $H_{ii} = -7.57$, $\zeta_1 = 3.3$, $c_1 = 0.55517$, $\zeta_2 = 1.5$, $c_2 = 0.6021$; Br 4s: $H_{ii} = -25.629999$, $\zeta_1 = 2.38$, $c_1 = 1.0$, 4p: $H_{ii} = -12.61$, $\zeta_1 = 2.38$, $c_1 = 1.0$.
- [22] J. Ren, W. Liang, M.-H. Whangbo, *CAESAR*, PrimeColor Software Inc., Raleigh, NC, USA, **1998**.

Received: May 25, 2010

Published Online: July 13, 2010

Humidity-Sensitive Magnet Composed of a Cyano-Bridged $\text{Co}^{\text{II}}\text{--Nb}^{\text{IV}}$ Dimetallic Assembly

Kenta Imoto,^[a] Daisuke Takahashi,^[a] Yoshihide Tsunobuchi,^[a] Wataru Kosaka,^[a]
Michio Arai,^[a] Hiroko Tokoro,^[a] and Shin-ichi Ohkoshi^{*[a]}

Keywords: Cyano-bridged assembly / Humidity response / Cobalt / Niobium / Magnetic properties

Nanoporous magnetic materials composed of metal-assembled complexes are expected to exhibit chemical sensitivity. In this work, we observed a humidity-induced reversible change between ferromagnetism and antiferromagnetism in a new type of a cobalt octacyanonitrate based magnet

in the high-humidity region. This humidity response is caused by the adsorption and desorption of non-coordinated water (so-called zeolitic water) molecules in the interstitial site. Such a phenomenon is achieved by the structural flexibility of an octacyanometalate-based magnet.

Introduction

Nanoporous magnetic materials composed of metal-assembled complexes are expected to exhibit chemical sensitivity because a gas or solvent molecule can penetrate into the lattice and directly act on spin sites. From this viewpoint, cyano-bridged metal assemblies are suitable systems.^[1] In 2004, humidity-induced magnetization and magnetic pole inversion due to changes in the Co coordination geometries between six- and four-coordinate were observed in $\text{Co}[\text{Cr}(\text{CN})_6]_{2/3} \cdot z\text{H}_2\text{O}$ and $(\text{Co}_{0.41}\text{Mn}_{0.59})[\text{Cr}(\text{CN})_6]_{2/3} \cdot z\text{H}_2\text{O}$,^[2] respectively. Furthermore, humidity-induced magnetism has been reported in $\text{Mn}[\text{Cr}(\text{CN})_6] \cdot (\text{dimethylethylenediamineH}) \cdot 2\text{H}_2\text{O}$ ^[3] and $\text{Mn}_{1.5}[\text{Mo}(\text{CN})_7] \cdot (\text{dimethylalaninolH}) \cdot 2\text{H}_2\text{O}$.^[4] In addition to these $[\text{M}(\text{CN})_6]$ - and $[\text{M}(\text{CN})_7]$ -based magnets, $[\text{M}(\text{CN})_8]$ -based magnets^[5,6] are also good candidates as nanoporous magnets because $[\text{M}(\text{CN})_8]$ -based magnets have a variety of coordination geometries with nanoporous structures. Herein we describe a humidity-induced reversible change between ferromagnetism and antiferromagnetism in a cobalt octacyanonitrate based magnet in the high-humidity region. This humidity response is due to the adsorption and desorption of non-coordinated water (so-called zeolitic water) molecules in the interstitial sites.

Results and Discussion

The target compound was prepared by adding an aqueous solution of $\text{K}_4[\text{Nb}(\text{CN})_8] \cdot 2\text{H}_2\text{O}$ ^[8a] to an aqueous solu-

tion of $\text{CoCl}_2 \cdot 6\text{H}_2\text{O}$. The resulting precipitate was a pink powder. Additionally, a single crystal of this compound was prepared by the diffusion method. Elemental analysis indicated the formula of the present compound to be $\text{Co}_2[\text{Nb}(\text{CN})_8] \cdot 8.0\text{H}_2\text{O}$.

Single-crystal X-ray analysis showed that the compound has a tetragonal crystal structure in the $I4/m$ space group with $a = 11.8879(11) \text{ \AA}$, $c = 13.1925(12) \text{ \AA}$, and $Z = 4$ (Figure 1, Figure S1, Tables S1–S3). The coordination geometries of the Co and Nb sites are pseudo-octahedral and square-antiprismatic, respectively. The four equatorial positions of the Co sites are coordinated by cyanide nitrogen atoms from $[\text{Nb}(\text{CN})_8]$, whereas the apical positions are coordinated by two oxygen atoms from the ligand water molecules. All eight CN groups of $[\text{Nb}(\text{CN})_8]$ are bridged to the

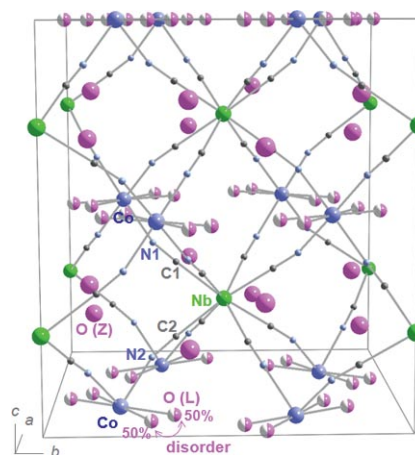


Figure 1. Crystal structure of $\text{Co}_2[\text{Nb}(\text{CN})_8] \cdot 8\text{H}_2\text{O}$. Blue, green, gray, light blue, and pink spheres represent Co, Nb, C, N, and O(Z) atoms of the zeolitic water molecules, respectively. The half pink/white spheres represent O(L) atoms of the ligand water molecules (disorder of 50%). H atoms are omitted for clarity.

[a] Department of Chemistry, School of Science, The University of Tokyo
7-3-1 Hongo, Bunkyo-ku, Tokyo 113-0033, Japan
Fax: +81-3-3812-1896
E-mail: ohkoshi@chem.s.u-tokyo.ac.jp
Supporting information for this article is available on the WWW under <http://dx.doi.org/10.1002/ejic.201000720>.

Co sites. The interstitial sites of the Co–NC–Nb framework contain four zeolitic water molecules. This structure is isostructural of $\text{Mn}_2[\text{Nb}(\text{CN})_8] \cdot 8.0\text{H}_2\text{O}$ ^[6a,6b] and $\text{Fe}_2[\text{Nb}(\text{CN})_8] \cdot 8.0\text{H}_2\text{O}$.^[6c] The XRD pattern of the powder sample corresponds to the crystal structure of the single crystal.

Magnetization vs. temperature plots show that at 80% RH the present compound exhibits a spontaneous magnetization with a Curie temperature (T_C) of 12 K (Figure 2a and Figure S2). The magnetization vs. external magnetic field plots indicate that the coercive field (H_C) value is 300 Oe at 2 K (Figure 2b), and the saturation magnetization (M_s) value is $5.2 \mu_B$ at 9 T (Figure S3). The observed M_s value suggests that the sample at 80% RH is a ferromagnet where the sublattice magnetizations of Co^{II} and Nb^{IV} are ordered in a parallel manner.^[7] The M_s and T_C values decrease as the humidity decreases. In particular, the magnetization and H_C values drastically decrease between 80% RH and 60% RH. The H_C value at 10% RH is almost zero, and the molar magnetic susceptibility (χ_M) vs. temperature plots show antiferromagnetism with a Néel temperature of 5 K (Figure S4). The temperature dependence of the magnetic susceptibility also supports these humidity dependences of magnetic properties (Figure S5). Conversely, increasing the humidity causes the magnetic properties to revert to the original ferromagnetic state.

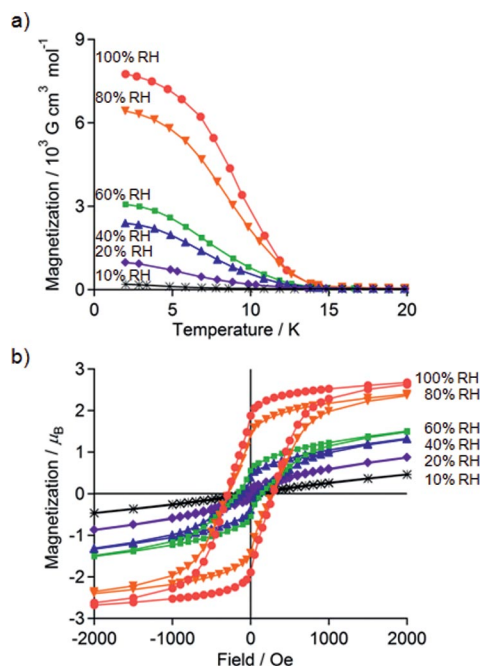


Figure 2. (a) Magnetization vs. temperature curves at an external magnetic field of 100 Oe for $\text{Co}_2[\text{Nb}(\text{CN})_8] \cdot z\text{H}_2\text{O}$. (b) Magnetization vs. external field curves at $T = 2$ K.

To elucidate the observed humidity response, the humidity dependences of the sample weight, IR spectrum, UV/Vis spectrum, Faraday effect, and XRD pattern were measured. The weight vs. humidity plots and IR spectra indicate that the sample weight and OH stretching peaks around

3400 cm^{-1} decrease as the humidity decreases (Figure 3a and Figure S6). By using the results of the sample weight vs. humidity plots, the z values of $\text{Co}_2[\text{Nb}(\text{CN})_8] \cdot z\text{H}_2\text{O}$ are estimated to change from $z = 8.0$ (100% RH) to 5.8 (15% RH) at 298 K (Figure 3a, inset). The UV/Vis reflectance spectra at 100% RH (Figure 3b, top) have a shoulder peak around 400 nm (Band 1) and absorption peaks around 500 nm (Band 2) and 1120 nm (Band 3), which are assigned to the ligand-to-metal charge transfer (LMCT) band of $[\text{Nb}^{\text{IV}}(\text{CN})_8]$ (Band 1), d-d (${}^4\text{T}_{1g} \rightarrow {}^4\text{T}_{1g}$, ${}^4\text{A}_{2g}$) transition (Band 2) and d-d (${}^4\text{T}_{1g} \rightarrow {}^4\text{T}_{2g}$) transition (Band 3) on the six-coordinate octahedral Co^{II} , respectively.^[8] These absorption bands are maintained nearly constant in the range of 100–20% RH (Figure 3b, center), indicating that ligand water molecules are not removed from Co^{II} but only zeolitic water molecules are reversibly adsorbed and desorbed in this humidity region. In contrast, below 15% RH, a small

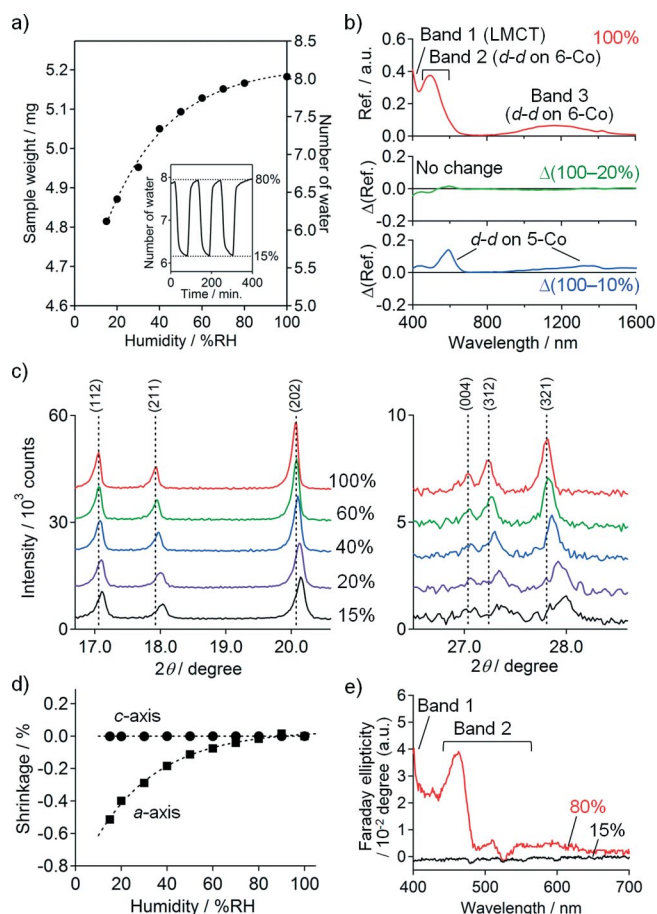


Figure 3. (a) Sample weight vs. humidity plots for $\text{Co}_2[\text{Nb}(\text{CN})_8] \cdot z\text{H}_2\text{O}$ between 100% and 15% RH. Dotted lines are eye guides. (Inset) Reversible change in weight between 80% and 15% RH. (b) Humidity dependence of the visible reflectance spectra at 100% RH (top), differential spectra between 100% and 20% RH (center), and between 100% and 10% RH (bottom). (c) Humidity dependence of the XRD patterns in the regions of $16.7^\circ \leq 2\theta \leq 20.6^\circ$ (left) and $26.5^\circ \leq 2\theta \leq 28.6^\circ$ (right). (d) Shrinking rate of a -axis (squares) and c -axis (dots) at different humidities, calculated by Rietveld analysis. Dotted lines are eye guides. (e) Faraday ellipticity (FE) spectra at 80% and 15% RH at 2 K after removal of the external magnetic field of 1 T.

amount of ligand water molecules is also released from Co^{II} (Figure 3b, bottom).^[9] The XRD patterns of the present compound show that several peaks [e.g., (202), (312), (321)] shift toward a higher angle, but other peaks [e.g., (004)] remain at the same angles as the humidity decreases (Figure 3c and Figure S7). This result suggests that lattice constants change anisotropically, i.e., the lattice parameter of the c -axis is constant but the a -axis decreases with decreasing humidity (Figure 3d). The Faraday ellipticity (FE) spectra of the sample in the range of 400–700 nm at 80% RH display FE effects at the positions of Bands 1 and 2 below T_{C} (Figure 3e), suggesting that the sample at high humidity is a ferromagnet. On the contrary, the sample at 15% RH did not exhibit an FE effect down to 2 K, suggesting the sample at low humidity is an antiferromagnet.

Based on these results, the present humidity response is understood as follows: In the change of humidity from 100% RH to 20% RH, only zeolitic water molecules desorb from the interstitial sites of the lattice.^[9] At the same time, the disorder of ligand water molecules is lost and the ab -plane of the tetragonal crystal structure is compressed. This change in the structure leads to a variation in the overlap of the magnetic orbitals on the Co and Nb ions, causing the sample to change into an antiferromagnet. In fact, Rietveld analysis of the sample at 20% RH (Figure S8 and Tables S4 and S5) shows that the bond situation of the Nb–C1–N1–Co moiety is different from the bond situation at 100% RH. Maybe, the superexchange interaction of this route changes to a negative value, resulting that the compound is converted to an antiferromagnet (Figure 4).

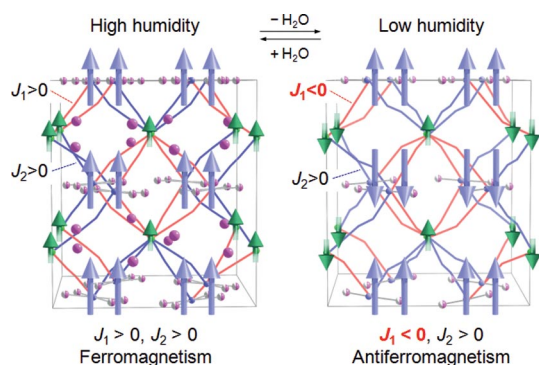


Figure 4. Schematic illustration of the magnetic ordering at high-humidity (left) and low-humidity (right) regions. J_1 and J_2 are superexchange interactions between Nb^{IV} ($S = 1/2$) and Co^{II} ($S = 3/2$) through –C1–N1– and –C2–N2– ligands, respectively. Pink spheres and half pink/white spheres represent O atoms of zeolitic water molecules and ligand water molecules, respectively. In the low humidity region, zeolitic water molecules desorb from the lattice.

Conclusions

In the present work, we observed a humidity-induced magnetic transition with a cobalt octacyanoniobate around 70% RH. This effect is ascribed to the adsorption and desorption of zeolitic water molecules in the interstitial site,

which cause the ferromagnet to change into an antiferromagnet. Such a phenomenon is achieved by the structural flexibility of an octacyanometalate-based magnet.

Experimental Section

Characterization: IR spectra were recorded with a JASCO FT/IR-4100 spectrometer by using samples scattered on a tape in the 4000–400 cm^{-1} region. XRD measurements were conducted with a Rigaku ULTIMA IV diffractometer using $\text{Cu-K}\alpha$ radiation ($\lambda = 1.5418 \text{ \AA}$) in the range of $10^\circ \leq 2\theta \leq 90^\circ$. Single-crystal X-ray data were collected with a Rigaku R-Axis RAPID imaging plate area detector with graphite-monochromated $\text{Mo-K}\alpha$ radiation. The crystal structure was solved by direct methods and refined on F^2 to $R1$ ($wR2$) = 0.0933 (0.2273) using 1115 reflections with $I > 2.00\sigma(I)$. CCDC-776326 contains the supplementary crystallographic data for this paper. These data can be obtained free of charge from The Cambridge Crystallographic Data Centre via www.ccdc.cam.ac.uk/data_request/cif. The UV/Vis reflectance spectra were measured with a Shimadzu UV-3100 spectrometer. Sample weight vs. humidity plots were measured with a humidity-controlled thermogravimetric system (TG-8120 RIGAKU). The humidity of the sample room was tuned by N_2 gas or air passed through water or a saturated aqueous solution of NaCl, NaBr, or K_2CO_3 . According to a similar procedure, magnetic-measurement samples were prepared by using a quartz cell. The humidity of each sample holder was measured with a humidity meter (CTH-1100 CUSTOM). Magnetic measurements on a polycrystalline sample were carried out by using a Quantum Design MPMS superconducting quantum interference device (SQUID) magnetometer.

Materials: The target compound was prepared as a powder by adding an aqueous solution of $\text{K}_4[\text{Nb}(\text{CN})_8] \cdot 2\text{H}_2\text{O}$ (2.5 mM) to an aqueous solution of $\text{CoCl}_2 \cdot 6\text{H}_2\text{O}$ (2.5 mM). Elemental analyses by inductively coupled plasma mass spectrometry and a thermogravimetric measurement indicated this compound has a composition of $\text{Co}_2[\text{Nb}(\text{CN})_8] \cdot 8.0\text{H}_2\text{O}$ at 100% RH. $\text{C}_8\text{H}_{16}\text{Co}_2\text{N}_8\text{NbO}_8$ (563.04): calcd. Co 20.9, Nb 16.5; found Co 20.8, Nb 16.2. IR: $\tilde{\nu} = 2145, 2157$ (CN stretching) cm^{-1} . A single crystal of this sample was prepared by diffusion of an aqueous solution of $\text{K}_4[\text{Nb}(\text{CN})_8] \cdot 2\text{H}_2\text{O}$ (100 mM) into an aqueous solution of $\text{CoCl}_2 \cdot 6\text{H}_2\text{O}$ (50 mM).

Supporting Information (see footnote on the first page of this article): Crystallographic data from single-crystal X-ray analysis, field-cooled magnetization and remanent magnetization plots at 100%RH, field dependence of magnetization at 80% RH, χ_{M} vs. T plots at 10% RH, $\chi_{\text{M}}T$ vs. T plots and χ_{M}^{-1} vs. T plots at 100% RH and 10% RH, humidity dependence of IR and XRD patterns, and crystallographic data from Rietveld analysis of the powder XRD pattern at 20% RH.

Acknowledgments

The present research was supported in part by a Grant-in-Aid for Young Scientists (S) from the Japan Society for the Promotion of Sciences (JSPS), a Grant for the Global COE Program “Chemistry Innovation through Cooperation of Science and Engineering” and the Photon Frontier Network Program from the Ministry of Education, Culture, Sports, Science, and Technology (MEXT), Japan, the Center for Nano Lithography & Analysis, The University of Tokyo, supported by MEXT Japan, the Izumi Science and Technology Foundation, and The Asahi Glass Foundation.

- [1] a) M. Verdager, A. Bleuzen, V. Marvaud, J. Vaissermann, M. Seuleiman, C. Desplanches, A. Scullier, C. Train, R. Garde, G. Gelly, C. Lomenech, I. Rosenman, P. Veillet, C. Cartier, F. Villain, *Coord. Chem. Rev.* **1999**, 190–192, 1023–1047; b) T. Malah, A. Marvilliers, E. Rivière, *Philos. Trans. R. Soc. A* **1999**, 357, 3139; c) O. Kahn, D. Gatteschi, J. S. Miller, F. Palacio, *NATO ARW Molecular Magnetic Materials*, Kluwer Academic Publishers, Dordrecht, **1991**; d) O. Kahn, *Molecular Magnetism*, VCH, New York, **1993**; e) K. R. Dunbar, R. A. Heintz, *Prog. Inorg. Chem.* **1997**, 45, 283–391; f) J. S. Miller, M. Drillon, *Magnetism: Molecules to Materials*, Wiley-VCH, Weinheim, **2005**; g) S. Ohkoshi, K. Hashimoto, *J. Photochem. Photobiol. C: Photochem. Rev.* **2001**, 2, 71–88; h) H. Tokoro, S. Ohkoshi, K. Hashimoto, *Appl. Phys. Lett.* **2003**, 82, 1245–1247; i) F. Varret, A. Goujon, K. Boukheddaden, M. Noguès, A. Bleuzen, M. Verdager, *Mol. Cryst. Liq. Cryst.* **2002**, 379, 333–340; j) A. Bleuzen, V. Escax, A. Ferrier, F. Villain, M. Verdager, P. Münsch, J.-P. Itié, *Angew. Chem.* **2004**, 116, 3814–3817; *Angew. Chem. Int. Ed.* **2004**, 43, 3728–3731; k) S. Margadonna, K. Prassides, A. N. Fitch, *Angew. Chem.* **2004**, 116, 6476–6479; *Angew. Chem. Int. Ed.* **2004**, 43, 6316–6319; l) T. Mahfoud, G. Molnár, S. Bonhommeau, S. Cobo, L. Salmon, P. Demont, H. Tokoro, S. Ohkoshi, K. Boukheddaden, A. Bousseksou, *J. Am. Chem. Soc.* **2009**, 131, 15049–15054; m) K. Inoue, K. Kikuchi, M. Ohba, H. Okawa, *Angew. Chem.* **2003**, 115, 4958–4961; *Angew. Chem. Int. Ed.* **2003**, 42, 4810–4813.
- [2] S. Ohkoshi, K. Arai, Y. Sato, K. Hashimoto, *Nat. Mater.* **2004**, 3, 857–861.
- [3] W. Kaneko, M. Ohba, S. Kitagawa, *J. Am. Chem. Soc.* **2007**, 129, 13706–13712.
- [4] J. Milon, M.-C. Daniel, A. Kaiba, P. Guionneau, S. Brandès, J.-P. Sutter, *J. Am. Chem. Soc.* **2007**, 129, 13872–13878.
- [5] a) R. Garde, C. Desplanches, A. Bleuzen, P. Veillet, M. Verdager, *Mol. Cryst. Liq. Cryst.* **1999**, 334, 587–595; b) B. Sieklucka, R. Podgajny, D. Pinkowicz, B. Nowicka, T. Korzeniak, M. Bałanda, T. Wasiutyński, R. Pełka, M. Makarewicz, M. Czapla, M. Rams, B. Gawel, W. Łasocha, *Cryst. Eng. Commun.* **2009**, 11, 2032–2039; c) Z. J. Zhong, H. Seino, Y. Mizobe, M. Hidai, A. Fujishima, S. Ohkoshi, K. Hashimoto, *J. Am. Chem. Soc.* **2000**, 122, 2952–2953; d) J. Larionova, M. Gross, M. Pilkington, H. Andres, H. Stoeckli-Evans, H. U. Güdel, S. Decurtins, *Angew. Chem.* **2000**, 112, 1667–1672; *Angew. Chem. Int. Ed.* **2000**, 39, 1605–1609; e) D. E. Freedman, M. V. Bennett, J. R. Long, *Dalton Trans.* **2006**, 2829–2834; f) G. Rombaut, S. Golhen, L. Ouahab, C. Mathonière, O. Kahn, *J. Chem. Soc., Dalton Trans.* **2000**, 3609–3614; g) R. Podgajny, T. Korzeniak, M. Bałanda, T. Wasiutyński, W. Errington, T. J. Kemp, N. W. Alcock, B. Sieklucka, *Chem. Commun.* **2002**, 1138–1139; h) Y. Arimoto, S. Ohkoshi, Z. J. Zhong, H. Seino, Y. Mizobe, K. Hashimoto, *J. Am. Chem. Soc.* **2003**, 125, 9240–9241; i) S. Ohkoshi, Y. Tsunobuchi, H. Takahashi, T. Hozumi, M. Shiro, K. Hashimoto, *J. Am. Chem. Soc.* **2007**, 129, 3084–3085.
- [6] a) J. M. Herrera, P. Franz, R. Podgajny, M. Pilkington, M. Biner, S. Decurtins, H. Stoeckli-Evans, A. Neels, R. Garde, Y. Dromée, M. Julve, B. Sieklucka, K. Hashimoto, S. Ohkoshi, M. Verdager, *C. R. Chim.* **2008**, 11, 1192–1199; b) M. Pilkington, S. Decurtins, *Chimia* **2000**, 54, 593–601; c) M. Arai, W. Kosaka, T. Matsuda, S. Ohkoshi, *Angew. Chem.* **2008**, 120, 6991–6993; *Angew. Chem. Int. Ed.* **2008**, 47, 6885–6887; d) R. Pradhan, C. Desplanches, P. Guionneau, J.-P. Sutter, *Inorg. Chem.* **2003**, 42, 6607–6609; e) W. Kosaka, K. Imoto, Y. Tsunobuchi, S. Ohkoshi, *Inorg. Chem.* **2009**, 48, 4604–4606; f) D. Pinkowicz, R. Podgajny, R. Pełka, W. Nitek, M. Bałanda, M. Makarewicz, M. Czapla, J. Żukrowski, C. Kapusta, D. Zaja, B. Sieklucka, *Dalton Trans.* **2009**, 7771–7777.
- [7] Since the ground Kramers doublet of an octahedral Co^{II} is populated, the sublattice magnetization of Co^{II} is $2.17 \mu_{\text{B}}$ ($g_{\text{Co}}J_{\text{Co}} = 13/3 \times 1/2$), whereas the sublattice magnetization of Nb^{IV} is $1 \mu_{\text{B}}$. Hence, the theoretical saturated magnetization of the ferromagnetic ordering is $5.3 \mu_{\text{B}}$ for the given formula.
- [8] a) P. M. Kiernan, W. P. Griffith, *J. Chem. Soc., Dalton Trans.* **1975**, 2489–2494; b) J. Burgess, *Metal Ions in Solution*, Ellis Horwood, New York, **1978**; c) R. G. Wilkins, *Kinetics and Mechanism of Reactions of Transition Metal Complexes*, Wiley-VCH, Weinheim, Germany, **1991**; d) L. G. Beauvais, M. P. Shores, J. R. Long, *J. Am. Chem. Soc.* **2000**, 122, 2763–2772; e) B. L. Vallee, B. Holmquist, *Methods for Determining Metal Ion Environments in Proteins: Structure and Function of Metalloproteins*, Elsevier/North-Holland, New York, **1980**.
- [9] At low humidity of 10% RH, a different absorption band appears around 590 nm in the UV/Vis spectrum (Figure 3b, bottom). The band is assigned to the d-d ($^4\text{A}_2 \rightarrow ^4\text{E}$, $^4\text{A}_2$) transition on five-coordinate square-pyramidal Co^{II} (5-Co^{II}). That is, the ligand water molecules are released from the Co ion.

Received: July 1, 2010

Published Online: August 17, 2010

Chromophoric Lewis Base Adducts of Methyltrioxorhenium: Synthesis, Catalysis and Photochemistry

Simone A. Hauser,^[a] Valentina Korinth,^[b] Eberhardt Herdtweck,^[a] Mirza Cokoja,^[a] Wolfgang A. Herrmann,^[a] and Fritz E. Kühn*^[a,b]

Keywords: Rhenium / Homogeneous catalysis / Photochemistry / Epoxidation / Stability constants

A series of chromophoric Lewis base adducts of methyltrioxorhenium (MTO) was examined. The ligands were pyridine derivatives with different size of the aromatic system and variable substituents, thus providing a variation of electronic and steric parameters. The complexes were fully characterised (UV/Vis, IR and NMR spectroscopy, single-crystal X-ray diffraction and elemental analysis) and their stability constants in dichloromethane were determined by means of UV/Vis spectroscopy. Moreover, this report presents a study of the influence of these N-donor ligands coordinated to MTO on the catalytic activity of epoxidation of 1-octene.

Each compound was tested twice; in a catalytic reaction under exclusion of light and in daylight. No significant differences in catalytic performance were found. The behaviour of the complexes under irradiation with UV light was investigated by means of ¹⁷O-NMR and UV/Vis spectroscopy. The herein exposed experiments aimed for probing potential beneficial effects of chromophoric N-donor ligands in MTO adducts, as they might activate the catalytic system by providing additional energy for weakening bonds that have to be broken during the catalytic cycle.

Introduction

Much research has been dedicated to the chemistry of methyltrioxorhenium (MTO) since its discovery by Beattie and Jones^[1] in the late 1970s and the improvement of the synthesis by Herrmann and co-workers^[2] some years later. The latter group discovered the ability of MTO to act as a versatile catalyst of various organic reactions.^[3] MTO can be used in several catalytic processes, for instance olefin metathesis^[4] and aldehyde olefination.^[5] Most recently, MTO has been successfully applied in deoxygenation of epoxides.^[6] However, the most important and thus best studied MTO-catalysed reaction is olefin epoxidation.^[7–9] Due to the strong Lewis acidity of the metal centre, undesired side reactions such as ring opening and diol formation are usually occurring. This can be prevented by addition of bases, mostly pyridine, bipyridine or pyrazole and their derivatives, as shown by Sharpless et al. and other groups.^[8,10–19] The photochemistry of MTO was for the first time under examination in the early 1990s.^[20,21] MTO solutions were found to be very sensitive to UV light, the rhenium-carbon bond was reported to be photolysed after a short irradiation

time, with subsequent formation of ReO₄[−] and ReO₃, at low and high concentrations.^[20] Some years later, the studies were extended to Lewis base adducts of MTO. Interesting properties of these adducts were published,^[22,23] but no further research was conducted in this direction. This prompted us to investigate the effect of a number of novel chromophoric Lewis base adducts of MTO with respect to the complex stability under irradiation with UV light.

Results and Discussion

Synthesis and Spectroscopic Characterisation

A series of chromophoric pyridine derivatives (**1–7**, Figure 1) was synthesised and the coordination to MTO was

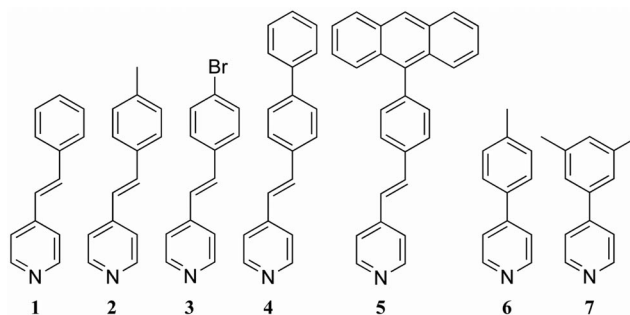


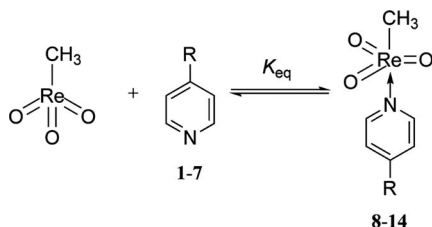
Figure 1. Overview of the pyridine derivatives employed as ligands for coordination to MTO.

[a] Chair of Inorganic Chemistry, Catalysis Research Center, Technische Universität München, Lichtenbergstrasse 4, 85748 Garching, Germany
Fax: +49-89-289-13473
E-mail: fritz.kuehn@ch.tum.de

[b] Molecular Catalysis, Catalysis Research Center, Technische Universität München, Lichtenbergstrasse 4, 85748 Garching, Germany

Supporting information for this article is available on the WWW under <http://dx.doi.org/10.1002/ejic.201000348>.

examined. Complexes **8–14** were formed by treatment of MTO with ligands **1–7** in a 1:1 ratio in diethyl ether at room temperature (Scheme 1). Subsequent cooling of the yellow solution led to precipitation of yellow crystals, which were isolated by filtration and purified by washing with *n*-hexane. The compounds obtained are stable to air, both in the solid state and in dichloromethane solution.



Scheme 1. Adduct formation of MTO with pyridine derivatives in solution.

Selected ^1H and ^{13}C NMR spectroscopic data of compounds **8–14** are shown in Table 1. The proton signals of the MTO methyl group of the complexes are considerably shifted to higher field, indicating the strength of the Re–N bond.^[15] The same effect is observed in the ^{13}C NMR spectra. The vicinal protons to the nitrogen of the ligand have a different electronic environment, similar to the methyl group of the MTO, which is manifested by a high-field shift compared to the free ligand.

Table 1. Selected ^1H and ^{13}C NMR spectroscopic data for complexes **8–14** in CDCl_3 .

| | $\alpha\text{-H}$ ligand, ^1H δ [ppm] | $\alpha\text{-H}$ adduct ^1H , δ [ppm] | Re-CH ₃ , ^1H δ [ppm] | Re-CH ₃ , ^{13}C δ [ppm] |
|-----------|--|---|---|--|
| MTO | – | – | 2.67 | 19.0 |
| 8 | 8.51 (1) | 8.29 | 2.03 | 24.7 |
| 9 | 8.55 (2) | 8.20 | 1.92 | 25.1 |
| 10 | 8.58 (3) | 8.26 | 1.96 | 24.0 |
| 11 | 8.59 (4) | 8.34 | 2.13 | 24.4 |
| 12 | 8.63 (5) | 8.33 | 2.00 | 24.9 |
| 13 | 8.63 (6) | 8.31 | 1.97 | 24.8 |
| 14 | 8.65 (7) | 8.32 | 1.98 | 24.4 |

In the IR spectra, a red-shift of Re = O bands compared to free MTO is observable. This gives rise to an enhanced electron density donated from the ligand to the Re centre, causing weakening of the Re=O bond (see Table 2).

Table 2. Characteristic IR vibrations of CH_3ReO_3 fragments (cm^{-1}) in **8–14**.

| MTO | 8 | 9 | 10 | 11 | 12 | 13 | 14 | Assignment |
|-----|----------|----------|---------------------|-----------|-----------|-----------|-----------|----------------------------|
| 998 | 934 | 936 | 931 | n.o. | n.o. | 934 | 931 | ReO ₃ sym str. |
| 965 | 927 | 926 | n.o. ^[a] | 927 | 928 | 927 | n.o. | ReO ₃ asym str. |

[a] Not observed.

X-ray Crystal Structure of Ligand **5** and Complexes **8–14**

The solid-state structure of the synthesised compounds **5** and **8–14** was measured; one example is shown in Figure 2. Selected bond lengths are given in Table 3. With one exception (compound **11**), the N-base ligand coordinates *trans* to

the methyl group to the rhenium centre. Complex **11**, however, exists in both *cis* and *trans* arrangements in the solid state. Together with the finding that only one peak is visible in the ^{17}O -NMR spectrum, this strongly indicates that packing forces are responsible for the solid-state configuration, rather than electronic or steric ligand effects. Moreover, this conclusion is in accordance with previously reported data.^[24]

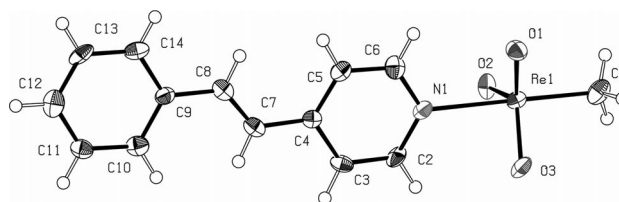


Figure 2. PLATON view of the solid-state structure of complex **8**. The thermal ellipsoids are shown at the 50% probability level.

Table 3. Selected bond lengths for complexes **8–14** (*trans* configuration) determined by single-crystal X-ray diffraction.

| | Re–N [Å] | Re–C [Å] | Re–O [Å] |
|--------------------------|----------|----------|--|
| MTO ^[a] | – | 2.074(4) | 1.703(2) |
| 8 | 2.422(5) | 2.113(7) | 1.712(3) 1.706(6) 1.726(7) |
| 9 | 2.445(5) | 2.094(6) | 1.718(4) 1.705(4) 1.707(4) |
| 10 ^[b] | 2.439(4) | 2.099(5) | 1.717(4) 1.716(3) 1.716(3) |
| | 2.438(5) | 2.102(6) | 1.711(3) 1.716(4) 1.720(3) |
| 11 ^[b] | 2.372(3) | 2.112(4) | 1.722(3) 1.719(3) 1.713(3) |
| | 2.439(3) | 2.081(5) | 1.714(3) 1.712(3) 1.714(3) |
| 12 | 2.418(2) | 2.091(3) | 1.720(2) 1.711(2) 1.714(2) |
| 13 | 2.417(3) | 2.092(4) | 1.716(4) 1.716(3) 1.722(3) |
| 14 ^[b] | 2.408(4) | 2.102(5) | 1.713(2) 2 × 1.708(4) 2.392(4) 2.101(5) 1.706(3) 2 × 1.694(4) |

[a] Values taken from ref.^[25]. [b] The values of the second crystallographically independent molecule are printed in *italics*.

Determination of Formation Constants

The formation constants of the MTO – ligand adducts **8–14** were determined by means of UV/Vis spectroscopy.^[26] Scheme 1 shows the equilibrium that is established in presence of MTO and a pyridine derivative. According to Equation (1), which is derived from the Lambert–Beer law (path length: 1 cm), the absorbance of the solution (*Abs*) changes in function of the presence of free ligand (L), uncoordinated MTO (M) and the MTO-ligand adduct (ML).

$$Abs = \varepsilon_L[L] + \varepsilon_M[M] + \varepsilon_{ML}[ML] \quad (1)$$

The adduct concentration [ML] can be expressed using the formation constant (K_{eq}) by taking into account the molar balance $[M]_T = [M] + [ML]$, leading to Equation (2).

$$Abs = \epsilon_L [L] + \epsilon_M [M] + \frac{\epsilon_{ML} [M]_T \cdot K_{eq} [L]}{1 + K_{eq} [L]} \quad (2)$$

Above 330 nm, the absorbance of MTO is negligible, i.e. $\epsilon_M \approx 0$.^[27] If the absorbance of the free ligands at the chosen wavelength can also be ignored, i.e. $\epsilon_L \approx 0$, then Equation (3) can be used to calculate the formation constant.

$$Abs = \frac{\epsilon_{ML} [M]_T \cdot K_{eq} [L]}{1 + K_{eq} [L]} \quad (3)$$

The values of the adduct formation constants (Table 4) are calculated by fitting of experimental absorbance data to Equation (2) or (3). Figure 3 shows the change in the absorption spectrum upon successive addition of MTO to a ligand solution in CH_2Cl_2 . In the case of the compound **10**, complex formation can be noticed at 350 nm. Thus, the values at this wavelength have been used for the curve fitting according to Equation (3) (see Figure 4).

Table 4. Formation constants of compounds **8–14** in CH_2Cl_2 .

| | Absorbance [nm] | Formation constant (K_{eq}) [L mol^{-1}] |
|-----------|-----------------|---|
| 8 | 340 | 431 ± 27 |
| 9 | 355 | 563 ± 88 |
| 10 | 350 | 386 ± 47 |
| 11 | 370 | 309 ± 36 |
| 12 | 335 | 78 ± 25 |
| 13 | 300 | 348 ± 93 |
| 14 | 300 | 286 ± 98 |

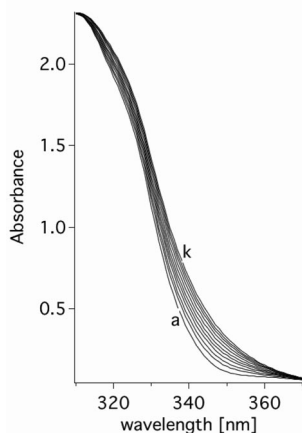


Figure 3. Change in the absorption in function of complex formation (**10**). (a) free ligand ($[3] = 0.1 \text{ mM}$), successive addition of 1 equiv. of MTO, (k) ligand with 10 equiv. MTO.

The values of the formation constants for complexes **8–14** are comparable to those reported in literature.^[26,28–30] Moreover, the influence of both the electronic and steric nature of the ligand can be seen. The stability of the adducts is higher when the ligand has electron-donating substituents and is less sterically crowded. The electronic effect is nicely seen when comparing the formation constant of

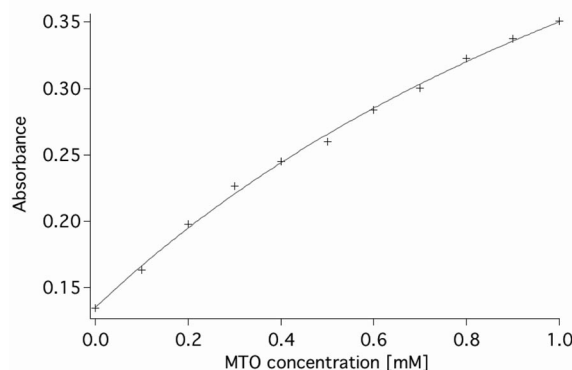


Figure 4. Curve fitting with Equation 3 for determination of formation constant of complex **10**.

complex **9** with that of complex **10**. The steric effect accounts for the difference in the value of the formation constant of complex **13** and complex **14**.

Application in Epoxidation Catalysis

The performance of ligands **2–7** was tested in the MTO-catalysed epoxidation of 1-octene with hydrogen peroxide. *tert*-Butylpyridine (*t*Bu-Pyr) was chosen as a benchmark ligand. A catalyst:ligand:oxidant:substrate ratio of 1:5:150:100 was used in all experiments, unless stated otherwise. The catalytic tests were performed at room temperature and twice with each ligand: once with exclusion of light and once in light with the goal to establish a statement about the supposed beneficial effect of chromophoric pyridine derivatives with respect to the already known advantages of simple pyridine derivatives in epoxidation catalysis with MTO.^[19] Further details are given in the Exp. Section. No significant diol formation or formation of other by-products could be observed.

Table 5 summarises the turnover frequencies (TOF) of the different catalytic systems tested. Maximum epoxide yield is obtained after 24 h reaction time, with a substrate conversion between 50 and 80% (Figure 5). *t*Bu-Pyr shows no significant advantage in catalytic performance compared to the chromophoric pyridine derivatives. Moreover, it can be noted that the advantage of running the catalytic reaction under exclusion of light is negligible with either type of pyridine ligand. The yields of 1-octene epoxide with the ligand additives tested within this work are comparable to

Table 5. Turnover frequencies [$\text{mol}(\text{epoxide}) \text{ mol}(\text{cat})^{-1} \text{ h}^{-1}$] determined after 5 min.

| Ligand | TOF [h^{-1}] | Yield [%], after 24 h with exclusion of light |
|-----------------|-------------------------|---|
| 2 | 63 | 76 |
| 3 | 44 | 69 |
| 4 | 65 | 69 |
| 5 | 46 | 65 |
| 6 | 49 | 73 |
| 7 | 41 | 72 |
| <i>t</i> Bu-Pyr | 35 | 71 |

the yield achieved with MTO alone.^[31] Nevertheless, they are far from those obtained with 3-methylpyrazole or pyrazole under the same conditions.^[31]

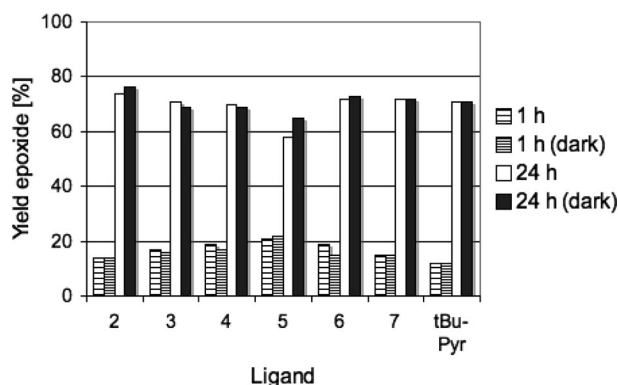


Figure 5. 1-Octene epoxide yields with different ligands.

Photostability of the Synthesised Compounds

One aim of this work is to probe potential beneficial effect of chromophoric Lewis bases in MTO adducts. They might activate the catalytic system by providing additional energy for weakening bonds that have to be broken during the catalytic cycle. However, photoinduced homolysis of the Re–CH₃ bond in solution is the most common way of degradation of MTO.^[20] Vogler et al. reported the photoassisted isomerisation of 4-styrylpyridine, where the complex remained intact, i.e. the MTO was not affected by UV-radiation.^[23] This led to the hypothesis that larger chromophoric systems might lead to stable MTO Lewis base adducts on the one hand, and act as a photosensitisers on the other hand. The most convenient approaches to study the stability or the photo-induced degradation of the MTO adducts are ¹⁷O-NMR and UV/Vis spectroscopy.

For the NMR studies, a 0.1 M solution of the complexes in CDCl₃ was used and treated with UV light ($\lambda = 368$ nm). In a second experiment, a fivefold excess of ligand was added to MTO, in order to mimic the reaction conditions of the catalytic tests (vide supra). The chemical shift of the oxygen atoms of the freshly synthesised complexes was found to be between 865 ppm and 885 ppm which is consistent with the reported literature values.^[32,33] Upon irradiation, already after 6 min a peak at $\delta = 563$ ppm was detected, which could be attributed to the perrhenate anion.^[32] This peak became more pronounced after longer irradiation time (see Figure 6). There was no significant difference in stability of the MTO in the two experiments performed. Noteworthy, all complexes synthesised in this work have shown the same behaviour under irradiation with UV light (see Supporting Information).

The UV/Vis spectra were recorded in CH₂Cl₂. A 0.1 M solution of selected complexes was irradiated with UV light and several samples were taken. Figure 7 shows the spectral change over a time span of 2 h. Ligand absorption is very strong, it shows a maximum at 325 nm. It partially overlaps

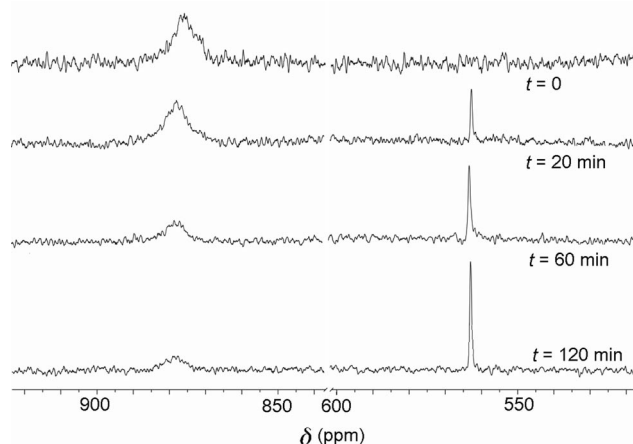


Figure 6. Time resolved ¹⁷O-NMR spectra of complex **11** before (top) and after irradiation with UV light. The signal of the MTO oxo moieties at $\delta = 879$ ppm is broadened due to fluxional equilibrium of complex formation, whereas the sharp peak at $\delta = 563$ ppm can be assigned [ReO₄[−]].

complex absorption as well as the absorbance pattern of free MTO.^[20] Upon photolytic degradation of MTO, the ligand is protonated. Thus, its absorbance spectrum changes by a shift of the maximum to 375 nm.

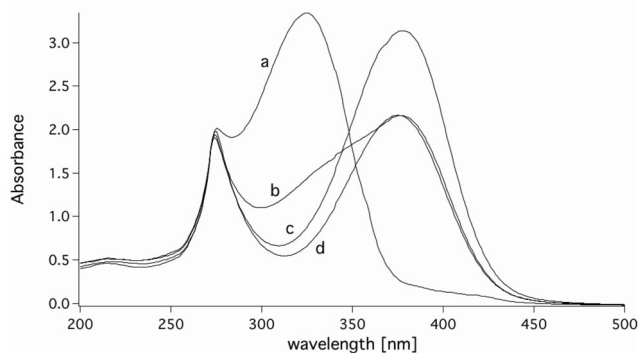


Figure 7. UV/Vis spectra of complex **11** in CH₂Cl₂ ($c = 0.16$ mM). (a) Initial spectrum; (b) after 20 min exposure to UV light; (c) after 60 min; (d) after 120 min, the decrease in intensity of the peak at 377 nm can be explained by precipitation of the perrhenate and protonated ligand.

The above-mentioned experiments clearly show that both the MTO and the ligands are affected by prolonged irradiation with UV light. Thus, no additional stability is brought to the adducts by the use of chromophoric pyridine derivatives. Despite of the use of chromophoric pyridine derivatives as ligands on MTO, the obtained adducts are not stable to UV light. However, as described above, the catalytic epoxidation is not influenced by light.

Conclusions

In this study, seven chromophoric pyridine derivatives were prepared and treated with MTO to form seven Lewis base adducts of MTO. They have been fully characterised and tested as catalysts in the epoxidation of 1-octene with

H₂O₂. With respect to the benchmark ligand *tert*-butylpyridine, the presented ligands do not show any advantages in the epoxidation of 1-octene, whether performed under exclusion of light or in daylight (see Figure 5). Moreover, the photochemistry of the complexes was studied by means of UV/Vis and ¹⁷O-NMR spectroscopy. The chromophoric ligands did not influence the adduct stability under UV irradiation. Complex decomposition occurred through the reported pathway,^[20] as formation of the perhenate anion was already observable after a short irradiation time with UV light (see Figure 6 and Figure 7).

Experimental Section

Materials and Methods: All experimental work was carried out using standard Schlenk techniques under argon. Solvents were dried by standard procedures (hexane and diethyl ether over Na/benzophenone; CH₂Cl₂ over CaH₂), distilled and stored under argon over molecular sieves. High resolution NMR spectra were measured with Bruker Avance DPX-400 (¹H: 400 MHz; ¹³C: 100.6 MHz; ¹⁷O: 54.2 MHz), and JEOL NMR GX-400 (¹H: 400 MHz; ¹³C: 100.6 MHz) spectrometers. The UV/Vis spectra were recorded on a JASCO UV/Vis V-550 spectrophotometer and the IR spectra on a Perkin–Elmer 1600 series FT-IR instrument. Microanalyses of the obtained products were performed in the Mikroanalytisches Labor of the Technical University of Munich, Garching, Germany. MTO was synthesised according to literature procedures.^[34]

Ligand Synthesis: Ligands 1–3 were synthesised by treating a solution of 4-picoline (2.48 mmol) in THF at –60 °C with an equimolar amount of lithium diisopropylamine in THF.^[35] The alcoholate was formed upon addition of the corresponding aldehyde, which was subsequently eliminated by refluxing in concentrated acetic acid for 18 h to form the C–C double bond. Purification was done by column chromatography on silica gel. The synthesis of ligands 4–7 was based on the Suzuki cross coupling mechanism described by Fu et al.^[36] The heteroaryl boronic acid reacted with an aryl bromide in refluxing dioxane, whereas the reaction was catalysed by [Pd₂(dba)₃] (dba = dibenzylideneacetone), PCy₃ and K₃PO₄ (aq.). Subsequent purification steps included filtration, extraction of the filtrate and column chromatography.

4-Styrylpyridine (1): Yield 314 mg (70%). ¹H NMR (400 MHz, CDCl₃, 25 °C): δ = 8.51 [d, *J*(H,H) = 4.8 Hz, 2 H, NC₂H₂C₂H₂C-], 7.48 [d, *J*(H,H) = 7.4 Hz, 2 H, -CC₂H₂C₂H₂CH], 7.35–7.24 (m, 4 H, NC₂H₂C₂H₂C-CHCH-CC₂H₂C₂H₂CH), 7.21 [d, *J*(H,H) = 9.8 Hz, 2 H, -CC₂H₂C₂H₂CH], 6.96 [d, *J*(H,H) = 15.9 Hz, 1 H, Pyr-CHCH-Ph] ppm. ¹³C NMR (100.6 MHz, CDCl₃, 25 °C): δ = 150.2 (2 C), 144.6 (2 C), 136.2 (1 C), 133.2 (1 C), 128.8 (2 C), 128.7 (2 C), 127.0 (1 C), 126.0 (2 C), 120.8 (1 C) ppm.

4-[2-(4-Methylphenyl)ethenyl]pyridine (2): Yield 386 mg (80%). ¹H NMR (400 MHz, CDCl₃, 25 °C): δ = 8.55 [d, *J*(H,H) = 6.0 Hz, 2 H, NC₂H₂C₂H₂C-], 7.43 [d, *J*(H,H) = 8.0 Hz, 2 H, NC₂H₂C₂H₂C-], 7.34 [d, *J*(H,H) = 6.0 Hz, 2 H, -CC₂H₂C₂H₂CCH₃], 7.27 [d, *J*(H,H) = 13.6 Hz, 1 H, -PhCHCHPyr-], 7.18 [d, *J*(H,H) = 7.6 Hz, 2 H, -CC₂H₂C₂H₂CCH₃], 6.95 [d, *J*(H,H) = 16.0 Hz, 1 H, -PhCHCHPyr-], 2.37 (s, 3 H, -CC₂H₂C₂H₂CCH₃) ppm. ¹³C NMR (100.6 MHz, CDCl₃, 25 °C): δ = 150.2 (1 C, NC₂H₂C₂H₂C-), 144.8 (2 C, NC₂H₂C₂H₂C-), 138.9 (1 C, -CC₂H₂C₂H₂CCH₃), 133.4 (1 C, -CC₂H₂C₂H₂CCH₃), 133.1 (1 C, -PhCHCHPyr-), 129.5 (2 C, -CC₂H₂C₂H₂CCH₃), 126.9 (2 C, -CC₂H₂C₂H₂CCH₃), 124.9 (1

C, -PhCHCHPyr-), 120.8 (2 C, NC₂H₂C₂H₂C-), 21.3 (1 C, -PhCH₃) ppm.

4-[2-(4-Bromophenyl)ethenyl]pyridine (3): Yield 503 mg (78%). ¹H NMR (400 MHz, CDCl₃, 25 °C): δ = 8.58 [d, *J*(H,H) = 6.0 Hz, 2 H, NC₂H₂C₂H₂C-], 7.50 [d, *J*(H,H) = 8.4 Hz, 2 H, -CC₂H₂C₂H₂CBr], 7.38 [d, *J*(H,H) = 8.4 Hz, 2 H, -CC₂H₂C₂H₂CBr], 7.34 [d, *J*(H,H) = 5.2 Hz, 2 H, NC₂H₂C₂H₂C-], 7.22 [d, *J*(H,H) = 16.4 Hz, 1 H, PyrCHCH-], 6.98 [d, *J*(H,H) = 16.4 Hz, 1 H, PyrCHCH-] ppm. ¹³C NMR (100.6 MHz, CDCl₃, 25 °C): δ = 150.30 (2 C, NC₂H₂C₂H₂C-), 144.23 (1 C, NC₂H₂C₂H₂C-), 135.13 (1 C, -CC₂H₂C₂H₂CBr), 132.02 (2 C, -CC₂H₂C₂H₂CBr), 131.87 (1 C, PyrCHCH-), 128.44 (2 C, -CC₂H₂C₂H₂CBr), 126.76 (1 C, PyrCHCH-), 122.68 (1 C, -CC₂H₂C₂H₂CBr), 120.85 (2 C, NC₂H₂C₂H₂C-) ppm.

4-[2-(Biphenyl)ethenyl]pyridine (4): Yield 980 mg (83%). ¹H NMR (400 MHz, CDCl₃, 25 °C): δ = 8.59 [d, *J*(H,H) = 8.0 Hz, 2 H, NC₂H₂C₂H₂C-], 7.63 (m, 7 H, -CC₂H₂C₂H₂C-CC₂H₂C₂H₂C-), 7.46 [t, *J*(H,H) = 8.0 Hz, 2 H, -CC₂H₂C₂H₂CH], 7.39 (m, 2 H, NC₂H₂C₂H₂C-), 7.35 [d, *J*(H,H) = 16.0 Hz, 1 H, Pyr-CHCH-Ph-Ph], 7.06 [d, *J*(H,H) = 16.0 Hz, 1 H, Pyr-CHCH-Ph-Ph] ppm. ¹³C NMR (100.6 MHz, CDCl₃, 25 °C): δ = 150.20 (2 C, NC₂H₂C₂H₂C-), 144.62 (1 C, NC₂H₂C₂H₂C-), 141.51 (1 C, -CC₂H₂C₂H₂CH), 140.38 (1 C, -CC₂H₂C₂H₂C-CC₂H₂C₂H₂CH), 135.16 (1 C, -CC₂H₂C₂H₂C-CC₂H₂C₂H₂CH), 132.71 (1 C, Pyr-CHCH-Ph-Ph), 128.85 (2 C, -CC₂H₂C₂H₂CH), 127.58 (1 C, -CC₂H₂C₂H₂CH), 127.47 (4 C, -CC₂H₂C₂H₂C-CC₂H₂C₂H₂CH), 126.95 (2 C, -CC₂H₂C₂H₂C-CC₂H₂C₂H₂CH), 125.99 (1 C, Pyr-CHCH-Ph-Ph), 120.83 (2 C, NC₂H₂C₂H₂C-) ppm.

4-[2-(4-Anthracenylphenyl)ethenyl]pyridine (5): Yield 880 mg (65%). ¹H NMR (400 MHz, CDCl₃, 25 °C): δ = 8.63 [d, *J*(H,H) = 4.9 Hz, 2 H], 8.52 (s, 1 H), 8.06 [d, *J*(H,H) = 8.6 Hz, 2 H], 7.77 [d, ³*J*(H,H) = 8.6 Hz, 2 H], 7.69 [d, *J*(H,H) = 8.6 Hz, 2 H], 7.47 [t, *J*(H,H) = 8.6, 7.4 Hz, 7 H], 7.37 [t, ³*J*(H,H) = 7.4, 7.4 Hz, 2 H], 7.18 [d, *J*(H,H) = 15.9 Hz, 1 H] ppm. ¹³C NMR (100.6 MHz, CDCl₃, 25 °C): δ = 150.2 (2 C), 144.7 (1 C), 139.5 (1 C), 136.3 (1 C), 135.4 (1 C), 132.9 (1 C), 131.8 (2 C), 131.4 (2 C), 130.1 (2 C), 128.4 (1 C), 127.0 (3 C), 126.8 (1 C), 126.6 (2 C), 126.3 (2 C), 125.5 (1 C), 125.1 (2 C), 120.9 (2 C) ppm.

4-Tolylpyridine (6): Yield 193 mg (60%). ¹H NMR (400 MHz, CDCl₃, 25 °C): δ = 8.63 [d, *J*(H,H) = 5.4 Hz, 2 H, NC₂H₂C₂H₂C-], 7.53 [d, *J*(H,H) = 8.0 Hz, 2 H, NC₂H₂C₂H₂C-], 7.48 [d, *J*(H,H) = 6.0 Hz, 2 H, -CC₂H₂C₂H₂CCH₃], 7.28 [d, *J*(H,H) = 8.0 Hz, 2 H, -CC₂H₂C₂H₂CCH₃], 2.40 (s, 3 H, -PhCH₃) ppm. ¹³C NMR (100.6 MHz, CDCl₃, 25 °C): δ = 150.2 (2 C, NC₂H₂C₂H₂C-), 148.2 (1 C, NC₂H₂C₂H₂C-), 139.2 [1 C, -CC₂H₂C₂H₂C(CH₃)], 135.2 [1 C, -CC₂H₂C₂H₂C(CH₃)], 129.8 [2 C, -CC₂H₂C₂H₂C(CH₃)], 126.8 [2 C, -CC₂H₂C₂H₂C(CH₃)], 121.4 (2 C, NC₂H₂C₂H₂C-), 21.2 (1 C, -PhCH₃) ppm.

4-(3,5-Dimethylphenyl)pyridine (7): Yield 450 mg (66%). ¹H NMR (400 MHz, CDCl₃, 25 °C): δ = 8.65 [d, *J*(H,H) = 6.8 Hz, 2 H, NC₂H₂C₂H₂C-], 7.50 [d, *J*(H,H) = 6.8 Hz, 2 H, NC₂H₂C₂H₂C-], 7.27 [s, 2 H, -CC₂H₂C₂(CH₃)₂CH], 7.10 [s, 1 H, -CC₂H₂C₂(CH₃)₂CH], 2.41 [s, 6 H, -CC₂H₂C₂(CH₃)₂CH] ppm. ¹³C NMR (100.6 MHz, CDCl₃, 25 °C): δ = 150.15 (2 C, NC₂H₂C₂H₂C-), 148.65 (1 C, NC₂H₂C₂H₂C-), 138.71 [2 C, -CC₂H₂C₂(CH₃)₂CH], 138.18 [1 C, -CC₂H₂C₂(CH₃)₂CH], 130.67 [1 C, -CC₂H₂C₂(CH₃)₂CH], 124.86 [2 C, -CC₂H₂C₂(CH₃)₂CH], 121.69 (2 C, NC₂H₂C₂H₂C-), 21.36 [2 C, -CC₂H₂C₂(CH₃)₂CH] ppm.

Typical Procedure for the Preparation of the Chromophoric Lewis Base Adducts of MTO: An equimolar amount of MTO and ligand was dissolved in diethyl ether and the solution was stirred for 1 h

before cooling the mixture in an ice bath. A yellow precipitate formed, which was filtered and washed with hexane. The solid was dried in vacuo and analysed by standard analysis methods.

Methyl(4-styrylpyridine)trioxorhenium (8): Yield 58 mg (76%). ^1H NMR (400 MHz, CDCl_3 , 25 °C): δ = 8.29 [d, $J(\text{H,H})$ = 6.2 Hz, 2 H, $\text{NC}_2\text{H}_2\text{C}_2\text{H}_2\text{C}-$], 7.54 [d, $J(\text{H,H})$ = 7.4 Hz, 2 H, $-\text{CC}_2\text{H}_2\text{C}_2\text{H}_2\text{CH}$], 7.45 (m, 6 H, $\text{NC}_2\text{H}_2\text{C}_2\text{H}_2\text{C}-\text{CHCH}-\text{CC}_2\text{H}_2\text{C}_2\text{H}_2\text{CH}$), 7.01 [d, $J(\text{H,H})$ = 17.2 Hz, 1 H, $\text{Pyr}-\text{CHCH}-\text{Ph}$], 2.03 (s, 3 H, $-\text{ReCH}_3$) ppm. ^{13}C NMR (100.6 MHz, CDCl_3 , 25 °C): δ = 147.2 (2 C), 135.6 (2 C), 135.5 (1 C), 129.3 (1 C), 128.9 (2 C), 127.3 (2 C), 124.7 (1 C), 121.9 (2 C), 24.7 (1 C) ppm. IR (KBr): $\tilde{\nu}$ = 1605 (vs), 1499 (w), 1449 (w), 1428 (w), 1384 (w), 1013 (m), 971 (m), 961 (w), 934 (vs), 927 (vs), 877 (w), 818 (m), 559 (w), 548 (m) cm^{-1} . $\text{C}_{14}\text{H}_{14}\text{NO}_3\text{Re}$ (430.47): calcd. C 39.06, H 3.28, N 3.25; found C 39.56, H 3.31, N 3.34.

Methyl[4-[2-(4-Methylphenyl)ethenyl]pyridine]trioxorhenium (9): Yield 53 mg (72%). ^1H NMR (400 MHz, CDCl_3 , 25 °C): δ = 8.20 [d, $J(\text{H,H})$ = 5.4 Hz, 2 H, $\text{NC}_2\text{H}_2\text{C}_2\text{H}_2\text{C}-$], 7.42 (m, 4 H, $\text{NC}_2\text{H}_2\text{C}_2\text{H}_2\text{C}-$, $-\text{CC}_2\text{H}_2\text{C}_2\text{H}_2\text{CCH}_3$), 7.30 [d, $J(\text{H,H})$ = 16.2 Hz, 1 H, $-\text{PhCHCHPyr}$], 7.20 [d, $J(\text{H,H})$ = 7.9 Hz, 2 H, $-\text{CC}_2\text{H}_2\text{C}_2\text{H}_2\text{CCH}_3$], 6.93 [d, $J(\text{H,H})$ = 16.2 Hz, 1 H, $-\text{PhCHCHPyr}$], 2.37 (s, 3 H, $-\text{PhCH}_3$), 1.92 (s, 3 H, $-\text{ReCH}_3$) ppm. ^{13}C NMR (100.6 MHz, CDCl_3 , 25 °C): δ = 147.94 (1 C, $\text{NC}_2\text{H}_2\text{C}_2\text{H}_2\text{C}-$), 147.06 (2 C, $\text{NC}_2\text{H}_2\text{C}_2\text{H}_2\text{C}-$), 139.66 (1 C, $-\text{CC}_2\text{H}_2\text{C}_2\text{H}_2\text{CCH}_3$), 135.48 (1 C, $-\text{CC}_2\text{H}_2\text{C}_2\text{H}_2\text{CCH}_3$), 132.76 (1 C, $-\text{PhCHCHPyr}$), 129.65 (2 C, $-\text{CC}_2\text{H}_2\text{C}_2\text{H}_2\text{CCH}_3$), 127.23 (2 C, $-\text{CC}_2\text{H}_2\text{C}_2\text{H}_2\text{CCH}_3$), 123.52 (1 C, $-\text{PhCHCHPyr}$), 121.85 (2 C, $\text{NC}_2\text{H}_2\text{C}_2\text{H}_2\text{C}-$), 25.08 (1 C, $-\text{ReCH}_3$), 21.36 (1 C, $-\text{PhCH}_3$) ppm. IR (KBr): $\tilde{\nu}$ = 3434 (w), 3025 (w), 1636 (m), 1602 (vs), 1514 (m), 1428 (m), 1384 (w), 1210 (w), 1183 (w), 1013 (s), 975 (m), 936 (vs), 926 (vs), 826 (s), 736 (w), 706 (w), 624 (m), 547 (s), 502 (m) cm^{-1} . $\text{C}_{15}\text{H}_{16}\text{NO}_3\text{Re}$ (444.50): calcd. C 40.53, H 3.63, N 3.15; found C 38.55, H 3.33, N 3.16.

[4-[2-(4-Bromophenyl)ethenyl]pyridine]methyltrioxorhenium (10): Yield 68 mg (79%). ^1H NMR (400 MHz, CDCl_3 , 25 °C): δ = 8.26 [d, $J(\text{H,H})$ = 6.2 Hz, 2 H, $\text{NC}_2\text{H}_2\text{C}_2\text{H}_2\text{C}-$], 7.52 [d, $J(\text{H,H})$ = 8.3 Hz, 2 H, $-\text{CC}_2\text{H}_2\text{C}_2\text{H}_2\text{CBr}$], 7.41 (m, 4 H, $\text{NC}_2\text{H}_2\text{C}_2\text{H}_2\text{C}-$, $-\text{CC}_2\text{H}_2\text{C}_2\text{H}_2\text{CBr}$), 7.25 [d, $J(\text{H,H})$ = 16.4 Hz, 1 H, $\text{Pyr}-\text{CHCH}$], 6.98 [d, $J(\text{H,H})$ = 16.2 Hz, 1 H, $\text{Pyr}-\text{CHCH}$], 1.96 (s, 3 H, $-\text{ReCH}_3$) ppm. ^{13}C NMR (100.6 MHz, CDCl_3 , 25 °C): δ = 147.3 (2 C), 147.0 (1 C), 134.5 (1 C), 134.1 (1 C), 132.1 (3 C), 128.7 (2 C), 125.4 (1 C), 123.5 (1 C), 122.0 (1 C), 24.0 (1 C) ppm. IR (KBr): $\tilde{\nu}$ = 3466 (w), 3048 (w), 2973 (w), 1895 (w), 1773 (w), 1637 (m), 1610 (vs), 1586 (s), 1497 (m), 1483 (m), 1428 (s), 1393 (m), 1385 (m), 1209 (m), 1070 (vs), 1017 (vs), 1008 (s), 975 (s), 970 (s), 928 (vs), 883 (m), 875 (m), 829 (vs), 738 (w), 674 (w), 583 (m), 557 (s), 542 (s), 496 (w) cm^{-1} . $\text{C}_{14}\text{H}_{13}\text{BrNO}_3\text{Re}$ (509.37): calcd. C 33.01, H 2.57, N 2.75; found C 32.88, H 2.53, N 2.78.

[4-[2-(Biphenyl)ethenyl]pyridine]methyltrioxorhenium (11): Yield 69 mg (80%). ^1H NMR (400 MHz, CDCl_3 , 25 °C): δ = 8.34 [d, $J(\text{H,H})$ = 6.2 Hz, 2 H, $\text{NC}_2\text{H}_2\text{C}_2\text{H}_2\text{C}-$], 7.62 (m, 6 H, $-\text{CC}_2\text{H}_2\text{C}_2\text{H}_2\text{C}-\text{CC}_2\text{H}_2\text{C}_2\text{H}_2\text{CH}$), 7.47–7.37 (m, 5 H, $\text{NC}_2\text{H}_2\text{C}_2\text{H}_2\text{C}-$, $-\text{CC}_2\text{H}_2\text{C}_2\text{H}_2\text{CH}$), 7.36 [d, $J(\text{H,H})$ = 16.2 Hz, 1 H, $\text{Pyr}-\text{CHCH}-\text{Ph}-\text{Ph}$], 7.04 [d, $J(\text{H,H})$ = 16.2 Hz, 1 H, $\text{Pyr}-\text{CHCH}-\text{Ph}-\text{Ph}$], 2.13 (s, 3 H, $-\text{ReCH}_3$) ppm. ^{13}C NMR (100.6 MHz, CDCl_3 , 25 °C): δ = 147.7 (2 C), 147.0 (1 C), 142.0 (1 C), 140.2 (1 C), 140.2 (1 C), 134.6 (2 C), 128.9 (2 C), 127.7 (2 C), 127.6 (2 C), 127.0 (2 C), 124.8 (1 C), 121.7 (2 C), 24.4 (1 C) ppm. IR (KBr): $\tilde{\nu}$ = 344 (w), 3032 (w), 1600 (s), 1487 (m), 1426 (m), 1204 (w), 1195 (w), 1015 (m), 976 (m), 934 (vs), 927 (vs), 879 (w), 836 (m), 765 (m), 737 (w), 690 (m), 638 (w), 561 (m), 529 (w) cm^{-1} . $\text{C}_{20}\text{H}_{18}\text{NO}_3\text{Re}$

(506.57): calcd. C 47.40, H 3.58, N 2.77; found C 47.33, H 3.58, N 2.77.

[4-[2-(4-Anthracenylphenyl)ethenyl]pyridine]methyltrioxorhenium (12): Yield 87 mg (84%). ^1H NMR (400 MHz, CDCl_3 , 25 °C): δ = 8.51 (s, 1 H), 8.33 [d, $J(\text{H,H})$ = 6.2 Hz, 2 H], 8.05 [d, $J(\text{H,H})$ = 8.3 Hz, 2 H], 7.76 [d, $J(\text{H,H})$ = 8.3 Hz, 2 H], 7.67 [d, $J(\text{H,H})$ = 8.7 Hz, 2 H], 7.47 (m, 7 H), 7.35 [m, $J(\text{H,H})$ = 15.6 Hz, 2 H], 7.15 [d, $J(\text{H,H})$ = 16.2 Hz, 1 H], 2.00 (s, 3 H, $-\text{ReCH}_3$) ppm. ^{13}C NMR (100.6 MHz, CDCl_3 , 25 °C): δ = 148.2 (2 C), 146.7 (1 C), 140.0 (1 C), 136.1 (1 C), 135.0 (1 C), 134.6 (1 C), 132.0 (2 C), 131.4 (2 C), 130.1 (2 C), 128.4 (1 C), 127.2 (3 C), 126.9 (1 C), 126.5 (2 C), 125.6 (2 C), 125.4 (1 C), 125.2 (2 C), 121.7 (2 C), 24.9 (1 C, $-\text{ReCH}_3$) ppm. IR (KBr): $\tilde{\nu}$ = 3434 (w), 3050 (w), 1607 (s), 1592 (m), 1443 (w), 1426 (m), 1412 (w), 1384 (m), 1066 (w), 1015 (m), 969 (w), 931 (vs), 881 (m), 827 (m), 790 (w), 735 (s), 653 (w), 635 (w), 613 (m), 568 (w), 554 (m) cm^{-1} . 541 (m), 422 (w) cm^{-1} . $\text{C}_{28}\text{H}_{22}\text{NO}_3\text{Re}$ (606.69): calcd. C 55.41, H 3.66, N 2.31; found C 55.80, H 3.72, N 2.24.

Methyl(4-tolylpyridine)trioxorhenium (13): Yield 67 mg (97%). ^1H NMR (400 MHz, CDCl_3 , 25 °C): δ = 8.31 [d, $J(\text{H,H})$ = 6.2 Hz, 2 H, $\text{NC}_2\text{H}_2\text{C}_2\text{H}_2\text{C}-$], 7.56 [d, $J(\text{H,H})$ = 6.2 Hz, 2 H, $\text{NC}_2\text{H}_2\text{C}_2\text{H}_2\text{C}-$], 7.52 [d, $J(\text{H,H})$ = 7.9 Hz, 2 H, $-\text{CC}_2\text{H}_2\text{C}_2\text{H}_2\text{CCH}_3$], 7.30 [d, $J(\text{H,H})$ = 7.5 Hz, 2 H, $-\text{CC}_2\text{H}_2\text{C}_2\text{H}_2\text{CCH}_3$], 2.41 (s, 3 H, $-\text{PhCH}_3$), 1.97 (s, 3 H, $-\text{ReCH}_3$) ppm. ^{13}C NMR (100.6 MHz, CDCl_3 , 25 °C): δ = 151.1 (1 C), 147.1 (2 C), 140.3 (1 C), 133.8 (1 C), 130.0 (2 C), 126.9 (2 C), 122.5 (2 C), 24.8 (1 C, $-\text{ReCH}_3$), 21.2 (1 C, $\text{Ph}-\text{CH}_3$) ppm. IR (KBr): $\tilde{\nu}$ = 33445 (m), 2925 (w), 1610 (s), 492 (m), 1384 (m), 1262 (w), 1227 (w), 1221 (w), 1073 (m), 1037 (w), 1010 (m), 934 (vs), 927 (vs), 854 (w), 811 (s), 721 (m), 559 (m), 498 (m) cm^{-1} . $\text{C}_{13}\text{H}_{14}\text{NO}_3\text{Re}$ (418.46): calcd. C 37.31, H 3.37, N 3.35; found C 37.05, H 3.41, N 3.34.

[4-[3,5-Dimethylphenyl]pyridine]methyltrioxorhenium (14): Yield 106 mg (70%). ^1H NMR (400 MHz, CDCl_3 , 25 °C): δ = 8.32 [d, $J(\text{H,H})$ = 6.4 Hz, 2 H, $\text{NC}_2\text{H}_2\text{C}_2\text{H}_2\text{C}-$], 7.56 [d, $J(\text{H,H})$ = 6.6 Hz, 2 H, $\text{NC}_2\text{H}_2\text{C}_2\text{H}_2\text{C}-$], 7.21 [s, 2 H, $-\text{CC}_2\text{H}_2\text{C}_2(\text{CH}_3)_2\text{CH}$], 7.11 [s, 1 H, $-\text{CC}_2\text{H}_2\text{C}_2(\text{CH}_3)_2\text{CH}$], 2.39 [s, 6 H, $-\text{CC}_2\text{H}_2\text{C}_2(\text{CH}_3)_2\text{CH}$], 1.98 (s, 3 H, $-\text{ReCH}_3$) ppm. ^{13}C NMR (100.6 MHz, CDCl_3 , 25 °C): δ = 151.4 (1 C), 147.2 (2 C), 139.0 (2 C), 136.8 (1 C), 131.5 (1 C), 125.0 (2 C), 122.8 (2 C), 24.4 (1 C), 21.3 (2 C) ppm. IR (KBr): $\tilde{\nu}$ = 3434 (w), 2916 (w), 1613 (vs), 1551 (w), 1507 (w), 1408 (w), 1385 (w), 1232 (w), 1073 (m), 1021 (m), 931 (vs), 828 (s), 664 (m), 589 (m), 561 (m), 434 (w), 418 (w) cm^{-1} . $\text{C}_{14}\text{H}_{16}\text{NO}_3\text{Re}$ (432.49): calcd. C 38.88, H 3.73, N 3.24; found C 38.88, H 3.73, N 3.24.

Single-Crystal X-ray Structure Determination of Compound 5: $\text{C}_{27}\text{H}_{19}\text{N}$; M_r = 357.43; crystal colour and shape: colourless fragment, crystal dimensions = $0.51 \times 0.56 \times 0.64$ mm; crystal system: monoclinic; space group: Cc (no. 9); a = 14.9971(6), b = 10.9497(4), c = 12.4175(5) Å; β = 114.048(2)°; V = 1862.14(13) Å³; Z = 4; μ ($\text{Mo}-K_\alpha$) = 0.073 mm^{-1} ; $\rho_{\text{calcd.}}$ = 1.275 g cm^{-3} ; θ range 2.38–25.34; data collected: 32910; independent data [$I_o > 2\sigma(I_o)$ /all data/ R_{int}]: 3360/3397/0.023; data/restraints/parameters: 3397/2/329; $R1$ [$I_o > 2\sigma(I_o)$ /all data] = 0.0255/0.0258; $wR2$ [$I_o > 2\sigma(I_o)$ /all data] = 0.0709/0.0713; GOF = 1.080; $\Delta\rho_{\text{max/min}}$ = 0.13/−0.12 e Å^{-3} .

Single-Crystal X-ray Structure Determination of Compound 8: $\text{C}_{14}\text{H}_{14}\text{NO}_3\text{Re}$; M_r = 430.47; crystal colour and shape: yellow fragment, crystal dimensions = $0.13 \times 0.18 \times 0.51$ mm; crystal system: monoclinic; space group: $P2_1$ (no. 4); a = 9.0054(2), b = 7.2442(2), c = 11.0721(3) Å; β = 109.3284(11)°; V = 681.60(3) Å³; Z = 2; μ ($\text{Mo}-K_\alpha$) = 8.916 mm^{-1} ; $\rho_{\text{calcd.}}$ = 2.098 g cm^{-3} ; θ range 1.95–25.39; data collected: 10806; independent data [$I_o > 2\sigma(I_o)$ /all data/ R_{int}]: 2275/2281/0.059; data/restraints/parameters: 2281/1/173;

$R1 [I_o > 2\sigma(I_o)/\text{all data}] = 0.0259/0.0259$; $wR2 [I_o > 2\sigma(I_o)/\text{all data}] = 0.0648/0.0648$; $\text{GOF} = 1.090$; $\Delta\rho_{\text{max/min}} = 2.27/-2.57 \text{ e } \text{\AA}^{-3}$.

Single-Crystal X-ray Structure Determination of Compound 9: $\text{C}_{15}\text{H}_{16}\text{NO}_3\text{Re}$; $M_r = 444.49$; crystal colour and shape: yellow fragment, crystal dimensions $0.15 \times 0.15 \times 0.43 \text{ mm}$; crystal system: monoclinic; space group: $P2_1/n$ (no. 14); $a = 9.1661(4)$, $b = 7.1741(3)$, $c = 22.3772(9) \text{ \AA}$; $\beta = 97.795(2)^\circ$; $V = 1457.89(11) \text{ \AA}^3$; $Z = 4$; $\mu (\text{Mo}-K_\alpha) = 8.341 \text{ mm}^{-1}$; $\rho_{\text{calcd.}} = 2.025 \text{ g cm}^{-3}$; θ range $1.84-25.36$; data collected: 29722; independent data $[I_o > 2\sigma(I_o)/\text{all data}/R_{\text{int}}]$: 2423/2564/0.058; data/restraints/parameters: 2564/0/183; $R1 [I_o > 2\sigma(I_o)/\text{all data}] = 0.0289/0.0307$; $wR2 [I_o > 2\sigma(I_o)/\text{all data}] = 0.0671/0.0680$; $\text{GOF} = 1.261$; $\Delta\rho_{\text{max/min}} = 0.85/-1.54 \text{ e } \text{\AA}^{-3}$.

Single-Crystal X-ray Structure Determination of Compound 10: $\text{C}_{14}\text{H}_{13}\text{BrNO}_3\text{Re}$; $M_r = 509.36$; crystal colour and shape: yellow fragment, crystal dimensions $0.05 \times 0.13 \times 0.53 \text{ mm}$; crystal system: triclinic; space group: $P\bar{1}$ (no. 2); $a = 5.9849(2)$, $b = 15.9131(6)$, $c = 17.0785(6) \text{ \AA}$; $\alpha = 66.0608(15)$, $\beta = 85.8488(15)$, $\gamma = 86.3720(14)^\circ$; $V = 1481.68(9) \text{ \AA}^3$; $Z = 4$; $\mu (\text{Mo}-K_\alpha) = 10.903 \text{ mm}^{-1}$; $\rho_{\text{calcd.}} = 2.283 \text{ g cm}^{-3}$; θ range $1.31-25.45$; data collected: 18921; independent data $[I_o > 2\sigma(I_o)/\text{all data}/R_{\text{int}}]$: 4839/5188/0.042; data/restraints/parameters: 5188/0/363; $R1 [I_o > 2\sigma(I_o)/\text{all data}] = 0.0264/0.0286$; $wR2 [I_o > 2\sigma(I_o)/\text{all data}] = 0.0697/0.0721$; $\text{GOF} = 1.048$; $\Delta\rho_{\text{max/min}} = 2.13/-1.85 \text{ e } \text{\AA}^{-3}$.

Single-Crystal X-ray Structure Determination of Compound 11: $\text{C}_{20}\text{H}_{18}\text{NO}_3\text{Re}$; $M_r = 506.56$; crystal colour and shape: yellow fragment, crystal dimensions $0.24 \times 0.35 \times 0.38 \text{ mm}$; crystal system: triclinic; space group: $P\bar{1}$ (no. 2); $a = 5.7288(3)$, $b = 11.4564(6)$, $c = 27.4120(14) \text{ \AA}$; $\alpha = 82.715(3)$, $\beta = 89.200(2)$, $\gamma = 77.895(2)^\circ$; $V = 1744.74(16) \text{ \AA}^3$; $Z = 4$; $\mu (\text{Mo}-K_\alpha) = 6.983 \text{ mm}^{-1}$; $\rho_{\text{calcd.}} = 1.929 \text{ g cm}^{-3}$; θ range $0.75-25.37$; data collected: 69973; independent data $[I_o > 2\sigma(I_o)/\text{all data}/R_{\text{int}}]$: 5347/6039/0.070; data/restraints/parameters: 6039/0/453; $R1 [I_o > 2\sigma(I_o)/\text{all data}] = 0.0217/0.0279$; $wR2 [I_o > 2\sigma(I_o)/\text{all data}] = 0.0507/0.0538$; $\text{GOF} = 1.068$; $\Delta\rho_{\text{max/min}} = 0.87/-0.52 \text{ e } \text{\AA}^{-3}$.

Single-Crystal X-ray Structure Determination of Compound 12: $\text{C}_{28}\text{H}_{22}\text{NO}_3\text{Re}$; $M_r = 606.68$; crystal colour and shape: yellow fragment, crystal dimensions $0.15 \times 0.18 \times 0.36 \text{ mm}$; crystal system: triclinic; space group: $P\bar{1}$ (no. 2); $a = 9.8694(3)$, $b = 10.9626(4)$, $c = 12.5154(7) \text{ \AA}$; $\alpha = 99.490(2)$, $\beta = 105.050(2)$, $\gamma = 112.906(1)^\circ$; $V = 1149.44(9) \text{ \AA}^3$; $Z = 2$; $\mu (\text{Mo}-K_\alpha) = 5.316 \text{ mm}^{-1}$; $\rho_{\text{calcd.}} = 1.753 \text{ g cm}^{-3}$; θ range $1.77-25.44$; data collected: 27800; independent data $[I_o > 2\sigma(I_o)/\text{all data}/R_{\text{int}}]$: 3917/3955/0.039; data/restraints/parameters: 3955/0/299; $R1 [I_o > 2\sigma(I_o)/\text{all data}] = 0.0139/0.0141$; $wR2 [I_o > 2\sigma(I_o)/\text{all data}] = 0.0356/0.0358$; $\text{GOF} = 1.078$; $\Delta\rho_{\text{max/min}} = 1.12/-0.44 \text{ e } \text{\AA}^{-3}$.

Single-Crystal X-ray Structure Determination of Compound 13: $\text{C}_{13}\text{H}_{14}\text{NO}_3\text{Re}$; $M_r = 418.46$; crystal colour and shape: yellow fragment, crystal dimensions $0.15 \times 0.20 \times 0.38 \text{ mm}$; crystal system: monoclinic; space group: $P2_1/c$ (no. 14); $a = 11.6924(4)$, $b = 14.3708(4)$, $c = 8.2219(3) \text{ \AA}$; $\beta = 110.3695(14)^\circ$; $V = 1295.13(8) \text{ \AA}^3$; $Z = 4$; $\mu (\text{Mo}-K_\alpha) = 9.381 \text{ mm}^{-1}$; $\rho_{\text{calcd.}} = 2.146 \text{ g cm}^{-3}$; θ range $1.86-25.39$; data collected: 4902; independent data $[I_o > 2\sigma(I_o)/\text{all data}/R_{\text{int}}]$: 2196/2260/0.028; data/restraints/parameters: 2260/0/165; $R1 [I_o > 2\sigma(I_o)/\text{all data}] = 0.0218/0.0225$; $wR2 [I_o > 2\sigma(I_o)/\text{all data}] = 0.0556/0.0561$; $\text{GOF} = 1.144$; $\Delta\rho_{\text{max/min}} = 1.12/-1.39 \text{ e } \text{\AA}^{-3}$.

Single-Crystal X-ray Structure Determination of Compound 14: $\text{C}_{14}\text{H}_{16}\text{NO}_3\text{Re}$; $M_r = 432.49$; crystal colour and shape: yellow needle, crystal dimensions $0.03 \times 0.05 \times 0.23 \text{ mm}$; crystal system: monoclinic; space group: $P2_1/m$ (no. 11); $a = 6.4763(9)$, $b = 11.652(2)$, $c = 18.930(3) \text{ \AA}$; $\beta = 93.705(6)^\circ$; $V = 1425.5(4) \text{ \AA}^3$; $Z = 4$; $\mu (\text{Mo}-K_\alpha) = 8.527 \text{ mm}^{-1}$; $\rho_{\text{calcd.}} = 2.015 \text{ g cm}^{-3}$; θ range $1.08-25.37$; data

collected: 35302; independent data $[I_o > 2\sigma(I_o)/\text{all data}/R_{\text{int}}]$: 2592/2741/0.048; data/restraints/parameters: 2741/0/195; $R1 [I_o > 2\sigma(I_o)/\text{all data}] = 0.0186/0.0200$; $wR2 [I_o > 2\sigma(I_o)/\text{all data}] = 0.0410/0.0416$; $\text{GOF} = 1.099$; $\Delta\rho_{\text{max/min}} = 1.09/-1.30 \text{ e } \text{\AA}^{-3}$.

CCDC-777693 (for **5**), -777694 (for **8**), -777695 (**9**), -777696 (for **10**), -777697 (for **11**), -777698 (for **12**), -777699 (for **13**), and -777700 (for **14**) contain the supplementary crystallographic data for this paper. These data can be obtained free of charge from The Cambridge Crystallographic Data Centre via www.ccdc.cam.ac.uk/data_request/cif.

Formation Constant Measurements: An UV/Vis spectrophotometric method was used to determine the formation constants of the chromophoric Lewis base adducts of MTO. Aliquots of a 0.1 mM solution of MTO in CH_2Cl_2 were successively added to a 0.1 mM solution of the ligand in CH_2Cl_2 in a quartz cuvette (path length 1 cm, total volume 3 mL). UV/Vis spectra of the homogeneous solutions at equilibrium containing the metal complex, the ligand and the adduct were recorded in the range of 200–400 nm before and after each addition of the MTO aliquot. The values of the formation constants were calculated by fitting the equilibrium absorbance at a certain wavelength to Equation (2) or (3) according to the chosen wavelength and the free ligand absorption using the IGOR computer program.

Catalysis: In a typical experiment, 1-octene (0.628 mL, 4 mmol), MTO (10 mg, 0.04 mmol), ligand (0.2 mmol), 0.200 mL of mesitylene (internal standard), 0.200 mL of toluene (internal standard) and 2.45 mL of CH_2Cl_2 were added to the reaction vessel under standard conditions at room temperature. The reaction started upon addition of H_2O_2 (35% aqueous solution) (0.55 mL, 6 mmol) under vigorous stirring. The course of the reaction was monitored by quantitative GC analysis. Samples (0.2 mL) were taken at specific time intervals, treated with Na_2SO_3 to quench the excess of peroxide and to remove water, filtered and diluted with dry CH_2Cl_2 before injection into a GC column. The conversion of 1-octene and the formation of octene epoxide were calculated from calibration curves ($r^2 = 0.999$) recorded prior to the reaction course.

Testing the Photostability of the Complexes: Selected ligands were treated with an equimolar amount of ^{17}O -labelled MTO (prepared by a published procedure^[31]) or in a fivefold excess and the ^1H and ^{17}O NMR spectra were recorded. The adduct solutions (0.1 M in CDCl_3) were then exposed to UV light and analysed again by ^1H and ^{17}O NMR spectroscopy. For the UV/Vis analysis, a 0.1 M solution of complex **11** in CH_2Cl_2 was prepared and exposed to UV light. Samples were taken over a timespan of 2 h, diluted with CH_2Cl_2 and the UV/Vis spectra were recorded.

Supporting Information (see also the footnote on the first page of this article): UV/Vis spectra of ligands and complexes, spectroscopic data for the determination of the stability constants and ^{17}O NMR spectra of selected complexes.

Acknowledgments

S. A. H. thanks the Bavarian elite network NanoCat for a Ph. D. grant and for financial support of the project.

- [1] R. I. Beattie, P. J. Jones, *Inorg. Chem.* **1979**, *18*, 2318–2319.
- [2] W. A. Herrmann, J. G. Kuchler, J. K. Felixberger, E. Herdtweck, W. Wagner, *Angew. Chem.* **1988**, *100*, 420–422; *Angew. Chem. Int. Ed. Engl.* **1988**, *27*, 394–396.
- [3] F. E. Kühn, A. Scherbaum, W. A. Herrmann, *J. Organomet. Chem.* **2004**, *689*, 4149–4164.

- [4] W. A. Herrmann, M. Wang, *Angew. Chem.* **1991**, *103*, 1709–1711; *Angew. Chem. Int. Ed. Engl.* **1991**, *30*, 1641–1643.
- [5] W. A. Herrmann, W. Wagner, U. N. Flessner, U. Volkhardt, H. Komber, *Angew. Chem.* **1991**, *103*, 1704–1706; *Angew. Chem. Int. Ed. Engl.* **1991**, *30*, 1636–1638.
- [6] J. E. Ziegler, M. J. Zdilla, A. J. Evans, M. M. Abu-Omar, *Inorg. Chem.* **2009**, *48*, 9998–10000.
- [7] W. A. Herrmann, R. W. Fischer, D. W. Marz, *Angew. Chem.* **1991**, *103*, 1706–1709; *Angew. Chem. Int. Ed. Engl.* **1991**, *30*, 1638–1641.
- [8] J. Rudolph, K. L. Reddy, J. P. Chiang, K. B. Sharpless, *J. Am. Chem. Soc.* **1997**, *119*, 6189–6190 and references cited therein.
- [9] F. E. Kühn, A. M. Santos, W. A. Herrmann, *Dalton Trans.* **2005**, 2483–2491 and references cited therein.
- [10] C. Copéret, H. Adolfson, K. B. Sharpless, *Chem. Commun.* **1997**, 1565–1566.
- [11] W. A. Herrmann, H. Ding, R. M. Kratzer, F. E. Kühn, J. J. Haider, R. W. Fischer, *J. Organomet. Chem.* **1997**, *549*, 319–322.
- [12] W. D. Wang, J. H. Espenson, *J. Am. Chem. Soc.* **1998**, *120*, 11335–11341.
- [13] W. A. Herrmann, R. M. Kratzer, H. Ding, W. R. Thiel, H. Glas, *J. Organomet. Chem.* **1998**, *555*, 293–295.
- [14] H. Adolfsson, A. Converso, K. B. Sharpless, *Tetrahedron Lett.* **1999**, *40*, 3991–3994.
- [15] F. E. Kühn, A. M. Santos, P. W. Roesky, E. Herdtweck, W. Scherer, P. Gisdakis, I. V. Yudanov, C. Di Valentin, N. Rösch, *Chem. Eur. J.* **1999**, *5*, 3603–3615.
- [16] C. Copéret, H. Adolfson, J. P. Chiang, A. K. Yudin, *J. Org. Chem.* **2000**, *65*, 8651–8658.
- [17] P. Ferreira, W. D. Xue, É. Bencze, E. Herdtweck, F. E. Kühn, *Inorg. Chem.* **2001**, *40*, 5834–5841.
- [18] M. J. Sabater, M. E. Domine, A. Corma, *J. Catal.* **2002**, *210*, 192–197.
- [19] P. Altmann, F. E. Kühn, *J. Organomet. Chem.* **2009**, *694*, 4032–4035.
- [20] H. Kunkely, T. Türk, C. Teixeira, C. de Meric de Bellefon, W. A. Herrmann, A. Vogler, *Organometallics* **1991**, *10*, 2090–2092.
- [21] W. A. Herrmann, F. E. Kühn, D. A. Fiedler, M. R. Mattner, M. R. Geisberger, H. Kunkely, A. Vogler, S. Steenken, *Organometallics* **1995**, *14*, 5377–5381.
- [22] H. Kunkely, A. Vogler, *J. Photochem. Photobiol. A: Chem.* **1996**, *94*, 135–138.
- [23] H. Kunkely, A. Vogler, *J. Photochem. Photobiol. A: Chem.* **1997**, *103*, 227–229.
- [24] M.-D. Zhou, S.-L. Zang, E. Herdtweck, F. E. Kühn, *J. Organomet. Chem.* **2008**, *693*, 2473–2477.
- [25] P. Wikrent, B. J. Drouin, S. G. Kukulich, J. C. Lilly, M. T. Ashby, W. A. Herrmann, W. Scherer, *J. Chem. Phys.* **1977**, *107*, 2187–2192.
- [26] A. M. Al-Ajlouni, A. Günyar, M.-D. Zhou, P. N. W. Baxter, F. E. Kühn, *Eur. J. Inorg. Chem.* **2009**, 1019–1026.
- [27] M. Y. Shatnawi, A. M. Al-Ajlouni, *Jordan J. Chem.* **2009**, *4*, 119–130.
- [28] S. M. Nabavizadeh, *Inorg. Chem.* **2003**, *42*, 4204–4208.
- [29] S. M. Nabavizadeh, *Dalton Trans.* **2005**, 1644–1648.
- [30] S. M. Nabavizadeh, A. Akbari, M. Rashidi, *Eur. J. Inorg. Chem.* **2005**, 2368–2375.
- [31] S. Yamazaki, *Org. Biomol. Chem.* **2007**, *5*, 2109–2113.
- [32] W. A. Herrmann, F. E. Kühn, P. W. Roesky, *J. Organomet. Chem.* **1995**, *485*, 243–251.
- [33] W. A. Herrmann, F. E. Kühn, M. U. Rauch, J. D. G. Correia, G. Artus, *Inorg. Chem.* **1995**, *34*, 2914–2920.
- [34] E. Tosh, H. K. M. Mitterpleininger, A. M. J. Rost, D. Veljanovski, W. A. Herrmann, F. E. Kühn, *Green Chem.* **2007**, *12*, 1296–1298.
- [35] V. Aranyos, J. Hjelm, A. Hagfeldt, H. Grennberg, *J. Chem. Soc., Dalton Trans.* **2001**, 1319–1325.
- [36] N. Kudo, M. Perseghini, G. C. Fu, *Angew. Chem. Int. Ed.* **2006**, *45*, 1282–1284.

Received: March 29, 2010
Published Online: July 23, 2010

Ordered Olivine-Type Lithium–Cobalt and Lithium–Nickel Phosphates Prepared by a New Precursor Method

Violeta Koleva,^{*,[a]} Ekaterina Zhecheva,^[a] and Radostina Stoyanova^[a]

Keywords: Lithium / Cobalt / Nickel / Organic-inorganic hybrid composites / X-ray diffraction

Single phases of olivine-type LiCoPO_4 and LiNiPO_4 were synthesized by thermal treatment of homogeneous lithium–metal–phosphate–formate precursors obtained by freeze drying of aqueous solutions of the corresponding metal formates and LiH_2PO_4 . The structure, thermal behavior, and morphology of the precursors were studied by IR spectroscopy, DTA, and SEM. Cobalt and nickel phosphate–formate precursors have a composition $\text{LiMH}_x(\text{PO}_4)(\text{HCOO})_{x-y}\text{H}_2\text{O}$, where the formate and phosphate groups are mainly deprotonated. For the Co precursor the formate and phosphate ions are randomly coordinated to both Co and Li cations, whereas for the Ni precursor there is a preferential coordina-

tion of the formate and phosphate ions around the Ni^{2+} and Li^+ ion, respectively. Thermal treatment of the precursors yields single phases of olivine-type LiCoPO_4 at 450 °C and LiNiPO_4 at 700 °C. Structural analysis evidences that both LiCoPO_4 and LiNiPO_4 have an ordered olivine-type structure without any Li to M disorder between the metal positions and lithium deficiency. The effect of the freeze-dried solution concentration and annealing temperature on the structure, crystallite size, and morphology of LiCoPO_4 and LiNiPO_4 has been discussed. The morphology of the cobalt and nickel phospho-olivines comprises isometric particles with mean sizes of 190 and 380 nm, respectively.

Introduction

Lithium–transition metal orthophosphates with olivine-type structure (LiMPO_4 , M = Fe, Mn, Co, and Ni) are the most intensive studied compounds as cathode materials for lithium-ion batteries in the last years. This is a consequence of their high cycling stability, tolerance to overcharge, and safety.^[1,2] The best electrochemical performance is achieved with the iron analogue LiFePO_4 . The electrochemical reaction takes place by reversible lithium intercalation in the olivine structure concomitantly with the oxidation/reduction of Fe^{2+} to Fe^{3+} , the operating voltage being 3.4 V. By simple replacement of iron by manganese, cobalt, and nickel, a higher operating voltage and energy density of the phospho-olivines can be achieved, which is beneficial for their electric vehicle applications. Cobalt and nickel phospho-olivines exhibit higher operating voltages (4.8 and 5.1 V vs. Li^+/Li) and energy densities (227.4 and 250.2 Wh/kg).^[3–5] The main drawback of the phospho-olivines is their low electronic and ionic conductivity. To overcome this drawback, specific synthesis methods have to be developed that aim to minimize the dimensions of the particles and/or to cover them with conductive substances. In this topic, a lot of work is carried out on the preparation of LiFePO_4 and LiMnPO_4 , whereas the reports on the preparation of LiCoPO_4 and LiNiPO_4 are limited.

LiCoPO_4 has been prepared by using solid-state reactions^[3,6,7] and soft chemistry routes.^[8–13] A common feature of all synthetic methods is the relatively high temperature where LiCoPO_4 is formed (600–800 °C and prolonged heating). Concerning LiNiPO_4 , solid-state reactions,^[4,14] sol-gel,^[9] and coprecipitation^[15] methods are used, but in all cases the synthesis temperature exceeds 775 °C.

Recently, we developed a phosphate–formate precursor method for the preparation of nano-sized olivine-type LiFePO_4 .^[16] The method is based on the formation of homogeneous lithium–iron–phosphate–formate precursors by freeze drying aqueous solutions containing lithium, iron(II), phosphate, and formate ions. Thermal treatment of the lithium–iron–phosphate–formate precursors at temperatures above 300 °C yields nanometric LiFePO_4 (particle sizes between 60 and 100 nm) containing up to 2 mass% carbon. The advantage of this method is related to the ability to control the morphology of lithium–iron–phosphate–formate precursors by a simple variation of the concentration of the freeze-dried solutions. This, on its turn, has an impact on the carbon content, particles size distribution, and electrochemical properties of target LiFePO_4 .^[17] The aptitude of the phosphate–formate precursor method to design simultaneously precursors and the target product has also been demonstrated with the preparation of nanocrystalline manganese phospho-olivine LiMnPO_4 .^[18] By this method a new structural modification of LiNiPO_4 (with Na_2CrO_4 -type structure) has been prepared.^[19]

In this paper we examine the applicability of the phosphate–formate precursor method for the preparation of co-

[a] Institute of General and Inorganic Chemistry, Bulgarian Academy of Sciences, Acad. G. Bonchev St, bl. 11, 1113 Sofia, Bulgaria
Fax: +359-2-8705024
E-mail: vkoleva@svr.igic.bas.bg

balt and nickel phospho-olivines, LiCoPO_4 and LiNiPO_4 . The precursors and target LiCoPO_4 and LiNiPO_4 compositions were characterized by XRD, IR spectroscopy, DTA, and SEM. The mechanism of cobalt and nickel phospho-olivines formation is discussed on the basis of iron and manganese analogues.

Results and Discussion

Composition and Structure of the Li–M–Phosphate–Formate Precursors (M = Co and Ni)

Freeze drying of the solution containing Li^+ , Co^{2+} or Ni^{2+} , PO_4^{3-} and HCOO^- in the ratio 1:1:1:2 yields amorphous powders with compositions as follows: pink $\text{LiCoH}_x(\text{PO}_4)_y(\text{HCOO})_x \cdot y\text{H}_2\text{O}$ ($x \approx 1$ and $y \approx 1.5$) and pale green $\text{LiNiH}_x(\text{PO}_4)_y(\text{HCOO})_x \cdot y\text{H}_2\text{O}$ ($x \approx 1.2$; $2.5 < y < 2.7$). The precursor compositions do not depend on the concentration of freeze-dried solutions. These results evidence for partial formic acid sublimation during the freeze-drying process: 1 and 0.8 mol of HCOOH are sublimated in the case of Co and Ni precursors, respectively. The same results were established for the iron and manganese phosphate–formate precursors,^[16,18] where only 1 mol of HCOOH is sublimated.

To examine the form and type of coordination of the anion groups in the freeze-dried compositions, IR spectroscopy was undertaken. Figures 1 and 2 give the IR spectra of Co and Ni freeze-dried precursors. For the sake of comparison, the IR spectra of $\text{M}(\text{HCOO})_2 \cdot 2\text{H}_2\text{O}$ and $\text{M}(\text{H}_2\text{PO}_4)_2 \cdot 2\text{H}_2\text{O}$ (M = Co, Ni) are also presented. The dihydrogen phosphates were synthesized as described elsewhere.^[20]

Three groups of IR bands due to the vibrations of formates, phosphates, and OH groups are resolved in the spectra of the precursors. It is noticeable that the concentration of the freeze-dried solution does not affect the IR profiles. The analysis of the IR spectra of both Co and Ni precursors reveals the presence of the characteristic IR vibrations due to deprotonated formate ions:^[21] $\nu_{\text{as}}(\text{COO})$ at 1607–1584 cm^{-1} ; $\delta(\text{CH})$ in the range 1399–1393 cm^{-1} ; $\nu_{\text{s}}(\text{COO})$ in the range 1378–1355 cm^{-1} , and $\delta_{\text{s}}(\text{OCO})$ in the range 795–774 cm^{-1} . All these characteristic vibrations are clearly seen in the IR spectra of the initial Co and Ni formate salts, $\text{M}(\text{HCOO})_2 \cdot 2\text{H}_2\text{O}$ (M = Co, Ni). Close inspection of Figure 2 shows that the wavenumbers of $\delta(\text{CH})$ and $\nu_{\text{s}}(\text{COO})$ vibrations are the same for the Ni precursor and for pure $\text{Ni}(\text{HCOO})_2 \cdot 2\text{H}_2\text{O}$. Therefore, one can suggest that for the Ni precursor the formate ions are predominantly coordinated to the Ni^{2+} ions. Contrary to Ni, it appears that for the Co precursors the formate ions are coordinated simultaneously to both Co^{2+} and Li^+ .

The vibrations associated with the deprotonated phosphate ion (PO_4^{3-}) are also well seen in the IR spectra of the Co(Ni) precursors (Figures 1 and 2). The two bands in the 1080–1008 cm^{-1} range for the Co precursors and the band at 1060 cm^{-1} for the Ni precursors are due to the asymmetric ν_3 stretching vibrations of the PO_4^{3-} ions. The doublets

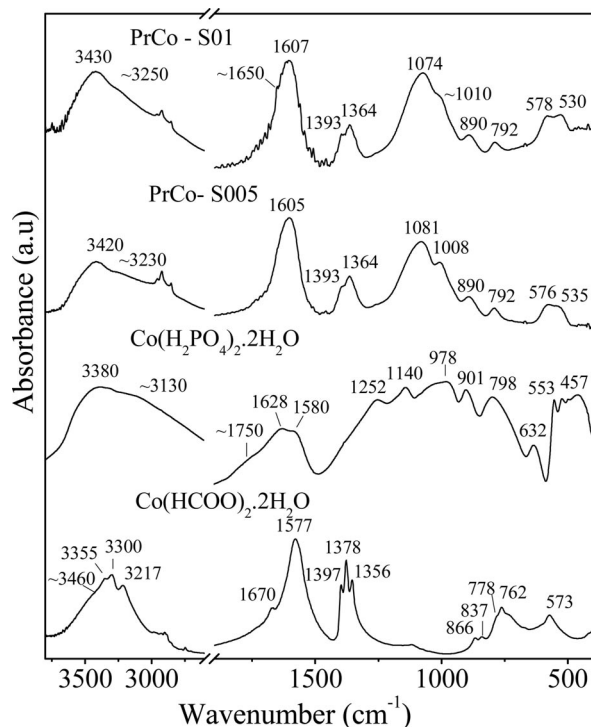


Figure 1. IR spectra of $\text{Co}(\text{HCOO})_2 \cdot 2\text{H}_2\text{O}$, $\text{Co}(\text{H}_2\text{PO}_4)_2 \cdot 2\text{H}_2\text{O}$, and lithium–cobalt–phosphate–formate precursors.

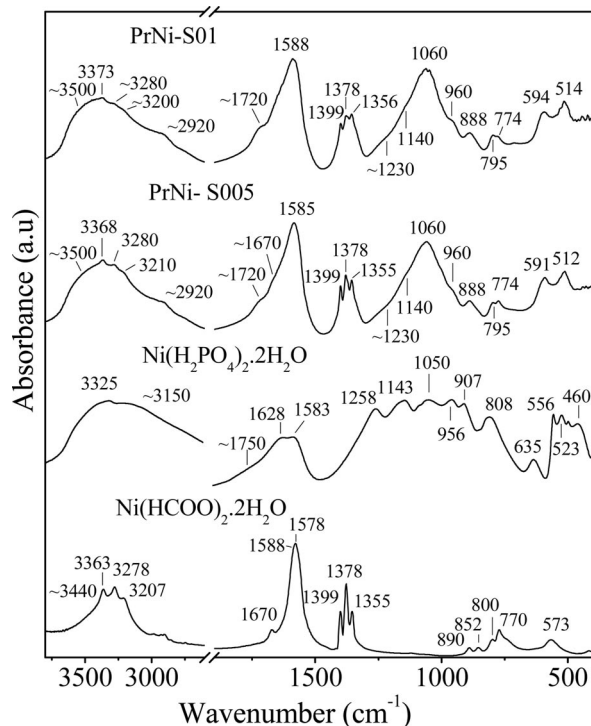


Figure 2. IR spectra of $\text{Ni}(\text{HCOO})_2 \cdot 2\text{H}_2\text{O}$, $\text{Ni}(\text{H}_2\text{PO}_4)_2 \cdot 2\text{H}_2\text{O}$, and lithium–nickel–phosphate–formate precursors.

at 578/530 and 594/514 cm^{-1} for the Co and Ni precursors, respectively, are associated with the asymmetric ν_4 bending PO_4^{3-} vibrations.^[22] It is worth mentioning that the positions of the ν_3 and ν_4 vibrations for the PO_4^{3-} ions in the

Ni precursors are close to those observed for Li_3PO_4 at 1040 and 592 cm^{-1} .^[23] Hence, it appears that the phosphate ions in the Ni precursors are preferentially coordinated around the Li^+ ions.

In addition, the Ni precursor exhibits three low intensive bands at 960, ca. 1230, and 1720 cm^{-1} (Figure 2). These bands can be attributed to the protonated forms of the coordinated anions – HCOOH and/or H_2PO_4^- or HPO_4^{2-} . To analyze this feature, the characteristic vibrations of protonated HCOOH and/or H_2PO_4^- or HPO_4^{2-} groups are taken into account: for HCOOH , the $\nu(\text{C}=\text{O})$, $\nu(\text{C}-\text{O})$, and $\gamma(\text{OH})$ vibrations are at 1700, 1260 and 975 cm^{-1} ,^[24] whereas for the protonated phosphate ions (H_2PO_4^- or HPO_4^{2-}) the out-of-plane $\delta(\text{OH})$ and in-plane $\gamma(\text{OH})$ bending POH vibrations are at 1230–1260 and 800–900 cm^{-1} .^[25,26] The comparison shows that the three additional bands at 1720, 1230, and 960 cm^{-1} are due to HCOOH rather than to protonated phosphate ions. The presence of small amount of protonated HCOOH is in accordance with the chemical composition of the Ni precursor, where the amount of formate species is higher than 1 mol.

In the range of the stretching OH vibrations, two bands at 3430 and ca. 3250 cm^{-1} are observed for the Co precursors, whereas there are four bands between 3500 and 3200 cm^{-1} for the Ni precursors. The bending water vibration is seen at $1650\text{--}1670\text{ cm}^{-1}$. For the Ni precursors, the positions of the four OH bands are close to that in initial $\text{Ni}(\text{HCOO})_2 \cdot 2\text{H}_2\text{O}$ (Figure 2). For the sake of comparison, for $\text{LiHCOO} \cdot \text{H}_2\text{O}$ these bands are at 3398 and 3109 cm^{-1} .^[27] This comparison shows that the water molecules are mainly coordinated to the nickel ions in the Ni precursors. The difference in the positions of OH vibrations for the cobalt precursors and $\text{Co}(\text{HCOO})_2 \cdot 2\text{H}_2\text{O}$ (Figure 1) and $\text{LiHCOO} \cdot \text{H}_2\text{O}$ ^[27] reveals that water molecules are coordinated to both cobalt and lithium ions in the cobalt precursors.

Summarizing, two features concerning the form and the type of coordination of the anionic groups and water molecules in the Co and Ni precursors can be outlined. First, in both types of precursors the formate and phosphate groups are mainly deprotonated. Second, there is a difference in respect to the type of coordination of the anionic groups and water molecules. Thus, in the Co precursors the formate and phosphate ions and the water molecules are coordinated to both types of cations without any preference. A similar feature was established for the Fe and Mn precursors obtained by the same freeze-drying method.^[16,18] Contrary, in the case of Ni precursors the formate ions and the water molecules prefer to coordinate the Ni^{2+} ions, whereas the phosphate ions coordinate the Li^+ ions. This is a specific feature of the Ni precursors obtained by freeze-drying of mixed phosphate–formate solutions.

The Ni and Co precursors exhibit not only a different structure, but also a different morphology. Figure 3 gives the SEM images of both precursors. Whereas the morphology of the Co precursors consists of flake-like aggregates, the Ni precursors display “cabbage”-like aggregates.

By increasing the concentration of the freeze-dried solutions, there is a slight tendency for increasing the aggregate dimensions of the Ni precursors. It is worth noting that a flake-like morphology was established for the iron and

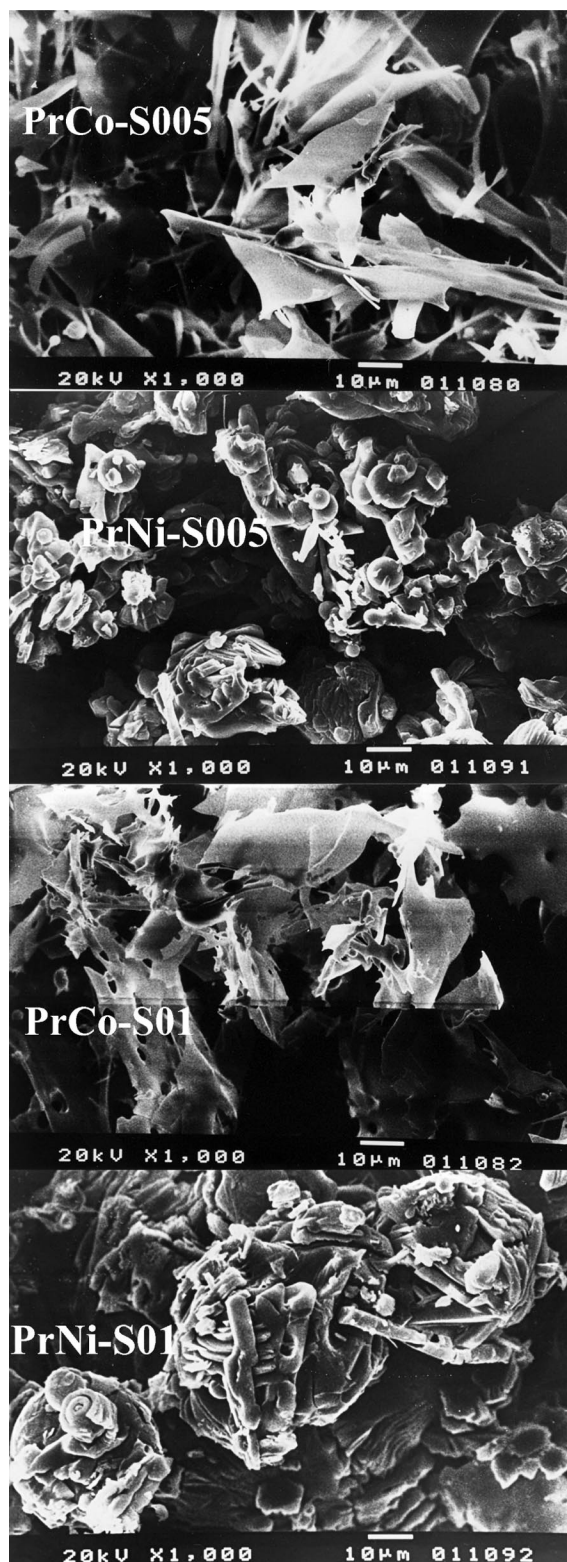


Figure 3. SEM images of LiCo- and LiNi-phosphate-formates precursors.

manganese phosphate–formate precursors. This result demonstrates once again the difference in the formation of the Ni precursors by freeze drying of solutions. The different structure and morphology of the Ni precursors as compared to that of Co, Mn, and Fe precursors can be related with the complex equilibria in the metal–phosphate–formate solutions.

The thermal properties of the Li–M–phosphate–formate ($M = \text{Co}, \text{Ni}$) precursors were followed by differential thermal analysis (Figures 4 and 5). For both compositions, endothermic peaks between 50 and 200 °C accompanied with a mass loss are clearly observed. These peaks can be related with dehydration processes, as was observed for the thermal decomposition of $M(\text{HCOO})_2 \cdot 2\text{H}_2\text{O}$ ($M = \text{Co}, \text{Ni}$)^[28,29] and LiHCOO .^[30] According to the TG curves they correspond to the release of 1.5 and 2.7 mol H_2O molecules from the Co and Ni precursor, respectively. Above 200 °C, the decomposition of the formate species occurs, which is registered on the DTA curves with several endo- and exothermic effects. In addition, the decomposition process is more complex and finishes at higher temperatures for the Ni precursor: the total mass loss for the Ni precursor up to 550 °C is 38.8%, whereas for the Co precursor the total mass loss is 31.1% up to 400 °C. This is a result of the appearance of more than one mol of formate species in the Ni precursor.

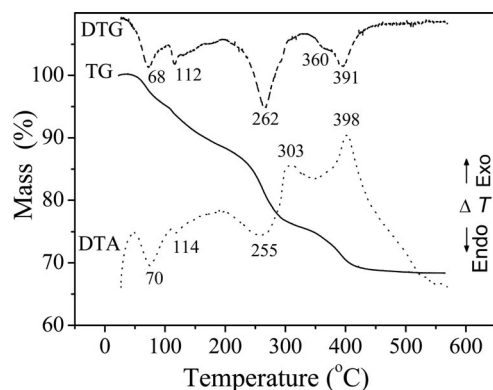


Figure 4. TG, DTA, and DTG curves for PrCo-S005.

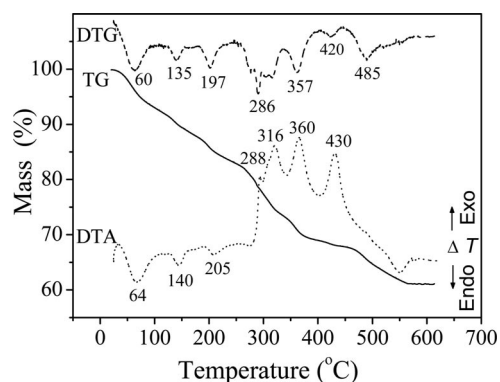


Figure 5. TG, DTA, and DTG curves for PrNi-S005.

Structural and Morphological Characterization of LiMPO_4 ($M = \text{Co}, \text{Ni}$)

LiCoPO_4

The XRD patterns of PrCo-S005 annealed between 350 and 600 °C is shown on Figure 6. The XRD analysis shows that olivine-type LiCoPO_4 is already formed at 350 °C. In addition, the partially decomposed precursor at 350 °C comprises also impurity phases including CoO , Li_3PO_4 , Co_3O_4 , $\text{Co}_2\text{P}_2\text{O}_7$, and an unknown phase with a strong diffraction peak at $2\theta = 22.14^\circ$. The phase composition is the same for the samples obtained from diluted and concentrated freeze-dried solutions. Further annealing of the samples leads to a decrease in the amount of the impurity phases, culminating at 450 °C in the formation of a single phase of well-crystallized LiCoPO_4 . To the best of our knowledge this is the lowest synthesis temperature that was reported for pure olivine-type LiCoPO_4 . The data obtained reveal that the formation of LiCoPO_4 from the phosphate–formate precursors takes place through interaction between Li_3PO_4 , $\text{Co}_2\text{P}_2\text{O}_7$, and cobalt oxides (CoO and/or Co_3O_4). The same mechanism of phospho-olivine formation was established also for LiMnPO_4 .^[18] Contrary to Co and Mn phospho-olivines, a single LiFePO_4 phase is formed directly after the release of the formic acid (i.e., at 350 °C), which is

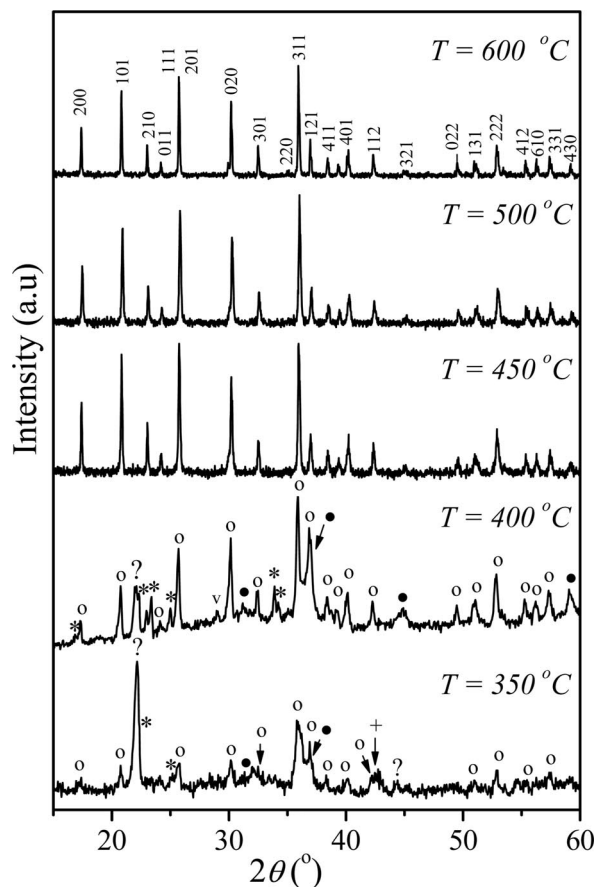


Figure 6. XRD patterns of PrCo-S005 annealed between 350 and 600 °C. Symbols: olivine-type LiCoPO_4 (○), Li_3PO_4 (*), CoO (+), Co_3O_4 (●), $\text{Co}_2\text{P}_2\text{O}_7$ (v), unknown phase (?).

accompanied with carbon deposition (up to 2.5 mass%).^[16] Contrary, no carbon was detected for the LiMnPO₄ and LiCoPO₄ samples. This demonstrates the different mechanism of formation of LiCo/MnPO₄ and LiFePO₄ from phosphate–formate precursors.

The XRD patterns of LiCoPO₄ obtained between 450 and 600 °C are satisfactory fitted by Rietveld analysis on the basis of the model of an ideal olivine structure, *SG Pnma* (Figure 7) and the structural parameters are given in Table 1. The lattice parameters and unit cell volumes seems to be insensitive towards both the annealing temperature and the concentration of the freeze-dried solutions. For the fitting procedure a possible Li/Co disorder between the *4a* and *4c* sites was also tried. However, after the refinement the occupancy factors of Li at *4a* and Co at *4c* tend to 1 (within the experimental error). For LiCoPO₄ annealed at 450 °C, the fitting procedure gives $R_b = 3.86$ with Li/Co disorder of 0.0035 ± 0.0015 vs. $R_b = 4.00$ without disorder; for LiCoPO₄ annealed at 500 °C – $R_b = 3.48$ with Li/Co disorder of 0.0018 ± 0.0014 vs. $R_b = 3.56$ without disorder; for LiCoPO₄ annealed at 600 °C – $R_b = 5.29$ with Li/Co disorder of 0.0044 ± 0.0014 vs. $R_b = 5.30$ without disorder. On the basis of the Rietveld refinement of neutron and X-ray powder diffraction, Ehrenberg et al.^[31] reported a Li deficiency at *4a* site (92% occupancy) for LiCoPO₄ obtained by the citric-assisted Pechini method at 600 °C. We have also tested a Li deficiency at *4a*, but the refinement results rejected this possibility: for LiCoPO₄ annealed at 450 °C R_b is 4.06 for *4a* site occupancy of 0.980 ± 0.020 ; for LiCoPO₄ annealed at 500 °C R_b is 3.53 for *4a* site occupancy of 1.010 ± 0.010 ; for LiCoPO₄ annealed at 600 °C R_b is 5.39 for *4a* site occupancy of 1.020 ± 0.020 . This means that LiCoPO₄ without any Li/Co disorder and Li deficiency is formed from phosphate–formate precursors between 450 and 600 °C. For comparison, LiMnPO₄ samples prepared by the same method at 500–600 °C are characterized by an ordered olivine-type structure, whereas at a lower temperature (450 °C) a small Li/Mn disorder of 2.6% between *4a* and *4c* sites was found.^[18]

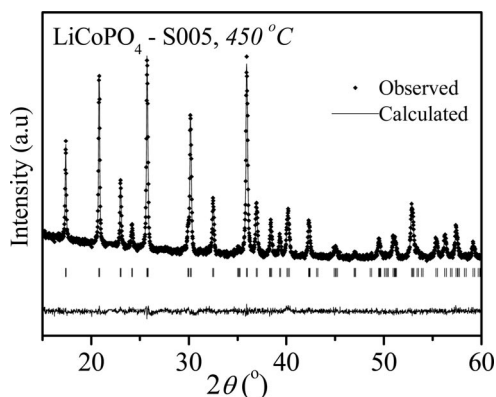


Figure 7. Rietveld refinement of the XRD pattern of PrCo-S005 annealed at 450 °C.

The results from XRD analysis are confirmed by the IR spectroscopic data (Figure 8). The decomposition of the

Table 1. Structural parameters of LiMPO₄ (M = Co and Ni) determined by Rietveld analysis.

| Atom | Site | <i>x</i> | <i>y</i> | <i>z</i> | <i>B</i> (Å ²) | SOF ^[a] |
|--|-----------|-----------|-----------|-----------|----------------------------|--------------------|
| LiCoPO ₄ -S005, 450 °C | | | | | | |
| <i>a</i> = 10.2026(3) Å, <i>b</i> = 5.9212(1) Å, <i>c</i> = 4.6995(1) Å | | | | | | |
| <i>V</i> = 283.907(16) Å ³ | | | | | | |
| <i>R</i> _{wp} = 11.7, <i>R</i> _b = 4.00, <i>R</i> _f = 3.57 | | | | | | |
| Li | <i>4a</i> | 0 | 0 | 0 | 1.1 | 1.0 |
| Co | <i>4c</i> | 0.2788(1) | 1/4 | 0.9791(5) | 0.9 | 1.0 |
| P | <i>4c</i> | 0.0958(3) | 1/4 | 0.4200(7) | 1.0 | 1.0 |
| O1 | <i>4c</i> | 0.0955(7) | 1/4 | 0.743(1) | 0.9 | 1.0 |
| O2 | <i>4c</i> | 0.4547(9) | 1/4 | 0.205(1) | 0.9 | 1.0 |
| O3 | <i>8d</i> | 0.1654(8) | 0.0458(7) | 0.2853(8) | 0.9 | 2.0 |
| LiCoPO ₄ -S005, 500 °C | | | | | | |
| <i>a</i> = 10.2045(2) Å, <i>b</i> = 5.9213(1) Å, <i>c</i> = 4.7002(1) Å | | | | | | |
| <i>V</i> = 284.012(14) Å ³ | | | | | | |
| <i>R</i> _{wp} = 10.90, <i>R</i> _b = 3.56, <i>R</i> _f = 3.76 | | | | | | |
| Li | <i>4a</i> | 0 | 0 | 0 | 1.2 | 1.0 |
| Co | <i>4c</i> | 0.2787(1) | 1/4 | 0.9789(4) | 1.3 | 1.0 |
| P | <i>4c</i> | 0.0951(3) | 1/4 | 0.4186(6) | 1.1 | 1.0 |
| O1 | <i>4c</i> | 0.0958(6) | 1/4 | 0.745(1) | 0.9 | 1.0 |
| O2 | <i>4c</i> | 0.4561(8) | 1/4 | 0.2060(9) | 0.9 | 1.0 |
| O3 | <i>8d</i> | 0.1670(5) | 0.0456(6) | 0.2848(7) | 0.9 | 2.0 |
| LiCoPO ₄ -S005, 600 °C | | | | | | |
| <i>a</i> = 10.2057(1) Å, <i>b</i> = 5.9228(1) Å, <i>c</i> = 4.7009(1) Å | | | | | | |
| <i>V</i> = 284.161(7) Å ³ | | | | | | |
| <i>R</i> _{wp} = 10.30, <i>R</i> _b = 5.29, <i>R</i> _f = 6.84 | | | | | | |
| Li | <i>4a</i> | 0 | 0 | 0 | 1.1 | 1.0 |
| Co | <i>4c</i> | 0.2787(1) | 1/4 | 0.9785(4) | 0.9 | 1.0 |
| P | <i>4c</i> | 0.0955(2) | 1/4 | 0.4204(6) | 1.0 | 1.0 |
| O1 | <i>4c</i> | 0.0978(5) | 1/4 | 0.744(1) | 0.9 | 1.0 |
| O2 | <i>4c</i> | 0.4543(7) | 1/4 | 0.2069(9) | 0.9 | 1.0 |
| O3 | <i>8d</i> | 0.1658(4) | 0.0456(6) | 0.2823(7) | 0.9 | 2.0 |
| LiNiPO ₄ -S005, 700 °C | | | | | | |
| <i>a</i> = 10.0384(1) Å, <i>b</i> = 5.85945(5) Å, <i>c</i> = 4.68020(5) Å | | | | | | |
| <i>V</i> = 275.288(5) Å ³ | | | | | | |
| <i>R</i> _{wp} = 8.32, <i>R</i> _b = 3.37, <i>R</i> _f = 4.83 | | | | | | |
| Li | <i>4a</i> | 0 | 0 | 0 | 1.1 | 1.0 |
| Ni | <i>4c</i> | 0.2757(1) | 1/4 | 0.9821(2) | 1.2 | 1.0 |
| P | <i>4c</i> | 0.0952(2) | 1/4 | 0.4199(4) | 1.1 | 1.0 |
| O1 | <i>4c</i> | 0.0996(3) | 1/4 | 0.7450(7) | 0.7 | 1.0 |
| O2 | <i>4c</i> | 0.4503(4) | 1/4 | 0.2019(6) | 0.7 | 1.0 |
| O3 | <i>8d</i> | 0.1647(3) | 0.0447(4) | 0.2760(4) | 0.7 | 2.0 |

[a] The site occupation factors (SOF) are given as number of atoms per formula unit.

LiCo precursors is completed for a short heating time at 350 °C (3 h) after the release of formic acid. The IR spectrum does not display any IR bands due to the formate ions vibrations. There are only bands due to the stretching PO and bending OPO vibrations. By extending the heating time from 3 to 10 h, the characteristic PO₄^{3−} ion vibrations become more resolved. The LiCo samples annealed at 450 °C exhibit the typical IR spectrum for well crystalline olivine-type LiCoPO₄:^[32] ν₃(PO₄) modes in the region 1149–976 and ν₄(PO₄) modes in the region 646–550 cm^{−1}. The bands at 521 and 471 cm^{−1} are suggested to originate mainly from Li⁺ translations.^[32] The bands positions are independent on the annealing temperature, which evidences the good thermal stability of the obtained LiCoPO₄ powders.

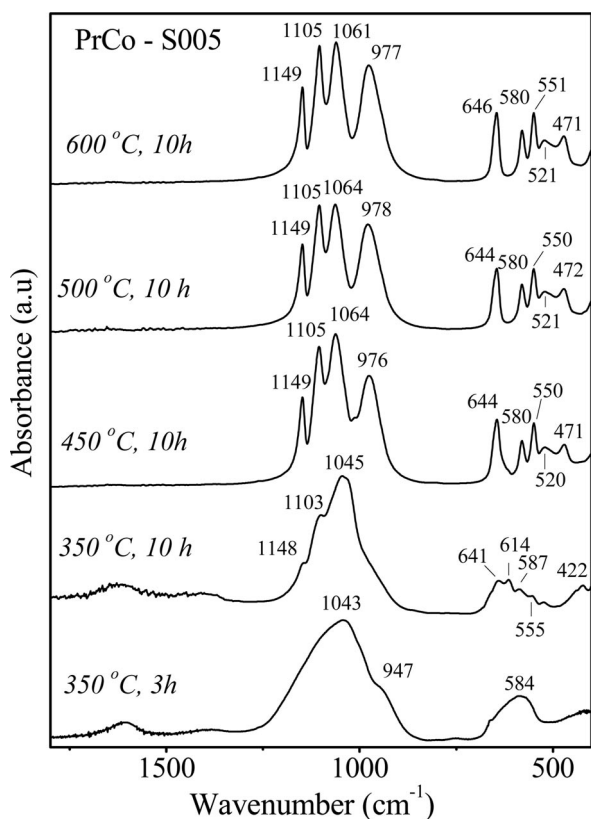


Figure 8. IR spectra of PrCo-S005 annealed between 350 and 600 °C.

The influence of the initial solution concentration and the annealing temperature on the LiCoPO_4 morphology is demonstrated by SEM analysis (Figure 9). The corresponding particles size distributions as determined from SEM analysis are also given (Figure 9, right). The morphology of LiCoPO_4 consists of isometric particles with close size distribution and does not depend on the solution concentration: the mean particles dimensions are around 185 ± 35 and 190 ± 30 nm for powders obtained at 500 °C from 0.05 and 0.10 M solutions, respectively (Figure 9A and B). By increasing the annealing temperature from 500 to 600 °C, there is a particle growth (around 230 ± 40 nm) and particle size distribution is slightly disturbed (Figure 9C). In addition, the crystallite sizes of LiCoPO_4 determined from the X-ray diffraction line broadening in the nanometric range (between 70 and 100 nm, Figure 10). On increasing the annealing temperature, the crystallite sizes tend to increase. Furthermore, the crystallite sizes slightly increase with the concentration of the freeze-dried solutions. It is worth mentioning that the crystallite sizes are slightly lower than the particle size dimensions determined from SEM analysis.

LiCoPO_4 obtained from phosphate-formate precursors is characterized with particles having small dimensions. In the literature, there are several reports on the formation of LiCoPO_4 with particle dimensions varying from 50 nm to 5 μm : for LiCoPO_4 obtained by solid-state reactions the particles were about 200–300 nm^[6] and 0.5–5 μm ,^[7] for

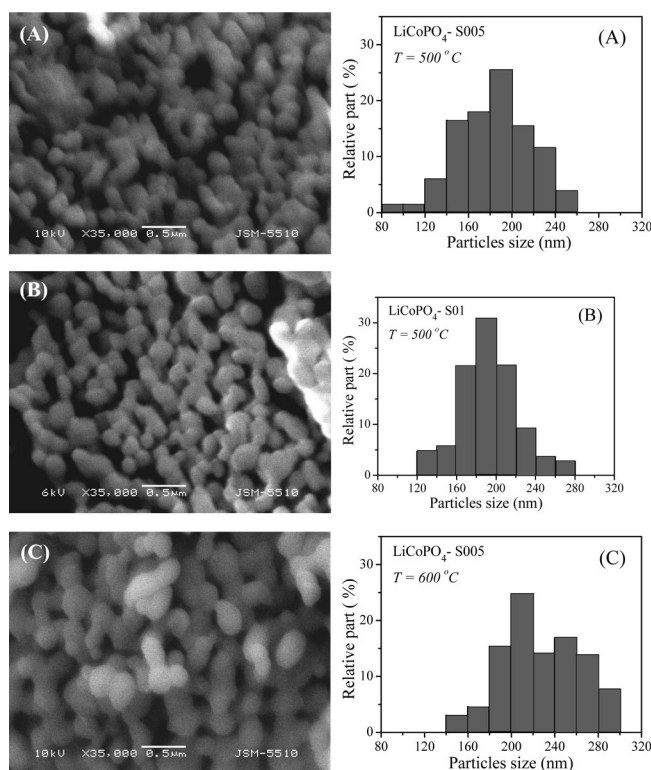


Figure 9. SEM images (left column) and corresponding particles size distributions (right column) of LiCoPO_4 .

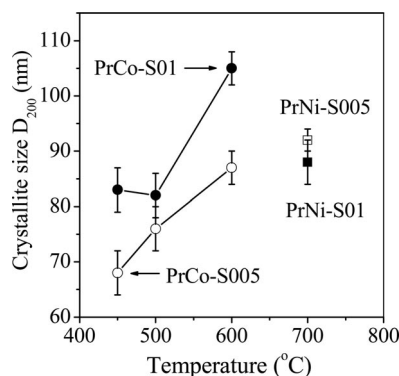


Figure 10. Dependence of the crystallite size D_{200} on the synthesis temperature for LiCoPO_4 and LiNiPO_4 prepared from two freeze-dried solutions. Symbols: LiCoPO_4 prepared from 0.05 M solution (\circ) and 0.10 M solution (\bullet), LiNiPO_4 prepared from 0.05 M solution (\square) and 0.10 M solution (\blacksquare).

LiCoPO_4 obtained by microwave heating the particles were about 400 nm² μm ,^[13] and for LiCoPO_4 prepared from citric acid assisted sol-gel method the particles were about 50 nm.^[9] The particles sizes of LiCoPO_4 were reduced to about of 100–150 nm by addition of conductive carbon during the synthesis^[6,13] or by subsequent high-energy ball milling.^[7] The comparison shows that the phosphate-formate precursor method allows preparing LiCoPO_4 with small particles, which will be favorable for its electrochemical performance.

Because the iron, manganese, and cobalt phosphate-formate precursors have a close structure and mor-

phology,^[16,18] it deserves to compare the particle dimensions and the crystallite sizes of the target LiMPO_4 olivines. The results show that the particle dimensions and crystallite sizes increase in the following order: $\text{LiFePO}_4 < \text{LiMnPO}_4 < \text{LiCoPO}_4$. The observed order can be related with the specific features of their formation: LiFePO_4 is directly formed after decomposition of the phosphate–formate precursor, whereas both LiMnPO_4 and LiCoPO_4 are a result of the solid-state reaction between the decomposition products. Further, the formation of LiCoPO_4 proceeds in air, whereas an argon atmosphere is needed for LiMnPO_4 .

LiNiPO_4

The XRD patterns of PrNi-S005 annealed at temperatures between 400 and 750 °C for 10 h are depicted in Figure 11. Thermal treatment of the LiNi–formate–phosphate precursors at 400 °C yields a phase mixture of metal Ni, NiO, and lithium phosphates phases like Li_3PO_4 and $\text{Li}_4\text{P}_2\text{O}_7$. LiNiPO_4 is formed at a temperature higher than 400 °C through a solid-state reaction between nickel oxide and lithium phosphates. A characteristic feature is that the LiNiPO_4 composition at 500 °C represents a phase mixture between two structural modifications: olivine-type and Na_2CrO_4 -type modifications (denoted also as β' -phase in^[33]). The mechanism of formation of the two forms of LiNiPO_4 from a LiNi–phosphate–formate precursor was discussed in our previous communication.^[19] The appearance of the metastable Na_2CrO_4 -type modification of LiNiPO_4 at 500 °C is a specific feature of the phosphate–formate precursor method for the Ni analogue. This reveals, most probably, once again the different structure and morphology of the nickel–phosphate–formate precursor.

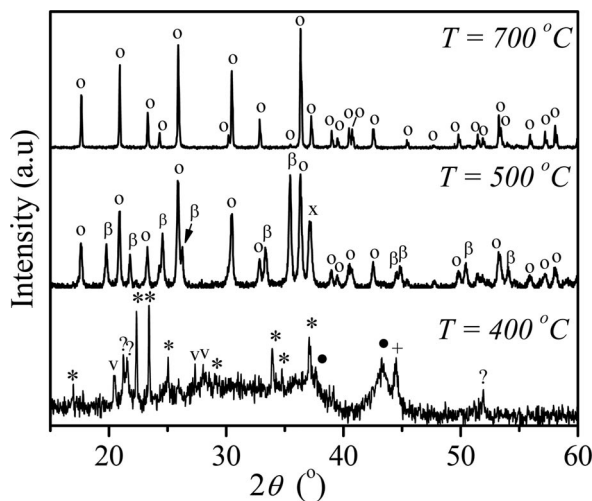


Figure 11. XRD patterns of PrNi-S005 annealed between 400 and 700 °C. Symbols: Li_3PO_4 (*), metal Ni (+), NiO (●), $\text{Li}_4\text{P}_2\text{O}_7$ (v), unknown phase (?), Na_2CrO_4 -type LiNiPO_4 (β), olivine-type LiNiPO_4 (○), common peak (x).

The temperature-induced transformation of the metastable Na_2CrO_4 -type to the olivine-type LiNiPO_4 is finished at 700 °C (Figure 11). Figure 12 and Table 1 give the results of the Rietveld refinement based on an ideal olivine-type

structure of the XRD pattern of LiNiPO_4 annealed at 700 °C. As in the case of LiCoPO_4 , the structural analysis reveals the formation of an olivine-type LiNiPO_4 phase, *SG Pnma*, without any Li/Ni disorder (between *4a* and *4c* positions) and Li deficiency: $R_b = 3.18$ with Li/Ni disorder of 0.004 ± 0.002 vs. $R_b = 3.29$ for *4a* site occupancy of 1.020 ± 0.020 vs. $R_b = 3.37$ without Li/Ni disorder and Li deficiency. In addition, the unit cell parameters of LiNiPO_4 do not depend on the concentration of the freeze-dried solutions.

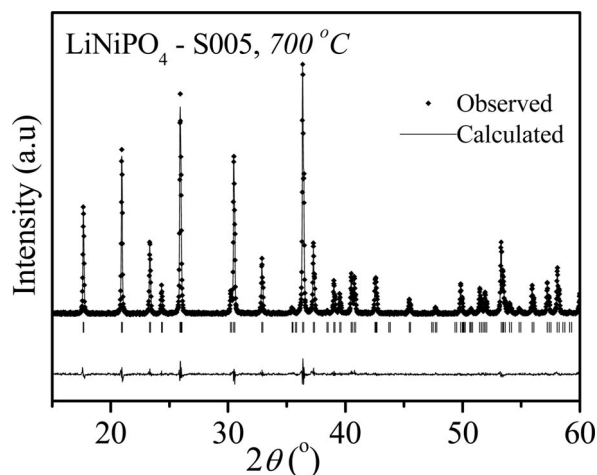


Figure 12. Rietveld refinement of the XRD pattern of PrNi-S005 annealed at 700 °C.

Figure 13 shows the IR spectra of the samples annealed between 400 and 700 °C. The IR spectrum at 400 °C is dominated by the absorption bands of phosphate groups in the regions of 1150–900 and 650–500 cm^{-1} . The weak bands around 1630, 1400, and 750 cm^{-1} are related with residual formate species. In accordance with the XRD data, the IR

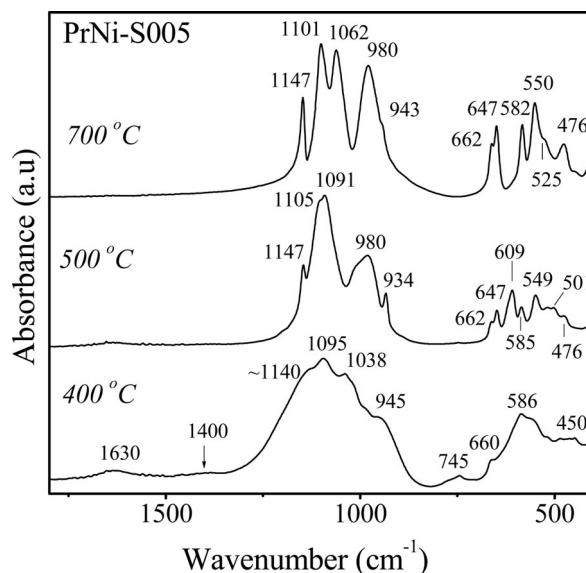


Figure 13. IR spectra of PrNi-S005 annealed between 400 and 700 °C.

spectrum of the sample annealed at 500 °C displays absorption bands due to the two LiNiPO_4 phases. The bands at 934, 609 and 501 cm^{-1} (ν_1 , ν_4 , and ν_2 modes, respectively) are attributed to the Na_2CrO_4 -type form only, whereas the residual bands originate from both forms. The IR spectrum of the sample at 700 °C fully coincides with that of pure olivine-type LiNiPO_4 ^[32] (Figure 13): $\nu_1(\text{PO}_4)$ vibration at 943 cm^{-1} , $\nu_3(\text{PO}_4)$ vibrations in the region $1147\text{--}980\text{ cm}^{-1}$, $\nu_4(\text{PO}_4)$ vibration in the region $662\text{--}550\text{ cm}^{-1}$, and Li^+ -translations in the range $525\text{--}476\text{ cm}^{-1}$.

Figure 14 depicts the SEM image of the olivine-type LiNiPO_4 prepared by the phosphate-formate method at 700 °C. As in the case of LiCoPO_4 , the morphology of LiNiPO_4 comprises isometric particles with a higher mean size of $380 \pm 70\text{ nm}$ and a broader particle size distribution. The particle size derived from SEM is larger than the crystallite size derived from XRD (about 90 nm, Figure 10). This means that the SEM particles are not single crystals. It is worth mentioning that there are no data in the literature for morphological characterization of LiNiPO_4 .

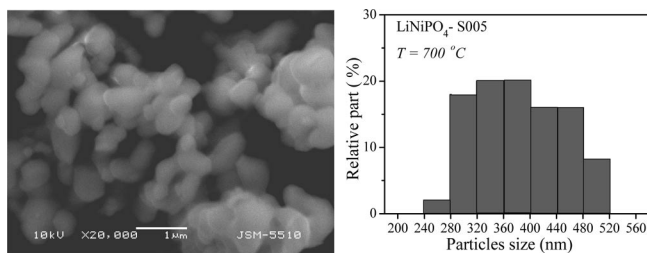


Figure 14. SEM image and particles size distribution of LiNiPO_4 annealed at 700 °C.

Conclusion

Homogeneous lithium-metal-phosphate-formate precursors with a composition $\text{LiMH}_x(\text{PO}_4)(\text{HCOO})_x \cdot y\text{H}_2\text{O}$ ($M = \text{Co}, \text{Ni}$) were prepared by freeze drying of aqueous solutions of the corresponding metal formates and LiH_2PO_4 . Cobalt and nickel precursors have different structure and morphology. Whereas in the Co precursors the formate and phosphates ions are randomly coordinated to both Co and Li cations, in the Ni precursors the formate ions are preferentially around Ni^{2+} and the phosphate ions are around Li^+ . The morphology of the Co precursors consists of flake-like aggregates, whereas the “cabbage”-like aggregates are formed for the Ni precursors. Nickel phosphate-formate precursors are decomposed at higher temperatures in comparison with the Co analogues. Thermal treatment of the precursors yields single olivine-type LiCoPO_4 at 450 °C and LiNiPO_4 at 700 °C with crystallite sizes of 65 and 90 nm, respectively. LiCoPO_4 and LiNiPO_4 phases display isometric particles with mean SEM particle dimensions of 185 and 380 nm, respectively. For both Co and Ni systems, the phosphate-formate precursor method yields olivine-type phase without any Li to M disorder (between 4a and 4c positions) and Li deficiency. A specific feature of LiNiPO_4 is that a phase mixture between olivine-

type and Na_2CrO_4 -type structural modifications is formed at 500 °C. The Na_2CrO_4 -type modification of LiNiPO_4 is transformed to olivine-type LiNiPO_4 at 700 °C.

Experimental Section

Preparation of Lithium-Cobalt-Phosphate-Formate and Lithium-Nickel-Phosphate-Formate Precursors: The starting reagents are $\text{M}(\text{HCOO})_2 \cdot 2\text{H}_2\text{O}$ ($M = \text{Co}, \text{Ni}$) and LiH_2PO_4 (Aldrich). The metal formate dihydrates, $\text{M}(\text{HCOO})_2 \cdot 2\text{H}_2\text{O}$, were prepared by neutralization of dilute formic acid solutions with the corresponding carbonates at 60–70 °C. The solutions were then filtered and concentrated. The crystals $\text{M}(\text{HCOO})_2 \cdot 2\text{H}_2\text{O}$ ($M = \text{Co}, \text{Ni}$) grew by cooling at room temperature. They are very stable upon storage, which ensures an exact stoichiometry of the target products. Transparent phosphate-formate solutions of lithium and cobalt (nickel, respectively) were obtained by mixing the solutions of $\text{M}(\text{HCOO})_2 \cdot 2\text{H}_2\text{O}$ ($M = \text{Co}$ or Ni) and LiH_2PO_4 keeping a stoichiometric ratio $M/\text{Li} = 1:1$. The pH value of both solutions before mixing was adjusted to $\text{pH} \approx 3$ with addition of a small quantity of HCOOH (1:1). In comparison with the iron and manganese salts, the solubility of $\text{Co}(\text{HCOO})_2$ and $\text{Ni}(\text{HCOO})_2$ in water is limited up to 2.7% at 25 °C. Therefore, in these cases the concentrations of freeze-dried solutions were varied between 0.05 and 0.10 M (with respect to the metal ions). The solutions thus prepared were frozen instantly with liquid nitrogen and dried in vacuo (20–30 mbar) for about 17 h at -20 °C with an Alpha-Christ Freeze Dryer. For the sake of simplicity, the precursors obtained from solutions with different concentrations will be further on denoted as PrCo-S005 and PrCo-S01 , PrNi-S005 and PrNi-S01 , i.e., obtained from 0.05 and 0.10 M solutions, respectively. After drying, the solid precursors were predecomposed at 350 and 400 °C for 3 h for cobalt and nickel precursors, respectively. The samples were further annealed at different temperatures from 350 to 750 °C for 10 h under static air atmosphere. The LiCoPO_4 and LiNiPO_4 samples obtained from the different precursors are denoted as $\text{LiCoPO}_4\text{-S005}$ and $\text{LiCoPO}_4\text{-S01}$, $\text{LiNiPO}_4\text{-S005}$ and $\text{LiNiPO}_4\text{-S01}$, respectively.

Methods for Sample Characterization: The metal content in starting $\text{M}(\text{HCOO})_2 \cdot 2\text{H}_2\text{O}$, the precursors, and LiMPO_4 ($M = \text{Co}, \text{Ni}$) samples was determined complexometrically. The lithium content was determined by atomic absorption analysis. Elemental analysis (C and H) was performed by using Elementar Analysensysteme GmbH (VarioEL analyzer). X-ray structural analysis was performed with a Bruker Advance 8 diffractometer with LynxEye detector by using Cu-K_α radiation. Step-scan recordings for structure refinement by the Rietveld method were carried out by using 0.02° 2θ steps of 10 s duration. The computer program FULLPROF was used in the calculations. The diffractometer point zero, the Lorentzian/Gaussian fraction of the pseudo-Voigt peak function, scale factor, the unit cell parameters (a , b , and c), the thermal factor for the 4a, 4c, and 8d positions and the line half-width parameters were determined. The crystallites size of LiMPO_4 was calculated by the Scherrer equation from the line width of the (200) reflection peak: $D_{200} = \lambda / [(\beta^2 - \beta_o^2)^{1/2} \cos \theta_{200}]$, where $\lambda(\text{Cu-K}_\alpha) = 0.15418\text{ nm}$, β is the peak width at the half height corrected with instrumental broadening, and θ_{hkl} is the Bragg angle. The line width was determined by profile analysis using a WinPlotr program. The IR spectra were recorded with a Fourier transform Nicolet Avatar-320 instrument using KBr pellets (resolution $< 2\text{ cm}^{-1}$). The thermal analysis (simultaneously obtained DTA, TG, and DTG curves) of the precursors was carried out by a “Stanton Redcroft” apparatus

in the temperature range up to 650 °C, a heating rate of 5 °C/min, and sample mass of 10 mg. The morphology of the precursors and LiMPO₄ powders was observed by JEOL (JSM-5300 and JSM-5510) scanning electron microscopes.

Acknowledgments

Authors are grateful for the financial support of the National Science Fund of Bulgaria (Ch 1701/2007) and the National Centre for New Materials (DO-02-82/2008).

- [1] A. K. Padhi, K. S. Nanjundaswamy, J. B. Goodenough, *J. Electrochem. Soc.* **1997**, *144*, 1188–1194.
- [2] M. S. Whittingham, Y. Song, S. Lutta, P. Y. Zavalij, N. Chernova, *J. Mater. Chem.* **2005**, *15*, 3362–3379.
- [3] K. Amine, H. Yasuda, M. Yamachi, *Electrochem. Solid State Lett.* **2000**, *3*, 178–179.
- [4] J. Wolfenstine, J. Allen, *J. Power Sources* **2005**, *14*, 389–390.
- [5] W. F. Howard, R. M. Spotnitz, *J. Power Sources* **2007**, *165*, 887–891.
- [6] J. M. Loris, C. Pérez Vicente, J. L. Tirado, *Electrochem. Solid State Lett.* **2002**, *5*, A234–A237.
- [7] B. Jin, H.-B. Gu, K.-W. Kim, *J. Solid State Electrochem.* **2008**, *12*, 105–111.
- [8] N. N. Bramnik, K. Nikolowski, D. M. Trots, H. Ehrenberg, *Electrochem. Solid State Lett.* **2008**, *11*, A89–A93.
- [9] Gangulibabu, D. Bhuvaneswari, N. Kalaiselvi, N. Jayaprakash, P. Periasamy, *J. Sol-Gel Sci. Technol.* **2009**, *49*, 137–144.
- [10] P. Deniard, A. M. Dulac, X. Rocquefelte, V. Grigorova, O. Lebacqz, A. Pasturel, S. Jobic, *J. Phys. Chem. Solids* **2004**, *65*, 229–233.
- [11] R. Vasanthi, D. Kalpana, N. G. Renganathan, *J. Solid State Electrochem.* **2008**, *12*, 961–969.
- [12] X. Huang, J. Ma, P. Wu, Y. Hu, J. Dai, Z. Zhu, H. Chen, H. Wang, *Mater. Lett.* **2005**, *59*, 578–582.
- [13] H. H. Li, J. Jin, J. P. Wei, Z. Zhou, J. Yan, *Electrochem. Commun.* **2009**, *11*, 95–98.
- [14] K. Rissouli, K. Benkhoulja, J. R. Ramos-Barrado, C. Julien, *Mater. Sci. Eng., B* **2003**, *98*, 185–189.
- [15] D. Shanmukaraj, R. Murugan, *Ionics* **2004**, *10*, 88–92.
- [16] V. Koleva, E. Zhecheva, R. Stoyanova, *J. Alloys Compd.* **2009**, *476*, 950–957.
- [17] E. Zhecheva, Ml. Mladenov, P. Zlatilova, V. Koleva, R. Stoyanova, *J. Phys. Chem. Solids* **2010**, *71*, 848–853.
- [18] V. Koleva, R. Stoyanova, E. Zhecheva, *Mater. Chem. Phys.* **2010**, *121*, 370–377.
- [19] V. Koleva, R. Stoyanova, E. Zhecheva, *Eur. J. Inorg. Chem.* **2010**, 127–131.
- [20] V. Koleva, H. Effenberger, *J. Solid State Chem.* **2007**, *180*, 956–967.
- [21] K. G. Kidd, H. H. Mantsch, *J. Mol. Spectrosc.* **1981**, *85*, 375–389.
- [22] K. Nakamoto, *Infrared and Raman Spectra of Inorganic and Coordination Compounds*, 4th ed., Wiley, New York, **1978**, p. 138.
- [23] A. Ait Salah, P. Jozwiak, K. Zaghib, J. Garbarczyk, F. Gendron, A. Manger, C. M. Julien, *Spectrochim. Acta* **2006**, *65A*, 1007–1113.
- [24] A. Novak, *Struct. Bonding (Berlin)* **1974**, *18*, 177–216.
- [25] J. Baran, T. Lis, M. Drozd, H. Ratajczak, *J. Mol. Struct.* **2000**, *516*, 185–202.
- [26] J. Xu, D. F. R. Gilson, I. S. Butler, *Spectrochim. Acta* **1998**, *A54*, 1869–1878.
- [27] K. Mouaïne, P. Becker, C. Carabatos-Nédelec, *Phys. Stat. Sol.* **1997**, *200*, 273–287.
- [28] P. Baraldi, *Spectrochim. Acta* **1979**, *35A*, 1003–1007.
- [29] V. Rosenband, A. Gany, *J. Mater. Proc. Technol.* **2004**, *153–154*, 1058–1061.
- [30] T. Meisel, Z. Halmos, K. Seybold, E. Pungor, *J. Thermal Anal.* **1975**, *7*, 73–80.
- [31] H. Ehrenberg, N. N. Bramnik, A. Senyshyn, H. Fuess, *Solid State Sci.* **2009**, *11*, 18–23.
- [32] M. Th. Paques-Ledent, P. Tarte, *Spectrochim. Acta* **1974**, *30A*, 673–689.
- [33] O. García-Moreno, M. Álvarez-Vega, F. García-Alvarado, J. García-Jaca, J. M. Gallardo-Amores, M. L. Sanjuán, U. Amador, *Chem. Mater.* **2001**, *13*, 1570–1576.

Received: April 12, 2010

Published Online: July 30, 2010

N,N,O Ligands Based on Triazoles and Transition Metal Complexes Thereof

Eike Hübner,^[a] Nina V. Fischer,^[a] Frank W. Heinemann,^[a] Utpal Mitra,^[b]
Viacheslav Dremov,^[b] Paul Müller,*^[b] and Nicolai Burzlaff*^[a]

Keywords: Scorpionate ligands / Tripod ligands / Coordination polymers / Zinc / Manganese / Ruthenium

The reaction of 2*H*-benzotriazole (**1**) with dichloroacetic acid leads to the symmetric bis(2*H*-benzotriazol-2-yl)methane (**2c**) in 40 % yield. Deprotonation of **2c** at the bridging methylene group and subsequent carboxylation with CO₂ yielded the new tripodal *N,N,O* ligand bis(2*H*-benzotriazol-2-yl)acetic acid Hbbta (**3**). The sterically less demanding sodium 3,3-bis(1*H*-1,2,4-triazol-1-yl)propionate Na[btp] (**5**) was obtained by saponification of methyl 3,3-bis(1*H*-1,2,4-triazol-1-yl)propionate (**4**). The heteroscorpionate ligand **3** was treated with [MnBr(CO)₅] and [RuCl₂(PPh₃)₃] to form the manganese tricarbonyl complex [Mn(bbta)(CO)₃] (**6**) and the air stable ruthenium complex [Ru(bbta)Cl(PPh₃)₂] (**7**). DFT calculations and the IR spectra of the carbonyl complex **6** reveal ligand **3**

to be a less electron-donating ligand compared to the bis(1*H*-pyrazol-1-yl)acetic acid Hbpza. In case of the 1*H*-1,2,4-triazole-based ligand **5** formation of coordination polymers were observed as proven by the synthesis of [Zn(btp)₂]_∞ (**8**) and [Mn(btp)₂]_∞ (**9**). Polymer **8** crystallises in linear chains of zinc atoms bridged by two molecules of ligand **5** each. These polymer chains show an interesting π -stacking interaction between uncoordinated triazole residues of the ligands. Deposition of the coordination polymer on highly ordered pyrolytic graphite (HOPG) was successful and was analysed by scanning tunnelling microscopy (STM). Reaction of Na[btp] (**5**) with MnSO₄·H₂O resulted in a metal organic framework (MOF) [Mn(btp)₂]_∞ (**9**).

Introduction

N,N,O ligands such as bis(1*H*-pyrazol-1-yl)acetic acids are a versatile class of ligands structurally related to the well-known hydrotris(1*H*-pyrazol-1-yl)borate (Tp) ligand. Efficient syntheses for achiral, chiral and enantiopure bis(1*H*-pyrazol-1-yl)acetic acids have been developed over the years since they have been introduced to coordination chemistry in 1999 by A. Otero.^[1] Various transition metal complexes bearing these tripodal, κ^3 -*N,N,O*-binding ligands indicate binding properties as weak electron-donating ligands, similar to the Tp ligands.^[2,3] Examples for transition metal complexes with manganese and ruthenium are [Mn(bdmpza)(CO)₃] and [Ru(bdmpza)(PPh₃)₃] {bdmpza: bis(3,5-dimethyl-1*H*-pyrazol-1-yl)acetate}.^[4–6] Furthermore, model complexes with biorelevant transition metals such as iron(II) and zinc(II) support the concept of bis(1*H*-pyrazol-1-yl)acetic acids to be good structural mimics for the active site of metalloenzymes with an 2-His-1-carboxylate motif.^[7–9]

Our recent work focuses on derivatives of such *N,N,O* ligands, to broaden the field of available heteroscorpionate ligands with various electronic and steric properties. So far examples of chiral bis(1*H*-pyrazol-1-yl)acetic acids,^[10] 3,3-bis(imidazol-2-yl)propionic acids^[11] or 2-[bis(1*H*-pyrazol-1-yl)methyl]phenolates^[12] have been obtained. Moreover, tricarbonylrhenium complexes are of particular interest as model compounds for radiopharmaceutical applications.^[13]

Introducing triazoles instead of pyrazoles or imidazoles as *N*-donor seems to be one reasonable option to establish a new field of *N,N,O* heteroscorpionate ligands. To the best of our knowledge, so far mainly bis(1*H*-1,2,4-triazol-1-yl)acetic acids have been applied in coordination chemistry, e.g. in cytotoxic copper(I) complexes or metal-organic frameworks (MOFs).^[14–16]

2*H*-Benzotriazole, which is well known to form a chelating *N,N*-donor ligand by reaction with dichloromethane,^[17] offers rather large steric demand but electron deficiency. Therefore, synthesis of bis(2*H*-benzotriazol-2-yl)acetic acid promises to result in an interesting ligand candidate. In contrast, 1*H*-1,2,4-triazole may act as small and sterically non-demanding *N*-donor.

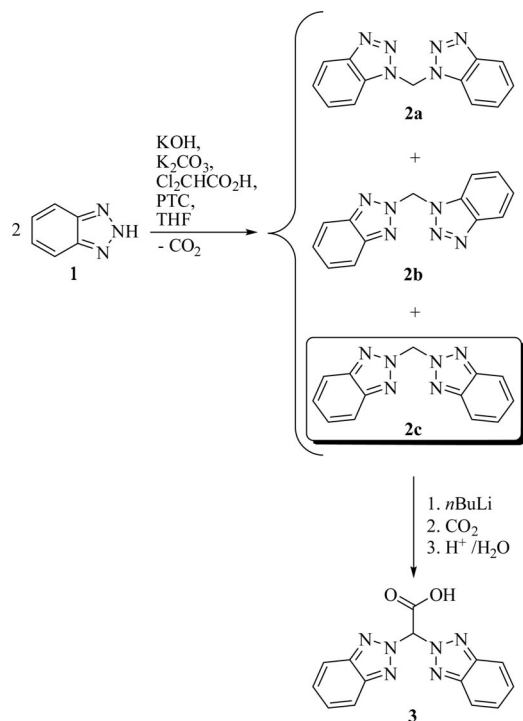
Ligand Design

Reaction of 2*H*-benzotriazole (**1**) with dichloromethane leads to the three possible isomers bis(1*H*-benzotriazol-1-yl)methane (**2a**), (1*H*-benzotriazol-1-yl)(2*H*-benzotriazol-2-yl)methane (**2b**) and bis(2*H*-benzotriazol-2-yl)methane (**2c**)

[a] Inorganic Chemistry, Department of Chemistry and Pharmacy & Interdisciplinary Center for Molecular Materials (ICMM), University of Erlangen-Nürnberg, Egerlandstraße 1, 91058 Erlangen, Germany
Fax: +49-9131-85-27387
E-mail: burzlaff@chemie.uni-erlangen.de

[b] Department of Physics & Interdisciplinary Center for Molecular Materials (ICMM), University of Erlangen-Nürnberg, Erwin-Rommel-Strasse 1, 91058 Erlangen, Germany

(Scheme 1).^[17,18] Almost independently from the reaction conditions the synthesis yields a mixture of all three isomers. A reaction with dichloromethane in the presence of KOH and a phase-transfer catalyst for example results in 40% **2a**, 31% **2b** and 6% **2c**.^[18] Isomer **2c** is the isomer required for the synthesis of a symmetric and bulky heteroscorpionate tripodal *N,N,O* ligand. Therefore, higher amounts of isomer **2c** would be desirable.



Scheme 1. Synthesis of the Hbta ligand **3**.

Instead of reacting **1** with dichloromethane, the reaction with dichloroacetic acid as starting material offers an alternative synthetic pathway. In the presence of K_2CO_3 , KOH and phase-transfer catalyst **2H**-benzotriazole (**1**) reacts with dichloroacetic acid to the desired isomer **2c** in yields up to 40% (Scheme 1).

Reaction of **2c** with *n*BuLi in THF leads to a dark blue anion, due to its large delocalized π -electron system. In analogy to the synthesis of Li[bdmpza], that is obtained from the corresponding bis(3,5-dimethyl-1*H*-pyrazol-1-yl)-methane,^[1] further reaction with dry gaseous carbon dioxide affords the bis(2*H*-benzotriazol-2-yl)acetic acid (Hbta) (**3**) after acidic workup. The presence of **3** is clearly indicated by a shift of the bridging CH 1H NMR signal from $\delta = 7.43$ ppm in **2c** to 8.25 ppm for **3**, as well as the appropriate mass spectrum. The IR resonance at 1763 cm^{-1} (THF) is assigned to the asymmetric carboxylate vibration. Finally, an X-ray analysis revealed the molecular structure of **3** (Figure 1).

Although, decarboxylation occurs during the reaction of 2*H*-benzotriazole with dichloroacetic acid, ligand **3** was found to be stable at room temperature as crystalline powder as well as in solution.

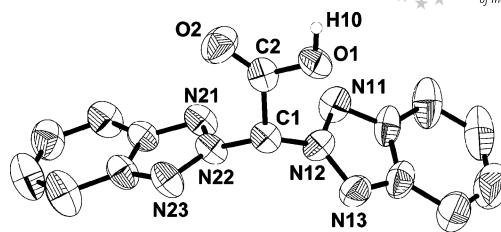
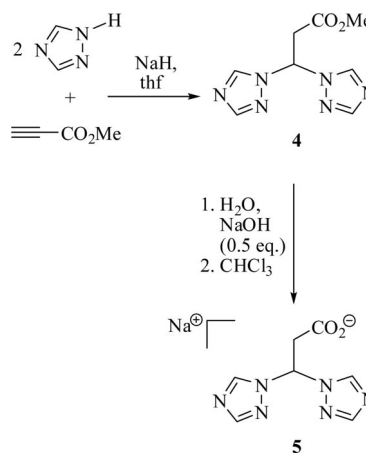


Figure 1. Molecular structure of bis(2*H*-benzotriazol-2-yl)acetic acid (**3**); thermal ellipsoids are drawn at the 50% probability level. Most hydrogen atoms have been omitted for clarity. Selected bond lengths [Å] and angles [°]: $d(C2-O1) = 1.320(5)$, $d(C2-O2) = 1.179(5)$, $d(C1-N12) = 1.440(5)$, $d(C1-N22) = 1.462(5)$, $\angle(N12,C1,N22) = 112.2(3)$.

Due to the annelated benzene rings, compound **3** represents a ligand with relatively large steric demand. Diez-Barra and co-workers recently published an interesting pathway to various esters of *N*-heterocyclic 3,3-bis(heteroaryl)propionic acids, such as methyl 3,3-bis(1*H*-1,2,4-triazol-1-yl)propionate (**4**).^[19] The corresponding acid, 3,3-bis(1*H*-1,2,4-triazol-1-yl)propionic acid or the salt sodium 3,3-bis(1*H*-1,2,4-triazol-1-yl)propionate (Nabtp) (**5**) are obtained by saponification of ester **4** in presence of water and NaOH in THF (Scheme 2). Due to the very good solubility of **5** in water, purification of **5** in the presence of excess base or other inorganic salts proved to be rather difficult.





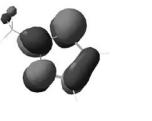

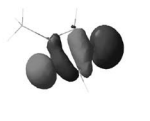

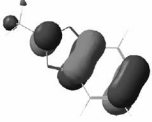
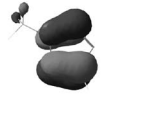

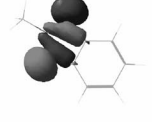
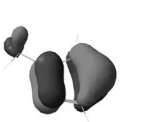

Scheme 2. Sodium 3,3-bis(1*H*-1,2,4-triazol-1-yl)propionate (Nabtp) (**5**) obtained by saponification of the ester methyl 3,3-bis(1*H*-1,2,4-triazol-1-yl)propionate (**4**).

However, saponification with a slight deficit of NaOH yields a mixture of **4** and **5**. Ester **4** was removed by washing with chloroform to yield the sodium propionate **5** as a colourless solid. Extracted ester **4** can be recirculated in a second saponification step. The sodium propionate **5** is clearly indicated by the absence of the resonance of the methyl ester at $\delta = 3.71$ ppm in the 1H -NMR spectra and the asymmetric carboxylate vibration at 1612 cm^{-1} (methanol). Ligand **3** represents on one side a new and sterically demanding bis(triazolyl)carboxylic acid whereas ligand **5** on the other side is sterically less demanding.

DFT Calculations

To gather some information about the electronical and coordination properties of the two ligands **3** and **5**, DFT calculations were performed. Comparison of the calculated frontier orbitals of 2-methyl-2*H*-benzotriazole, 1-methyl-1*H*-1,2,4-triazole and 1-methyl-1*H*-pyrazole (Table 1) gives information about the donor and acceptor properties of the binding nitrogen sites of **3** and **5**. The frontier orbitals of 2-methyl-2*H*-benzotriazole are assumed to be comparable to those of the 2*H*-benzotriazol-2-yl donor in **3**, the frontier orbitals of 1-methyl-1*H*-1,2,4-triazole to those of the 1*H*-1,2,4-triazol-1-yl donor in **5** and the frontier orbitals of 1-methyl-1*H*-pyrazole to those of the 1*H*-pyrazol-1-yl donor in bis(1*H*-pyrazol-1-yl)acetic acids. The binding behaviour of histidine according to Holm and co-workers is dominated by its frontier orbitals.^[20] Recently, we and others successfully discussed the binding of imidazole- and pyrazole-based *N,N,O* ligands by means of their frontier orbitals.^[11]

Table 1. Comparison of the Kohn–Sham orbitals of 2-methyl-1*H*-benzotriazole, 1-methyl-1*H*-triazole and 1-methyl-1*H*-pyrazole.

| 2-Methyl-2 <i>H</i> -benzotriazole | 1-Methyl-1 <i>H</i> -1,2,4-triazole | 1-Methyl-1 <i>H</i> -pyrazole |
|---|---|---|
|  |  |  |
| Ia) LUMO + 1 (−2.0518 eV) | Ib) LUMO (0.7791 eV) | Ic) LUMO (−0.2829 eV) |
|  |  |  |
| IIa) HOMO (−5.4827 eV) | IIb) HOMO (−6.1943 eV) | IIc) HOMO (−5.6571 eV) |
|  |  |  |
| IIIa) HOMO − 1 (−6.0617 eV) | IIIb) HOMO − 1 (−6.2515 eV) | IIIc) HOMO − 1 (−5.7849 eV) |
|  |  |  |
| IVa) HOMO − 2 (−6.7646 eV) | IVb) HOMO − 2 (−6.9316 eV) | IVc) HOMO − 2 (−6.3999 eV) |

The orbital plots show the capability of **3** to act as π -acceptor (LUMO+1, Table 1, Ia) as well as the pyrazoles (LUMO, Ic) do. Noticeable is the energetically low and strongly delocalised LUMO+1. The orbital plot of the HOMO (IIa) points out the π -donor character of the 1*H*-benzotriazole ligands in accordance to the pyrazoles (IIc). σ -Donor binding properties (HOMO−2, IVa) are provided similar to pyrazoles (HOMO−2, IVc).

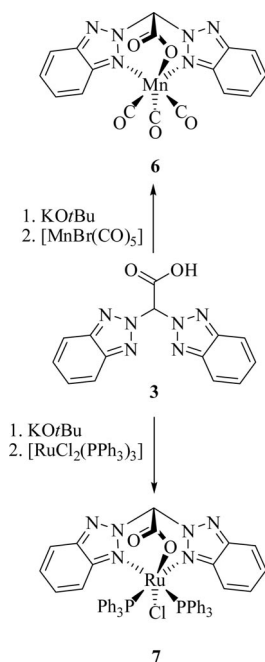
Solely the HOMO−1 (IIIa) does not seem to be involved in the interaction between the frontier orbitals and the metal centre. Obviously, all considered orbitals apart from the HOMO−2 show conspicuous delocalisation in the aromatic benzene ring. Over all, bis(2*H*-benzotriazol-2-yl)acetic acid should be able to act as σ -donor, π -donor and π -acceptor. The π -donor properties may be less distinctive due to the delocalization into the aromatic system. The two possible nitrogen binding sites in **3** do not show up any differences in the orbital plots, due to the molecular symmetry. Coordination towards the metal centre with one of the nitrogen donors will always lead to the same product.

In contrast, ligand **5** shows some differences regarding the two possible N donors. Both can act as π -acceptors (LUMO, Ib) and σ -donors (HOMO, IIb) although coordination will not lead to the same product due to the broken symmetry. N2 has a smaller orbital coefficient in one of the two orbitals suitable for π -donors compared to N4 (IVb, HOMO−2). On the other hand N4 has a total lack of π -donors capabilities compared to N2 in IIIb (HOMO−1). In total, due to missing delocalisation, the orbitals of **5** seem to show some similarity to those of the pyrazole donor. Especially N2 can be compared to the nitrogen of a pyrazole-based ligand. But **5** provides two different binding sites, both able to act as donor and acceptor.

Besides a discussion of the orbital plots, the HOMO–LUMO energy gap allows to estimate further properties based on the concept of chemical hardness. Molecules with a large HOMO–LUMO energy gap are considered to be hard, molecules with a small energy gap are considered to be soft.^[21] Following the calculated orbital energies in Table 1, ligand **3** must clearly be accepted to be the softest of the three ligands discussed here. The low HOMO–LUMO energy gap can be explained by the strongly delocalized structure of 2*H*-benzotriazole. Due to the DFT calculations performed here and well-known errors of the resulting orbital energies, no further estimations on the reactivity of these ligands towards metal fragments are extracted from these results.^[22] Furthermore, the different coordination properties of the two possible bindings sites N2 and N5 of 1-methyl-1*H*-1,2,4-triazole cannot be explained by means of the HOMO–LUMO energy gap.

Metal Complexes

Deprotonation of the carboxylate donor allows ligand **3** to react as a monoanionic *N,N,O* ligand with organometallic precursors such as [MnBr(CO)₃] and [RuCl₂(PPh₃)₃] (Scheme 3).



Scheme 3. Synthesis of $[\text{Mn}(\text{bbta})(\text{CO})_3]$ (**6**) and $[\text{Ru}(\text{bbta})\text{Cl}(\text{PPh}_3)_2]$ (**7**).

The facial *N,N,O*-binding behaviour of ligand **3** is clearly indicated by the IR stretching frequencies of the complex $[\text{Mn}(\text{bbta})(\text{CO})_3]$ (**6**), which is obtained by a reaction of the potassium salt of **3** with $[\text{MnBr}(\text{CO})_5]$. The IR spectrum of complex **3** exhibits a single A' and two close A'' and A' signals [**6**: $\tilde{\nu}$ (THF) = 2047, 1963, 1933 cm^{-1}]. This is typical for an unsymmetric “piano stool” carbonyl complex.^[4] An IR signal observed at 1707 cm^{-1} is assigned to the asymmetric carboxylate vibration. The formation of **6** is backed by the appropriate MH^+ signal of the FAB mass spectrum. Although the NMR spectra of **6** are broad, complex **6** shows a clear set of signals for the carbonyl residues at δ = 218.3 and 221.0 ppm in the $^{13}\text{C}\{^1\text{H}\}$ NMR spectrum. The signal occurring at δ = 162.0 ppm is assigned to the carboxylate donor. Table 2 shows a comparison of the characteristic IR signals of **6** to analogous tricarbonyl complexes, which allows to estimate the electronic properties of **3**.^[4]

Table 2. IR data of complexes $[\text{MnL}(\text{CO})_3]$ with various tripodal ligands.

| Ligand L | bbta | bpza ^[4] | bdmpza ^[4] | Tp ^[4] |
|---|------------------|---------------------|-----------------------|-------------------|
| $\tilde{\nu} [\text{MnL}(\text{CO})_3]$ | 2047, 1963, 1933 | 2041, 1946, 1925 | 2036, 1942, 1915 | 2033, 1930 |

The IR stretching vibrations at higher wavenumbers indicate in total (σ - and π -bonding as well as π -back bonding) that ligand **3** is a less electron-donating ligand compared to the other ligands. This may be explained by the large delocalized π -electron system of 2*H*-benzotriazole and electron density located at the benzene rings instead of then *N*-donor as indicated by the DFT calculations. Therefore, Hbbta may be the *N,N,O* ligand providing the most electron deficiency at the metal center from this series of ligands, meanwhile providing noticeable steric demand.

Unfortunately, **6** turned out to be rather unstable towards external influences such as heat and light. After some hours at daylight, complex **6** already decomposes to an orange solid. As known from the synthesis of **3**, higher temperatures lead to decarboxylation. Therefore, heating of **6** in solution above 40 °C leads to decomposition indicated by the appearance of several signals in the IR carbonyl region (1900–2050 cm^{-1}). Consequently, synthesis of **6** affords temperatures of 30 °C or lower which causes a longer reaction time compared to the synthesis of $[\text{Mn}(\text{bpza})(\text{CO})_3]$.^[4] Purification of **6** by means of column chromatography was only successful with stabilized THF as solvent, leading to residues of butylated hydroxytoluene (BHT) in the product. Attempts of an analogous reaction of ligand **3** with $[\text{ReBr}(\text{CO})_5]$ instead of $[\text{MnBr}(\text{CO})_5]$ failed, probably due to a slower reaction, which leads to decomposition.

To further investigate the steric demand and coordination properties of ligand **3**, the ruthenium complex $[\text{Ru}(\text{bbta})\text{Cl}(\text{PPh}_3)_2]$ (**7**) was synthesized analogously to the preparation of $[\text{Ru}(\text{bdmpza})\text{Cl}(\text{PPh}_3)_2]$.^[5] Reaction of the potassium salt of **3** with $[\text{RuCl}_2(\text{PPh}_3)_3]$ leads to $[\text{Ru}(\text{bbta})\text{Cl}(\text{PPh}_3)_2]$ (**7**), a light orange powder, as indicated by the FD mass peak (Scheme 3). It is well known, that in case of sterically less demanding ligands such as bpza, two diastereomers are obtained, while sterically more demanding ligands such as bdmpza lead to just one symmetrical isomer.^[5] The ^{31}P NMR spectrum shows only one singlet for the PPh_3 ligands (δ = 33.3 ppm). This suggests that only one isomer was formed by the reaction. This is backed by the absence of more than one set of benzotriazole signals in the $^{13}\text{C}\{^1\text{H}\}$ NMR spectrum. An X-ray structure determination doubtlessly reveals the symmetrical structure of **7** (Figure 2).

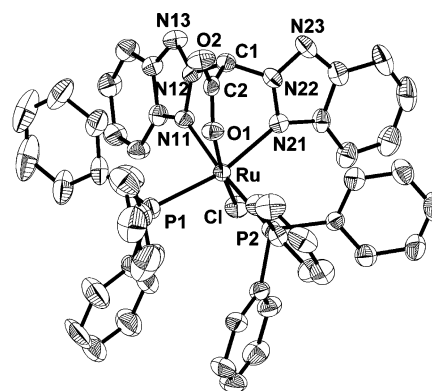


Figure 2. Molecular structure of $[\text{Ru}(\text{bbta})\text{Cl}(\text{PPh}_3)_2]$ (**7**); thermal ellipsoids are drawn at the 50% probability level. Hydrogen atoms have been omitted for clarity. Selected bond lengths [Å] and angles [°]: $d(\text{C}2-\text{O}1) = 1.272(6)$, $d(\text{C}2-\text{O}2) = 1.211(6)$, $d(\text{Ru}-\text{N}11) = 2.118(4)$, $d(\text{Ru}-\text{N}21) = 2.182(4)$, $d(\text{Ru}-\text{O}1) = 2.106(3)$, $d(\text{Ru}-\text{Cl}) = 2.4070(16)$, $d(\text{Ru}-\text{P}1) = 2.3488(18)$, $d(\text{Ru}-\text{P}2) = 2.3415(15)$, $\angle(\text{N}11, \text{Ru}, \text{N}21) = 78.59(16)$, $\angle(\text{N}11, \text{Ru}, \text{O}1) = 87.54(15)$, $\angle(\text{N}21, \text{Ru}, \text{O}1) = 86.53(14)$, $\angle(\text{O}1, \text{Ru}, \text{Cl}) = 170.34(10)$, $\angle(\text{O}1, \text{Ru}, \text{P}1) = 83.82(11)$, $\angle(\text{O}1, \text{Ru}, \text{P}2) = 95.92(11)$, $\angle(\text{N}11, \text{Ru}, \text{P}1) = 91.19(13)$, $\angle(\text{N}11, \text{Ru}, \text{P}2) = 173.10(12)$, $\angle(\text{N}11, \text{Ru}, \text{Cl}) = 86.07(12)$, $\angle(\text{N}21, \text{Ru}, \text{P}1) = 166.24(11)$, $\angle(\text{N}21, \text{Ru}, \text{P}2) = 95.62(12)$, $\angle(\text{N}21, \text{Ru}, \text{Cl}) = 85.11(11)$, $\angle(\text{Cl}, \text{Ru}, \text{P}1) = 103.53(5)$, $\angle(\text{Cl}, \text{Ru}, \text{P}2) = 89.72(5)$, $\angle(\text{P}1, \text{Ru}, \text{P}2) = 95.11(6)$.

Signals at $\delta = 83.3$ ppm and 164.6 ppm are assigned to the bridging CH and the CO_2^- carboxylate donor. Due to the ambient temperature reaction conditions, no decomposition by decarboxylation was observed. The pure compound **7** itself, was found to be remarkably stable against air. No indication of oxidation of the ruthenium centre was notified even after weeks. Due to the stability of complex **7**, and the weak electron-donating properties of ligand **3**, compound **7** promises to be an interesting precursor for organometallic ruthenium complexes. Further work might focus on ligand exchange reactions with $[\text{Ru}(\text{bbta})\text{Cl}(\text{PPh}_3)_2]$, e.g. the exchange of PPh_3 or Cl by cumulynidene ligands.

In contrast to the potassium salt of **3**, reaction of the sodium salt **5** with $[\text{MnBr}(\text{CO})_5]$ does not lead to the corresponding manganese tricarbonyl complex. During the reaction in THF a bright-yellow substance precipitates. IR spectra of the reaction mixture shows three carbonyl absorption bands at $\tilde{\nu} = 2032, 1936, 1908 \text{ cm}^{-1}$. The lower signals may be in accordance with the expected more electron-donating properties of **5** compared to **3** as shown by the DFT-calculations, but these results have to be interpreted with caution, since the spectra were obtained from the crude suspension of the reaction mixture. Any attempts to purify the obtained insoluble substances failed. Similar formation of insoluble and unisolable products was observed by the reaction of **5** with $[\text{ReBr}(\text{CO})_5]$ and $[\text{RuCl}_2(\text{PPh}_3)_3]$. Reaction of **5** with $\text{Zn}(\text{ClO}_4)_2$ in methanol immediately precipitates a white powder, too (Scheme 4). IR spectra of this zinc complex **8** show an absorption band assigned to the asymmetric carboxylate vibration at $\tilde{\nu} = 1634 \text{ cm}^{-1}$, indicating coordination of ligand **5** via the carboxylate donor. NMR spectra in D_2O , in which the obtained zinc complex **8** slowly dissolves, show the resonances of the free ligand **5**. Finally, an X-ray structure determination explains the unusual behaviour of **8** (see Figures 3 and 4). Obviously, a linear coordination polymer $[\text{Zn}(\text{btp})_2]_\infty$ (**8**) has been formed. Each zinc atom is tetrahedrally coordinated by four ligands, each binding towards the metal centre with the carboxylate group as O-donor or the nitrogen atom at 4-position of the triazole residue as N-donor (Figure 3). The bond lengths are in the typical range for a tetrahedral coordinated zinc centre with *N,O*-donor ligands, as comparison with $[\text{Zn}(\text{bd/bpza})\text{Cl}]$ [$d(\text{Zn}-\text{O}): 1.990(2) \text{ \AA}$, $d(\text{Zn}-\text{N}): 2.053(2), 2.067(3) \text{ \AA}$

shows.^[7] Two ligands act as bridging ligands towards a second metal centre at a time each. This results in a linear alignment of the zinc atoms (see Figures 3 and 4). In total, every zinc atom is connected to two other zinc centres. Each bridge is built up by two ligands. This results in the total formula ratio of $\text{Zn}/\text{btp} = 1:2$.

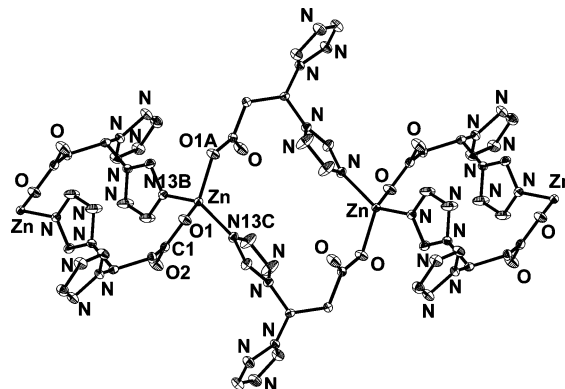


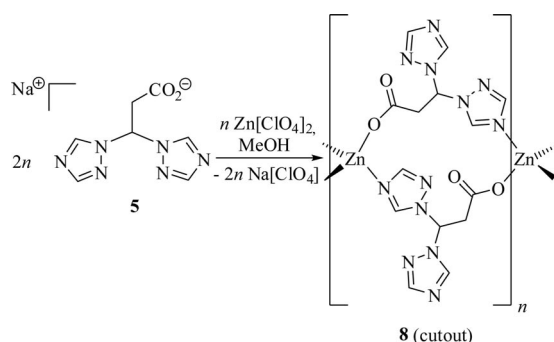
Figure 3. Molecular structure of $[\text{Zn}(\text{btp})_2]_\infty$ (**8**); a cutout of a linear chain with three zinc atoms is shown; thermal ellipsoids are drawn at the 50% probability level. Hydrogen atoms have been omitted for clarity. Selected bond lengths [\AA] and angles [$^\circ$]: $d(\text{Zn}-\text{O}1) = 1.9494(11)$, $d(\text{Zn}-\text{N}13) = 2.0045(13)$, $d(\text{C}1-\text{O}1) = 1.2745(19)$, $d(\text{C}1-\text{O}2) = 1.2301(19)$, $\angle(\text{O}1, \text{Zn}, \text{O}1\text{A}) = 100.41(7)$, $\angle(\text{O}1, \text{Zn}, \text{N}13\text{B}) = 121.34(5)$, $\angle(\text{O}1, \text{Zn}, \text{N}13\text{C}) = 104.48(5)$, $\angle(\text{N}13\text{B}, \text{Zn}, \text{N}13\text{C}) = 106.02(8)$, $d(\text{Zn}-\text{Zn}) = 6.773 \text{ \AA}$, centroid-centroid distance of the triazole rings: 5.043 \AA .

This bridging coordination is possible, since every ligand coordinates via the *N*-donor in 4-position of only one of the two triazole rings. The second triazole ring of each ligand is not coordinated to any metal centre and remains free. The two coordinated triazole rings of the two bridging ligands are aligned coplanar to each other (Figure 3). The centroid-centroid distance of these triazole rings is rather large with 5.043 \AA . Each chain of the linear coordination polymer additionally shows interaction with adjacent chains (Figure 4) by a coplanar orientation of the uncoordinated triazole rings (centroid-centroid distance: 3.618 \AA).

The short distance of these triazole rings let us assume a π -stacking interaction since a comparison with the centroid-centroid distance in hexagonal graphite shows only a slightly smaller distance ($d = 3.354 \text{ \AA}$).^[23]

The formation of linear coordination polymers explains the poor solubility of the zinc complex **8**. In water or D_2O the compound probably slowly dissociates to give the free ligand and $\text{Zn}_{\text{aq}}^{2+}$, which explains the identical NMR spectra of **5** and **8**, and crystallizes again as coordination polymer. This coordination behaviour of **5** may also explain the insoluble products obtained by reaction of **5** with other metal salts although the products could not be crystallized so far. It is noteworthy that recently Klein Gebbink and co-workers obtained a linear coordination polymer with the *N,N,O* ligand 3,3-bis(1-methyl-2*H*-imidazol-2-yl)propionate.^[24]

Recent studies have shown that the real space structure of metal coordination complexes can be investigated by scanning tunnelling microscopy (STM).^[25] Therefore a



Scheme 4. Formation of a linear coordination polymer $[\text{Zn}(\text{btp})_2]_\infty$ (**8**).

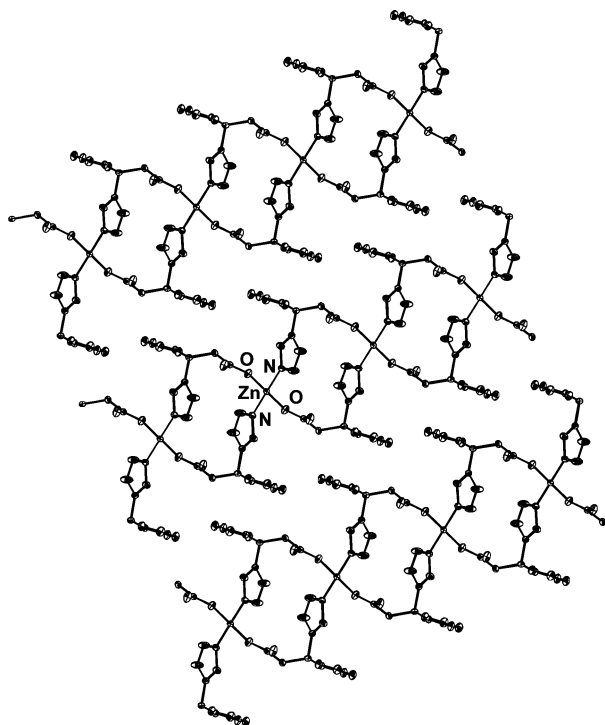


Figure 4. Molecular structure of $[\text{Zn}(\text{btp})_2]_\infty$ (**8**); thermal ellipsoids are drawn at the 50% probability level. Hydrogen atoms have been omitted for better clarity. A cutout of three adjacent linear polymer chains is shown. Centroid–centroid distance of the triazole rings in π -stacking arrangement: 3.618 Å.

10^{-9} M aqueous solution of **8** was drop coated on highly oriented pyrolytic graphite (HOPG) and investigated by STM in ambient conditions.

$[\text{Zn}(\text{btp})_2]_\infty$ (**8**) was found to form stable, straight lines (Figure 5, a). This can be attributed to a template effect of the substrate, stabilizing the polymer in positions of minimal energy along step edges and subsurface defect lines. As seen in Figure 5 (b) the minimum observed width of the structures is approx. 2.7 nm, roughly the diameter of a double chain. Therefore we have to assume a strong tendency to form clustered chains. This can be attributed to the π -stacking interaction of the non coordinating triazole rings as observed in the crystal structure. The measured periodicity along the chain is 1.5 nm. This is very close to the distance between every 2nd triazole ring. This can be ex-

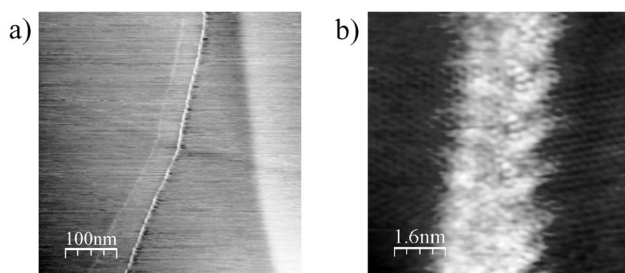


Figure 5. STM topographies showing a) the aggregation of linear polymer strands on the surface; and b) STM topography indicating a double stranded polymer on the surface.

pected if one considers sticking to the surface with one ring parallel and one perpendicular to the plane. Due to this strong clustering high resolution topography and spectroscopy where not achieved, even while atomic resolution of the graphite background was routinely observed.

Following a procedure similar to the successful synthesis of $[\text{Zn}(\text{btp})_2]_\infty$ (**8**), but employing $\text{MnSO}_4 \cdot \text{H}_2\text{O}$ instead of $\text{Zn}(\text{ClO}_4)_2$, we found the formation of the two-dimensional coordination polymer $[\text{Mn}(\text{btp})_2]_\infty$ (**9**). Instead of the split $\nu(\text{C}=\text{N})$ bands we observed in case of $[\text{Zn}(\text{btp})_2]_\infty$ (**8**) [$\tilde{\nu} = 1530 \text{ cm}^{-1}$ and 1513 cm^{-1}], now only one signal at 1521 cm^{-1} for $\nu(\text{C}=\text{N})$ is observed in the IR spectrum (KBr) of **9**. This can be explained by a closer look at the molecular structure of **9**, gained by X-ray structure determination. Three different metal centres coordinate the two triazole donors and the carboxylate functionality each. Hence, all carboxylate and triazol moieties have the same electronic environment. A cutout of the coordination geometry of one manganese atom is shown in Figure 6.

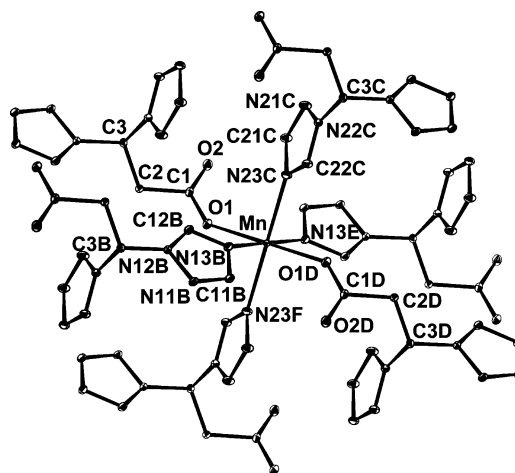


Figure 6. Molecular structure of $[\text{Mn}(\text{btp})_2]_\infty$ (**9**); thermal ellipsoids are drawn at the 50% probability level. Hydrogen atoms have been omitted for better clarity. A cutout of the surrounding of one manganese ion is shown. Selected bond lengths [Å] and angles [°]: $d(\text{Mn}-\text{O}1) = 2.1297(11)$, $d(\text{Mn}-\text{N}13\text{B}) = 2.2806(13)$, $d(\text{Mn}-\text{N}23\text{C}) = 2.2678(13)$, $d(\text{C}1-\text{O}1) = 1.2673(18)$, $d(\text{C}1-\text{O}2) = 1.2371(19)$, $\angle(\text{O}1, \text{Mn}, \text{O}1\text{D}) = 180.00$, $\angle(\text{O}1, \text{Mn}, \text{N}13\text{B}) = 88.10(5)$, $\angle(\text{O}1, \text{Mn}, \text{N}23\text{C}) = 92.84(5)$, $\angle(\text{N}13\text{B}, \text{Mn}, \text{N}23\text{C}) = 90.56(5)$.

The manganese center is octahedrally coordinated by six different ligands. Two ligands are coordinating through the carboxylate functionalities in *trans*-position towards each other. The left coordination sites are occupied by the N-atoms of the 4-position of four triazole rings, belonging to four different btp ligands. Recently, M. Du and S. R. Batten and co-workers reported on the coordination properties of bis(1*H*-1,2,4-triazol-1-yl)acetate (btza).^[16] It is noteworthy, that reaction of $\text{Mn}(\text{OAc})_2$ with Hbtza afforded a coordination polymer $\{[\text{Mn}(\text{btza})_2(\text{OH}_2)_2] \cdot 2\text{H}_2\text{O}\}_\infty$, in which the manganese centers are coordinated by four independent ligands each, two coordinated by the carboxylates and two by the triazole rings. Two further coordination sites have been occupied by additional water molecules. Evidently, by the elongation of the carbon backbone from acetate to pro-

pionate, a full occupation of the manganese coordination sites by ligands and vice versa becomes possible.

This results in an array of coordination polymer sheets. Within a sheet all the manganese atoms are situated in one plane [$d(\text{Mn}-\text{Mn}) = 8.064, 8.279$ and 9.538 \AA], shielded by the ligands from above and from below. The top view on such a sheet is given in Figure 7.

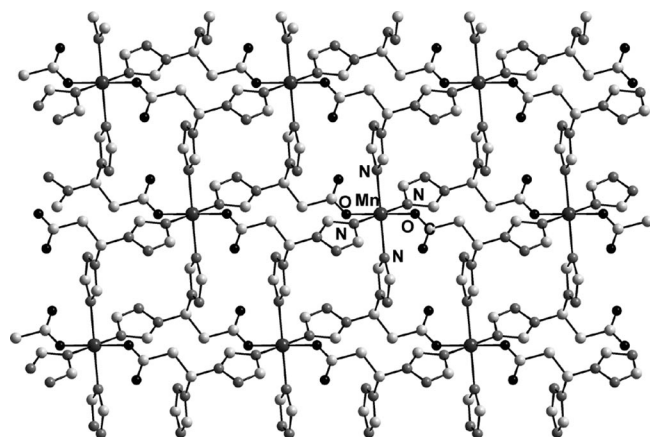


Figure 7. Molecular structure of $[\text{Mn}(\text{btp})_2]_\infty$ (9); hydrogen atoms have been omitted for better clarity. Cutout of a coordination polymer sheet is shown (top view).

Interestingly, no solvent molecules are intercalated into the structures of 9 and 8, respectively, although incorporated water molecules were observed for the analogous coordination polymers derived from btza.^[16] In coordination polymer $[\text{Mn}(\text{btp})_2]_\infty$ (9), the stacked sheets are interlocked into each other, leaving no larger spaces within the structure [$d(\text{O2}-\text{N11}\{\text{other sheet}\}) = 3.512 \text{ \AA}$]. A short distance between the uncoordinated carboxylate oxygen atom O2 and C3 of the neighbouring sheet [$d(\text{O2}-\text{C3}\{\text{other sheet}\}) = 3.329 \text{ \AA}$] might indicate hydrogen bonds in between the sheets. Figure 8 shows the side view on the arrangement of the polymer sheets in the crystal structure, showing the coordination polyhedra of the manganese atoms.

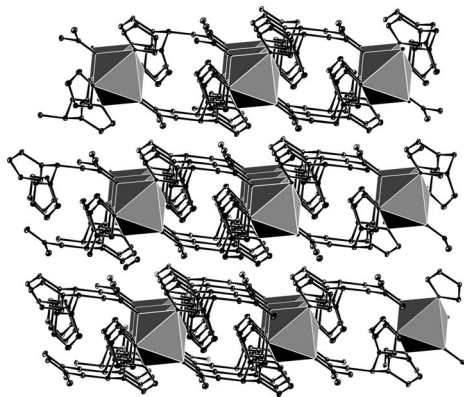


Figure 8. Molecular structure of $[\text{Mn}(\text{btp})_2]_\infty$ (9); cutouts of three adjacent coordination polymer sheets are shown (side view, polyhedral representation of the octahedral coordination of the manganese atoms).

Conclusions

In conclusion, the syntheses of 3 and 5 lead to two new ligands with interesting coordination properties. Ligand 3 shows $\kappa^3\text{-}N,N,O$ -coordination as it is well-known from other tripodal monoanionic N,N,O ligands. Estimation of the electronic properties of 3 via synthesis of the manganese tricarbonyl complex $[\text{Mn}(\text{bbta})(\text{CO})_3]$ (7) and DFT calculations show 3 to be a rather weak electron-donating ligand. Furthermore, synthesis of $[\text{Ru}(\text{bbta})\text{Cl}(\text{PPh}_3)_2]$ (6) might enable the future synthesis of various organometallic complexes. In contrast to 3, ligand 5 does not show tripodal binding towards metal centres but prefers the formation of coordination polymers as proven by the synthesis of $[\text{Zn}(\text{btp})_2]_\infty$ (8) and $[\text{Mn}(\text{btp})_2]_\infty$ (9). Interestingly, 8 assembles as linear chains of zinc ions, connected by two bridging ligands 5. The chains show interactions via π -stacking of the uncoordinated triazole residue. The coordination polymer $[\text{Mn}(\text{btp})_2]_\infty$ (9) shows two-dimensional polymer sheets.

Experimental Section

General Remarks: All operations regarding manganese carbonyl and ruthenium complexes were carried out under an inert gas atmosphere by using conventional Schlenk techniques. All solvents (analytical-grade purity) were degassed and stored under nitrogen atmosphere. The yields refer to analytically pure substances and were not optimised. IR spectra were recorded by use of a Varian Excalibur FTS-3500 FT-IR spectrometer in CaF_2 cuvettes (0.2 mm). ^1H and $^{13}\text{C}\{^1\text{H}\}$ NMR spectra: Bruker AC 250 MHz, Bruker DPX300, Bruker DPX400, δ values relative to TMS or the deuterated solvent. Mass spectra were recorded on a modified Finnigan MAT 312 using either EI or FAB technique or on a Jeol JMS-700 using FD technique. Elemental analysis: Euro EA 3000 (Euro Vector) and EA 1108 (Carlo Erba). Chemicals were used as purchased without further purification. Methyl bis(1,2,4-triazol-1-yl)propionate, $[\text{MnBr}(\text{CO})_5]$ and $[\text{RuCl}_2(\text{PPh}_3)_2]$ were synthesized according to literature.^[19,26–28]

Synthesis of Bis(2H-benzotriazol-2-yl)methane (2c): 2H-Benzotriazole (11.9 g, 100 mmol), K_2CO_3 (24.9 g, 180 mmol), KOH powder (10.1 g, 180 mmol) and benzyltriethylammonium chloride (1.00 g, 4.39 mmol) are suspended in THF (500 mL). Dichloroacetic acid (6.45 g, 50.0 mmol) is added and the white suspension heated under reflux for 96 h. The solvent is removed in vacuo and the remaining residue dissolved in water (250 mL). The aqueous solution is extracted with ethyl ether ($5 \times 200 \text{ mL}$) and the combined organic layers dried with Na_2SO_4 . Evaporation of the ethyl ether at room temperature to approx. 500 mL affords a first fraction of a mixture containing large amounts of the undesirable isomers. Decanting of the diethyl ether solution and evaporation of the remaining diethyl ether affords 2c in colourless crystals; yield 5.01 g (20.0 mmol, 40%); ^1H NMR (250 MHz, CDCl_3 , 25 °C): $\delta = 7.38$ and 7.78 [AA'BB' pattern, $^3J(\text{H,H}) = 6.7$, $^4J_{\text{H,H}} = 3.1 \text{ Hz}$, 8 H, Ar-H], 7.43 (s, 2 H, $\text{CH}_{\text{bridge}}$) ppm. $^{13}\text{C}\{^1\text{H}\}$ NMR (62.9 MHz, CDCl_3 , 25 °C): $\delta = 71.6$ (C_{bridge}), 118.6 (C_{aryl}), 127.6 (C_{aryl}), 145.2 (CN_{aryl}) ppm.

Bis(2H-benzotriazol-2-yl)acetic Acid (3): A solution of 2c (0.826 g, 3.30 mmol) in dry THF was treated with $n\text{BuLi}$ (2.10 mL, 1.6 M in n -hexane, 3.36 mmol) at -80°C . The dark blue solution is stirred for 2 h and warmed up to -40°C . Dry carbon dioxide is passed

in for a period of 3 h, meanwhile the colour changes from dark blue over dark red to light yellow. The solvent is removed in vacuo and the remaining residue dissolved in water (100 mL) and acidified with diluted HCl to pH = 7. The aqueous phase is extracted with ethyl ether (2 × 100 mL) to remove impurities. The aqueous solution is further acidified to pH = 3 and extracted with ethyl ether (3 × 200 mL) and the combined organic layers dried with Na₂SO₄ and concentrated in vacuo. The yellowish residue is recrystallised from acetone to yield **3** as colourless crystals; yield 0.243 g (0.826 mmol, 25%); m.p. 151–153 °C (dec.). ¹H NMR (300 MHz, CDCl₃, 25 °C): δ = 7.44, 7.90 (AA'BB' pattern, ³J_{H,H} = 3.6, ⁴J_{H,H} = 3.0 Hz, 8 H, Ar-H), 8.25 (s, 1 H, CH_{bridge}) ppm. ¹³C{¹H} NMR (75.5 MHz, [D₆]DMSO, 25 °C): δ = 80.3 (C_{bridge}), 118.3 (CH_{aryl}), 127.8 (CH_{aryl}), 143.9 (CN_{aryl}), 163.3 (CO₂H) ppm. IR (THF): ν̄ = 1763 [s (CO₂H)], 1563 [m (C=N)] cm⁻¹. FD-MS: *m/z* (%) = 296 (100) [MH⁺], 250 (46) [M⁺ – CO₂]. C₁₄H₁₀N₆O₂ (294.27 g mol⁻¹): calcd. C 57.14, H 3.43, N 28.56; found C 57.40, H 3.48, N 28.49.

Synthesis of Sodium 3,3-Bis(1*H*-1,2,4-triazol-1-yl)propionate (5): To methyl 3,3-bis(1*H*-1,2,4-triazol-1-yl)propionate (1.00 g, 4.50 mmol) a solution of pure NaOH (0.090 g, 2.25 mmol, 0.5 equiv.) in water (100 mL) is stirred for 24 h at ambient temperature. The solvent is removed in vacuo at 40 °C and the residue is extracted five times with chloroform to remove not reacted methyl ester and dried in vacuo. The chloroform may be removed in vacuo to recover methyl bis(1,2,4-triazol-1-yl)propionate.

5 was obtained as a white powder; yield 0.434 g (1.89 mmol, 84%); m.p. >260 °C (dec.). ¹H NMR (300 MHz, D₂O, 25 °C): δ = 3.61 (d, ³J_{H,H} = 7.1 Hz, 2 H, CH₂), 7.27 (t, ³J_{H,H} = 7.1 Hz, 1 H, CH_{bridge}), 8.10 (s, 2 H, H_{triazole}), 8.84 (s, 2 H, H_{triazole}) ppm. ¹³C{¹H} NMR (75.5 MHz, D₂O, 25 °C): δ = 40.7 (CH₂), 69.8 (C_{bridge}), 145.2 (C_{triazole}), 152.8 (C_{triazole}), 175.1 (COO⁻) ppm. IR (MeOH): ν̄ = 1612 [s (CO₂⁻)], 1511 [m (C=N)] cm⁻¹. FD-MS (after addition of dil. HCl): *m/z* (%) = 210 (60) [MH⁺], 140 (10) [M⁺ – tz]. C₇H₇N₆NaO₂ (230.16 g mol⁻¹): calcd. C 36.53, H 3.07, N 36.51; found C 36.86, H 3.16, N 36.86.

Synthesis of [Ru(bbta)Cl(PPh₃)₂] (7): To Hbbta (**3**) (0.100 g, 0.340 mmol) in dry THF (50 mL) *t*BuOK (0.038 g, 0.339 mmol) was added and the reaction mixture stirred at ambient temperature for 30 min. To the resulting white suspension [RuCl₂(PPh₃)₃] (0.326 g, 0.34 mmol) was added and stirred for additional 2 h and the dark-brown suspension changes colour to orange. The solvent is removed in vacuo and the remaining residue washed with water (2 × 10 mL) and little ethyl ether, pentane (2 × 10 mL) and methanol (2 × 5 mL) to yield **7** as bright orange powder.

Crystallisation from chloroform yields orange crystals suitable for X-ray structure determination.

Yield 0.195 g (0.20 mmol, 59%); m.p. >140 °C (dec.). ¹H NMR (400 MHz, CDCl₃, 25 °C): δ = 6.7–7.6 (m, 38 H, H_{aryl}), 7.94 (s, 1 H, CH_{bridge}) ppm. ¹³C{¹H} NMR (101 MHz, CDCl₃, 25 °C): δ = 83.3 (CH_{bridge}), 118.3 (CH_{aryl}), 120.2 (CH_{aryl}), 127.2 (vt, ³J_{C,P} = 5 Hz, *m*-PPh₃), 127.7 (m, *i*-PPh₃), 129.1 (*p*-PPh₃), 134.9 (vt, ²J_{C,P} = 5 Hz, *o*-PPh₃), 135.1 (d, ¹J_{C,P} = 2 Hz, CH_{aryl}), 135.4 (CH_{aryl}), 145.0 (CN_{aryl}), 146.4 (CN_{aryl}), 164.6 (CO₂⁻) ppm. ³¹P{¹H} NMR (121.5 MHz, CDCl₃, 25 °C): δ = 33.3 (PPh₃) ppm. IR (THF): ν̄ = 1967 [s (CO₂⁻)], 1690 [w (CN)] cm⁻¹. FD-MS: *m/z* (%) = 954 (5) [M⁺], 662 (44) [MH⁺ – bbta], 262 (50) [(PPh₃)₃]. C₅₀H₃₉ClN₆O₂·P₂Ru (954.37 g mol⁻¹): calcd. C 62.93, H 4.12, N 8.81; found C 62.27, H 4.19, N 8.60.

Synthesis of [Mn(bbta)(CO)₃] (6): To Hbbta (**3**) (0.294 g, 1.00 mmol) in dry THF (50 mL) *t*BuOK (0.112 g, 1.00 mmol) was added and the reaction mixture stirred at ambient temperature for

30 min. To the resulting white suspension [MnBr(CO)₅] (0.275 g, 1.00 mmol) was added, the reaction mixture heated to 30 °C and controlled by IR on a regular basis. After 72 h the reaction was completed and the solution filtered. The filtrate was concentrated in vacuo and after washing with water (2 × 5 mL) and little diethyl ether dried in vacuo to yield **6** as a yellow, light and heat sensitive solid; yield 0.186 g (0.430 mmol, 43%); m.p. >60 °C (slow dec.), >200 °C (fast dec.). ¹H NMR (300 MHz, CDCl₃, 25 °C): δ = 7.6–8.1 (m, broad, 8 H, H_{aryl}), 7.83 (br., 1 H, CH_{bridge}) ppm. ¹³C{¹H} NMR (75.5 MHz, CDCl₃, 25 °C): δ = 80.4 (CH_{bridge}), 115.8 (CH_{aryl}), 120.3 (CH_{aryl}), 129.3 (CH_{aryl}), 131.5 (CH_{aryl}), 144.7 (CN_{aryl}), 146.3 (CN_{aryl}), 162.0 (COOH), 218.3 (CO), 221.0 (CO) ppm. IR (THF): ν̄ = 2047 [s (C=O)], 1963 [s (C=O)], 1933 [s (C=O)], 1707 [s (CO₂⁻)] cm⁻¹. FAB-MS: *m/z* (%) = 433 (25) [MH⁺], 349 (13) [MH⁺ – 3CO], 307 (25) [MH⁺ – 3CO – CO₂]. C₁₇H₉MnN₆O₅ (432.23 g mol⁻¹): calcd. C 47.24, H 2.10, N 19.44; found: Due to the instability of **6** against light and heat, no sample free of a stabilizing agent (BHT) could be purified.

Synthesis of [Zn(btp)₂]_∞ (8): To a solution of Nabtp (**5**) (0.230 g, 1.00 mmol) in methanol (20 mL) a solution of zinc perchlorate hexahydrate (0.186 g, 0.499 mmol) in methanol (10 mL) is slowly added. Immediately, **8** precipitates as a fine white powder. The suspension is stirred for 15 min at ambient temperature, the residue filtered off, washed with methanol and dried in vacuo, to give **8** as a colourless powder.

Crystallisation from water affords colourless blocks suitable for X-ray structure determination.

Yield 0.187 g (0.390 mmol, 78%); m.p. >240 °C (dec.).

IR (KBr): ν̄ = 1634 [s (CO₂⁻)], 1530 (w) and 1513 [w (C=N)] cm⁻¹. C₁₄H₁₄N₁₂O₄Zn (479.73 g mol⁻¹): calcd. C 35.05, H 2.94, N 35.04; found C 34.78, H 2.93, N 34.78.

Due to the coordination polymer properties of **8** further analytical methods failed. NMR spectra in D₂O show similar resonances as in case of the free ligand **5**.

Synthesis of [Mn(btp)₂]_∞ (9): A test tube was charged with btpNa (0.101 g, 0.439 mmol) and MnSO₄ × H₂O (0.037 g, 0.219 mmol), and water (5 mL) was added. The tube was heated at 70 °C for 4 d. After cooling, pale yellow crystals had formed, that were collected, triturated with water (5 × 5 mL), and dried in vacuo at 80 °C to yield **9** a pale yellow powder; yield 0.066 g, 0.141 mmol, 64%; m.p. >311 °C (dec.). IR (KBr): ν̄ = 3436 (br), 3114 (m), 1621 [s (CO₂⁻)], 1521 [s (C=N)], 1438 (w), 1395 (m), 1340 (w), 1266 (w), 1199 (w), 1131 (m), 1007 (w), 908 (w), 822 (w), 673 (m), 552 (w) cm⁻¹. C₁₄H₁₄MnN₁₂O₄ (469.28 g mol⁻¹): calcd. C 35.83, H 3.01, N 35.82; found C 35.85, H 3.05, N 35.95.

Calculations

All DFT-calculations and full geometry optimizations were carried out by using Jaguar 6.0012^[29] running on Linux 2.4.18–14smp on five Athlon MP 2800+ dual-processor workstations (Beowulf-cluster) parallelized with MPICH 1.2.4. MM+ calculated structures were used as starting geometries. Complete geometry optimizations were carried out on the implemented N31G6* basis set and the BP86 density functional. Orbital plots^[22] were obtained using Maestro 7.0.113, the graphical interface of Jaguar.^[29]

STM Measurements

The STM imaging was carried out under ambient conditions using a home-built, low-drift microscope and RHK100 control electronics. A drop of aqueous 10⁻⁹ M sample solution was placed onto a freshly cleaved HOPG surface and left to dry. Sections without molecules clearly showed atomic resolution of the underlying

Table 3. Details of the structure determination for **3**, **7**, **8** and **9**.

| | 3 | 7 | 8 | 9 |
|--|---|---|---|--|
| Empirical formula | C ₁₄ H ₁₀ N ₆ O ₂ | C ₅₀ H ₃₉ ClN ₆ O ₂ P ₂ Ru | C ₁₄ H ₁₄ N ₁₂ O ₄ Zn | C ₁₄ H ₁₄ MnN ₁₂ O ₄ |
| Formula mass /g mol ⁻¹ | 294.28 | 954.33 | 239.87 | 234.66 |
| Crystal colour/habit | colourless block | red plate | colourless block | colourless block |
| Crystal system | monoclinic | monoclinic | monoclinic | triclinic |
| Space group | <i>P</i> 2 ₁ / <i>c</i> | <i>P</i> 2 ₁ / <i>c</i> | <i>C</i> 2/ <i>c</i> | <i>P</i> $\bar{1}$ |
| <i>a</i> /Å | 9.836(3) | 18.183(8) | 22.8880(11) | 7.7640(4) |
| <i>b</i> /Å | 9.7389(15) | 10.654(5) | 6.1072(2) | 8.0636(4) |
| <i>c</i> /Å | 14.726(3) | 22.591(6) | 13.4816(7) | 8.2794(5) |
| α /° | 90.00 | 90.00 | 90.00 | 108.605(3) |
| β /° | 99.220(17) | 93.08(3) | 92.934(3) | 104.916(5) |
| γ /° | 90.00 | 90.00 | 90.00 | 92.918(4) |
| <i>V</i> /Å ³ | 1392.4(6) | 4370(3) | 1882.01(15) | 469.66(4) |
| θ /° | 2.10–25.91 | 1.81–25.46 | 3.43–29.52 | 2.74–28.99 |
| <i>h</i> | –12 to 12 | –21 to 21 | –31 to 31 | –10 to 10 |
| <i>k</i> | –11 to 11 | –12 to 0 | –8 to 8 | –10 to 10 |
| <i>l</i> | –18 to 18 | 0 to 27 | –18 to 18 | –11 to 11 |
| <i>F</i> (000) | 608 | 1952 | 976 | 239 |
| <i>Z</i> | 4 | 4 | 4 | 1 |
| μ (Mo- <i>K</i> α) /mm ⁻¹ | 0.101 | 0.542 | 1.359 | 0.757 |
| Crystal size /mm | 0.3 × 0.25 × 0.15 | 0.65 × 0.2 × 0.18 | 0.12 × 0.09 × 0.08 | 0.18 × 0.18 × 0.07 |
| <i>D</i> _{calcd.} /g cm ⁻³ , <i>T</i> /K | 1.404, 293(2) | 1.450, 293(2) | 1.693, 150(2) | 1.659, 150(2) |
| Reflections collected | 5225 | 8312 | 24456 | 13616 |
| Indep. Reflections | 2675 | 8088 | 2639 | 2491 |
| Obs. refl. (>2 σ <i>I</i>) | 840 | 5080 | 2310 | 2224 |
| Parameter | 203 | 560 | 141 | 142 |
| Weight parameter <i>a</i> | 0.0407 | 0.0736 | 0.0241 | 0.0477 |
| Weight parameter <i>b</i> | 0 | 0.0813 | 2.0966 | 0.1519 |
| <i>R</i> ₁ (obsd.) | 0.0545 | 0.0480 | 0.0287 | 0.0278 |
| <i>R</i> ₁ (overall) | 0.2665 | 0.1248 | 0.0371 | 0.0340 |
| <i>wR</i> ₂ (obsd.) | 0.0975 | 0.1219 | 0.0605 | 0.0889 |
| <i>wR</i> ₂ (overall) | 0.1402 | 0.1484 | 0.0628 | 0.0864 |
| Diff. peak/hole /e Å ⁻³ | 0.189/–0.195 | 0.725/–0.590 | 0.400/–0.369 | 0.414/–0.302 |

graphite substrate. Typically, tunnelling currents between 10 and 200 pA were employed. The bias voltage was ± 72.9 mV. The scan frequency was varied between 2 to 5 Hz. Resolution was 256×256 points. Manually cut Pt/Ir(10%) tips were used.

X-ray Structure Determinations

Single crystals of **3**, **7**, **8** and **9** were mounted with Paratone-N or glue on a glass fibre. A modified Siemens P4-Diffractometer and a Bruker–Nonius Kappa-CCD and an Enraf–Nonius CAD4 Mach3 diffractometer were used for data collection (graphite monochromator, Mo-*K* α radiation, $\lambda = 0.71073$ Å). The structures were solved by using direct methods and refined with full-matrix least-squares against F^2 {Siemens SHELX-97}.^[30] A weighting Scheme was applied in the last steps of the refinement with $w = 1/[\sigma^2(F_o^2) + (aP)^2 + bP]$ and $P = [2Fc^2 + \max(F_o^2, 0)]/3$. Most hydrogen atoms were included in their calculated positions and refined in a riding model. The proton of carboxylic acids (**3**) was found and its coordinates were refined freely. All details and parameters of the measurements are summarised in Table 3. The structure pictures were prepared with the program Diamond 2.1e.^[31]

CCDC-766896 (for **3**), -766897 (for **7**), -766898 (for **8**) and -766899 (for **9**) contain the supplementary crystallographic data for this paper. These data can be obtained free of charge from The Cambridge Crystallographic Data Centre via www.ccdc.cam.ac.uk/data_request/cif.

Acknowledgments

Generous financial support by the Deutsche Forschungsgemeinschaft (DFG) (SFB 583) is gratefully acknowledged.

- [1] A. Otero, J. Fernández-Baeza, J. Tejada, A. Antiñolo, F. Carrillo-Hermosilla, E. Díez-Barra, A. Lara-Sánchez, M. Fernández-López, M. Lanfranchi, M. A. Pellinghelli, *J. Chem. Soc., Dalton Trans.* **1999**, 3537–3539.
- [2] A. Otero, J. Fernández-Baeza, A. Antiñolo, J. Tejada, A. Lara-Sánchez, L. Sánchez-Barba, M. T. Expósito, A. M. Rodríguez, *Dalton Trans.* **2003**, 1614–1619.
- [3] C. Pettinari, R. Pettinari, *Coord. Chem. Rev.* **2005**, 249, 663–691.
- [4] N. Burzlaff, I. Hegelmann, B. Weibert, *J. Organomet. Chem.* **2001**, 626, 16–23.
- [5] A. López-Hernández, R. Müller, H. Kopf, N. Burzlaff, *Eur. J. Inorg. Chem.* **2002**, 671–677.
- [6] R. Müller, E. Hübner, N. Burzlaff, *Eur. J. Inorg. Chem.* **2004**, 2151–2159.
- [7] A. Beck, B. Weibert, N. Burzlaff, *Eur. J. Inorg. Chem.* **2001**, 521–527.
- [8] I. Hegelmann, A. Beck, C. Eichhorn, B. Weibert, N. Burzlaff, *Eur. J. Inorg. Chem.* **2003**, 339–347.
- [9] A. Beck, A. Barth, E. Hübner, N. Burzlaff, *Inorg. Chem.* **2003**, 42, 7182–7188.
- [10] L. Peters, N. Burzlaff, *Polyhedron* **2004**, 23, 245–251.
- [11] L. Peters, E. Hübner, N. Burzlaff, *J. Organomet. Chem.* **2005**, 690, 2009–2016.
- [12] J. Elfle, F. Platzmann, N. Burzlaff, *Eur. J. Inorg. Chem.* **2007**, 5173–5176.
- [13] U. Abram, R. Alberto, *J. Braz. Chem. Soc.* **2006**, 17, 1486–1500.
- [14] a) M. Giorgetti, L. Guadagnini, S. G. Fiddy, C. Santini, M. Pellei, *Polyhedron* **2009**, 28, 3600–3606; b) S. Alidori, G. Gioia Lobbia, G. Papini, M. Pellei, M. Porchia, F. Refosco, F. Tisato, J. S. Lewis, C. Santini, *J. Biol. Inorg. Chem.* **2008**, 13,

- 307–315; c) C. Marzano, M. Pellei, D. Colavito, S. Alidori, G. Gioia Lobbia, V. Gandin, F. Tisato, C. Santini, *J. Med. Chem.* **2006**, 49, 7317–7324.
- [15] Y. Ling, H.-Y. Gao, L. Zhang, *Acta Crystallogr., Sect. E* **2007**, 63, m193–m195.
- [16] M. Du, Z.-H. Zhang, L.-F. Tang, X.-G. Wang, X.-J. Zhao, S. R. Batten, *Chem. Eur. J.* **2007**, 13, 2578–2586.
- [17] L. Avila, J. Elguero, S. Juliá, J. M. del Mazo, *Heterocycles* **1983**, 20, 1787–1792.
- [18] E. Díez-Barra, A. de la Hoz, A. Sánchez-Migallón, J. Tejada, *Heterocycles* **1992**, 34, 1365–1373.
- [19] E. Díez-Barra, J. Guerra, V. Hornillos, S. Merino, J. Tejada, *Tetrahedron Lett.* **2004**, 45, 6937–6939.
- [20] R. H. Holm, P. Kennepohl, E. I. Solomon, *Chem. Rev.* **1996**, 96, 2239–2314.
- [21] R. G. Pearson, *Proc. Natl. Acad. Sci. USA* **1986**, 83, 8440–8441.
- [22] R. Stowasser, R. Hoffmann, *J. Am. Chem. Soc.* **1999**, 121, 3414–3420.
- [23] R. W. G. Wyckoff, *Crystal Structures*, vol. 1, John Wiley & Sons, New York, London, **1963**.
- [24] P. C. A. Bruijninx, M. Lutz, J. P. den Breejen, A. L. Spek, G. van Koten, R. J. M. Klein Gebbink, *J. Biol. Inorg. Chem.* **2007**, 12, 1181–1196.
- [25] K. Petukhov, M. S. Alam, H. Rupp, S. Strömsdörfer, P. Müller, A. Scheurer, R. W. Saalfrank, J. Kortus, A. Postnikov, M. Ruben, L. K. Thompson, J.-M. Lehn, *Coord. Chem. Rev.* **2009**, 253, 2387–2398.
- [26] D. Vitali, F. Calderazzo, *Gazz. Chim. Ital.* **1972**, 102, 586–596.
- [27] E. W. Abel, G. Wilkinson, *J. Chem. Soc.* **1959**, 1501–1505.
- [28] P. S. Hallmann, T. A. Stephenson, G. Wilkinson, *Inorg. Synth.* **1970**, 12, 237–240.
- [29] *Jaguar*, version 6.0, Schrödinger, LLC, New York, NY, **2005**.
- [30] G. M. Sheldrick, *Acta Crystallogr., Sect. A* **2008**, 64, 112–122.
- [31] K. Brandenburg, M. Berndt, Diamond – Visual Crystal Structure Information System, Crystal Impact GbR, Bonn (Germany), **1999**; for a software review see: W. T. Pennington, *J. Appl. Crystallogr.* **1999**, 32, 1028–1029.

Received: April 8, 2010

Published Online: August 4, 2010

Enhancing Magnetic and Magnetotransport Properties by Topotactic Reduction of the $\text{Sr}_2\text{Fe}_{1.33}\text{Mo}_{0.66}\text{O}_6$ Double Perovskite

Carlos Alberto López,^[a] María del Carmen Viola,^[a] José Carmelo Pedregosa,^{*,[a]} José Antonio Alonso,^[b] and María Teresa Fernández-Díaz^[c]

Keywords: Double perovskites / Magnetic properties / Hydrogen reduction

$\text{Sr}_2\text{Fe}_{1.33}\text{Mo}_{0.66}\text{O}_6$ (alternately written as $\text{Sr}_3\text{Fe}_2\text{MoO}_9$) perovskite has been prepared in polycrystalline form by thermal treatment, in air, of previously decomposed citrate precursors. This material has been studied by X-ray and neutron powder diffraction (XRPD and NPD), magnetic and transport measurements. At room temperature, the crystal structure is cubic with $a = 7.8585(2) \text{ \AA}$ and $V = 485.30(2) \text{ \AA}^3$, defined in the space group $Fm\bar{3}m$. Magnetic measurements indicate a ferromagnetic ordering below $T_C = 246 \text{ K}$. As prepared, the sample is an electrical insulator. A topotactic reduction of the stoichiometric sample performed at 600, 700, and 800 °C, in H_2/N_2 flows, leads to the oxygen-deficient double perovskites, $\text{Sr}_2\text{Fe}_{1.33}\text{Mo}_{0.66}\text{O}_{6-\delta}$ with increasing δ values. The evolution of the crystal structure upon reduction has been

studied from XRPD and NPD data. For the sample obtained at 800 °C, exhibiting the largest δ value, the low-temperature evolution from NPD data was investigated between 2 K and 500 K: in all the temperature range the crystal structure is cubic with space group $Fm\bar{3}m$; at room temperature $a = 7.87060(6) \text{ \AA}$ and $V = 487.555(6) \text{ \AA}^3$. The magnetic behavior of this reduced sample suggests the presence of ferromagnetic domains characterized by Curie temperatures with $T_C > 400 \text{ K}$. The conductivity dramatically increases upon H_2 reduction. Moreover, this reduced sample exhibits magnetoresistance, as high as 2.5 % at room temp. for $H = 5 \text{ T}$. Magnetic and magnetotransport results are consistent with a large component of itinerancy for down-spin Mo t_{2g} electrons, injected through hydrogen reduction.

Introduction

The search for materials with improved magnetotransport properties has been a challenging topic during the last decade in the field of transition metal oxides, stimulated by their potential technological applications.^[1] In particular, due to the observation of colossal magnetoresistance (CMR), the manganese perovskites rapidly became promising materials.^[2] However, a few years after the discovery of the CMR effect the attention focused on some double perovskite oxides as well. The revival of interest in this family was triggered by a report on $\text{Sr}_2\text{FeMoO}_6$,^[3] demonstrating that in the electronic structure only minority spins are present at the Fermi level; this material was shown to exhibit intrinsic tunneling-type magnetoresistance (TMR) at room temp.^[3,4] In a simple picture, FeO_6 and MoO_6 octahedra alternate along the three directions of the crystal structure of $\text{Sr}_2\text{FeMoO}_6$; the ferrimagnetic structure can be described as an ordered arrangement of parallel Fe^{3+} ($S = 5/2$) magnetic moments antiferromagnetically coupled with Mo^{5+} ($S = 1/2$) spins.

Despite the large number of double perovskites informed up to now, only some reports exist about compounds with stoichiometry $\text{A}_3\text{B}'_2\text{B}''\text{O}_9$. This particular type of stoichiometry is apparently more complex, but these oxides are also double perovskites $\text{A}_2\text{B}'_{1.33}\text{B}''_{0.66}\text{O}_6$ whose crystallographic formula can be re-written as $\text{A}_2[\text{B}']_a[\text{B}'_{1/3}\text{B}''_{2/3}]_b\text{O}_6$, where a and b denote the crystallographic sites in the corresponding space group. They, thus, display an intrinsic partial disordering over half of the perovskite ($\text{B}'_{1/3}\text{B}''_{2/3}$) positions. Furthermore, this composition offers the possibility of changing the oxidation states of the B' and B'' ions and consequently modifying the electrical and magnetic properties.

Some double perovskites have recently been reported as ferrimagnets with T_C 's, in some cases, above room temp. Previously we have prepared and studied the magnetic properties of $\text{Sr}_3\text{Fe}_2\text{MoO}_9$, $\text{Sr}_3\text{Fe}_2\text{UO}_9$, and $\text{Sr}_3\text{Fe}_2\text{TeO}_9$ and observed a ferrimagnetic behaviour below $T_C = 280 \text{ K}$, $T_C = 330 \text{ K}$ and $T_C = 717 \text{ K}$ respectively.^[5–7] Our main finding is that these intrinsically “disordered” perovskites, containing a random distribution of Fe and Mo, U or Te at the B'' positions, exhibit a strong magnetic scattering on the low-angle Bragg positions of the neutron diffraction patterns, originating upon naturally-occurring groups of Fe^{3+} cations in which strong antiferromagnetic (AFM) Fe–O–Fe superexchange interactions are promoted, similar to those existing in the LaFeO_3 perovskite.

[a] Área de Química General e Inorgánica “Dr. Gabino F. Puelles”, Departamento de Química, Facultad de Química, Bioquímica y Farmacia, Universidad Nacional de San Luis, Chacabuco y Pedernera, 5700 San Luis, Argentina

[b] Instituto de Ciencia de Materiales de Madrid, CSIC, Cantoblanco, 28049 Madrid, Spain

[c] Institut Laue-Langevin, B. P. 156, 38042 Grenoble Cedex 9, France

On the other hand, some recent experiments have shown that electron doping may improve the magnetic and electrical properties and induce a substantial rising of the Curie temperature. Two routes are possible in order to attain this electron doping effect in double perovskites. One of them consists of partially substituting divalent by trivalent ions in the A site. It has been previously reported that the replacement of A^{2+} by Ln^{3+} in $A_2FeB''O_6$ (where $B'' = Mo$) induces magnetic and structural changes.^[8] When doping with La, an important fraction of the injected electrons is localized at Mo sites, which is harmful concerning the potential applicability, since it promotes the occurrence of anti-site disordering between Fe and Mo cations.^[9–11] This route is not always successful, for instance when $B'' = W$.^[12]

Other possibility to obtain electron doping is via chemical reduction by topotactical removal of oxygen atoms. We have recently demonstrated that semi-metallic behaviour and CMR properties can be induced by this procedure in the insulating Sr_2CoMoO_6 double perovskite.^[13] A strict control of the reduction conditions is necessary to reach the maximum level of oxygen vacancies avoiding phase segregations and elemental B' formation.^[14]

Although doping and chemical reduction have been shown to be fruitful in $A_2B'B''O_6$ double perovskites, the utilization of these procedures on $A_3B'_2B''O_9$ ($A_2B'_{1.33}B''_{0.66}O_6$) double perovskites are scarce in the literature.^[15] For the previously mentioned reasons, in this work we focus on the preparation and characterization of reduced $Sr_2Fe_{1.33}Mo_{0.66}O_{6-\delta}$ oxides; we describe the synthesis and structural characterization of three materials obtained via topotactical reduction in $H_2/5\% N_2$ atmosphere at 600, 700, and 800 °C, with increasing δ values. The sample reduced at 800 °C was selected for a temperature-dependent NPD study, in complement with magnetization and magnetotransport measurements; we describe substantial changes experienced by the magnetic response upon controlled H_2 reduction which leads to the induction of non-negligible *MR* properties at room temperature.

Results

Crystallographic Structure

The structural refinement of the oxygen-stoichiometric $Sr_2Fe_{1.33}Mo_{0.66}O_6$ sample was performed from combined XRPD and NPD data at room temp. The good agreement between the observed and calculated XRPD and NPD patterns after the refinement is shown in parts a and b of Figure 1. The present sample was successfully refined as cubic in the space group $Fm\bar{3}m$ in agreement with G. Y. Liu et al.^[16] Trials to refine the crystal structure in the tetragonal

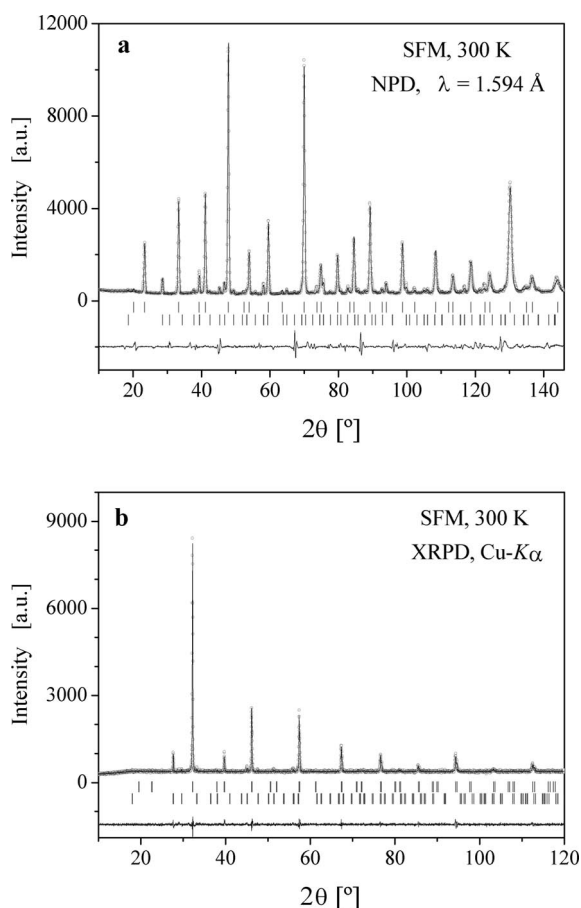


Figure 1. Observed (circles), calculated (full line) and difference (bottom) Rietveld profiles at room temp. for $Sr_2Fe_{1.33}Mo_{0.66}O_6$ after a combined XDR-NPD refinement; the second series of tick marks correspond to the Bragg reflections for the $SrMoO_4$ impurity phase. (a) NDP and (b) XRPD.

Table 1. Positional and displacement parameters for stoichiometric and reduced samples, in the cubic $Fm\bar{3}m$ space group, from combined NPD and XRPD data at room temp.

| | SFM | SFM60 | SFM70 | SFM80 |
|---|------------|------------|------------|------------|
| a [Å] | 7.8585(2) | 7.8678(2) | 7.8685(2) | 7.87060(6) |
| V [Å ³] | 485.30(2) | 487.04(2) | 487.16(2) | 487.555(6) |
| Sr $8c$ ($\frac{1}{4}, \frac{1}{4}, \frac{1}{4}$) | | | | |
| $(\beta_{11} = \beta_{22} = \beta_{33}) \times 10^4$ | 33(1) | 37(1) | 41(1) | 30(1) |
| Fe/Mo $4b$ ($\frac{1}{2}, \frac{1}{2}, \frac{1}{2}$) [#] | | | | |
| $(\beta_{11} = \beta_{22} = \beta_{33}) \times 10^4$ | 15(3) | 31(2) | 34(2) | 5(3) |
| Occ Fe/Mo | 0.84/0.16 | 0.77/0.23 | 0.74/0.26 | 0.73/0.27 |
| (Fe/Mo) $4b$ -O | 1.9025(6) | 1.943(6) | 1.936(6) | 1.952(4) |
| Fe/Mo $4a$ (0,0,0) [#] | | | | |
| $(\beta_{11} = \beta_{22} = \beta_{33}) \times 10^4$ | 21(2) | 13(2) | 18(2) | 21(4) |
| Occ Fe/Mo | 0.49/0.51 | 0.56/0.44 | 0.59/0.41 | 0.60/0.40 |
| (Fe/Mo) $4a$ -O | 2.0267(6) | 1.990(6) | 1.998(6) | 1.983(4) |
| O $24e$ ($x, 0, 0$) | | | | |
| x | 0.2579(3) | 0.253(2) | 0.254(2) | 0.252(1) |
| $\beta_{11} \times 10^4$ | 13(2) | 32(2) | 30(3) | 20(1) |
| $(\beta_{22} = \beta_{33}) \times 10^4$ | 71(2) | 83(1) | 92(2) | 73(1) |
| Occ | 1 | 0.970(3) | 0.968(3) | 0.963(3) |
| Magnetic moment | | | | |
| μ_B/B site | — | 1.76(2) | 2.02(3) | 2.04(2) |
| Reliability factors | | | | |
| R_p (%) NPD; XRPD | 5.79; 4.46 | 4.12; 4.10 | 4.88; 4.83 | 2.96; 5.03 |
| R_{wp} (%) NPD; XRPD | 7.84; 5.74 | 5.20; 5.19 | 6.16; 6.15 | 3.99; 6.33 |
| R_{exp} (%) NPD; XRPD | 2.75; 4.84 | 4.80; 4.74 | 5.66; 5.56 | 1.43; 5.80 |
| χ^2 | 4.9 | 1.6 | 1.7 | 7.8 |
| R_{Bragg} (%) NPD; XRPD | 2.02; 4.24 | 2.48; 4.66 | 2.90; 4.54 | 1.64; 4.26 |
| R_{Mag} (%) | — | 7.75 | 6.61 | 5.81 |

$I4/m$ space group, as reported previously by Viola et al. for a $\text{Sr}_3\text{Fe}_2\text{MoO}_9$ phase obtained at 1100°C did not yield a better fit than that obtained for the cubic model.^[5] The difference between the $Fm\bar{3}m$ and the $I4/m$ refinements is very subtle, but the cubic model certainly leads to a superior agreement between observed and calculated intensities for certain superstructure reflections, such as (121)+(013) (tetragonal model) vs. (311) (cubic model).

In the $Fm\bar{3}m$ space group (No. 225), $Z = 4$, the unit-cell parameter is related to a_0 (ideal cubic perovskite, $a_0 \approx 3.9 \text{ \AA}$) as $a = 2a_0$. Sr atoms were located at the $8c$ ($1/4, 1/4, 1/4$) positions, Fe/Mo at $4a$ (0,0,0) and at $4b$ ($1/2, 1/2, 1/2$) sites, and oxygen atoms at the $24e$ ($x, 0, 0$) positions. For this space group $Fm\bar{3}m$ there are two possible sites for B type cations, namely, $4a$ and $4b$. In double perovskites with stoichiometry $\text{A}_2\text{B}'\text{B}''\text{O}_6$ there is the possibility of total order of B-type

cations between these two sites, which would correspond to a crystallographic formula $\text{A}_2[\text{B}']_{4b}[\text{B}'']_{4a}\text{O}_6$ for this cubic symmetry. For perovskites with stoichiometry $\text{A}_3\text{B}'_2\text{B}''\text{O}_9$, total order is intrinsically impossible. Thus, if one wants to assure certain degree of disorder in this kind of perovskites, the $\text{A}_3\text{B}'_2\text{B}''\text{O}_9$ stoichiometry is ideal. In order to obtain a better picture of the distribution of the B cations in the two crystallographic sites and to consider the degree of disorder, we can write the crystallographic formula as $\text{A}_2[\text{B}'_{1-\alpha}\text{B}''_{\alpha}]_{4b}[\text{B}'_{1/3+\alpha}\text{B}''_{2/3-\alpha}]_{4a}\text{O}_6$, where $0 \leq \alpha \leq 1/3$. Thus, if $\alpha = 0$ we have maximum order (but not full order), and if $\alpha = 1/3$ we have maximum disorder. The composition for maximum disorder, i.e. $\text{A}_2[\text{B}'_{2/3}\text{B}''_{1/3}]_{4b}[\text{B}'_{2/3}\text{B}''_{1/3}]_{4a}\text{O}_6$, corresponds to B cations randomly distributed. Based on the preceding discussion we can define the degree of order (DO) as $\text{DO} = 1 - 3\alpha$. For maximum order $\text{DO} = 1$ and for random

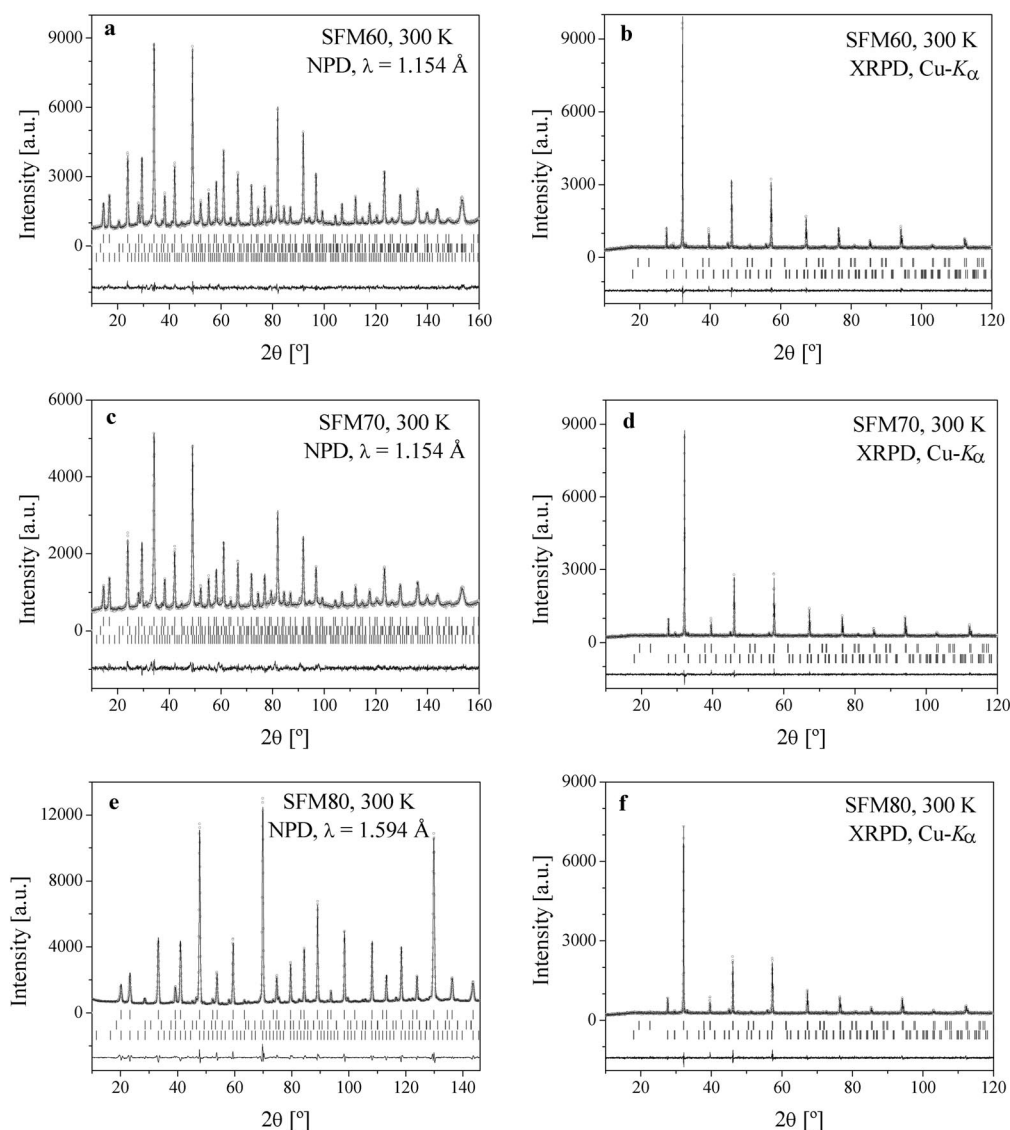


Figure 2. Observed (circles), calculated (full line) and difference (bottom) high resolution Rietveld profiles at room temp. for SFM60, SFM70 and SFM80 samples after a combined XDR-NPD refinement. (a); (c) and (e) NPD: The second and third series of tick marks correspond to the Bragg reflections for the SrMoO_4 impurity phase and the magnetic structure, respectively. (b); (d) and (f) XRPD: The second series of tick marks corresponds to the Bragg reflections for the SrMoO_4 impurity phase.

distribution $\text{DO} = 0$. DO values are obtained from the refinements of occupancies of B cations in $4a$ and $4b$ sites. The most important structural parameters of the crystallographic structure and the discrepancy factors after the refinements are listed in Table 1.

For the reduced $\text{Sr}_2\text{Fe}_{1.33}\text{Mo}_{0.66}\text{O}_{6-\delta}$ samples the combined structural refinement from NPD and XRPD data at room temp. were also successfully performed in the $Fm\bar{3}m$ space group. As the $\text{Sr}_2\text{Fe}_{1.33}\text{Mo}_{0.66}\text{O}_{6-\delta}$ phases are magnetic at room temp. we included a model for the magnetic structure, as described below. SrMoO_4 was also included in the refinements as a second phase, defined in the space group $I4_1/a$.^[17] From the scale factor of the main and secondary phases we estimated the following impurity levels as wt.-%: 6.2(2)%, 6.0(2)%, 5.9(2)% and 5.8(2)% of SrMoO_4 for the SFM, SFM60, SFM70, SFM80 samples. In the final refinement, the occupancy parameter of oxygen atom was checked, obtaining an occupation of 97.0(3)%, 96.8(3)% and 96.3% for SFM, SFM60, SFM70, SFM80, respectively at room temp. An excellent agreement between observed and calculated for both NPD and XRPD profiles was obtained for this model, as illustrated in Figure 2 for SFM60, SFM70, and SFM80 samples. Table 1 includes the final atomic coordinates and discrepancy factors after the refinement.

In order to confirm the symmetry observed by NPD and XRD, an electron diffraction study along some selected zone axis was carried out for a selected sample, SFM70, at room temp. The electron micrographs are presented in Figure 3. The a , b , and c panels correspond to the zone axes $[0\ 0\ -1]$, $[1\ -1\ 0]$, and $[1\ -1\ 1]$, respectively. Figure 3 (d) shows the microcrystal where the diffraction patterns were taken. In Figure 3 (a) the $(h00)$ and $(0k0)$ ($h, k = 2n + 1$) reflections are extinct due to the face-centered symmetry

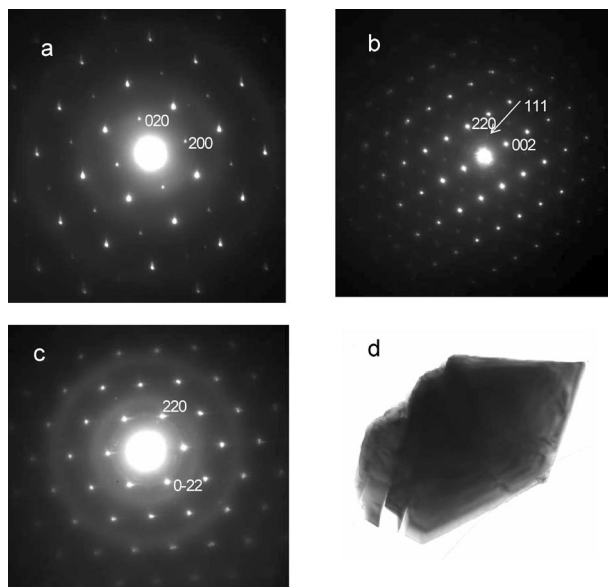


Figure 3. Electron diffraction patterns of SFM70 recorder at room temp. corresponding to the zone axes a) $[0\ 0\ -1]$, b) $[1\ -1\ 0]$ and c) $[1\ -1\ 1]$. d) Image of the microcrystal where the diffraction patterns were taken, recorded with a magnification of 80000 \times .

of the space group ($Fm\bar{3}m$). However, the superstructure corresponding to the unit cell doubling ($a = 2a_0$) is perfectly noticeable in the b panel, along the $[1\ -1\ 0]$ zone axis, were the $(1\ 1\ 1)$, $(3\ 1\ 1)$ etc. reflections are visible, although very weak.

The thermal evolution of the crystallographic structure was investigated from NPD data collected at 2, 150, 250, 300, 350, 450 and 500 K for SFM80. The cubic model (space group $Fm\bar{3}m$) was considered in all cases. The thermal evolution of the a unit-cell parameter is shown in Figure 4. The average thermal expansion coefficient from 2 K to 500 K is $11.9 \times 10^{-6} \text{ K}^{-1}$. Table 2 includes the final atomic coordinates, ordered magnetic moments and discrepancy factors for different temperatures. Furthermore, for each temperature the oxygen occupancy vacancies were refined and the resulting δ values, corresponding to the formula $\text{Sr}_2\text{Fe}_{1.33}\text{Mo}_{0.66}\text{O}_{6-\delta}$, are shown in Table 2. The inset a of Figure 4 also shows a lineal evolution of the a parameter with the δ values for SFM, SFM60, SFM70 and SFM80. At $T = 2 \text{ K}$, $\delta = 0.20(2)$; there is a negligible evolution of δ with T (within the experimental errors) until 450 K, but at 500 K this value decreases slowly, reaching $\delta = 0.16(2)$.

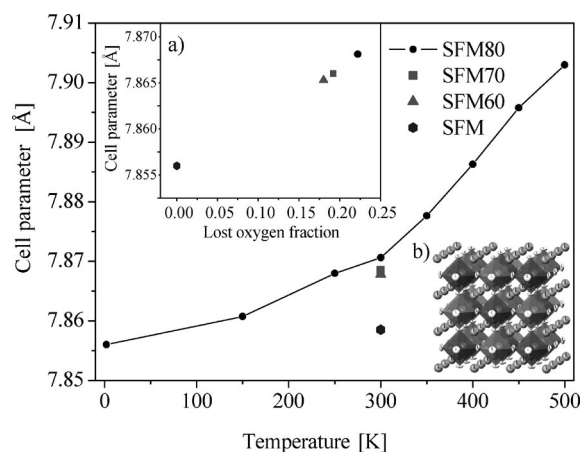


Figure 4. Thermal evolution of the a unit-cell parameter for SFM80 double perovskites obtained from NPD. The symbols correspond to the cell parameter of SFM, SFM60 and SFM70 at room temp. The inset a) shows the variations of the unit-cell parameter with the oxygen deficiency (δ). The inset b) is a view of the cubic crystal structure of both double perovskites; each $[\text{B}]_{4b}\text{O}_6$ octahedron is corner linked to six $[\text{B}]_{4a}\text{O}_6$ octahedral.

Thermal Analysis

Figure 5 shows the thermal evolution of δ values obtained by TPR and TGA (in H_2/N_2 5%/95%) methods of the oxygen-stoichiometric perovskites ($\text{Sr}_2\text{Fe}_{1.33}\text{Mo}_{0.66}\text{O}_6$) in comparison with those from TGA (re-oxidations) and NPD techniques for SFM60, SFM70 and SFM80.

TPR profiles show two reductions processes. The first peak with a maximum at 380 $^\circ\text{C}$ indicates the beginning of the reduction process. After this peak the H_2 consumption stays approximately constant up to 800 $^\circ\text{C}$. A second peak

Table 2. Structural parameters after the refinement of NPD data for SFM80 at different temperatures.

| SFM80 | 2 K | 150 K | 250 K | 300 K ^[a] | 350 K | 400 K | 450 K | 500 K |
|--|------------|------------|------------|----------------------|------------|------------|------------|------------|
| <i>a</i> [Å] | 7.85598(8) | 7.86070(8) | 7.86794(8) | 7.87060(6) | 7.87761(8) | 7.88628(8) | 7.89576(9) | 7.90295(8) |
| <i>V</i> [Å ³] | 484.843(8) | 485.717(9) | 487.062(9) | 487.555(6) | 488.859(8) | 490.474(8) | 492.245(9) | 493.591(9) |
| Sr 8c (1/4, 1/4, 1/4) | | | | | | | | |
| ($\beta_{11} = \beta_{22} = \beta_{33}$) $\times 10^4$ | 8(1) | 14(1) | 20(1) | 30(1) | 27(1) | 33(1) | 39(1) | 47(1) |
| Fe/Mo 4b (1/2, 1/2, 1/2) ^{#[b]} | | | | | | | | |
| ($\beta_{11} = \beta_{22} = \beta_{33}$) $\times 10^4$ | −16(3) | −12(4) | −4(5) | 5(3) | 4(7) | 11(14) | 15(33) | 19(14) |
| Fe/Mo 4a (0,0,0) ^{#[b]} | | | | | | | | |
| ($\beta_{11} = \beta_{22} = \beta_{33}$) $\times 10^4$ | 16(4) | 18(4) | 16(6) | 21(4) | 17(8) | 15(15) | 16(34) | 20(15) |
| O 24e (x,0,0) | | | | | | | | |
| <i>X</i> | 0.253(1) | 0.252(2) | 0.252(2) | 0.252(1) | 0.251(2) | 0.251(3) | 0.249(5) | 0.251(2) |
| $\beta_{11} \times 10^4$ | 8(2) | 8(2) | 11(2) | 20(1) | 13(2) | 15(2) | 20(2) | 25(2) |
| ($\beta_{22} = \beta_{33}$) $\times 10^4$ | 59(2) | 61(2) | 63(1) | 73(1) | 67(1) | 69(1) | 70(1) | 75(1) |
| Occ | 0.967(3) | 0.966(3) | 0.966(3) | 0.963(3) | 0.964(3) | 0.966(2) | 0.968(3) | 0.973(2) |
| δ | 0.20(2) | 0.20(2) | 0.20(2) | 0.22(2) | 0.22(2) | 0.20(2) | 0.19(2) | 0.16(2) |
| Magnetic Moment | | | | | | | | |
| μ_B /B site | 2.71(3) | 2.53(3) | 2.28(3) | 2.04(2) | 1.89(3) | 1.56(3) | 1.22(4) | – |
| Reliability factors | | | | | | | | |
| <i>R</i> _p (%) | 4.19 | 3.94 | 3.77 | 2.96 | 3.59 | 3.28 | 3.65 | 3.71 |
| <i>R</i> _{wp} (%) | 6.17 | 5.81 | 5.66 | 3.99 | 5.45 | 5.08 | 5.52 | 5.20 |
| <i>R</i> _{exp} (%) | 2.45 | 2.38 | 2.37 | 1.43 | 2.34 | 2.33 | 2.19 | 1.99 |
| χ^2 | 6.3 | 5.9 | 5.7 | 7.8 | 5.4 | 4.7 | 6.4 | 6.8 |
| <i>R</i> _{Bragg} (%) | 2.53 | 2.49 | 2.25 | 1.64 | 2.0 | 2.09 | 1.87 | 1.8 |
| <i>R</i> _{Mag} (%) | 7.28 | 7.27 | 7.38 | 5.81 | 7.28 | 9.09 | 12.9 | – |

[a] From combined NPD and XRPD data. [b] The Fe/Mo occupancy factors are fixed to those refined at 300 K (see Table 1).

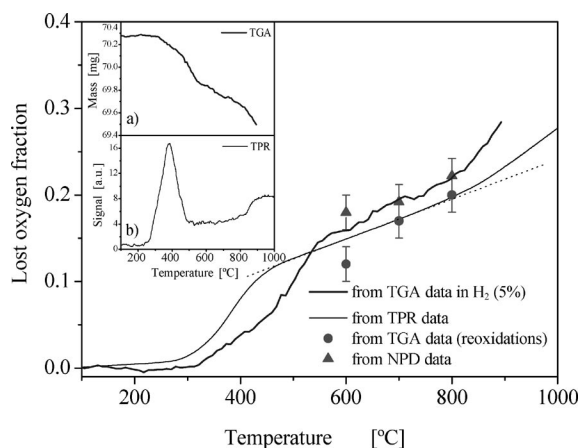


Figure 5. Thermal evolution of the oxygen deficiency (δ) obtained from TGA (in H_2/N_2 5%/95%) and TPR data for SFM. The symbols show the δ values obtained from TGA (by re-oxidations) and NPD data for SFM60, SFM70 and SFM80. The dash dot line indicates the interval temperature where the increase of δ is gradual. The inset a) and b) show the TGA and TPR experiments of the SFM respectively.

is observed between 820 and 1000 °C. The H_2 mass consumed during the reduction experiment was calculated from TPR data. The H_2 mass is proportional to the area under TPR curve, and the δ value is proportional to the H_2 mass. This curve shows a region between 470 and 800 °C where the increase of δ is constant. This temperature region was used to prepare the reduced samples. The same behavior of the thermal evolutions of the oxygen deficiency is observed from TGA data (in H_2/N_2 5%/95%) (see Figure 5).

Figure 6 illustrates the TGA (re-oxidation) curves in air of the oxygen-deficient perovskites ($Sr_2Fe_{1.33}Mo_{0.66}O_{6-\delta}$). The reduced samples are stable in an air flow up to 150 °C;

above this temperature, an oxidation process starts which it is assumed to lead back to the oxidized form of the $Sr_2Fe_{1.33}Mo_{0.66}O_6$ perovskite. The weight gain corresponds to the incorporation of 0.12(2), 0.17(2) and 0.20(2) oxygen atoms per formula for SFM60, SFM70 and SFM80, respectively. These values, within the experimental errors, are in agreement with the refinements neutron values, TGA (in H_2/N_2 5%/95%) and TPR data (see Figure 5).

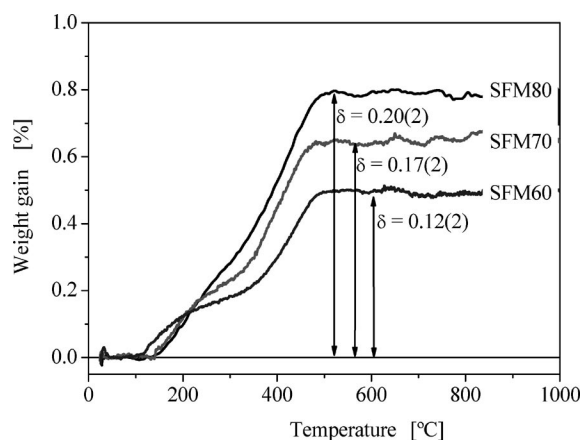


Figure 6. TGA curves of the reduced samples (re-oxidation), obtained in air flow at 5 °C min^{−1}.

Magnetic Data

The magnetic susceptibility vs. temperature curves are displayed in Figure 7. For the oxygen-stoichiometric sample there is a spontaneous increment of the susceptibility below 246 K, followed by a divergence of the zero-field-cooled (ZFC) and field-cooled (FC) curves. The presence of mag-

netic irreversibilities is symptomatic of a large degree of disordering or magnetic frustration in this sample. The reciprocal susceptibility shows a perfectly linear plot in the high-temperature range $300\text{ K} < T < 400\text{ K}$; a trial fit to the Curie–Weiss law gives a characteristic paramagnetic temperature $\theta_{\text{Weiss}} = -364\text{ K}$, and a value of the effective paramagnetic moment $\mu_{\text{eff}} = 6.81\text{ }\mu_{\text{B}}/\text{f.u.}$ Assuming the electronic configuration $\text{Fe}^{3+}(3d^5)\text{--}\text{Mo}^{6+}(4d^0)$, the magnetism only arises from trivalent Fe ($S = 5/2$). For the $\text{Sr}_2\text{Fe}_{1.33}\text{Mo}_{0.66}\text{O}_6$ formula, a predicted paramagnetic moment of $6.83\text{ }\mu_{\text{B}}/\text{f.u.}$ should be obtained in the absence of short range magnetic interactions, in excellent agreement with the observed value.

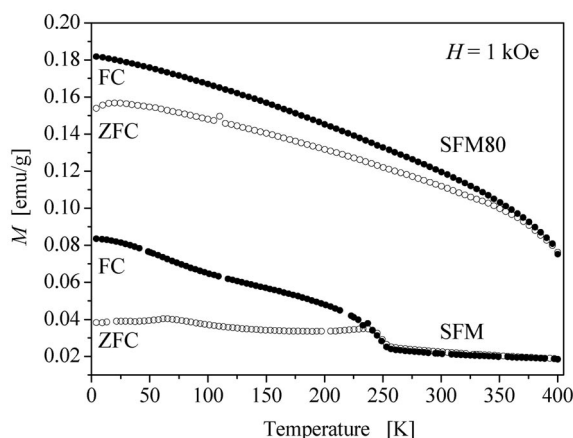


Figure 7. Field-cooled (FC) and zero-field-cooled (ZFC) magnetic susceptibility vs. temperature curves for the SFM and SFM80.

For the reduced sample (SFM80), the magnetic ordering temperature is dramatically enhanced, lying above the maximum measuring temperature of 400 K ; below 350 K the zero-field-cooled (ZFC) and field-cooled (FC) curves exhibit a distinct evolution. The FC curve shows a progressive increment of the susceptibility as temperature decreases, reminiscent of the spontaneous evolution characteristic of a ferromagnet, although a very small saturation magnetization is reached at low temperatures, of only $0.013\text{ }\mu_{\text{B}}/\text{f.u.}$ with a measuring field of $H = 1\text{ kOe}$. The ZFC curve shows a less pronounced susceptibility increment as temperature decreases.

The magnetization vs. magnetic field curve for the reduced sample at 4 K is plotted in Figure 8. Even at the lowest temperature, the magnetization is very far from saturation for the maximum applied field of $H = 5\text{ T}$, reaching a maximum value of $0.22\text{ }\mu_{\text{B}}/\text{f.u.}$ The M - H loops are characteristic of a weak ferro- or ferrimagnetic system. A weak ferromagnetic response exists but the predominant character is linear with the field. The linear high-field response was studied in magnetic fields up to 4 T . By subtracting the linear high-field dependence from the M - H curve measured at 4 K (inset Figure 8), the magnitude of the spontaneous moment at this temperature can be estimated. The measured magnetic moment is mainly determined by the Fe^{3+} ions. The spontaneous (uncompensated) site moment obtained becomes $\mu = 0.054\text{ }\mu_{\text{B}}/\text{f.u.}$

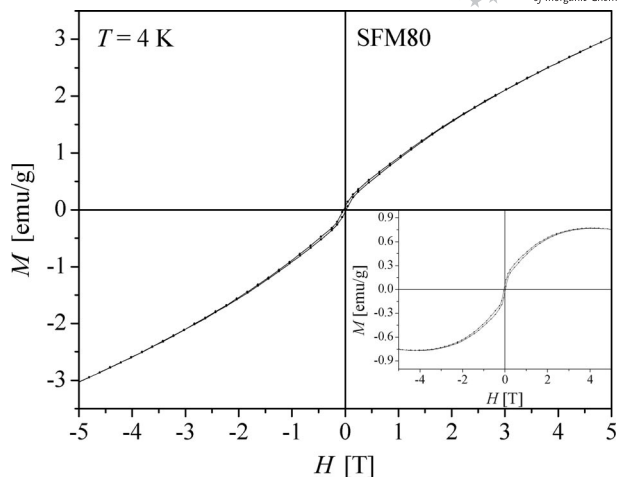


Figure 8. Magnetization vs. applied field measured at 4 K for SFM80. The inset shows the spontaneous magnetization vs. applied field at 4 K , obtained by subtracting the linear high field response from the measured hysteresis curve.

Transport and Magnetotransport

The electrical resistance of the stoichiometric $\text{Sr}_2\text{Fe}_{1.33}\text{Mo}_{0.66}\text{O}_6$ perovskite resulted to be too high to be measured (above 10^8 Ohms at room temp.); this compound must be considered as an insulator. On the contrary, the reduced sample (SFM80) shows a lower resistance. The experimental data were obtained from room temperature to 220 K ; below this temperature, the resistance was inaccessible in our experimental set-up. The electrical resistance was also measured under an external magnetic field ($H = 5\text{ T}$). As shown in Figure 9 at room temp. the resistance of SFM80 is $2.7 \times 10^5\text{ Ohms}$. The resistance gradually increases at lower temperatures, showing a semiconductor-like or thermally activated behavior. In Figure 9 (inset) we plot $\ln(R)$ vs. T^{-1} and a linear behaviour is observed. This can be associated with a thermal activated electronic conduction mechanism [$R = R_0 \exp(\Delta E_g/kT)$], giving $\Delta E_g =$

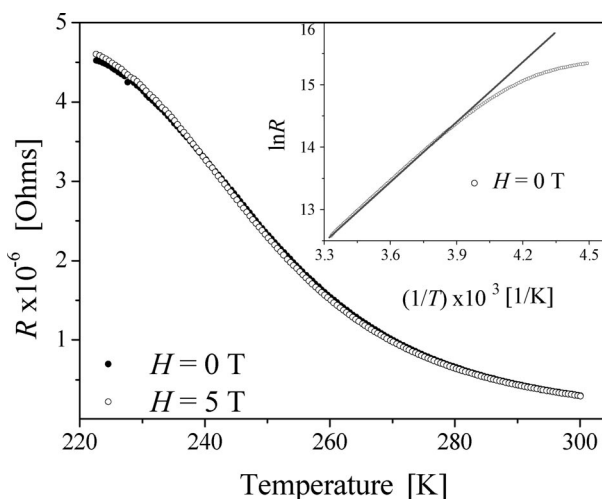


Figure 9. Resistance vs. temperature curves at 0 and 5 T for SFM80. The inset shows the logarithm of the electrical resistance vs. the reciprocal temperature at 0 T .

0.28 eV. This ΔE_g value could correspond to the energy gap between the valence and the conduction bands.

The Figure 10 shows the thermal evolution of the magnetoresistance, defined as $MR(T) = 100 \times [R(H = 0 \text{ T}, T) - R(H = 5 \text{ T}, T)]/R(H = 5 \text{ T}, T)$. A negative magnetoresistance is observed, reaching a maximum value of MR is -2.5% . MR shows a plateau between 300 and 260 K, and below this temperature it regularly increases as temperature diminishes, reaching positive values below 240 K. The inset shows the normalized magnetoresistance vs. magnetic field isotherm at 300 K, where a relatively weak low-field component is observed.

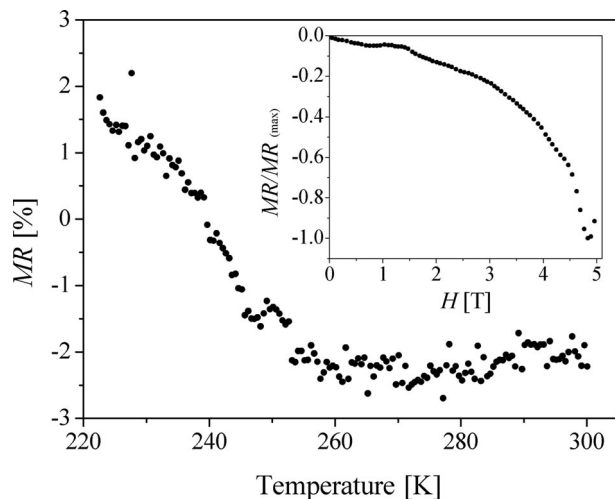


Figure 10. Magnetoresistance vs. temperature at 5 T for reduced the SFM80, calculated from $MR(T) = 100 \times [R(H = 0 \text{ T}, T) - R(H = 5 \text{ T}, T)]/R(H = 5 \text{ T}, T)$. The inset shows the normalized magnetoresistance vs. magnetic field isotherm at 300 K. The oxygen-stoichiometric sample was found to be an insulator; thus, R and MR could not be measured.

Magnetic Structure

The NPD data collection for SFM60, SFM70 and SFM80 at room temp. showed a progressively strong magnetic contribution to the scattering on allowed Bragg positions ($k = 0$), mainly on the (111) reflection, suggesting a ferro- or ferrimagnetic long-range ordering. This behavior is also observed below room temperature for SFM80. (Figure 11). This is surprising in this strongly disordered sample, taking into account that the saturation magnetization is very small, of hardly $0.22 \mu_B/\text{f.u.}$ with an applied field of 5 T. We would have expected that the structural disordering at the B positions of the perovskite had led to the absence of long-range magnetic ordering between Fe and Mo magnetic moments. As it will be discussed later, we believe that this magnetic scattering originates from Fe-rich regions in which neighboring Fe^{3+} spins exhibit AFM superexchange interactions via Fe–O–Fe paths. We have thus modeled the magnetic structure as a perfect AFM arrangement of Fe spins with alternating directions, occupying all the B positions of a perovskite structure with the same unit-cell and positional parameters as the host $\text{Sr}_2\text{Fe}_{1.33}\text{Mo}_{0.66}\text{O}_{6-\delta}$. We

have constrained the scale factors of both structural and magnetic models, and refined the magnitude of the Fe magnetic moments. The thermal variation of the magnitude of the ordered Fe magnetic moments for SFM80 is displayed in Figure 12 (see also Table 2).

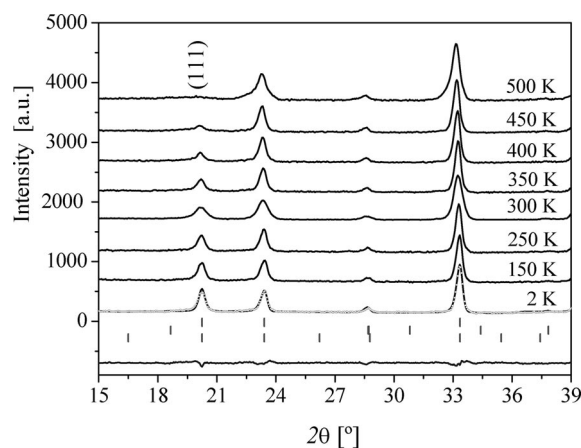


Figure 11. Thermal evolution of the NPD patterns for the reduced sample, highlighting the appearance at low temperatures of a magnetic contribution to the scattering on the low-angle reflections, especially on the (111) Bragg position.

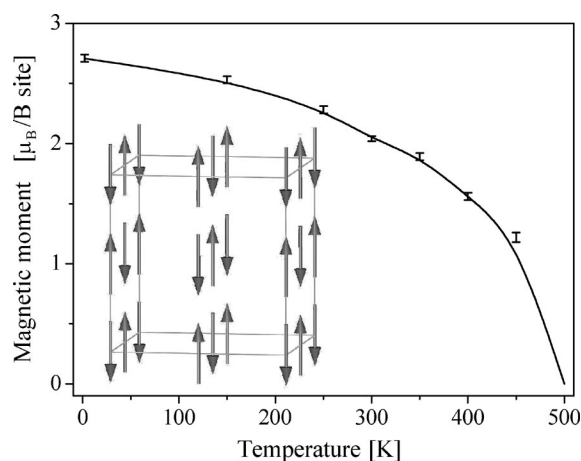


Figure 12. Thermal dependence of the ordered magnetic moments refined from NPD data. The inset in shows a schematic view of the magnetic structure of the reduced sample.

Discussion

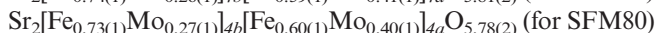
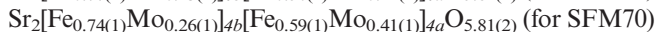
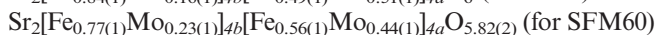
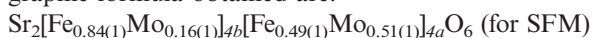
The perovskite structure ABO_3 can be viewed as a network of corner-sharing BO_6 octahedra, with the A cations occupying the voids formed by these octahedra. If the size of A cations becomes small, the BO_6 octahedra tilt in order to optimize the A–O contacts. $\text{Sr}_2\text{Fe}_{1.33}\text{Mo}_{0.66}\text{O}_6$ adopts the well-known $(\text{NH}_4)_3\text{FeF}_6$ structure, in which $(\text{Fe}_{1-a}\text{Mo}_a)_{4b}\text{O}_6$ and $(\text{Fe}_{1/3+a}\text{Mo}_{2/3-a})_{4a}\text{O}_6$ octahedra alternate along the three crystallographic directions. Given the size of Sr^{2+} cations, the octahedral network is not tilted, keeping $\text{B}_{4b}\text{O} - \text{B}_{4a}$ angles of 180° .

The presence of the reduction effect is supported by the variations in the unit-cell parameters, which increase progressively from the SFM sample to the SFM80 oxide. The lineal increase in the cell parameters is attributed to the reduction of molybdenum ions with the concomitant increase of the ionic radius. This process is illustrated in Figure 4 (inset a).

As it was mentioned above, the oxygen-stoichiometric $\text{Sr}_2\text{Fe}_{1.33}\text{Mo}_{0.66}\text{O}_6$ perovskite has been prepared in air, in such a way that, from the chemical point of view, a hexavalent oxidation state is expected for Mo cations with Fe cations being trivalent. The electronic configuration for this sample is $\text{Fe}^{3+}(3d^5)\text{-Mo}^{6+}(4d^0)$, which also accounts for the electrical insulator behavior. The reduction process to give $\text{Sr}_2\text{Fe}_{1.33}\text{Mo}_{0.66}\text{O}_{6-\delta}$ introduces, nominally, 2δ extra electrons that can partially occupy hybridized Mo $4d$ t_{2g} and Fe $3d$ t_{2g} states. However, the findings from Mössbauer spectroscopy clearly indicate that Fe is in a trivalent state upon reduction of the sample at 800°C (Fe^0 is not observed) and, hence, a mixed $\text{Mo}^{6+}/\text{Mo}^{5+}$ valence state is induced in the reduced sample under the mentioned conditions.^[14] In the TPR curve this process can be followed; the oxygen loss begins with a strong peak centered at 380°C and then δ increases regularly up to 820°C . As Fe^{3+} is observed by Mössbauer spectroscopy the extra electrons occupy hybridized Mo $4d$ t_{2g} states.^[14] Above this temperature the extra H_2 consumption shows a increment associated to $\text{Fe}^{3+} \rightarrow \text{Fe}^{2+}$ reduction involving a change in the stoichiometry in $\text{Sr}_2\text{Fe}_{1+x}\text{Mo}_{1-x}\text{O}_6$ from $x = 1/3$ to $1/3 > x > 0$.^[14] This study allowed us to determine the experimental condition that maximize the number of oxygen vacancies keeping a Fe/Mo ratio = 2; these conditions were used to prepare SFM80. For this reason this optimized sample was subsequently selected for an in-depth magnetic and transport characterization.

The refined site occupancies for the stoichiometric and reduced samples (Table 1) show that the Fe/Mo long-range ordering is only partial. The DO values calculated are 0.52, 0.31, 0.22 and 0.19 for SFM, SFM60, SFM70 and SFM80, respectively. This decrease in the degree of order is originated by the progressive reduction of Mo^{6+} to Mo^{5+} , yielding a diminution of the ionic radii difference between Fe and Mo cations, which is the driving force for the long-range ionic ordering ($r_{\text{Fe}^{III}} = 0.645 \text{ \AA}$; $r_{\text{Mo}^V} = 0.61 \text{ \AA}$ and $r_{\text{Mo}^{VI}} = 0.59 \text{ \AA}$).^[18]

From the combined XRPD and NPD data the crystallographic formula obtained are:



From the crystallography formula obtained after the combined refinement at room temp. the oxygen vacancies content are 3.0(3)%, 3.2(3)% and 3.7(3)% for SFM60, SFM70 and SFM80, respectively. The removal of one oxygen atom corresponds to two injected electrons per formula. Since Mo is more easily reducible than Fe, Mo is present in 66% as Mo^{5+} in the optimized sample SFM80, the formula

being rewritten as $\text{Sr}_2\text{Fe}_{1.33}\text{Mo}^{\text{VI}}_{0.23}\text{Mo}^{\text{V}}_{0.44}\text{O}_{5.78}$. The amount of Mo^{5+} determined by thermogravimetric analysis is 60%, in good agreement with the mentioned structural data.

In the oxygen-stoichiometric material, nominally containing only Fe^{3+} and Mo^{6+} , the lack of an itinerant Mo electron prevents the magnetic coupling across Fe–O–Mo paths, in such a way that the only possible magnetic superexchange mechanism would take place via Fe–O–Fe paths, in Fe-rich regions of the crystal containing neighboring Fe^{3+} spins, promoted by the anti-site disordering of this sample. However in the reduced sample a coupling across Fe–O–Mo is also possible due to new electronic configurations $\text{Fe}^{3+}(3d^5)\text{-O-Mo}^{5+}(4d^1)$.

In order to understand this situation for $\text{Sr}_2[\text{Fe}_{1-a}\text{Mo}_a]_{4b}\text{-}[\text{Fe}_{1/3+a}\text{Mo}_{2/3-a}]_{4a}\text{O}_{6-\delta}$, it is necessary to first consider the statistical distribution of the coordination environments of the paramagnetic cations. Firstly, the majority of Fe^{3+} (the only paramagnetic cation present in the oxygen-stoichiometric sample) is located on the 4b-site, Fe_{4b} , and it is coordinated to either Mo_{4a} or Fe_{4a} with fractional occupancies $2/3-a$ and $1/3+a$, respectively. The remaining Fe^{3+} on the 4a-site, Fe_{4a} , is coordinated to either Mo_{4b} or Fe_{4b} with fractional occupancies a and $1-a$. For m independent events, each of which has two possible outcomes A and B with probabilities P_A and P_B , respectively, the probability P of A occurring n times (and B therefore occurring $m-n$ times) is given by the following expression^[19]

$$P = {}^mC_n \cdot P_A^n \cdot P_B^{(m-n)}$$

where mC_n is the number of possible ways that the given combination of events can occur and is given by

$${}^mC_n = m!/(m-n)!n!$$

The probability over all Fe on 4a and 4b sites, with fractional occupancies, $f_{(\text{Fe}4a)}$ and $f_{(\text{Fe}4b)}$ is

$$P_{\text{Fe}} = f_{(\text{Fe}4a)} \cdot P_{\text{Fe}(4a)} + f_{(\text{Fe}4b)} \cdot P_{\text{Fe}(4b)}$$

and it was normalized such that

$$\Sigma P_{\text{Fe}} = 100$$

In the same way, the probability is calculated for Mo. Values of mC_n and the calculated statistical probability distribution of all possible coordination environments for Fe and Mo are given in Table 3.

From this statistical distribution of the coordination environments of the cations, a simplified image can be built to represent this situation. Parts a and b of Figure 13 show a magnetic ordering in the stoichiometric and reduced (SFM80) samples respectively; only one layer of B cations is shown for the sake of simplicity. A ferrimagnetic coupling between up Fe^{3+} spins at 4b sites (black in Figure 13, a) and down Fe^{3+} spins at 4a positions (grey in Figure 13, a) would ideally give a net magnetization of $5(0.84-0.49) = 1.75(1) \mu_B/\text{f.u.}$, but this would require a perfect coherence between Fe-rich patches, as illustrated in Figure 13 (a). For a cubic lattice where 4b and 4a positions are statistically occupied by 0.84(2) and 0.49(2) Fe ions respectively the probability of finding Fe–(Fe_6) and Fe–(Fe_5Mo) coordinations are 34.1% (= 13.8% + 20.3%), thus the long range magnetic connections through $\text{Fe}_{4b}\text{-O-Fe}_{4a}\text{-O-Fe}_{4b}$ exceed the 31% percolation limit of a simple cubic lattice.

Table 3. Probability, P , for all possible distributions of six-coordinated species for Fe and Mo atoms, where mC_n is the number of ways in which a particular distribution can occur.

| Fe(–) | mC_n | P_{Fe} | Mo(–) | mC_n | P_{Mo} |
|--|-----------|----------|---------------------------------|-----------|----------|
| Sr₂Fe_{1.33}Mo_{0.66}O₆ | | | | | |
| Mo ₆ | 1 | 1.1 | Fe ₆ | 1 | 27.1 |
| FeMo ₅ | 6 | 6.4 | Fe ₅ Mo | 6 | 32.6 |
| Fe ₂ Mo ₄ | 15 | 15.6 | Fe ₄ Mo ₂ | 15 | 19.9 |
| Fe ₃ Mo ₃ | 20 | 21.5 | Fe ₃ Mo ₃ | 20 | 11.3 |
| Fe ₄ Mo ₂ | 15 | 21.2 | Fe ₂ Mo ₄ | 15 | 6.3 |
| Fe ₅ Mo | 6 | 20.3 | FeMo ₅ | 6 | 2.5 |
| Fe ₆ | 1 | 13.8 | Mo ₆ | 1 | 0.4 |
| Sr₂Fe_{1.33}Mo_{0.66}O_{6-δ} | | | | | |
| Mo ₆ | 1 | 0.2 | Fe ₆ | 1 | 10.9 |
| FeMo ₅ | 6 | 2.3 | Fe ₅ Mo | 6 | 27.6 |
| Fe ₂ Mo ₄ | 15 | 9.5 | Fe ₄ Mo ₂ | 15 | 31.1 |
| Fe ₃ Mo ₃ | 20 | 22.1 | Fe ₃ Mo ₃ | 20 | 20.3 |
| Fe ₄ Mo ₂ | 15 | 31.1 | Fe ₂ Mo ₄ | 15 | 8.1 |
| Fe ₅ Mo | 6 | 25.4 | FeMo ₅ | 6 | 1.9 |
| Fe ₆ | 1 | 9.4 | Mo ₆ | 1 | 0.2 |

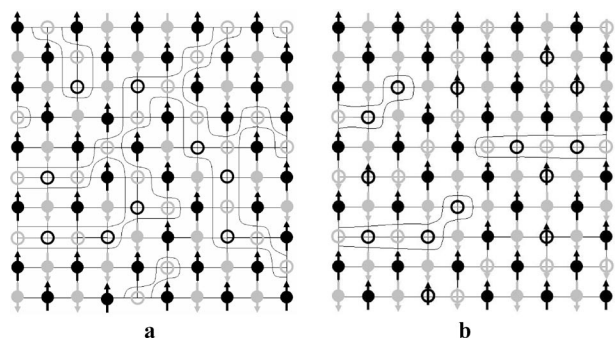


Figure 13. Ideal schematic view of the magnetic coupling in (a) oxygen-stoichiometric and (b) reduced sample. These double perovskites contains randomly distributed Fe (full circle) and Mo (circle) at $4a$ (black) and $4b$ (grey) positions.

In the reduced (SFM80) phase this situation is different, since the Fe-rich regions are magnetically connected through Mo⁵⁺(4d¹). Figure 13 (b) illustrates this situation, where a ferrimagnetic coupling between Fe³⁺ or Mo⁵⁺ spin at $4b$ sites and Fe³⁺ or Mo⁵⁺ spin at $4a$ sites, would ideally give a net magnetization of 0.36 μ_B /f.u. which comes from considering an antiparallel coupling between the Fe and Mo spins occupying the $4b$ and $4a$, with the different relative occupations obtained by NPD and XRPD experiment.

The calculated magnetic moment is bigger than that obtained from the experimental data. The difference probably arises from the non-perfect coherence between Fe-rich patches. Notice that the total absence of coherence between isolated Fe-rich patches would lead, on average, to a null saturation magnetization.

On one hand, the introduction of oxygen vacancies is in the origin of the enhanced FM T_C , due to the concomitant introduction of extra electrons in the system, but, at the same time, the physical absence of these oxygens hinders the establishment of a homogeneous FM state, disturbing

both the superexchange Fe–O–Fe interactions and the electronic conduction paths. This fact generates a decrease of the saturation moment and the increment in the resistance.

The coexistence of important electronic conductivity and FM interactions below T_C accounts for the magnetotransport properties, as observed in other half-metallic FM double perovskites. In the absence of band-structure calculations, we can speculate that the extra itinerant Mo electrons occupy down-spin bands and they are shared among Fe and Mo atoms. Nevertheless, the parallelism with Sr₂FeMoO₆ is not complete, because there is a significant difference with the Sr₂Fe_{1.33}Mo_{0.66}O_{6-δ} system; the necessary electrons have been introduced by chemical reduction through the introduction of oxygen vacancies.

The measured MR would be a result of the spin dependent scattering of the charge carriers through the FM clusters; this scattering is reduced when an external magnetic field is applied thus aligning the orientation of the isolated clusters. The maximum value of MR (2.5%) occurs at room temp. obtained from the MR vs. T curves (Figure 10). However, the observed increase of MR with increasing temperature is different to that exhibited in other double perovskites, namely, Sr₂FeMoO₆, in which the main component of MR is attributable to grain boundary tunneling effects that take place at temperatures well below T_C . In our sample the MR vs. T behaviour (Figure 10) is comparable to that exhibited in Sr₃Fe₂ReO₉ reported by Pannunzio-Miner et al.^[20] For this sample a similar 2:1 (Fe/B'') ratio as B-site disorder are comparable with our sample, besides their electronic configurations. This dependence of the MR with the temperature can be associated with irreversible relaxations of the magnetic domains inside the sample. The temperature can help to reverse the magnetization mechanism of magnetic clusters or ferrimagnetic regions. On the contrary, at low temperature, these ferrimagnetic regions could be perfectly correlated.

The magnetic susceptibility measurements by SFM80 (Figure 7) show that the magnetic ordering temperature is above 400 K; an extrapolation from the ZFC curve (fit to a Brillouin curve) gives an estimated T_C of 470 K. This is in good agreement with the temperature-dependent NPD data that show that the long-range magnetic ordering is established between 450 and 500 K.

We have fit the magnetic contributions to the neutron scattering by modeling an AFM structure consisting of a perfect arrangement of Fe cations occupying all of the B positions of a perovskite structure with the same unit-cell parameters as the crystallographic Sr₂Fe_{1.33}Mo_{0.66}O_{6-δ} phase. A comparative analysis of the magnetic moment values at room temp. show a gradual increment with the oxygen vacancy content (Table 1). The refinement of the magnitude of the magnetic moments on the Fe positions in SFM80 at 2 K, gives an ordered magnetic moment of 2.71(3) μ_B , with constrained scale factors for the crystal and magnetic structure. Notice that this is only the average ordered component of the magnetic moment over all the B positions of the perovskite. Our picture thus shows a disordered Fe/Mo pattern in which the Fe–O–Fe superexchange

AFM interactions are comparable to those existing in $R\text{FeO}_3$ ferrites (R = rare earths), as shown in the inset of Figure 12.

Conclusions

Three reduced samples of stoichiometry $\text{Sr}_2\text{Fe}_{1.33}\text{Mo}_{0.66}\text{O}_{6-\delta}$ have been stabilized by topotactical removal of oxygen atoms in the parent $\text{Sr}_2\text{Fe}_{1.33}\text{Mo}_{0.66}\text{O}_6$ compound at increasing temperatures. Annealing in a H_2 flow at 800 °C (SFM80) constitutes the optimum conditions to produce the best non-stoichiometric $\text{Sr}_2\text{Fe}_{1.33}\text{Mo}_{0.66}\text{O}_{6-\delta}$ phase with $\delta = 0.22(2)$, as determined from NPD data at room temp. The crystal structure is cubic, space group $Fm\bar{3}m$, in the temperature range 2 K to 500 K; the average thermal expansion coefficient is $11.9 \times 10^{-6} \text{ K}^{-1}$. The crystallographic formula obtained at room temp. $\text{Sr}_2[\text{Fe}_{0.73(1)}\text{Mo}_{0.27(1)}]_{4b}[\text{Fe}_{0.60(1)}\text{Mo}_{0.40(1)}]_{4a}\text{O}_{5.78(2)}$, involves an important anti-site disordering, which accounts for the observed magnetic properties. The magnetic ordering temperature lies within the temperature interval 450–500 K, as shown from NPD data, where a distinct magnetic contribution is noted on the low-angle Bragg reflections; this T_C is enhanced with respect to the parent oxygen-stoichiometric compound ($T_C = 250 \text{ K}$). This high magnetic-ordering temperature is the result of direct superexchange Fe–O–Fe interactions combined with the presence of itinerant down-spin Mo t_{2g} electrons, induced by the electron doping effect associated with the oxygen removal. However, as a result of the important anti-site disordering, the saturation magnetization is very low even at low temperatures: the spontaneous (uncompensated) site moment obtained becomes $\mu = 0.054 \mu_B/\text{f.u.}$ For this reason, the magnetic structure has been successfully refined with an antiferromagnetic (instead of ferromagnetic) model, with ordered magnetic moments on the Fe site of $2.71(3) \mu_B$ at 2 K. The electron-doping effect also has a strong influence on the electronic conductivity, which dramatically increases upon H_2 reduction. Moreover, the reduced samples exhibit magnetoresistance, as high as 2.5% at room temp. for $H = 5 \text{ T}$.

Experimental Section

General: The parent $\text{Sr}_2\text{Fe}_{1.33}\text{Mo}_{0.66}\text{O}_6$ double perovskite was prepared as a black polycrystalline powder from citrate precursors obtained by soft chemistry procedures, similar to the method proposed by Viola et al.^[5] Stoichiometric amounts of analytical grade $\text{Sr}(\text{NO}_3)_2$, $\text{Fe}(\text{NO}_3)_3 \cdot 9\text{H}_2\text{O}$, and $(\text{NH}_4)_6\text{Mo}_7\text{O}_{24} \cdot 4\text{H}_2\text{O}$ were dissolved in citric acid. The citrate and nitrate solutions were slowly concentrated, leading to organic resins containing a random distribution of the cations involved at an atomic level. These resins were first dried at 180 °C and then slowly decomposed at temperatures up to 600 °C. All the organic materials and nitrates were eliminated in a subsequent treatment at 800 °C in air, for 2 h, giving rise to highly reactive precursor materials. The resulting black powder was then treated in air at 1000 °C for 24 h and fired at 1300 °C in two periods totaling 12 h and the sample was furnace-cooled to room temperature. This sample is labeled SFM. The oxygen-deficient

$\text{Sr}_2\text{Fe}_{1.33}\text{Mo}_{0.66}\text{O}_{6-\delta}$ perovskites were prepared by topotactic reduction of the oxygen-stoichiometric perovskite in an H_2/N_2 (5%/95%) flow at 600, 700 and 800 °C for 10 h. The rate of heating and cooling was $5 \text{ }^\circ\text{C min}^{-1}$. Thermal treatments longer than 10 h did not produce changes in the obtained samples, suggesting that the reduction products reach equilibrium with the atmosphere before this treatment time. These reduced samples are labeled SFM60; SFM70 and SFM80, respectively. The conditions for the $\text{Sr}_2\text{Fe}_{1.33}\text{Mo}_{0.66}\text{O}_6$ reduction, were established from Thermal Programmed Reduction (TPR) data and previous Mössbauer spectroscopy results.^[14] The initial identification and characterization of the samples was carried out by X-ray powder diffraction, XRPD.

The crystallographic study for stoichiometric $\text{Sr}_2\text{Fe}_{1.33}\text{Mo}_{0.66}\text{O}_6$ and reduced $\text{Sr}_2\text{Fe}_{1.33}\text{Mo}_{0.66}\text{O}_{6-\delta}$ samples were carried out from XRPD patterns collected at about 300 K (room temp.). The experimental XRPD patterns obtained on a diffractometer Rigaku D-MAX-IIIIC with $\text{Cu-K}\alpha$ ($\lambda = 1.5406 \text{ \AA}$) radiation. The data were collected over a range of $10\text{--}120^\circ$ (2θ) with a step of 0.02° ; the effective counting time was 5 s per step.

For the structural refinements, NPD patterns of SFM and SFM80 were collected at room temp. (room temperature) at the high-resolution D2B neutron diffractometer of ILL-Grenoble. The high-flux mode was used. Additionally, measurements at 2, 150, 250, 350, 450 and 500 K were performed for the SFM80 sample. A wavelength of 1.594 \AA was selected from a Ge monochromator. For the SFM60 and SFM70 samples the NPD patterns were collected at 300 K at the high resolution HRPT diffractometer of the SINQ spallation source at the Paul Scherrer Institute, Villigen, Switzerland with $\lambda = 1.154 \text{ \AA}$. The patterns were refined by the Rietveld method using the FULLPROF refinement program.^[21,22] A pseudo-Voigt function was chosen to generate the line shape of the diffraction peaks. A SrMoO_4 minor impurity was included as a second crystallographic phase in the refinements. In the final runs, the following parameters were refined: scale factors for the main and impurity phases, background coefficients, zero-point error, unit cell parameters, pseudo-Voigt corrected for asymmetry parameters, positional coordinates, anisotropic thermal factors, and antisite disorder of Fe/Mo and occupancy factors for oxygen atoms. The coherent scattering lengths for Sr, Fe, Mo, and O were 7.02, 9.45, 6.72, and 5.803 fm, respectively.

Electron microscopy was performed at room temp. in a JEOL 2000 FII with an acceleration potential of 200 kV. The SFM70 sample was thoughtfully ground, dispersed in *n*-butanol and placed on a Cu grid coated with C.

The Thermal Programmed Reduction (TPR) of the stoichiometric sample was performed with Quantchrome equipment, model Chembet 3000 TPR/TPD. The mass of sample used was 182 mg under 20 mL/min of H_2/N_2 (5%/95%) with heating rate of $5 \text{ }^\circ\text{C/min}$.

Thermogravimetric analysis of the reduced samples was performed in a Shimadzu TG-50H thermal analyzer apparatus using flowing air at 50 mL/min from 25 °C to 1000 °C, at a heating rate of $5 \text{ }^\circ\text{C/min}$. About 18 mg of the sample was used in the experiment. Moreover, measurements using flowing H_2/N_2 (5%/95%) were collected for the about 70 mg of stoichiometric sample in the same conditions.

The magnetization measurements for SFM and SFM80 were measured with a commercial SQUID magnetometer on powdered samples, in the temperature range of 5–400 K; transport and magnetotransport measurements were performed by the conventional four probe technique, under magnetic fields up to 5 T in a PPMS

system from Quantum Design. For the resistance and magnetotransport measurements, polycrystalline powder of SFM80 was pressed in bar-shaped pellets and sintered at 800 °C for 6 h in Ar flow.

Acknowledgments

We are grateful for financial support from the Argentinean Agencia Nacional de Promoción Científica y Tecnológica (ANPCYT) (grant no. PICT 25459), the Secretaría de Ciencia y Técnica de la Universidad Nacional de San Luis (SECYT-UNSL) (grant no. 7707), and the Consejo Nacional de Investigaciones Científicas y Técnicas (CONICET) (PIP no. 6246) and the Spanish Ministerio de Ciencia y Innovación (MICINN) (grant no. MAT2007-60536). We are also grateful to the Institut Laue Langevin (ILL) for allowing us to use their facilities. We thank Dr. A. Landa for the collection of the electron diffraction patterns. C. A. L. is grateful for a CONICET fellowship and J. C. P. is a member of CONICET.

- [1] J. L. Simonds, *Phys. Today* **1995**, 48, 26–32.
- [2] M. B. Salamon, M. Jaime, *Rev. Mod. Phys.* **2001**, 73, 583–628.
- [3] K. I. Kobayashi, T. Kimura, H. Sawada, K. Terakura, Y. Tokura, *Nature* **1998**, 395, 677.
- [4] T. H. Kim, M. Uehara, S. W. Cheong, S. Lee, *Appl. Phys. Lett.* **1999**, 74, 1737–1739.
- [5] M. C. Viola, J. A. Alonso, J. C. Pedregosa, R. E. Carbonio, *Eur. J. Inorg. Chem.* **2005**, 1559–1564.
- [6] R. M. Pinacca, M. C. Viola, J. C. Pedregosa, R. E. Carbonio, J. A. Alonso, *J. Mater. Chem.* **2005**, 15, 4648–4653.
- [7] M. S. Augsburger, M. C. Viola, J. C. Pedregosa, R. E. Carbonio, J. A. Alonso, *J. Mater. Chem.* **2006**, 16, 4235–4242.
- [8] J. Navarro, J. Nogués, J. S. Muñoz, J. Fontcuberta, *Phys. Rev. B* **2003**, 67, 1744161–1744166.
- [9] C. Frontera, D. Rubí, J. Navarro, J. L. García-Muñoz, C. Ritter, J. Fontcuberta, *Phys. B* **2004**, 350, E285–E288.
- [10] D. Rubí, C. Frontera, G. Herranz, J. L. García-Muñoz, J. Fontcuberta, C. Ritter, *J. Appl. Phys.* **2004**, 95, 7082–7084.
- [11] C. Frontera, D. Rubí, J. Navarro, J. L. García-Muñoz, J. Fontcuberta, C. Ritter, *Phys. Rev. B* **2003**, 68, 0124121–0124124.
- [12] C. A. López, M. C. Viola, R. D. Sánchez, R. E. Carbonio, M. T. Díaz, J. C. Pedregosa, *J. Solid State Chem.* **2008**, 181, 3095–3102.
- [13] M. C. Viola, M. J. Martínez-Lope, J. A. Alonso, P. Velasco, J. L. Martínez, J. C. Pedregosa, R. E. Carbonio, M. T. Fernández-Díaz, *Chem. Mater.* **2002**, 14, 812–818.
- [14] C. A. López, M. C. Viola, J. C. Pedregosa, R. C. Mercader, *Mater. Res. Bull.*, manuscript accepted (*Assessment of the optimum degree of $\text{Sr}_3\text{Fe}_2\text{MoO}_9$ electron-doping through oxygen removal: An X-ray powder diffraction and ^{57}Fe Mössbauer spectroscopy study*).
- [15] S. A. Ivanov, S. G. Eriksson, R. Tellgran, H. Rundlof, P. Nordblad, J. Eriksen, *J. Solid State Chem.* **2006**, 179, 2645–2655.
- [16] G. Y. Liu, G. H. Rao, X. M. Feng, H. F. Yang, Z. W. Ouyang, W. F. Liu, J. K. Liang, *J. Alloys Compd.* **2003**, 353, 42–47.
- [17] E. Guermen, E. Daniels, J. S. King, *J. Chem. Phys.* **1971**, 55, 1093–1097.
- [18] R. D. Shannon, *Acta Crystallogr., Sect. A* **1976**, 32, 751–767.
- [19] J. H. Conway, R. K. Guy, *The Book of Numbers*, Springer, New York, **1996**.
- [20] E. V. Pannunzio Miner, J. M. De Paoli, J. A. Alonso, M. García-Hernández, R. D. Sánchez, R. E. Carbonio, *Phys. B* **2007**, 398, 397–400.
- [21] H. M. Rietveld, *J. Appl. Crystallogr.* **1969**, 2, 65–71.
- [22] J. Rodríguez-Carvajal, *Phys. B* **1993**, 192, 55–69.

Received: March 18, 2010
Published Online: July 28, 2010

Multistep Anchoring Route of Luminescent (5-Amino-1,10-phenanthroline)-tris(dibenzoylmethane)europium(III) on Si(100)

Guglielmo G. Condorelli,^{*,[a]} Cristina Tudisco,^[a] Alessandro Motta,^[a]
Alessandro Di Mauro,^[a] Fabio Lupo,^[a] Antonino Gulino,^[a] and Ignazio L. Fragalà^[a]

Keywords: Monolayers / Luminescence / Surface chemistry / Silicon / Metal complexes

A multistep route for the covalent anchoring of (5-amino-1,10-phenanthroline)tris(dibenzoylmethane)europium(III) molecules on silicon (100) has been developed. The anchoring route consists of Si functionalization with *N*-hydroxysuccinimide (NHS) activated carboxylic acid, followed by nucleophilic substitution at the carboxylic acid sites. Characterization of the resulting Si based hybrid materials was achieved by using several complementary techniques: X-ray photoelectron spectroscopy (XPS), attenuated total reflection FTIR spectroscopy (ATR-FTIR), AFM and fluorescence spec-

troscopy. Comparison of results obtained for NHS activated Si surfaces with those of inert alkyl functionalized Si surfaces proved the covalent anchoring of the Eu complex and ruled out the presence of physisorbed Eu species. The 1.8 nm thickness of the grafted layer, estimated by atomic-force lithography, is compatible with the presence of the anchored complex on the surface. Fluorescence measurements proved that luminescence properties are retained in the grafted complex.

Introduction

Functionalization of inorganic surfaces with specific organic molecules and metal complexes is a theme of major interest in contemporary inorganic chemistry because of potential applications in the fabrication of advanced materials^[1] performing specific functions such as memory storage,^[2] molecular switches^[3] and sensing.^[4] In this field, monolayers covalently bound to technological substrates such as Si^[5] and SiO₂^[6] represent very attractive systems since they allow facile integration in electronic devices and offer the possibility to make durable devices by stable covalent bonds. Different approaches can be followed for the covalent functionalization of SiO₂ and Si surfaces. The first is based on the bonding of appropriate molecules to the surface hydroxy groups of the substrate. In this context, suitable molecules are alkoxy-,^[7] chloro-^[8] and allylsilanes^[9] and various organometallics.^[10] However, this approach needs strictly controlled experimental conditions to ensure clean and complete monolayer formation and avoid side reactions. On the other hand, direct linking of functional molecules on H-terminated Si surfaces, through thermal or photochemical hydrosilylation of multiple bonds, appears to be an easier and cleaner alternative approach.^[5a,11,12] In this context, we have recently explored direct^[13] and

multistep^[14,15] silicon anchoring routes for different inorganic complexes. In particular, multistep anchoring routes have the advantage of allowing the anchoring of a large variety of functional complexes often not suited for the direct hydrosilylation reaction.^[16] An example of the successful application of a multistep approach is for the surface binding of biological molecules in so-called DNA chips.^[17,18] Si-anchoring of inorganic complexes by ligand exchange reactions has been developed and successfully applied for the covalent bonding of single molecular magnets (SMM) on a ligand prefunctionalized silicon surface.^[14] A similar ligand exchange route has been applied to the silicon anchoring of a Ni β -diketonate complex in the vapour phase.^[15] However, this approach can have significant drawbacks if changing the metal environment affects the functional properties of the inorganic complex. This point must be taken into account for the anchoring of luminescent lanthanide complexes. Although 4f levels in lanthanide compounds have been generally considered essentially atomic in nature,^[19] emission of trivalent lanthanides and, in particular, of Eu^{III} complexes, is strongly influenced by the metal environment because of the effective intramolecular energy transfer from the coordinated ligands to the luminescent lanthanide ion.^[20] Photoluminescence (PL) of trivalent europium ions is relevant because of the involvement of Eu^{III} compounds in efficient light conversion in molecular devices such as phosphors in full-colour flat-panel displays, laser materials, for sensing, as bioprobes and as memory devices.^[21] In fact, despite the limited applications of some lanthanide β -diketonate complexes due to their poor stability, Eu^{III} β -diketonate complexes also coordinated by a

[a] Dipartimento di Scienze Chimiche, University of Catania, ISTM-CNR and INSTM UdR of Catania, V.le A. Doria 6, 95125 Catania, Italy
Fax: +39-095-580138
E-mail: guidocn@unict.it

Supporting information for this article is available on the WWW under <http://dx.doi.org/10.1002/ejic.201000272>.

phenanthroline ligand find application since the neutral ligand induces luminescence as well as thermal and photostability.^[22] In addition, the immobilization of Eu^{III} luminescent complexes on Si represents an approach for the fabrication of hybrid inorganic/organic materials showing SMM properties.

The luminescence properties of (5-amino-1,10-phenanthroline)tris(dibenzoylmethane)europium(III) molecules (**1**) grafted on quartz substrates have been observed recently.^[23] In this work, a new grafting route suited for the anchoring of **1** on H-terminated Si surfaces has been developed. This anchoring route is based on silicon prefunctionalization with NHS activated carboxylic acid, followed by nucleophilic substitution of the amine group of **1** at the carboxylic acid site. This study describes a grafting strategy to obtain a Eu complex molecular monolayer that, to the best of our knowledge, has not been used previously for lanthanide or other inorganic complexes. In addition, we demonstrate that the experimental conditions adopted for grafting are fundamental to address an intact covalent assembly of the Eu complex to the functionalized Si(100) substrate, thus maintaining the luminescence behaviour of the molecule and resulting in a luminescent molecular material with the potential for integration in optoelectronic devices.

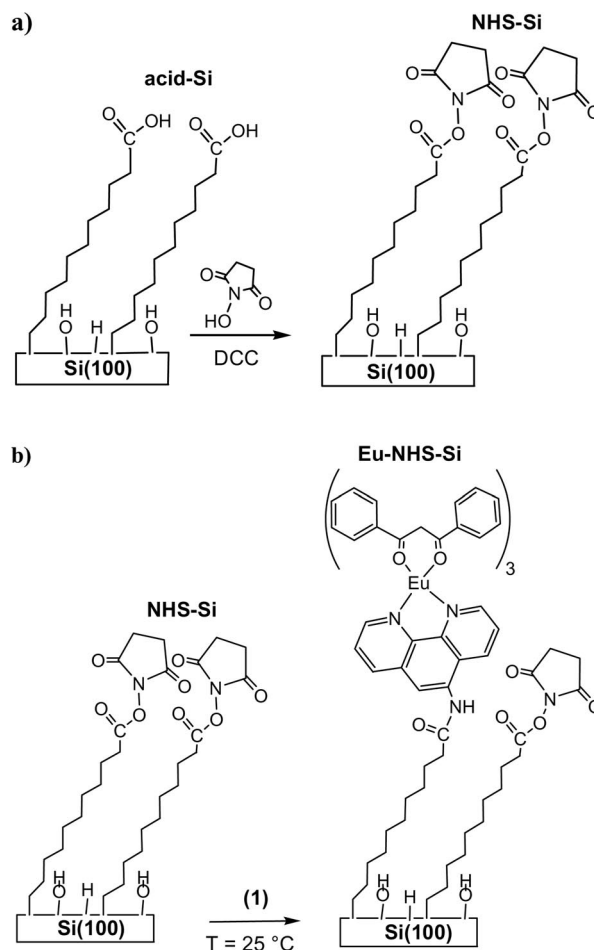
In addition, the role of the different functional surface groups (carboxylic acid, NHS ester and alkyl moieties) on the anchoring process of **1** has been evaluated. Characterization of these Si based hybrid materials, which is a crucial challenge for the development of new devices, has been achieved by using several complementary techniques: XPS, ATR-FTIR, AFM and fluorescence spectroscopy.

Results and Discussion

NHS Ester Functionalization of the Silicon Surface

Si(100) surfaces were functionalized with NHS-ester activated carboxylic groups following a three step route: i) grafting of methyl protected 10-undecenoic acid on Si; ii) hydrolysis of the methyl ester leading to undecanoyl acid functionalized Si (acid-Si) and, finally, iii) NHS ester formation (NHS-Si). In addition, Si(100) surfaces functionalized with a 1-decyl monolayer (decyl-Si) were also prepared as reference materials. Both approaches for the synthesis of decyl-Si as well as acid-Si have been optimized in previous studies.^[14,15,24] Similarly, both chemical and structural characterizations of decyl-Si and acid-Si were performed adopting XPS, ATR-FTIR and AFM as widely reported in the previous studies.^[14,15,24]

The formation of NHS-Si from the reaction of acid-Si with NHS is demonstrated by XPS and ATR-FTIR (Scheme 1, a). The appearance of the XPS N 1s signal in the nitrogen energy region of NHS-Si is an indication of the presence of NHS on the surface (Figure 1). The band position at 402.1 eV is typical of the NHS nitrogen atom bound to an oxygen atom, according to literature data on NHS ester monolayers.^[25]



Scheme 1. a) Formation of NHS-Si species on Si(100) and b) subsequent anchoring of the Eu complex.

The XPS O 1s spectral region of NHS-Si shows two components (Figure 1). The main band centred at 532.7 eV, already present in the spectra of acid-Si, is due to both carboxylic acid groups and oxidized silicon (SiO₂). The second component, centred at higher binding energy (BE), 535.3 eV, is typical evidence of the C–O–N oxygen atom in the NHS ester.^[25] The C 1s regions of acid-Si and NHS-Si show the characteristic structure of carboxylic acid and its derivatives (Figure 1). Both acid-Si and NHS-Si show the component due to aliphatic hydrocarbons at 285.0 eV. In addition, the carboxylic C 1s signals at 289.8 and 289.6 eV indicate acid-Si^[15] and NHS-Si,^[25] respectively.

ATR-FTIR measurements provide further information useful to monitor surface reactions. Two spectral regions are diagnostic, namely that of C–H stretching between 3050 and 2800 (Figure 2, a) and that of carbonyl stretching between 1700 and 1800 cm^{−1} (Figure 2, b). The C–H stretching region is similar for both acid-Si and NHS-Si. The main bands at 2926–2927 and 2856–2857 cm^{−1} are assigned to the $\tilde{\nu}_a(\text{CH}_2)$ and $\tilde{\nu}_s(\text{CH}_2)$ stretching modes of the undecanoyl backbone, respectively.^[26,27] Figure 2 (b) compares the carbonyl stretching of acid-Si and NHS-Si. A shift of the carbonyl stretching from 1721 (for acid-Si) to 1748 cm^{−1} (for NHS-Si) is evident, as expected for the ester formation.^[25b]

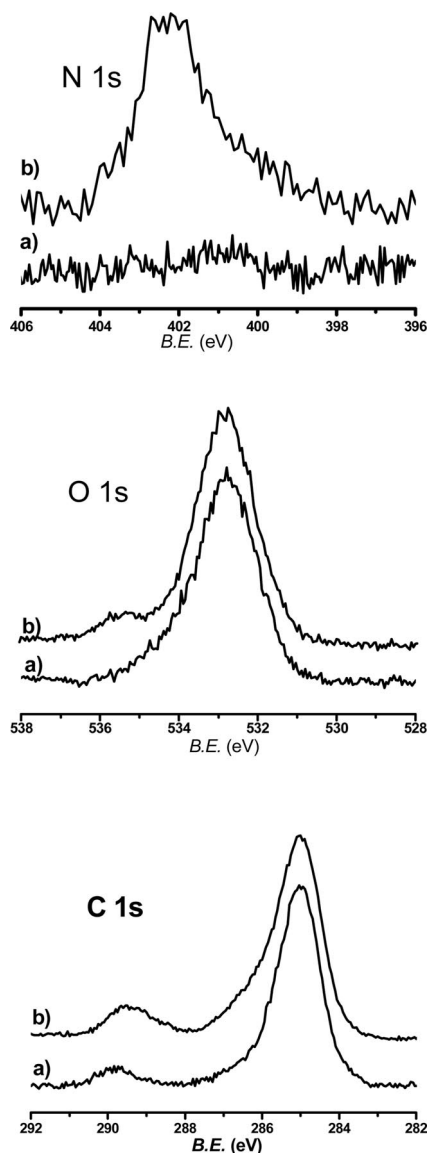


Figure 1. High resolution N 1s, O 1s and C 1s XPS spectral regions (takeoff angle 45°) of a) acid-Si; and b) NHS-Si.

Anchoring of Complex 1 on the Functionalized Silicon Surface

Covalent anchoring of the Eu complex has been performed by treatment of NHS-Si with an ethyl acetate solution of **1**. Both the presence and spectral positions of the XPS Eu 3d_{5/2} and N 1s bands of the **1** treated NHS-Si surface (Eu-NHS-Si) are indications of a successful surface reaction (Figure 3). The N 1s region shows two bands: one at 400.0 eV (N_{phen}), assigned to the nitrogen atoms of the coordinated aminophenanthroline ligand,^[28] and the other at 402.1 eV (N_{NHS}), due to unreacted NHS sites. The intensity ratio of these two bands, N_{NHS}/N_{phen} = 1, allows estimation of a 25% yield of the NHS sites with complex **1** (Table 1). A reaction yield much lower than 100% is expected also for a homogeneous substrate coverage with **1**, as shown by AFM images (vide infra), because of the larger size of **1** compared to the NHS esters (from DFT modelling

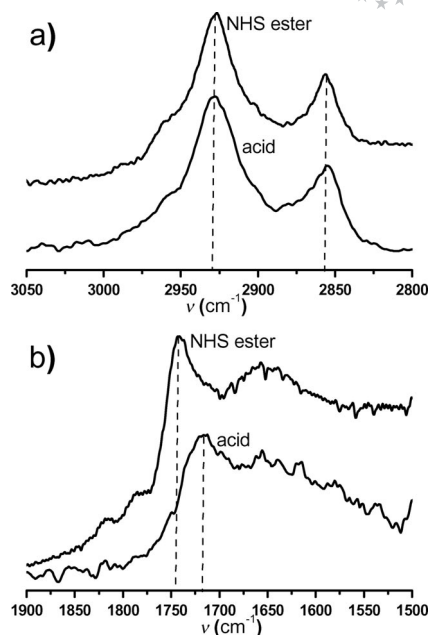


Figure 2. ATR-FTIR absorption spectra for NHS-Si and acid-Si samples in the a) C–H stretching region and b) in the C=O stretching region.

2.0 and 0.2 nm², respectively). The position of the Eu 3d_{5/2} band (1135.9 eV) is consistent with the presence of Eu^{III} in the coordination environment of **1**. XPS spectra of powders of complex **1** are reported for comparison (Figure 3).

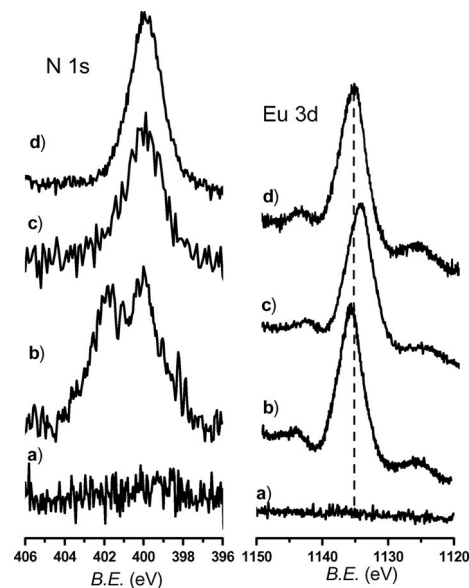


Figure 3. XPS spectra relative to N 1s and Eu 3d regions of a) **1**-treated decyl-Si; b) Eu-NHS-Si; c) Eu-acid-Si and d) **1** powder.

In addition, the XPS elemental composition of Eu-NHS-Si (Table 1) shows an N_{phen}/Eu atomic ratio of 2.9, consistent with the theoretical value of N_{phen}/Eu = 3 for complex **1**. Further experiments were performed to rule out any possible physisorption or alternative anchoring through coordinative interactions with eventually unreacted carboxylic acid groups. Thus, decyl-Si and acid-Si were similarly

Table 1. XPS atomic concentrations of NHS-Si, decyl-Si and acid-Si surface after treatment with **1**.

| | Mole fraction [%] | | | N | | Eu |
|-----------------------|-------------------|-------|-------|--------|--------|------|
| | Si | O | C | 402 eV | 400 eV | |
| 1-treated Decyl-Si | 44.3 | 13.6 | 40.7 | – | – | – |
| Eu-acid-Si | 28.17 | 33.16 | 37.31 | – | 0.59 | 0.85 |
| Eu-NHS-Si | 44.36 | 18.60 | 34.96 | 0.88 | 0.89 | 0.31 |

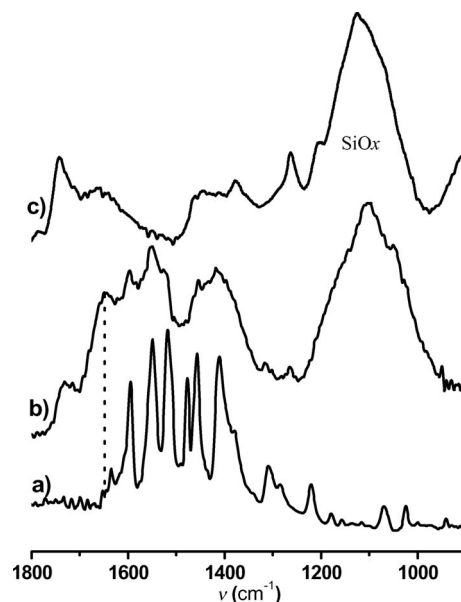
treated with the ethyl acetate solution of **1**. After treatment with **1**, the decyl-Si sample did not show the presence of nitrogen or europium (part a of Figure 3 and Table 1), thus indicating no complex physisorption.

In contrast, treatment of acid-Si with **1** (Eu-acid-Si) leads to surface modifications as indicated by the presence of the N 1s and Eu 3d bands in the XPS spectra (Figure 3, c). The single N 1s feature at 400.0 eV is consistent with the presence of the coordinated aminophenanthroline ligand, but the position of the Eu 3d_{5/2} band at 1135.1 eV is slightly shifted compared to that of the powders and Eu-NHS-Si (Figure 3, d). In addition, the different elemental compositions (Table 1) of Eu-acid-Si vs. Eu-NHS-Si reveal different reactivities of **1** towards acid-Si or NHS-Si surfaces. In fact, in the case of Eu-acid-Si, the N_{phen}/Eu ratio (0.69) is quite different from the almost theoretical value (3) observed for Eu-NHS-Si. This is consistent with a relevant displacement of the phenanthroline ligand. Moreover, complex **1** can also exchange one or more β -diketonate ligands with carboxylate groups of acid-Si leading to a different coordination environment for Eu^{III}. The observed shift at lower BE (−0.8 eV) of the Eu 3d_{5/2} in the XPS spectra of Eu-acid-Si, with respect to that of the powder samples, is consistent with this exchange, as previously reported for a parent Eu compound.^[29]

Therefore, results obtained for Eu-NHS-Si are consistent with the anchoring of **1** through a nucleophilic attack of its $-NH_2$ group to the NHS activated carboxylic acid terminations (Scheme 1, b). Finally, it is worth noting that NHS-Si provides a better surface passivation, compared to acid-Si. In fact, the Si 2p XPS spectral region of Eu-acid-Si shows an evident band centred at 102.5 eV due to SiO_x species, whilst the same feature is much less intense in the case of Eu-NHS-Si (Supporting Information: Figure S1). This result agrees well with the observed higher oxygen content (Table 1) in Eu-acid-Si than that in Eu-NHS-Si.

Eu-NHS-Si has been further characterized by ATR-FTIR analysis and AFM lithography. Figure 4 compares the ATR-FTIR spectra of Eu-NHS-Si, NHS-Si and complex **1** reference powder in the region between 1800 and 900 cm^{−1}. The Eu-NHS-Si spectrum shows new features compared to the original NHS-Si surface. The broad features in the 1600–1400 cm^{−1} region can be assigned to the convolution of the β -diketonate vibrations, which are clearly visible also in the spectrum of **1** powder. This suggests that the β -diketonate coordination environment is maintained after the surface anchoring. The band at 1650 cm^{−1}, absent in both spectra of NHS-Si and **1** powder,

is assigned to the typical $\tilde{\nu}(C=O)$ stretches of the amide bond,^[25,30] formed from the reaction of **1** with the carboxylic groups on the surface. The wide absorption band centred at 1100 cm^{−1} is assigned to SiO_x species, formed during chemical manipulations. The low feature observed in the 1750–1720 cm^{−1} range is due to C=O stretches of unreacted and partially hydrolyzed NHS ester groups.

Figure 4. ATR-FTIR absorption spectra of a) **1** powder, b) Eu-NHS-Si and c) NHS-Si.

The surface morphology studies were carried out by AFM. Comparison of statistical parameters (mean particle height, R_{mean} , and the surface roughness, R.M.S.) among prefunctionalized surfaces (acid-Si and NHS-Si) and Eu-NHS-Si indicates relevant surface modifications after the anchoring of **1**. The acid-Si surface appears very flat and homogeneous with R.M.S. = 0.12 nm and R_{mean} = 0.3 nm (Figure 5, a). No significant differences were found for NHS-Si. Relevant morphology differences were found for the Eu-NHS-Si (Figure 5, b). The typical vertical size of the observed features (R_{mean}) is about 0.6 nm and the roughness (R.M.S. = 0.24 nm) is clearly higher than that of acid-Si.

Monolayer thicknesses of acid-Si and Eu-NHS-Si were evaluated using AFM lithography (contact mode)^[31] and compared to results of DFT modelling (Figure 6, a) in order to obtain information on the geometric arrangement of the related molecules on Si(100). Thus, grafted molecules were removed along straight lines by rastering different areas ($0.5 \times 1.5 \mu m^2$) of the surface with the AFM tip under a suitable constant force (0.24 μN). The scratch obtained on acid-Si shows an average depth of 0.3 ± 0.1 nm, smaller than that expected for chain extended undecenoic acid. This could be explained by the presence of some bent chains due to a possible interaction between the chain carboxylic acid end groups with the Si–OH termination of SiO_x species formed during the hydrolysis step (Figure 6, b). The scratch obtained on Eu-NHS-Si has an average depth of

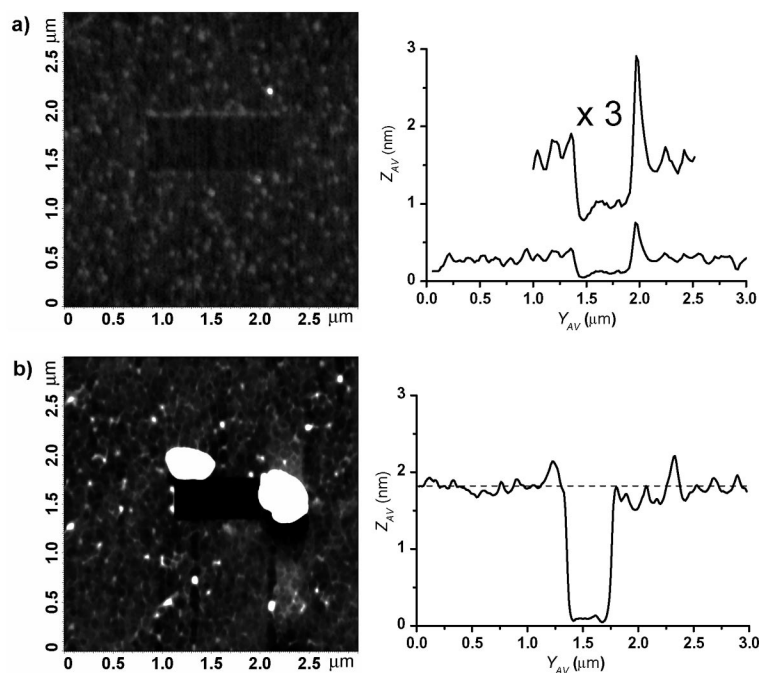


Figure 5. AFM images and average cross section profiles of a) acid-Si and b) Eu-NHS-Si. The two large features on the scratch edge are due to the material removed from the scratch.

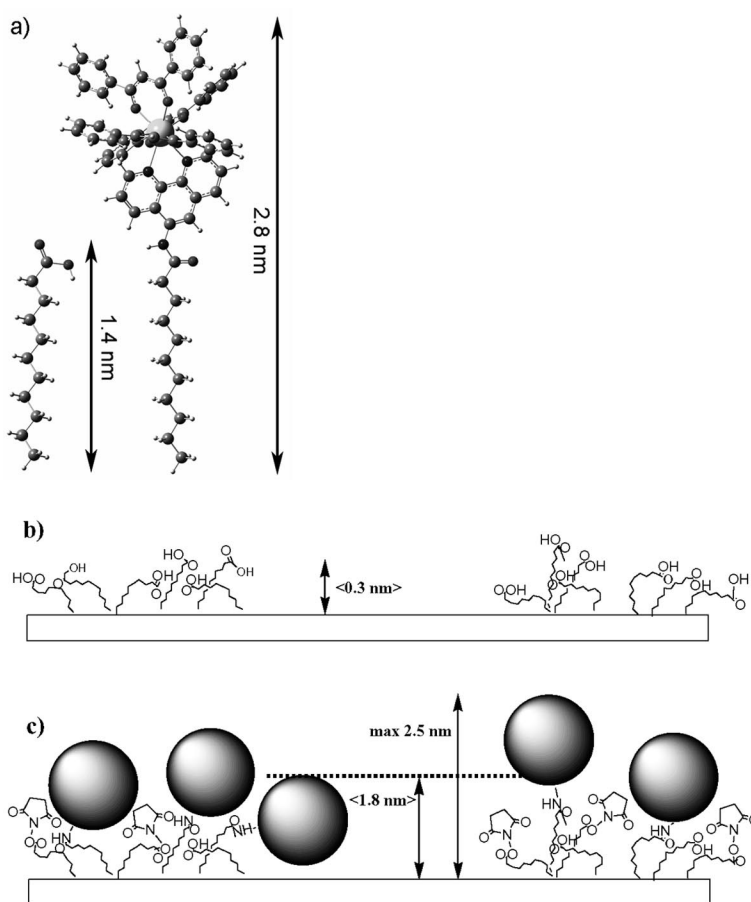


Figure 6. a) Estimated dimensions of 10-undecenoic acid and of **1** bonded to the undecenoic chain; b) possible arrangement of the carboxylic chains on the Si(100) surface compatible with the depth of the scratch on acid-Si (a similar arrangement can be proposed for NHS-Si); c) proposed arrangement of complex **1** anchored to the silicon surface, compatible with the depth of the scratch on Eu-NHS-Si.

1.8 ± 0.1 nm. Such a value is compatible with the presence of **1** (whose diameter is approximately 1.4 nm) over unordered undecanoyl chains (Figure 6, c). In addition, the presence of 2.5 nm height features is highly compatible with the total size of the amide formed between undecenoic acid and **1**.

Luminescence Properties of the Functionalized Surfaces

It is well known that luminescence effects in rare earth complexes are due to f–f transitions. In addition, often emission arising from the organic ligand excited states and from f–d transitions (e.g. Ce^{3+}) is also observed. In the case of Eu^{III} β -diketonate complexes, the emission spectra consist of $^5\text{D}_0 \rightarrow ^7\text{F}_J$ transitions ($J = 0-4$) mainly dominated by the $^5\text{D}_0 \rightarrow ^7\text{F}_1$ and $^5\text{D}_0 \rightarrow ^7\text{F}_2$ emissions at 590 and 613 nm, respectively.^[32,33] In general, luminescence properties of Eu^{III} complexes depend on the energy transfer properties of ligands since excited organic ligands act as light harvesting groups that, in turn, promote intramolecular energy transfer from the triplet state to an excited state of Eu^{3+} .^[34] Therefore, emission occurs from the lowest excited state ($^5\text{D}_0$) to the ground state ($^7\text{F}_J$) of Eu^{3+} and the presence of organic ligands, namely β -diketonates and phenanthroline, whose triplet states are higher in energy than the emissive $^5\text{D}_0$ excited state determines an efficient energy transfer process.^[20,32–34] However, intensities of the emission spectra related to Eu^{3+} intra-4f⁶ transitions between the $^5\text{D}_0$ and $^7\text{F}_{0-4}$ levels do not depend on the energy transfer mechanisms but on the excitation wavelength^[23,34a,35] and on the local environment around the europium ion.^[34,36]

Figure 7a displays the emission spectra of **1** powders physisorbed on Si in the 560–650 nm range, adopting two excitation wavelengths, $\lambda_{\text{ex}} = 265$ and 340 nm, corresponding to the absorption of the phenanthroline ligand^[32,37] and to the π - π^* transition of the β -diketonate, respectively.^[32] The spectrum consists of the characteristic sharp emission peaks at 578 ($^5\text{D}_0 \rightarrow ^7\text{F}_0$), 590 ($^5\text{D}_0 \rightarrow ^7\text{F}_1$) and 611 nm ($^5\text{D}_0 \rightarrow ^7\text{F}_2$).

Emission spectra of Eu-acid-Si and Eu-NHS-Si are shown in parts b and c of Figure 7. A good overlap between the spectra of powders and the functionalized surfaces is evident. However, the relative intensities of the $^5\text{D}_0 \rightarrow ^7\text{F}_1$ and $^5\text{D}_0 \rightarrow ^7\text{F}_2$ transitions are different for the two functionalized surfaces and this difference can be related to different chemical environments around Eu^{III} in the two cases. In fact, the $^5\text{D}_0 \rightarrow ^7\text{F}_1$ transition does not depend on the chemical environment around the Eu^{3+} ion due to its magnetic dipole nature. By contrast, the $^5\text{D}_0 \rightarrow ^7\text{F}_2$ transition is influenced by the perturbing field of the ligand arrangement.^[33,36] The intensity ratio between the $^5\text{D}_0 \rightarrow ^7\text{F}_2$ and $^5\text{D}_0 \rightarrow ^7\text{F}_1$ transitions ($I_{^5\text{D}_0 \rightarrow ^7\text{F}_2}/I_{^5\text{D}_0 \rightarrow ^7\text{F}_1}$ at 340 nm) in the Eu-NHS-Si sample ($\approx 4:1$) is similar to that observed for **1** powders on Si ($\approx 5:1$), but higher than that observed in Eu-acid-Si spectra ($\approx 2:1$). These results suggest that the anchoring of **1** on NHS activated surfaces occurs without significant degradation of the Eu coordination environment. By contrast, the direct grafting of **1** on the free acid leads to some

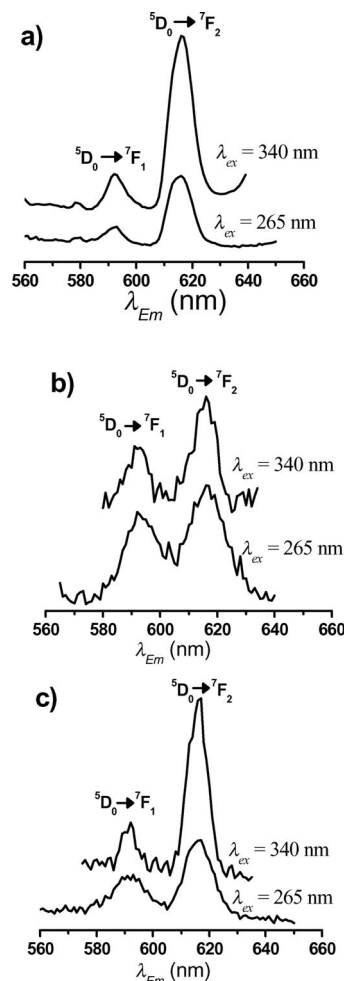


Figure 7. Emission spectra of a) physisorbed **1** powder on Si, b) Eu-acid-Si and c) Eu-NHS-Si.

modification of the original Eu environment.^[36c] According to the XPS results (vide supra), these changes can be related to the partial displacement of the phenanthroline ligand. Moreover, substitution of β -diketonate ligands with the carboxylate groups of the acid-Si monolayer occurs. All the present findings agree well with results obtained for a previously adopted anchoring procedure that takes advantage of siloxane-based functionalized silica surfaces.^[23] Therefore, it emerges that siloxane procedures are best suited for transparent silica substrates whereas the NHS mediated route is more appropriate for grafting on silicon to produce monolayers that can be integrated in electronic devices.

Conclusions

A multistep synthetic strategy to anchor the Eu complex on the silicon surface has been developed. The anchoring strategy is based on the nucleophilic attack of primary amine groups of aminophenanthroline ligands to NHS activated carboxylic acid groups of prefunctionalized Si surfaces. The role of the NHS activation and, in turn, of the nucleophilic substitution, was demonstrated by comparing

the reactivity of **1** with differently functionalized surfaces, NHS-Si, acid-Si and decyl-Si. The surface reaction on NHS activated carboxylic groups does not significantly change the ligand arrangement of **1** during the anchoring process whereas direct reaction on the carboxylic acid leads to the exchange/dissociation of some ligands, thus changing the Eu coordination environment. The synthetic protocol was assessed by combining a suitable control experiment on decyl-functionalized Si(100). Fluorescence measurements provided indications of the Eu^{III} chemical environment and geometric arrangement on the surface. In particular, photoluminescence analysis showed that luminescence properties are retained in the monolayer thus suggesting that this material is suitable for application in the photonic field. The overall results indicate that the nature of silicon prefunctionalization affects the Eu environment and, hence, the luminescence properties can be modulated by chemical design of suitable grafted ligands. Finally, it is noteworthy that there are not many covalently assembled films based on lanthanide complexes and, likewise, there are relatively few covalently Si-bonded monolayers exhibiting photoluminescence.

Experimental Section

General: All chemicals, unless otherwise noted, were commercially available and used as received. Solvents for substrate cleaning were purified by distillation. 1-decene for monolayer preparation was distilled under reduced pressure with Na metal. Complex **1** was purchased from Aldrich and used as received.

1-Decyl-Functionalized Si (decyl-Si): 1-Decene (10 mL) was placed in a small flask fitted with a nitrogen inlet and deoxygenated with dry nitrogen for 1 h. Subsequently, Si(100) substrates were treated in a piranha solution for 12 min, rinsed in double distilled water for 2 min, etched in 1.0% hydrofluoric acid for 90 s, rinsed with double distilled water, immediately immersed in the alkene and heated to reflux at 200 °C for 2 h under slow N₂ bubbling to prevent bumping. After cooling to room temperature, the samples were removed from the flask and sonicated twice in dichloromethane for 5 min.

Undecanoyl Acid Functionalized Si (acid-Si): Methyl 10-undecenoate was grafted on to Si according to the procedure above. The methyl protected acid was hydrolyzed with potassium *tert*-butoxide in DMSO,^[38] according to a method reported by Strother et al.^[39] The grafted surfaces were dipped in a solution of potassium *tert*-butoxide in DMSO (250 mM) for 30 s at room temperature followed by rinsing in acidified water (100 mM HCl).

Undecanoyl Acid NHS Ester Functionalized Si (NHS-Si). NHS-Si was obtained by placing the acid-Si sample in a solution of NHS (20 mM) and dicyclohexylcarbodiimide (DCC, 20 mM) in anhydrous ethyl acetate, under dry N₂ bubbling for 1 h.

Anchoring of **1:** Prefunctionalized silicon substrates (NHS-Si, acid-Si or decyl-Si) were immersed in anhydrous ethyl acetate solutions of **1** and stirred for 16 h in a glove box at room temperature. Substrates were removed from the solution and cyclically (5 min) sonicated in dichloromethane, 2-propanol and double distilled water, followed by drying with a nitrogen flux, to remove physisorbed species.

Characterization Techniques: The XPS spectra were run with a PHI ESCA/SAM 5600 Multitechnique spectrometer equipped with a monochromatized Al-K_α X-ray source. The BE scale was calibrated by centring the hydrocarbon/adventitious C 1s peak at 285 eV.

Infrared spectra of the monolayers were recorded with a Harrick GATR germanium single reflection ATR accessory, collecting 800 scans (scan range 400–4000 cm^{−1}, resolution 4 cm^{−1}) per spectrum.

AFM images were obtained with a NT-MTD instrument apparatus. The noise level before and after each measurement was 0.01 nm. AFM characterizations were performed in a high-amplitude mode (tapping mode) to avoid any possible modification of the grafted organic layer on the surfaces caused by the interactions with the tip whose nominal curvature radius is 10 nm. In order to account for tip contribution, AFM data were deconvoluted with PC software ZOD 2.0 from Goh^[40] assuming an ideal AFM probe with a tip radius of 10 nm. In addition, the same tip was used for a set of measurements on different samples, in order to allow a fair comparison among samples.^[41]

Fluorescence spectra on Si monolayers were obtained with a spectrofluorimeter SPEX FLUOROLOG 111, equipped with a solid plate sample holder for detection in front face. The acquisition mode used was signal/reference, thus correcting the emission spectra for the detection/optical response of the spectrometer. The integration time and slit width were 2 s and 5.5 nm, respectively. Two excitation wavelengths (λ_{ex}) were used: λ_{ex} = 265 and 340 nm.

Supporting Information (see also the footnote on the first page of this article): Figure S1. XPS spectra of Si 2p region of a) Eu-NHS-Si and b) Eu-acid-Si.

Acknowledgments

This work was supported by the Ministero dell' Istruzione, dell' Università e della Ricerca (MIUR) through the FIRB 2003 project (Nr. RBNE033KMA), by the Consorzio Interuniversitario Nazionale per la Scienza e la Tecnologia dei Materiali (INSTM) through the PRISMA “Molecular systems grafted on silicon for integrated sensing devices” project and by the Istituto di Scienza e Tecnologie Molecolari del Centro Nazionale delle Ricerche (ISTM-CNR) within the PROMO project: “Nanostrutture organiche, organo-metalliche polimeriche ed ibride: ingegnerizzazione supramolecolare delle proprietà fotoniche e dispositivistica innovativa per optoelettronica”.

- [1] a) G. P. Lopinski, D. D. M. Wayner, R. A. Wolkow, *Nature* **2000**, *406*, 48–51; b) G. P. Lopinski, D. J. Moffatt, D. D. M. Wayner, R. A. Wolkow, *Nature* **1998**, *392*, 909–911; c) P. Kruse, E. R. Johnson, G. A. DiLabio, R. A. Wolkow, *Nanoletters* **2002**, *2*, 807–810; d) R. L. Cicero, C. E. D. Chidsey, G. P. Lopinski, D. D. Wayner, R. A. Wolkow, *Langmuir* **2002**, *18*, 305–307; e) S. J. Lee, D. R. Bae, W. S. Han, S. S. Lee, J. H. Jung, *Eur. J. Inorg. Chem.* **2008**, 1559–1564.
- [2] a) Z. Liu, A. A. Yassery, J. S. Lindsey, D. F. Bocian, *Science* **2003**, *302*, 1543–1545; b) M. Mannini, F. Pineider, P. Saintavit, C. Danieli, E. Otero, C. Sciancalepore, A. M. Talarico, M.-A. Arrio, A. Cornia, D. Gatteschi, R. Sessoli, *Nat. Mater.* **2009**, *8*, 194–197.
- [3] C. Tsekouras, O. Johansson, R. Lomoth, *Chem. Commun.* **2009**, 3425–3427.
- [4] a) A. Gulino, T. Gupta, M. Altman, S. Lo Schiavo, P. G. Mineo, I. L. Fragalà, G. Evmenenko, P. Dutta, M. E. van der Boom, *Chem. Commun.* **2008**, 2900–2902; b) A. Gul-

- ino, T. Gupta, P. G. Mineo, M. E. van der Boom, *Chem. Commun.* **2007**, 4878–4880; c) A. B. Descalzo, R. Martínez-Mañez, F. Sancenón, K. Hoffmann, K. Rurack, *Angew. Chem. Int. Ed.* **2006**, *45*, 5924–5948.
- [5] a) J. M. Buriak, *Chem. Rev.* **2002**, *102*, 1271–1308; b) A. Aurora, F. Cattaruzza, C. Della Volpe, G. Di Santo, A. Flamini, C. Mangano, S. Morpurgo, P. Pallavicini, R. Zanoni, *Chem. Eur. J.* **2007**, *13*, 1240–1250.
- [6] A. Ulman, *Chem. Rev.* **1996**, *96*, 1533–1554.
- [7] a) T. Gupta, M. E. van der Boom, *Angew. Chem. Int. Ed.* **2008**, *47*, 5322–5326; b) I. Haller, *J. Am. Chem. Soc.* **1978**, *100*, 8050–8055.
- [8] a) A. Gulino, G. G. Condorelli, P. Mineo, I. Fragalà, *Nanotechnology* **2005**, *16*, 2170–2175; b) A. Ulman, *Adv. Mater.* **2004**, *16*, 573–582; c) S. Di Bella, N. Leonardi, G. Consiglio, S. Sortino, I. Fragalà, *Eur. J. Inorg. Chem.* **2004**, 4561–4565; d) A. Y. Fadeev, T. J. McCarthy, *Langmuir* **2000**, *16*, 7268–7274.
- [9] T. Shimada, K. Aoki, Y. Shinoda, T. Nakamura, N. Tokunaga, S. Inagaki, T. Hayashi, *J. Am. Chem. Soc.* **2003**, *125*, 4688–4689.
- [10] a) S. Boutet, B. Jousseau, T. Toupance, M. Biesemans, R. Willem, C. Labrugue, L. Delattre, *Chem. Mater.* **2005**, *17*, 1803–1811; b) K. L. Purvis, G. Lu, J. Schwartz, S. L. Bernasek, *J. Am. Chem. Soc.* **2000**, *122*, 1808–1809; c) E. L. Bruner, A. R. Span, S. L. Bernasek, J. Schwartz, *Langmuir* **2001**, *17*, 5696–5702.
- [11] a) A. B. Sieval, A. L. Demirel, J. M. Nissink, M. R. Linford, J. H. van der Maas, W. H. de Jeu, H. Zuithof, E. J. R. Sudhölter, *Langmuir* **1998**, *14*, 1759–1768; b) Q.-Y. Sun, L. C. P. M. de Smet, B. van Lagen, M. Giesbers, P. C. Thune, J. van Engelenburg, F. A. de Wolf, H. Zuithof, E. J. R. Sudhölter, *J. Am. Chem. Soc.* **2005**, *127*, 2514–2523.
- [12] a) X. Bin, T. K. Mischki, C. Fan, G. P. Lopinski, D. D. M. Wayner, *J. Phys. Chem. C* **2007**, *111*, 13547; b) T. L. Lassetter, B. H. Clare, N. L. Abbott, R. J. Hamers, *J. Am. Chem. Soc.* **2004**, *126*, 10220–10221; c) X. Wang, Y. Chen, K. A. Gibney, S. Erramilli, P. Mohanty, *Appl. Phys. Lett.* **2008**, *92*, 013903/1–013903/3.
- [13] a) G. Pellegrino, A. Motta, A. Cornia, I. Spitaleri, I. L. Fragalà, G. G. Condorelli, *Polyhedron* **2009**, *28*, 1758–1763; b) S. Di Bella, G. G. Condorelli, A. Motta, A. Ustione, A. Cricenti, *Langmuir* **2006**, *22*, 7952–7955.
- [14] a) G. G. Condorelli, A. Motta, G. Pellegrino, A. Cornia, L. Gorini, I. L. Fragalà, C. Sangregorio, L. Sorace, *Chem. Mater.* **2008**, *20*, 2405–2411; b) G. G. Condorelli, A. Motta, I. L. Fragalà, F. Giannazzo, V. Raineri, A. Caneschi, D. Gatteschi, *Angew. Chem. Int. Ed.* **2004**, *43*, 4081–4084.
- [15] G. G. Condorelli, A. Motta, C. Bedoya, A. Di Mauro, G. Pellegrino, E. Smecca, *Inorg. Chim. Acta* **2007**, *360*, 170–178.
- [16] T. P. Sullivan, W. T. S. Huck, *Eur. J. Org. Chem.* **2003**, 17–29.
- [17] a) M. C. Pirrung, *Angew. Chem. Int. Ed.* **2002**, *41*, 1276–1289; b) A. R. Pike, L. H. Lie, R. A. Eagling, L. C. Ryder, S. N. Patole, B. A. Connolly, B. R. Horrocks, A. Houlton, *Angew. Chem. Int. Ed.* **2002**, *41*, 615–617; c) T. Strother, W. Cai, X. Zhao, R. J. Hamers, L. M. Smith, *J. Am. Chem. Soc.* **2000**, *122*, 1205–1209.
- [18] a) W. Liao, F. Wei, M. X. Qian, X. S. Zhao, *Sens. Actuators B* **2004**, *101*, 361–367; b) W. Liao, F. Wei, D. Liu, M. X. Qian, G. Yuan, X. S. Xin Zhao, *Sens. Actuators B* **2006**, *114*, 445–450; c) F. Wei, B. Sun, W. Liao, J. Ouyang, X. S. Zhao, *Biosens. Bioelectron.* **2003**, *18*, 1149–1155.
- [19] a) B. O. Roos, R. Lindh, P. Malmqvist, V. Veryazov, P.-O. Widmark, A. C. Borin, *J. Phys. Chem. A* **2008**, *112*, 11431–11435; b) C. Adamo, P. Maldivi, *J. Phys. Chem. A* **1998**, *102*, 6812–6820; c) S. Di Bella, A. Gulino, G. Lanza, I. L. Fragalà, D. Stern, T. J. Marks, *Organometallics* **1994**, *13*, 3810–3815.
- [20] a) M. Jiang, X. Zhai, M. Liu, *Langmuir* **2005**, *21*, 11128–11135; b) Y. Li, B. Yan, H. Yang, *J. Phys. Chem. C* **2008**, *112*, 3959–3968; c) C. H. Chang, M. H. Yun, W. Choi, *J. Synth. Met.* **2004**, *145*, 1–6.
- [21] a) J.-C. G. Bünzli, *Acc. Chem. Res.* **2006**, *39*, 53–61; b) S. Ida, C. Ogata, D. Shiga, K. Izawa, K. Ikeue, Y. Matsumoto, *Angew. Chem. Int. Ed.* **2008**, *47*, 2480–2483; c) A.-S. Chauvin, S. Comby, M. Baud, C. De Piano, C. Duhot, J. C. G. Bünzli, *Inorg. Chem.* **2009**, *48*, 10687–10696; d) Y. Su, L. Li, G. Li, *Chem. Commun.* **2008**, *34*, 4004–4006; e) J. P. Leonard, P. Jensen, T. McCabe, J. E. O'Brien, R. D. Peacock, P. E. Kruger, T. Gunnlaugsson, *J. Am. Chem. Soc.* **2007**, *129*, 10986–10987; f) K. Hanaoka, K. Kikuchi, S. Kobayashi, T. Nagano, *J. Am. Chem. Soc.* **2007**, *129*, 13502–13509; g) N. S. Murray, S. P. Jarvis, T. Gunnlaugsson, *Chem. Commun.* **2009**, 4559–4961; h) C. G. Gulgas, T. M. G. Reineke, *Inorg. Chem.* **2008**, *47*, 1548–1559; i) E. Brunet, O. Juanes, J. C. Rodriguez-Ubis, *Curr. Chem. Biol.* **2007**, *1*, 11–39.
- [22] K. Aslan, M. Wu, J. R. Lakowicz, C. D. Geddes, *J. Am. Chem. Soc.* **2007**, *129*, 1524–1525.
- [23] A. Gulino, F. Lupo, G. G. Condorelli, A. Motta, I. L. Fragalà, *J. Mater. Chem.* **2009**, *19*, 3507–3511.
- [24] a) A. Gulino, F. Lupo, G. G. Condorelli, P. Mineo, I. L. Fragalà, *Chem. Mater.* **2007**, *19*, 5102–5109; b) G. G. Condorelli, A. Motta, M. Favazza, P. Nativo, I. L. Fragalà, D. Gatteschi, *Chem. Eur. J.* **2006**, *12*, 3558–3566.
- [25] a) T. Bocking, M. James, H. G. L. Coster, T. C. Chilcott, K. D. Barrow, *Langmuir* **2004**, *20*, 9227–9235; b) M. Yang, R. L. M. Teeuwen, M. Giesbers, J. Baggerman, A. Arafat, F. A. de Wolf, J. C. M. van Hest, H. Zuithof, *Langmuir* **2008**, *24*, 7931–7938.
- [26] D. Lin-Vien, N. B. Colthup, W. G. Fateley, J. G. Grasselli in *The Handbook of Infrared and Raman Characteristic Frequencies of Organic Molecules*, Academic Press, San Diego, CA, **1991**, pp. 134–141.
- [27] P. Martin, S. Marsaudon, L. Thomas, B. Desbat, J.-P. Aimè, B. Bennetau, *Langmuir* **2005**, *21*, 6934–6943.
- [28] a) W. Mo, H. Liu, H. Xiong, M. Li, G. Li, *Appl. Catal. A* **2007**, *333*, 172–176; b) D. Hengshan, M. Hongzhu, W. Bo, Y. Shiyang, *Polyhedron* **1997**, *16*, 427–431; c) T. Yoshida, S. Sawada, *Bull. Chem. Soc. Jpn.* **1975**, *48*, 3379–3380.
- [29] F. Mercier, C. Alliot, L. Bion, N. Thromat, P. Toulhoat, *J. Electron Spectrosc. Relat. Phenom.* **2006**, *150*, 21–26.
- [30] O. Andersson, M. Lundquist, L. Tegler, S. Börjegen, L. Baltzer, L. Österlund, *ChemPhysChem* **2007**, *8*, 712–722.
- [31] X. N. Xie, H. J. Chung, C. H. Sow, A. T. S. Wee, *Mater. Sci. Eng. R* **2006**, *54*, 1–48.
- [32] a) A. Bellusci, G. Barberio, A. Crispini, M. Ghedini, M. La Deda, D. Pucci, *Inorg. Chem.* **2005**, *44*, 1818–1825; b) M. O. Ahmed, J.-L. Liao, X. Chen, S.-A. Chen, J. H. Kaldis, *Acta Crystallogr., Sect. E* **2003**, *59*, m29–m32; c) J. Peng, N. Takada, N. Minami, *Thin Solid Films* **2002**, *405*, 224–227.
- [33] a) L. L. Kong, B. Yan, J. Li, *J. Solid State Chem.* **2009**, *182*, 1631–1637; b) x. Guo, H. Guo, L. Fu, R. Deng, W. Chen, J. Feng, S. Dang, H. Zhang, *J. Phys. Chem. C* **2009**, *113*, 2603–2610.
- [34] a) L. D. Carlos, R. A. S. Ferreira, V. De Zea Bermudes, S. J. L. Ribeiro, *Adv. Mater.* **2009**, *21*, 509–534; b) A. M. Klonkowski, S. Lis, M. Pietraszkiewicz, Z. Hnatejko, K. Czarnobaj, M. Elbanowski, *Chem. Mater.* **2003**, *15*, 656–663.
- [35] E. O. Oh, Y. H. Kim, C. M. Whang, *J. Electroceram.* **2006**, *17*, 335–338.
- [36] a) D.-J. Qian, K.-Z. Yang, H. Nakahara, K. Fukuda, *Langmuir* **1997**, *13*, 5925–5932; b) R. F. Silva, M. E. D. Zaniquelli, O. A. Serra, I. L. Torroni, S. G. C. de Castro, *Thin Solid Films* **1998**, *324*, 245–252; c) G. Malandrino, M. Bettinelli, A. Speghini, I. L. Fragalà, *Eur. J. Inorg. Chem.* **2001**, 1039–1044.
- [37] a) M. R. A. Da Silva, A. G. Trovò, R. F. P. Nogueira, *J. Hazard. Mater.* **2007**, *146*, 508–513; b) C. Peng, H. Zhang, J. Yu, Q. Meng, L. Fu, H. Li, L. Sun, X. Guo, *J. Phys. Chem. B* **2005**, *109*, 15278–15287; c) M. T. Ramirez-Silva, M. Momez-Hernandez, M. L. Pacheco-Hernandez, A. Rojas-Hernandez, L. Galicia, *Spectrochim. Acta A* **2004**, *60*, 781–789.

- [38] a) F. C. Chang, N. F. Wood, *Tetrahedron Lett.* **1964**, 40, 2969–2973; b) P. G. Gassman, W. N. Shenk, *J. Org. Chem.* **1976**, 42, 918–920.
- [39] T. Strother, W. Cai, X. Zhao, R. J. Hamers, L. M. Smith, *J. Am. Chem. Soc.* **2000**, 122, 1205–1209.
- [40] P. Markiewicz, M. C. Goh, *Langmuir* **1994**, 10, 5–7.
- [41] R. A. McAloney, M. Sinyor, V. Dudnik, M. C. Goh, *Langmuir* **2001**, 17, 6655–6663.

Received: March 9, 2010
Published Online: July 23, 2010

Routes to Ruthenium–Fluoro Cations of the Type $[\text{RuL}_2(\text{CO})_n\text{F}]^+$ ($n = 2, 3$; $\text{L} = \text{PR}_3, \text{NHC}$): A Play-Off between Solvent, L and Weakly Coordinating Anion

Karl S. Coleman,^{[a][‡]} John Fawcett,^[a] Duncan A. J. Harding,^[a] Eric G. Hope,^{*,[a]}
Kuldip Singh,^[a] and Gregory A. Solan^{*,[a]}

Keywords: Ruthenium / Fluorides / Cations / Lewis acids / Phosphane ligands / Carbene ligands / *N*-Heterocyclic carbenes / Weakly coordinating anions (WCAs)

Interaction of *cis,cis,trans*- $[\text{RuF}_2(\text{CO})_2(\text{PPh}_3)_2]$ (**1a**) with BF_3 in acetonitrile affords the dicationic adduct $[\text{Ru}(\text{NCMe})_2(\text{CO})_2(\text{PPh}_3)_2](\text{BF}_4)(\text{B}_2\text{F}_7)$ (**2**), which can be readily carbonylated to form $[\text{Ru}(\text{CO})_4(\text{PPh}_3)_2](\text{BF}_4)_2$ (**3**). In contrast, reaction of **1a** with BF_3 in dichloromethane leads to the neutral ruthenium–fluoro species $[\text{RuF}(\text{FBF}_3)(\text{CO})_2(\text{PPh}_3)_2]$ (**4**); facile displacement of the bound FBF_3 ligand in **4** occurs on treatment with CO or PPh_3 to afford cationic $[\text{RuF}(\text{CO})_2(\text{L})(\text{PPh}_3)_2](\text{BF}_4)$ [$\text{L} = \text{CO}$ (**5a**), PPh_3 (**5b**)]. On the other hand, reaction of **1a** with PF_5 in dichloromethane furnishes the coordinatively unsaturated 16-electron salt $[\text{RuF}(\text{CO})_2(\text{PPh}_3)_2](\text{PF}_6)$ (**6**). Metathesis of the PF_6 anion in **6** with $\text{KB}(\text{Ar}^F)_4$ [$\text{Ar}^F = 3,5\text{-(CF}_3)_2\text{-C}_6\text{H}_3$] in dichloromethane results in rapid decomposition, while in the presence of CO solvent exchange (CH_2Cl_2) takes

place to yield chloride-containing $[\text{RuCl}(\text{CO})_3(\text{PPh}_3)_2]\text{-}[\text{B}(\text{Ar}^F)_4]$ (**7**). Unexpectedly, **1a** proved unreactive towards tris(pentafluorophenyl)borane in dichloromethane. However, by substituting the triphenylphosphane ligands in **1a** with better donor phosphanes or with an *N*-heterocyclic carbene (NHC) [to give *cis,cis,trans*- $[\text{RuF}_2(\text{CO})_2(\text{L})_2]$ [$\text{L} = \text{PEt}_2\text{Ph}$ (**1b**), $\text{P}(\text{CCPh})\text{Ph}_2$ (**1c**), IPr (1,3-bis(2,6-diisopropylphenyl)imidazol-2-ylidene) (**1d**)], fluoride abstraction could be achieved using $\text{B}(\text{C}_6\text{F}_5)_3$ to give 16-electron $[\text{RuF}(\text{CO})_2(\text{L})_2][\text{FB}(\text{C}_6\text{F}_5)_3]$ ($\text{L} = \text{PEt}_2\text{Ph}$ (**8b**), $\text{P}(\text{CCPh})\text{Ph}_2$ (**8c**), IPr (**8d**)). Carbonylation of **8d** proceeds smoothly to generate the coordinatively saturated species $[\text{RuF}(\text{CO})_3(\text{IPr})_2][\text{FB}(\text{C}_6\text{F}_5)_3]$ (**9**) in high yield. Single crystal X-ray structures are presented for **2**, **3**, **5a/3**, **7** and **9**.

Introduction

Recent years have seen a surge of interest in the development of late-transition metal–fluoro complexes due, in part, to their potential for mediating selective and efficient carbon–fluorine bond forming reactions in organic synthesis.^[1–10] With reference to ruthenium(II) chemistry, cationic ruthenium monofluoro complexes have shown great promise. For example, Mezzetti et al. reported that the 16-valence-electron salt $[\text{Ru}(\text{dppp})_2\text{F}](\text{PF}_6)$ ($\text{dppp} = 1,3\text{-bis}(\text{diphenylphosphanyl})\text{propane}$) could fluorinate a range of organic molecules containing activated carbon–halide bonds.^[10] However, routes to such cationic complexes are not straightforward and can often necessitate the use of toxic thallium-based metathesis reagents in combination with the corresponding ruthenium–chloride precursor. A more elegant route might involve the selective abstraction of a fluoride ligand from a neutral ruthenium difluoro species with a suitable Lewis acid. In recent years we have de-

veloped reliable routes to a general family of complexes of the type *cis,cis,trans*- $[\text{RuF}_2(\text{CO})_2(\text{L})_2]$ (**1**) (Figure 1) that can bear an assortment of different ancillary ligands (L) including organo–phosphanes^[11] and *N*-heterocyclic carbenes (NHCs).^[12]

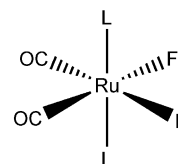


Figure 1. *cis,cis,trans*- $[\text{RuF}_2(\text{CO})_2(\text{L})_2]$ (**1**); $\text{L} = \text{PR}_3, \text{NHC}$.

As part of a preliminary investigation into the chemistry of **1**, we recently reported that a variety of cationic bis(NHC) complexes are accessible when using boron trifluoride as the Lewis acid.^[12] However, so far this synthetic approach has not been conducive to the formation of isolable monofluoro cations of the type $[\text{RuF}(\text{CO})_n(\text{L})_2]^+$ [$n = 2$ (16 electron), 3 (18 electron)]. We reasoned that the nature of the Lewis acid, the coordinating capacity of the resulting fluoro-containing anion, the solvent employed and the ancillary ligand L in **1**, would each influence the ability to generate the desired cationic species. To this end we report in this work a broad study of the chemistry of **1** by: (i) ex-

[a] Department of Chemistry, University of Leicester, University Road, Leicester LE1 7RH, UK
E-mail: egh1@le.ac.uk
gas8@le.ac.uk

[‡] Current address: Chemistry Department, University of Durham, South Road, Durham DH1 3LE, UK

ploring the reactivity of bis(triphenylphosphane)-containing $[\text{RuF}_2(\text{CO})_2(\text{PPh}_3)_2]$ (**1a**) towards boron trifluoride as a function of the solvent employed; (ii) probing the reactivity of **1a** towards phosphorus pentafluoride; (iii) evaluating tris(pentafluorophenyl)borane as the Lewis acid; (iv) varying the coligands at the ruthenium centre in a study of $[\text{RuF}_2(\text{CO})_2(\text{L})_2]$ [$\text{L} = \text{PEt}_2\text{Ph}$ (**1b**), $\text{P}(\text{CCPh})\text{Ph}_2$ (**1c**), IPr (1,3-bis(2,6-diisopropylphenyl)imidazol-2-ylidene) (**1d**)].

Results and Discussion

1. Reactivity of **1a** towards BF_3

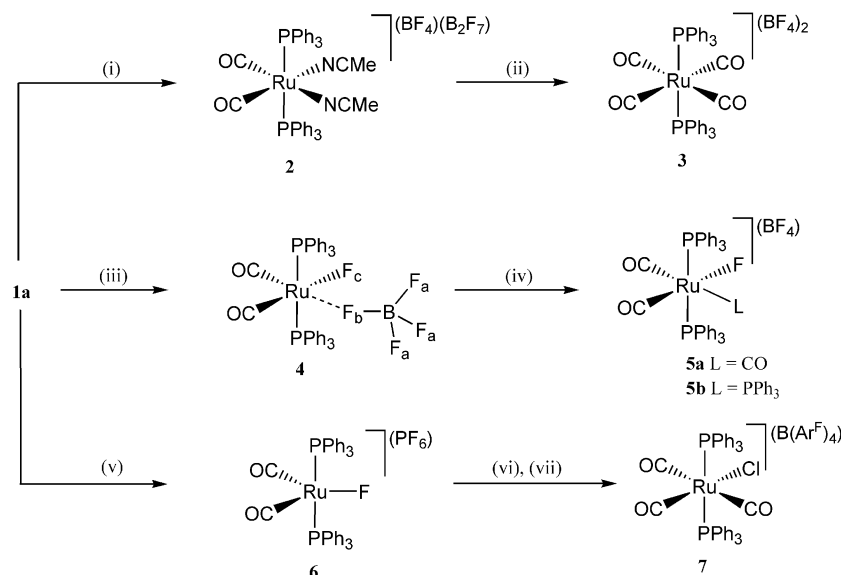
Interaction of **1a** with $\text{BF}_3 \cdot \text{OEt}$ in acetonitrile at room temperature gave on workup $[\text{Ru}(\text{NCMe})_2(\text{CO})_2(\text{PPh}_3)_2](\text{BF}_4)(\text{B}_2\text{F}_7)$ (**2**) as an air- and moisture-sensitive white solid in good yield (Scheme 1). Substitution of the labile acetonitrile ligands in **2** to give $[\text{Ru}(\text{CO})_4(\text{PPh}_3)_2](\text{BF}_4)_2$ (**3**) could also be readily achieved on carbonylation. Both **2** and **3** have been characterised by a combination of multinuclear NMR (^1H , ^{19}F , ^{31}P) and IR spectroscopy along with FAB mass spectrometry (see Table 1 and Exp. Section). In addition, both complexes have been the subject of single-crystal X-ray diffraction studies.

Crystals of **2** and **3** suitable for X-ray determinations were both grown by vapour diffusion of hexane into saturated dichloromethane solutions of the respective complex. Each structure consists of a distorted octahedral dicationic unit charge-balanced by either two tetrafluoroborate anions (**3**) or one tetrafluoroborate anion and one heptafluorodiborate anion (**2**). In **3** the ruthenium atom is located on a centre of symmetry. Perspective views of the dicationic units in **2** and **3** are shown in Figures 2 and 3, respectively; selected bond lengths and angles are collected in Tables 2 and 3, respectively. Within the cation in **2**, the two triphenylphosphane ligands are disposed *trans* [$\text{P}(1)\text{--Ru}(1)\text{--}$

$\text{P}(2)$ $176.31(4)^\circ$] with the two pairs of carbonyl and acetonitrile ligands configured mutually *cis*. In **3**, the triphenylphosphane ligands are again mutually *trans* [$\text{P}(1)\text{--Ru}(1)\text{--P}(1\text{A})$ $180.00(9)^\circ$] but with four carbonyl ligands now occupying the equatorial belt. Between structures a slight elongation of the metal–phosphorus bond lengths is evident on conversion of **2** to **3** [$\text{Ru}(1)\text{--P}(1)$ $2.4294(11)$ Å, $\text{Ru}(1)\text{--P}(2)$ $2.4318(11)$ Å (**2**) vs. $2.4528(18)$ Å (**3**)]. This elongation in **3** presumably takes place in order to allow the four equatorial carbonyl ligands to maximise their back-bonding capacity. It is worth noting that crystallographically characterised examples of dicationic mononuclear ruthenium carbonyl complexes are rare.^[13] There are no intermolecular contacts in either structure.

In the ^{19}F NMR spectra of both **2** and **3**, a single resonance with a chemical shift characteristic of a BF_4 counterion is visible [$\delta = -155.7$ (**2**), -156.0 ppm (**3**)]; the presence of two inequivalent borate counterions for **2**, as evidenced in the solid state, is not apparent in solution. Their ^{31}P NMR spectra confirm that the two triphenylphosphane phosphorus atoms in each molecule are located in equivalent positions with a singlet resonance. The $\nu(\text{CO})$ bands [2095 , 2050 cm^{-1} (**2**); 2084 cm^{-1} (**3**)] in the IR spectra are seen at notably higher wavenumbers than those observed in precursor **1a** (2045 , 1973 cm^{-1}),^[11b] no doubt reflecting the dicationic nature of the complexes; an additional strong $\nu(\text{CN})$ band at 2319 cm^{-1} in **2** confirms the presence of the bound acetonitrile ligands. Furthermore, the FAB mass spectra of **2** and **3** support the formulations with fragmentation peaks corresponding to the loss of acetonitrile (**2**) or carbonyl (**3**) from the corresponding dications.

With the intent of preventing the abstraction of both fluoride ligands in **1a**, the reaction was then attempted in the presence of a noncoordinating solvent. Hence, reaction of **1a** with BF_3 at -78°C in dichloromethane afforded $[\text{RuF}(\text{FBF}_3)(\text{CO})_2(\text{PPh}_3)_2]$ (**4**) in near-quantitative yield



Scheme 1. Reagents and conditions: (i) $\text{BF}_3 \cdot \text{OEt}_2$ (xs), MeCN, r.t.; (ii) CO, CH_2Cl_2 , r.t.; (iii) BF_3 , CH_2Cl_2 , -78°C ; (iv) CO or PPh_3 , CH_2Cl_2 , r.t.; (v) PF_5 , CH_2Cl_2 , r.t.; (vi) $\text{KB}(\text{Ar}^F)_4$, CH_2Cl_2 , r.t.; (vii) CO, CH_2Cl_2 , r.t.

Table 1. Spectroscopic data for the new complexes **2–9**.

| | $\nu(\text{CO})$ [cm^{-1}] ^[a] | ^1H NMR [δ] ^[b] | ^{19}F NMR [δ] ^[c] | ^{31}P NMR [δ] ^[d] | FAB-MS |
|-----------|--|--|--|---|---|
| 2 | 2095 (s), 2050 (s), $\nu(\text{CN})$ 2319 (br) | 7.50–7.30 (m, 30 H, Ar–H), 1.67 (s, 6 H, CH_3) | –155.7 (s, BF_4) | 27.2 (s, RuP_2) | 362 [$\text{MH} - \text{B}_3\text{F}_{11} - \text{MeCN}$] ²⁺ |
| 3 | 2084 (s) | 7.65–7.40 (m, 30 H, Ar–H) | –156.0 (s, BF_4) | 21.6 (s, RuP_2) | 328 [$\text{MH} - 2\text{BF}_4 - 3\text{CO}$] ²⁺ |
| 4 | 2072 (s), 2002 (s) | 7.5–7.30 (m, 30 H, Ar–H) | –149.5 [d, 3F, $^2J(\text{FF}) = 78$, F_a], –237.6 (m, 1F, F_b), –330.0 [dm, 1F, $^2J(\text{F}_b\text{F}_c) = 87$, F_c] | 23.4 (br. s, RuP_2) | ^[e] |
| 5a | 2163 (m), 2103 (s), 2077 (s) | 7.50–7.60 (m, 30 H, Ar–H) | –156.0 (s, 4F, BF_4), –438.0 [t, 1F, $^1J(\text{PF}) = 20$, RuF] | 22.8 (d, $^2J(\text{PF}) = 20$, RuP_2) | 701 [$\text{M} - \text{BF}_4 - \text{CO}$] ⁺ , 673 [$\text{M} - \text{BF}_4 - 2\text{CO}$] ⁺ , 653 [$\text{M} - \text{BF}_4 - 2\text{CO} - \text{F}$] ⁺ |
| 5b | 2054 (s), 1985 (s) | 7.50–7.30 (m, 45 H, Ar–H) | –155.9 (s, 4F, BF_4), –393.7 [app. q, 1F, $^2J(\text{PF}) = 22$, RuF] | 9.4 [dt, $^2J(\text{PF}) = 22$, $^2J(\text{PP}) = 29$, RuP_{cis}], 14.3 [dd, $^2J(\text{PP}) = 29$, $^2J(\text{PF}) = 22$, $\text{RuP}_{\text{trans}}$] | 963 [$\text{M} - \text{BF}_4$ – PPh_3] ⁺ |
| 6 | 2073 (s), 2006 (s) | 7.70–7.30 (m, 30 H, Ar–H) | –72.7 [d, 6F, $^1J(\text{PF}) = 713$, PF_6], –345.1 [t, 1F, $^1J(\text{PF}) = 19$, RuF] | 16.6 [d, $^2J(\text{PF}) = 20$, RuP_2], –144.2 [sept, $^1J(\text{PF}) = 711$, PF_6] | 653 [$\text{M} - \text{F} - \text{CO} - \text{PF}_6$] ⁺ , 625 [$\text{M} - \text{F} - 2\text{CO} - \text{PF}_6$] ⁺ |
| 7 | 2073 (s), 2011 (s) | 7.60–7.35 (m, 30 H, Ar–H) | –62.4 (s, 6F, Ar– CF_3) | 17.3 (s, RuP_2) | 689 [$\text{M} - \text{B}(\text{Ar}^{\text{F}})_4 - 2\text{CO}$] ⁺ , 654 [$\text{MH} - \text{B}(\text{Ar}^{\text{F}})_4 - 2\text{CO} - \text{Cl}$] ⁺ , 625 [$\text{MH} - \text{B}(\text{Ar}^{\text{F}})_4 - 3\text{CO} - \text{Cl}$] ⁺ |
| 8b | 2066 (s), 2005 (s) | ^[f] | ^[f] | ^[f] | 576 [$\text{M} - \text{BF}(\text{C}_6\text{F}_5)_3 - \text{CO}$] ⁺ , 557 [$\text{M} - \text{BF}(\text{C}_6\text{F}_5)_3 - \text{CO} - \text{F}$] ⁺ |
| 8c | 2070 (s), 2005 (s), $\nu(\text{C}\equiv\text{C})$ 2177 (s) | 7.99 (m, 2 H, Ar–H), 7.76 (m, 4 H, Ar–H), 7.37 (m, 24 H, Ar–H) | –135.0 (m, 6F, ArF), –160.0 [t, 3F, $^3J(\text{FF}) = 22$, $p\text{-Ar-F}$], –165.2 (m, 6F, Ar–F), –182.4 (s, 1F, BF), –351.9 [t, 1F, $^3J(\text{PF}) = 20$, RuF] | –1.9 [t, $^3J(\text{PF}) = 20$, RuP_2] | 720 [$\text{M} - \text{BF}(\text{C}_6\text{F}_5)_3 - \text{CO}$] ⁺ , 692 [$\text{M} - \text{BF}(\text{C}_6\text{F}_5)_3 - 2\text{CO}$] ⁺ , 673 [$\text{M} - \text{BF}(\text{C}_6\text{F}_5)_3 - 2\text{CO} - \text{F}$] ⁺ |
| 8d | 2063 (s), 2011 (s) | 7.42 [t, 4 H, $^3J(\text{HH}) = 7.7$, $p\text{-Ar-H}$], 7.17 [d, 8 H, $^3J(\text{HH}) = 7.8$, $m\text{-Ar-H}$], 6.97 (s, 4 H, NCHCHN), 2.41 [ps t, 4 H, $^3J(\text{HH}) = 6.6$, CH_3CH], 2.24 [ps t, 4 H, $^3J(\text{HH}) = 6.2$, CH_3CH], 1.27 [d, 12 H, $^3J(\text{HH}) = 6.3$, CH_3CH], 1.06 (m, 12 H, CH_3CH) | –135.1 (m, 6F, Ar–F), –162.0 [t, 3F, $^3J(\text{FF}) = 20$, $p\text{-Ar-F}$], –166.4 (m, 6F, Ar–F), –190.9 (s, br, 1F, BF), –291.3 (s, 1F, RuF) | ^[g] | 953 [$\text{M} - \text{BF}(\text{C}_6\text{F}_5)_3$] ⁺ |
| 9 | 2062 (s), 2011 (s) | 7.41 [t, 4 H, $^3J(\text{HH}) = 7.9$, $p\text{-Ar-H}$], 7.15 [d, 8 H, $^3J(\text{HH}) = 7.6$, $m\text{-Ar-H}$], 7.10 (s, 4 H, NCHCHN), 2.22 [sept, 4 H, $^3J(\text{HH}) = 6.7$, CH_3CH], 0.96 [d, 12 H, $^3J(\text{HH}) = 6.8$, CH_3CH], 0.93 [d, 12 H, $^3J(\text{HH}) = 6.8$, CH_3CH] | –135.1 (m, 6F, Ar–F), –161.9 [t, 3F, $^3J(\text{FF}) = 20$, Ar–F], –166.3 (m, 6F, Ar–F), –189.9 (s, br, 1F, BF), –432.6 (s, 1F, RuF) | ^[g] | 953 [$\text{M} - \text{BF}(\text{C}_6\text{F}_5)_3 - \text{CO}$] ⁺ |

[a] Recorded with a Perkin-Elmer Spectrum One ATR-FTIR spectrometer. [b] Recorded in CDCl_3 at 293 K, chemical shifts in ppm relative to SiMe_4 , coupling constants in Hz. [c] Recorded in CDCl_3 at 293 K (**2**, **3**, **6–9**) or in $[\text{D}_6]\text{acetone}$ at 184 K (**4**) and 293 K (**5a**, **5b**), chemical shifts in ppm relative to CFCl_3 , coupling constants in Hz. [d] Recorded in CDCl_3 at 293 K or $[\text{D}_6]\text{acetone}$ at 203 K (**3**) and 293 K (**5a**, **5b**), chemical shifts in ppm relative to 85% H_3PO_4 , coupling constants in Hz. [e] Not recorded. [f] Because of solubility problems acceptable NMR spectra could not be obtained. [g] No phosphorus atoms present.

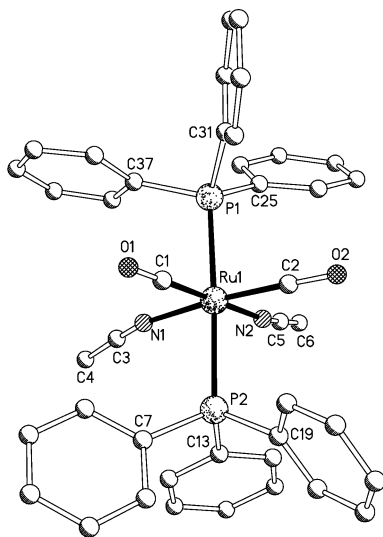


Figure 2. Molecular structure of the dicationic unit in **2** including a partial atom numbering scheme; all hydrogen atoms have been omitted for clarity.

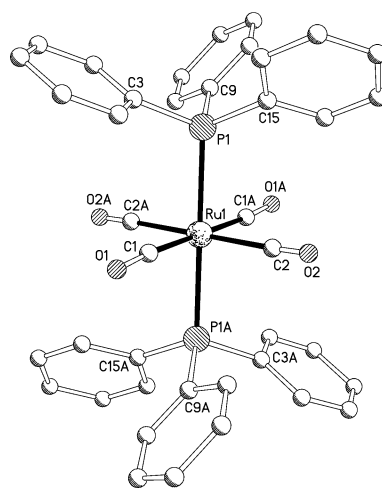


Figure 3. Molecular structure of the dicationic unit in **3** including a partial atom numbering scheme; all hydrogen atoms have been omitted for clarity.

Table 2. Selected bond lengths [\AA] and angles [$^\circ$] for **2**.

| | | | |
|--|-----------|-----------------|------------|
| Bond lengths | | | |
| Ru(1)–C(1) | 1.889(4) | Ru(1)–P(1) | 2.4294(11) |
| Ru(1)–C(2) | 1.887(4) | Ru(1)–P(2) | 2.4318(11) |
| Ru(1)–N(1) | 2.096(3) | C(5)–N(2) | 1.126(5) |
| Ru(1)–N(2) | 2.073(3) | C(3)–N(1) | 1.128(5) |
| Range of B–F (in BF_4 and B_2F_7 anions): 1.363(6)–1.513(8) | | | |
| Bond angles | | | |
| P(1)–Ru(1)–P(2) | 176.31(4) | C(1)–Ru(1)–N(2) | 176.55(15) |
| C(1)–Ru(1)–C(2) | 92.33(16) | C(1)–Ru(1)–P(1) | 90.47(12) |
| C(1)–Ru(1)–N(1) | 95.19(15) | C(1)–Ru(1)–P(2) | 90.51(12) |

Table 3. Selected bond lengths [\AA] and angles [$^\circ$] for **3**.

| | | | |
|--------------------------------------|----------|------------------|------------|
| Bond lengths | | | |
| Ru(1)–C(1) | 1.960(8) | Ru(1)–P(1) | 2.4528(18) |
| Ru(1)–C(2) | 1.938(9) | | |
| Range of B–F (anions): 1.2738–1.4920 | | | |
| Bond angles | | | |
| C(1)–Ru(1)–C(2) | 89.9(4) | C(1)–Ru(1)–P(1) | 94.1(2) |
| C(1)–Ru(1)–C(2A) | 90.1(4) | C(1)–Ru(1)–P(1A) | 85.9(2) |
| C(1)–Ru(1)–C(1A) | 180.0(5) | P(1)–Ru(1)–P(1A) | 180.00(9) |

The atoms labelled with A are generated by symmetry ($1 - x, -y, -z$)

(Scheme 1). The ^{19}F NMR spectrum of **4** (recorded in $[\text{D}_6]$ -acetone at -89°C), confirmed the presence of a bound FBF_3 unit with two signals attributable to F_a and F_b in a 3:1 ratio (see Scheme 1 for labelling). The signal for F_a takes the form of doublet because of the two-bond coupling to F_b , and its chemical shift ($\delta = -149.5$ ppm) is typical of a fluorine atom bound to a trivalent boron atom. The signal for F_b is poorly resolved because of the coupling to F_a , the *trans* phosphane ligands and the ruthenium-bound F_c , while its chemical shift ($\delta = -237.6$ ppm) is comparable with that found in related complexes containing a Ru– F_b –B linkage.^[14] Equally, the signal for Ru– F_c is poorly resolved, but a doublet with a coupling constant of 87 Hz is detectable, which can be assigned to a $^2J(\text{F}_c\text{F}_b)_{\text{cis}}$ coupling; its chemical shift ($\delta = -330.0$ ppm) is in the region associated with fluoride terminally bound to ruthenium.^[11] Similarly, the low temperature $^{31}\text{P}\{^1\text{H}\}$ NMR spectrum of **4** was poorly resolved with a broad resonance at $\delta = 23.4$ ppm attributable to the equivalent *trans*-configured triphenylphosphanes. It is uncertain why the spectra are broad even at low temperature but it is likely that this is a result of the lability of the FBF_3 ligand in solution (vide infra). The IR spectrum of **4** shows two $\nu(\text{CO})$ bands typical of a *cis* arrangement of carbonyl ligands while six bands for the $\nu(^{10}\text{BF})$ and $\nu(^{11}\text{BF})$ stretches are visible for the coordinated FBF_3 group.^[15] The capacity of $[\text{BF}_4]^-$ to coordinate to an electron-deficient centre is well established spectroscopically and a number of ruthenium complexes containing such ligands have been crystallographically characterised.^[12,16]

In order to probe the anticipated lability of the bound FBF_3 group in **4**, its reactivity towards donor ligands was examined. Hence, treatment of **4** with CO or triphenylphosphane in dichloromethane at room temperature gave

$[\text{RuF}(\text{CO})_2(\text{L})(\text{PPh}_3)_2](\text{BF}_4)$ [$\text{L} = \text{CO}$ (**5a**), PPh_3 (**5b**)] in near quantitative yields (Scheme 1). Complex **5a** has previously been synthesised by an alternative route and indeed its spectroscopic properties closely match the data reported in this work.^[11b] The ^{19}F NMR spectrum of **5b** shows two signals, one corresponding to the discrete BF_4 counterion ($\delta = -155.9$ ppm) and the other to the bound fluoride ($\delta = -393.7$ ppm), the latter taking the form of an apparent quartet. This multiplicity is presumably an overlapping doublet of triplets with the metal-bound fluoride ligand coupling to the *cis* triphenylphosphane and the equivalent *trans* triphenylphosphanes. The signal for the coordinated fluoride is substantially upfield shifted when compared to precursor **4** but falls in the range found for previously reported monofluoro ruthenium cationic compounds.^[10a,11c,14] The $^{31}\text{P}\{^1\text{H}\}$ NMR spectrum of **5b** reveals two mutually coupled resonances at $\delta = 9.4$ and $\delta = 14.3$ ppm in a 1:2 ratio along with additional doublet multiplicities for each signal from the $^2J(\text{PF})_{\text{cis}}$ couplings (ca. 22 Hz).

Unexpectedly during an attempt to grow crystals of **4** suitable for a single X-ray diffraction study, the structure of **5a** was determined as part of a 50:50 superimposed mixture with complex **3**. Furthermore, the fluoride ligand within the cationic component in **5a** was disordered across four equatorial sites resulting in an overall 12.5% fluoride site occupancy. An attempt to solve the structure in the *P1* and *Cc* space groups rather than the *C2/c* space group (the preferred one), gave the same disorder problems. As a consequence the affected carbonyl and fluoride atoms were refined isotropically and thus reliable discussion of the associated metric data is limited. Nevertheless, the Ru–F distances of ca. 2.117 \AA fall in the range found for related ruthenium(II) complexes.^[10a,11,12] It should be mentioned that such CO/F scrambling has been noted elsewhere.^[12] A view of the superimposed cations is shown in Figure 4; selected

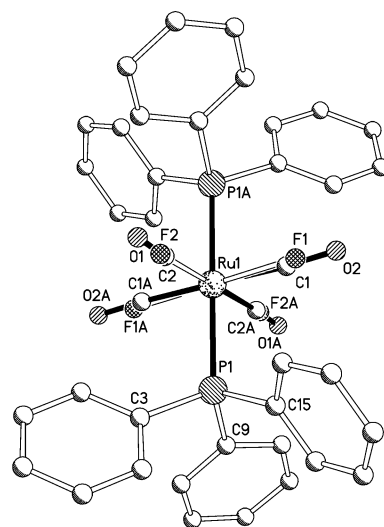


Figure 4. Molecular structure of the disordered cationic unit in **5a/3** including a partial atom numbering scheme; all hydrogen atoms have been omitted for clarity.

bond lengths are listed in Table 4. It would seem probable that **5a/3** represents a decomposition product formed during the crystallisation of **4**.

Table 4. Selected bond lengths [Å] and angles [°] for **5a/3**.^[a]

| | |
|---|------------|
| Bond lengths | |
| Ru(1)–P(1) | 2.4410(18) |
| Range of B–F (anion): 1.315(12)–1.372(11) | |
| Bond angles | |
| P(1A)–Ru(1)–P(1) | 180.00(8) |

[a] The atoms labelled with A are generated by symmetry ($1 - x + 1/2, -y + 1/2$).

2. Reactivity of **1a** towards PF₅

On the basis of spectroscopic and crystallographic studies it has previously been proposed that the coordinating ability of fluoro-containing anions decreases in the order $[\text{BF}_4]^- > [\text{PF}_6]^-$.^[17] With a view to exploiting this trend to prepare coordinatively unsaturated cationic monofluoro complexes, **1a** was treated with PF₅ in dichloromethane at ambient temperature; complex $[\text{RuF}(\text{CO})_2(\text{PPh}_3)_2](\text{PF}_6)$ (**6**) was isolated in high yield as a white solid (Scheme 1). Characterisation by multinuclear NMR spectroscopy supports the formulation of **6** as a 16-electron ruthenium–fluoro cation charge-balanced by a discrete hexafluorophosphate anion. In the ¹⁹F NMR spectrum the PF₆ anion is seen as a characteristic doublet at $\delta = -72.7$ ppm with a ¹J(PF) coupling constant (ca. 71.3 Hz) that is mirrored in the septet signal found in the ³¹P NMR spectrum. Unlike **4**, the bound fluoride takes the form of a triplet [¹J(PF) = 19 Hz] in the ¹⁹F NMR spectrum, while the ³¹P NMR spectrum displays a doublet for the equivalent phosphane ligands coupling to the *cis* fluoride. Attempts at recording the NMR spectrum at a lower temperature (−80 °C, in CD₂Cl₂) gave no evidence of any interaction with the ruthenium centre.

With the aim to indisputably confirm that the $[\text{PF}_6]^-$ anion in **6** undergoes only minimal anion–metal interactions in solution (cf. **4**), an anion exchange reaction with the well-documented “superweak” coordinating anion $[\text{B}(\text{Ar}^{\text{F}})_4]^-$ [$\text{Ar}^{\text{F}} = 3,5\text{-(CF}_3)_2\text{C}_6\text{H}_3$]^[18] was undertaken. Hence, **6** was treated with the potassium salt of the borate in dichloromethane at room temperature (Scheme 1). The ³¹P and ¹⁹F NMR spectra of the product indicated that anion metathesis had been successful, however, it was apparent that rapid decomposition of the product occurred in solution. To circumvent this instability carbon monoxide was introduced and $[\text{RuCl}(\text{CO})_3(\text{PPh}_3)_2][\text{B}(\text{Ar}^{\text{F}})_4]$ (**7**) was isolated in good yield. Complex **7** was characterised by multinuclear NMR spectroscopy, IR spectroscopy, mass spectrometry and by microanalysis (see Table 1 and Exp. Section). A single-crystal X-ray diffraction study was also performed.

Crystals of **7** suitable for the X-ray determination were grown by slow diffusion of hexane into a saturated dichlo-

romethane solution containing the complex. A perspective view of the cation in **7** is shown in Figure 5; selected bond lengths are collected in Table 5. The structure reveals the presence of the cationic unit charge-balanced by a discrete $[\text{B}(\text{Ar}^{\text{F}})_4]^-$ counterion. Within the cation the two triphenylphosphane ligands are disposed mutually *trans*, with the equatorial sites being filled by three carbonyl ligands and a chloride so as to complete an essentially octahedral geometry. The metal–phosphorus bond lengths [Ru(1)–P(1) 2.419(3) Å, Ru(1)–P(2) 2.437(4) Å] are comparable with those found in **2** and similar to those found in the structurally related salt $[\text{RuCl}(\text{CO})_2(\text{NH}=\text{NPh})(\text{PPh}_3)_2](\text{ClO}_4)$.^[19] There are no inter-ion contacts of note.

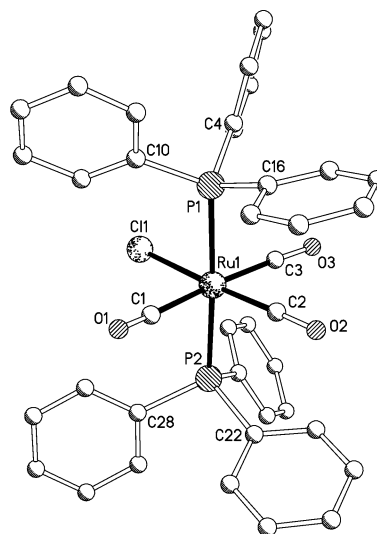


Figure 5. Molecular structure of the cationic unit in **7** including a partial atom numbering scheme; all hydrogen atoms have been omitted for clarity.

Table 5. Selected bond lengths [Å] and angles [°] for **7**.

| | | | |
|---|-----------|------------------|------------|
| Bond lengths | | | |
| Ru(1)–Cl(1) | 2.411(3) | Ru(1)–C(3) | 1.981(14) |
| Ru(1)–C(1) | 1.965(12) | Ru(1)–P(1) | 2.419(3) |
| Ru(1)–C(2) | 1.911(11) | Ru(1)–P(2) | 2.437(4) |
| Range of B–C (anion): 1.607(16)–1.657(14) | | | |
| Bond angles | | | |
| Cl(1)–Ru(1)–C(1) | 93.5(3) | Cl(1)–Ru(1)–P(1) | 88.64(11) |
| Cl(1)–Ru(1)–C(2) | 177.3(4) | Cl(1)–Ru(1)–P(2) | 88.38(11) |
| Cl(1)–Ru(1)–C(3) | 90.6(4) | P(1)–Ru(1)–P(2) | 176.80(13) |

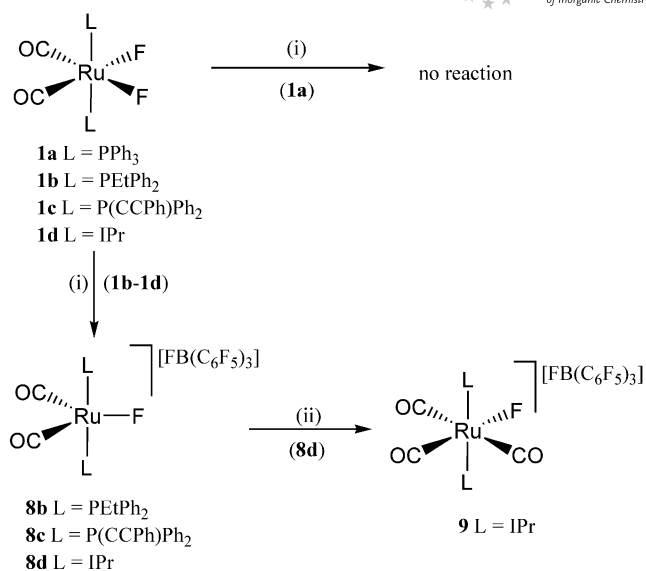
Inspection of the upfield region of the ¹⁹F NMR spectrum of **7** confirmed the absence of a signal corresponding to a bound fluoride while a signal characteristic of the CF₃ resonances for the borate were clearly visible more downfield ($\delta = -62.4$ ppm). In the ³¹P{¹H} NMR spectrum the presence of a singlet is in agreement with the *trans* configuration of the phosphane ligands and the absence of a neighbouring fluorine ligand. The positive FAB mass spectrum reveals fragmentation peaks arising from the loss of both carbonyl and chloride ligands from the cationic unit, while the negative FAB mass spectrum shows a peak corresponding to the $[\text{B}(\text{Ar}^{\text{F}})_4]^-$ anion.

It would seem likely that **7** is formed by halide exchange with the dichloromethane present as solvent. Indeed, fluoride exchange between a fluoro-containing transition-metal complex and a chlorinated solvent is not uncommon.^[20] Significantly, however, the exchange of the $[\text{PF}_6]^-$ for a non-coordinating $[\text{B}(\text{Ar}^{\text{F}})_4]^-$ anion appears to have facilitated this exchange reaction. It is therefore tempting to suggest that the $[\text{PF}_6]^-$ anion in **6** does in fact (though not revealed in the NMR spectra) exert some mild stabilisation to the 16-electron $[\text{RuF}(\text{CO})_2(\text{PPh}_3)_2]^+$ cation that inhibits the exchange process. Conversely with $[\text{B}(\text{Ar}^{\text{F}})_4]^-$ as the anion, the “naked” 16-electron cation is now susceptible to halide exchange.

3. Reactivity of **1a–1d** towards $\text{B}(\text{C}_6\text{F}_5)_3$

In recent years tris(pentafluorophenyl)borane has often been employed as a Lewis acid for the abstraction of a variety of anionic ligands and generally the resultant anions have been regarded as noncoordinating or weakly coordinating.^[18,21] To explore its use as a Lewis acid for fluoride abstraction, **1a** was treated with $\text{B}(\text{C}_6\text{F}_5)_3$ in dichloromethane at ambient temperature (Scheme 2). Unexpectedly, an analysis of the reaction mixture by NMR spectroscopy revealed only the presence of unreacted starting material. Given that reaction of **1a** with BF_3 readily occurs, it was postulated that $\text{B}(\text{C}_6\text{F}_5)_3$ was not a strong enough Lewis acid to abstract a fluoride ion from **1a**. It was, therefore, reasoned that an increase in the lability of the Ru–F bond in **1** might facilitate the transformation. Hence the reactivity of $\text{B}(\text{C}_6\text{F}_5)_3$ towards *cis,cis,trans*- $[\text{RuF}_2(\text{CO})_2(\text{L})_2]$ [**L** = PEt_2Ph (**1b**), $\text{P}(\text{CCPh})\text{Ph}_2$ (**1c**), IPr (**1d**)] was investigated in which the two PPh_3 groups in **1a** were replaced by more electron-donating ancillary ligands. Thus, treatment of **1b–1d** with $\text{B}(\text{C}_6\text{F}_5)_3$ in dichloromethane at room temperature gave the 16-electron $[\text{RuF}(\text{CO})_2(\text{L})_2][\text{FB}(\text{C}_6\text{F}_5)_3]$ (**L** = PEt_2Ph (**8b**), $\text{P}(\text{CCPh})\text{Ph}_2$ (**8c**), IPr (**8d**)) compounds as pale-yellow solids in high yield (Scheme 2). In the case of **8b** the poor solubility of the product precluded characterisation by NMR spectroscopy. Otherwise all the complexes have been characterised by a combination of IR spectroscopy, ^1H , ^{19}F and ^{31}P NMR spectroscopy, FAB mass spectrometry and elemental analysis (see Table 1 and Exp. Section).

In the FAB mass spectra of **8b–8d**, peaks consistent with the cationic unit or fragmentation peaks corresponding to the loss of carbonyl ligands are evident. In the ^{19}F NMR spectra of **8c** and **8d**, a signal for the B–F fluoride within the anion was clearly visible [δ = -182.4 ppm (**8c**), -190.9 ppm (**8d**)], while the Ru–F resonance could be seen upfield [δ = -351.9 ppm (**8c**), -291.3 ppm (**8d**)] as a triplet for **8c** ($^2J(\text{PF}) = 20$ Hz) or as a singlet for **8d**. In the ^{31}P NMR spectrum of **8c**, a mutually coupled doublet was observed corroborating the presence of a single metal-bound fluoride. In **8d** the equivalency of the resonances resulting from the two IPr groups observed in the ^1H NMR spectrum supports their *trans* configuration. For all three salts, the $\nu(\text{CO})$ bands were found at higher wavenumbers than those for their corresponding difluoro precursor,^[11,12] reflecting



Scheme 2. Reagents and conditions: (i) $\text{B}(\text{C}_6\text{F}_5)_3$, CH_2Cl_2 , r.t.; (ii) CO , CH_2Cl_2 , r.t.

the cationic nature of the complexes. In **8c** the presence of a nonbonded alkyne unit was confirmed by the presence of the $\nu(\text{C}\equiv\text{C})$ band at 2177 cm^{-1} in its IR spectrum.

Carbonylation of **8d** under ambient conditions proved facile affording $[\text{RuF}(\text{CO})_3(\text{L})_2][\text{FB}(\text{C}_6\text{F}_5)_3]$ (**9**) as a white solid in quantitative yield. Confirmation of its formulation was made on the basis of IR spectroscopy, multinuclear NMR spectroscopy, mass spectrometry and elemental analysis. A crystal of **9** was also subject to a single-crystal X-ray diffraction study. Unfortunately, the data was not stable to full anisotropic refinement due to poor crystal quality. Nevertheless, the gross structure revealed the presence of a coordinatively saturated fluoro cation along with a noncoordinating $[\text{FB}(\text{C}_6\text{F}_5)_3]^-$ anion; a view of the cationic unit in **9** is depicted in Figure 6. Notably, crystallographically characterised examples of complexes containing

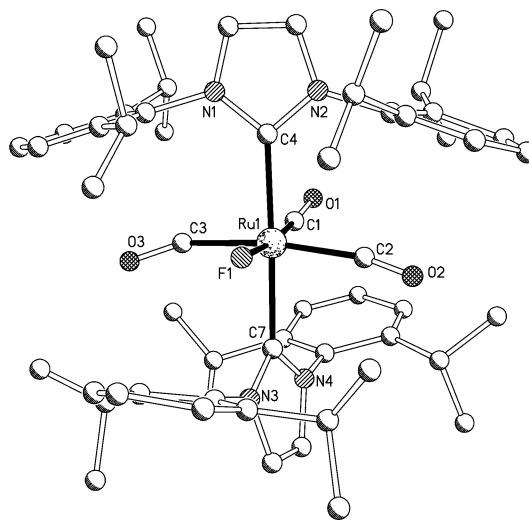


Figure 6. Molecular structure of the cationic unit in **9** including a partial atom numbering scheme; all hydrogen atoms have been omitted for clarity.

a $[\text{FB}(\text{C}_6\text{F}_5)_3]^-$ anion are rare.^[22] As expected the ^{19}F resonances for the borate anion remained unaffected on carbonylation but the resonance arising from the ruthenium-bound fluoride ion underwent a considerable upfield shift when compared to that in **8d** [$\delta = -432.6$ ppm (**9**) vs. -291.3 ppm (**8d**)]. A similar shift in the Ru–F resonance has previously been observed for the carbonylation of $[\text{RuF}(\text{dppp})_2][\text{PF}_6]$.^[10a]

Interestingly the formally 16-electron complexes **8c** and **8d** appear stable in solution. By analogy with **6**, it would seem plausible that the $[\text{FB}(\text{C}_6\text{F}_5)_3]^-$ ion also provides some subtle stabilisation to the electron-deficient ruthenium centre (although not detectable by NMR spectroscopy). As with **4**, any contact the anion in **8** exhibits with the metal centre can readily be removed on introduction of CO.

Conclusions

By systematic variation of the Lewis acid, solvent and electronic properties of **1**, ruthenium–fluoro cations of the type $[\text{RuL}_2(\text{CO})_n\text{F}]^+$ ($n = 2, 3$) have been successfully isolated. In the case of the formally 16-electron cations ($n = 2$), it would appear that the coordinating nature of the anion is vital for providing some mild stabilisation (see **4**, **6** and **8**); with a “superweak” anion like $[\text{B}(\text{Ar}^F)_4]^-$ decomposition occurs.

Experimental Section

General Remarks: All reactions, unless otherwise stated, were carried out under an atmosphere of dry, oxygen-free nitrogen, using standard Schlenk-line or metal vacuum-line techniques or in a nitrogen purged dry box. Solvents were distilled under nitrogen from appropriate drying agents and degassed prior to use.^[23] The infrared spectra were recorded with a Perkin–Elmer Spectrum One FTIR spectrometer on solid samples. The ES (electrospray) and the FAB mass spectra were recorded using a micromass Quattro LC mass spectrometer and a Kratos Concept spectrometer with methanol or 3-nitrobenzyl alcohol as the matrix, respectively. ^1H , ^{31}P , ^{19}F and ^{13}C NMR spectra were recorded with a Bruker spectrometer (ARX 250, AM 300 or DRX 400 MHz) at ambient temperature; chemical shifts (δ) for the ^1H and ^{13}C NMR spectra were referenced internally to TMS ($\delta = 0$ ppm) while the ^{19}F and ^{31}P NMR were referenced externally to CFCl_3 ($\delta = 0$ ppm) and 85% H_3PO_4 ($\delta = 0$ ppm), respectively. Elemental analyses were performed at the Science Technical Support Unit, London Metropolitan University.

Dicarbonylbis(triphenylphosphane)ruthenium difluoride (**1a**),^[11a] dicarbonylbis(ethylphenylphosphane)ruthenium difluoride (**1b**),^[11a] dicarbonylbis(phenylethynylphenylphosphane)ruthenium difluoride (**1c**)^[11c] and bis{1,3-bis(2,6-diisopropylphenyl)imidazol-2-ylidene}dicarbonylruthenium difluoride (**1d**)^[12] were prepared according to previously reported procedures. All other chemicals were obtained commercially and used without further purification.

Synthesis of 2: A Schlenk vessel was charged, in a dry box, with **1a** (0.250 g, 0.347 mmol) and acetonitrile (20 mL) was introduced. $\text{BF}_3 \cdot \text{OEt}_2$ (1 mL, excess) was added dropwise to the stirred solution at room temperature forming a colourless solution. After stirring at room temperature for 10 h, all volatiles were removed under re-

duced pressure to afford a white solid. Following crystallisation from firstly dichloromethane/diethyl ether (1:100) and secondly from dichloromethane/hexane (1:100), **2** could be obtained as an air- and moisture-sensitive white powder (0.332 g, 95%). Single crystals suitable for an X-ray diffraction study were grown by slow diffusion of hexane into a saturated dichloromethane solution of **2**. $\text{C}_{42}\text{H}_{36}\text{B}_3\text{F}_{11}\text{N}_2\text{O}_2\text{P}_2\text{Ru}$ (1004.90): calcd. C 50.15, H 3.58, N 2.79; found C 50.26, H 3.61, N 2.74. FAB mass spectrum, $m/z = (-\text{FAB})$ 87 (BF_4). IR (solid state): $\tilde{\nu} = 2319$ (br, CN), 2095 (s, CO), 2050 (s, CO), 1483 (s), 1432 (s), 1066 (BF_4), 836 (s), 744 (s), 685 (s) cm^{-1} . See Table 1 for additional spectroscopic data.

Synthesis of 3: A Schlenk vessel was charged with **2** (0.300 g, 0.299 mmol) and dichloromethane (10 mL) was introduced. Carbon monoxide was bubbled through the solution at ambient temperature for 30 min. The resulting colourless solution was transferred to a second vessel containing diethyl ether (200 mL) and the precipitate was collected by filtration. Recrystallisation of the solid from dichloromethane/hexane (1:150) gave **3** as an air- and moisture-sensitive white solid (0.259 g, 95%). Single crystals suitable for an X-ray diffraction study were grown by slow diffusion of hexane into a saturated dichloromethane solution of **3**. FAB mass spectrum, $m/z = (-\text{FAB})$ 87 (BF_4). IR (solid state): $\tilde{\nu} = 3059$ (br), 2084 (s, CO), 1479 (s), 1432 (s), 1049 (vs., BF_4), 747 (s), 691 (s) cm^{-1} . See Table 1 for additional spectroscopic data.

Synthesis of 4: Complex **1a** (0.03 g, 0.04 mmol) was loaded, in the dry-box, into a prefluorinated FEP (perfluoroethylene/propylene copolymer) tube [4 mm outside diameter (o.d.)]. The FEP tube was connected to a metal vacuum line and the connectors were passivated. Dichloromethane (0.3 mL) was condensed into the tube at -196°C under a static vacuum. The contents were warmed to -78°C and then placed under boron trifluoride gas (1 atm) giving a yellow solution. The solvent was then removed under reduced pressure to give **4** as an off-white solid (0.030 g, 90%). See Table 1 for spectroscopic data.

Synthesis of 5a: A preseasoned FEP tube (6 mm o.d.) was charged, in the dry box, with **4** (0.100 g, 0.13 mmol). The apparatus was reconnected to the line and the connectors were passivated. Dichloromethane (0.8 mL) was condensed into the reaction tube at -196°C under a static vacuum. The tube was warmed to -78°C and placed under carbon monoxide (2 atm) and slowly warmed to room temperature. The reaction vessel was left to stand for 3 h with occasional agitation after which all the solid had dissolved. All volatiles were removed under reduced pressure to give **5a** as an off-white solid (0.092 g, 89%). See Table 1 for spectroscopic data.

Synthesis of 5b: A preseasoned FEP tube (6 mm o.d.) was charged, in the dry box, with **4** (0.100 g, 0.13 mmol) and triphenylphosphane (0.367 g, 0.14 mmol, 1.1 equiv.). The apparatus was reconnected to the line and the connectors were passivated. Dichloromethane (0.8 mL) was condensed into the reaction tube at -196°C under a static vacuum. The tube was warmed to room temperature and left for 2 h with occasional agitation. All volatiles were removed under reduced pressure to give an off-white solid, which was washed with warm hexane to give **5b** (0.108 g, 81%). See Table 1 for spectroscopic data.

Synthesis of 6: A preseasoned FEP tube (6 mm o.d.) was charged, in the dry box, with **1a** (0.250 g, 0.347 mmol). The apparatus was reconnected to the line and the satellite connectors were passivated. Dichloromethane (2 mL) was condensed into the vessel at -196°C and the solution was warmed to ambient temperature whereupon dissolution of the solid occurred. The resulting yellow solution was cooled to -50°C and placed under PF_5 (1.3 atm). The reaction vessel was closed and the reaction mixture was stirred and warmed

(cautiously) to room temperature. The yellow solution was recooled to $-50\text{ }^{\circ}\text{C}$ and PF_5 was reintroduced and the uptake of the gas monitored. This process was repeated until the consumption of PF_5 had ceased. All volatiles were removed under reduced pressure to give $[\text{RuF}(\text{CO})_2(\text{PPh}_3)_2](\text{PF}_6)$ (**6**) as an air- and moisture-sensitive yellow powder (0.280 g, 97%). FAB mass spectrum, $m/z = (-\text{FAB})$ 145 (PF_6). IR (solid state): $\tilde{\nu} = 2073$ (s, CO), 2006 (s, CO), 1479 (s), 1432 (s), 1094 (s), 831 (br), 741 (s), 688 (s) cm^{-1} .

Synthesis of 7: A Schlenk vessel was charged, in a dry box, with **6** (0.200 g, 0.237 mmol), potassium tetra(3,5-bis(trifluoromethyl)phenyl)borate (0.214 g, 0.237 mmol) and dichloromethane (10 mL) were then introduced. The reaction mixture was stirred at ambient temperature for 5 h. Following filtration, carbon monoxide was bubbled through the stirred solution at room temperature for 30 min. The resulting clear solution was transferred to a vessel containing diethyl ether (200 mL) and the resulting precipitate isolated by filtration. Recrystallisation from dichloromethane/hexane (1:100) afforded **7** as air- and moisture-sensitive white crystals (0.285 g, 75%). Single crystals suitable for an X-ray diffraction study were grown by slow diffusion of hexane into a saturated dichloromethane solution of **7**. $\text{C}_{71}\text{H}_{42}\text{BClF}_{24}\text{O}_3\text{P}_2\text{Ru}\cdot 0.5\text{CH}_2\text{Cl}_2$ (1650.3): calcd. C 52.00, H 2.60; found C 52.00, H 2.59. FAB mass spectrum, $m/z = (-\text{FAB})$ 863 $\{[\text{B}(\text{Ar}^{\text{F}})_4]\}$. IR (solid state): $\tilde{\nu} = 2073$ (s, CO), 2011 (s, CO), 1435 (s), 1351 (s), 1270 (vs), 1131 (br), 881 (s) cm^{-1} .

Synthesis of 8: (i) **L** = PEtPh_2 (**8b**): A preseasoned FEP tube (6 mm o.d.) was charged, in the dry box, with **1b** (0.100 g, 0.161 mmol) and tris(pentafluorophenyl)borane (0.82 g, 0.161 mmol). The apparatus was reconnected to the line and the satellite connectors were passivated. Dichloromethane (3 mL) was condensed into the vessel at $-196\text{ }^{\circ}\text{C}$ and the solution warmed to ambient temperature whereupon dissolution of the solid occurred. After stirring the resulting colourless solution at room temperature overnight, all volatiles

were removed under reduced pressure to give $[\text{RuF}(\text{CO})_2(\text{PPh}_2\text{Et})_2][\text{FB}(\text{C}_6\text{F}_5)_3]$ (**8b**) as an air- and moisture-sensitive white powder (0.173 g, 95%). $\text{C}_{48}\text{H}_{30}\text{BF}_{17}\text{O}_2\text{P}_2\text{Ru}\cdot 2\text{CH}_2\text{Cl}_2$ (1304.80): calcd. C 46.00, H 2.60; found C 46.14, H 1.95. FAB mass spectrum, $m/z = (-\text{FAB})$ 531 $[\text{FB}(\text{C}_6\text{F}_5)_3]$. IR (solid state): $\tilde{\nu} = 3357$ (w), 2962 (w), 2066 (s, CO), 2005 (s, CO), 1641 (s), 1512 (s), 1459 (s), 1257 (s), 1092 (br), 1014 (br), 966 (br), 792 (s) cm^{-1} . See Table 1 for additional spectroscopic data.

(ii) **L** = $\text{P}(\text{CCPh})\text{Ph}_2$ (**8c**): The title complex was isolated in a similar manner to that used for **8b**, using **1c** (0.200 g, 0.262 mmol) and tris(pentafluorophenyl)borane (0.133 g, 0.261 mmol). Removal of all volatiles under reduced pressure gave $[\text{RuF}(\text{CO})_2(\text{PPh}_2\text{CCPh})_2][\text{FB}(\text{C}_6\text{F}_5)_3]$ (**8c**) as an air- and moisture-sensitive white powder (0.32 g, 96%). $\text{C}_{60}\text{H}_{30}\text{BF}_{17}\text{O}_2\text{P}_2\text{Ru}$ (1278.80): calcd. C 56.29, H 2.35; found C 56.29, H 2.29. FAB mass spectrum, $m/z = (-\text{FAB})$ 531 $[\text{FB}(\text{C}_6\text{F}_5)_3]$. IR (solid state): $\tilde{\nu} = 3010$ (br), 2177 (s, $\text{C}\equiv\text{C}$), 2070 (s, CO), 2005 (s, CO), 1509 (s), 1461 (s), 1279 (s), 1091 (br), 965 (w), 739 (s) cm^{-1} . See Table 1 for additional spectroscopic data.

(iii) **L** = **IPr** (**8d**): The title complex was isolated in a similar manner to that used for **8b**, using **1c** (0.253 g, 0.261 mmol) and tris(pentafluorophenyl)borane (0.133 g, 0.261 mmol). Removal of all volatiles under reduced pressure gave $[\text{RuF}(\text{CO})_2(\text{IPr})_2][\text{FB}(\text{C}_6\text{F}_5)_3]$ (**8d**) as an air- and moisture-sensitive white powder (0.352 g, 91%). $\text{C}_{74}\text{H}_{72}\text{BF}_{17}\text{N}_4\text{O}_2\text{Ru}\cdot 3\text{CH}_2\text{Cl}_2$ (1737.80): calcd. C 53.16, H 4.48, N 3.22; found C 53.63, H 4.75, N 2.89. FAB mass spectrum, $m/z = (-\text{FAB})$ 531 $[\text{FB}(\text{C}_6\text{F}_5)_3]$. IR (solid state): $\tilde{\nu} = 2966$ (w), 2063 (s, CO), 2011 (s, CO), 1510 (s), 1454 (br), 1275 (s), 1088 (br), 959 (w), 801 (s), 756 (s) cm^{-1} . See Table 1 for additional spectroscopic data.

Synthesis of 9: Carbon monoxide was bubbled through a stirred solution of **8d** (0.200 g, 0.132 mmol) in dichloromethane (5 mL) for 30 min. Removal of all volatiles under reduced pressure afforded a

Table 6. Crystallographic and data processing parameters for **2**, **3**, **5a/3**, **7** and **9**^[a].

| | 2 | 3 | 5a/3 | 7 | 9 |
|---|--|---|--|--|--|
| Empirical formula | $\text{C}_{42}\text{H}_{36}\text{B}_3\text{F}_{11}\text{N}_2\text{O}_2\text{P}_2\text{Ru}$ | $\text{C}_{40}\text{H}_{30}\text{B}_2\text{F}_8\text{O}_4\text{P}_2\text{Ru}$ | $\text{C}_{78}\text{H}_{60}\text{B}_3\text{F}_{14}\text{O}_6\text{P}_4\text{Ru}_2$ | $\text{C}_{71.5}\text{H}_{43}\text{BCl}_2\text{F}_{24}\text{O}_3\text{P}_2\text{Ru}$ | $\text{C}_{75}\text{H}_{172}\text{BF}_{17}\text{N}_4\text{O}_3\text{Ru}$ |
| M_r [g mol^{-1}] | 1005.17 | 911.27 | 1717.71 | 1650.78 | 1512.25 |
| Crystal size [mm] | $0.37 \times 0.12 \times 0.05$ | $0.12 \times 0.10 \times 0.06$ | $0.21 \times 0.07 \times 0.04$ | $0.06 \times 0.15 \times 0.20$ | $0.26 \times 0.20 \times 0.14$ |
| Temperature [K] | 150(2) | 150(2) | 150(2) | 150(2) | 150(2) |
| Crystal system | monoclinic | triclinic | monoclinic | triclinic | monoclinic |
| Space group | $P2_1/c$ | $P\bar{1}$ | $C2/c$ | $P\bar{1}$ | Cc |
| a [Å] | 21.865(3) | 10.2154(18) | 22.614(12) | 13.321(3) | 18.227(6) |
| b [Å] | 9.8073(15) | 10.904(2) | 13.342(12) | 18.143(4) | 23.267(6) |
| c [Å] | 20.139(3) | 11.313(2) | 12.807(8) | 18.330(4) | 16.982(5) |
| α [°] | 90 | 113.046(2) | 90 | 107.813(4) | 90 |
| β [°] | 92.785(3) | 99.606(3) | 101.329(15) | 104.632(4) | 102.298(7) |
| γ [°] | 90 | 95.918(3) | 90 | 110.705(4) | 90 |
| U [Å ³] | 4313.5(11) | 1123.4(4) | 3789(4) | 3607.1(13) | 7037(3) |
| Z | 4 | 1 | 2 | 2 | 4 |
| D_c [Mg m^{-3}] | 1.548 | 1.347 | 1.506 | 1.520 | 1.427 |
| $F(000)$ | 2024 | 458 | 1730 | 1650 | 3104 |
| $\mu(\text{Mo-K}\alpha)$ [mm^{-1}] | 0.524 | 0.489 | 0.570 | 0.444 | 0.319 |
| Reflections collected | 30094 | 8172 | 14310 | 26234 | 27059 |
| Independent reflections | 7598 | 3923 | 3726 | 12583 | 13525 |
| R_{int} | 0.0568 | 0.0276 | 0.0870 | 0.1576 | 0.0934 |
| Restraints/parameters | 0/570 | 0/229 | 0/247 | 0/884 | 2/401 |
| Final R indices | $R_1 = 0.0465$ | $R_1 = 0.1057$ | $R_1 = 0.0747$ | $R_1 = 0.0960$ | $R_1 = 0.1008$ |
| $[I > 2\sigma(I)]$ | $wR_2 = 0.1028$ | $wR_2 = 0.3029$ | $wR_2 = 0.1782$ | $wR_2 = 0.1860$ | $wR_2 = 0.2522$ |
| All data | $R_1 = 0.0671$ | $R_1 = 0.1118$ | $R_1 = 0.1098$ | $R_1 = 0.2487$ | $R_1 = 0.1232$ |
| | $wR_2 = 0.1101$ | $wR_2 = 0.3133$ | $wR_2 = 0.1915$ | $wR_2 = 0.2399$ | $wR_2 = 0.2764$ |
| Goodness of fit on F^2 (all data) | 1.000 | 1.378 | 1.108 | 0.863 | 1.027 |

[a] Data in common: $R_1 = \Sigma||F_o| - |F_c||/\Sigma|F_o|$, $wR_2 = \{\Sigma[w(F_o^2 - F_c^2)^2/\Sigma w(F_o^2)^2]\}^{1/2}$, $w^{-1} = [\sigma^2(F_o)^2 + (aP)^2]$, $P = [\max(F_o^2, 0) + 2(F_c^2)]/3$, where a is a constant adjusted by the program; goodness of fit = $[\Sigma(F_o^2 - F_c^2)^2/(n - p)]^{1/2}$ where n is the number of reflections and p the number of parameters.

white solid, which was recrystallised from dichloromethane/hexane affording $[\text{RuF}(\text{CO})_2(\text{IPr})_2][\text{FB}(\text{C}_6\text{F}_5)_3]$ (**8d**) as an air- and moisture-sensitive white powder (0.192 g, 94%). Single crystals suitable for an X-ray diffraction study were grown by diffusion of hexane vapour into a saturated dichloromethane solution of **9**. $\text{C}_{75}\text{H}_{72}\text{BF}_{17}\text{N}_4\text{O}_3\text{Ru}$ (1510.80); calcd. C 59.56, H 4.76, N 3.71; found C 59.72, H 4.94, N 3.75. FAB mass spectrum, $m/z = (-\text{FAB})$ 531 $[\text{FB}(\text{C}_6\text{F}_5)_3]$. IR (solid state): $\tilde{\nu} = 2969$ (s), 2062 (s, CO), 2011 (s, CO), 1513 (s), 1457 (vs), 1275 (s), 1088 (s), 962 (s), 750 (s), 671 (s) cm^{-1} . See Table 1 for additional spectroscopic data.

Crystallographic Studies: Data collections for **2**, **3**, **5a/3**, **7** and **9** were carried out with a Bruker APEX 2000 CCD diffractometer using graphite-monochromated Mo- K_α radiation ($\lambda = 0.71073 \text{ \AA}$). Details of the data collection, refinement and crystal data are listed in Table 6. The data were corrected for Lorentz and polarization effects and empirical absorption corrections were applied. Structure solution by direct methods and structure refinement on F^2 employed SHELXTL version 6.10.^[24] Hydrogen atoms were included in calculated positions (C–H: 0.93–0.98 \AA) riding on the bonded atom with isotropic displacement parameters set to $1.5U_{\text{eq}}(\text{C})$ for methyl H atoms and $1.2U_{\text{eq}}(\text{C})$ for all other H atoms. All non-H atoms, apart from the disordered fluorine substituents in the CF_3 groups of the anion in **7** and the disordered CO/F groups in **5a/3**, were refined with anisotropic displacement parameters. Data was also collected for **9** but did not prove stable to full anisotropic refinement (see Supporting Information).

CCDC-757375 (for **2**), -757376 (for **3**), -757377 (for **5a/3**), -757378 (for **7**) and -757379 (for **9**) contain the supplementary crystallographic data for this paper. These data can be obtained free of charge from The Director, CCDC, 12 Union Road, Cambridge CB2 1EZ, UK (Fax: +44-1223-336033; E-mail: deposit@ccdc.cam.ac.uk or www: <http://www.ccdc.cam.ac.uk>).

Acknowledgments

We acknowledge the Engineering and Physical Sciences Research Council (EPSRC) for financial support.

- [1] a) V. V. Grushin, *Acc. Chem. Res.* **2010**, *43*, 160–171; b) J. Goodman, V. V. Grushin, R. B. Larichev, S. A. Macgregor, W. J. Marshall, C. D. Roe, *J. Am. Chem. Soc.* **2009**, *131*, 4236–4238; c) V. V. Grushin, W. J. Marshall, *Organometallics* **2008**, *27*, 4825–4828; d) V. V. Grushin, W. J. Marshall, *Angew. Chem. Int. Ed.* **2002**, *41*, 4476–4479; e) V. V. Grushin, *Angew. Chem. Int. Ed.* **1998**, *37*, 994–996; f) S. L. Fraser, M. Y. Antipin, V. N. Khroustlyov, V. V. Grushin, *J. Am. Chem. Soc.* **1997**, *119*, 4769–4770; g) M. C. Pilon, V. V. Grushin, *Organometallics* **1998**, *17*, 1774–1781; h) W. J. Marshall, D. L. Thorn, V. V. Grushin, *Organometallics* **1998**, *17*, 5427–5430; i) V. V. Grushin, *Chem. Eur. J.* **2002**, *8*, 1006–1014.
- [2] D. V. Yandulov, T. N. Tran, *J. Am. Chem. Soc.* **2007**, *129*, 1342–1358.
- [3] D. A. Watson, M. Su, G. Teverovskiy, Y. Zhang, J. Garcia-Fortanet, T. Kinzel, S. L. Buchwald, *Science* **2009**, *321*, 1661–1664.
- [4] K. L. Hull, W. Q. Anani, M. S. Sanford, *J. Am. Chem. Soc.* **2006**, *128*, 7134–7135.
- [5] X. Wang, T.-S. Mei, J. Q. Yu, *J. Am. Chem. Soc.* **2009**, *131*, 7520–7521.
- [6] T. Furuya, D. Benitez, E. Tkatchouk, A. E. Strom, P. Tang, W. A. Goddard III, T. Ritter, *J. Am. Chem. Soc.* **2010**, *132*, 3793–3807.
- [7] A. Vigalok, *Chem. Eur. J.* **2008**, *14*, 5102–5108.
- [8] a) S. A. Macgregor, D. C. Roe, W. J. Marshall, K. M. Bloch, V. I. Bakhmutov, V. V. Grushin, *J. Am. Chem. Soc.* **2005**, *127*, 15304–15321; b) W. J. Marshall, V. V. Grushin, *Organometallics* **2004**, *23*, 3343–3347.
- [9] a) S. L. Chatwin, M. G. Davidson, C. Doherty, S. M. Donald, R. F. R. Jazzar, S. A. Macgregor, G. J. McIntyre, M. F. Mahon, M. K. Whittlesey, *Organometallics* **2006**, *25*, 99–110; b) S. P. Reade, D. Nama, M. F. Mahon, P. S. Pregosin, M. K. Whittlesey, *Organometallics* **2007**, *26*, 3484–3491.
- [10] a) P. Barthazy, R. M. Stoop, M. Worle, A. Togni, A. Mezzetti, *Organometallics* **2000**, *19*, 2844–2852; b) A. Mezzetti, C. Becker, *Helv. Chim. Acta* **2002**, *85*, 2686–2703; c) A. Togni, A. Mezzetti, P. Barthazy, C. Becker, I. Devillers, R. Frantz, L. Hintermann, M. Perseghini, M. Sanna, *Chimia* **2001**, *55*, 801–805; d) C. Becker, I. Kieltch, D. Broggini, A. Mezzetti, *Inorg. Chem.* **2003**, *42*, 8417–8429; e) P. Barthazy, L. Hintermann, R. M. Stoop, M. Worle, A. Mezzetti, A. Togni, *Helv. Chim. Acta* **1999**, *82*, 2448–2453.
- [11] a) K. S. Coleman, J. Fawcett, J. H. Holloway, E. G. Hope, D. R. Russell, *J. Chem. Soc., Dalton Trans.* **1997**, 3557–3562; b) S. A. Brewer, K. S. Coleman, J. Fawcett, J. H. Holloway, E. G. Hope, D. R. Russell, P. G. Watson, *J. Chem. Soc., Dalton Trans.* **1995**, 1073–1076; c) D. A. J. Harding, E. G. Hope, J. Fawcett, G. A. Solan, *J. Organomet. Chem.* **2007**, *692*, 5474–5480; d) D. A. J. Harding, E. G. Hope, G. A. Solan, J. Fawcett, *Acta Crystallogr., Sect. C* **2007**, *63*, m383–m384.
- [12] J. Fawcett, D. A. J. Harding, E. G. Hope, K. Singh, G. A. Solan, *Dalton Trans.* **2009**, 6861–6870.
- [13] a) E. Bernhardt, C. Bach, B. Bley, R. Wartchow, U. Westphal, I. H. T. Sha, B. von Ahsen, C. Wang, H. Willner, R. C. Thompson, F. Aubke, *Inorg. Chem.* **2005**, *44*, 4189–4205; b) D. Ooyama, M. Sato, *Appl. Organomet. Chem.* **2004**, *18*, 380–381; c) J. M. Goicoechea, M. F. Mahon, M. K. Whittlesey, P. G. A. Kumar, P. S. Pregosin, *Dalton Trans.* **2005**, 588–597.
- [14] W. Beck, R. Kramer, E. Lipmann, U. Nagel, K. Noiternig, M. Steimann, *Chem. Ber.* **1993**, *126*, 927–932.
- [15] a) W. Beck, K. Sunkel, *Chem. Rev.* **1988**, *88*, 1405–1421; b) A. P. Caughan Jr., Z. Dori, J. A. Ibers, *Inorg. Chem.* **1974**, *13*, 1657–1667.
- [16] a) M. Ogasawara, D. Huang, W. E. Streib, J. C. Huffman, N. Gallego-Planas, F. Maseras, O. Eisenstein, K. G. Caulton, *J. Am. Chem. Soc.* **1997**, *119*, 8642–8651; b) F. A. Cotton, J. Lu, A. Yokochi, *Inorg. Chim. Acta* **1998**, *275*, 447–452; c) G.-L. Xu, C. G. Jablonski, T. Ren, *Inorg. Chim. Acta* **2003**, *343*, 387–390.
- [17] R. V. Honeybrook, W. H. Hersh, *Inorg. Chem.* **1989**, *28*, 2869–2886.
- [18] For reviews see: a) I. Krossing, I. Raabe, *Angew. Chem. Int. Ed.* **2004**, *43*, 2066–2090; b) C. Reed, *Acc. Chem. Res.* **1998**, *31*, 133–139; c) S. H. Strauss, *Chem. Rev.* **1993**, *93*, 927–942, and references cited therein.
- [19] B. L. Haymore, J. A. Ibers, *J. Am. Chem. Soc.* **1975**, *97*, 5369–5379.
- [20] a) W. W. Dukat, J. H. Holloway, E. G. Hope, M. R. Rieland, P. J. Townson, R. L. Powell, *J. Chem. Soc., Chem. Commun.* **1993**, 1429–1430; b) J. H. Holloway, E. G. Hope, P. J. Townson, R. L. Powell, *J. Fluorine Chem.* **1996**, *76*, 105–107.
- [21] a) X. Hu, I. Castro-Rodriguez, K. Meyer, *J. Am. Chem. Soc.* **2004**, *126*, 13464–13673; b) N. Millot, C. C. Santini, B. Fenet, J.-M. Basset, *Eur. J. Inorg. Chem.* **2002**, 3328–3335, and references cited therein; c) G. Erker, *Dalton Trans.* **2005**, 1883–1890.
- [22] a) R. Taube, S. Wache, J. Sieler, *J. Organomet. Chem.* **1993**, *459*, 335–347; b) M.-C. Chen, J. A. S. Roberts, T. J. Marks, *Organometallics* **2004**, *23*, 932–935.
- [23] W. L. F. Armarego, D. D. Perrin, *Purification of Laboratory Chemicals*, Butterworth Heinemann, 4th ed., **1996**.
- [24] G. M. Sheldrick, *SHELXTL*, version 6.10, Bruker AXS, Madison, Wisconsin, USA, **2000**.

Received: April 14, 2010

Published Online: August 16, 2010

On a TiNiSi-Type Superstructure: Synthesis, Crystal and Electronic Structures of CaAgGe and Its Mn-Substituted Derivative

Siméon Ponou^{[a],†}

Dedicated to Professor Bernd Harbrecht on the occasion of his 60th birthday

Keywords: Solid-state structures / Intermetallic phases / Zintl phases / TiNiSi-type superstructure

The compound CaAgGe and its Mn-substituted derivative $\text{CaMn}_{0.07}\text{Ag}_{0.93}\text{Ge}$ were synthesized by reaction of the element mixtures at high temperature. Their structures were refined from single-crystal X-ray diffraction data. CaAgGe crystallizes in the isomorphic (i_3) superstructure of the TiNiSi type (CaCuGe type). The LMTO band structure calculations predicted the CaAgGe phase to be metallic. In addition, it appeared that the valence electron concentration is critical for the atomic ordering and the resulting superstructure. Thus, CaAgGe is one electron short per asymmetric unit, but a drastic narrowing of the electron shortage is achieved

through the more complex atomic ordering in the supercell, relative to the simple TiNiSi type subcell. This results in the formation of $\{\text{Ge}_2\}$ dumbbells in the supercell, which ascribe greater electronic flexibility to the structure. Despite the fact that CaAgGe is not a Zintl phase in the strict definition as valence balanced intrinsic semiconductor, its structural aspects and transport properties can still be understood within the Zintl concept. The formal Zintl phase $\text{Ca}_3\text{MnAg}_2\text{Ge}_3$ could be predicted from the theoretical calculations, but no significant phase width was observed experimentally in the substituted derivative $\text{Ca}_3\text{Mn}_{0.21}\text{Ag}_{2.79}\text{Ge}_3$.

1. Introduction

Understanding the driving forces behind the atomic distribution in intermetallic phases is a critical step towards the control of the atomic order in intermetallic crystal structures and, at present, this remains one of the most challenging tasks in metal research.^[1–2] In this context, equiatomic ternary phases with the formulation RTX (R = electropositive metal, T = transition metal and, X = late- or post-transition element) with the TiNiSi-type^[3] structure (an ordered ternary variant of the KHg_2 or CeCu_2 type) provide a nice playground for experimental and theoretical studies, because they crystallize with a variety of atomic ordering that often leads to various superstructures.^[4–8] The TiNiSi structural family is known for its remarkable structural and electronic flexibility as it accommodates a wide range of elements, electron counts, and geometrical features.^[4–5] For instance, assuming the Zn/Ag d^{10} as pseudocore electrons,^[9] we have in the series CaAgX the binary phase CaAg_2 ^[10] with 4 valence electrons (ve) per formula unit (fu) crystallizing with the KHg_2 structure (S.G. *Imma*) similarly to the ternary phase CaAgZn (5 ve/fu).^[11] The

same KHg_2 type was previously reported for the ternary CaAgGe (7 ve/fu) with Ag and Ge randomly distributed in the Hg site.^[12] Further, the Zintl phase CaAgSb (and CaMgGe)^[13–14] with 8 ve/fu adopts the ordered variant TiNiSi type (S.G. *Pnma*). Recently, we reported the phase $\text{CaAg}_{0.98}\text{Ge}_{1.02}$ in an isomorphic superstructure of the TiNiSi type with a tripling of the *a*-axis (i_3 , minimal isomorphic subgroup of index 3) and, an almost complete ordering of the atomic sites.^[15] The occurrence of the superstructure in this structural family is well known, like for instance EuAuGe and CaPdGe (i_2 , space group *Imm2*),^[16] YPdSi^[7] (i_2 , S.G. *Pmmm*), as well as CaCuGe (i_3 , S.G. *Pmna*) and YbAuSn (i_3 , S.G. *Imm2*), or even CaAuSn (i_5 , S.G. *Pmna*).^[6] But, the origin of the superstructure has been scarcely discussed. In fact, it is difficult to find a simple valence rule for the TiNiSi type structure when the R component is a transition metal as evidenced by bonding analysis in the MTSi series (with M = Sc, Ti, V, Cr, Mn, Fe, Co, Ni; and T = Co, Ni) by Hoffmann and co-workers.^[4] But the valence electrons concentration (vec) seems to be critical for the formation and stability of many compounds with the TiNiSi type structure especially when the electropositive metal (at Ti position) is a s-block element. Therefore, it is important to study the structure–property relationships in this class of materials in order to determine the structure directing factors and to understand the origin of the structural isomorphism. Such structural variations are usually caused by

[a] Division of Polymer and Materials Chemistry, Lund University, Box 124, 22100 Lund, Sweden
Fax: +46-46-222-4012
E-mail: Simeon.Ponou@polymat.lth.se

[†] Permanent address: Department of Chemistry, Ecole Normale Sup., B. P. 47, Yaounde, Cameroon

either varying bonding principles or valence electrons concentration, or both.

The KHg_2 -type is an orthorhombically distorted variant of the aristotyl AlB_2 .^[3] In the former, a puckering and interconnection of the 6^3 planar condensed hexagon layers results in a four-bonded three-dimensional (4b-3D) network of Hg-type atoms.^[8] The two main structural features of the 4b-3D net are large channels encapsulating the electropositive metal and atomic ladders of edge-sharing squares with locally distorted tetrahedral coordination of the atoms. In the ordered TiNiSi type structures like CaMgGe ,^[14] the Ge atoms are exclusively coordinated by Mg and vice-versa. In contrast, the atomic distribution in the isomorphic phase is markedly different. In CaCuGe , 2/3 of the atomic square-ladders have direct Cu–Cu and Ge–Ge homonuclear contacts, while the remaining 1/3 of ladders, have exclusively heteronuclear Cu–Ge bonds. Here, the occurrence of *exo*-bonded $\{\text{Ge}_2\}$ dumbbells in the superstructure is noteworthy since it implies the formation of homonuclear covalent bonds, not observed in the simple TiNiSi type subcell. With this paper we report on the synthesis and structural characterization of CaAgGe and the Mn-substituted derivative $\text{Ca}_3\text{Mn}_\delta\text{Ag}_{3-\delta}\text{Ge}_3$ ($\delta \approx 0.21$). Both phases crystallized with an isomorphic (i_3) superstructure of the TiNiSi type. The electronic band structure obtained from the LMTO method and the bonding analysis have provided some more insights on the largely documented electronic and structural flexibility of the TiNiSi type and related structures and, on the validity of the Zintl–Klemm concept, as well as on the origin of the superstructure.

2. Results and Discussion

The most relevant details of the crystal structure determination and refinement are listed in Table 4. CaAgGe and

its Mn-substitution derivative crystallize in an isomorphic superstructure (i_3) of the TiNiSi type (Pearson code oP36) with a tripling of the a -axis and, is isotypic with the Cu homologue CaCuGe .^[6] This is in contrast with a previous description of CaAgGe in the KHg_2 type with Ge and Ag mixing at Hg position.^[12] There are nine crystallographically independent atomic positions in the unit cell, all at special position (Table 1). In the Mn-substituted phase, one Ag position is mixed with a slight amount of Mn. As shown in Figure 1, the (AgGe) substructure is an orthorhombic

Table 1. Atomic coordinates and equivalent isotropic displacement parameters for CaAgGe and the Mn-substituted phase. U_{eq} is defined as one third of the trace of the orthogonalized U_{ij} tensor.

| Atom | Wyck. | x | y | z | $U_{\text{eq}}/\text{\AA}^2$ |
|--|-------|------------|-----|-----------|------------------------------|
| $\text{Ca}_3\text{Ag}_3\text{Ge}_3$ | | | | | |
| Ag1 | 4c | 0.26336(3) | 1/4 | 0.5877(1) | 0.0130(2) |
| Ag2 | 4c | 0.40425(3) | 1/4 | 0.5797(1) | 0.0132(2) |
| Ag3 | 4c | 0.06432(4) | 1/4 | 0.5824(1) | 0.0173(2) |
| Ge1 | 4c | 0.22801(5) | 1/4 | 0.9170(1) | 0.0115(3) |
| Ge2 | 4c | 0.60269(5) | 1/4 | 0.5889(1) | 0.0132(3) |
| Ge3 | 4c | 0.42677(5) | 1/4 | 0.9078(1) | 0.0114(3) |
| Ca1 | 4c | 0.5005(1) | 1/4 | 0.2813(3) | 0.0125(6) |
| Ca2 | 4c | 0.8334(1) | 1/4 | 0.2932(3) | 0.0121(4) |
| Ca3 | 4c | 0.1676(1) | 1/4 | 0.2924(3) | 0.0137(4) |
| $\text{Ca}_3\text{Mn}_{0.21}\text{Ag}_{2.79}\text{Ge}_3$ | | | | | |
| Ag1 | 4c | 0.26317(3) | 1/4 | 0.5853(1) | 0.0102(2) |
| Ag2 | 4c | 0.40386(3) | 1/4 | 0.5786(1) | 0.0103(2) |
| Ag3/Mn ^[a] | 4c | 0.06301(4) | 1/4 | 0.5792(1) | 0.0136(2) |
| Ge1 | 4c | 0.22775(4) | 1/4 | 0.9144(1) | 0.0088(2) |
| Ge2 | 4c | 0.60202(4) | 1/4 | 0.5932(1) | 0.0100(2) |
| Ge3 | 4c | 0.42641(4) | 1/4 | 0.9067(1) | 0.0102(2) |
| Ca1 | 4c | 0.5007(1) | 1/4 | 0.2849(2) | 0.0112(4) |
| Ca2 | 4c | 0.8337(1) | 1/4 | 0.2956(2) | 0.0089(3) |
| Ca3 | 4c | 0.1672(1) | 1/4 | 0.2893(2) | 0.0100(3) |

[a] 20.7(1)% Mn occupancy.

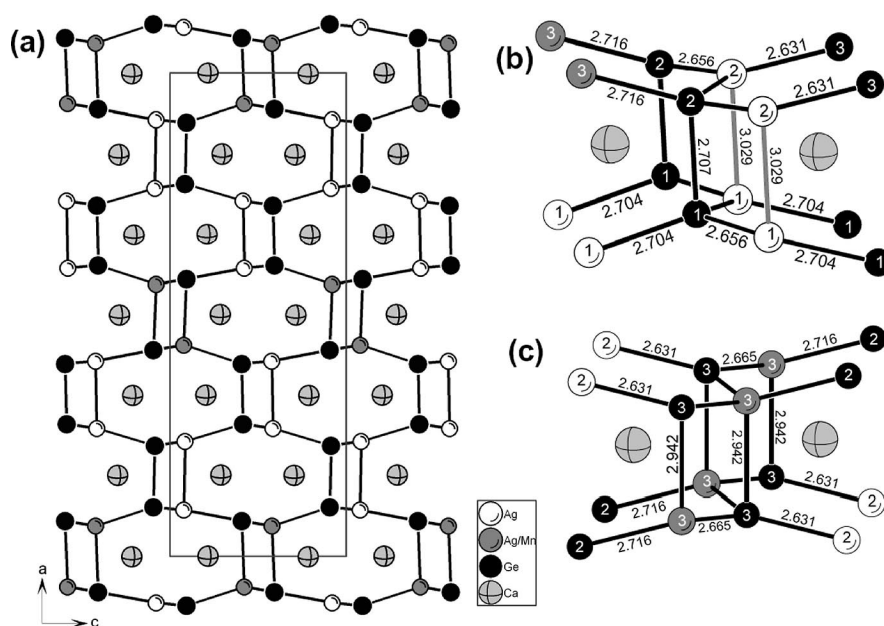


Figure 1. (a) Projection of the structure of CaAgGe and, some structural details of the two types of atomic square ladders with (b) hetero- and (c) homonuclear contacts. The atom numbers assignment is according to Table 1, and the bond length are in \AA .

four-bonded three-dimensional (4b-3D) net with distorted tetrahedral, and ladder polymers of four-membered rings. This structural class derives from the aristotyp AlB_2 through an orthorhombic distortion. Hence, the 4b-3D network is topologically constructed by puckering the two-dimensional sheets of condensed hexagons (6^3 net), running perpendicular to the a -axis, and connecting them along the a -direction to form one-dimensional ladders of edge-sharing four-membered rings, and large channels running along the b -direction. The main structural difference between superstructure of CaAgGe and the TiNiSi type subcell is the existence of two types of atomic square ladders in the former, as a result of the different layers stacking. In CaAgGe, 2/3 of the atomic square ladders show direct Ag–Ag contact (albeit quite long) and Ge–Ge bonds; and the remaining 1/3 of ladders the Ge atoms are exclusively coordinated by Ag and vice-versa, typical of the simple TiNiSi structure. Another similarity between the ladders with only heteronuclear type bonds and the TiNiSi type subcell is that the more electronegative Ge atoms, have a strongly distorted tetrahedral local coordination geometry (rather trigonal pyramidal), indicating insignificant s – p orbitals mixing. In contrast, the surrounding of the less electronegative Ag atom (mixed with Mn atoms in the substituted phase) corresponds to distorted tetrahedral coordination geometry and, may be assumed as sp^3 hybridized. Therefore, the CaAgGe structure is best described as a minimal isomorphic (i_3) superstructure of the TiNiSi type with a tripling of the subcell a -axis. Noteworthy, in the YbAuSn structure, the majority 2/3 of the atomic ladders are “hetero” type, and 1/3 “homo” type. Further comparison with YPdSi (i_2)^[7] where half of the ladders feature homonuclear contacts and the remaining half, only heteronuclear Si–Pd bonds, whereas in CaPdGe and EuAuGe (i_2)^[16] only “homo” type atomic ladders are observed. In CaAuSn (i_3)^[6] the relative fraction “homo” and “hetero” type ladders become 2/5 and 3/5, respectively. Here, the ladders with only Sn–Au hetero type contact show almost similar Sn and Au coordination geometries and, since this is more typical to the KHg_2 type structure, in that sense, the CaAuSn structure may be viewed as an ordered isomorphic superstructure of the KHg_2 type with a quintupling of the subcell b -axis.

The shortest Ge–Ag distances in CaAgGe range from 2.636(1) Å to 2.724(1) Å and are comparable with the sum of the covalent radii of Ge (1.22 Å) and Ag (1.44 Å) (Table 2). Longer bond lengths are also observed with Ag3–Ge3 2.97 Å and Ge1–Ge2 2.705(2) Å in the dumbbells, both markedly longer than the sum of the Pauling’s atomic radii.^[17] These long bond lengths are found between the puckered layers in the stacking direction. The Ge1–Ge2 bond length is longer than that in the zigzag chains of CaGe ($d_{\text{Ge–Ge}} = 2.592$ Å)^[18] and, also longer than the distances observed in “isolated” Ge–Ge dumbbells, like in Ca_5Ge_3 [$d_{\text{Ge–Ge}}$ from 2.568 to 2.575(1) Å].^[19] Similar long Ge–Ge bond length of about 2.73 Å in the dumbbells was also observed in the Cu homologue CaCuGe .^[6] These longer than expected Ge–Ge and Ag–Ge distances indicate

that the interactions between the layers are somewhat weaker than *intra*-layer interactions. Also, the long Ag1–Ag2 distance [3.041(1) Å] suggests only weak interactions. Finally, the double rows of the Ca cations are located in the large channels of the anionic network with irregular octagon-like shape. These Ca atoms are quite apart from the anionic network with Ca–Ge and Ca–Ag distances ranging from 3.10 to 3.36 Å and from 3.11 to 3.65 Å, respectively. These distances are comparable with the Ca–Ge and Ca–Ag distances found in the corresponding binary phases. The inclusion of Mn atoms at the relatively low level do not induce very significant changes in the crystal data as expected from the rather similar atomic size of Ag (1.44 Å) and Mn (1.37 Å). Nevertheless, a noticeable trend into the shrinkage of the unit cell parameters and bond lengths in the substituted phase is obvious. The cell volume is reduced from 780.8 to 774 Å³ upon substitution. The most significant bond shrinkage is for the Ag3–Ge3 which is reduced by 0.016 Å (about 0.6%), for the shortest, and by 0.028 Å (0.9%) for the longest. In contrast, the longer than expected Ge1–Ge2 bond length remains essentially unchanged (2.705 in the pristine vs. 2.707 Å in the Mn-substituted). Similarly, the other bond lengths in the anionic framework are also almost unchanged.

Table 2. Selected interatomic distances.

| Atom pairs | Distance /Å | |
|------------------------|-------------------------------------|----------------|
| | $\text{Ca}_3\text{Ag}_3\text{Ge}_3$ | Mn-substituted |
| Ag1–Ge1 ($\times 2$) | 2.665(1) | 2.656(1) |
| Ag1–Ge1 | 2.709(1) | 2.704(1) |
| Ag1–Ag2 | 3.041(1) | 3.029(1) |
| Ag2–Ge3 | 2.636(1) | 2.631(1) |
| Ag2–Ge2 ($\times 2$) | 2.654(1) | 2.656(1) |
| Ag3–Ge3 ($\times 2$) | 2.681(1) | 2.665(1) |
| Ag3–Ge2 | 2.724(1) | 2.716(1) |
| Ag3–Ge3 | 2.970(1) | 2.942(1) |
| Ge1–Ge2 | 2.705(2) | 2.707(1) |
| Ca1–Ag3 ($\times 2$) | 3.110(2) | 3.117(1) |
| Ca1–Ge3 ($\times 2$) | 3.153(2) | 3.154(1) |
| Ca1–Ag3 | 3.184(2) | 3.167(2) |
| Ca1–Ag2 ($\times 2$) | 3.268(1) | 3.253(1) |
| Ca1–Ge3 | 3.350(2) | 3.350(2) |
| Ca1–Ge2 ($\times 2$) | 3.355(1) | 3.355(1) |
| Ca2–Ge3 | 3.104(2) | 3.080(2) |
| Ca2–Ge2 ($\times 2$) | 3.123(2) | 3.108(1) |
| Ca2–Ge1 ($\times 2$) | 3.124(2) | 3.113(1) |
| Ca2–Ge1 | 3.226(2) | 3.229(2) |
| Ca2–Ag1 ($\times 2$) | 3.239(2) | 3.230(1) |
| Ca2–Ag2 | 3.318(2) | 3.313(2) |
| Ca2–Ag3 ($\times 2$) | 3.330(2) | 3.334(1) |
| Ca2–Ag1 | 3.365(2) | 3.365(2) |
| Ca3–Ag1 ($\times 2$) | 3.175(2) | 3.167(1) |
| Ca3–Ge3 ($\times 2$) | 3.198(2) | 3.182(1) |
| Ca3–Ag2 ($\times 2$) | 3.237(2) | 3.210(1) |
| Ca3–Ge1 | 3.238(3) | 3.229(2) |
| Ca3–Ge2 | 3.321(3) | 3.326(2) |
| Ca3–Ge1 ($\times 2$) | 3.360(2) | 3.359(1) |

Electron and Bonding Requirements

The calcium atoms, as the most electropositive component of CaAgGe have most likely transferred their

two valence electrons to the $[\text{Ag}_3\text{Ge}_3]$ network. To a first approximation, the ionic formula may be written as $3\text{Ca}^{2+}[\text{Ag}_3\text{Ge}_3]^{6-}$. And, assuming that Ag atoms are cationic, the Zintl chemistry treatment,^[20] can be expressed by the formulation 3Ca^{2+} , $\{3\text{Ag}^+(1\text{b-Ge}^{3-})_2(0\text{b-Ge}^{4-})_1\}$, (0b-, 1b-, ... stand for zero- and one-bonded, ... , respectively). This leads us to a one electron deficiency per asymmetric unit. Alternatively, if we consider Ag to be acting as pseudo-main group element as discussed in many phases,^[9] since the Ag–Ag contact in the “homo” type ladders are too distant to be considered as bonding, we can write: 3Ca^{2+} , $\{(3\text{b-Ag}^{2-})_2(4\text{b-Ag}^{3-})_1(4\text{b-Ge}^0)_3\}$ resulting in again in a one electron short system per asymmetric unit. Interestingly, in the hypothetical simple TiNiSi type, CaAgGe is also one electron short per formula unit in both counting schemes which is translated into 3 electrons deficiency relative to the supercell $\text{Ca}_3\text{Ag}_3\text{Ge}_3$. Hence, we can conclude that according to the Zintl concept, the superstructure has a beneficial effect on the structure electronic stabilization as it allows a reduction of the electron shortage from 1 to 1/3 electron per formula unit relative to the simple TiNiSi structure.

More generally, many ternary equiatomic phases in the *s*–*d*–*p* system adopting the TiNiSi type may be described as electron precise phase within the Zintl concept. Indeed, $\text{CaPdSn}^{[5]}$ is a Zintl phase according to the ionic formula $\text{Ca}^{2+}\text{Pd}^{2+}\text{Sn}^{4-}$ (with purely formal charge assignment). A rare example of an ordered one electron deficient phase with the TiNiSi type is $\text{CaPdIn}^{[5]}$. But here, the implementation of the Zintl concept is complicated by the fact that the transition metal, Pd is the more electronegative element and occupied the Si position in the structure (Pd 2.20 and In 1.78 in the Pauling's scale). With these findings, it is tempting to relate the occurrence of superstructure in CaAgGe to the charge optimization. But varying bonding principles have also strong influence on the phase stability as in the case of CaPdIn . Therefore, theoretical band structure calculations have been conducted in order to gain deeper insight into the nature of the cooperative bonding in the solid, and to verify the applicability of the Zintl concept as well as to explain an eventual electronic origin of the superstructure.

Electronic Band Structure

The density of states (DOS) were calculated for CaAgGe and the homologue CaCuGe for comparison. As seen from Figure 2, the DOS curves of both phases are very similar, except the shift in the energy scale of the Ag/Cu *d*-orbitals states from the bottom to the middle of the valence band region as emphasized in the projected DOS (PDOS). These filled Ag-4*d* (or Cu-3*d*) states occur in narrow bands of essentially localized, soft-core orbitals around ca. –4 eV (or –3 eV, respectively) well below the Fermi level (E_F). In addition they are not visible in the corresponding energy section of the Ag–Ge interactions –COHP diagram (Figure 3) discussed below. Thus, in the following discussions the Ag-*d*¹⁰ will be assumed as pseudo-core electrons.^[21]

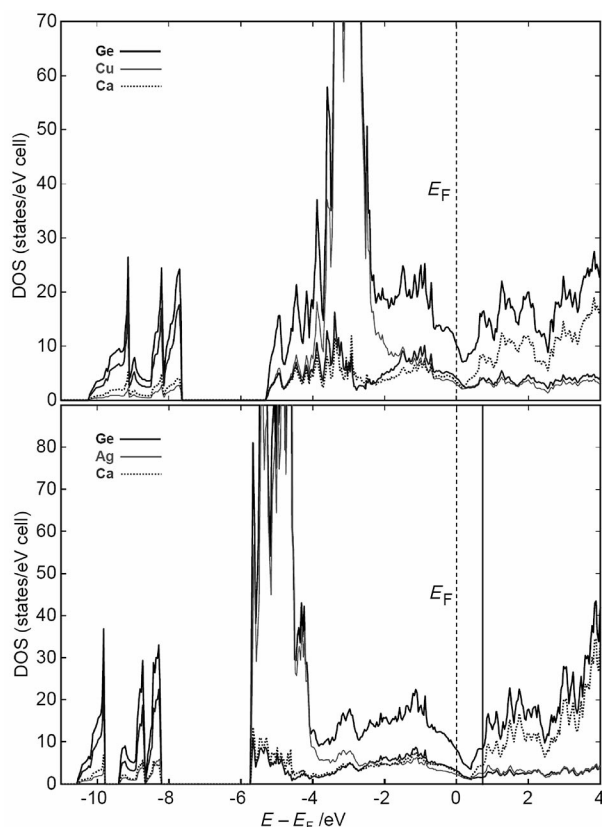


Figure 2. Total and projected DOS (see legend) of the CaAgGe (bottom): the Fermi level (dashed line) is taken as point of zero energy, and the solid above E_F corresponds to the Zintl phase (208 ve/cell). On top the DOS of the Cu homologue CaCuGe is given for comparison.

The formation of a deep pseudo-gap near (above) the Fermi level (at ca. +0.4 eV) is a sign that the atomic interactions in the systems are nearly optimized, with strong localization of the bonding electrons. Two other distinctive regions of the occupied states in the DOS plot of CaAgGe are noticeable. Firstly, the three localized bands between –8 and –11 eV below E_F which are essentially contributed from the Ge-4*s* states, with very little Ca and Ag states. Hence, the Ge-*s* orbital is basically localized at rather low energy, with negligible Ge 4*s*–4*p* orbitals mixing, in agreement with the distorted and rather trigonal coordination environment of the corresponding Ge atoms. Secondly, the region between –4 eV and the Fermi energy is contributed from Ge-4*p* orbitals as well as from a strong mixture of Ag-5*s* and Ag-5*p* orbitals, consistent with *sp*³ hybridized Ag atoms. However, in this latter portion of the DOS the Ca contributions are non negligible and, they become even higher than those of Ag-*p* orbitals, in the portion roughly between –2.5 eV and the pseudo-gap. This is mainly due to the strong overlapping of the Ca-*d* orbital states with the valence band, and this is one of the reasons why the compound is predicted to be metallic. Above the pseudo-gap, the DOS is largely dominated by Ca, while Ge and Ag have minor, but otherwise similar contributions. This is an indication of the large charge transfer between cationic and anionic

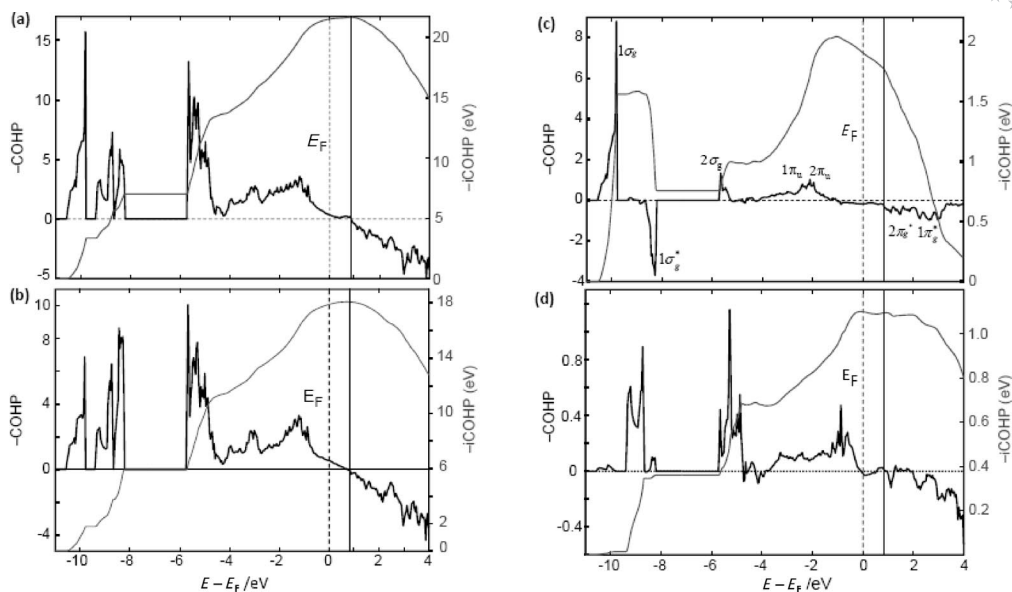


Figure 3. Calculated $-COHP$ diagrams and its integration ($-iCOHP$) for: (a) all interactions within the anionic network of CaAgGe; (b) shorter *intra-layer* bonds corresponding to interactions within the puckered 6^3 hexagons layers; (c) Ge1–Ge2 interactions, and (d) the Ag3–Ge3 longer (*out-layer*) bond. The vertical solid line above E_F marks the position of the Zintl phase limit of 208 ve/cell.

substructures. Nevertheless the respectable Ca contributions to the states below the E_F indicate non negligible covalent character in the Ca–Ge bonding interactions, though these bonds may be assumed as mainly ionic.

According to the integrated DOS (iDOS), the deep pseudo gap at ca. +0.4 eV above E_F , does not correspond to the filling of all valence bands. Indeed, we have a total of 204 ve/cell up to E_F and, 206 ve/cell up to the pseudo gap. This is lower than the expected 208 ve/cell for a charge balanced (Zintl) phase. Within the rigid band approximation, the Zintl phase will be obtained at ca. +0.90 eV above E_F . Thus, CaAgGe is an electron deficient phase, but will perhaps be charge optimized at slightly lower electron count than predicted by implementing the Zintl concept and the octet rule. It is therefore important to identify the possible unusual mechanism which is associated with the charge optimization in this open valence-shell phase and the subsequent phase stability.

In a previous analysis of the bonding in the TiNiSi type structure using the semi-empirical tight binding extended Hückel (eH) calculations, Hoffmann and co-workers^[4–5] have suggested that the bonding interactions in this family of structures should be optimized at 17 ve/fu instead of the 18 ve/fu expected from the Zintl concept and the octet rule. They attributed this unusual valence rule to the antibonding nature of the orbital interactions at the Fermi level, which originated from the electrostatic repulsion between bonding atomic pair within the featuring atomic square ladders. They concluded that the electron shortage is prompted to compensate the destabilizing effects of these antibonding interactions at E_F . For CaAgGe, so far, our analysis indicated that the charge in the supercell would apparently be optimized at 17.2 ve/fu (206 ve/cell) and, a priori this would suggest that the superstructure is not meant to stabilize the

system, since from the eH analysis the TiNiSi subcell will be charge optimized for 17 ve/fu. It is therefore important to see if the DFT calculations will lead to the same valence rule for the hypothetical TiNiSi type of CaAgGe. As represented in Figure 4, the DOS and COHP curves of the hypothetical CaAgGe with TiNiSi subcell, with the PDOS of the three different atomic components, indicates that E_F is located at relatively high DOS, and a deep energy pseudo-gap is visible at ca. +1 eV, above the Fermi level (68 ve/cell or 17 ve/fu), and corresponds to 72 ve/cell (i.e. 18 ve/fu), as expected for a Zintl phase. Thus, the electron count derived from eH calculations for some TiNiSi type is in contradiction with the results of our LMTO calculations. Moreover, the $-COHP$ diagram in the hypothetical TiNiSi subcell (Figure 4, b) for all Ag–Ge interactions indicates some significant bonding levels above E_F and, that the bonding in the anionic network will be optimized at 72 ve/cell as predicted by the Zintl concept. Therefore, the TiNiSi type subcell for CaAgGe will result in an electron deficient phase. Noteworthy, the Ag-*d* levels here are more localized than in the supercell as they form a distinct band roughly between –5.5 and –4.0 eV below E_F , without overlapping with the valence band. Most likely, the widening of the corresponding Ag-*d* band in the supercell, leading to the mixing with the valence band, is an indication of Ag-*d* orbitals contributions to the overall bonding of the system, probably as the result of the direct Ag–Ag contact in the “homo” type atomic square ladders. To validate further the assumption that the electron count for this class compounds with the TiNiSi type structure is optimized for 18 ve/fu instead of 17 ve/fu as suggested by the semi-empirical eH method, the electronic structure of the homologous Zintl phase CaAgSb was also calculated with the LMTO method. As seen in Figure 5, a very narrow energy gap is opened in the DOS

plot (Figure 5, a) at the Fermi level, while the other portions of the electronic structure remain virtually identical to that of the hypothetical TiNiSi subcell of CaAgGe with respect to their relevant aspects. Moreover, the –COHP diagram (Figure 5, b) of the all Ag–Sb interactions in the structure indicates they are optimized at E_F with typical features of covalent interactions. These confirm CaAgSb as a charged balanced phase as predicted from the Zintl concept.

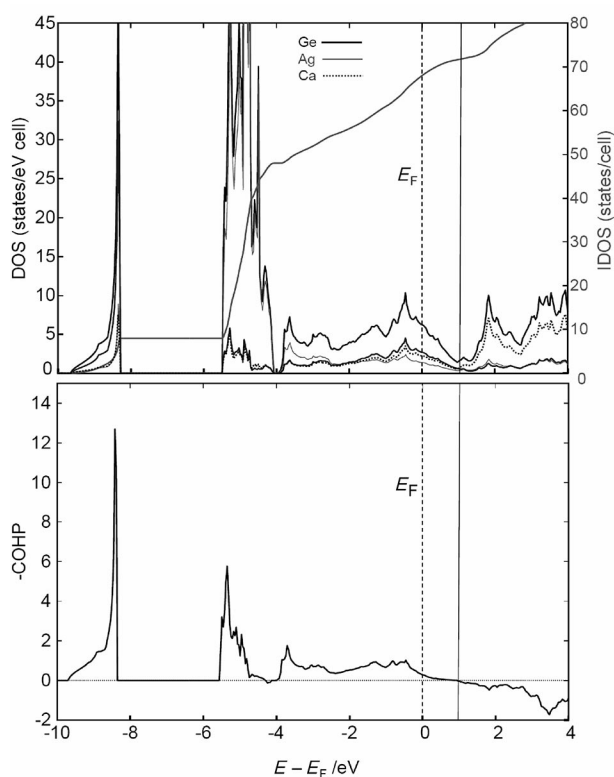


Figure 4. (a) Total and projected DOS (see legend) of the hypothetical TiNiSi subcell of CaAgGe. (b) Average –COHP diagrams of the Ag–Ge interactions in the anionic framework. The Fermi level is taken as point of zero energy. The solid line above E_F marks the position of the Zintl phase at 72 ve/cell.

The reasons why the DFT analysis differs from the eH method are yet to be thoroughly accessed, but this is very common for intermetallic systems in which the approximations of the semi-empirical method are translated in an exaggeration in the extent of the charge transfer from the cations to the anionic substructure and, corollary, in the magnitude of the antibonding interactions. The latter is weighted in the eH method by the crystal orbital overlap population Crystal orbital overlap population analysis (COOP)^[22] analogue of the COHP. Therefore, we can conclude that for CaAgGe the electron deficiency is reduced in the superstructure as opposed to the simple TiNiSi type structure, and this confirms that electronic factors are behind the occurrence of the superstructure. Nevertheless, in the latter, CaAgGe remains electron deficient (albeit to a much less extent), and the question of the phase stability is still open. At this point, it should be mentioned that several

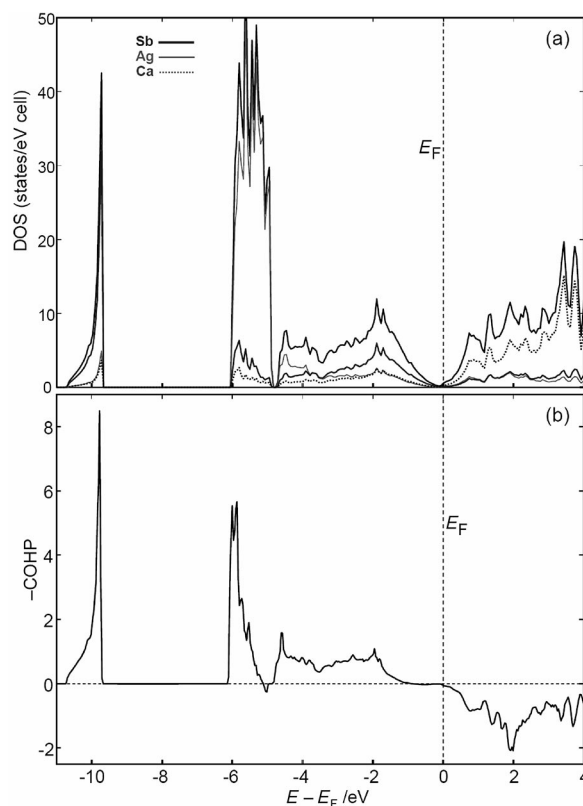


Figure 5. (a) Total DOS and PDOS (see legend) of the Zintl phase CaAgSb with the TiNiSi-type structure. (b) Average –COHP diagrams of the Ag–Sb interactions in the anionic framework.

examples of phases with an open valence-shell are reported in the literature.^[23–24] In general, such apparently electron short compounds with respect to the classical closed-shell bonding Scheme seems to develop when an interplay of other factors that govern the formation and stability of intermetallic compounds, like Madelung energy or packing efficiency, eventually overcome the usually dominant electronic effects.^[25] In some case, a judicious adjustments of the bonding characteristics are realized using the flexibility of some peculiar subunits of the structure. In the TiNiSi type, the electronic flexibility was ascribed to the antibonding states at E_F , arising from the intrinsic nature of the interactions within the atomic square ladders (vide supra).^[4–5] In addition, the ability of the anionic network to be distorted anisotropically, owing to its lower orthorhombic symmetry, is the main factor behind the geometrical flexibility. Another flexible subunit with strong ability for electronic stabilisation is the homoatomic dimer. For instance, {Sb₂} dumbbells in the series Ae₁₁Cd₆Sb₁₂ (Ae = Sr, Ba)^[26] were found to ascribe a greater flexibility to the system, critical to the stability of the phase which features unusually long Cd–Sb covalent bonds (ca. 3.55 Å). The {Ge₂} dimers and atomic square ladders are the two main features of the anionic network in CaAgGe structure. Therefore, it is worth to evaluate their respective contributions to the electronic stability of the phase. Thus, in order to investigate further the stabilizing factors of this electron short phase, a more

detailed analysis of the relative bond strength in the anionic framework were conducted using the –COHP diagram and its integration (–iCOHP). In Figure 3 (a) the –COHP curve for all interactions within the $\{\text{Ag}_3\text{Ge}_3\}$ anionic network is shown. The interactions are bonding below E_F and antibonding above ca. +0.9 eV, with an energy gap (non bonding) well above E_F and separating the two regions. These are typical features of covalent bonds, but with some unoccupied bonding states above E_F , confirming that the phase is electron deficient, and more electrons are needed to fully optimize the system. To evaluate the atomic ladders flexibility, we have to compare the bond strength within and between the puckered 6^3 layers form by the $\{\text{Ag}_3\text{Ge}_3\}$ hexagons, since their interconnection along the a -direction generates the atomic square Ladders. In Table 3 where the –iCOHP values of the most relevant interactions are summarized, it appears that all *intra*-layer bonds are strengthened, while all but one *out*-layer bonds, the Ag1–Ag2, are conversely weaken when the overall charge of the system is optimized from 204 ve/cell at E_F to 208 ve/cell. All the twelve Ag–Ge bonds of the unit cell yielded an average value of 1.813 eV/bond up to E_F . The nine *intra*-layer bonds (Figure 3, b) have an average –iCOHP value of 2.011 eV/bond, almost twice as strong as the remaining four *out*-layer bonds (Figure 3, c) where we have 1.100 eV/bond in average. These confirm that the interactions between the puckered 6^3 hexagon layers are weaker than those within them, in agreement with the bond lengths. Moreover, the –COHP curve of the Ge1–Ge2 dimers (Figure 3, d) is very typical of the molecular dumbbells with two pairs of filled, degenerate bonding and antibonding orbitals with π -character, in analogy with the I_2 molecule.^[27] The molecular orbitals may be simplified, due to the negligible mixing between the s - and p -orbitals of Ge as follows: $1\sigma_g$ $1\sigma_u^*$ $2\sigma_g$ $1\pi_u$ $2\pi_u$ $1\pi_u^*$ $2\pi_g^*$ $2\sigma_u^*$. This simplistic description is possible even though the dimers in this structure are not isolated but rather *exo*-bonded to Ag atoms. Anyway, the Ge1–Ge2 electronic structure here resembles that of an isolated Ge_2^{6-} . The –iCOHP value of 1.908 eV/bond at E_F for the Ge1–Ge2 bond indicates relatively stronger than anticipated interactions in view of the long bonding distance; but the bond is clearly non-optimized with antibonding states at E_F . In $\text{Ae}_{11}\text{Cd}_6\text{Sb}_{12}$, a quite similar electronic structure was obtained for $\{\text{Sb}_2\}$ dimer from the same –COHP analysis, but there the bond was well optimized with a clear energy gap at E_F .^[26] For the $\{\text{Ge}_2\}$ dimer in CaAgGe structure, the levels of the overlapping $1\pi_u^*$ and $2\pi_g^*$ molecular orbitals are shifted to the vicinity of the Fermi energy and, this together with the absence of an energy gap at E_F are most likely the result of the, significantly longer Ge–Ge distance as compared to the sum of Pauling radii. Further, at +0.9 eV above E_F where the overall bonding in the anionic framework would be optimized (i.e. 208 ve/cell), the Ge–Ge bond will be weakened to 1.753 eV/bond, meaning that an optimization of the electron count of the system is not favourable for this bond. Conversely, the Ag3–Ge3 bond is roughly optimized with 1.880 eV/bond at E_F , but some weak antibonding interactions are visible at E_F as well. But

this bond will be less sensitive to an increase of the valence electron count (Figure 3, e) since the –iCOHP value at 208 ve/cell will be 1.911 eV/bond, meaning a moderate bond strengthening. This may partly explained why the Ag/Mn mixing is observed only at Ag3 position, and why it is so limited. Thus, the $\{\text{Ge}_2\}$ dumbbells may have the greatest stabilization effect to compensate the instability generated by of the electron shortage, because of the bond strengthening as well as the large antibonding nature of the states at E_F . Indeed, the absence of an energy gap at the Fermi energy ascribes some electronic flexibility to the structure.^[28] The fact that the aliovalent Mn for Ag substitution was achieved without disturbing the structure, providing an experimental evidence of the superstructure electronic flexibility. Therefore, the overall stability of the system is realized through the achievement of the right balance between the magnitude of the antibonding interactions at E_F in the $\{\text{Ge}_2\}$ dumbbells and the destabilising effect of the electron shortage which results in non-occupied bonding states at, and above E_F . This mechanism involves a fine tuning of the bonds strength (distance) between the puckered hexagons layers represented by the Ge1–Ge2 and the longest Ag3–Ge3 bond lengths in the structure. Meanwhile, it was recently proposed that an unusual strong participation of the cations (here Ca) in the overall bonding may also help in compensating the instability arising from the electron shortage, as proposed in the $\text{Ba}_5\text{In}_4\text{Bi}_5$ structure.^[24]

Table 3. Calculated –iCOHP values of the relevant bonds in the CaAgGe.

| Atom pairs | Distance /Å | –iCOHP (/eV/bond) up to E_F | –iCOHP (/eV/bond) up to +0.9 eV |
|-------------------------|-------------|-------------------------------|---------------------------------|
| Ge1–Ge2 | 2.705 | 1.908 | 1.753 |
| Ag1–Ge1 ($\times 2$) | 2.665 | 2.032 | 2.058 |
| Ag1–Ge1 | 2.709 | 1.931 | 1.957 |
| Ag1–Ag2 | 3.041 | 0.730 | 1.196 |
| Ag2–Ge2 ($\times 2$) | 2.654 | 2.074 | 2.099 |
| Ag2–Ge3 | 2.636 | 2.149 | 2.161 |
| Ag3–Ge3 ($\times 2$) | 2.681 | 1.880 | 1.912 |
| Ag3–Ge3 | 2.969 | 1.101 | 1.095 |
| Ag3–Ge2 | 2.724 | 1.844 | 1.880 |
| all <i>intra</i> -layer | 2.636–2.724 | 1.989 | 2.011 |

Lastly, the Ag1–Ag2 bond is relatively weak as expected, with an –iCOHP value of 0.730 eV/bond, up to the Fermi energy. Above, they are some unoccupied bonding states, and it will be strengthened at 208 ve/cell to 1.1956 eV/bond. Nevertheless, the contribution of this bond to the phase stability remains negligible.

3. Conclusion

The isostructural CaAgGe and the Mn-substituted derivative adopt an isomorphic superstructure of the ubiquitous TiNiSi type with a tripling of the a -axis, as a result of a different atomic ordering compared to the subcell. The electronic band structure calculations on a DFT levels confirmed CaAgGe as a slightly electron deficient phase, as predicted by implementing the Zintl concept. But, our cal-

culations demonstrate that the superstructure may be driven by the electron shortage, since the latter is predicted to be larger in the simple TiNiSi type subcell. It is also determined that the overall phase stability is achieved through a judicious adjustments of the bonding characteristics of the peculiar subunits of the structure (dumbbells and square ladders), that have strong ability for electronic stabilisation. Further optimization of the structure could be predicted by the calculations and somewhat partially confirmed experimentally through the aliovalent Ag for Mn substitution. Nevertheless, the formally Zintl phase $\text{Ca}_3\text{MnAg}_2\text{Ge}_3$ could not be obtained perhaps because of the competitive formation of other phases. Possibly, the charge optimization according to the classical view of the valence rule will remain elusive here, because of the inherent flexibility of the pristine phase. Furthermore, when using aluminium as substituting element, we found that the superstructure is suppressed and a random Ag/Al mixing is observed in the solid solution $\text{CaAg}_{1-x}\text{Al}_x\text{Ge}$ with x close to 0.5 as expected from the Zintl concept.^[29]

4. Experimental Section

4.1. Synthesis: All manipulations of the starting materials and products were done in an argon-filled glove-box with an O_2 and H_2O level < 0.1 ppm. For the synthesis mixtures of the elements (all from ABCR GmbH, Karlsruhe, Germany) Ca (granules, 99.5%), Ag (60 μm powder, 99.9%), Ge (50 μm powder, 99.999%) and, Mn (powder, 99%+) were loaded in niobium ampoules (\varnothing 9 mm) which were sealed on both ends by arc-melting and, in turn, enclosed in evacuated fused silica tubes to protect the former from air oxidation at high temperature.

CaAgGe was obtained as a pure phase by reacting the mixture with a composition $\text{Ca}/\text{Ag}/\text{Ge} = 3:2:2$ at $1000^\circ\text{C}/4$ h followed by slow cooling to room temperature at the rate of $-6^\circ\text{C}/\text{h}$; a 50% Ca excess appears to be important to obtain large single crystals, suitable for X-ray diffraction experiments, but also to avoid the formation of by-products like CaAg_2Ge_2 (ThCr₂Si₂ type).^[3] In an attempt to prepare the charge-optimized Zintl phase $\text{Ca}_3\text{MnAg}_2\text{Ge}_3$ with 1/3 of the Ag substituted by divalent Mn, the corresponding stoichiometric mixture was used (also with 50% Ca excess) and, the previous temperature procedure was applied. This procedure yielded the phase $\text{Ca}_3\text{Mn}_{0.21(1)}\text{Ag}_{2.79(1)}\text{Ge}_3$ with lower than expected Mn content from the refinement of the data from single-crystal X-ray diffraction, and confirmed by EDS analysis. Further attempts to increase the Mn content by either larger amount of Mn in the reaction mixtures or higher reaction temperature were unsuccessful, as their resulted in roughly similar refined composition (within 3σ standard deviation) and, in the formation of other phases like the solid solution $\text{Ca}_3\text{Mn}_{0.43}\text{Ag}_{0.87}\text{Ge}_{2.70}$ ^[29] with the Sc_3NiSi_3 type^[30] and CaMnGe as the major phase.^[31] Previous endeavours to prepare the hypothetical Mg-substituted charge-balanced phase $\text{Ca}_3\text{MgAg}_2\text{Ge}_3$ were also elusive, and always produced phases with higher Mg content, $\text{CaMg}_{1-x}\text{Ag}_x\text{Ge}$ ($x < 0.15$) in the simple TiNiSi type subcell.^[32]

4.2. EDS Analysis: The single crystals of the Mn-substituted phase that were used in X-ray diffraction experiment as well as the bulk sample were analysed by the Energy Dispersive X-ray Spectroscopy (EDS) technique using a field emission scanning electron microscope (JSM-7000F, JEOL, Japan) operating at 15 kV and equipped

with an energy dispersive X-ray spectrometer (INCAx-sight, Oxford Instruments, UK). Elemental cobalt was used as standard, and corrections for atomic number, absorption, and fluorescence were applied. The analysis on several single crystals of the substituted phase confirmed the presence of all four elements with the atomic ratio $\text{Ca}/\text{Mn}/\text{Ag}/\text{Ge} = 34(1):1.0(1):34(1):31(1)$, roughly close to the refined values.

4.3. X-ray Powder Diffraction: The samples were routinely characterized by X-ray powder diffraction using an X'Pert-Pro diffractometer using $\text{Cu-K}\alpha$ radiation ($\lambda = 1.5406 \text{ \AA}$) in the 2θ range of $5\text{--}90^\circ$. The generator voltage was 45 kV and the tube current was 40 mA. The measured X-ray powder patterns of the resultant products were indexed using crystal data obtained from single crystal diffraction experiments.

4.4. Single Crystal X-ray Data: The single crystals of CaAgGe ($0.10 \times 0.08 \times 0.04 \text{ mm}$) and the Mn-substituted phase ($0.15 \times 0.12 \times 0.08 \text{ mm}$) were isolated from the crushed samples and the data were collected at 295 K on an Xcalibur3 diffractometer equipped with a CCD camera using $\text{Mo-K}\alpha$ radiation ($\lambda = 0.71073 \text{ \AA}$) from an enhanced optic X-ray tube operating at 50 kV and 40 mA, and a detector-to-crystal distance of 50 mm (Table 4). Data integration and numerical absorption correction were carried out with the *CrysAlis* software package.^[33] The space group *Pnma* was confirmed by the systematic absent reflections and successful structure refinement. The structure solution and refinement were carried out using the SHELXTL software package.^[34]

Table 4. Selective details on X-ray single crystal data collection and refinement parameters.

| Chemical formula | CaAgGe | $\text{CaMn}_{0.07(1)}\text{Ag}_{0.93(1)}\text{Ge}$ |
|-------------------------------------|---|--|
| Formula weight | 661.62 | 650.64 |
| Crystal color and habit | silver metallic rod | silver metallic rod |
| Temperature | 293(2) K | 293(2) K |
| Crystal system / space group | orthorhombic / <i>Pnma</i> (no. 62) | orthorhombic / <i>Pnma</i> (no. 62) |
| Unit cell parameters | $a = 21.581(1) \text{ \AA}$, $b = 4.5827(3) \text{ \AA}$, $c = 7.8947(5) \text{ \AA}$ | $a = 21.5244(6) \text{ \AA}$, $b = 4.5622(2) \text{ \AA}$, $c = 7.8820(3) \text{ \AA}$ |
| Unit cell volume / Z | $780.79(8) \text{ \AA}^3 / 12$ | $774.00(5) \text{ \AA}^3 / 12$ |
| density calculated | 5.63 g/cm^3 | 5.58 g/cm^3 |
| Abs. coeff. ($\text{Mo-K}\alpha$) | 20.64 mm^{-1} ($\lambda = 0.71073 \text{ \AA}$) | 20.64 mm^{-1} ($\lambda = 0.71073 \text{ \AA}$) |
| <i>F</i> (000) | 1188 | 1170 |
| Absorption correction | empirical | empirical |
| Index range | $-32 \leq h \leq 30$, $6 \leq k \leq 4$, $-10 \leq l \leq 11$ | $-31 \leq h \leq 17$, $6 \leq k \leq 6$, $-10 \leq l \leq 11$ |
| Reflections collected | 6768 ($R_\sigma = 0.0394$) | 7008 ($R_\sigma = 0.0287$) |
| Independent reflections | 1445 ($R_{\text{int}} = 0.0478$) | 1436 ($R_{\text{int}} = 0.0326$) |
| Observed refl. [$I > 2\sigma(I)$] | 876 | 932 |
| Refinement method | full-matrix least squares on F^2 | full-matrix least squares on F^2 |
| Parameters/restraints | 56/0 | 57/0 |
| Goodness-of-fit on F^2 | 1.083 | 1.085 |
| Final <i>R</i> indices | $R_1 = 0.0465$ / [$I > 2\sigma(I)$] | $R_1 = 0.0305$ / [$I > 2\sigma(I)$] |
| Final <i>R</i> indices (all data) | $wR_2 = 0.1017$ $R_1 = 0.0881$ / $wR_2 = 0.1141$ | $R_1 = 0.0521$ / $wR_2 = 0.1009$ |
| Weighting parameters ^[a] | $a = 0.0476$ | $a = 0.0472$ |
| Extinction coefficient | 0.0056(3) | 0.0060(3) |
| Residual map [$e/\text{\AA}^3$] | 1.73/−1.83 | 1.84/−1.96 |

[a] $w = 1/[\sigma^2(F_o^2) + (a \cdot P)^2 + b \cdot P]$, $P = [\max(F_o^2, 0) + 2 \times F_c^2]/3$.

Further details on the crystal structure investigations may be obtained from the Fachinformationszentrum Karlsruhe, 76344 Eggenstein-Leopoldshafen, Germany (Fax: +49-7247-808-666; E-mail: crysdata@fiz-karlsruhe.de), on quoting the depository numbers CSD-421236 for CaAgGe and CSD-421235 for CaMn_{0.07}Ag_{0.93}Ge.

4.5. Electronic Bands Structure Calculations: The electronic structures and the chemical bonding of CaAgGe, and for comparison CaCuGe, were investigated on the basis of the density-functional theory (DFT) using the tight-binding linear-muffin-tin-orbital (TB-LMTO-ASA) approach and the local-density approximation (LDA) within the program LMTO47c.^[35] The hypothetical TiNiSi type subcell for CaAgGe was also considered to access its stability and compared to that of the formally charge balanced Zintl phase CaAgSb.

The radii of the muffin-tin spheres were determined by an automatic procedure subject to a 16% overlap restriction,^[36] and no additional empty spheres were necessary. The k-space integration was performed by the tetrahedron method on a set of 280 irreducible k points and, the basis set employed was Ca-4s/(4p)/3d, Ge-4s/4p/(3d), Sb-5s/5p/(4d), and Ag-5s/5p/4d (down-folded orbitals in parentheses). The crystal orbital Hamilton population (COHP)^[37] was used for the analysis of the relative bond strength. Since the COHP is an energy partition, negative/positive values indicate bonding/antibonding interactions. The integration of the COHP (iCOHP) is used as a qualitative measure of mainly covalent bond strength between pairs of interacting atoms in the structure. The Fermi level in all figures is taken as the zero energy level, and the COHP are drawn by reversing their values with respect to the energy scale (i.e., -COHP vs. *E*). By doing this, the calculated values become negative for antibonding and positive for bonding interactions.

Acknowledgments

Financial support from the Wenner-Gren Foundation is gratefully acknowledged. The author tanks Prof. Sven Lidin for continuous supports, Dr. Kjell Jansson for assistance during the EDS analysis and, Dr. Daniel Grüner for fruitful discussions on the LMTO method.

- [1] G. J. Miller, *Eur. J. Inorg. Chem.* **1998**, 523.
- [2] G. J. Miller, C.-S. Lee, W. Choe, in: G. Meyer, D. Naumann, L. Wesemann (Eds.), *Inorganic Chemistry Highlights*, Cea, Berlin, **2002**.
- [3] Villars, P. *Pearson's Handbook of Crystallographic data for Intermetallic Phases*, **1997**.
- [4] G. A. Landrum, R. Hoffmann, J. Evers, H. Boysen, *Inorg. Chem.* **1998**, 37, 5754–5763.
- [5] G. Nuspl, K. Polborn, J. Evers, G. A. Landrum, R. Hoffmann, *Inorg. Chem.* **1996**, 35, 6922–6932.
- [6] D. Kußmann, R.-D. Hoffmann, R. Pöttgen, *Z. Anorg. Allg. Chem.* **1998**, 624, 1727–1735.
- [7] a) Yu. M. Prots', R. Pöttgen, W. Jeitschko, *Z. Anorg. Allg. Chem.* **1998**, 624, 425–432; b) B. Sendlinger, Dissertation, Ludwig-Maximilian-Universität, München, **1993**.
- [8] R.-D. Hoffmann, R. Pöttgen, *Z. Kristallogr.* **2001**, 216, 127–145.
- [9] J. Köhler, M.-H. Whangbo, *Solid State Sci.* **2008**, 10, 444–449.
- [10] L. D. Calvert, R. S. Dunsmore, L. V. Kuhi, R. S. Tse, *Acta Crystallogr.* **1957**, 10, 775–775.
- [11] M. Pani, F. Merlo, M. L. Fornasini, *Z. Kristallogr.* **2007**, 222, 218–225.
- [12] F. Merlo, M. Pani, M. L. Fornasini, *J. Alloys Compd.* **1996**, 232, 289–295.
- [13] F. Merlo, M. Pani, M. L. Fornasini, *J. Less-Common Met.* **1990**, 166, 319.
- [14] B. Eisenmann, H. Schäfer, A. Weiss, *Z. Anorg. Allg. Chem.* **1972**, 391, 241–254.
- [15] S. Ponou, S. Lidin, *Z. Kristallogr. New Cryst. Struct.* **2008**, 223, 329–330.
- [16] R. Pöttgen, *J. Mater. Chem.* **1995**, 5, 505.
- [17] L. Pauling, *The Nature of the Chemical Bond*, 3rd ed., Cornell University Press, Ithaca, NY, **1960**.
- [18] O. Schob, E. Parthe, *Acta Crystallogr.* **1965**, 19, 214–224.
- [19] a) B. Eisenmann, H. Schäfer, *Z. Naturforsch. Teil B* **1974**, 29, 460–463; b) A. E. Leon-Escamilla, J. D. Corbett, *J. Solid State Chem.* **2001**, 159, 149.
- [20] H. Schäfer, B. Eisenmann, W. Müller, *Angew. Chem. Int. Ed. Engl.* **1973**, 12, 694.
- [21] J. Köhler, M.-H. Whangbo, *Chem. Mater.* **2008**, 20, 2751–2756.
- [22] a) R. Hoffmann, *J. Chem. Phys.* **1963**, 39, 1397; b) R. Hoffmann, *Solids and Surfaces: A Chemist's View of Bonding in Extended Structures*, VCH Publishers, New York, **1988**.
- [23] a) D.-K. Seo, J. D. Corbett, *J. Am. Chem. Soc.* **2001**, 123, 4512; b) L. Chi, J. D. Corbett, *Inorg. Chem.* **2001**, 40, 3596; c) D.-K. Seo, J. D. Corbett, *J. Am. Chem. Soc.* **2000**, 122, 9621–9627.
- [24] S. Ponou, T. F. Fässler, G. Tobias, E. Canadell, A. Cho, S. C. Sevov, *Chem. Eur. J.* **2004**, 10, 3615–3621.
- [25] U. Häussermann, S. Amerioun, L. Eriksson, C.-S. Lee, G. J. Miller, *J. Am. Chem. Soc.* **2002**, 124, 4371.
- [26] S.-Q. Xia, S. Bobev, *J. Comput. Chem.* **2008**, 29, 2125–2133.
- [27] F. Hulliger, R. J. Schmelzer, *J. Solid State Chem.* **1978**, 26, 389.
- [28] a) C. Kranenberg, D. Johrendt, A. Mewis, *Z. Anorg. Allg. Chem.* **1999**, 625, 1787; b) C. Kranenberg, D. Johrendt, A. Mewis, *Solid State Sci.* **2002**, 4, 261–265.
- [29] S. Ponou, S. Lidin, to be submitted for publication.
- [30] B. Ya. Kotur, E. I. Gladyshevskii, *Sov. Phys. Crystallogr.* **1983**, 28, 271.
- [31] W. Doerrscheidt, H. Schaefer, *Z. Naturforsch. Teil B* **1976**, 31, 1050–1052.
- [32] C. Banenzoué, S. Ponou, J. N. Lambi, *Acta Crystallogr. Sect. E* **2009**, 65, i90.
- [33] Oxford Diffraction, *CrysAlis CCD and CrysAlis RED* **2006**, p171.31.2.
- [34] *SHELXTL*, version 5.1, Bruker AXS Inc., Madison, WI, **1998**.
- [35] O. Jepsen, A. Burkhardt, O. K. Andersen, *The TB-LMTO-ASA Program*, version 4.7, Max-Planck-Institut für Festkörperforschung, Stuttgart, Germany, **1999**.
- [36] O. Jepsen, O. K. Andersen, *Z. Phys.* **1995**, B97, 35.
- [37] R. Dronskowski, P. Blöchl, *J. Phys. Chem.* **1993**, 97, 8617.

Received: April 20, 2010
Published Online: July 28, 2010

Mononuclear Copper(I) Complexes Containing Redox-Active 1,2-Bis(aryl-imino)acenaphthene Acceptor Ligands: Synthesis, Crystal Structures and Tuneable Electronic Properties

Thomas Kern,^[a] Uwe Monkowius,^{*[a]} Manfred Zabel,^[b] and Günther Knör^{*[a]}

Keywords: Copper / Electronic spectra / Solvatochromism / Charge transfer

A series of pseudo-tetrahedral copper(I) complexes carrying bis(imino)acenaphthene (BIAN) ligands as acceptor subunits and various phosphane derivatives was prepared and characterized by elemental analysis, X-ray crystallography and spectroscopic techniques. The electronic spectra of the compounds are dominated by low-lying metal-to-ligand charge transfer (MLCT) transitions which could be systematically modified by different substituent patterns at the diimine acceptor subunit and by variations of the electron donating properties and bite angles of the phosphane moiety. A qualitative model based on frontier-orbital overlap arguments is

introduced to describe the observed variations in optical spectra, excited state energies, solvatochromic behaviour, charge transfer character, and extent of electronic coupling following moderate changes in orbital mixing. Due to their readily tuneable properties and the potential of the BIAN ligands to reversibly store up to four redox equivalents, these systems are of considerable interest for the development of novel multi-electron transfer photosensitizers which are based on the abundant and environmentally benign transition metal copper.

Introduction

There is currently an increasing interest in the development of novel catalyst systems based on cheap, abundant and environmentally benign metal ions. Especially, the replacement of quite expensive second- and third-row transition elements, such as the commonly employed rhenium, ruthenium, iridium, palladium or platinum coordination compounds by first-row transition metals or main group elements as catalytically active centres is gaining more and more attention.^[1–5] In this context, copper-based reagents offer an attractive alternative to complexes of the noble metals, according to their prominent role in enzymatic redox catalysis^[6,7] and to the significance of Cu-containing heterogeneous catalysts^[8,9] already used in many important technical processes.

In order to promote multi-electron transfer reactivity, which is crucially required for many permanent substrate transformation processes, individual copper centres are frequently attached to other redox-active subunits. This may be achieved by the formation of multinuclear metal complexes or by establishing an efficient coupling to organic

ligands, which are acting as electron transfer cofactors. Following this latter strategy, we have combined a mononuclear copper centre with 1,2-bis(aryl-imino)acenaphthene (Ar-BIAN) derivatives as redox-active bidentate *N*-donor chelates.^[10,11] The strong π -acceptor properties of Ar-BIAN ligands have already been successfully employed to introduce exceptionally low-lying metal-to-ligand charge transfer (MLCT) transitions in several d⁶ chlorotricarbonyl Re^I complexes,^[12] and the beneficial properties of these compounds have soon led to interesting applications such as low-band-gap sensitizers in bulk-heterojunction photovoltaic devices.^[13,14] Similar bathochromic shifts of charge transfer transitions expanding far into the visible spectral region of the solar spectrum could also be expected for the corresponding d¹⁰ Cu^I derivatives of 1,2-bis(aryl-imino)acenaphthene, which should be able to significantly improve the efficiency of new types of solar cells based on conventional copper 2,2'-bipyridine sensitizers.^[15,16] Moreover, the properties of Ar-BIAN derivatives are particularly attractive for the development of novel types of photocatalysts, since the delocalized π -electron system of these ligands has recently been demonstrated to reversibly store up to four electrons upon consecutive two-electron reductions,^[17] thus acting as a potential electron reservoir for catalytic multi-electron reactions.

Here, we report the synthesis, structural characterization and spectroscopic properties of a series of air-stable mononuclear Cu^I Ar-BIAN systems with Ar = phenyl, *p*-tolyl, *p*-methoxyphenyl or *o*-bis(isopropyl)phenyl and additional phosphane-based mono- or bidentate P, PP and PO ligands

[a] Institut für Anorganische Chemie, Johannes Kepler Universität Linz, 4040 Linz, Austria
E-mail: uwe.monkowius@jku.at
guenther.knoer@jku.at

[b] Zentrale Analytik der Universität Regensburg, Röntgenstrukturanalyse, Universitätsstr. 31, 93053 Regensburg, Germany

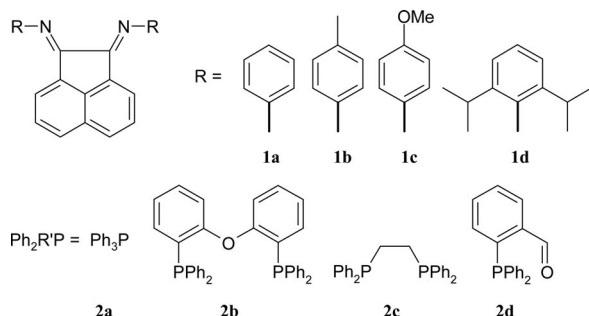
Supporting information for this article is available on the WWW under <http://dx.doi.org/10.1002/ejic.201000061>.

in the coordination sphere of the copper centre. The suitability of these systems to accumulate reduction equivalents and to act as a redox relay for catalytic applications will also be discussed in this paper.

Results and Discussion

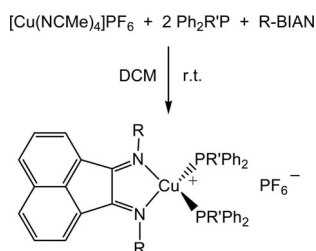
Syntheses

The series of Ar-BIAN compounds (**1a–1d**) and phosphane derivatives (**2a–2d**) studied as ligands for copper(I) in this work is summarized in Scheme 1.



Scheme 1.

Reaction of the 1,2-bis(arylimino)acenaphthene derivatives **1a–1d** with $[\text{Cu}(\text{NCCMe}_3)_4]\text{PF}_6$ as a low-valent copper precursor and different phosphane ligands in CH_2Cl_2 leads to deeply coloured compounds, which are obtained as crystalline materials upon precipitation with *n*-pentane. All metal complexes isolated were stable in the solid state with respect to air and moisture. They were characterized by elemental analysis and ^1H NMR, FTIR and ESI-MS spectroscopic methods. In the case of the heteroleptic compounds **1–3** carrying mono or bidentate phosphane ligands, red or violet crystals were formed according to the stoichiometric reaction shown in Scheme 2.



Scheme 2.

In another case, the initially expected formation of the heteroleptic Ar-BIAN phosphane derivative was incomplete, and a defined copper(I) complex **4** carrying only one phosphorus donor **2d** was obtained following the general conditions of Scheme 2. This compound could also be produced in comparable yield, when the correct 1:1 stoichiometry was applied. Surprisingly, the combinations **1c/2a** and **1a/2d** result in the formation of a product mixture in only low yields. Recrystallisation gave only a few crystals of the unintended compounds shown in Figure S1–S3 (Supporting

Information). Therefore, no further chemical analyses were performed. Interestingly, with some other substituents **R** in the Ar-BIAN ligand series, the homoleptic bis-1,2-diimine complexes were isolated as unexpected main products under the standard reaction conditions applied. These almost black compounds showed very interesting spectroscopic and redox properties, which will be presented in a separate publication.

The remarkable variety of coordination patterns of the isolated species formed by a supposedly straightforward synthetic procedure is a typical feature, which reflects the well-known lability of copper(I) phosphane complexes in solution.^[18,19] Therefore, it is important to keep in mind that the preparation of defined species requires a delicate balance and control of the reaction conditions, and that a thorough structural characterization of the products becomes necessary. On the other hand, however, this feature may be quite advantageous for potential catalytic applications of such systems, since rapid ligand exchange at a labile substrate binding site similar to the reduced forms of mononuclear “type 2” copper centres in oxidoreductases^[7] is a highly desirable feature for functional enzyme mimics and bio-inspired catalysis.^[3]

Structural Studies

Single crystals suitable for X-ray diffraction of compounds **1**, **2**, and **4** were obtained from acetonitrile/pentane. Crystals of **1** and **2** are monoclinic with $P2_1/n$ ($Z = 4$). **4** crystallizes in the monoclinic space group $P2_1/c$ ($Z = 4$) with one molecule of ethyl ether in the asymmetric unit. Characteristic bond lengths and angles are summarized in Table 1. In compounds **1** and **2**, the copper atom is coordinated by the BIAN and phosphane ligands in a distorted tetrahedral environment (see Figures 1 and 2). In analogy to other Cu^{I} complexes of **2b** there are no sub-van der Waals contacts between the oxygen atom of the phosphane ligand and the copper atom in **2**.^[20] In contrast, the copper centre in complex **4** is coordinated by the BIAN and one phosphane ligand and shows a distorted trigonal-planar coordination geometry (Figure 3). Due to the weak contacts between the copper centre and the oxygen atom of the alde-

Table 1. Bond lengths and angles of **1**, **2**, and **4**.

| Bond length [Å] | 1 | 2 | 4 |
|-----------------|----------|----------|----------|
| Cu1–N1 | 2.132(3) | 2.068(2) | 2.045(2) |
| Cu1–N2 | 2.088(3) | 2.087(2) | 2.080(2) |
| Cu1–P1 | 2.246(1) | 2.252(1) | 2.172(1) |
| Cu1–P2 | 2.280(1) | 2.224(1) | – |
| Cu1–O1 | – | – | 2.495(2) |
| Bond angles [°] | | | |
| N1–Cu1–N2 | 79.2(1) | 80.1(1) | 81.8(1) |
| P1–Cu1–P2 | 119.4(1) | 112.3(1) | – |
| P1–Cu1–O1 | – | – | 75.9(1) |
| N1–Cu1–P1 | 121.1(1) | 105.9(1) | 141.1(1) |
| N2–Cu1–P2 | 108.4(1) | 112.6(1) | – |
| N2–Cu1–P1 | 118.9(1) | 111.7(1) | 133.6(1) |
| N2–Cu1–O1 | – | – | 108.7(1) |

hyde function [Cu1–O1 2.495(2) Å] the copper atom lies out of the plane defined by the atoms N1, N2, and P1. With the exception of the Cu1–N1 distance in **1** [2.132(3) Å] all Cu–N distances are very similar (2.045–2.088 Å). Likewise, **1** and **2** exhibit similar Cu–P distances (2.224 and 2.280 Å),

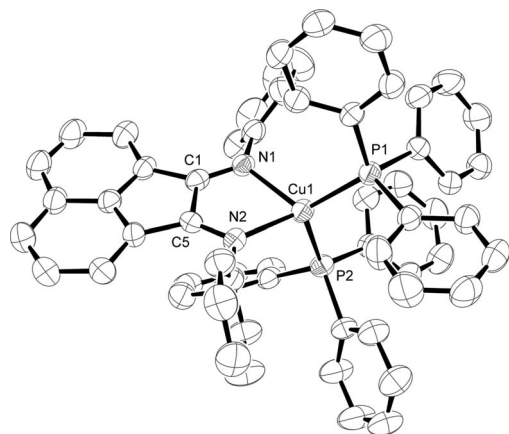


Figure 1. Complex cation in crystals of **1** (ORTEP, displacement ellipsoids at the 50% probability level).

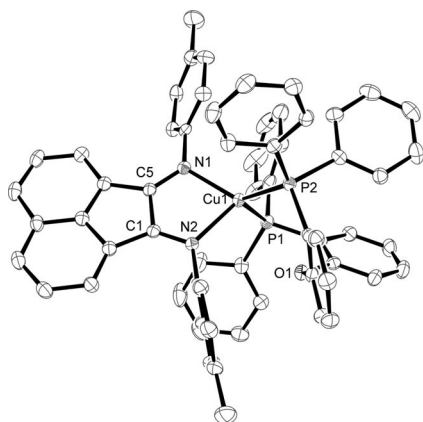


Figure 2. Complex cation in crystals of **2**.

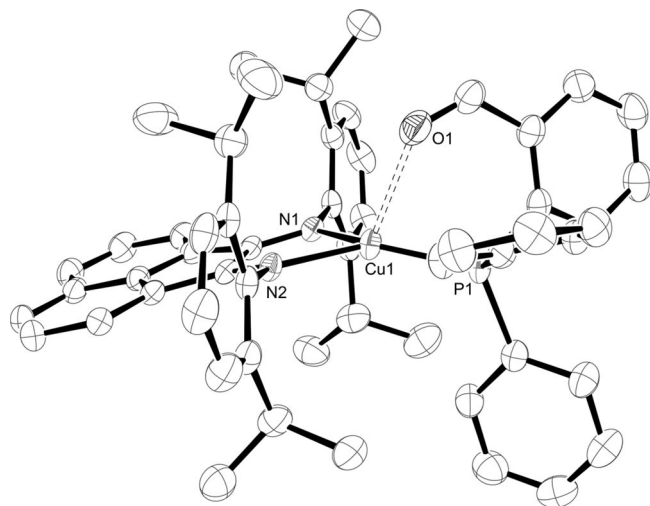


Figure 3. Complex cation in crystals of **4**.

whereas in **4** this bond is significantly shorter [Cu1–P1 2.172(1) Å]. The bite angle of the BIAN ligand lies in a narrow range [79.2(1)–81.8(1)°] comparable to other Cu–BIAN complexes.^[11] The lower steric flexibility of the chelating DPEPhos ligand **2b** leads to a smaller P–Cu–P angle in **2** compared to **1** [**1**: 119.4(1)° vs. **2**: 112.3(1)°].

Electronic Spectra

The absorption spectra of all copper(I) Ar-BIAN complexes investigated in this study display various electronic transitions below 400 nm and an additional broad chromophoric feature in the visible spectral region (Figure 4, Table 2).

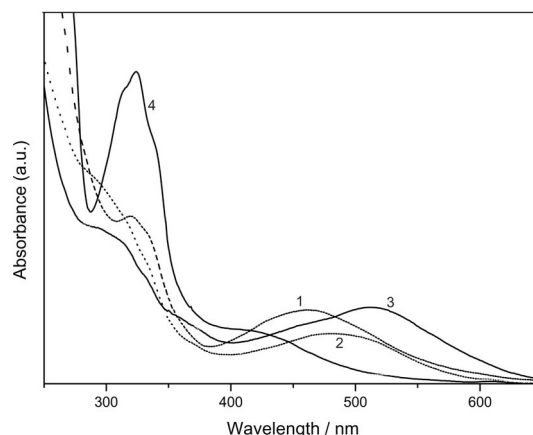


Figure 4. Electronic absorption spectra of compounds **1–4** in DCM solutions.

Table 2. UV/Vis spectroscopic data of the complexes **1–4** in DCM solution at 298 K.

| | λ_{max} [nm] (ϵ [L/(mol·cm)]) |
|----------|---|
| 1 | 461 (7400), 332 <i>sh</i> (16400), 319 (18100), 255 <i>sh</i> (45000) |
| 2 | 481 (12100), 333 <i>sh</i> (28500), 315 <i>sh</i> (40900) |
| 3 | 518 (6800), 310 <i>sh</i> (29800), 289 <i>sh</i> (33100) |
| 4 | 405 <i>sh</i> (7500), 340 <i>sh</i> (7400), 323 (33300), 312 <i>sh</i> (31700), 257 <i>sh</i> (62200) |

The shorter-wavelength bands are dominated by the typical structured intraligand (IL) transitions localized at the Ar-BIAN π -electron system,^[12] which are only slightly shifted with respect to the corresponding UV absorptions of the free diimine ligands. The broad chromophoric visible bands are ascribed to metal-to-ligand charge transfer (MLCT) transitions from predominately copper(I) localized d-electrons to the lowest unoccupied π^* -orbitals of the Ar-BIAN ligand.^[21] While metal centered ds- and dp-excited states may be present at higher energies, no other low-lying transitions involving the copper valence electrons are expected due to the d^{10} electronic configuration of the central metal. The phosphane moiety of the complexes also does not directly contribute to significant spectral features, since the IL bands of these subunits are covered by the more intense diimine-based $\pi\pi^*$ -transitions of the compounds.

The charge transfer assignment of the visible spectral bands of the complexes, which is in agreement with the regular spectroscopic properties of many other copper(I) diimine systems such as the extensively studied phenanthroline derivatives,^[22–24] is strongly supported by the occurrence of a conspicuous negative solvatochromism, shifting the visible absorption maxima of all compounds to higher energy with increasing solvent polarity. This characteristic effect, resulting in drastic colour changes in compounds such as **1**, can be quantified by applying different solvent polarity scales such as the empirical E^*_{MLCT} parameters^[25] (Figure 5).

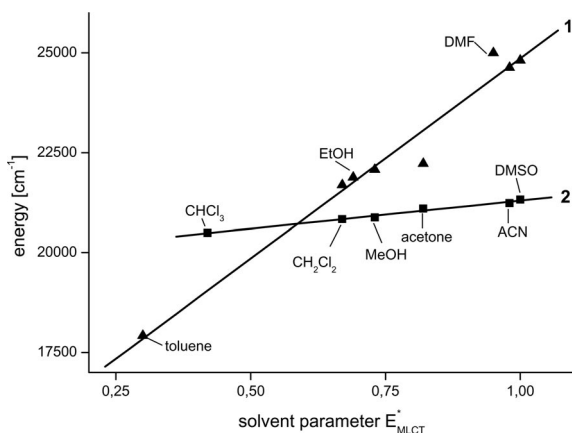


Figure 5. Correlation of the charge transfer transition energies of compounds **1** (▲) and **2** (■) with the E^*_{MLCT} values of different solvents.

A reasonably linear correlation is observed for the solvatochromic behaviour of all compounds investigated in this study, although for **1** a significant deviation from a simple polarity character of solvent interactions seems to be operative in systems containing a carbonyl group, such as DMF and acetone (Figure 5). In this context it is interesting to recall that the preparation of copper Ar-BIAN complex with the carbonyl containing phosphane ligand (compound **4**) also leads to larger deviations from the regular synthetic pathways. Therefore, it is tempting to speculate about dominant exchange equilibria between phosphane and carbonyl ligands in solution as a general property of these copper(I) compounds. This feature should be very useful for the development of catalytic cycles involving carbonyl group containing substrates, but still has to be further confirmed by a more systematic study exceeding the scope of this work.

Another support for the proposed MLCT assignment of the lowest-lying electronic transitions of the copper Ar-BIAN complexes is provided by the results of TD-DFT calculations, which clearly indicate the charge transfer character of the frontier orbital (HOMO–LUMO) transition resulting in a shift of electron density from the electron-rich copper phosphane donor moiety to the 1,2-diimine acceptor side of the molecule. The excited state with the highest calculated oscillator strength results predominately from such a transition (Figure 6, S6, and Table S2).

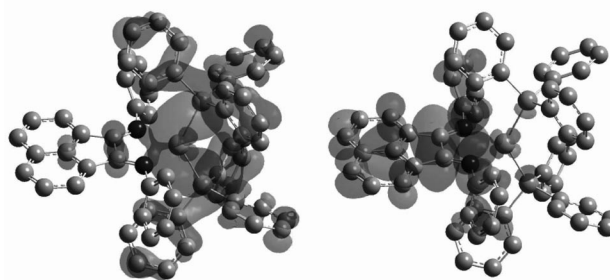


Figure 6. Contour plots of the highest occupied (left) and the lowest unoccupied molecular orbitals of complex **1** [DFT calculation at the B3LYP/6-31G(d,p) level].

It turns out that the HOMO of the heteroleptic complexes is not purely localized at the copper d-orbitals, but also carries a substantial portion of admixed phosphane ligand character, as illustrated in Figure 6. Therefore, the phosphane moiety, although spectroscopically attracting minor attention, can not only be regarded as a spectator subunit with regard to the photophysical properties, but significantly modifies the electronic structure and orbital coupling of the systems as will be described later in more detail. The LUMO predominately consists of the π -electron system of the coordinating diazabutadiene moiety ($\text{N}=\text{C}-\text{C}=\text{N}$), which is forced to stay rigid because of the aromatic acenaphthene backbone.^[10] The LUMO-energy of the ligands can be moderately influenced by variations of substituents R, which are situated in *p*-position of the non-coplanar aryl groups directly attached to the nitrogen atoms of the diazabutadiene moiety. This allows to lower the MLCT transition energies by increasing the π -acceptor strength of the Ar-BIAN system. In a certain solvent, the bathochromic shift of the charge-transfer band maximum slightly increases in the series $\text{R} = \text{OMe} < \text{Me} < \text{H} < \text{COOMe}$, which linearly correlates to the trend predictable by the Hammett σ_p parameters, as already observed before in a similar system.^[12]

A much more drastic effect on the electronic structure, however, is induced by small modifications at the phosphane moiety of the heteroleptic Ar-BIAN copper complexes. For example, the exchange of $\text{R} = \text{H}$ (**1a**) vs. Me (**1b**) at the Ar-BIAN acceptor side should induce a moderate blue-shift of approximately 500 cm⁻¹ for the MLCT transition of complex **2** relative to **1**.^[12] In contrast to this prediction, the MLCT band of **2** is actually 900 cm⁻¹ red-shifted, because the additional structural variation at the phosphane moiety overcompensates the expected effect of the methyl groups. It therefore turns out that the partially mixed copper-phosphane character of the metal-dominated donor subunit of the complexes deserves more attention for a detailed discussion of origin and properties of the lowest-lying charge transfer transitions. In Figure 7, a simplified MO picture is provided to illustrate some of the relevant interactions involving the $d\pi$ and π^* frontier orbitals of the compounds, assuming a pseudo-tetrahedral ligand sphere around the copper(I) center.

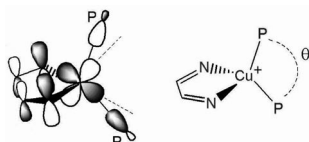


Figure 7. Metal–ligand frontier orbital overlap interactions in pseudotetrahedral copper(I) diazabutadiene complexes carrying additional P-donor ligands.

As shown in this qualitative picture, the P-localized lone-pairs of the phosphane σ -donor moiety may directly interact with one of the occupied $d\pi$ -orbitals of the copper center in a tetrahedral environment. This orbital interaction induces a destabilization of the copper(I) oxidation state and thus should lead to a decreasing excitation energy (bathochromic shift) of the corresponding MLCT transitions in heteroleptic complexes carrying 1,2-diimine acceptor ligands. According to angular orbital model considerations, the destabilization of the copper d-orbital shown in Figure 7 can be minimized by increasing the angle θ between the Cu-center and the two σ -donor ligands situated at the corners of the tetrahedron. In fact, when two individual phosphane ligands are coordinated, as is the case in compound **1**, a quite large distortion from the idealized tetrahedral geometry occurs, and the P–Cu–P angle θ reaches a value of 119.4° , which is exceeding the hypothetical rectangular arrangement corresponding to a maximum d-orbital overlap by almost 30° . In the case of compound **2**, where a P–Cu–P angle of 112.3° is imposed by the chelating bisphosphane ligand, the corresponding overlap integral should be larger due to the reduced bite angle.^[26] Therefore, the d-orbital destabilization (wavelength of the MLCT maximum) and the effects of admixed phosphane electron density are expected to be higher in **2** ($\lambda_{\text{max}} = 481 \text{ nm}$) compared to **1** ($\lambda_{\text{max}} = 461 \text{ nm}$). Within a series of phosphanes of very similar basicity, as is the case with the coordinating P atoms in the σ -donor ligands **2a** and **2b**, in fact the bite angle θ seems to be a dominant parameter for tuning the excited state energies of such types of complexes. A calculated Walsh diagram supporting such arguments is given in Figure 8: whereas the HOMO energy is pushed up with decreasing P–Cu–P angle θ the energies of the LUMOs are hardly effected upon changing of θ (Figure S8).

Besides variations in the P–Cu–P angle, larger changes of the σ -donor strength of different phosphane ligands will also lead to modifications of orbital mixing and MLCT energies, with electron rich phosphanes such as **2c** resulting in even stronger effects than decreasing bite-angles, and thus shifting the lowest-lying electronic transitions significantly to the red ($\lambda_{\text{max}} = 518 \text{ nm}$ in **3**).^[27] Removal of one of the phosphorus ligands and thus lowering the average ligand field around the copper center has the opposite effect, resulting in higher MLCT transition energies in compounds such as **4**.

While all these electronic effects discussed here certainly determine the optical properties of the compounds, another crucial frontier orbital interaction has the potential to

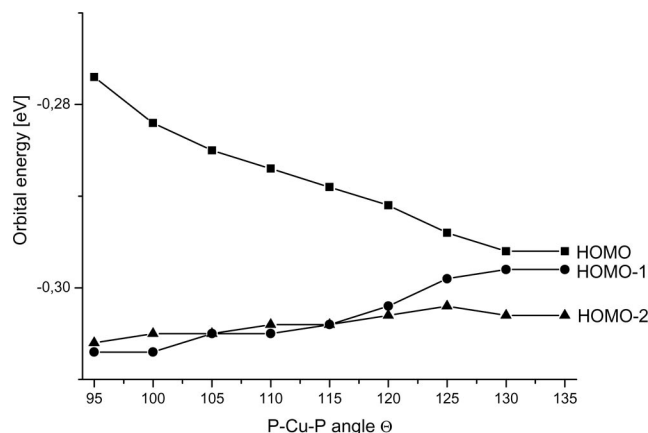


Figure 8. Walsh-diagram illustrating the effects of variable phosphane bite angles θ on the three highest occupied orbital energies of the copper complex cation $[(\text{Ph-BIAN})\text{Cu}(\text{PPh}_3)_2]^+$ obtained by single point calculations at the B3LYP/6-31G(d,p) level.

strongly influence the chromophore delocalization and therefore the actual charge transfer character of the corresponding excited states, which again will control the expected photoreactivity of the compounds. As can be seen in Figure 7, the copper $d\pi$ -orbital directly influenced by the phosphane donor moiety has the proper symmetry to interact with the π -electron system of the 1,2-diimine acceptor site. Since the N–Cu–N bite angle of the Ar-BIAN ligands (79° in **1** and 80° in **2**) is quite small and nearly approaches the 72° value of an aromatic five-membered ring such as a cyclopentadienyl anion, this π -interaction should not be neglected. In principle, for symmetry reasons, the π -orbital overlap with the copper center may only influence the HOMO–1 (ψ_1) and the LUMO (ψ_3^*) of the diazabutadiene fragment (see Figures 7 and 9), while the HOMO (ψ_2) and LUMO+1 (ψ_4^*) linear combinations remain non-bonding. The lowest unoccupied MO (ψ_3^*) of the Ar-BIAN ligand depicted in Figure 9 has the largest orbital coefficients at the nitrogen atoms directly connected to the copper(I) center.^[28] Therefore, the LUMO is predominately affected by this orbital interaction.

Whenever the electron density of the copper phosphane donor fragment is rising and the energy of the $d\pi$ -orbital is high, also the mixing with the 1,2-diimine-based LUMO becomes more pronounced. As a consequence, the MLCT states are not only red-shifted, but at the same time become more delocalized between the copper center and the Ar-BIAN acceptor side. The corresponding excited states will no longer display pure charge transfer properties and less pronounced dipole moment changes will occur between ground- and MLCT-excited states. Experimentally, this feature is drastically illustrated by the different solvatochromic behaviour of complexes **1** and **2** (Figure 5), where the less delocalized derivative **1** carrying monophosphane ligands contains the more typical charge transfer chromophore with obviously much larger electron density rearrangements occurring in the lowest excited state.

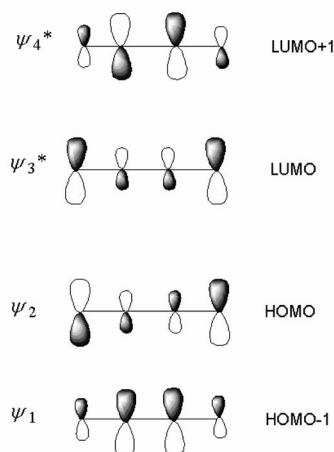


Figure 9. Approximate composition of the π -molecular orbitals of 1,4-diazabutadiene.

When such typical MLCT states with a pronounced charge transfer characteristics are populated, the transition metal center in terms of a classical radical pair model formally reaches the copper(II) oxidation state with a d^9 electron configuration. At the same time, the Ar-BIAN ligand is formally reduced by one electron to form a radical anion. According to the Jahn–Teller effect, a distortion of the pseudo-tetrahedral coordination sphere around copper(II) occurs when the molecule is relaxing from the initial Franck–Condon state to reach a significantly flattened thermally equilibrated excited state geometry.^[22] In the course of this relaxation process, the copper(II) oxidation state is stabilized and nucleophilic substrate or solvent molecules may approach the coordinatively unsaturated “axial” sites at the Cu center. In terms of the orbital interactions discussed above, it is important to note that this well-established flattening distortion occurring in the charge transfer excited state will also lead to an orbital decoupling of the donor and acceptor subunits in the compounds, since the $d\pi$ -overlap of copper with the diazabutadiene moiety shown in Figure 7 is gradually lost with an increasing distortion of the tetrahedron and should even vanish completely in a square planar system.

By comparison of the redox properties of known rhenium(I) Ar-BIAN complexes^[12] with the corresponding data available for phenanthroline-copper(I) and -rhenium(I) complexes,^[18,29] it can be predicted that the MLCT-excited copper(I) Ar-BIAN systems such as **1** should be very versatile redox reagents for photoinduced electron transfer processes in solution.^[30] Besides the possibility of back-electron transfer re-forming the copper(I) ground state species, the decoupled 1,2-diimine radical anion subunit of the MLCT excited species might for example further react in a secondary electron transfer process by reductive quenching involving a donor substrate. This type of reaction, which is expected to be favoured due to a low reorganization energy, should then result in the formation of the diamagnetic Ar-BIAN²⁻ dianion^[17,29] in the coordination sphere of copper and thus could store two reduction equivalents on an elec-

tronically decoupled acceptor ligand. Such a process is extremely useful for the development of photocatalytic systems suitable for multi-electron transfer reactions similar to the ones involving biologically relevant organic redox cofactors such as hydroquinones, NADH or reduced flavines, which have evolved in natural systems as efficient redox relays for the prevention of free radical product formation and undesired catalyst degradation processes.

Of course, this ideal situation for photoredox reactivity gradually changes in the more delocalized MLCT cases occurring in compounds such as **3**, where the formal copper oxidation states are less settled and coupling between the copper center and the Ar-BIAN ligand might be dominant also in the excited states due to the larger orbital interactions. As a consequence, besides the differences in solvatochromic features also the structural changes following the MLCT excitation should be less pronounced in this case. Such drastic differences in excited state distortion are well-known to strongly influence the luminescence properties and photochemical reactivity of other copper 1,2-diimine complexes.^[22] A systematic study, which is certainly necessary to further support all the basic concepts developed in the present work is currently underway.

Conclusions

Pseudo-tetrahedral copper(I) complexes carrying bis-(imino)acenaphthene ligands are versatile new photosensitizers with rather low-lying metal-to-ligand charge transfer (MLCT) states which are expected to be suitable for photoredox processes. Their electronic properties can be systematically modified by different substituents at the diimine acceptor subunit and by variations of the electron donating properties and bite angles of the phosphane moiety. Especially, the delocalization between central metal and the ligands is quite sensitive to minor structural distortions at the phosphane ligand site and thus can be exploited to dictate excitation energies, solvatochromism, charge transfer reactivity and the stability of the copper(I) oxidation state in these complexes. The suitability of such systems for the accumulation of reduction equivalents and to act as a multi-electron redox reagent for catalytic applications seems very promising. Therefore, such copper-based systems may become an attractive alternative to classical photosensitizers such as ruthenium polypyridine complexes in the context of typical applications such as dye-sensitized solar cells or photocatalytic redox reactions.

Experimental Section

General Methods: All chemicals were purchased in reagent-grade quality and directly used as received. Unless otherwise stated, commercially available organic solvents of standard quality were purified and dried according to the accepted general procedures. Elemental analyses were performed at the Centre for Chemical Analysis of the Faculty of Natural Sciences of the University of Regensburg. Electronic absorption spectra were recorded with a Cary 300 Bio UV/Vis spectrophotometer using 1-cm quartz cells. NMR spec-

tra were recorded with a Bruker Digital Avance NMR spectrometer DPX200 (^1H : NMR 200.1 MHz; ^{13}C : 50.3 MHz; $T = 303\text{ K}$). The chemical shifts are reported in ppm relative to external standards (solvent residual peak), and coupling constants are given in Hertz. The spectra were analysed as being first order. Error of reported values: 0.01 ppm for ^1H NMR, 0.1 ppm for ^{13}C NMR and 0.1 Hz for coupling constants. The solvent used is reported for each spectrum. Mass spectra were recorded with a LCQ DECA XP Plus (ESI). Infrared spectra were recorded with a FT-IR-Spectrometer Paragon PC.

Computational Details: The Gaussian03 program was used in the calculations.^[31] Initial coordinates were taken from the corresponding X-ray crystal structure if available. All quantum-chemical calculations were carried out using a density functional theory (DFT) based method with the hybrid B3LYP^[32] functional. The 6-31G(d,p) basis set^[33] was used through the calculations, whereas for the complexed metal a LanL2DZ basis set^[34] was applied. The obtained geometries were verified to correspond to a real minimum by establishing an absence of imaginary IR frequencies. The electronic transition energies and oscillator strengths were calculated using the time-dependent density functional response theory (TD-DFT)^[35] at the B3LYP/6-31G(d',p') level.^[36] Single point energies were calculated applying the B3LYP/6-31G(d,p) method. The parameters from the optimized geometry were held fixed while the bond P–Cu–P angle θ were changed from 95–135° in intervals of 5°.

Synthesis: The preparation of all compounds described in this work was carried out according to the following general procedure: stoichiometrical amounts of $[\text{Cu}(\text{NCCH}_3)_4]\text{PF}_6$ and the phosphane ligand in 20 mL of dichloromethane were stirred at room temperature for 2 h and then combined with a solution of the Ar-BIAN ligand in 5 mL of dichloromethane. This reaction mixture was stirred for an additional hour. After this period, approximately 10 mL of *n*-pentane were added to fully precipitate the complex

formed. The product was washed with *n*-pentane, filtered and dried in vacuo.

[(Ph-BIAN)(Ph₃P)₂Cu]PF₆ (1): Reaction of $[\text{Cu}(\text{NCCH}_3)_4]\text{PF}_6$ (100 mg, 0.27 mmol) with Ph-BIAN (**1a**, 89.29 mg, 0.27 mmol) and PPh₃ (**2a**, 140.74 mg, 0.54 mmol) yielded 208.68 mg (73%) as a red powder. ^1H NMR (200 MHz, CDCl_3): $\delta = 8.19$ (d, $^3J = 8.54\text{ Hz}$, 2 H, *o*-H-An), 8.13 (d, $^3J = 7.02\text{ Hz}$, 2 H, *p*-H-An), 7.86 (dd, $^3J = 7.88\text{ Hz}$, 2 H, *p*-H-An), 7.62–7.34 (m, 40 H, Ph-H) ppm. ^{13}C NMR (50 MHz, CDCl_3): $\delta = 162.45$ (+, N=C, 2 C), 146.43 (+, N-C, 2 C), 129.36–133.38 (–, aromatic, 4 C), 130.84 (+, 6 C), 125.23 (+, 4 C) ppm. MS (ESI, $\text{MeOH}/\text{CHCl}_3$): m/z (%) = 658.28 (100) $[\text{M} - \text{PPh}_3]^+$, 436.00 (24.33) $[(\text{Ph} - \text{BIAN})\text{Cu} + \text{MeCN}]^+$, 395.20 (1.91) $[(\text{Ph} - \text{BIAN})\text{Cu}]^+$. $\text{C}_{60}\text{H}_{46}\text{CuF}_6\text{N}_2\text{P}_3$ (1065.5): calcd. C 67.64, H 4.35, N 2.63; found C 68.76, H 4.48, N 2.30. UV/Vis (CH_2Cl_2): λ (log ϵ) = 255 *sh* (4.65), 319 (4.26), 332 *sh* (4.22), 461 nm (3.87). IR (KBr): $\tilde{\nu} = 3054$ (m, =C–H), 1736 (s, C=O), 1652 (s, C=N–), 1440 (s, P–C), 1280 (s, C–N), 840 (ss, P–F) cm^{-1} .

[(Tol-BIAN)(DPEPhos)Cu]PF₆ (2): Reaction of $[\text{Cu}(\text{NCCH}_3)_4]\text{PF}_6$ (100 mg, 0.27 mmol) with Tol-BIAN (**1b**, 97.25 mg, 0.27 mmol) and DPEPhos (**2b**, 144.50 mg, 0.27 mmol) yielded 234.75 mg (79%) as a violet powder. ^1H NMR (200 MHz, CDCl_3): $\delta = 8.29$ (d, $^3J = 8.54\text{ Hz}$, 2 H, *o*-H-An), 8.13 (d, $^3J = 7.70\text{ Hz}$, 2 H, *p*-H-An), 7.58 (dd, $^3J = 7.68\text{ Hz}$, 2 H, *m*-H-An), 6.74–6.65 (m, 34 H, Ph-H), 6.30 (d, $^3J = 8.55\text{ Hz}$, 2 H, Ph-H), 2.40 (s, 6 H, Me) ppm. MS (ESI, $\text{MeOH}/\text{CHCl}_3$): m/z (%) = 962.28 (100) $[\text{M}]^+$, 601.33 (53.98) $[\text{M} - (\text{Tol-BIAN})]^+$, 642.53 (14.19) $[\text{Cu} + \text{DPEPhos} + \text{MeCN}]^+$. $\text{C}_{62}\text{H}_{48}\text{CuF}_6\text{N}_2\text{OP}_3$ (1107.5): calcd. C 67.24, H 4.37, N 2.53; found C 66.93, H 4.56, N 2.22. UV/Vis (CH_2Cl_2): λ (log ϵ) = 315 *sh* (4.61), 333 *sh* (4.46), 481 nm (4.08). IR (KBr): $\tilde{\nu} = 3054$ (m, =C–H), 1654 (s, C=N–), 1436 (s, P–C), 1280 (w, C–N), 842 (ss, P–F) cm^{-1} .

[(MeO-Ph-BIAN)(dppe)Cu]PF₆ (3): Reaction of $[\text{Cu}(\text{NCCH}_3)_4]\text{PF}_6$ (100 mg, 0.27 mmol) with MeO-Ph-BIAN (**1c**, 105.3 mg, 0.27 mmol) and dppe (**2c**, 106.9 mg, 0.27 mmol) yielded 211.83 mg

Table 3. Crystal data, data collection and structure refinement for compounds **1**, **2**, and **4**.

| | 1 | 2 | 4 |
|---|--|---|---|
| Formula | $\text{C}_{60}\text{H}_{46}\text{CuN}_2\text{P}_2\cdot\text{PF}_6$ | $\text{C}_{62}\text{H}_{48}\text{CuN}_2\text{OP}_2\cdot\text{PF}_6$ | $\text{C}_{55}\text{H}_{55}\text{CuN}_2\text{OP}\cdot\text{C}_4\text{H}_{10}\text{O}\cdot\text{PF}_6$ |
| M_w [g/mol] | 1065.50 | 1107.48 | 1073.62 |
| Crystal size [mm] | $0.28 \times 0.24 \times 0.20$ | $0.22 \times 0.18 \times 0.12$ | $0.32 \times 0.29 \times 0.11$ |
| Crystal system | monoclinic | monoclinic | monoclinic |
| Space group | $P2_1/n$ | $P2_1/n$ | $P2_1/c$ |
| a [Å] | 15.262(12) | 14.395(10) | 15.4477(1) |
| b [Å] | 17.002(16) | 17.457(10) | 18.3784(1) |
| c [Å] | 20.145(18) | 21.240(2) | 19.3020(1) |
| α [°] | 90 | 90 | 90 |
| β [°] | 8.65(10) | 94.68(9) | 98.518(1) |
| γ [°] | 90 | 90 | 90 |
| V [Å ³] | 5168.1(8) | 5319.64(7) | 5419.47(6) |
| ρ_{ber} [mg cm ^{−3}] | 1.369 | 1.383 | 1.316 |
| Z | 4 | 4 | 4 |
| μ [mm ^{−1}] | 0.579 | 1.982 | 1.662 |
| T [K] | 296(1) | 123 | 123 |
| θ range [°] | 2.57–26.94 | 3.28–62.24 | 2.89–62.21 |
| λ [Å] | 0.71073 | 1.54184 | 1.54184 |
| Reflections collected | 70487 | 25805 | 71918 |
| Unique reflections | 11172 [$R(\text{int}) = 0.1468$] | 8146 [$R(\text{int}) = 0.0273$] | 8517 [$R(\text{int}) = 0.0398$] |
| Observed reflections [$I > 2\sigma(I)$] | 4427 | 6201 | 6579 |
| Data/restraints/parameters | 11172/0/649 | 8146/0/679 | 8517/0/659 |
| Absorption correction | analytical | semi-empirical | semi-empirical |
| $T_{\text{min.}}, T_{\text{max.}}$ | 0.9212, 0.7981 | 1.00000, 0.77370 | 1.00000, 0.59687 |
| $\sigma_{\text{fin.}}$ (max/min) [e Å ^{−3}] | 0.425/−0.252 | 0.707/−0.475 | 0.896/−0.394 |
| R_1 [$I \geq 2\sigma(I)$] | 0.0477 | 0.0369 | 0.0394 |
| wR_2 | 0.1060 | 0.1015 | 0.1165 |

(79%) as a red powder. ^1H NMR (200 MHz, CDCl_3): δ = 8.62 (d, 3J = 8.02 Hz, 2 H, *o*-H-An), 6.84–7.49 (m, 32 H, Ph-H), 3.93 (s, 6 H, Me), 2.39 (t, 3J = 5.32 Hz, 4 H) ppm. ^{13}C NMR (50 MHz, CDCl_3): δ = 24.94 (+, dd, $^2J_{\text{CP}}$ = 18.95 Hz; 2 C), 55.30 (–, 2 C), 114.53 (–, 4 C), 131.87 (–, dd, J = 7.95 Hz, Ph), 131.41 (+, Ph), 130.75 (+, Ph), 130.46 (–, Ph), 128.69 (–, m, Ph), 127.82 (–, Ph), 124.08 (–, Ph), 158.42 (–, 2 C) ppm. $\text{C}_{52}\text{H}_{44}\text{CuF}_6\text{N}_2\text{O}_2\text{P}_3$ (999.39): calcd. 62.50, H 4.44, N 2.80; found C 61.97, H 4.09, N 2.68. UV/Vis (CH_2Cl_2): λ (log ϵ) = 289 *sh* (4.52), 310 *sh* (4.47), 518 nm (3.83). IR (KBr): $\tilde{\nu}$ = 3052 (m, C–H), 1638 (s, C=N–), 1446 (s, P–C), 1295 (s, C–N), 1246 (s, C–O), 839 (ss, P–F) cm^{-1} .

[(iPr₂-Ph-BIAN)(PCHO)Cu]PF₆ (4): Reaction of $[\text{Cu}(\text{NCCH}_3)_4]\text{PF}_6$ (100 mg, 0.27 mmol) with Pr₂-Ph-BIAN (**1d**, 134.3 mg, 0.27 mmol) and PCHO (**2d**, 140.7 mg, 0.54 mmol) yielded 168.95 mg (63%) of a brown powder. ^1H NMR (200 MHz, CDCl_3): δ = 9.67 (s, 1 H, CHO), 8.21 (d, 3J = 8.14 Hz, 2 H, *o*-H-An), 7.93–7.99 (m, 1 H), 7.77 (dd, 3J = 7.64 Hz, 1 H), 7.16–7.62 (m), 6.97 (m, 4 H), 6.86 (d, 3J = 7.17 Hz, 2 H), 3.07 (sept, 3J = 6.68 Hz, Me₂C–H), 1.26 (br., 1 H, Me), 0.93 (br., 23 H, Me) ppm. $\text{C}_{55}\text{H}_{55}\text{CuF}_6\text{N}_2\text{O}_2\text{P}_3$ (999.54): calcd. C 66.09, H 5.55, N 2.80; found C 64.36, H 4.62, N 2.68. UV/Vis (CH_2Cl_2): λ (log ϵ) = 257 *sh* (4.79), 312 *sh* (4.60), 323 (4.52), 340 *sh* (3.87), 405 *sh* nm (3.88). IR (KBr): $\tilde{\nu}$ = 2959 (m, C–H), 1670 (s, C=O), 1641 (s, C=N–), 1435 (s, P–C), 1297 (s, C–N), 837 (ss, P–F) cm^{-1} .

Crystal Structures: Diffraction data for crystals of the compounds **1** and **8** were collected with a STOE-IPDS diffractometer^[37] with graphite-monochromated Mo- K_α radiation (λ = 0.71073 Å), whereas crystal data of **2**, **4**, **6** and **7** were collected with an Oxford Diffraction Gemini Ultra CCD diffractometer with multilayer optics and Cu- K_α radiation (λ = 1.5418 Å). Further crystallographic and refinement data can be found in Table 3 and Table S1. The structures were solved by direct methods (SIR-97)^[38] and refined by full-matrix least-squares an F^2 (SHELXL-97).^[39] The H atoms were calculated geometrically and a riding model was applied during the refinement process.

CCDC-756603 (for **1**), -756606 (for **2**) and -756601 (for **4**), contain the supplementary crystallographic data for this paper. These data can be obtained free of charge from The Cambridge Crystallographic Data Centre via www.ccdc.cam.ac.uk/data_request/cif.

Supporting Information (see also the footnote on the first page of this article): Further experimental details on synthesis, structures, and quantum chemical calculations.

Acknowledgments

Partial support of this work by the Austrian Science Fund (FWF) project P21045: “Bio-inspired Multielectron Transfer Photosensitizers”) and the European Commission (ERA Chemistry Project I316: “Selective Photocatalytic Hydroxylation of Inert Hydrocarbons”) is gratefully acknowledged.

- [1] J. Messinger, *ChemSusChem* **2009**, 2, 47.
- [2] P. Du, J. Schneider, G. Luo, W. W. Brennessel, R. Eisenberg, *Inorg. Chem.* **2009**, 48, 4952.
- [3] G. Knör, *Chem. Eur. J.* **2009**, 15, 568.
- [4] M. W. Kanan, D. G. Nocera, *Science* **2008**, 321, 1072.
- [5] H. Tributsch, *Electrochim. Acta* **2007**, 52, 2302.
- [6] Y. Lee, K. D. Karlin, in: *Concepts and Models in Bioinorganic Chemistry* (Eds.: H.-B. Kraatz, N. Metzler-Nolte), Wiley-VCH, **2006**.
- [7] M. Rolf, F. Tuczek, *Angew. Chem. Int. Ed.* **2008**, 47, 2344.
- [8] C. Ratnasamy, J. P. Wagner, *Catal. Rev.* **2009**, 51, 325.

- [9] C. L. Bracey, P. R. Ellis, G. J. Hutchings, *Chem. Soc. Rev.* **2009**, 38, 2231.
- [10] N. J. Hill, I. Vargas-Baca, A. H. Cowley, *Dalton Trans.* **2009**, 240, and references cited therein.
- [11] Some related copper(II) and dimeric copper(I) complexes carrying Ar-BIAN ligands have recently been investigated, see: a) U. El-Ayaan, A. Paulovicova, Y. Fukuda, *J. Mol. Struct.* **2003**, 645, 205; b) U. El-Ayaan, A. Paulovicova, S. Yamada, Y. Fukuda, *J. Coord. Chem.* **2003**, 56, 373; c) U. El-Ayaan, F. Murata, S. El-Derby, Y. Fukuda, *J. Mol. Struct.* **2004**, 692, 209; d) K. V. Vasudevan, M. Findlater, A. H. Cowley, *Chem. Commun.* **2008**, 1918.
- [12] G. Knör, M. Leirer, T. E. Keyes, J. G. Vos, A. Vogler, *Eur. J. Inorg. Chem.* **2000**, 749.
- [13] H. L. Wong, L. S. M. Lam, K. W. Cheng, K. Y. K. Man, W. K. Chan, C. Y. Kwong, A. B. Djurišić, *Appl. Phys. Lett.* **2004**, 84, 2557.
- [14] C. S. K. Mak, H. L. Wong, Q. Y. Leung, W. Y. Tam, W. K. Chan, A. B. Djurišić, *J. Organomet. Chem.* **2009**, 694, 2770.
- [15] T. Bessho, E. C. Constable, M. Grätzel, A. Hernandez-Redondo, C. E. Housecroft, W. Klyberg, Md. K. Nazeeruddin, M. Neuburger, S. Schaffner, *Chem. Commun.* **2008**, 3717.
- [16] E. C. Constable, A. Hernandez-Redondo, C. E. Housecroft, M. Neuburger, S. Schaffner, *Dalton Trans.* **2009**, 6634.
- [17] I. Fedushkin, A. A. Sakatova, V. K. Cherkasov, V. A. Chudakova, S. Dechert, M. Hummert, H. Schuhmann, *Chem. Eur. J.* **2003**, 9, 5778.
- [18] For monodentate copper(I) phosphane complexes see: S. J. Lipard, J. J. Mayerle, *Inorg. Chem.* **1972**, 11, 753, and references cited therein.
- [19] For bidentate phosphane-copper(I) complexes, see: S. Berners-Price, R. K. Johnson, C. K. Mirabelli, L. F. Faucette, F. L. McCabe, P. J. Sadler, *Inorg. Chem.* **1987**, 26, 3383, and references cited therein.
- [20] U. Monkowius, S. Ritter, B. König, M. Zabel, H. Yersin, *Eur. J. Inorg. Chem.* **2007**, 4597; U. Monkowius, Y. N. Svartsov, M. Zabel, H. Yersin, *Inorg. Chem. Com.* **2007**, 10, 1473.
- [21] It is well known that heteroleptic diimine-phosphane Cu^I complexes of the type $[(\text{NN})\text{CuP}_2]^+$ undergo ligand scrambling reactions in solution forming the species $[(\text{NN})_2\text{Cu}]^+$ and $[\text{CuP}_n]^+$. Under our experimental conditions we rule out the presence of such complexes. The homoleptic cations $[(\text{NN})_2\text{Cu}]^+$ feature an absorption band at longer wavelength. This and further results will be presented separately.
- [22] a) O. Horváth, K. L. Stevenson, *Charge Transfer Photochemistry of Coordination Compounds*, VCH, New York, **1993**, p. 45; b) S. Sakaki, H. Mizutani, Y.-i. Kase, *Inorg. Chem.* **1992**, 31, 4575.
- [23] D. R. McMillin, K. M. McNett, *Chem. Rev.* **1998**, 98, 1201.
- [24] a) N. Armaroli, G. Accorsi, F. Cardinali, A. Listorti, *Top. Curr. Chem.* **2007**, 280, 69; b) N. Armaroli, G. Accorsi, G. Bergamini, P. Ceroni, M. Holler, O. Moudam, C. Duhayon, B. Delavaux-Nicot, F. Nierengarten, *Inorg. Chim. Acta* **2007**, 360, 1032.
- [25] D. M. Manuta, A. J. Lees, *Inorg. Chem.* **1983**, 22, 3825.
- [26] T. A. Albright, J. K. Burdett, M.-H. Whangbo, *Orbital Interactions in Chemistry*, Wiley, New York, **1985**, p. 9.
- [27] Note that the presence of a methoxy group in complex **3** makes the Ar-BIAN ligand a less favourable electron acceptor than the one in complex **2**. This effect alone should induce a blue-shift of approximately 500 cm^{-1} for the MLCT maximum instead of the observed 1500 cm^{-1} red-shift.
- [28] This can be readily derived by qualitative Hückel MO considerations for the parent system butadiene: I. Fleming, *Frontier Orbitals and Organic Chemical Reactions*, Wiley, New York, **1976**, p. 17.
- [29] a) K. Kalyanasundaram, *Photochemistry of Polypyridine and Porphyrin Complexes*, Academic Press, London, **1992**; b) S. Sakaki, H. Mizutani, Y.-i. Kase, K.-j. Inokuchi, T. Arai, T. Hamada, *J. Chem. Soc., Dalton Trans.* **1996**, 1909.

- [30] Cyclovoltammograms of **1** (DCM, Pt, 0.2 V/s) display two reversible waves at -0.67 V and -0.91 V vs. SCE ascribed to reduction processes of the Ar-BIAN ligand, and an irreversible oxidation with $E_{\text{pa}} = +1.10$ V vs. SCE tentatively assigned to the copper (I/II) redox couple. Rough estimates for the MLCT excited state redox potentials (electronic origin around 600 nm or 2.07 eV) are therefore $+1.40$ V and -0.97 V vs. SCE ($+1.64$ V and -0.73 V vs. NHE) for reductive and oxidative quenching processes, respectively.
- [31] M. J. Frisch, G. W. Trucks, H. B. Schlegel, G. E. Scuseria, M. A. Robb, J. R. Cheeseman, J. A. Montgomery Jr., T. Vreven, K. N. Kudin, J. C. Burant, J. M. Millam, S. S. Iyengar, J. Tomasi, V. Barone, B. Mennucci, M. Cossi, G. Scalmani, N. Rega, G. A. Petersson, H. Nakatsuji, M. Hada, M. Ehara, K. Toyota, R. Fukuda, J. Hasegawa, M. Ishida, T. Nakajima, Y. Honda, O. Kitao, H. Nakai, M. Klene, X. Li, J. E. Knox, H. P. Hratchian, J. B. Cross, V. Bakken, C. Adamo, J. Jaramillo, R. Gomperts, R. E. Stratmann, O. Yazyev, A. J. Austin, R. Cammi, C. Pomelli, J. W. Ochterski, P. Y. Ayala, K. Morokuma, G. A. Voth, P. Salvador, J. J. Dannenberg, V. G. Zakrzewski, S. Dapprich, A. D. Daniels, M. C. Strain, O. Farkas, D. K. Malick, A. D. Rabuck, K. Raghavachari, J. B. Foresman, J. V. Ortiz, Q. Cui, A. G. Baboul, S. Clifford, J. Cioslowski, B. B. Stefanov, G. Liu, A. Liashenko, P. Piskorz, I. Komaromi, R. L. Martin, D. J. Fox, T. Keith, M. A. Al-Laham, C. Y. Peng, A. Nanayakkara, M. Challacombe, P. M. W. Gill, B. Johnson, W. Chen, M. W. Wong, C. Gonzalez, J. A. Pople, *Gaussian 03*, Revision C.02, Gaussian, Inc., Wallingford CT, **2004**.
- [32] A. D. Becke, *Phys. Rev. A* **1988**, *38*, 3098; C. T. Lee, W. T. Yang, R. G. Parr, *Phys. Rev. B* **1988**, *37*, 785; A. D. Becke, *J. Chem. Phys.* **1993**, *98*, 5648.
- [33] R. Ditchfield, W. J. Hehre, J. A. Pople, *J. Chem. Phys.* **1971**, *54*, 724; W. J. Hehre, R. Ditchfield, J. A. Pople, *J. Chem. Phys.* **1972**, *56*, 2257; V. A. Rassolov, M. A. Ratner, J. A. Pople, P. C. Redfern, L. A. Curtiss, *J. Comput. Chem.* **2001**, *22*, 976.
- [34] P. J. Hay, W. R. Wadt, *J. Chem. Phys.* **1985**, *82*, 270; W. R. Wadt, P. J. Hay, *J. Chem. Phys.* **1985**, *82*, 284; P. J. Hay, W. R. Wadt, *J. Chem. Phys.* **1985**, *82*, 299.
- [35] R. E. Stratmann, G. E. Scuseria, M. J. Frisch, *J. Chem. Phys.* **1998**, *109*, 8218.
- [36] a) G. A. Petersson, A. Bennett, T. G. Tensfeldt, M. A. Al-Laham, W. A. Shirley, J. Mantzaris, *J. Chem. Phys.* **1988**, *89*, 2193; b) G. A. Petersson, M. A. Al-Laham, *J. Chem. Phys.* **1991**, *94*, 6081.
- [37] *Stoe IPDS software*, version 2.89, Stoe & Cie GmbH, Darmstadt, Germany, **1998**.
- [38] A. Altomare, G. Cascarano, C. Giacovazzo, A. Guagliardi, *J. Appl. Crystallogr.* **1993**, *26*, 343.
- [39] G. M. Sheldrick, *SHELXL-97*, Program for crystal structure refinement, University of Göttingen, Germany, **1997**.

Received: January 21, 2010
Published Online: July 27, 2010

Discovery and Synthetic Value of a Novel, Highly Crowded Cyclopentadienylphosphane $\text{Ph}_2\text{P-Cp}^{\text{TM}}\text{H}$ and Its Ferrocenyl-Bisphosphane dppf^{TM}

Alex R. Petrov,^[a] Michael Elfferding,^[a] Juri Möbus,^[a] Klaus Harms,^[a]
Konstantin A. Rufanov,^[a,b] and Jörg Sundermeyer^{*[a]}

Keywords: Phosphane ligands / Cyclopentadienyl ligands / Sandwich complexes / Phosphanes / Ferrocenes / Palladium complexes

Base-catalysed condensation of $\text{Ph}_2\text{P-C}_5\text{H}_5$ (**1**) with an excess of acetone leads to a fulvene-like diphenyl(4,4,6-trimethyl-4,5-dihydropentalen-2-yl)phosphane $\text{Ph}_2\text{P-C}_{11}\text{H}_{13}$ (**3**) as a product of double condensation. Carbometallation of **3** with MeLi, followed by aqueous work-up, results in formation of a new cyclopentadienylphosphane bearing a highly sterically demanding, anellated 1,1,3,3-tetramethylcyclopentane moiety (**4**, $\text{Ph}_2\text{P-Cp}^{\text{TM}}\text{H}$). It reacts with chalcogene oxidants (H_2O_2 , S_8 , Se) to form the corresponding phosphane chalcogenides $\text{Ph}_2\text{P}(=\text{X})\text{Cp}^{\text{TM}}\text{H}$, X = O (**5**), S (**6**), Se (**7**) in high yields. Quaternization of **4** with MeI gives the phosphonium salt **8** as a single isomer in high yield. Dehydrohalogenation of **8** by reaction with *n*BuLi gives Cp^{TM} -phosphonium ylide $\text{Ph}_2\text{P}(\text{Cp}^{\text{TM}})\text{Me}$ (**9**). An alternative protocol towards **9** that includes deprotonation of **8** with benzylpotassium followed by *P*-alkylation is superior and gives **9** in more than 95 % yield. Staudinger reaction of **4** with *t*BuN₃ gives only

P-amino-cyclopentadienylidenephosphorane $\text{Ph}_2\text{P}(\text{Cp}^{\text{TM}})\text{-NHtBu}$ (**10**), whereas with Me_3SiN_3 only the tautomeric *P*-imino-cyclopentadienylphosphane $\text{Ph}_2\text{P}(\text{NSiMe}_3)\text{Cp}^{\text{TM}}\text{H}$ (**11**) was isolated. Hydrolysis of **11** with wet MeCN leads to the new parent *P*-amino-cyclopentadienylidenephosphorane $\text{Ph}_2\text{P}(\text{Cp}^{\text{TM}})\text{NH}_2$ (**12**). Treatment of **4** with benzylpotassium followed by transmetalation with FeCl_2 leads to the sterically most crowded ferrocenyl-bisphosphane $[(\text{Ph}_2\text{P-Cp}^{\text{TM}})_2\text{Fe}]$ (**13**, dppf^{TM}) in high yield. Its X-ray diffraction analysis reveals an *anti*-orientation of phosphane functionalities at both cyclopentadienyl rings. However, upon reaction of dppf^{TM} with $[\text{PdCl}_2(\text{MeCN})_2]$, a constrained *syn*-orientation is achieved in the product $[(\text{dppf}^{\text{TM}})\text{PdCl}_2]$ (**14**). Halogen exchange by reaction of **14** with NaI leads to the corresponding $[(\text{dppf}^{\text{TM}})\text{PdI}_2]$ (**15**). Molecular structures of **4**, **9**, **13** and **15** have been confirmed by XRD studies.

Introduction

Cyclopentadienylphosphane ligands $[\text{R}_2\text{P}\{-\text{Cp}\}]$, $\{\text{Cp}\}$ = (non)-substituted Cp, Ind or Flu are useful building blocks, broadly applied in organometallic chemistry.^[1] As structural motive they can be found in very useful ligands such as dppf $[(\text{Ph}_2\text{P-C}_5\text{H}_4)_2\text{Fe}]$ or CTC-Q-Phos $[(\text{Ph}_5\text{C}_5)\text{Fe}\{-\text{C}_5\text{H}_4\text{P}(t\text{Bu})_2\}]$. Most frequently $\text{R}_2\text{P}\{-\text{Cp}\}$ are represented in the literature by phosphanes $\text{R}_2\text{P-C}_5\text{H}_5$ (R = Me, Ph),^[2] $\text{R}_2\text{P-C}_5\text{Me}_4\text{H}$ (R = Me,^[3] Ph^[4]), $(t\text{Bu})_2\text{P-C}_5\text{H}_5$,^[5] 3-indenyl- $(\text{Ph}_2\text{P-C}_9\text{H}_7)$ ^[6] and 9-fluorenyl- $(\text{Ph}_2\text{P-C}_{13}\text{H}_9)$,^[7] that with exception of 9-fluorenyl derivatives, show fluxional behaviour in solutions and appear as mixtures of isomers.

Commonly $\text{R}_2\text{P}\{-\text{Cp}\}$ are synthesized by nucleophilic substitution of $\text{R}_2\text{P-X}$ (X = Hal, OAlk) with anionic forms of appropriate cyclopentadienes. Nevertheless, their further derivatization is very scarcely described in the literature.^[2]

For our systematic investigation of chelating organophosphorus(V) ligands of the general type $[\text{R}_2\text{P}(\text{X})\text{Z}]^-$ (X, Z = S, NR', CH₂, CHR', Cp, Ind, Flu; as for X = Z and X ≠ Z)^[8,9] it was necessary to synthesize $\text{Ph}_2\text{P}\{-\text{Cp}\}$ phosphanes, bearing sterically demanding substituents, e.g. a *tert*-butyl group, at the C₅ ring. Besides simple metathesis of *t*BuCp anion with Ph_2PCl , such ligand motive may be achieved by carbometallation with MeLi of corresponding 6,6-dimethylfulvene that is easily accessible by a condensation of acetone with $\{\text{Cp}\}\text{H}$ using 5–10 mol-% of pyrrolidine, as a catalyst, in methanol. The reaction is highly chemoselective and, as a rule, high yields of fulvenes are reported.^[10] However, even minor changes of the reaction conditions were found to be highly crucial to its further transformation. Here we report our discovery of a new, highly crowded cyclopentadienylphosphane, $\text{Ph}_2\text{P-Cp}^{\text{TM}}\text{H}$, its reactivity and synthetic potential.

Results and Discussion

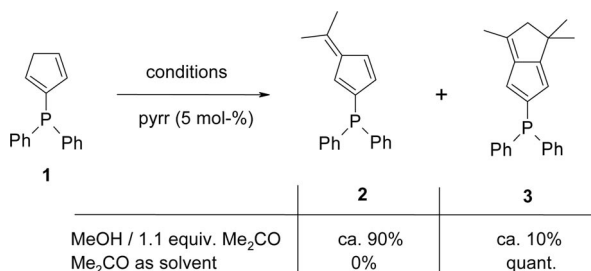
Synthesis and Molecular Structure of $\text{Ph}_2\text{P-Cp}^{\text{TM}}\text{H}$

Condensation reaction of $\text{Ph}_2\text{P-C}_5\text{H}_5$ (**1**)^[2] with one equivalent of acetone (MeOH, 10 mol-% pyrrolidine) leads

[a] Fachbereich Chemie, Philipps-Universität Marburg, Hans-Meerwein-Str., 35032 Marburg, Germany
Tel: +49-6421-2825693
E-mail: jsu@staff.uni-marburg.de

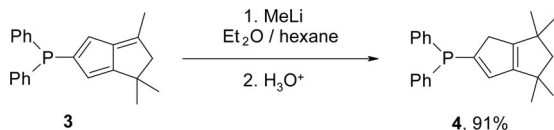
[b] Chemical Diversity Research Institute, Rabochaya 2a, Khimki, Moscow Region 141410, Russia

to the selective formation of the expected fulvenylphosphane $\text{Ph}_2\text{P-C}_8\text{H}_9$ (**2**) (Scheme 1). The product precipitates from the reaction mixture as a bright yellow, air-stable crystalline solid, ^{31}P NMR (C_6D_6): $\delta_{\text{P}} = -16.8$ ppm. Monitoring of the reaction by ^{31}P NMR spectroscopy indicated formation of ca. 10% of an unidentified impurity ($\delta_{\text{P}} = -13.9$ ppm). By working in acetone as solvent, formation of **2** was quantitative within minutes, however it was followed by conversion of **2** into this new compound **3** within 4 h as monitored by ^{31}P NMR spectroscopy. The structure and composition of thus formed $\text{Ph}_2\text{P-C}_{10}\text{H}_{13}$ (**3**) as annelated phosphane (Scheme 1) have been confirmed by multinuclear and 2D NMR spectroscopic techniques, mass spectra and elemental analysis.



Scheme 1.

Further carbometallation of **3** with MeLi in ether or hexane as solvent followed by protonation of thus derived carbanion leads to a new annelated tetramethylpentalenyl-substituted phosphane ($\text{Ph}_2\text{PCp}^{\text{TMH}}$) **4**, that, compared to its 3-*t*Bu-substituted analogue, is higher both by its steric impact and symmetry (Scheme 2). However, if the reaction with MeLi is performed in THF a deprotonation of the exocyclic fulvene methyl group of **3** rather than a carbometallation took place. Phosphane $\text{Ph}_2\text{P-Cp}^{\text{TMH}}$ (**4**) was purified by preparative flash chromatography under anaerobic conditions. This pale yellow needle-like crystalline material with a faint phosphane-like odour is fairly air-stable and can be handled and stored under aerobic conditions without decomposition for months. The solubility of **4** is very high in common organic solvents, but becomes moderate in those ones of the higher polarity (CH_3CN , MeOH) as well as in cold lower alkanes (pentane, hexane). The molecular structure of **4** was confirmed by multinuclear NMR spectroscopy, mass spectrometry, elemental and XRD single crystal structure analysis.



Scheme 2.

Crystals of the compound **4**, suitable for X-ray diffraction analysis, were obtained by slow cooling of its hot concentrated ethanol solution. It crystallizes in the monoclinic space group $P2_1/c$ with four molecules per cell unit. In the

structure the bridging H_2C -group of the aliphatic ring is disordered with occupancies of 0.49/0.51; only one conformation is shown in Figure 1. As expected, the phosphorus atom is threefold coordinated by two phenyl groups and a Cp^{TMH} -moiety – all are twisted in a propeller-like arrangement. The unsaturated Cp ring is essentially planar [$\Delta_{\text{max}} = 0.0002(2)$ Å for C8]. The C4 and C6 atoms of the aliphatic ring deviate only by values of 0.053 and 0.073(2) Å from the Cp^{TMH} -ring plane.

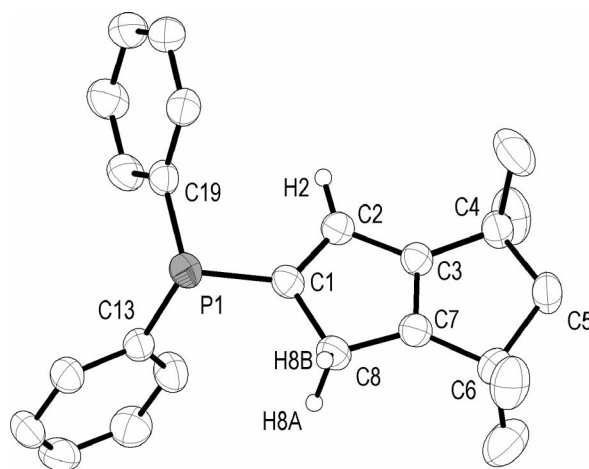
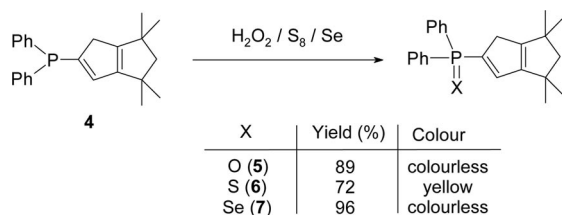


Figure 1. Molecular structure of compound **4**. All hydrogen atoms, except of those at the Cp-ring, have been omitted for clarity. Selected bond lengths [Å] and angles [°]: P1–C1 1.807(2), P1–C13 1.832(2), P1–C19 1.833(2), C1–C2 1.348(2), C2–C3 1.475(2), C3–C7 1.334(2), C7–C8 1.487(2), C1–C8 1.517(2); C1–P1–C13 103.1(1), C13–P1–C19 102.3(1), C19–P1–C1 100.7(1), C1–C8–C7 102.7(1), C3–C2–C1–C8 0.2(2), C2–C3–C7–C8 0.2(2).

The average P-C_{Ph} bond length is of 1.832(3) Å and falls in the typical range of other phosphanes Ar_3P (1.82–1.84 Å).^[11] However, the P-C1 bond length is slightly shorter [1.807(2) Å]. The olefinic bonds lengths are alternating and are shorter at C1–C2 and C3–C7 with 1.348(2) and 1.334(2) Å, respectively then other ones in the Cp ring [C2–C3 1.475(2), C7–C8 1.487(2), C1–C8 1.517(2) Å]. All C-P-C angles [100.7(1), 102.3(1) and 103.1(1) Å] lie in the typical range reported for triarylphosphanes.^[11] Although several free indenyl- and fluorenylphosphanes are known,^[12] to the best of our knowledge, **4** is the first free diorgano-cyclopentadienylphosphane characterized by X-ray crystallography.

Reactivity of $\text{Ph}_2\text{P-Cp}^{\text{TMH}}$ as Phosphane

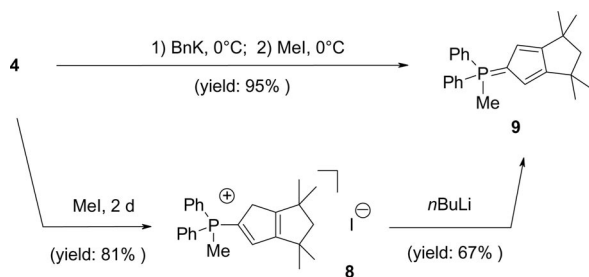
The phosphane **4** is readily oxidized by H_2O_2 (30% solution in water) in THF, elemental sulfur in toluene and red selenium in CHCl_3 to form corresponding chalcogenido phosphanes as air-stable, crystalline solids in high yields (Scheme 3).



Scheme 3.

As expected and confirmed by NMR spectroscopy, only one tautomeric form is observed for all these compounds. Steric hindrance of the tetramethyltrimethylene backbone prevents their dimerization by the Diels–Alder reaction typically found for the parent C₅-unsubstituted derivatives Ph₂P(X)C₅H₅ (X = O, S).^[2]

Quaternization of **4** with an excess of MeI leads to the expected phosphonium salt [Ph₂P(CpTMH)Me]⁺ I[−] (**8**) (Scheme 4) as an air-stable, non-hygroscopic solid, that appears as a single isomer (δ_P = 12.2 ppm). It is worth to mention, that sterically less hindered Ph₂P-Cp and Ph₂P-Ind upon reaction with MeI lead to the mixtures of allylic and vinylic isomers; for the Cp-derivative, Diels–Alder type dimerization products were also obtained.^[13,14] Dehydrohalogenation of the salt **8** with *n*BuLi leads to the formation of cyclopentadienyliden-phosphorane Ph₂P(CpTM)Me (**9**) as a pale yellow, crystalline solid in 67% yield. A superior protocol towards **9** includes deprotonation of **4** with BnK followed by in situ quaternization of thus obtained anionic derivative with an excess of MeI that chemoselectively leads to *P*-alkylation and gives **9** in almost quantitative yield.

Scheme 4. Two alternative reaction sequences toward synthesis of **9**.

Single crystals, suitable for X-ray diffraction analysis, were obtained by storing of concentrated ether solution to 0 °C. Compound **9** crystallizes in the triclinic space group *P* $\bar{1}$ with two independent molecules in the unit cell. The molecular structure of one of these molecules is drawn in Figure 2.

The P1–C1 bond length in **9** is significantly shorter [1.714(2) Å] than in parent **4**, this is in good agreement with those in other cyclopentadienylidenephosphoranes.^[15] An alternating order of C–C bond lengths at the C₅ ring was observed: the short bonds are C2–C3 and C7–C8 [1.373(3) and 1.385(3) Å], whereas C1–C2, C3–C7 and C1–C8, respectively, are long [1.425(3), 1.404(3) and 1.441(3) Å].

Earlier, we reported the Staudinger reactions of a series of R₂P–{Cp} with organic azides.^[8] Successful formation of

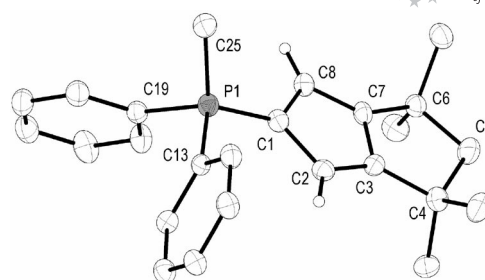
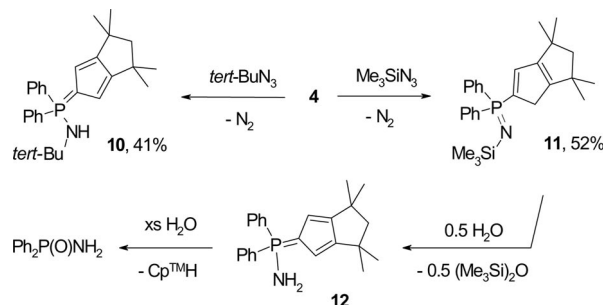


Figure 2. Molecular structure of Ph₂P(CpTM)Me (**9**). All hydrogen atoms have been omitted for clarity. Only one independent molecule is drawn. Selected bond lengths [Å] and angles [°]: P1–C1 1.714(2), P1–C13 1.803(2), P1–C19 1.802(3), P1–C25 1.795(3), C1–C2 1.425(3), C2–C3 1.373(3), C3–C7 1.404(3), C7–C8 1.385(3), C1–C8 1.441(3), C1–P1–C13 107.37(12), C13–P1–C19 106.62(11), C19–P1–C1, 113.98(13), C1–P1–C25 113.72(13), C13–P1–C25 109.15(13), C19–P1–C25 105.74(13).

the *CpPN* derivatives has been confirmed also for the entitled ligand **4** (Scheme 5). Thus reaction of **4** with *t*BuN₃ proceeds at ambient temperature yielding a yellow, microcrystalline solid as the single *P*-amino-cyclopentadienylidenephosphorane tautomer Ph₂P(CpTM)NH(*t*Bu) (**10**). The position of the NH-proton at δ = 2.04 ppm in **10** was also established by the HMQC spectroscopy. The ³¹P NMR resonance of **10** (δ = 17.1 ppm) appears essentially at the same δ_P as those ones of *CpPN*-ligands R₂P(C₅Me₄)NHAd (R = Me: 17.6 ppm,^[8] and R = Ph: 17.8 ppm^[16]). The reaction of **4** with the less reactive Me₃SiN₃ was found to be extremely slow and gave the desired product only if Me₃SiN₃ was used as a solvent at the reflux temperature (5 d, ca. 100 °C). The ³¹P NMR monitoring the reaction mixture after 14 h of heating reveals absence of both starting material **4** and its Staudinger phosphazide adduct (δ = −27 ppm) and two new resonances at ca. −5 (major) and 23 ppm (minor). The major signal appears in the characteristic *P*-iminophosphane region and belongs to the target **11**, whereas the minor signal is attributed to its tautomeric *P*-aminophosphorane form similar to **10**.^[9] **11**, the better soluble tautomer was extracted from the reaction mixture into hexane. It comprises a highly air-sensitive, crystalline solid, that easily hydrolyzes, when in solution: first, by water traces with release of (Me₃Si)₂O to *P*-amino-cyclopentadienylidenephosphorane **12**, and further by excess of water with release of free CpTMH and precipitation of a colorless, crystalline solid, identified as diphenylphosphinic

Scheme 5. Reactions of **4** with organic azides.

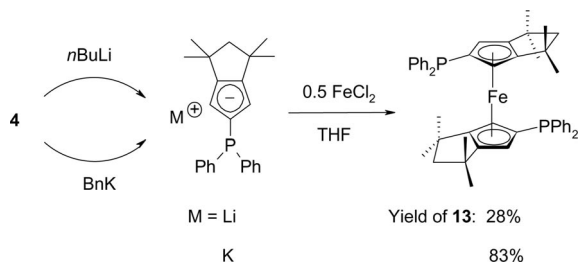
acid amide $\text{Ph}_2\text{P}(\text{O})\text{NH}_2$ [$\delta_{\text{P}}(\text{THF}) = 25.0$ ppm, m.p. 161–162 °C].^[17]

Further studies of thus obtained organophosphorus(V) derivatives **5–12** of the title phosphane $\text{Ph}_2\text{P-Cp}^{\text{TM}}\text{H}$ (**4**) as chelating ligands in organometallic chemistry are the focus of our current investigations.

Reactivity of $\text{Ph}_2\text{P-Cp}^{\text{TM}}\text{H}$ as Bifunctional Ligand

We have studied a possibility to use **4** as a bifunctional ligand in the synthesis of a bis-phosphanyl-substituted ferrocene and its further use as chelating, electron-rich and sterically demanding ligand towards PdCl_2 .

Direct transmetalation of lithiated **4** by ferrous chloride [$\text{FeCl}_2(\text{THF})_n$] gave the desired ferrocene **13** in 28% isolated yield (Scheme 6). A possible explanation for such a poor yield might be a partial deprotonation of $\text{Ph}_2\text{P-Cp}^{\text{TM}}\text{H}$ due to its low kinetic CH-acidity compared to unsubstituted $\text{Ph}_2\text{P-C}_5\text{H}_5$ (**1**) or the low nucleophilicity of the lithium salt. Benzylpotassium [PhCH_2K] is known as superior deprotonating reagent and its use instead of $n\text{BuLi}$ gave rise to **13** in 83% isolated yield as a bright-orange, air-stable, non-volatile solid. Being analogous to the prominent chelate ligand [$\{\text{Ph}_2\text{P-C}_5\text{H}_4\}_2\text{Fe}$] (dppf),^[18] we call this derivative **13** dppfTM.



Scheme 6. Yield dependence of **13** on deprotonation agent.

The ^{31}P NMR spectroscopy reveals a single up-field shifted resonance at -15.8 ppm. In the ^1H NMR spectrum, the geminal protons of the CH_2 -group and the methyl groups are, as expected, diastereotopic. The high conformational rigidity in solution is presented in the ^{13}C NMR spectroscopy – the resonances to *ortho*- and *ipso*-Ph carbons, observed at $\delta = 134.6$ and 141.2 ppm, resp., show *pseudo*-triplet pattern ($|^2J_{\text{CP}} + ^6J_{\text{CP}}| = 10.5$ Hz, $|^1J_{\text{CP}} + ^5J_{\text{CP}}| = 6.8$ Hz, resp.). This coupling pattern is in contrast to those reported for the unsubstituted ferrocene (dppf),^[19] which shows for these resonances solely two doublets.

Orange crystals of **13**, suitable for X-ray structure determination, were grown by slow cooling of its concentrated alcohol solution. The molecular structure of ferrocene with ellipsoids of 50% of probability is presented in Figure 3.

Complex **13** crystallizes in the triclinic space group $P\bar{1}$ with one molecule in the unit cell. The iron atom lies on the crystallographic inversion center, the molecule as a whole is centrosymmetric. The molecule has a strictly *anti*-conformation of substituents at both C_5 -rings. The distance between the iron atom and centroid (Z) of the C_5 -ring

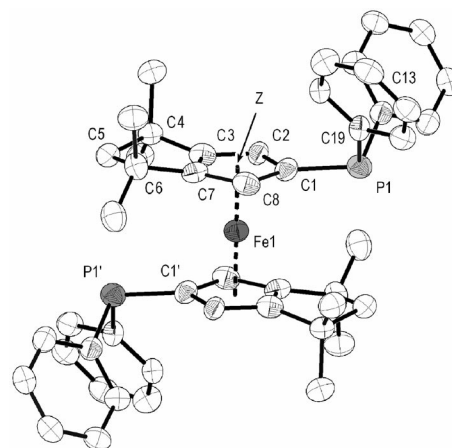
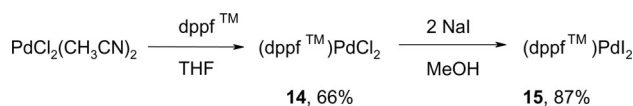


Figure 3. The molecular structure of [$(\text{Cp}^{\text{TM}}\text{PPh}_2)_2\text{Fe}$] (**13**). Hydrogen atoms have been omitted for clarity (Z = centroid of C_5 -ring). Selected bond lengths [Å] and angles [°]: P1–C1 1.832(1), P1–C13 1.833(1), P1–C19 1.853(1), C1–C2 1.441(1), C2–C3 1.406(1), C3–C7 1.400(1), C7–C8 1.427(1), C8–C1 1.437(1), Z···Fe1 1.682(1), Fe1–C1 2.084(1), C1–P1–C13 101.2(2), C13–P1–C19 99.7(2), C19–P1–C1 100.1(1), C8–C1–P1–C19 46.6(1), C2–C1–P1–C13 24.5(1), P1–Z–P1' 180.00(2).

[1.682(1) Å] is slightly longer than those in [$(\text{C}_5\text{H}_4\text{PPh}_2)_2\text{Fe}$] [1.646(5) Å],^[20] [$(\text{Me}_4\text{C}_5\text{PPh}_2)_2\text{Fe}$] [1.653(1) Å].^[21] Bond lengths and angles involving the phosphorus atoms compare well with the values in triphenylphosphane, [$(\text{C}_5\text{H}_4\text{PPh}_2)_2\text{Fe}$] and **4** (vide supra). All Fe1–C₅ distances lie in a narrow range varying from 2.064(1)–2.088(1) Å.

Reaction of **13** with [$\text{PdCl}_2(\text{CH}_3\text{CN})_2$] gives an light purple microcrystalline solid of composition [$(\text{dppf}^{\text{TM}})\text{PdCl}_2$] (**14**) in 66% yield. Further halogen exchange was achieved by reaction of **14** with an excess of NaI in MeOH (Scheme 7). Thus, [$(\text{dppf}^{\text{TM}})\text{PdI}_2$] (**15**) was isolated as a deep purple microcrystalline solid in 87% yield, higher than in the analogous synthesis of the [$(\text{dppp})\text{PdI}_2$] reported recently.^[22] Identification of both compounds was completed by microanalysis and multinuclear NMR spectroscopy.



Scheme 7.

NMR spectra of **14** and **15** are rather similar and spectroscopic characteristics will be discussed for **14** as representative. In its ^1H NMR spectrum four resonances for methyl groups were observed whereas two diastereotopic methyl groups are observed in dppfTM. Moreover, the protons at the C_5 ring appear as *two* resonances at 3.64 (s) and 4.11 (d, $^3J_{\text{HP}} = 2.5$ Hz) ppm. In the ^{13}C NMR spectrum two diastereotopic *para*- and *ipso*-Ph carbon resonances were observed. These findings confirm the molecular rigidity in solution and a helical structure with low degree or absence of Δ -/ Λ interconversion.

Single crystals of palladium complex **15**, suitable for X-ray diffraction analysis, were obtained by a slow evapora-

tion of its chloroform solution. The compound crystallizes in the orthorhombic space group $Pca2_1$ with four molecules per unit cell (Figure 4).

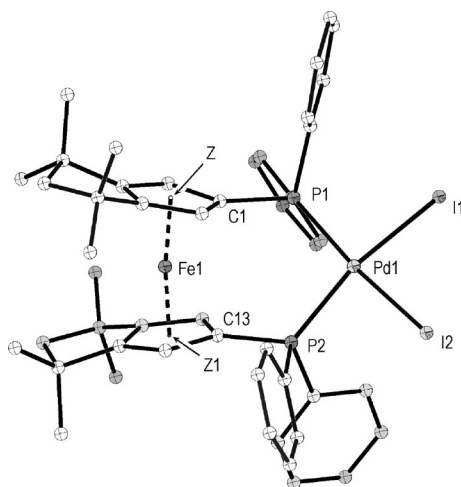


Figure 4. The molecular structure of $[(dppf^{TM})PdI_2]$ (**15**). All H-atoms have been omitted for clarity (Z = centroid of C_5 -ring). Selected bond lengths [Å] and angles [°]: Pd1–I1 2.639(2), Pd1–I2 2.652(2), Pd1–P1 2.293(1), Pd1–P2 2.298(1), P1–C1 1.808(2), P2–C13 1.801(2), Fe–Z 1.683(1), Fe–Z1 1.675(1), I1–Pd1–I2 90.2(1), P1–Pd1–I1 86.3(1), P2–Pd1–I2 86.3(1), P1–Pd1–P2 99.3(1), Z–Pd1–Z1 172.0(1).

The palladium atom has a distorted square-planar geometry. The similar distortion was reported for complexes $[(dppf)PdI_2]$ (Hal = Br, I).^[23]

The P1–Pd1–P2 bite angle is of $99.3(1)^\circ$ and comparable with those of in series $[(dppf)PdHal_2]$ (Hal = Cl – I: 98.9 – 99.9°). The I1–Pd1–I2 angle is of $90.2(1)^\circ$ and slightly larger than those in $dppf$ complexes (Hal = Cl – I: 87.2 – 87.8°).^[22,24] The most interesting feature is the dramatic distortion of both C_5 rings in the molecule. The Z–Fe–Z1 angle of $172.0(1)^\circ$ is the lowest value in the whole series of the $[(dppf)PdHal_2]$ [Hal = Cl: $179.5(1)^\circ$, Br $177.8(1)^\circ$, I: $178.3(1)^\circ$].^[22,23]

Conclusions

Simple pyrrolidine catalyzed condensation of the known phosphane $Ph_2P-C_5H_5$ (**1**) with acetone leads to the formation of two different condensation products: either with 1 equiv. of acetone to yield diphenyl(6,6-dimethylfulven-2-yl)phosphane (**2**) or with two equiv. of acetone when reacted in acetone as a solvent to yield diphenyl(4,4,6-trimethyl-4,5-dihdropentalen-2-yl)-phosphane (**3**). Subsequent carbometallation of **3** with MeLi resulted in the first air-stable, sterically highly crowded tetramethypentalenylphosphane **4**. This cyclopentadienylphosphane ($Ph_2P-Cp^{TM}H$) appeared to be thermodynamically stable with respect to its dimerisation and it is the first compound of this class that has been crystallographically characterized. The oxidation reactions of $Ph_2P-Cp^{TM}H$ with H_2O_2 , S_8 and Se yield exclusively the corresponding chalcogenides $Ph_2P-(X)Cp^{TM}H$, X = O (**5**), X = S (**6**), X = Se (**7**). Quaterni-

zation of **4** with MeI proceeds smoothly to $[Ph_2P(Cp^{TM}H)-Me]^+ I^-$ (**8**), its dehydrohalogenation by reaction with $nBuLi$ gives P -methyl-cyclopentadienylidenephosphorane $Ph_2P-(Cp^{TM})Me$ (**9**). An alternative protocol towards **9**, the deprotonation of **8** with benzyl potassium followed by P -alkylation is superior and gives **9** in more than 95% yield. The NMR spectroscopy of the phosphane **4**, its chalcogenides **5**–**7** as well as the phosphonium salt **8** shows the presence of a single vinylic isomer in all cases. Compounds **4** and **9** have been structurally characterized by X-ray diffraction analyses.

The Staudinger reaction of **4** with $tBuN_3$ gives tautomer $Ph_2P(Cp^{TM})NHtBu$ (**10**) that exists exclusively in P -amino-cyclopentadienylidenephosphorane form, whereas with Me_3SiN_3 the major tautomer has the form of P -imino-cyclopentadienylphosphane $Ph_2P(NSiMe_3)Cp^{TM}H$ (**11**). Hydrolysis of **11** with wet MeCN leads after tautomerization to the novel P -amino-cyclopentadienylidenephosphorane $Ph_2P(Cp^{TM})NH_2$ (**12**).

Finally, ferrocene $[(\eta^5-Cp^{TM}PPh_2)_2Fe]$ (**13**) was synthesized by metallation of $Ph_2P-Cp^{TM}H$ with $[PhCH_2K]$ and transmetallation with $FeCl_2$. In analogy to its known predecessor $dppf$ it is named $dppf^{TM}$. Despite of its extreme steric bulk and stereochemical rigidity, ferrocene **13** has been applied as a bidentate phosphane ligand for the synthesis of palladium complexes $[(dppf^{TM})PdCl_2]$ (**14**) and $[(dppf^{TM})PdI_2]$ (**15**). Both **13** and **15** have also been characterized by X-ray diffraction analysis. The reported high-yield chemical transformation from cheap starting materials as well as proof of ligand properties will stimulate further development with respect to introducing other substituents at the phosphorus atom or via carbometallation at the reactive fulvene functionality.

Experimental Section

General Considerations: All manipulations were performed under purified argon or nitrogen using standard high vacuum or Schlenk or glovebox techniques. Solvent grade acetone, acetonitrile and MeOH were used without purification. Hexane and THF were distilled under argon employing standard drying agents.^[25] $Ph_2P-C_5H_5$ (**1**)^[2] and anhydrous metal salts $FeCl_2$,^[26] $[PdCl_2(MeCN)_2]$ ^[27] were prepared according to the literature procedures. Ph_2PCl (95%, techn.) was used as supplied from Acros. NMR spectra were recorded at $+25^\circ C$ on a Bruker ARX200 and Bruker AMX300. Elemental analyses were performed at the Analytical Laboratory of the Chemistry Department/Philipps-University of Marburg. EI mass spectra were obtained on a Varian MAT CH7A (70 eV), ESI mass spectra on a FINNIGAN TSQ 700 spectrometer. Melting points were determined with a Büchi melting point B-540 apparatus.

Fulvenylphosphane 2 ($Ph_2P-C_8H_6$): To a stirred solution of phosphane **1** (745 mg, 2.98 mmol) in methanol (10 mL), acetone (0.24 mL, 3.72 mmol, 1.1 equiv.) and pyrrolidine (0.1 mL, ca. 1.3 mmol, ca. 5 mol-%) were added at ambient temperature. The reaction mixture progressively turns deep yellow. The solution was stirred for 4 h whereupon a bright yellow, microcrystalline solid forms. It was filtered off and dried in vacuo for 4 h; yield 59% (510 mg); m.p. 83.0 – $83.5^\circ C$. 1H NMR (300.1 MHz, C_6D_6 , $25^\circ C$):

$\delta = 1.59, 1.67$ ($2 \times s, 2 \times 3\text{H}, 2 \times \text{Me}$), 6.52 (m, 1 H, CH), 6.56 (m, 1 H, CH), 6.71 (m, 1 H, CH), 7.07 (m, 6 H, Ph), $7.55\text{--}7.64$ (m, 4 H, *o*-Ph) ppm. $^{13}\text{C}\{^1\text{H}\}$ NMR (75.5 MHz, C_6D_6 , 25°C): $\delta = 22.6$ (s, Me), 122.4 (d, $J_{\text{C,P}} = 4.1$ Hz, C_{CS}), 128.7 (d, $^3J_{\text{C,P}} = 7.0$ Hz, *m*-Ph), 128.7 (s, *p*-Ph), 129.0 (d, $J_{\text{C,P}} = 22$ Hz, *P*- C_{CS}), 133.6 (d, $J_{\text{C,P}} = 12.8$ Hz, *ipso*-Ph), 134.0 (d, $^2J_{\text{P,C}} = 19.4$ Hz, *o*-Ph), 138.5 (d, $^1J_{\text{C,P}} = 11.1$ Hz, C_{CS}), 140.9 (d, $J_{\text{P,C}} = 10.3$ Hz, C_{CS}), $143.8, 149.6$ ($2 \times$ d, $J_{\text{C,P}} = 7.8, J_{\text{C,P}} = 2.5$ Hz, $\text{C}=\text{CMe}_2$) ppm. $^{31}\text{P}\{^1\text{H}\}$ NMR (81.0 MHz, C_6D_6 , 25°C): $\delta = -16.8$ ppm. EI-MS: m/z (%) = 290 (100) [M^+], 275 (1) [$\text{M}^+ - \text{Me}$], 213 (1) [$\text{M}^+ - \text{Ph}$]. $\text{C}_{20}\text{H}_{19}\text{P}$ (290.35): calcd. C 82.73, H 6.60; found C 82.91, H 6.63.

Fulvenylphosphane 3 ($\text{Ph}_2\text{P-C}_{11}\text{H}_{13}$): To a stirred solution of phosphane 1 (6.20 g, 24.8 mmol) in acetone (40 mL), pyrrolidine (0.5 mL, 6.4 mmol, 25 mol-%) was added at ambient temperature. The reaction mixture turns gradually deep orange. The proceeding of the reaction was monitored by $^{31}\text{P}\{^1\text{H}\}$ NMR spectroscopy of the reaction mixture sample. After the reaction completed (ca. 4 h), all volatiles were removed in vacuo and resulting orange, viscous oil was dried for 4 h at 60°C under high vacuum. The obtained crude product was crystallized twice from hexane (2×20 mL) at -30°C to give a bright yellow, microcrystalline solid in 44% yield (4.0 g); m.p. $93\text{--}94^\circ\text{C}$. ^1H NMR (300.1 MHz, C_6D_6 , 25°C): $\delta = 1.12$ (s, 6 H, Me_2C), 1.59 (q, $^4J_{\text{H,H}} = 1.2$ Hz, 3 H, $\text{MeC}=\text{C}$), 2.44 (s, 2 H, CH_2), 5.97 (s, 1 H, CH), 6.27 (dd, $^3J_{\text{H,P}} = 3.0, ^4J_{\text{H,H}} = 1.2$ Hz, 1 H, CH), 7.09 (m, 6 H, *m*-*p*-Ph), 7.65 (m, 4 H, *o*-Ph) ppm. $^{13}\text{C}\{^1\text{H}\}$ NMR (75.5 MHz, C_6D_6 , 25°C): $\delta = 16.4$ (s, $\text{MeC}=\text{C}$), 29.2 (s, Me_2C), 37.7 (Me_2C), 61.3 (s, CH_2), 115.7 (d, $^2J_{\text{C,P}} = 17.6$ Hz, HC), 117.3 (d, $^2J_{\text{C,P}} = 17.1$ Hz, HC), 128.6 (s, Ph), 128.7 (s, Ph), 134.3 (d, $^2J_{\text{C,P}} = 19.8$ Hz, *o*-Ph), 138.4 (d, $^1J_{\text{C,P}} = 11.3$ Hz, *ipso*-Ph), 148.7 (d, $J_{\text{C,P}} = 8.1$ Hz, *F*lv), 151.3 (d, $J_{\text{C,P}} = 13.6$ Hz, *F*lv), 153.2 (d, $J_{\text{C,P}} = 3.0$ Hz, *F*lv), 161.6 (d, $J_{\text{C,P}} = 5.8$ Hz, *F*lv) ppm. $^{31}\text{P}\{^1\text{H}\}$ NMR (81.0 MHz, C_6D_6 , 25°C): $\delta = -13.9$ ppm. EI-MS: m/z (%) = 331 (22.5) [$\text{M}^+ + \text{H}$], 330 (100) [M^+], 315 (18.6) [$\text{M}^+ - \text{CH}_3$], 253 (8.3) [$\text{M}^+ - \text{Ph}$]. $\text{C}_{23}\text{H}_{23}\text{P}$ (330.41): calcd. C 83.61, H 7.02; found C 83.31, H 6.64.

Phosphane 4 ($\text{Ph}_2\text{P-Cp}^{\text{TMH}}$): To a solution of fulvenylphosphane 3 (5.28 g, 16.0 mmol) in diethyl ether (50 mL), MeLi solution (1.6 M in ether, 15 mL, 24 mmol) was added at 0°C during 15 min followed by stirring at ambient temperature for 1 h. The reaction mixture was quenched with methanol (3.5 mL). The clear, supernatant solution was decanted from the sticky residue and all volatiles were removed in vacuo. The residue was extracted into hexane (100 mL) and the solution was filtered through a Celite® pad. Cooling the solution to -80°C overnight gives a pale yellow, crystalline material, which was isolated by low temperature filtration and dried in vacuo for 1 h. A pale yellow, crystalline solid was obtained in yield of 91% (5.04 g); m.p. $108\text{--}109^\circ\text{C}$. An almost colorless sample was obtained by crystallization from SiMe_4 at -30°C ; m.p. $109.0\text{--}109.3^\circ\text{C}$. ^1H NMR (300.1 MHz, C_6D_6 , 25°C): $\delta = 1.02$ (s, 6 H, Me_2C), 1.11 (s, 6 H, Me_2C), 1.94 [s, 2 H, $\text{CH}_2(\text{CMe}_2)_2$], 2.89 (t, $^4J_{\text{H,H}} = 1.5$ Hz, 1 H, $\text{H}_2\text{C}_{\text{CS}}$), 7.76 (dt, $^3J_{\text{H,P}} = 5.4, ^4J_{\text{H,H}} = 1.5$ Hz, 1 H, HC_{CS}), 7.05 (m, 6 H, *m*-*p*-Ph), 7.53 (m, 4 H, *o*-Ph) ppm. $^{13}\text{C}\{^1\text{H}\}$ NMR (75.5 MHz, C_6D_6 , 25°C): $\delta = 30.0, 30.4$ ($2 \times$ s, $2 \times \text{CMe}_2$), 37.6 (d, $^2J_{\text{C,P}} = 9.8$ Hz, $\text{H}_2\text{C}_{\text{CS}}$), $40.2, 41.8$ ($2 \times$ s, $2 \times \text{CMe}_2$), 61.6 [s, $\text{CH}_2(\text{CMe}_2)_2$], $128.6, 128.7$ ($2 \times$ s, *m*-*p*-Ph), 133.7 (d, $^1J_{\text{C,P}} = 19.7$ Hz, *ipso*-Ph), 139.0 (d, $^2J_{\text{C,P}} = 24.1$ Hz, *o*-Ph), 139.4 (d, $J_{\text{C,P}} = 10.9$ Hz, C_{CS}), 145.8 (d, $J_{\text{C,P}} = 14.8$ Hz, C_{CS}), 155.8 (d, $J_{\text{C,P}} = 8.2$ Hz, C_{CS}), 160.6 (s, C_{CS}) ppm. $^{31}\text{P}\{^1\text{H}\}$ NMR (81.0 MHz, C_6D_6 , 25°C): $\delta = -14.5$ ppm. EI-MS: m/z (%) = 347 (1.4) [$\text{M}^+ + \text{H}$], 346 (34.5) [M^+], 331 (100) [$\text{M}^+ - \text{Me}$], 269 (1) [$\text{M}^+ - \text{Ph}$]. $\text{C}_{24}\text{H}_{27}\text{P}$ (346.45): calcd. C 83.21, H 7.86; found C 83.38, H 7.79.

Phosphane Oxide 5 ($[\text{Ph}_2\text{P}(\text{O})\text{Cp}^{\text{TMH}}]$): To a stirred solution of phosphane 4 (490 mg, 1.42 mmol) in THF (10 mL), aq. H_2O_2

(ca. 30%, ca. 1.6 mmol) was added in one portion at ambient temperature. An exothermic reaction takes place. The stirring was continued for 0.5 h after that the volatiles were completely removed in high vacuum. The traces of water were removed by azeotropic drying with toluene (50 mL). The solid residue was washed with cold hexane (2×5 mL), crystallized from hot heptane and dried in vacuo; yield 71% (365 mg) of a colorless, microcrystalline solid; m.p. $162.9\text{--}163.3^\circ\text{C}$. ^1H NMR (300.1 MHz, C_6D_6 , 25°C): $\delta = 0.97, 1.02$ ($2 \times$ s, 2×6 H, $2 \times \text{Me}_2\text{C}$), 1.90 [s, 2 H, $\text{CH}_2(\text{CMe}_2)_2$], 3.10 (s, 2 H, $\text{H}_2\text{C}_{\text{CS}}$), 6.95 (d, $^3J_{\text{C,P}} = 8.7$ Hz, 1 H, HC_{CS}), 7.05 (m, 6 H, *m*-*p*-Ph), 7.89 (m, 4 H, *o*-Ph) ppm. $^{13}\text{C}\{^1\text{H}\}$ NMR (75.5 MHz, C_6D_6 , 25°C): $\delta = 29.8, 30.1$ ($2 \times$ s, $2 \times \text{Me}_2\text{C}$), 36.8 (d, $^2J_{\text{C,P}} = 12.6$ Hz, $\text{H}_2\text{C}_{\text{CS}}$), $40.1, 41.8$ ($2 \times$ s, $2 \times \text{Me}_2\text{C}$), 61.4 [s, $\text{CH}_2(\text{CMe}_2)_2$], $128.5, 128.7$ ($2 \times$ s, *m*-*p*-Ph), 131.1 (d, $J_{\text{C,P}} = 2.7$ Hz, C_{CS}), 132.2 (d, $J = 10.9$ Hz, *o*-Ph), 141.6 (d, $J = 9.8$ Hz, HC_{CS}), 155.0 (d, $^3J_{\text{C,P}} = 14.8$ Hz, $\text{C}_{\text{CS}}\text{CMe}_2$), 164.2 (s, $\text{C}_{\text{CS}}, \text{C}_{\text{CS}}\text{CMe}_2$) ppm. $^{31}\text{P}\{^1\text{H}\}$ NMR (81.0 MHz, C_6D_6 , 25°C): $\delta = +18.1$ ppm. EI-MS: m/z (%) = 362 (19) [M^+], 347 (87) [$\text{M}^+ - \text{Me}$]. $\text{C}_{24}\text{H}_{27}\text{OP}$ (362.4): calcd. C 79.53, H 7.51; found C 79.78, H 6.98.

Phosphane Sulfide 6 ($[\text{Ph}_2\text{P}(\text{S})\text{Cp}^{\text{TMH}}]$): Sulfur powder (340 mg, 1.33 mmol, 1 equiv.) was added to a stirred solution of phosphane 4 (460 mg, 1.33 mmol) in toluene (12 mL) at ambient temperature. A slightly exothermic reaction with dissolution of sulfur was observed. The reaction mixture was stirred for additional 2 h. The solvent was removed in vacuo and the solid residue obtained was triturated with hexane. The formed precipitate was filtered off and washed with small amount of hexane. Yield 72% (360 mg) of yellow powder with the melting point of $133\text{--}134^\circ\text{C}$. The sample of analytical purity was obtained by crystallization from hot heptane solution: yellow, crystalline solid; m.p. $134.4\text{--}134.7^\circ\text{C}$. ^1H NMR (300.1 MHz, C_6D_6 , 25°C): $\delta = 0.96, 1.00$ ($2 \times$ s, 2×6 H, Me_2C), 1.87 [s, 2 H, $\text{CH}_2(\text{CMe}_2)_2$], 3.20 (s, 2 H, $\text{H}_2\text{C}_{\text{CS}}$), 6.94 (d, $^3J_{\text{C,P}} = 9.5$ Hz, 1 H, HC_{CS}), 7.01 (m, 6 H, *m*-*p*-Ph), 7.97 (m, 4 H, *o*-Ph) ppm. $^{13}\text{C}\{^1\text{H}\}$ NMR (75.5 MHz, C_6D_6): $\delta = 29.8, 30.1$ ($2 \times$ s, $2 \times \text{Me}_2\text{C}$), 36.8 (d, $^2J_{\text{C,P}} = 12.6$ Hz, $\text{H}_2\text{C}_{\text{CS}}$), $40.1, 41.8$ ($2 \times$ s, $2 \times \text{Me}_2\text{C}$), 61.4 [s, $\text{CH}_2(\text{CMe}_2)_2$], 128.5 (m, *m*-*p*-Ph), 131.1 (d, $J_{\text{C,P}} = 2.7$ Hz, C_{CS}), 132.2 (d, $J = 10.9$ Hz, *o*-Ph), 141.6 (d, $J = 9.8$ Hz, HC_{CS}), 155.0 (d, $^3J_{\text{C,P}} = 14.8$ Hz, $\text{C}_{\text{CS}}\text{CMe}_2$), 164.2 (s, $\text{C}_{\text{CS}}\text{CMe}_2$) ppm. $^{31}\text{P}\{^1\text{H}\}$ NMR (81.0 MHz, C_6D_6 , 25°C): $\delta = +31.4$ ppm. EI-MS: m/z (%) = 378 (55) [M^+], 363 (65) [$\text{M}^+ - \text{Me}$]. $\text{C}_{24}\text{H}_{27}\text{PS}$ (378.5): calcd. C 76.16, H 7.19; found C 76.46, H 7.13.

Phosphane Selenide 7 ($[\text{Ph}_2\text{P}(\text{Se})\text{Cp}^{\text{TMH}}]$): Red selenium powder (119 mg, 1.55 mol, 1.07 equiv.) was added to a solution of phosphane 4 (498 mg, 1.44 mmol) in chloroform (5 mL). The heterogenic reaction mixture was heated under reflux for 5 h. The excess of red selenium was removed by filtration through a Celite® pad. Removal of the solvent from the filtrate gives a brown, foamy solid; yield 96% (588 mg) of brown solid. The sample of analytical purity with the melting point of $143\text{--}144^\circ\text{C}$ was obtained by slow crystallization from hot heptane. Colorless, crystalline solid; m.p. $147.7\text{--}148.0^\circ\text{C}$. ^1H NMR (300.1 MHz, C_6D_6 , 25°C): $\delta = 0.95, 1.00$ ($2 \times$ s, 2×6 H, $2 \times \text{Me}_2\text{C}$), 1.86 [s, 2 H, $\text{CH}_2(\text{CMe}_2)_2$], 3.25 (s, 2 H, $\text{H}_2\text{C}_{\text{CS}}$), 6.94 (d, $^3J_{\text{C,P}} = 9.8$ Hz, 1 H, HC_{CS}), 6.99 (m, 6 H, *m*-*p*-Ph), 7.97 (m, 4 H, *o*-Ph) ppm. $^{13}\text{C}\{^1\text{H}\}$ NMR (75.5 MHz, CDCl_3 , 25°C): $\delta = 30.0, 30.5$ ($2 \times$ s, $2 \times \text{Me}_2\text{C}$), 36.8 (d, $^2J_{\text{C,P}} = 12.7$ Hz, $\text{H}_2\text{C}_{\text{CS}}$), $40.2, 42.1$ ($2 \times$ s, $2 \times \text{Me}_2\text{C}$), 61.3 [s, $\text{CH}_2(\text{CMe}_2)_2$], 128.6 (d, $^3J_{\text{C,P}} = 12.1$ Hz, *m*-Ph), 131.5 (d, $^4J_{\text{C,P}} = 3.3$ Hz, *p*-Ph), 132.4 (d, $^2J_{\text{C,P}} = 11.0$ Hz, *o*-Ph), 132.5 (d, $^1J_{\text{C,P}} = 78$ Hz, *ipso*-Ph), 138.3 (d, $^1J_{\text{C,P}} = 83$ Hz, *P*- C_{CS}), 143.2 (d, $^2J_{\text{C,P}} = 9.9$ Hz, HC_{CS}), 154.9 (d, $^3J_{\text{C,P}} = 15.4$ Hz, $\text{C}_{\text{CS}}\text{CMe}_2$), 165.0 (d, $^3J_{\text{C,P}} = 7.2$ Hz, $\text{C}_{\text{CS}}\text{CMe}_2$) ppm. $^{31}\text{P}\{^1\text{H}\}$ NMR (81.0 MHz, C_6D_6 , 25°C): $\delta = 22.3$ ($^1J_{\text{P,Se}} = 710$ Hz) ppm. $^{77}\text{Se}\{^1\text{H}\}$ NMR (76 MHz, C_6D_6 , 25°C): $\delta = -260.8$ (d, $^1J_{\text{Se,P}} = 741$ Hz) ppm. EI-MS: m/z (%) = 426 (32.8) [M^+], 265

(84.5) [$M^+ - Cp^{TM}$]. $C_{24}H_{27}PSe$ (425.41): calcd. C 67.76, H 6.40; found C 68.06, H 6.87.

Phosphonium Salt 8 [$Ph_2P(Cp^{TM}H)Me$] $^+I^-$: To a solution of phosphane **4** (350 mg, 1.00 mmol) in CH_2Cl_2 (5 mL), MeI (0.15 mL, ca. 2.4 mmol) was added and resulting solution was stirred for 48 h. Progress of the reaction was monitored by $^{31}P\{^1H\}$ NMR spectroscopy. After that all volatiles were removed in vacuo, ether (10 mL) was added. Vigorous stirring results in formation of a pale yellow, powdery solid that was filtered off and dried in high vacuum; yield 81% (395 mg); m.p. 195–200 °C 1H NMR (200.1 MHz, $CDCl_3$, 25 °C): δ = 1.23, 1.26 (2 \times s, 2 \times 6 H, 2 \times Me_2C), 2.12 [s, 2 H, $H_2C(CMe_2)_2$], 3.00 (d, $^2J_{H,P}$ = 13.5 Hz, MeP), 3.32 (br. d, $^4J_{H,H}$ = 2.0 Hz, 2 H, H_2C_{CS}), 7.29 (dt, $^3J_{H,P}$ = 9.6, $^4J_{H,H}$ = 2.0 Hz, 1 H, HC_{CS}), 7.69–7.83 (m, 10 H, Ph) ppm. $^{13}C\{^1H\}$ NMR (50.1 MHz, $CDCl_3$, 25 °C): δ = 12.2 (d, $^2J_{C,P}$ = 58 Hz, Me_2P), 29.9, 30.3 (2 \times s, 2 \times Me_2C), 38.0 (d, $^2J_{C,P}$ = 13 Hz, H_2C_{CS}), 40.2, 42.5 (2 \times s, 2 \times Me_2C), 61.1 [s, $H_2C(CMe_2)_2$], 120.5 (d, $^1J_{C,P}$ = 91 Hz, *ipso-Ph*), 122.2 (d, $^1J_{C,P}$ = 96 Hz, $P-C_{CS}$), 130.5 (d, $^3J_{C,P}$ = 12.7 Hz, *m-Ph*), 132.8 (d, $^2J_{C,P}$ = 10.5 Hz, *o-Ph*), 134.9 (d, $^4J_{C,P}$ = 2.8 Hz, *p-Ph*), 151.5 (d, $^2J_{C,P}$ = 10.7 Hz, HC_{CS}), 156.3 (d, $^3J_{C,P}$ = 16.5 Hz, $P-C=CH-C_{CS}CMe_2$), 171.0 (d, $^3J_{C,P}$ = 7.3 Hz, $CH_2-C_{CS}CMe_2$) ppm. $^{31}P\{^1H\}$ NMR (81.0 MHz, $CDCl_3$, 25 °C): δ = +12.2 ppm. ESI-MS: m/z (%) = 361 [$Ph_2P(Cp^{TM}H)Me$] $^+$. $C_{25}H_{30}IP$ (488.39): calcd. C 61.48, H 6.19; found C 61.31, H 6.35.

Methylenephosphorane 9 [$Ph_2P(Cp^{TM})Me$]. **a) By Deprotonation of 8**: To a suspension of phosphonium salt **8** (320 mg, 0.66 mmol) in THF (20 mL), *n*BuLi (1.6 M, 0.4 mL, 0.64 mmol) was added at 0 °C. The reaction mixture was stirred at same temperature for 1 h and for further 14 h at ambient temperature. The pale yellow suspension formed was filtered through a Celite® pad and the filtrate was concentrated in high vacuum to yield a waxy residue. Crystallization from ether gives a pale yellow microcrystalline solid; yield 67% (155 mg).

b) By Successive Reactions with [BnK] and MeI: To a solution of **4** (1.04 g, 3.00 mmol) in 20 mL of THF, solution of [BnK] (400 mg, 3.08 mmol) in THF (5 mL) was added drop-by-drop at 0 °C. After addition was completed the orange reaction mixture was stirred for 15 min and MeI (0.3 mL, 1.6 equiv.) was added within 5 min at room temp. After an exothermic reaction ceased, the pale yellow suspension was filtered through a Celite® pad, washed with THF (5 mL) and the filtrate was completely evaporated under vacuum yielding a yellow viscous oil. Addition of ether (20 mL) results in crystallization with deposition of a pale yellow, microcrystalline solid. An additional crop of product can be obtained by storing the mother liquor at –30 °C; yield 95% (1.02 g); m.p. 203–204 °C. 1H NMR (300.1 MHz, C_6D_6 , 25 °C): δ = 1.56 (d, $^2J_{C,H}$ = 13.0 Hz, 3 H, MeP), 1.72 (s, 12 H, 2 \times Me_2C), [d, $^6J_{C,H}$ = 0.6 Hz, 2 H, $CH_2(CMe_2)_2$], 6.02 (d, $^3J_{C,H}$ = 3.6 Hz, 2 H, HC_{CS}), 6.86 (m, 4 H, *m-Ph*), 6.96 (m, 2 H, *p-Ph*), 7.24–7.31 (m, 4 H, *o-Ph*) ppm. $^{13}C\{^1H\}$ NMR (50.1 MHz, C_6D_6 , 25 °C): δ = 12.2 (d, $^1J_{C,P}$ = 62 Hz, MeP), 33.3 (s, 2 \times Me_2C), 39.6 (d, $^4J_{C,P}$ = 1.7 Hz, Me_2C), 64.9 [s, $CH_2(CMe_2)_2$], 78.6 (d, $^1J_{C,P}$ = 108 Hz, $P-C_{CS}$), 103.5 (d, $^2J_{C,P}$ = 16.5 Hz, HC_{CS}), 128.6 (d, $^3J_{C,P}$ = 12.1 Hz, *m-Ph*), 129.5 (d, $^1J_{C,P}$ = 86 Hz, *ipso-Ph*), 131.8 (d, $^4J_{C,P}$ = 2.8 Hz, *p-Ph*), 132.5 (d, $^2J_{C,P}$ = 10.5 Hz, *o-Ph*), 145.7 (d, $^3J_{C,P}$ = 18.2 Hz, Me_2CC_{CS}) ppm. $^{31}P\{^1H\}$ NMR (81.0 MHz, C_6D_6 , 25 °C): δ = +4.2 ppm. ESI-MS: m/z (%) = 361 [$M^+ + H$]. $C_{25}H_{29}P$ (360.48): calcd. C 83.30, H 7.98; found C 82.97, H 8.21.

P-Aminophosphorane 10 [$Ph_2P(Cp^{TM})NHtBu$]: To a solution of phosphane **4** (360 mg, 1.04 mmol) in THF (10 mL), *t*BuN₃ (500 mg, 5.0 mmol, 5.0 equiv.) was added at ambient temperature. The reaction mixture was stirred for 5 h. The proceeding of the

reaction was monitored by $^{31}P\{^1H\}$ NMR spectroscopy. After the reaction completed, all volatiles were removed in vacuo and the solid residue was triturated with acetonitrile, whereupon a yellow solid forms. The latter was filtered off and dried at high vacuum; yield 41% (170 mg) of a yellow, microcrystalline solid; m.p. 165.5–166.5 °C. The sample of the analytical purity was obtained by crystallization from concd. hot acetonitrile solution (m.p. 166.3–166.7 °C). The compound has high solubility in aromatic solvents, THF; it is weakly soluble in acetonitrile, ether and aliphatic solvents. 1H NMR (300.1 MHz, C_6D_6 , 25 °C): δ = 0.90 (s, 9 H, *t*Bu), 1.69 (s, 12 H, 2 \times Me_2C), 2.07 (d, $^2J_{H,P}$ = 5.1 Hz, 1 H, NH), 2.47 [s, 2 H, $CH_2(CMe_2)_2$], 6.16 (d, $^3J_{C,P}$ = 4.0 Hz, 2 H, HC_{CS}), 7.03 (m, 6 H, *m-Ph*), 7.83–7.90 (m, 4 H, *o-Ph*) ppm. $^{13}C\{^1H\}$ NMR (75.5 MHz, C_6D_6 , 25 °C): δ = 31.4 (d, $^3J_{C,P}$ = 3.9 Hz, $NCMe_3$), 33.3 (s, 2 \times Me_2C), 39.6 (d, $^4J_{C,P}$ = 1.7 Hz, 2 \times Me_2C), 53.1 (d, $^2J_{C,P}$ = 2.2 Hz, CMe_3), 64.9 [s, $CH_2(CMe_2)_2$], 80.5 (d, $^1J_{C,P}$ = 118 Hz, $P-C_{CS}$), 106.1 (d, $^2J_{C,P}$ = 16 Hz, HC_{CS}), 128.5 (d, $^3J_{C,P}$ = 12 Hz, *m-Ph*), 131.5 (d, $^1J_{C,P}$ = 105 Hz, *ipso-Ph*), 131.7 (d, $^4J_{C,P}$ = 2.8 Hz, *p-Ph*), 133.9 (d, $^2J_{C,P}$ = 9.9 Hz, *o-Ph*), 146 ($^3J_{C,P}$ = 18.7 Hz, Me_2CC_{CS}) ppm. $^{31}P\{^1H\}$ NMR (81.0 MHz, C_6D_6 , 25 °C): δ = +17.0 ppm. EI-MS: m/z (%): 417 (100) [M^+], 340 (70) [$M^+ - Ph$], 412 (25) [$M^+ - Me$]. $C_{28}H_{36}NP$ (417.56): calcd. C 80.54, H 8.69, N 3.35; found C 80.25, H 8.57, N 3.38.

P-Iminophosphane 11 [$Ph_2P(NSiMe_3)Cp^{TM}H$]: A suspension of phosphane **4** (334 mg, 0.96 mmol) in Me_3SiN_3 (1.0 mL, ca. 7.5 mmol) was stirred at 100 °C for 18 h, whereupon slow N₂ evolution takes place. The color of reaction mixture turns progressively brown. The proceeding of the reaction was performed by ^{31}P NMR spectroscopy of the crude reaction mixture. After the reaction proceeded to 87%, it was terminated. Removal of all volatiles in vacuo yields a light brown semisolid mass, which was extracted into hexane (10 mL). Filtration from a small amount of amorphous, brown solid followed by removal of the solvent results in the formation of the light brown crystalline product (m.p. 94.0–94.5 °C). The moisture and air-sensitive compound **11** shows very high solubility in all common aprotic solvents at room temp. A sample of analytical purity was obtained by crystallization from acetonitrile; m.p. 94.5–94.7 °C. 1H NMR (300.1 MHz, C_6D_6 , 25 °C): δ = 0.39 (s, 9 H, $SiMe_3$), 1.00, 1.04 (2 \times s, 2 \times 6 H, 2 \times Me_2C), 1.91 [s, 2 H, $CH_2(CMe_2)_2$], 3.03 (dd, $^3J_{H,P}$ = 1.0, $^4J_{H,H}$ = 1.7 Hz, 2 H, H_2C_{CS}), 6.95 (dt, $^4J_{H,H}$ = 1.7, $^3J_{H,P}$ = 9.0 Hz, HC_{CS}), 7.05 (m, 6 H, *m-Ph*), 7.80–7.90 (m, 4 H, *o-Ph*) ppm. $^{13}C\{^1H\}$ NMR (75.5 MHz, C_6D_6 , 25 °C): δ = 4.5 (d, $^2J_{C,P}$ = 3.3 Hz, $SiMe_3$), 29.9, 30.3 (2 \times s, 2 \times Me_2C), 36.6 (d, $^2J_{C,P}$ = 12.7 Hz, H_2C_{CS}), 40.0, 41.7 (2 \times s, 2 \times Me_2C), 61.6 [s, $CH_2(CMe_2)_2$], 128.2 (d, $^3J_{C,P}$ = 10.6 Hz, *m-Ph*), 130.7 (d, $^4J_{C,P}$ = 2.8 Hz, *p-Ph*), 131.9 (d, $^2J_{C,P}$ = 10.5 Hz, *o-Ph*), 136.8 (d, $^1J_{C,P}$ = 104 Hz, *ipso-Ph*), 140.3 (d, $^2J_{C,P}$ = 11 Hz, HC_{CS}), 144.6 (d, $^1J_{C,P}$ = 108 Hz, $P-C_{CS}$) ppm. 155.5 (d, $^3J_{C,P}$ = 14.9 Hz, $C_{CS}CMe_2$), 162.7 (d, $^3J_{C,P}$ = 6.6 Hz, $C_{CS}CMe_2$) ppm. $^{31}P\{^1H\}$ NMR (81.0 MHz, C_6D_6): δ = –7.8 ppm. EI-MS: m/z (%): 433 (34) [M^+], 360 (100) [$M^+ - SiMe_3$]. $C_{27}H_{36}NPSi$ (433.65): calcd. C 74.78, H 8.37, N 3.23; found C 73.71, H 8.36, N 3.16.

P-Aminophosphorane 12 [$Ph_2P(Cp^{TM})NH_2$]: This compound was isolated accidentally as a small amount of colorless precipitate by crystallization attempt from solvent-grade acetonitrile. Therefore, the synthesis of compound **12** was not optimized; m.p. 172.0–173.0 °C. 1H NMR (300.1 MHz, C_6D_6 , 25 °C): δ = 1.66 (s, 12 H, 2 \times Me_2C), 2.10 (br. s, 2 H, NH_2), 2.42 [s, 2 H, $CH_2(CMe_2)_2$], 5.68 (d, $^3J_{CP}$ = 3.4 Hz, 2 H, HC_{CS}), 6.87–7.03 (m, 6 H, *m-Ph*), 7.48–7.56 (m, 4 H, *o-Ph*) ppm. $^{13}C\{^1H\}$ NMR (50.1 MHz, C_6D_6 , 25 °C): δ = 33.2 (s, 2 \times Me_2C), 39.5 (s, 2 \times Me_2C), 64.8 [s, $CH_2(CMe_2)_2$], 82.0 (d, $^1J_{C,P}$ = 110 Hz, $P-C_{CS}$), 104.8 (d, $^2J_{C,P}$ = 17.8 Hz, HC_{CS}), 128.3 (d, $^3J_{C,P}$ = 12.6 Hz, *m-Ph*), 131.1 (d, $^1J_{C,P}$ =

102 Hz, *ipso-Ph*), 131.7 (d, $^4J_{C,P}$ = 2.5 Hz, *p-Ph*), 132.4 (d, $^2J_{C,P}$ = 10.7 Hz, *o-Ph*), 146.0 (d, $^3J_{C,P}$ = 19.3 Hz, Me_2CC_5) ppm. $^{31}P\{^1H\}$ NMR (81.0 MHz, C_6D_6 , 25 °C): δ = +22.1 ppm. EI-MS: m/z (%): 361 (100) [M^+], 284 (32) [$M^+ - Ph$]. $C_{24}H_{28}NP$ (361.47): calcd. C 79.75, H 7.81, N 3.88; found C 80.30, H 8.18, N 3.98.

Ferrocene Derivative 13 [$(\eta^5-Cp^{TM}PPh_2)_2Fe$], (dppfTM): To a solution of phosphane **4** (690 mg, 2.05 mmol) in THF (25 mL), a solution of [PhCH₂K] (255 mg, 1.98 mmol) in THF (10 mL) at 0 °C was added followed by addition of solid FeCl₂ (64 mg, 0.50 mmol). A dark brown suspension forms. The reaction mixture was stirred for 2 h at room temp., after that all volatiles were removed in vacuo and residue was extracted with hexane; solvent was stripped off yielding a brown-orange, foamy residue. This was dissolved in acetonitrile, treated with ultrasound whereupon an orange-pink solid forms. It was filtered off and dried in high vacuum; yield 83% (620 mg). Ferrocene **13** is highly soluble in hydrocarbons, aromatic solvents, ethers, ethanol and virtually insoluble in methanol and acetonitrile; m.p. 180.5 °C (dec. > 188 °C). 1H NMR (300.1 MHz, C_6D_6 , 25 °C): δ = 1.16 (s, 6 H, 2 × *Me*), 1.25 (s, 6 H, 2 × *Me*), 1.68, 2.42 [2 × d of AB system, $^2J_{H,H}$ = 12.8 Hz, 2 × 1 H, diastereotopic $H_2C(CMe_2)$], 4.00 (s, 2 H, HC_{C_5}), 7.06 (m, 6 H, *p-/m-Ph*), 7.60 (m, 4 H, *o-Ph*) ppm. $^{13}C\{^1H\}$ NMR (75.5 MHz, C_6D_6 , 25 °C): δ = 31.3 (s, *Me*), 32.7 (s, *Me*), 37.9 (s, CMe_2), 59.2 (s, CH_2), 63.7 (pst, $^2J_{C,P}$ + $^3J_{C,P}$ = 7.6 Hz, HC_{C_5}), 109.6 (s, C_5CMe_2), 128.4, 128.7 (2 × s, *m-/p-Ph*), 134.6 (pst, $^2J_{C,P}$ + $^6J_{C,P}$ = 10.5 Hz, *o-Ph*), 141.2 (pst, $^1J_{C,P}$ + $^5J_{C,P}$ = 6.8 Hz, *ipso-Ph*) ppm. $^{31}P\{^1H\}$ NMR (81.0 MHz, C_6D_6 , 25 °C): δ = −16.7 ppm. ESI-MS: m/z (%) = 747.2 [$M^+ + H$]. $C_{48}H_{52}FeP_2$ (746.7): calcd. C 77.21, H 7.02; found C 76.62, H 7.13.

Palladium Complex 14 [(dppfTM)PdCl₂]: To a solution of ferrocene **13** (500 mg, 0.67 mmol, 1.07 equiv.) in THF (10 mL), [PdCl₂(MeCN)₂] (160 mg, 0.63 mmol) was added and reaction mixture was stirred for 24 h. During that period a lustrous, purple-

orange, microcrystalline precipitate forms. It was filtered off and dried in high vacuum; yield 66% (395 mg). The compound is air-stable and shows high solubility in CH₂Cl₂ and low solubility in THF; not soluble in aromatic solvents, hexane, ether, acetone, lower alcohols; m.p. > 250 °C. 1H NMR (300.1 MHz, C_6D_6 , 25 °C): δ = 1.00, 1.03, 1.08, 1.39 (4 × s, 4 × 3 H, 4 × *Me*), 1.76, 2.30 (2 × d of AB system, $^2J_{H,H}$ = 13.4 Hz, 2 × 1 H, *exo-lendo-CH₂*), 3.64 (s, 1 H, HC_{C_5}), 4.11 (d, $^3J_{H,P}$ = 2.5 Hz, 1 H, HC_{C_5}), 7.33–7.65 (m, 8 H, *Ph*), 8.11 (m, 2 H, *Ph*) ppm. $^{13}C\{^1H\}$ NMR (75.5 MHz, C_6D_6 , 25 °C): δ = 29.4, 30.4, 31.7, 32.7 (4 × s, 4 × *Me*), 36.3, 38.1 (2 × s, 2 × CMe_2), 58.1 [s, $CH_2(CMe_2)_2$], 62.2 (s, HC_{C_5}), 66.5 (pst, $^2J_{C,P}$ + $^4J_{C,P}$ = 20.2 Hz, HC_{C_5}), 71.1 (dd, $^1J_{C,P}$ = 56, $^3J_{C,P}$ = 4 Hz, $P-C_{C_5}$), 112.6 (pst, $^3J_{C,P}$ + $^5J_{C,P}$ = 5.4 Hz, C_5CMe_2), 127.2, 128.1 (2 × pst, $^3J_{C,P}$ + $^5J_{C,P}$ = 11.0, $^3J_{C,P}$ + $^5J_{C,P}$ = 11.6 Hz, 2 × *m-Ph*), 130.0, 131.6 (2 × s, 2 × *p-Ph*), 133.7 (pst, $^2J_{C,P}$ + $^4J_{C,P}$ = 9.2 Hz, *o-Ph*), 134.6 (d, $^1J_{C,P}$ = 60 Hz, *ipso-Ph*), 135.6 (pst, $^2J_{C,P}$ + $^4J_{C,P}$ = 12.4 Hz, *o-Ph*) ppm. $^{31}P\{^1H\}$ NMR (121.0 MHz, CD_2Cl_2 , 25 °C): δ = +30.3 ppm. ESI-MS: m/z (%): 924.2 [M^+]. $C_{48}H_{52}Cl_2FeP_2Pd$ (924.07): calcd. C 62.39, H 5.67; found C 62.05, H 5.81.

Palladium Complex 15 [(dppfTM)PdI₂]: A stirred suspension of complex **14** (166 mg, 0.18 mmol) and NaI (660 mg, 4.4 mmol, ca. 24 equiv.) in MeOH (30 mL) was refluxed for 10 min. After that the reaction mixture was cooled to room temperature and major amount of inorganic salts was removed by centrifugation. The filtrate was collected by decantation and the solid was extracted in the same way three times. The solvent from combined organic phases was removed in vacuo and the brown residue was extracted with CH₂Cl₂. The subsequent filtration and removal of the solvent yield a deep purple, microcrystalline solid; yield 87% (173 mg). The compound shows very high solubility in CH₂Cl₂; marginally soluble in THF and insoluble in MeCN and Et₂O; m.p. > 250 °C. 1H NMR (300.1 MHz, $CDCl_3$, 25 °C): δ = 1.01, 1.06, 1.039 (3 × s,

Table 1. Details of the crystal data, structural resolution and refinement procedure for compounds **4**, **9**, **13** and **15**.

| | 4 | 9 | 13 | 15 |
|---|------------------------------------|---|--|--|
| Empirical formula | C ₂₄ H ₂₇ P | C ₂₅ H ₂₉ P | C ₄₈ H ₅₂ FeP ₂ | C ₄₈ H ₅₂ FeI ₂ P ₂ Pd |
| Fw /g mol ^{−1} | 346.43 | 360.45 | 746.69 | 1106.89 |
| Crystal color, habit | colorless, prism | colorless, needle | dark red, prism | light red, plate |
| Crystal size /mm | 0.30 × 0.18 × 0.12 | 0.36 × 0.08 × 0.04 | 0.08 × 0.05 × 0.03 | 0.21 × 0.06 × 0.03 |
| Crystal system | monoclinic | triclinic | triclinic | orthorhombic |
| Space group | <i>P</i> 2 ₁ / <i>c</i> | <i>P</i> $\bar{1}$ | <i>P</i> $\bar{1}$ | <i>Pca</i> 2 ₁ |
| <i>Z</i> | 4 | 4 | 1 | 4 |
| <i>a</i> /Å | 6.4001(3) | 10.5140(11) | 8.8276(18) | 26.3109(17) |
| <i>b</i> /Å | 37.8489(13) | 13.1131(13) | 11.002(3) | 11.4236(7) |
| <i>c</i> /Å | 8.4024(4) | 15.7793(17) | 11.123(3) | 14.8667(7) |
| α /° | 90 | 89.722(8) | 80.50(2) | 90 |
| β /° | 96.017(6) | 72.761(8) | 71.261(17) | 90 |
| γ /° | 90 | 86.898(8) | 84.658(19) | 90 |
| Volume /Å ³ | 2024.16(15) | 2074.6(4) | 1008.0(4) | 4468.4(5) |
| $d_{\text{calcd.}}$ /g cm ^{−3} | 1.137 | 1.154 | 1.230 | 1.645 |
| μ /mm ^{−1} | 0.139 | 0.138 | 0.486 | 2.212 |
| <i>F</i> (000) | 744 | 776 | 396 | 2192 |
| Diffraction type | IPDS1 | IPDS2 | IPDS2 | IPDS2 |
| Temperature /K | 173(2) | 100(2) | 130(2) | 100(2) |
| Number of reflections collected | 12322 | 23974 | 8283 | 20064 |
| Number of independent reflections | 3874 | 23794 | 3532 | 7797 |
| Absorption correction | semi-empirical | none | integration | semi-empirical |
| <i>R</i> (int) | 0.0510 | "HKLF 5" refinement, no merging, BASF = 0.157 | 0.1276 | 0.0745 |
| GOF | 0.956 | 0.690 | 0.763 | 0.898 |
| <i>R</i> 1 [<i>I</i> > 2σ(<i>I</i>)] | 0.0379 | 0.00583 | 0.0551 | 0.0439 |
| <i>wR</i> ₂ (all data) | 0.0953 | 0.1313 | 0.0980 | 0.0767 |

3 H, 6 H, 3 H, 4 × Me), 1.75, 2.30 (2 × d of AB system, $^2J_{H,H} = 12.6$ Hz, 2 × 1 H, *exo-lendo-CH₂*), 3.55 (s, 1 H, *HC_{CS}*), 3.94 (d, $^2J_{H,P} = 3.3$ Hz, 1 H, *HC_{CS}*), 7.30–7.44 (m, 5 H, *Ph*), 7.51–7.63 (m, 3 H, *Ph*), 8.00–8.06 (m, 2 H, *Ph*) ppm. $^{13}C\{^1H\}$ NMR (75.5 MHz, $CDCl_3$, 25 °C): $\delta = 30.0$, 31.2, 32.4, 33.5 (4 × s, 4 × Me), 36.8, 38.5 (2 × s, 2 × *CMe₂*), 58.7 [s, *CH₂(CMe₂)₂*], 62.7 (s, *HC_{CS}*), 67.0 (pst, $^2J_{C,P} + ^4J_{C,P} = 21$ Hz, *HC_{CS}*), 73.9 (dd, $^1J_{C,P} = 47$, $^3J_{C,P} = 6$ Hz, *P-C_{CS}*), 112.4 (d, $^3J_{C,P} = 6.6$ Hz, *C_{CS}CMe₂*), 112.5 (pst, $^3J_{C,P} + ^5J_{C,P} = 2.2$ Hz, *C_{CS}CMe₂*), 127.4, 128.2 (2 × pst, 2 × $^3J_{C,P} + ^5J_{C,P} = 11.6$ Hz, *m-Ph*), 130.3, 131.6 (2 × s, 2 × *p-Ph*), 132.2 (d, $^1J_{C,P} = 54$ Hz, *ipso-Ph*), 134.8, 135.9 (2 × pst, $^2J_{C,P} + ^4J_{C,P} = 9.4$ Hz, $^2J_{C,P} + ^4J_{C,P} = 12.5$ Hz, 2 × *o-Ph*), 136.6 (d, $^1J_{C,P} = 55$ Hz, *ipso-Ph*) ppm. $^{31}P\{^1H\}$ NMR (81.0 MHz, $CDCl_3$, 25 °C): $\delta = +19.9$ ppm. ESI-MS: *m/z* (%): 1106.4 [*M*⁺]. $C_{48}H_{52}FeI_2P_2Pd$ (1106.97): calcd. C 52.08, H 4.74; found C 52.53, H 4.65.

X-ray Crystallographic Studies: The crystals of compounds were grown by cooling of their concentrated solutions: 4, 13 (EtOH, +25 °C), 9 (Et₂O, 0 °C) and 15 (CH₂Cl₂, 0 °C). Diffraction data were collected with STOE IPDS1 (for 4, 9) and IPDS2 (for 13, 15) diffractometers using graphite monochromated Mo-*K_α* radiation ($\lambda = 0.71073$ Å). Crystal data and structure refinement details are collected in Table 1. All structures were solved by direct methods and expanded by difference-Fourier synthesis using SIR2004 (Giacovazzo, 2004) and refined by the full-matrix least-squares procedure based on *F₂*, using the SHELXL-97 (Sheldrick, 1997) computer program. ORTEP plots of all molecular structures were generated with Diamond 3.1, Crystal Impact software.

CCDC-746654 (for 4), -746655 (for 9), -746656 (for 13), -746657 (for 15) contain the supplementary crystallographic data for this paper. These data can be obtained free of charge from The Cambridge Crystallographic Data Centre via www.ccdc.cam.ac.uk/data_request/cif.

Acknowledgments

K. A. R. thanks Deutsche Akademischer Austausch Dienst (DAAD) for funding of a research fellowship at Philipps-Universität Marburg within the Ostpartnerschaftsprogramm. Financial support of Deutsche Forschungsgemeinschaft (DFG) (SPP-1166) is gratefully acknowledged.

- [1] a) P. Jutzi, *Chem. Rev.* **1986**, 86, 983–996; b) K. A. Fallis, G. K. Anderson, N. G. Rath, *Organometallics* **1992**, 11, 885–888; c) C. J. Schaverien, R. Ernst, W. Terlouw, P. Schut, O. Sudmeijer, P. H. M. Budzelaar, *J. Mol. Catal. A* **1998**, 128, 245–256; d) J. H. Shin, T. Hascal, G. Parkin, *Organometallics* **1999**, 18, 6–9; e) J. H. Shin, B. M. Bridgewater, G. Parkin, *Organometallics* **2000**, 19, 5155–5159; f) V. V. Kotov, E. V. Avtomonov, J. Sundermeyer, K. Harms, D. A. Lemenovskii, *Eur. J. Inorg. Chem.* **2002**, 678–691.
- [2] F. Mathey, J.-P. Lampin, *Tetrahedron* **1975**, 31, 2685–2690.
- [3] a) M. Visseaux, A. Dormond, M. M. Kubicki, C. Moïse, D. Baudry, M. Ephritikhine, *J. Organomet. Chem.* **1992**, 433, 95–106; b) K. A. Rufanov, A. R. Petrov, V. V. Kotov, F. Laquai, J. Sundermeyer, *Eur. J. Inorg. Chem.* **2005**, 3805–3807.
- [4] H. Schumann, T. Ghodsi, L. Esser, E. Hahn, *Chem. Ber.* **1993**, 126, 591–594.
- [5] O. I. Kolodyazhnyi, *Zh. Obshch. Khim.* **1980**, 50, 1885–1886.
- [6] a) K. A. Fallis, G. K. Anderson, N. P. Rath, *Organometallics* **1992**, 11, 885–888; b) J. J. Adams, D. E. Berry, O. J. Curnow, G. M. Fern, M. L. Hamilton, H. J. Kitto, J. R. Pipal, *Aust. J. Chem.* **2003**, 56, 1153–1160.
- [7] a) S. P. Mesyats, E. N. Tsvetkov, E. S. Petrov, M. I. Terekhova, A. I. Shatenshein, M. I. Kabachnik, *Izv. Akad. Nauk SSSR, Ser. Khim.* **1974**, 2489–2496; b) L. Baiget, M. Bouslikhane, J. Escudie, G. C. Nemes, I. Silaghi-Dumitrescu, L. Silaghi-Dumitrescu, *Phosphorus Sulfur Silicon Relat. Elem.* **2003**, 178, 1949–1961.
- [8] K. A. Rufanov, A. Spannenberg, *Mendeleev Commun.* **2008**, 18, 32–34.
- [9] A. R. Petrov, K. A. Rufanov, B. Ziemer, P. Neubauer, V. V. Kotov, J. Sundermeyer, *Dalton Trans.* **2008**, 909–915.
- [10] a) K. J. Stone, P. D. Little, *J. Org. Chem.* **1984**, 49, 1849–1853; b) I. Erden, F.-P. Xu, A. Sadoun, W. Smith, G. Sheff, M. Osun, *J. Org. Chem.* **1995**, 60, 813–820.
- [11] The av. C–P bond length for Ph_3P (1.83 Å): J. J. Daly, *J. Chem. Soc.* **1964**, 3799–3810; 1.84 Å for $P(o-EtC_6H_4)_3$: N. Fey, J. A. S. Howell, J. D. Lovatt, P. C. Yates, D. Cunningham, P. McArdle, H. Gottlieb, S. J. Coles, *Dalton Trans.* **2006**, 5464–5475; 1.83 Å for $P(2,6-Me_2C_6H_3)_3$: R. A. Shaw, M. Woods, T. S. Cameron, B. Dahlen, *Chem. Ind. (London)* **1971**, 151–152.
- [12] For diphenyl(inden-1-yl)phosphane, see: K. A. Fallis, G. K. Anderson, N. P. Rath, *Organometallics* **1992**, 11, 885–888; for tri(inden-3-yl)phosphane, see: T. Cantrell, P. Perrotin, B. Twamley, P. J. Shapiro, *Acta Crystallogr., Sect. E* **2007**, 63, o2044–o2045; for [2-(dimethylamino)inden-1-yl]diphenylphosphane see: J. Cipot, D. Wechsler, M. Stradiotto, R. McDonald, M. J. Ferguson, *Organometallics* **2003**, 22, 5185–5192; for (S_P)-(fluoren-9-yl)(menthyl)(phenyl)phosphane, see: E. Vedejs, Y. Donde, *J. Org. Chem.* **2000**, 65, 2337–2343.
- [13] J. H. Brownie, M. C. Baird, H. Schmider, *Organometallics* **2007**, 26, 1433–1443.
- [14] For diphenyl(indenyl)phosphane both isomeric forms of the phosphonium salts can be isolated: J. H. Brownie, M. C. Baird, *J. Organomet. Chem.* **2008**, 693, 2812–2817.
- [15] 1.718(2) Å for $Ph_3PC_5H_4$: H. L. Ammon, G. L. Wheeler, P. H. Watts Jr., *J. Am. Chem. Soc.* **1973**, 95, 6158–6163; av. 1.727 Å for $Ph_2P(C_5H_4)Me$: see ref.^[13] for a substituted indenylidene (C_9H_6) compound. 1.733(4) Å for $Ph_2P(C_9H_6)CH_2Ph$: K. A. Rufanov, B. Ziemer, M. Hummert, S. Schutte, *Eur. J. Inorg. Chem.* **2004**, 4759–4763; 1.756(5) Å for $Et_3P(C_5Ph_4)$: J. J. Eisch, Y. Qian, A. L. Rheingold, *Eur. J. Inorg. Chem.* **2007**, 1576–1584.
- [16] A. Petrov, K. Rufanov, K. Harms, J. Sundermeyer, *Mend. Commun.* **2009**, manuscript in preparation.
- [17] a) S. Freeman, M. J. P. Harger, *J. Chem. Soc. Perkin Trans. 1* **1989**, 571–578; S. Schlecht, S. Chitsaz, B. Neumüller, K. Dehnke, *Z. Naturforsch., Teil B* **1998**, 53, 17–22.
- [18] J. J. Bishop, A. Davison, M. L. Katcher, D. W. Lichtenberg, R. E. Merrill, J. C. Smart, *J. Organomet. Chem.* **1971**, 27, 241–249.
- [19] M. B. Gholivand, A. Babakhanian, M. Joshaghani, *Anal. Chim. Acta* **2007**, 584, 302–307.
- [20] U. Casellato, D. Ajo, G. Valle, B. Corain, B. Longato, R. Grazi-ani, *J. Crystallogr. Spectrosc. Res.* **1988**, 18, 583–588.
- [21] G. Trouve, R. Broussier, B. Gautheron, M. M. Kubicki, *Acta Crystallogr., Sect. C* **1991**, 47, 1966–1967.
- [22] J. Barkley, M. Ellis, S. J. Higgins, M. K. McCart, *Organometallics* **1998**, 17, 1725–1731.
- [23] T. J. Colacot, H. Qian, R. Cea-Olivares, S. Hernandez-Ortega, *J. Organomet. Chem.* **2001**, 637–639, 691–697.
- [24] T. Hayashi, M. Konishi, Y. Kobori, M. Kumada, T. Higuchi, K. Hirotsu, *J. Am. Chem. Soc.* **1984**, 106, 158–163.
- [25] W. L. F. Armarego, D. D. Perrin, *Purification of Laboratory Chemicals*, 4th ed., Butterworth-Heinemann, **1996**.
- [26] P. Kovacic, N. O. Brace, *Inorg. Synth.* **1960**, 6, 172–173.
- [27] Ch. J. Mathews, P. J. Smith, T. Welton, *J. Mol. Catal. A* **2003**, 206, 77–82.

Received: December 31, 2009
Published Online: July 28, 2010

Magneto–Structural Correlations in Discrete $\text{Mn}^{\text{II}}\text{--W}^{\text{V}}$ Cyano-Bridged Assemblies with Polyimine Ligands

Robert Podgajny,^{*,[a]} Tomasz Korzeniak,^[a] Paweł Przychodzeń,^[a] Carlos Gimenez-Saiz,^[b] Michał Rams,^[c] Michał Kwaśniak,^[c] and Barbara Sieklucka^[a]

Keywords: Manganese / Tungsten / Cyanides / Molecular squares / Magnetic properties / Structure elucidation

We present the magneto–structural correlations for two novel discrete cyano-bridged assemblies based on cationic complexes of manganese(II) with diimine ligands and octacyanotungstate(V) ions. The crystal structure of $[\text{Mn}^{\text{II}}(\text{terpy})(\text{dmf})(\text{H}_2\text{O})_2][\text{Mn}^{\text{II}}(\text{terpy})(\text{H}_2\text{O})(\text{dmf})(\mu\text{-NC})\text{W}^{\text{V}}(\text{CN})_7]_2 \cdot 6\text{H}_2\text{O}$ (**1**) (terpy = 2,2';6',2''-terpyridine, dmf = dimethylformamide) contains dinuclear $\{\text{Mn}^{\text{II}}\text{W}^{\text{V}}\}^-$ cyano-bridged anions, while the crystal structure of $[\text{Mn}^{\text{II}}(\text{phen})_3]_2[\text{Mn}^{\text{II}}(\text{phen})_2(\mu\text{-NC})_2\text{W}^{\text{V}}(\text{CN})_6]_2(\text{ClO}_4)_2 \cdot 9\text{H}_2\text{O}$ (**2**) (phen = 1,10-phenanthroline) is built of tetranuclear $\{\text{Mn}^{\text{II}}_2\text{W}^{\text{V}}_2\}^{2-}$ square anions. Intramolecular Mn–W magnetic interactions through the cyano bridges are represented by magnetic coupling constants $J = -39\text{ cm}^{-1}$ for the $\{\text{Mn}^{\text{II}}\text{W}^{\text{V}}\}^-$ unit in **1** and $J_1 = -25.7$ and $J_2 = -16.7\text{ cm}^{-1}$ for the $\{\text{Mn}^{\text{II}}_2\text{W}^{\text{V}}_2\}^{2-}$ unit in **2**. J and J_1 represent

relatively strong W–CN–Mn interactions and are ascribed to the bridges in *b* positions of TPRS-8 (trigonal prism square-face bicapped) of $[\text{W}(\text{CN})_8]^{3-}$ polyhedra, favoring the strongest electronic interactions between the $d_{z^2}\text{--}d_{x^2-y^2}$ orbital of W and the π^* orbitals of CN^- , whereas J_2 is related to the *m* vertex of $[\text{W}(\text{CN})_8]^{3-}$. The magnetic properties of **1** and **2** are compared with reference compounds and discussed in the context of the type of coordination polyhedra of $[\text{W}(\text{CN})_8]^{3-}$ as well as the metric parameters of cyano-bridged W–CN–Mn linkages. We found the type of coordination polyhedra and bridging mode of $[\text{W}(\text{CN})_8]^{3-}$ to be the most important factors influencing the magnitude of the Mn–W magnetic interaction.

Introduction

The interest in achieving novel functional materials has stimulated extensive research on the design and synthesis of polynuclear complexes. Cyanometalates able to act as divergent polytopic linking units offer a variety structural and functional features including a broad scope of coordination numbers and geometries, redox activity, and magnetic moments.^[1–9] The great success of Prussian blue analogues and other hexacyano-bridged hybrid materials was due to the observation of up to room temperature magnets,^[10] light-,^[11] pressure-,^[12] and solvent-tunable^[13] magnets, cyano-centered linkage isomerism,^[14] chiral magnets,^[15] high-nuclearity discrete systems including high-spin molecules,^[16] as well as magnetically ordered nanoparticles,^[17] nanolayers,^[18] and nanolayered composites.^[19] Over the last decade octacyanometalates $[\text{M}(\text{CN})_8]^{3-/4-}$ have been employed for crystal engineering of molecular magnetic materials. A

number of factors including the low energy barrier for the transformation between geometries [ideal square-antiprism (SAPR-8), dodecahedron (DD-8), and trigonal prism square-face bicapped (TPRS-8)],^[20] electrochemical lability between paramagnetic $4d^1$ (Nb^{IV} , Mo^{V}) or $5d^1$ (W^{V}) and diamagnetic $4d^2$ (Mo^{IV}) or $5d^2$ (W^{IV}) valence configurations,^[21] and a tendency to grow conveniently, leads to monocrystalline bimetallic solids with a novel potential in the construction of functional cyano-bridged networks.^[8,22–24] The highest magnetic ordering temperatures (T_c) of up to 62 K were regularly observed in $\{\text{Mn}^{\text{II}}[\text{M}(\text{CN})_8]\}$ networks.^[23] A T_c of 138 K was recently reported for mixed valence $\{\text{V}^{\text{II}}, \text{V}^{\text{III}}[\text{Nb}(\text{CN})_8]\}$.^[24] In addition, we have reported a relatively high increase in T_c from 25 to 62 K observed upon the dehydration of $\{\text{Mn}^{\text{II}}(\text{imH})_2[\text{Nb}^{\text{IV}}(\text{CN})_8] \cdot 4\text{H}_2\text{O}\}_\infty$.^[23g]

In the context of designing magnetically ordered networks, calculating the intermetallic magnetic coupling constant, $J_{\text{MnW}(\text{Mo}, \text{Nb})}$, is of interest. In order to establish correlations between the local magnetic interactions and the geometry of $[\text{W}(\text{CN})_8]^{3-}$ ions in polynuclear 3d–5d cyano-bridged assemblies, we present two novel discrete manganese(II) octacyanotungstate(V) compounds. In Figure 1 we present an overview of the relevant structural motifs observed for discrete $\text{Mn}^{\text{II}}\text{W}^{\text{V}}$, $\text{Mn}^{\text{II}}\text{Mo}^{\text{V}}$, and $\text{Mn}^{\text{II}}\text{Nb}^{\text{IV}}$ species.^[25] The magnetic moment originating from Mn^{II} ($3d^5$) couples antiferromagnetically with the W^{V} (Mo^{V} , Nb^{IV})

[a] Faculty of Chemistry, Jagiellonian University, Ingardena 3, 30-060 Kraków, Poland
Fax: +48-126-340-515
E-mail: podgajny@chemia.uj.edu.pl

[b] Institute for Material Science, University of Valencia Polígono La Coma, 46980 Paterna, Spain

[c] M. Smoluchowski Institute of Physics, Jagiellonian University, Reymonta 4, 30-059 Kraków, Poland

Supporting information for this article is available on the WWW under <http://dx.doi.org/10.1002/ejic.201000280>.

magnetic moment in all known cyano-bridged molecules and networks giving rise to total ground state spins (S) of up to 39/2, with values of $J_{\text{MnW(Mo,Nb)}}$ ranging from -10 to -24 cm^{-1} , calculated using the standard $\mathbf{H} = -\sum_{ij} \mathbf{S}_i \cdot \mathbf{S}_j$ Heisenberg Hamiltonian or DFT methods. Within our research on low nuclearity species,^[26] we take advantage of the properties of phen and terpy to synthesize two novel systems $[\text{Mn}^{\text{II}}(\text{terpy})(\text{dmf})(\text{H}_2\text{O})_2][\text{Mn}^{\text{II}}(\text{terpy})(\text{H}_2\text{O})(\text{dmf})(\mu\text{-NC})\text{W}^{\text{V}}(\text{CN})_8]_2 \cdot 6\text{H}_2\text{O}$ (**1**) and $[\text{Mn}^{\text{II}}(\text{phen})_3]_2[\text{Mn}^{\text{II}}(\text{phen})_2(\mu\text{-NC})_2\text{W}^{\text{V}}(\text{CN})_6]_2(\text{ClO}_4)_2 \cdot 9\text{H}_2\text{O}$ (**2**). The structures of **1** and **2** comprise dinuclear and square tetranuclear cyano-bridged skeletons, respectively. The J_{MnW} values reach ca. -39 cm^{-1} indicating slightly stronger Mn–W interaction compared to the systems reported previously. Furthermore, we compare the structural and magnetic features of **2** with those of two reference systems: $[\text{Mn}^{\text{II}}(\text{tpzt})(\text{OAc})(\text{H}_2\text{O})_2]_2\{\{\text{Mn}^{\text{II}}(\text{tpzt})(\text{MeOH})_{1.58}(\text{H}_2\text{O})_{0.42}\}_2\{\text{W}^{\text{V}}(\text{CN})_8\}_2\} \cdot 5\text{MeOH} \cdot 9.85\text{H}_2\text{O}$ (**3**)^[25a] [$\text{tpzt} = 2,4,6\text{-tris}(2\text{-pyridyl})\text{-}1,3,5\text{-triazine}$, $\text{OAc} = \text{acetate}$] and $[\{\text{Mn}^{\text{II}}(\text{bpy})_2(\text{ox})\}][\{\text{Mn}^{\text{II}}(\text{bpy})_2\}\{\text{W}^{\text{V}}(\text{CN})_8\}_2] \cdot 4\text{H}_2\text{O}$ (**4**)^[25b] ($\text{bpy} = 2,2'\text{-bipyridine}$, $\text{ox} = \text{oxalate}$) in the context of the presence of topologically identical, yet structurally different $\{\text{Mn}_2\text{W}_2\}^{2-}$ squares in all three structures. The magneto-structural correlations take into account the differences in the type of coordination polyhedra, the bridging modes of $[\text{W}(\text{CN})_8]^{3-}$, and the metric parameters of the cyano-bridged linkage.

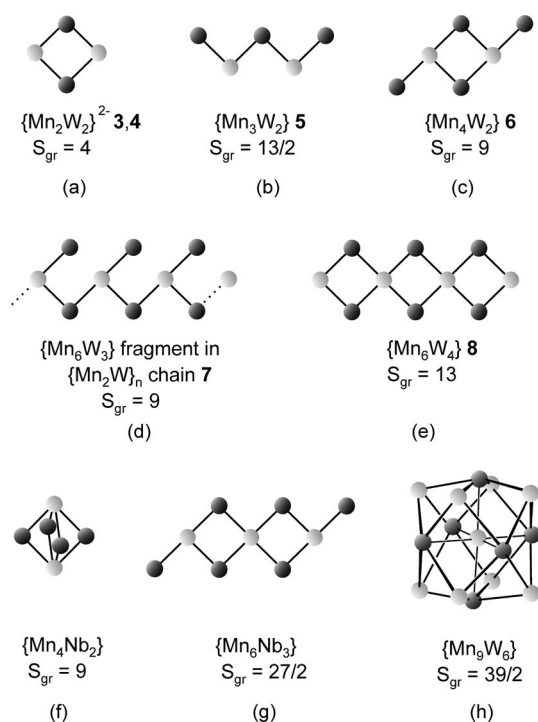


Figure 1. Structural motifs observed for Mn^{II}W^V, Mn^{II}Mo^V, and Mn^{II}Nb^{IV} species together with the relevant ground state spins $S^{\text{[25]}}$ including the reference Mn–W compounds **3–8** (a–e).^[25a–25c] Color scheme used: W, Mo, Nb = light gray, Mn = dark gray, cyano-bridges = black line.

Results and Discussion

Crystal Structure of 1

The asymmetric unit of **1** consists of two structurally different $[\text{Mn}(\text{terpy})(\text{H}_2\text{O})(\text{dmf})(\mu\text{-NC})\text{W}^{\text{V}}(\text{CN})_8]^-$ $[\{\text{MnW}\}^-]$ cyano-bridged anions (Figure 2), one $[\text{Mn}(\text{terpy})(\text{H}_2\text{O})_2(\text{dmf})]^{2+}$ cation and six molecules of water of crystallization. Selected bond lengths and angles are presented in Table 1 and Table S1. The coordination polyhedra of the $[\text{W}(\text{CN})_8]^{3-}$ units were determined using two criteria: (i) the shape-determining angles^[20a] defined as the deviation from planarity of atoms forming a trapezoid in an ideal dodecahedron (ϕ angles) and the dihedral angles at the shape-determining edges (δ angles) (see Figure S1 and Table S3 in the Supporting Information) and (ii) the continuous shape measures method (CSM)^[27] (Table S4).

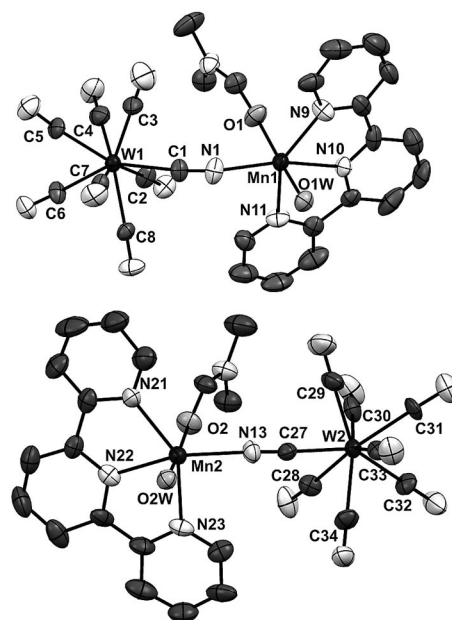


Figure 2. The cyano-bridged $\{\text{MnW}\}^-$ units of **1** with selected atom labeling. 50% Probability ellipsoids are shown. Color scheme used: W, Mn = black, C = dark grey, O = grey, N = pale grey.

Table 1. Distances [Å] and angles [°] of cyano bridges in **1** and **2**.

| 1 | | | |
|------------|-----------|-------------|-----------|
| W1–C1 | 2.202(14) | Mn1–N1 | 2.176(14) |
| C1–N1 | 1.14(2) | Mn1–N1–C1 | 150.8(12) |
| W1–C1–N1 | 174.2(14) | W1...Mn1 | 5.31 |
| W2–C13 | 2.169(13) | Mn2–N13 | 2.199(12) |
| C13–N27 | 1.15(2) | Mn2–N13–C27 | 149.6(12) |
| W2–C13–N27 | 177.2(14) | W2...Mn2 | 5.32 |
| 2 | | | |
| W1–C1 | 2.150(8) | Mn1a–N1 | 2.176(14) |
| C1–N1 | 1.143(9) | Mn1a–N1–C1 | 167.6(7) |
| W1–C1–N1 | 177.9(7) | W1...Mn1a | 5.43 |
| W1–C5 | 2.183(7) | Mn1–N5 | 2.249(6) |
| C5–N5 | 1.135(9) | Mn1–N5–C5 | 159.9(6) |
| W1–C5–N5 | 174.9(6) | W1...Mn1 | 5.46 |

The $[\text{W}(\text{CN})_8]^{3-}$ moiety exhibits geometry very close to TPRS-8, whereas $[\text{W}_2(\text{CN})_8]^{3-}$ adopts TPRS-8 geometry with some admixture of SAPR-8 character, with W–C bond lengths and almost linear W–C–N angles typical for this class of compounds.^[23,25] In each $\{\text{MnW}\}^-$ unit the bridging ligand is positioned at the noncapped square-face corner of TPRS-8 $[\text{W}(\text{CN})_8]^{3-}$, denoted as the *b* position (Figure 3).^[20b] The metric parameters of the cyano-bridging linkages Mn1–N1–C1–W1 and Mn2–N13–C27–W2 are represented by Mn–N bond lengths of 2.176 and 2.199 Å, strongly bent Mn–N–C angles of 150.8 and 149.6°, almost linear W–C–N angles of 174.2 and 177.2°, and intramolecular Mn···W distances of 5.31 and 5.32 Å, respectively. The coordination spheres of the Mn1 and Mn2 centers are similar and can be described as having distorted octahedral geometry with bond lengths in the range 2.18–2.29 Å. The distortion is mainly caused by the coordination of the rigid terpy ligand, conferring the formation of five-membered rings with $\text{N}_{\text{terpy}}\text{--Mn--N}_{\text{terpy}}$ bite angles of approximately 72° and N–C–N torsion angles in range 2.21–8.28°. The cyano bridge is coordinated to the manganese center in the plane formed by three N atoms from the terpy ligand. The coordination sphere is completed by one water and one dmf molecule. In the $[\text{Mn}_3(\text{terpy})(\text{H}_2\text{O})_2(\text{dmf})]^{2+}$ complex, the Mn center adopts a distorted octahedral geometry with the coplanar coordination of terpy and dmf, and the axial positions are occupied by two water molecules. The stereochemical arrangement around Mn centers seems to be controlled mainly by steric hindrance of the terpy ligand and the $[\text{W}^{\text{V}}(\text{CN})_8]^{3-}$ ion or dmf molecule, respectively, resulting in the *trans* arrangement of bulky ligands in the coordination sphere. Nonbridged metal ions are separated by distances longer than 7.3 Å.

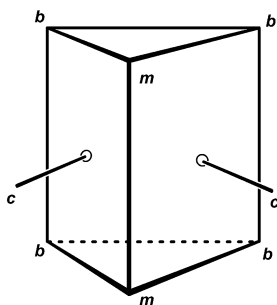


Figure 3. Three geometrically different vertices in TPRS-8 geometry.^[20b]

The 3D supramolecular architecture is stabilized by a hydrogen bond network formed by terminal cyano ligands, coordinated water, and crystallized water molecules with donor···acceptor distances in the range 2.6–2.9 Å and face-to-face π – π stacking interactions between the terpy pyridyl rings with average interplanar distance of 3.5 Å (Figure S2, Supporting Information).

Crystal Structure of **2**

The structure of **2** consists of a tetranuclear $[\text{Mn}^{\text{II}}(\text{phen})_2(\mu\text{-NC})_2\text{W}^{\text{V}}(\text{CN})_7]^{2-}$ $[\{\text{Mn}_2\text{W}_2\}^{2-}]$ unit (Figure 4), two

$[\text{Mn}^{\text{II}}(\text{phen})_3]^{2+}$ cations, two ClO_4^- anions, and seven crystallographically independent sites of water of crystallization with complete or partial occupancy, resulting in nine water molecules per formula unit. The bond lengths and angles are presented in Table 1 and Table S2.

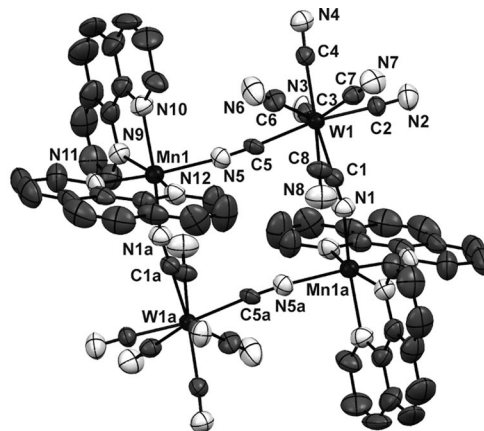


Figure 4. The cyano-bridged $\{\text{Mn}_2\text{W}_2\}^{2-}$ unit of **2** with selected atom labeling. 50% Probability ellipsoids are shown. Color scheme used: W, Mn = black, C = dark grey, N = pale grey. Symmetry operations: a) 1 – *x*, 1 – *y*, 1 – *z*.

The geometry of the octacyanotungstate unit can be generally described as TPRS-8, with very similar shape parameters to those of the $[\text{W}_2(\text{CN})_8]^{3-}$ in **1** (Table S3 and Table S4). The octacyanotungstate ion forms two cyano bridges to manganese centers, resulting in the formation of tetranuclear unit. The first bridging ligand, N1C1, is positioned at the noncapped square-face corner of TPRS-8 $[\text{W}(\text{CN})_8]^{3-}$ (*b* position), and the second, N5C5, is positioned at one of the corners between the capping ligands, denoted as the *m* position (Figure 3).^[20b] The metric parameters of the respective cyano bridges are represented by Mn–N bond lengths of 2.167 and 2.249 Å, Mn–N–C angles of 167.54 and 159.85°, almost linear W–C–N angles of 177.98 and 174.85°, and intramolecular Mn···W distances of 5.43 and 5.46 Å. The coordination sphere of the *cis*- $[\text{Mn}(\text{phen})_2(\text{NC})_2]$ displays slightly distorted octahedral geometry with all Mn1–N bonds in the range 2.167–2.292 Å. The tetrameric anion is formed from the coordination of two cyano ligands to the Mn center with a N1a–Mn1–N5 angle of 92.5(2)°. The tungsten corner of the tetranuclear unit has a C1–W1–C5 angle of 81.0(3)°, showing a deviation from ideal square geometry. The Mn2 centers coordinate three phen ligands in an almost regular octahedral geometry with Mn2–N bond lengths between 2.224 and 2.287 Å. The shortest intermolecular contacts outside the $\{\text{Mn}_2\text{W}_2\}^{2-}$ unit are Mn2···W1 distances of 7.76 and 7.93 Å.

The crystal lattice is stabilized by face-to-face π – π stacking interactions between the phen ligands with the appropriate interplanar distances of approximately 3.5 Å and by moderately strong hydrogen bonds. In the crystal lattice of **2** two kinds of crystallized H_2O molecules can be distinguished (Figure S3). The six H_2O per formula unit located at O1W, OW2, and OW3 sites, are involved in hydrogen bonding interactions with terminal cyano ligands and oxy-

gen atoms of perchlorate anions and, thus, may be treated as strongly bonded. The remaining three H₂O molecules represented by O4W, O5W, O6W, and O7W sites are delocalized within the channels walled by the phen ligands of {Mn₂W₂}²⁻ units and ClO₄⁻ anions parallel to the *a* crystallographic direction. These positions are excluded from the hydrogen bonding network and participate only in weak intermolecular contacts with the carbon and nitrogen atoms of the phen rings and oxygen atoms of the ClO₄⁻ anions.

Magnetic Properties

The temperature dependence of $\chi T(T)$ per formula unit measured at 1 kOe for **1** is presented in Figure 5 (a). At 300 K, the χT value of 13.3 cm³ K mol⁻¹ is close to 13.8 cm³ K mol⁻¹ expected for three uncoupled Mn^{II} ($S = 5/2$) centers and two W^V ($S = 1/2$) centers, assuming $g = 2.0$. On cooling the χT value decreases slowly indicating that the dominant interactions within {MnW}⁻ units are antiferromagnetic. After reaching a smooth minimum at around 60 K, χT starts to increase, which is presumably caused by the intermolecular ferromagnetic interactions between the mono- and dinuclear units in **1**. The χT measured below 25 K is affected by a small ferromagnetic impurity with $T_c = 22$ K that is demonstrated by irreversibility in the ZFC/FC measurement (ZFC = zero field cooling, FC = field cooling) (Figure S4, a). The presence of the unavoidable impurity was observed in various quantities in samples from three separate syntheses. For this reason the data below 30 K were excluded from the analysis. The $M(H)$ curve tends to saturate reaching 13.4 N β per formula unit at 50 kOe (Figure S4, b), being very close to 13 N β expected for **1** for antiferromagnetic coupling between W^V and Mn^{II}, which confirms the sign of the interactions.

We modeled the magnetic data of **1** assuming the dominant interactions within the {MnW}⁻ units, and the effective intermolecular interaction (for all kinds of intermolecular interactions in the crystal lattice within the regime of mean field approximation^[28]) in accordance with its molecular structure. One antiferromagnetic Mn^{II} ($S = 5/2$)-W^V ($S = 1/2$) exchange coupling constant J was assumed. The Heisenberg Hamiltonian, H_2 , for the dinuclear species {MnW}⁻ in magnetic field

$$H_2 = -J(S_{\text{Mn}}S_{\text{W}}) - g\beta H\Sigma(S_{\text{Mn}}^z + S_{\text{W}}^z)$$

was solved numerically, and the [Mn(terpy)(H₂O)₂(dmf)]²⁺ contribution was added to get the susceptibility χ_0 of noninteracting complexes. The intermolecular interaction was included as

$$\chi = \chi_0(1 - \chi_0 zJ'/N_A g^2 \beta^2)$$

Fitting the $\chi T(T)$ above 30 K gives $J = -39(2)$, $zJ' = 0.32(2)$ cm⁻¹, and $g = 1.99(2)$.

The temperature dependence of $\chi T(T)$ per formula unit measured at 1 kOe for **2** is presented in Figure 5 (b). At 300 K, the χT value of 16.3 cm³ K mol⁻¹ is lower than 18.25 cm³ K mol⁻¹ expected for four uncoupled Mn^{II} ($S =$

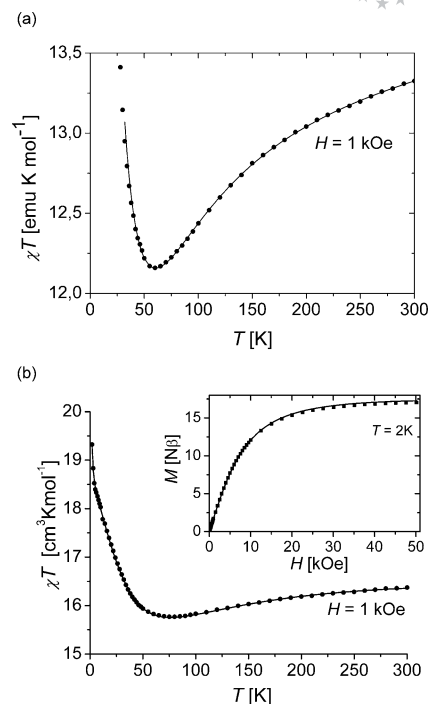


Figure 5. Magnetic characteristics for **1** and **2**: $\chi T(T)$ dependences for **1** (a) and **2** (b); [$M(H)$ dependence inset in (b)]. Straight lines represent the best fits.

$5/2$) centers and two W^V ($S = 1/2$) centers, assuming $g = 2.0$. On cooling the χT value decreases slowly, reaching a smooth minimum at 78 K, then starts to increase rapidly to 19.3 cm³ K mol⁻¹ at 2 K revealing a very smooth inflection at around 4 K. The value of $\chi T = 19.3$ cm³ K mol⁻¹ at 2 K is between the low temperature limits $(\chi T)_{\text{LT}}$ of 18.75 and 29.75 cm³ K mol⁻¹, calculated for {Mn₂W₂}²⁻ units with antiferro- and ferromagnetic W-Mn interactions, respectively, and the uncoupled [Mn(phen)₃]²⁺ complex, assuming $g_{\text{av}} = 2$. The $\chi T(T)$ dependence above 30 K with the minimum around 80 K, suggests the presence of antiferromagnetic W-Mn interactions within the {Mn₂W₂}²⁻ units. The $M(H)$ curve tends to saturate reaching 17 N β per formula unit at 50 kOe (see inset in Figure 5, b), and is very close to the magnetization of saturation of 18 N β (assuming $g_{\text{av}} = 2$) expected for **2** in the case of antiferromagnetic coupling between W^V and Mn^{II}, which confirms the nature of these interactions. The intermolecular ferromagnetic interactions including mono- and tetranuclear complexes may be operating at low temperatures.

Due to the substantially different Mn-N bond lengths and Mn-N-C angles of the cyano bridges within the {Mn₂W₂}²⁻ unit, the magnetic system of **2** can be treated as a tetranuclear Mn^{II} ($S = 5/2$)-W^V ($S = 1/2$) unit with two different antiferromagnetic exchange coupling constants J_1 and J_2 , and two isolated Mn ($S = 5/2$) centers. The Heisenberg Hamiltonians

$$H_4 = -J_1(S_{\text{Mn1}}S_{\text{W1}} + S_{\text{Mn2}}S_{\text{W2}}) - J_2(S_{\text{Mn1}}S_{\text{W2}} + S_{\text{Mn2}}S_{\text{W1}}) + g\mu_B H(S_{\text{Mn1}}^z + S_{\text{Mn2}}^z + S_{\text{W1}}^z + S_{\text{W2}}^z)$$

and

$$\mathbf{H}_1 = g\beta H \mathbf{S}_{\text{Mn}}$$

were solved numerically, which includes diagonalization of a 144×144 matrix. The molar magnetization of the sample was calculated as

$$M = M_4 + 2M_1$$

where $M_{1,4} = N_A \sum_n (-\partial E_n^{1,4}/H) \exp(-E_n^{1,4}/k_B T) / \sum_n \exp(-E_n^{1,4}/k_B T)$

and $E_n^{1,4}$ denote the eigenvalues of $\mathbf{H}_{1,4}$ respectively. Much weaker effective interunit interactions involving tetramers and monomers were approximated in terms of the molecular field model, where

$$H = H_{\text{ext}} + \gamma M \text{ and } \gamma = 2zJ'/N_A g^2 \beta^2.$$

This model was also solved numerically, which also allowed us to calculate the nonlinear $M(H)$ dependence. The calculations were performed with the diamagnetic contribution taken into account. The best agreement with the experimental data was obtained for $J_1 = -25.7(7)$, $J_2 = -16.7(7)$, $zJ' = 0.020(7) \text{ cm}^{-1}$, and $g = 1.95(5)$. This set of parameters satisfactorily reproduces both $\chi(T)$ and $M(H)$ dependencies, which is visible in Figure 4 (b). Reducing the number of fitted parameters by assuming that J_1 and J_2 are equal, results in the value of $J_1 = J_2 = -21(2) \text{ cm}^{-1}$.

The mean g values of 1.99 (**1**) and 1.97 (**2**) obtained from the fitting procedure are very similar to those observed for mononuclear $[\text{W}^{\text{V}}(\text{CN})_8]^{3-}$ salts (1.963–1.974)^[21b] and for *cis*- $[\text{Mn}^{\text{II}}(\text{phen})_2\text{Cl}_2]$ (1.97).^[29] They also conform to the mean g values found for a range of cyano-bridged W–Mn species.^[23a,23c,23d,25a–25c] No sign of magnetic anisotropy was observed in the magnetic characteristics [i.e. frequency dependent signals of $\chi'(T)$ and $\chi''(T)$ or a magnetic hysteresis loop] under the experimental conditions employed.

Discussion

The calculated negative values of J_{MnW} of -39 , -25.7 , and -16.7 cm^{-1} indicate relatively strong Mn–W magnetic interactions.^[23c,25] Magnetic coupling in octacyanometalate–Mn(II) species depends on several structural features: (i) the type of coordination polyhedra of the $[\text{W}(\text{CN})_8]^{3-}$ moiety, (ii) the bridge position in respect to the magnetic orbitals of $[\text{W}(\text{CN})_8]^{3-}$, and (iii) the metric parameters of cyano-bridged linkages, which include Mn–N distances, Mn–N–C angles, and, indirectly, Mn···W distances. The coordination polyhedron of $[\text{W}(\text{CN})_8]^{3-}$ and the bridge position imply the amount of the spin density delocalized on the cyanide orbitals, increasing from the A vertex of DD via the SAPR vertex towards the B vertex of DD for $[\text{Mo}(\text{CN})_8]^{3-}$ and $[\text{W}(\text{CN})_8]^{3-}$, which was shown by DFT calculations.^[23c,23f,25f,25g,30] The $[\text{W}(\text{CN})_8]^{3-}$ moiety exhibits TPRS-8 geometry in **1** and **2**. The analysis of possible interactions of the ground state orbital of mixed d_{z^2} and $d_{x^2-y^2}$ character in TPRS-8 with the π -accepting orbitals of the CN^- ligands allows us to estimate qualitatively the increasing trend of the spin density delocalized from metal orbitals

to ligand orbitals: c positions $< m$ positions $< b$ positions (Figure 3).^[20b] W–C, Mn–N, and Mn···W distances naturally govern the extent of exchange coupling. DFT calculations have shown that the decrease in the Mn–N–C angle from 180 to 140° leads to the moderate increase (of about 20–30%) in the strength of antiferromagnetic Mn–W coupling in the case of dinuclear species.^[25g]

The relatively strong Mn–W interaction in the dinuclear $\{\text{MnW}\}^-$ units, represented by $J_{\text{MnW}} = -39 \text{ cm}^{-1}$, assigned to the W–CN–Mn linkage in **1** is the consequence of the superposition of three structural features: (i) the location of cyano-bridges at b positions of TPRS-8 implying that the highest spin density is delocalized on the CN^- orbitals, (ii) the relatively short Mn–N distances of 2.176 and 2.199 Å and W···Mn distances of 5.32 and 5.31 Å, and (iii) the high degree of bending of the Mn–N–C angles of 150.8 and 149.6°.

In the case of the square cyano-bridged $\{\text{Mn}_2\text{W}_2\}^{2-}$ units in **2**, two magnetic coupling constants, $J_1 = -25.7(7)$ and $J_2 = -16.7(7) \text{ cm}^{-1}$, were calculated according to the two different types of Mn–NC–W linkages observed. The geometry of the $[\text{W}(\text{CN})_8]^{3-}$ polyhedron in **2** is TPRS-8 with some admixture of SAPR-8 (Tables S3 and S4). The W–C1–N1–Mn1a linkage is located at the b position and is characterized by a relatively short Mn–N distance of 2.167 Å, a W···Mn distance of 5.43 Å, and a relatively small degree of bending (Mn–N–C 167.6°). The W–C5–N5–Mn1 linkage is located at the m position and is characterized by long Mn–N and W···Mn distances (2.249 and 5.46 Å, respectively) and a slightly higher degree of bending (Mn–N–C 159.9°) compared to the former. Thus, we assign J_1 to the W–C1–N1–Mn1a linkage and J_2 to the W–C5–N5–Mn1 linkage. A smaller value of J_1 compared to J_{MnW} of -39 cm^{-1} for **1** may be due some admixture of SAPR-8 in the TPRS-8 octacyanide polyhedron in **2**, decreasing to some extent the difference between the spin density delocalized on π^* CN^- orbitals at positions b , m , and c of TPRS-8 as well as due to longer Mn···W distances in **2**.

Table 2 presents the complete set of key parameters for molecular cyano-bridged MnW units constituting **1** and **2**. For comparison purposes we have also included the relevant parameters for the selected reference compounds **3**–**8** (Figure 1).^[25a–25c] The type of coordination polyhedra of octacyanotungstate in the reference compounds were re-examined and determined using shape-determining angles (**3**, **4**) (Table S3) and shape parameters (**3**–**8**) (Table S4).

The square cyano-bridged $\{\text{Mn}_2\text{W}_2\}^{2-}$ units of a total ground spin state $S = 4$ are present in reference compounds **3**^[25a] and **4**.^[25b] In **3**, the $[\text{W}(\text{CN})_8]^{3-}$ moiety has an approximate SAPR-8 geometry, which implies almost identical spin density delocalized onto π^* orbitals of each CN^- ligand. The average Mn–N and W···Mn distances of 2.19 and 5.42 Å, respectively, are shorter than those of 2.21 and 5.45 Å found in **2**. The average angle Mn–N–C of 163° in **3** is almost identical that of 163.8° in **2**. The antiferromagnetic interaction in **3** represented by the average $J_{\text{av}} = -15.6 \text{ cm}^{-1}$ for **3** is weaker than that of **2** ($J_{\text{av}} = -21.2 \text{ cm}^{-1}$). The location of CN^- bridges at the b and m positions of in

Table 2. Bridging modes of [W(CN)₈]³⁻, geometry of cyano bridges, and intramolecular J_{MnW} coupling constants for dinuclear {MnW}⁻ 1 and tetranuclear square {Mn₂W₂}²⁻ units in 2–4 and other cyano-bridged MnW units in 5–8.^[25a–25c]

| Compound | Polyhedron ^[a] | W–C [Å] | Mn–N [Å] | Mn–N–C/deg | Mn···W [Å] | <i>J</i> _{MnW} [cm ^{–1}] | Ref. |
|---|---------------------------|---------|----------|------------|------------|---|------------------------------|
| {MnW} [–] units | | | | | | | |
| 1 | TPRS-8(<i>b</i>) | 2.202 | 2.176 | 150.8 | 5.31 | –39 | this work |
| | TPRS-8(<i>b</i>) | 2.167 | 2.199 | 149.6 | 5.32 | | |
| Square-like {Mn ₂ W ₂ } ^{2–} units | | | | | | | |
| 2 | TPRS-8(<i>b</i>) | 2.150 | 2.167 | 167.6 | 5.43 | –25.7 | this work |
| | TPRS-8(<i>m</i>) | 2.183 | 2.249 | 159.9 | 5.46 | –16.7 | this work |
| 3 | SAPR-8 | 2.158 | 2.221 | 169.3 | 5.49 | –15.6 ^[b] | ^[25a] , this work |
| | SAPR-8 | 2.163 | 2.156 | 156.7 | 5.34 | | |
| 4 | DD-8 (A) | 2.140 | 2.245 | 169.2 | 5.51 | –20.4 ^[b] | ^[25b] , this work |
| | DD-8 (A) | 2.172 | 2.168 | 167.4 | 5.43 | | |
| Other cyano-bridged MnW units ^[c] | | | | | | | |
| 5 {Mn ₃ W ₂ } | DD-8 (A,A) | 2.263 | 2.21 | 163.2 | 5.46 | –12.0 | ^[25c] , this work |
| 6 {Mn ₄ W ₂ } | SAPR-8 | 2.162 | 2.21 | 160 | 5.41 | –12.2 ^[d] | ^[25a] , this work |
| 7 {Mn ₆ W ₃ } | SAPR-8 | 2.157 | 2.22 | 156 | 5.37 | –12.2 ^[d] | ^[25a] , this work |
| 8 {Mn ₆ W ₄ } | SAPR-8 | 2.165 | 2.23 | 168.2 | 5.49 | –12.4 ^[d] | ^[25a] , this work |

[a] The dominant polyhedra are indicated, for a detailed description see Tables S3 and S4; the notation (A) and (A,A) indicates the apical position of bridging CN⁻ ligands in the DD-8 polyhedron, and the notation (*b*) and (*m*) indicates the positions of the bridging CN⁻ ligands in the TPRS-8 polyhedron. [b] The average J_{MnW} values of -7.8 cm^{-1} for **3** and -10.2 cm^{-1} for **4**, calculated originally with $H_4 = -2J_1(S_{\text{Mn}1}S_{\text{W}1} + S_{\text{Mn}2}S_{\text{W}2} + S_{\text{Mn}1}S_{\text{W}2} + S_{\text{Mn}2}S_{\text{W}1})$ Hamiltonian, were multiplied by a factor of 2, for the sake of comparison. [c] The average values of interest are given for all cyano linkages due to the simplified magnetic interaction models applied. [d] The J_{MnW} values were originally calculated using the Hamiltonians relative to the molecular structure of MnW units and multiplied by the factor of 2 for the sake of comparison.

TPRS-8 for **2** seems to overcome the effect of shortening the Mn–N and Mn···W distances on going from **2** to **3**. This indicates the dominating influence of the coordination polyhedra type over the length of Mn–N bonds by the bridging mode present in {Mn₂W₂}²⁻ units in **2** and **3**. In **4** we found an A,A bridging mode in the [W(CN)₈]³⁻ moiety of DD-8 geometry. One bridge is relatively short (Mn–N = 2.168, W···Mn 5.43 Å) compared to the other (Mn–N = 2.245, W···Mn 5.51 Å), and both have a similar degree of bending (Mn–N–C angles of 169.2 and 167.4°). The average value of $J_{\text{MnW}} = -20.4 \text{ cm}^{-1}$ for **4** is located between those of **2** and **3**. Weaker Mn–W coupling is expected for **4**, which may be favored by relatively long average Mn–N (2.21 Å) and W···Mn (5.47 Å) distances, poorly bent Mn–N–C angles (168.3°) as well as a substantial contribution of A,A bridging geometry in the DD-8 polyhedron. However, the more complicated model of magnetic interactions in **4**, including intramolecular interactions within the [{Mn^{II}-(bpy)₂}(ox)]²⁺ dinuclear unit, was applied.

The discussion of J_{MnW} values obtained for **1** and **2** may be extended to the other discrete MnW cyano-bridged systems with different types of molecular structure including zig-zag, decorated zig-zag, decorated squares, and ribbons of vertex sharing squares topology presented for compounds **5–8** (Figure 1, Table 2).^[25a,25c] In **5**, two bridges of very similar metric parameters occur at the A,A positions of the [W(CN)₈]³⁻ dodecahedron, which may explain the relatively small value of J_{MnW} of -12 cm^{-1} . The average J_{MnW} values close to -12 cm^{-1} calculated for compounds **6–8**, may be explained in terms of the domination of the SAPR-8 geometry of [W(CN)₈]³⁻.

DFT calculations theoretically predict that increasing the number of cyano bridges may result in the decrease of the calculated J value for some cases of 3d hexacyanochromate(III)-based molecules.^[31] The magnitude of J_{MnW} values for the whole series **1–8** seems to obey this general trend (Table 2).

Conclusions

The novel low nuclearity cyano-bridged {Mn^{II}W^V}⁻ and {Mn^{II}₂W^V₂}²⁻ species, based on [W(CN)₈]³⁻ of TPRS-8 geometry, exhibit relatively strong magnetic interactions through cyano bridges represented by intramolecular Mn–W magnetic coupling constants $J = -39 \text{ cm}^{-1}$ for {Mn^{II}W^V}⁻ units and $J_1 = -25.7$ and $J_2 = -16.7 \text{ cm}^{-1}$ for {Mn^{II}₂W^V₂}²⁻ units. The J and J_1 constants are ascribed to the bridges in *b* positions of TPRS-8 [W(CN)₈]³⁻ polyhedra, favoring the strongest electronic interactions between the $d_{z^2}-d_{x^2-y^2}$ orbital of W and π^* orbitals of CN⁻. We found that the most important factors influencing the magnitude of the Mn–W magnetic interactions are the type of coordination polyhedra and bridging mode of [W(CN)₈]³⁻. We demonstrate that TPRS-8 geometry, decreasing the symmetry of [M(CN)₈]³⁻ ion, differentiates the extent of magnetic coupling within M^{II}–NC–M linkage in the manner alternative to the DD-8.

Experimental Section

Materials: All reagents were purchased from commercial sources (Sigma–Aldrich) and used as received. Sodium octacyanotungst-

ate(V)^[32] and cesium octacyanotungstate(V)^[33] salts were synthesized according to the published procedures.

Safety Warning: Perchlorate salts of transition metals are potentially explosive, therefore should be used in small amounts and handled with care.

Syntheses

[Mn^{II}(terpy)(dmf)(H₂O)₂][Mn^{II}(terpy)(H₂O)(dmf)(μ-NC)W^V(CN)₇]₂·6H₂O (1): A solution of terpy (0.116 g, 0.50 mmol) in methanol (10 mL) was added slowly to a methanolic solution of Mn(ClO₄)₂·6H₂O (0.181 g, 0.50 mmol, 10 mL) with constant stirring. A yellow solid was formed immediately and dmf (5 mL) was added dropwise, followed by slow addition of an aqueous solution of Na₃[W(CN)₈]·4H₂O (0.330 g, 0.62 mmol, 10 mL). After 10 min of stirring, the resulting brown solution was allowed to stand, and brown plate-shaped crystals were formed after two days; yield 79 mg, 23%. C₇₀H₇₄Mn₃N₂₈O₁₃W₂ (2048.01): calcd. C 41.0, H 3.6, N 19.2; found C 41.1, H 3.2, N 19.3. IR spectrum in the ν̄(CN) region: 2152 m, 2190 m is consistent with the presence of W^V–CN–Mn^{II} and W^V–CN stretching modes.^[34]

[Mn^{II}(phen)₃]₂[Mn^{II}(phen)₂(μ-NC)₂W^V(CN)₆]₂(ClO₄)₂·9H₂O (2): To an acetonitrile solution of [Mn(phen)₂(H₂O)₂](ClO₄)₂ (0.50 g, 0.77 mmol, 10 mL) was slowly added an aqueous solution of Cs₃[W(CN)₈]·2H₂O (0.579 g, 0.70 mmol, 10 mL), followed by addition of dmf (5 mL). A light brown precipitate removed by filtration, and the resulting solution was allowed to stand. The product forms amber plate-like crystals which were collected by filtration after two days; yield 60 mg, 10%. C₁₃₆H₁₁₂Cl₂Mn₄N₃₆O₁₄W₂ (2·3H₂O) (3132.92): calcd. C 52.14, H 3.60, N 16.09; found C 52.60, H 3.02, N 16.44. IR spectrum in the ν̄(CN) region: 2144 m, 2177 m is consistent with the presence of W^V–CN–Mn^{II} and W^V–CN stretching modes.^[34]

Physical Measurements: Infrared spectra were recorded with a Bio-Rad FTS 165 FT-IR and a Bruker EQUINOX 55 FT-IR spectrometer. Elemental analyses were performed on a EuroVector EuroEA instrument. Magnetic measurements were performed using a Quantum Design MPMS5-XL magnetometer with finely grounded polycrystalline samples. Temperature-dependent molar magnetic susceptibility, χ(*T*) and χ*T*(*T*), were obtained in the temperature (*T*) range 1.8–300 K at the magnetic field *H* of 1000 Oe. Temperature-dependent real magnetic susceptibility χ'(*T*) and imaginary magnetic susceptibility χ''(*T*) were measured at *H*_{ac} = 5 Oe. The field dependent magnetization *M*(*H*) data were obtained in the *H* range of 0–50 kOe at *T* = 2 K. The signal corrections of the sample holder and diamagnetism contributions were included in the magnetic coupling calculations.

X-ray Crystallography and Structure Solutions: The crystal structures of compounds were determined from single-crystal X-ray diffraction data collected at 292(2) K for **1** and **2**. Data were collected with a Nonius KappaCCD diffractometer using a graphite-monochromated Mo-*K*_α radiation source (λ = 0.71073 Å). Complete crystallographic data and data collection parameters are summarized in Table 3. DENZO and SCALEPACK programs^[35] were used for cell refinements and data reduction. The structures were solved by direct methods using the SIR97 program^[36] with the WinGX graphical user interface.^[37] The structure refinements were carried out with SHELX-97.^[38] No absorption corrections were performed. In all compounds the hydrogen atoms on carbon atoms were included at calculated positions and refined with a riding model. Hydrogen atoms of water molecules were not located for **1** and **2**.

Table 3. Crystallographic data for **1** and **2**.

| | 1 | 2 |
|--|--|---|
| Empirical formula | C ₇₀ H ₇₄ Mn ₃ N ₂₈ O ₁₃ W ₂ | C ₁₃₆ H ₉₈ Cl ₂ Mn ₄ N ₃₆ O ₁₇ W ₂ |
| Formula weight | 2048.09 | 3166.86 |
| Temperature | | 292(2) K |
| Wavelength | | 0.71073 Å |
| Crystal system | orthorhombic | monoclinic |
| Space group | <i>P</i> 2 ₁ 2 ₁ 2 ₁ | <i>P</i> 2 ₁ / <i>c</i> |
| Unit cell | <i>a</i> = 13.66640(14) Å | <i>a</i> = 12.3632(2) Å |
| Dimensions | <i>b</i> = 14.8099(2) Å | <i>b</i> = 34.0769(4) Å |
| | <i>c</i> = 40.9140(6) Å | <i>c</i> = 18.7915(2) Å |
| Volume | 8280.91(19) Å ³ | 6845.25(16) Å ³ |
| <i>Z</i> | 4 | 2 |
| Density (calculated) | 1.643 Mg/m ³ | 1.536 Mg/m ³ |
| Absorption coefficient | 3.289 mm ^{−1} | 2.148 mm ^{−1} |
| <i>F</i> (000) | 4068 | 3168 |
| Crystal size | 0.20 × 0.15 × 0.15 mm | 0.20 × 0.15 × 0.15 mm |
| θ range for data collection | 1.46 to 27.48° | 2.25 to 26.77° |
| Index ranges | 0 ≤ <i>h</i> ≤ 17, 0 ≤ <i>k</i> ≤ 19, 0 ≤ <i>l</i> ≤ 53 | 0 ≤ <i>h</i> ≤ 15, 0 ≤ <i>k</i> ≤ 39, −23 ≤ <i>l</i> ≤ 23 |
| Reflections collected | 17914 | 23650 |
| Independent reflections | 17914 [<i>R</i> (int) = 0.0000] | 14244 [<i>R</i> (int) = 0.0675] |
| Completeness to θ = 27.61° | 97.8% (θ 27.48) | 97.6% |
| Absorption correction | | none |
| Refinement method | | Full-matrix least-squares on <i>F</i> ² |
| Data/restraints/parameters | 17914/0/1061 | 14244/68/924 |
| Goodness-of-fit on <i>F</i> ² | 1.029 | 0.994 |
| Final <i>R</i> indices | <i>R</i> ₁ = 0.0786, | <i>R</i> ₁ = 0.0627, |
| [<i>I</i> > 2σ(<i>I</i>)] | <i>wR</i> ₂ = 0.1997 | <i>wR</i> ₂ = 0.1630 |
| <i>R</i> indices (all data) | <i>R</i> ₁ = 0.1123, | <i>R</i> ₁ = 0.1092, |
| | <i>wR</i> ₂ = 0.2333 | <i>wR</i> ₂ = 0.1913 |
| Largest diff. peak/hole | 1.220/−2.019 e Å ^{−3} | 0.964/−1.396 e Å ^{−3} |

In **1**, O10A and O10B correspond to a water molecule which is disordered over two positions separated by 1.34 Å with refined occupancies of 0.607 and 0.393. There are five other water molecules of crystallization with full occupancy in the asymmetric unit, giving a total of six water molecules of crystallization in the formula unit. In **2** the oxygen atoms of the perchlorate anion were found to be disordered between two different positions with refined partial occupancies of 0.6635 and 0.3365. Seven crystallographically independent water molecules were found in **2**, of these O1W, O2W, and O3W have occupancies of 1.0, while O4W, O5W, O6W, and O7W have occupancies of 0.5, 0.5, 0.5, and 0.25, respectively, giving a total of nine water molecules in the formula unit. The oxygen atoms with partial occupancies were not refined anisotropically. All other non-hydrogen atoms were refined anisotropically.

CCDC-768846 (for **1**) and -768847 (for **2**) contain the supplementary crystallographic data for this paper. These data can be obtained free of charge from The Cambridge Crystallographic Data Centre via www.ccdc.cam.ac.uk/data_request/cif.

Supporting Information (see also the footnote on the first page of this article): Bond lengths and angles for **1** and **2**, shape determining angles for **1–4**, continuous shape measures for **1–8**, including the description of CShM method, views of noncovalent intermolecular interactions for **1** and **2**, and χ(*T*) ZFC/FC and *M*(*H*) signals for **1**.

Acknowledgments

The study has been partially supported by The European Commission (EC), within NoE project MAGMANet, contract no. NMP3-CT-2005-515767, and by the Polish Ministry of Science and Higher Education within research projects 1535/B/H03/2009/36 and 0087-B-H03-2008-34.

- [1] K. R. Dunbar, R. A. Heintz, in: *Prog. Inorg. Chem.* (Ed.: K. D. Karlin), John Wiley & Sons, **1997**, vol. 45, pp. 283–391.
- [2] M. Ohba, H. Okawa, *Coord. Chem. Rev.* **2000**, 198, 313–328.
- [3] J. Černák, M. Orendáč, I. Potočník, J. Chomič, A. Orendáčová, J. Skorupa, A. Feher, *Coord. Chem. Rev.* **2002**, 224, 51–66.
- [4] C. J. Shorrock, H. Jong, R. J. Batchelor, D. B. Leznoff, *Inorg. Chem.* **2003**, 42, 3917–3924.
- [5] S. Kitagawa, R. Kitaura, Sh. Noro, *Angew. Chem. Int. Ed.* **2004**, 43, 2334–2375.
- [6] J. A. Real, A. B. Gaspar, M. C. Munoz, *Dalton Trans.* **2005**, 2062–2079.
- [7] S. Tanase, F. Tuna, Ph. Guionneau, Th. Maris, G. Rombaut, C. Mathoniere, M. Andruh, O. Kahn, J.-P. Sutter, *Inorg. Chem.* **2003**, 42, 1625–1631.
- [8] P. Przychodzeń, T. Korzeniak, R. Podgajny, B. Sieklucka, *Coord. Chem. Rev.* **2006**, 250, 2234–2260.
- [9] M. Ohba, K. Yoneda, G. Augusti, M. C. Munoz, A. B. Gaspar, J. A. Real, M. Yamasaki, H. Ando, Y. Nakao, S. Sasaki, S. Kitagawa, *Angew. Chem. Int. Ed.* **2009**, 48, 4767–4771.
- [10] M. Verdaguer, A. Bleuzen, V. Marvaud, J. Vaisserman, M. Seuleiman, C. Desplanches, C. Train, R. Garde, G. Gelly, C. Lomenech, I. Rosenman, P. Veillet, C. Cartier, F. Villain, *Coord. Chem. Rev.* **1999**, 190–192, 1023–1047.
- [11] a) S. Ohkoshi, K. Hashimoto, *J. Photochem. Photobiol. C: Photochem. Rev.* **2001**, 2, 71–88; b) N. Shimamoto, S. Ohkoshi, O. Sato, K. Hashimoto, *Inorg. Chem.* **2002**, 41, 678–684; c) R. Le Bris, J.-D. Cafun, C. Mathoniere, A. Bleuzen, J.-F. Letard, *New J. Chem.* **2009**, 33, 1255–1261.
- [12] a) M. Ohba, W. Kaneko, S. Kitagawa, T. Maeda, M. Mito, *J. Am. Chem. Soc.* **2008**, 130, 4475–4484; b) W. Kaneko, M. Mito, S. Kitagawa, M. Ohba, *Chem. Eur. J.* **2008**, 14, 3481–3489.
- [13] a) W. Kaneko, M. Ohba, S. Kitagawa, *J. Am. Chem. Soc.* **2007**, 129, 13706–13712; b) N. Yanai, W. Kaneko, K. Yoneda, M. Ohba, S. Kitagawa, *J. Am. Chem. Soc.* **2007**, 129, 3496–3497.
- [14] a) W. E. Buschmann, J. Enslin, Ph. Gülich, J. S. Miller, *Chem. Eur. J.* **1999**, 5, 3019–3028; b) W. Kosaka, K. Nomura, K. Hashimoto, S. Ohkoshi, *J. Am. Chem. Soc.* **2005**, 127, 8590–8591; c) E. Coronado, M. C. Giménez-López, T. Korzeniak, G. Levchenko, F. M. Romero, A. Segura, V. García-Baonza, J. C. Cezar, F. M. F. de Groot, A. Milner, M. Paz-Pasternak, *J. Am. Chem. Soc.* **2008**, 130, 15519–15532.
- [15] a) K. Inoue, H. Imai, P. S. Ghalsasi, K. Kikuchi, M. Ohba, H. Okawa, J. V. Yakhmi, *Angew. Chem. Int. Ed.* **2001**, 40, 4242–4245; b) W. Kaneko, S. Kitagawa, M. Ohba, *J. Am. Chem. Soc.* **2007**, 129, 248–249.
- [16] a) D. Li, R. Clérac, O. Roubeau, E. Harté, C. Mathoniere, R. Le Bris, St. M. Holmes, *J. Am. Chem. Soc.* **2008**, 130, 252–258; b) V. Marvaud, C. Decroix, A. Scullier, C. Guyard-Duhayon, J. Vaissermann, F. Gonnet, M. Verdaguer, *Chem. Eur. J.* **2003**, 9, 1677–1691; c) M. Shatruk, K. E. Chamber, A. V. Prosvirin, K. R. Dunbar, *Inorg. Chem.* **2007**, 46, 5155–5165; d) C. P. Berlinguette, K. R. Dunbar, *Chem. Commun.* **2005**, 2451–2453.
- [17] M. Clemente-Leon, E. Coronado, A. Lopez-Munoz, D. Repetto, Ch. Mingotaud, D. Brinzei, L. Catala, T. Mallah, *Chem. Mater.* **2008**, 20, 4642–4652.
- [18] a) J. T. Culp, J.-H. Park, F. Frye, Y.-D. Huh, M. W. Meisel, D. R. Talham, *Coord. Chem. Rev.* **2005**, 249, 2642–2648; b) F. A. Frye, D. M. Pajeroski, J.-H. Par, D. R. Talham, *Chem. Mater.* **2008**, 20, 5706–5713.
- [19] E. Coronado, C. Marti-Gastaldo, E. Navarro-Moratalla, A. Ribera, *Inorg. Chem.* **2010**, 49, 1313–1315.
- [20] a) E. L. Muetterties, L. J. Guggenberger, *J. Am. Chem. Soc.* **1974**, 96, 1748; b) J. K. Burdett, R. Hoffmann, R. C. Fay, *Inorg. Chem.* **1978**, 17, 2553–2568.
- [21] a) A. Samotus, J. Szklarzewicz, *Coord. Chem. Rev.* **1993**, 125, 63; b) P. M. Kiernan, W. P. Griffith, *J. Chem. Soc., Dalton Trans.* **1975**, 2489.
- [22] a) B. Nowicka, M. Rams, K. Stadnicka, B. Sieklucka, *Inorg. Chem.* **2007**, 46, 8123–8125; b) S. Ohkoshi, Y. Tsunobuchi, H. Takahashi, T. Hozumi, M. Shiro, K. Hashimoto, *J. Am. Chem. Soc.* **2007**, 129, 3084–3085; c) H. Higashikawa, K. Okuda, J. Kishine, N. Masuhara, K. Inoue, *Chem. Lett.* **2007**, 36, 1022–1023; d) S. Ohkoshi, H. Tokoro, T. Hozumi, Y. Zhang, K. Hashimoto, C. Mathoniere, I. Bord, G. Rombaut, M. Verelst, Ch. Cartier dit Moulin, F. Villain, *J. Am. Chem. Soc.* **2006**, 128, 270–277; e) S. Ohkoshi, Y. Hamada, T. Matsuda, Y. Tsunobuchi, H. Tokoro, *Chem. Mater.* **2008**, 20, 3048–3054; f) M. Arai, W. Kosaka, T. Matsuda, S. Ohkoshi, *Angew. Chem. Int. Ed.* **2008**, 47, 6885–6887.
- [23] a) Z. J. Zhong, H. Seino, Y. Mizobe, M. Hidai, M. Verdaguer, S. Ohkoshi, K. Hashimoto, *Inorg. Chem.* **2000**, 39, 5059–5101; b) M. Pilkington, S. Decurtins, *Chimia* **2000**, 54, 593–601; c) Y. Song, S. Ohkoshi, Y. Arimoto, H. Seino, Y. Mizobe, R. Hashimoto, *Inorg. Chem.* **2003**, 42, 1848–1856; d) T. Kashi-gawi, S. Ohkoshi, H. Seino, Y. Mizobe, K. Hashimoto, *J. Am. Chem. Soc.* **2004**, 126, 5024–5025; e) R. Podgajny, D. Pinkowicz, T. Korzeniak, W. Nitek, M. Rams, B. Sieklucka, *Inorg. Chem.* **2007**, 46, 10416–10425; f) D. Pinkowicz, R. Podgajny, W. Nitek, M. Makarewicz, M. Czapla, M. Mihalik, M. Bałanda, B. Sieklucka, *Inorg. Chim. Acta* **2008**, 361, 3957–3962; g) D. Pinkowicz, R. Podgajny, M. Bałanda, M. Makarewicz, B. Gaweł, W. Łasocha, B. Sieklucka, *Inorg. Chem.* **2008**, 47, 9745–9747; h) W. Kosaka, K. Hashimoto, S. Ohkoshi, *Bull. Chem. Soc. Jpn.* **2008**, 81, 992–994.
- [24] W. Kosaka, K. Imoto, Y. Tsunobuchi, S. Ohkoshi, *Inorg. Chem.* **2009**, 48, 4604–4606.
- [25] a) H. Zhao, M. Shatruk, A. V. Prosvirin, K. R. Dunbar, *Chem. Eur. J.* **2007**, 13, 6573–6589; b) Z.-X. Wang, X.-L. Li, T.-W. Wang, Y.-Z. Li, S. Ohkoshi, K. Hashimoto, Y. Song, X.-Z. You, *Inorg. Chem.* **2007**, 46, 10990–10995; c) R. Podgajny, C. Desplanches, B. Sieklucka, R. Sessoli, V. Villar, C. Paulsen, W. Wernsdorfer, Y. Dromzée, M. Verdaguer, *Inorg. Chem.* **2002**, 41, 1323–1327; d) Th. S. Venkatakrishnan, R. Rajamani, S. Ramasesha, J.-P. Sutter, *Inorg. Chem.* **2007**, 46, 9569–9574; e) Zh. J. Zhong, H. Seino, Y. Mizobe, M. Hidai, A. Fujishima, S. Ohkoshi, K. Hashimoto, *J. Am. Chem. Soc.* **2000**, 122, 2952–2953; f) E. Ruiz, G. Rajaraman, S. Alvarez, B. Gillon, J. Stride, R. Clérac, J. Lariónova, S. Descurtins, *Angew. Chem. Int. Ed.* **2005**, 44, 2711–2715; g) Y.-Q. Zhang, Ch.-L. Luo, *Dalton Trans.* **2008**, 4575–4584.
- [26] T. Korzeniak, C. Desplanches, R. Podgajny, C. Giménez-Saiz, K. Stadnicka, M. Rams, B. Sieklucka, *Inorg. Chem.* **2009**, 48, 2865–2872.
- [27] a) D. Casanova, J. Cirera, M. Llunell, P. Alemany, D. Avnir, S. Alvarez, *J. Am. Chem. Soc.* **2004**, 126, 1755–1763; b) S. Alvarez, P. Alemany, D. Casanova, J. Cirera, M. Llunell, D. Avnir, *Coord. Chem. Rev.* **2005**, 249, 1693–1708; c) D. Casanova, M. Llunell, P. Alemany, S. Alvarez, *Chem. Eur. J.* **2005**, 11, 1479–1494; d) M. Llunell, D. Casanova, J. Cirera, J. M. Bofill, P. Alemany, S. Alvarez, M. Pinsky, D. Avnir, *Shape*, version 1.1b, University of Barcelona, Barcelona, Spain, **2005**. The description of CShM method together with the significance of shape parameters are given in the Supporting Information (Table S4).
- [28] O. Kahn, *Molecular Magnetism*; VCH Publishers, New York, **1993**, p. 131.
- [29] S. McCann, M. McCann, M. T. Casey, M. Jackman, M. Deveraux, V. McKee, *Inorg. Chim. Acta* **1998**, 279, 24–29.

- [30] D. Visinescu, C. Desplanches, I. Imaz, V. Bahers, R. Pradhan, F. A. Villamena, Ph. Guionneau, J.-P. Sutter, *J. Am. Chem. Soc.* **2006**, *128*, 10202–10212.
- [31] a) Y.-Q. Zhang, Ch.-L. Luo, *Eur. J. Inorg. Chem.* **2006**, 2292–2298; b) Y.-Q. Zhang, Ch.-L. Luo, *J. Phys. Chem. A* **2006**, *110*, 5096–5101.
- [32] A. Samotus, *Pol. J. Chem.* **1973**, *47*, 653.
- [33] C. R. Dennis, A. J. van Wyk, S. S. Basson, J. G. Leipoldt, *Transition Met. Chem.* **1992**, *17*, 471.
- [34] R. Podgajny, T. Korzeniak, K. Stadnicka, Y. Dromzee, N. W. Alcock, W. Errington, K. Kruczała, M. Bałanda, T. J. Kemp, M. Verdaguer, B. Sieklucka, *Dalton Trans.* **2003**, 3458–3468.
- [35] Z. Otwinowski, W. Minor, DENZO-SCALEPACK, *Processing of X-ray Diffraction Data Collected in Oscillation Mode*, in: *Methods Enzymol.* (Eds. C. W. Carter Jr., R. M. Sweet), Academic Press, New York, **1997**; *Macromolecular Crystallography*, part A, vol. 276.
- [36] A. Altomare, M. C. Burla, M. Camalli, G. Cascarano, C. Giacovazzo, A. Guagliardi, A. G. G. Moliterni, G. Polidori, R. Spagna, *J. Appl. Crystallogr.* **1999**, *32*, 115–119.
- [37] L. J. Farrugia, *J. Appl. Crystallogr.* **1997**, *32*, 837.
- [38] G. M. Sheldrick, *SHELXL-97*, University of Göttingen, Germany, **1997**.

Received: March 11, 2010
Published Online: July 27, 2010

Binuclear Cyclopentadienylmanganese Carbonyl Thiocarbonyls: Four-Electron Donor Bridging Thiocarbonyl Groups of Two Types and a Bridging Acetylenedithiolate Ligand

Zhong Zhang,^[a,b] Qian-shu Li,^{*[a,c]} Yaoming Xie,^[d] R. Bruce King,^{*[a,d]} and Henry F. Schaefer III^[d]

Keywords: Manganese / Cyclopentadienyl ligands / Density functional calculations / Metal-metal interactions / Metal thiocarbonyls

As a starting point, the mononuclear cyclopentadienylmanganese carbonyl thiocarbonyls $[\text{CpMn}(\text{CS})(\text{CO})_n]$ ($\text{Cp} = \eta^5\text{-C}_5\text{H}_5$; $n = 2, 1, 0$) and binuclear derivatives $[\text{Cp}_2\text{Mn}_2(\text{CS})_2(\text{CO})_n]$ ($n = 3, 2, 1, 0$) have been studied by density functional theory (DFT). For coordinately saturated binuclear $[\text{Cp}_2\text{Mn}_2(\text{CS})_2(\text{CO})_3]$, the four electron donor end-on CE ($\text{E} = \text{O}, \text{S}$) bridged structures are preferred energetically over the normal CE ($\text{E} = \text{O}, \text{S}$) bridged structures, analogous to $[\text{Cr}_2(\text{CS})_2(\text{CO})_9]$. The lowest energy structure for $[\text{Cp}_2\text{Mn}_2(\text{CS})_2(\text{CO})_2]$ has one four-electron donor bridging $\eta^2\text{-}\mu\text{-CS}$ group. However, this structure is thermodynamically unstable with respect to disproportionation into $[\text{Cp}_2\text{Mn}_2(\text{CS})_2(\text{CO})_3]$ and $[\text{Cp}_2\text{Mn}_2(\text{CS})_2(\text{CO})]$. Only two structures are found for $[\text{Cp}_2\text{Mn}_2(\text{CS})_2(\text{CO})]$ as is the case for the carbonyl analogue $[\text{Cp}_2\text{Mn}_2(\text{CO})_3]$. The global minimum of

$[\text{Cp}_2\text{Mn}_2(\text{CS})_2(\text{CO})]$, a singlet triply bridged structure, is very favorable energetically with respect to loss of a CO group, disproportionation into $[\text{Cp}_2\text{Mn}_2(\text{CS})_2(\text{CO})_2] + [(\text{Cp})_2\text{Mn}_2(\text{CS})_2]$, and dissociation into mononuclear fragments. The lowest energy structure for $[\text{Cp}_2\text{Mn}_2(\text{CS})_2]$ is a triplet structure with two bridging CS groups and the $\text{Mn}\equiv\text{Mn}$ triple bond required to give each Mn atom a 17-electron configuration for a binuclear triplet. A higher energy singlet $[\text{Cp}_2\text{Mn}_2(\text{CS})_2]$ structure is found with a very short $\text{Mn}\equiv\text{Mn}$ distance of about 2.1 Å suggesting the formal quadruple bond required to give each Mn atom the favored 18-electron configuration. In other higher energy singlet and triplet $[\text{Cp}_2\text{Mn}_2(\text{CS})_2]$ structures the two CS ligands have coupled to form an acetylenedithiolate ligand bridging the two manganese atoms.

1. Introduction

The chemistry of cyclopentadienylmanganese carbonyls dates back to 1954 shortly after the discovery of ferrocene with the independent syntheses by Fischer and Jira^[1] and by Piper, Cotton, and Wilkinson^[2] of the mononuclear derivative $[(\eta^5\text{-C}_5\text{H}_5)\text{Mn}(\text{CO})_3]$ (Figure 1), commonly known as cymantrene. This compound, with the favored 18-electron configuration for the manganese atom, is the most stable and least chemically reactive of the simple mononuclear and binuclear first row transition metal cyclopentadienylmetal carbonyls. This stability allows extensive organic chemistry to be done on the cyclopentadienyl (Cp) ring of cymantrene without disturbing the $\text{Mn}(\text{CO})_3$ unit.^[3]

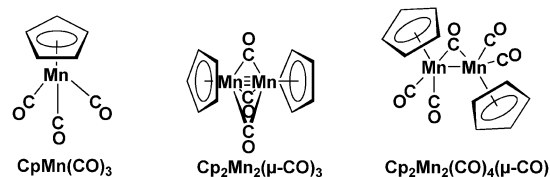


Figure 1. Structures of some cyclopentadienylmanganese carbonyl derivatives.

About 30 years after the discovery of $[(\eta^5\text{-C}_5\text{H}_5)\text{Mn}(\text{CO})_3]$, the first binuclear cyclopentadienylmanganese carbonyl $[(\eta^5\text{-Me}_5\text{C}_5)_2\text{Mn}_2(\mu\text{-CO})_3]$ (Figure 1) was synthesized by the photolysis of $[(\eta^5\text{-Me}_5\text{C}_5)\text{Mn}(\text{CO})_3]$ in tetrahydrofuran followed by spontaneous decomposition of the intermediate $[(\eta^5\text{-Me}_5\text{C}_5)\text{Mn}(\text{CO})_2(\text{C}_4\text{H}_8)]$.^[4] The resulting $[(\eta^5\text{-Me}_5\text{C}_5)_2\text{Mn}_2(\mu\text{-CO})_3]$ was shown by X-ray diffraction to have three bridging CO groups and a very short $\text{Mn}\equiv\text{Mn}$ distance of 2.17 Å, suggesting the triple bond required to give each manganese atom the favored 18-electron configuration.^[5]

To date no other binuclear cyclopentadienylmanganese carbonyl derivatives have been synthesized as stable compounds. However, $[(\eta^5\text{-C}_5\text{H}_5)_2\text{Mn}_2(\text{CO})_4(\mu\text{-CO})]$ (Figure 1) has been detected as a transient intermediate from the flash

[a] Center for Computational Quantum Chemistry, South China Normal University, Guangzhou 510631, P. R. China

[b] College of Science, Northwest A&F University, Yanlin, Shanxi 712100, P. R. China

[c] Institute of Chemical Physics, Beijing Institute of Technology, Beijing 100081, P. R. China

[d] Department of Chemistry and Center for Computational Chemistry, University of Georgia, Athens, Georgia 30602, USA

Supporting information for this article is available on the WWW under <http://dx.doi.org/10.1002/ejic.201000172>.

photolysis of $[\text{CpMn}(\text{CO})_3]$ in heptane solution.^[6] The iso-valent binuclear cyclopentadienylrhodium carbonyl chemistry is considerably more extensive. Thus $[(\eta^5\text{-Me}_5\text{C}_5)_2\text{-Re}_2(\text{CO})_4(\mu\text{-CO})]$ with a bridging CO group and formal Re–Re single bond,^[7] $[(\eta^5\text{-Me}_5\text{C}_5)_2\text{Re}_2(\text{CO})_2(\mu\text{-CO})_2]$ with two terminal CO groups and two semibridging CO groups and a formal Re=Re double bond,^[8] and $[(\eta^5\text{-Me}_5\text{C}_5)_2\text{-Re}_2(\mu\text{-CO})_3]$ with three bridging CO groups and a formal Re≡Re triple bond^[9] have all been synthesized as stable compounds that have been structurally characterized by X-ray crystallography. The entire series of binuclear $(\eta^5\text{-C}_5\text{H}_5)_2\text{-M}_2(\text{CO})_n$ derivatives for both manganese and rhenium ($\text{M} = \text{Mn}^{[10]}$ and $\text{Re}^{[11]}$ $n = 5, 4, 3, 2$) have been studied recently by density functional theory (DFT) methods.

The extensive chemistry of metal carbonyls makes of interest the corresponding chemistry of analogous metal thiocarbonyls. However, the instability of carbon monosulfide, CS, at temperatures above -100°C makes the synthesis of metal thiocarbonyls much more difficult than the synthesis of metal carbonyls, where the readily available and extremely stable carbon monoxide can be used as a source of carbonyl groups, even if the reaction requires high pressures of carbon monoxide. Because of the instability of carbon monosulfide, indirect methods must be used to introduce thiocarbonyl groups into transition metal complexes, using compounds such as carbon disulfide (CS_2) or thiophosgene ($\text{S}=\text{CCl}_2$) as sources of CS groups.^[12–16]

The stability of the $[(\eta^5\text{-C}_5\text{H}_5)\text{MnL}_3]$ system allows the entire series of cyclopentadienylmanganese carbonyl thiocarbonyls $[(\eta^5\text{-C}_5\text{H}_5)\text{Mn}(\text{CS})_n(\text{CO})_{3-n}]$ ($n = 1, 2, 3$) to be synthesized.^[17,18] Thus the mononuclear mono(thiocarbonyl) $[(\eta^5\text{-C}_5\text{H}_5)\text{Mn}(\text{CS})(\text{CO})_2]$ is obtained in good yield by the conversion of $[(\eta^5\text{-C}_5\text{H}_5)\text{Mn}(\text{CO})_3]$ to the cyclooctene complex $[(\eta^5\text{-C}_5\text{H}_5)\text{Mn}(\text{CO})_2(\eta^2\text{-C}_8\text{H}_{14})]$ followed by reaction with PPh_3 in CS_2 solution.^[18] This sequence of reactions can be continued to convert $[(\eta^5\text{-C}_5\text{H}_5)\text{Mn}(\text{CS})(\text{CO})_2]$ to $[(\eta^5\text{-C}_5\text{H}_5)\text{Mn}(\text{CS})_2(\text{CO})]$ and finally even $[(\eta^5\text{-C}_5\text{H}_5)\text{Mn}(\text{CS})_2(\text{CO})]$ to $[(\eta^5\text{-C}_5\text{H}_5)\text{Mn}(\text{CS})_3]$, although the yields decrease as the number of thiocarbonyl groups increases. Despite the availability and stability of the entire mononuclear series $[(\eta^5\text{-C}_5\text{H}_5)\text{Mn}(\text{CS})_n(\text{CO})_{3-n}]$ ($n = 1, 2, 3$), no binuclear cyclopentadienylmanganese carbonyl thiocarbonyls $[(\eta^5\text{-C}_5\text{H}_5)_2\text{Mn}_2(\text{CS})_m(\text{CO})_n]$ have yet been synthesized.

Because of the difficulty of synthesizing metal thiocarbonyls as compared with similar metal carbonyls, theoretical studies on metal thiocarbonyl chemistry are important for predicting the potential most productive areas of metal thiocarbonyl chemistry in order to focus synthetic studies on the most interesting targets. In this connection, we have used density functional theory to study mononuclear and binuclear thiocarbonyl derivatives. To date, these theoretical studies have been restricted to the first row transition metals and to compounds containing only carbonyl and thiocarbonyl groups. In this connection, our theoretical studies on $[\text{Fe}_2(\text{CS})_2(\text{CO})_n]$,^[19] $[\text{Co}_2(\text{CS})_2(\text{CO})_{n-1}]$,^[20] and $[\text{Cr}_2(\text{CS})_2(\text{CO})_{n+2}]$ ($n = 7, 6, 5, 4$)^[21] indicate not only that CS is a preferred bridging ligand to CO but also that four-electron

donor CS groups are frequently found in the low energy structures of binuclear derivatives in preference to higher order metal-metal multiple bonds. Moreover, for $[\text{Cr}_2(\text{CS})_2(\text{CO})_9]$, isolobal with $[(\eta^5\text{-C}_5\text{H}_5)_2\text{Mn}_2(\text{CS})_2(\text{CO})_5]$, the four-electron donor CE ($\text{E} = \text{O}, \text{S}$) bridged structures are energetically preferred over structures with direct Cr–Cr bonds.^[21] Furthermore, such structures are thermodynamically viable with respect to dissociation into the corresponding mononuclear fragments. These points make of interest a theoretical study on $[(\eta^5\text{-C}_5\text{H}_5)_2\text{Mn}_2(\text{CS})_2(\text{CO})_n]$ ($n = 3, 2, 1, 0$) derivatives with the following questions of particular interest:

- (1) Are structures with four-electron donor CE ($\text{E} = \text{O}, \text{S}$) bridges without Mn–Mn bonds energetically preferred over structures with manganese–manganese bonds for $[(\eta^5\text{-C}_5\text{H}_5)_2\text{Mn}_2(\text{CS})_2(\text{CO})_5]$ isoelectronic with $[\text{Cr}_2(\text{CS})_2(\text{CO})_9]$?
- (2) Are structures with four-electron donor $\eta^2\text{-}\mu\text{-CS}$ groups energetically preferred over structures with higher order manganese–manganese bonds for the unsaturated $[(\eta^5\text{-C}_5\text{H}_5)_2\text{Mn}_2(\text{CS})_m(\text{CO})_n]$ derivatives, as they are for $\text{M}_2(\text{CS})_2(\text{CO})_n$ derivatives?

Compounds of the type $[(\eta^5\text{-C}_5\text{H}_5)_2\text{Mn}_2(\text{CS})_2(\text{CO})_n]$ ($n = 3, 2, 1, 0$) were included in this study because of the prospects of synthesizing or at least generating them from the stable and readily obtained^[17,18] $[(\eta^5\text{-C}_5\text{H}_5)\text{Mn}(\text{CS})(\text{CO})_2]$.

2. Theoretical Methods

Electron correlation effects were considered using density functional theory (DFT) methods, which have evolved as a practical and effective computational tool, especially for organometallic compounds.^[22–30] Two DFT methods were used in this study. The first functional is the popular B3LYP method, which is the hybrid HF/DFT method using a combination of the three-parameter Becke exchange functional (B3) with the Lee–Yang–Parr (LYP) generalized gradient correlation functional.^[31,32] The other DFT method used in this paper is BP86, which combines Becke's 1988 exchange functional (B) with Perdew's 1986 gradient-corrected correlation functional method (P86).^[33,34] It has been noted elsewhere that the BP86 method may be somewhat more reliable than B3LYP for the type of organometallic systems considered in this paper, particularly for vibrational frequencies.^[35–37]

Our DZP basis sets for carbon, oxygen, and sulfur add one set of pure spherical harmonic d functions with orbital exponents $a_d(\text{C}) = 0.75$, $a_d(\text{O}) = 0.85$, and $a_d(\text{S}) = 0.70$ to the standard Huzinaga–Dunning–Hay contracted DZ sets.^[38–40] The C and O basis sets are designated as (9s5p1d/4s2p1d) and the S basis set is designated as (12s8p1d/6s4p1d). For H, a set of p polarization functions $a_p(\text{H}) = 0.75$ is added to the standard Huzinaga–Dunning–Hay contracted DZ set. For Mn, in our loosely contracted DZP basis set, the Wachters primitive set^[41] is augmented by two sets of p functions and one set of d functions, contracted following Hood, Pitzer and Schaefer,^[42] and designated (14s11p6d/10s8p3d). For $[\text{CpMn}(\text{CS})(\text{CO})_2]$, $[\text{CpMn}(\text{CS})$

(CO)], [CpMn(CS)], [Cp₂Mn₂(CS)₂(CO)₃], [Cp₂Mn₂(CS)₂(CO)₂], [Cp₂Mn₂(CS)₂(CO)], and [Cp₂Mn₂(CS)₂], there are 247, 217, 187, 464, 434, 404, and 374 contracted Gaussian functions, respectively.

The geometries of all structures were fully optimized using the B3LYP/DZP and BP86/DZP methods. Vibrational frequencies were determined by evaluating analytically the second derivatives of the energy with respect to the nuclear coordinates. The corresponding infrared intensities were also evaluated analytically. All of the computations were carried out with the Gaussian 03 program,^[43] exercising the fine grid option (75 radial shells, 302 angular points) for evaluating integrals numerically,^[44] while the tight (10⁻⁸ hartree) designation is the default for the self-consistent field (SCF) convergence.

In the search for minima using all currently implemented DFT methods, low magnitude imaginary vibrational frequencies are suspect because of significant limitations in the numerical integration procedures. Thus all imaginary vibrational frequencies with a magnitude less than 100i cm⁻¹ are considered questionable, and are given less weight in the analysis.^[44–46] Therefore, we do not always follow such low imaginary vibrational frequencies.

The optimized structures are listed in Tables 1–5 and depicted in Figures 2–8. Each [Cp_aMn_a(CS)_a(CO)_b] structure is designated as **ab-c**, where **a** is the number of manganese atoms (the same as the number of CS groups), **b** is the number of CO groups, and **c** orders the structures according to their relative energies. Triplet structures are indicated by **T**. Thus the lowest energy structure of [Cp₂Mn₂(CS)₂(CO)₃] is designated **23-1**. In the text, energies are listed as 5.9(2.9) kcal/mol corresponding to the results from the B3LYP(BP86) methods, and bond lengths are listed in the same way.

3. Results and Discussion

3.1 Mononuclear Derivatives

Three structures have been optimized for [CpMn(CS)(CO)_n] (*n* = 2, 1, 0) (Figure 2 and Table 1). Structure **12-1** with a tiny imaginary frequency of 18i(19i) cm⁻¹ is still a genuine minimum since the tiny imaginary

frequency is removed by using a finer integration grid of (120, 974). The predicted ν(CO) and ν(CS) vibrational frequencies of 1994, 1951, and 1303 cm⁻¹ agree well with the experimental values^[17] of 2006, 1954, and 1266 cm⁻¹. Structures **11-1** and **10-1** are found to be genuine minima with all real vibrational frequencies. These structures derive from **12-1** by loss of one CO group or two CO groups, respectively. The Mn–C(S) and C=S distances gradually decrease and increase, respectively, from 1.769(1.763) Å and 1.565(1.580) Å in **12-1** to 1.748(1.737) and 1.581(1.600) Å in **10-1**, indicating both stronger σ-bonding and π-back-bonding as CO groups are lost.

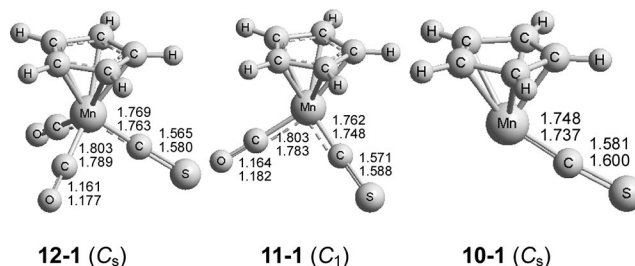


Figure 2. Optimized structures for mononuclear derivatives. In Figures 2–8 the upper distances are obtained by the B3LYP method and the lower distances by the BP86 method.

Table 1. The ν(CO) and ν(CS) stretching frequencies and infrared intensities predicted by the BP86 method for the mononuclear [CpMn(CS)(CO)_n] (*n* = 2, 1, 0) derivatives.

| | ν(CO) | ν(CS) |
|-------------------------------|---------------------------------|---------------------------|
| 12-1 (C _s) | 1994 (a', 678), 1951 (a'', 818) | 1303 (a', 648) |
| Exp. ^[17] | 2006 s, 1954 s | 1266 s (CS ₂) |
| Exp. ^[17] | 2010 s, 1959 s | 1271 s (Nujol) |
| 11-1 (C ₁) | 1941 (a, 825) | 1277 (a, 553) |
| 10-1 (C _s) | | 1249 (a', 488) |

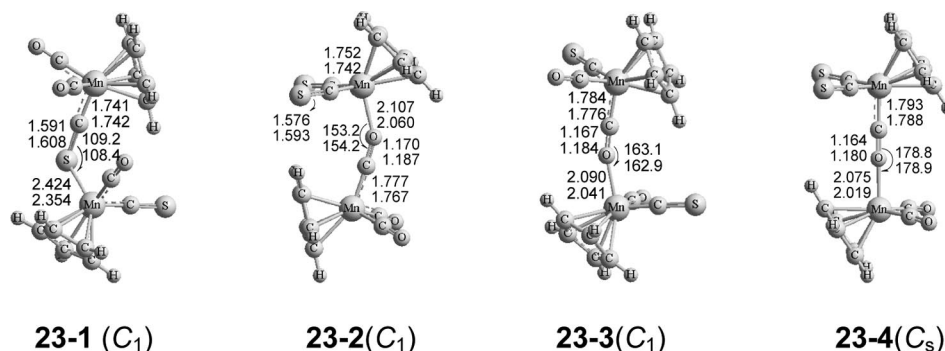


Figure 3. Four optimized [Cp₂Mn₂(CS)₂(CO)₃] structures with a single four-electron donor bridging CE (E = O, S) group but without direct Mn–Mn bonding.

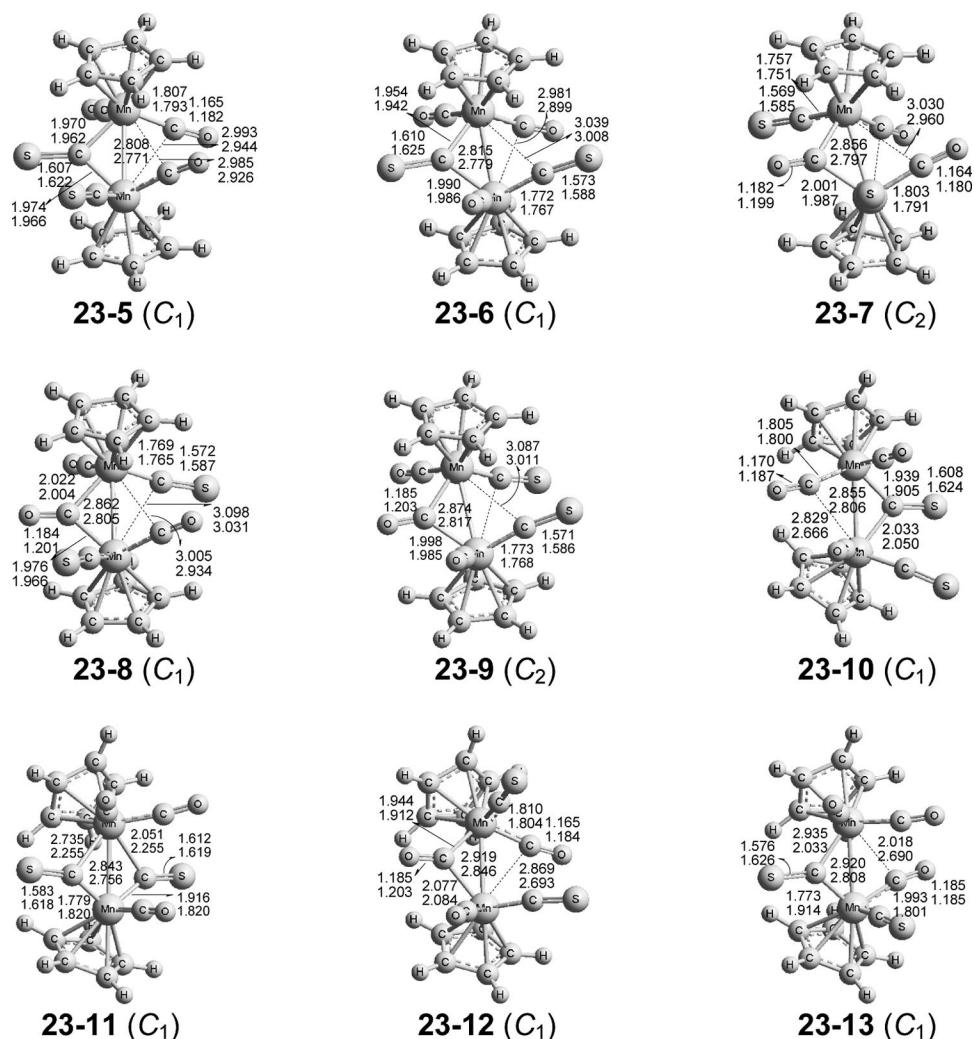


Figure 4. Nine optimized $[\text{Cp}_2\text{Mn}_2(\text{CS})_2(\text{CO})_3]$ structures with direct Mn–Mn interactions.

include four structures with a single four-electron donor bridging CE ($\text{E} = \text{O}, \text{S}$) group but without direct Mn–Mn bonding, five structures with one normal bridging group

and two semi-bridging groups, and four structures with two bridging groups. All of these structures are reported to be genuine minima with no imaginary vibrational frequencies.

Table 2. Relative energies (ΔE in kcal/mol) and Mn...Mn distances ($R_{\text{Mn-Mn}}$ in Å) for the four energetically competitive optimized $[\text{Cp}_2\text{Mn}_2(\text{CS})_2(\text{CO})_3]$ structures with a single four-electron donor bridging CE ($\text{E} = \text{O}, \text{S}$) group but without direct Mn...Mn bonding. None of the structures has any imaginary vibrational frequencies.

| | | 23-1 (C_1) | 23-2 (C_1) | 23-3 (C_1) | 23-4 (C_s) |
|-------|--------------------|-----------------------|-----------------------|-----------------------|-----------------------|
| B3LYP | ΔE | 0.0 | 1.7 | 2.5 | 4.2 |
| | $R_{\text{Mn-Mn}}$ | 4.715 | 4.888 | 5.030 | 5.030 |
| BP86 | ΔE | 0.0 | 5.5 | 7.0 | 9.2 |
| | $R_{\text{Mn-Mn}}$ | 4.663 | 4.872 | 4.934 | 4.988 |

The four lowest energy $[\text{Cp}_2\text{Mn}_2(\text{CS})_2(\text{CO})_3]$ structures all have an end-on CE group bonded to one manganese atom through the carbon atom and to the other manganese atom through the chalcogen atom (O or S). In these structures the manganese atoms are too far apart from each other (4.6 to 5.0 Å; see Table 2) for any direct manganese-manganese bonding (Figure 3 and Table 2). Structure **23-1** is found to be the global minimum of $[\text{Cp}_2\text{Mn}_2(\text{CS})_2(\text{CO})_3]$ by the B3LYP method, but lies 1.5 kcal/mol above a fifth structure **23-5** (Figure 4) by the BP86 method. The Mn–S

Table 3. Relative energies (ΔE in kcal/mol), and Mn–Mn distances ($R_{\text{Mn-Mn}}$, in Å) for the $[\text{Cp}_2\text{Mn}_2(\text{CS})_2(\text{CO})_3]$ structures with direct Mn–Mn bonds. None of these structures has any imaginary vibrational frequencies.

| | | 23-5 (C_1) | 23-6 (C_1) | 23-7 (C_2) | 23-8 (C_1) | 23-9 (C_2) | 23-10 (C_1) | 23-11 (C_1) | 23-12 (C_1) | 23-13 (C_1) |
|-------|--------------------|-----------------------|-----------------------|-----------------------|-----------------------|-----------------------|------------------------|------------------------|------------------------|------------------------|
| B3LYP | ΔE | 4.6 | 5.3 | 6.6 | 7.8 | 9.6 | 11.9 | 12.5 | 14.7 | 15.1 |
| | $R_{\text{Mn-Mn}}$ | 2.808 | 2.815 | 2.856 | 2.862 | 2.874 | 2.855 | 2.843 | 2.919 | 2.920 |
| BP86 | ΔE | –1.5 | –0.6 | 0.1 | 1.3 | 3.2 | 6.2 | 6.1 | 9.0 | 6.5 |
| | $R_{\text{Mn-Mn}}$ | 2.771 | 2.779 | 2.797 | 2.805 | 2.817 | 2.806 | 2.756 | 2.846 | 2.808 |

distance of 2.424(2.354) Å in **23-1** indicates an end-on four-electron donor bridged CS group and no direct Mn...Mn interaction. Structure **23-1** can be characterized by a $\nu(\text{CS})$ vibrational frequency at 1225 cm⁻¹ for the bridging CS group (Table S1 in the Supporting Information). A related four-electron donor bridging thiocarbonyl group has been found experimentally in ($\eta^6\text{-MeC}_6\text{H}_5$)Cr(CO)₂[CS→Cr(CO)₅], which is stable enough to be isolated and characterized by X-ray crystallography.^[47] The experimental Cr–C, C–S, S–Cr distances and Cr–C–S angle are 1.747 Å, 1.604 Å, 2.486 Å, and 110.4° respectively, in ($\eta^6\text{-MeC}_6\text{H}_5$)Cr(CO)₂[CS→Cr(CO)₅]. These structural parameters are very similar to the corresponding Mn–C, C–S, S–Mn distances and Mn–C–S angle of 1.741 Å, 1.60 ± 0.01 Å, 2.39 ± 0.06 Å, and 108.8 ± 0.6°, respectively, predicted in this research for the related [Cp₂Mn₂(CS)₂(CO)₃] structure **23-1**. This suggests stronger π -back bonding when three carbonyl groups in a Cr(CO)₅ unit are replaced by a the weaker π -acceptor $\eta^5\text{-C}_5\text{H}_5$ ligand in an isoelectronic CpMn unit.

The [Cp₂Mn₂(CS)₂(CO)₃] structure **23-2**, at 1.7(5.5) kcal/mol above **23-1** is predicted to have a nearly end-on bridging CO group (Figure 3 and Table 2). The next two related structures, namely **23-3** and **23-4**, are predicted to lie 2.5(7.0) and 4.2(9.2) kcal/mol above **23-1**, respectively. The C=O distances in the bridging carbonyl group decrease monotonically from 1.170(1.187) Å in **23-2** to 1.164(1.180) Å in **23-4**, suggesting decreasing π -back-bonding from the Mn atom. In addition, the Mn–O(C) distances gradually decrease from 2.107(2.060) Å in **23-2** to 2.075(2.019) Å in **23-4**, indicating increasing σ -bonding from oxygen to the Mn atom. In going from **23-4** to **23-2** via **23-3**, the Mn–O–C angles deviate increasingly from linearity (180°). This may be attributed to effective orbital overlap of the two fragments. These [Cp₂Mn₂(CS)₂(CO)₃] structures can be characterized by a rather low $\nu(\text{CO})$ frequency of 1810 ± 4 cm⁻¹, assigned to the four-electron donor end-on bridging carbonyl group. Related end-on bridging carbonyl groups have been found experimentally in ($\eta^6\text{-C}_6\text{Me}_6$)₂Ti(CH₃)←OC(CO)₂Mo($\eta^5\text{-C}_5\text{H}_5$)^[48] and in ($\eta^5\text{-C}_5\text{Me}_5$)₂V←OCV(CO)₅^[49] which are stable enough to be isolated and structurally characterized by X-ray crystallography. These derivatives have Ti–O(C) and V–O(C) distances of 2.057 Å and 2.075 Å, respectively, which are close to the 2.09 ± 0.02 Å Mn–O(C) distances for the nearly linear end-on bridging carbonyl groups in structures **23-2** to **23-4**.

The [Cp₂Mn₂(CS)₂(CO)₃] structure **23-5** with a bridging CS group and two semi-bridging CO groups is reported to lie 4.6(–1.5) kcal/mol above(below) **23-1**. The Mn–Mn distance of 2.808(2.771) Å in **23-1** is shortened by about 0.05(0.04) Å relative to that in the lowest energy predicted structure^[10] for [Cp₂Mn₂(CO)₅]. This arises mainly from the effect of the bridging CS group. The following four [Cp₂Mn₂(CS)₂(CO)₃] structures (from **23-6** to **23-9**) are rather similar to structure **23-5** except for different arrangements of the CS groups. The energies of these four structures are predicted to lie at most 9.6(3.2) kcal/mol above

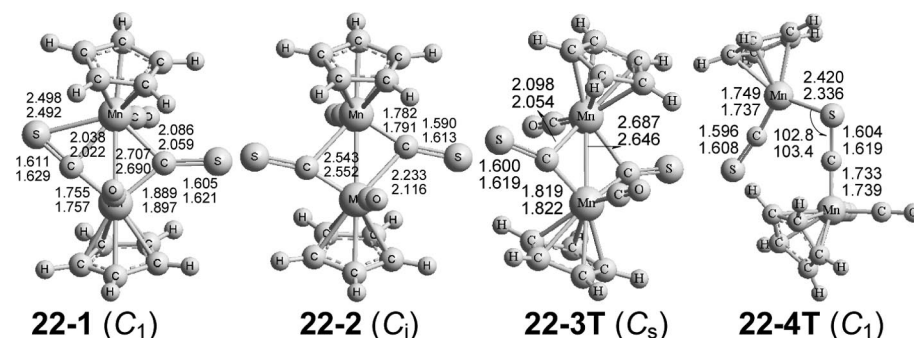
23-1. The Mn–Mn distances in these five structures are predicted to fall in the narrow range 2.84 ± 0.04(2.79 ± 0.03) Å, corresponding to the formal Mn–Mn single bonds required to give each manganese atom the favored 18-electron configuration.

Several doubly bridged [Cp₂Mn₂(CS)₂(CO)₃] structures were found (Figure 4 and Table 3). Thus structure **23-10**, at 11.9(6.2) kcal/mol above **23-1**, is predicted to have a normal two-electron donor bridging CS group and a semibridging CO group (Figure 4 and Table 3). The long Mn–C distance to the semibridging CO group is predicted to be 2.829(2.666) Å. The [Cp₂Mn₂(CS)₂(CO)₃] structure **23-11**, at 12.5(6.1) kcal/mol above **23-1**, has two bridging CS groups. The B3LYP method indicates one of these CS groups to be a semibridging CS group with a short Mn–C(S) distance of 1.779 Å and a long Mn–C(S) distance of 2.735 Å. However, the BP86 method predicts the Mn–C(S) distances to the corresponding CS group to be more nearly equal at 1.820 and 2.255 Å. A similar situation occurs in structure **23-13**, at 15.1(6.5) kcal/mol above **23-1**, for which the B3LYP method gives very unequal Mn–C(S) distances of 1.773 and 2.935 Å to the bridging thiocarbonyl group, whereas the BP86 method give more nearly equal Mn–C(S) distances of 1.914 and 2.033 Å. The remaining [Cp₂Mn₂(CS)₂(CO)₃] structure, namely **23-12** with a normal bridging CO group and a semibridging CO group, lies 14.7(9.0) kcal/mol above **23-1**. The Mn–Mn distances of 2.89 ± 0.03 (2.83 ± 0.06) Å in these four structures correspond to formal single bonds thereby giving both manganese atoms the favored 18-electron configuration.

3.2.2 [Cp₂Mn₂(CS)₂(CO)₂]

The potential energy surface of [Cp₂Mn₂(CS)₂(CO)₂] is very complicated since no less than 22 structures have been optimized for [Cp₂Mn₂(CS)₂(CO)₂]. The details of all of these 22 structures are of limited chemical interest, particularly since [Cp₂Mn₂(CS)₂(CO)₂] is shown to be thermodynamically unstable with respect to disproportionation into [Cp₂Mn₂(CS)₂(CO)₃] and [Cp₂Mn₂(CS)₂(CO)]. Four selected structures (Figure 5 and Table 4) are discussed here as representatives of the different structure types and spin states.

The lowest energy structure for [Cp₂Mn₂(CS)₂(CO)₂], namely **22-1** (Figure 5 and Table 4), is reported to be a genuine minimum with no imaginary vibrational frequencies. Structure **22-1** has two non-equivalent bridging CS groups. One of the CS groups in **22-1** has a very short Mn–S distance of 2.498(2.492) Å suggesting a four-electron donor bridging $\eta^2\text{-}\mu\text{-CS}$ group. This is also indicated by a relatively low $\nu(\text{CS})$ frequency of 1124 cm⁻¹ (Table S2 in the Supporting Information). The other CS group is a normal two-electron donor bridging CS group. The predicted Mn–Mn distance of 2.707(2.690) Å in **22-1** corresponds to a formal single bond, thereby giving both manganese atoms the favored 18-electron configuration in a [Cp₂Mn₂(CS)₂(CO)₂] structure with one four-electron donor bridging $\eta^2\text{-}\mu\text{-CS}$ group.

Figure 5. Four optimized structures for $[\text{Cp}_2\text{Mn}_2(\text{CS})_2(\text{CO})_2]$.Table 4. Relative energies (ΔE in kcal/mol), and Mn–Mn distances ($R_{\text{Mn–Mn}}$, in Å) for four selected $[\text{Cp}_2\text{Mn}_2(\text{CS})_2(\text{CO})_2]$ structures. None of the structures has any imaginary vibrational frequencies except for **22-2** with an imaginary frequency of $59i\text{ cm}^{-1}$ (BP86).

| | | 22-1 (C₁) | 22-2 (C₁) | 22-3T (C_s) | 22-4T (C₁) |
|-------|--------------------|-----------------------------|-----------------------------|------------------------------|------------------------------|
| B3LYP | ΔE | 0 | 9.9 | 0.9 | 7.2 |
| | $R_{\text{Mn–Mn}}$ | 2.707 | 2.543 | 2.687 | >4.0 |
| BP86 | ΔE | 0 | 8.7 | 9.0 | 25.9 |
| | $R_{\text{Mn–Mn}}$ | 2.690 | 2.552 | 2.646 | >4.0 |

The second lowest energy structure of $[\text{Cp}_2\text{Mn}_2(\text{CS})_2(\text{CO})_2]$, namely **22-2**, is also a singlet with two bridging CS groups (Figure 5 and Table 4) and is predicted to lie 9.9(8.7) kcal/mol above **22-1**. Structure **22-2** is predicted to be a genuine minimum by B3LYP but has a small imaginary frequency of $59i\text{ cm}^{-1}$ with the BP86 method. Structure **22-2** is derived from the doubly CS-bridged $[\text{Cp}_2\text{Mn}_2(\text{CS})_2(\text{CO})_3]$ structure **23-11** (Figure 4) by loss of a terminal CO group from the upper Mn atom with concurrent bending of the $\eta^5\text{-C}_5\text{H}_5\text{Mn}$ bond to fill the resulting gap. The Mn=Mn distance of 2.543(2.552) Å is about 0.2 Å shorter than that in **23-11**, suggesting the formal Mn=Mn double bond required to give both Mn atoms the favored 18-electron rare gas configurations.

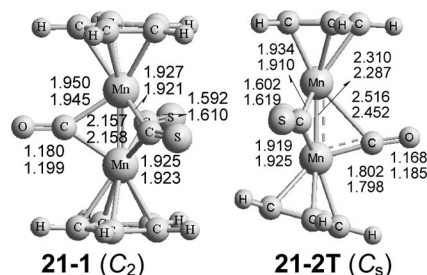
The lowest energy triplet $[\text{Cp}_2\text{Mn}_2(\text{CS})_2(\text{CO})_2]$ structure **22-3T** with only two-electron donor CO and CS groups (Figure 5 and Table 4) lies 0.9(9.0) kcal/mol above **22-1** with no imaginary vibrational frequencies. Structure **22-3T** is closely related to **22-2** in that both structures have two bridging two-electron donor CS groups. However, the 2.687(2.646) Å Mn–Mn distance in **22-3T** is significantly longer than that in **22-2** and corresponds to a formal single bond, thereby giving both manganese atoms the 17-electron configurations for a binuclear triplet.

The last of the 22 total $[\text{Cp}_2\text{Mn}_2(\text{CS})_2(\text{CO})_2]$ structures reported in this paper is **22-4T**, lying 7.2(25.9) kcal/mol above **22-1** with no imaginary vibrational frequencies (Figure 5 and Table 4). Structure **22-4T** may be derived from the global minimum of $[\text{Cp}_2\text{Mn}_2(\text{CS})_2(\text{CO})_2]$ (**23-1** in Figure 3) by loss of a terminal CO group from the $\text{CpMn}(\text{CS})(\text{CO})$ fragment. The Mn–S distance of 2.420(2.336) Å in **22-4T** is slightly shorter than that in **23-1** and the bridging C=S distance of 1.604(1.619) Å in **22-4T** is slightly longer than that in **23-1**. The predicted $\nu(\text{CS})$ vi-

brational frequency of 1198 cm^{-1} (Table S2 in the Supporting Information) for the four-electron donor end-on bridging CS group in **22-4T** is 27 cm^{-1} lower than that in **23-1**.

3.2.3 $[\text{Cp}_2\text{Mn}_2(\text{CS})_2(\text{CO})]$

Only two distinct structures were found for $[\text{Cp}_2\text{Mn}_2(\text{CS})_2(\text{CO})]$ within 20 kcal/mol of the global minimum **21-1** (Figure 6). Both of these structures are triply bridged, with two bridging CS groups and one bridging CO group. Attempts to optimize singly bridged structures of $[\text{Cp}_2\text{Mn}_2(\text{CS})_2(\text{CO})]$ led to the triply bridged structures **21-1** or **21-2T**.

Figure 6. Two optimized $[\text{Cp}_2\text{Mn}_2(\text{CS})_2(\text{CO})]$ structures.

The singlet global minimum $[\text{Cp}_2\text{Mn}_2(\text{CS})_2(\text{CO})]$ structure **21-1** has no imaginary vibrational frequencies. The predicted triply bridged Mn=Mn distance in **21-1** is very short at 2.157(2.158) Å, consistent with the triply bridged triple bond required to give both manganese atoms the favored 18-electron configuration. This predicted Mn=Mn bond length in **21-1** is very close to the experimental Mn=Mn distance of 2.17 Å in the isovalent triply bridged structure $[\text{Cp}_2\text{Mn}_2(\mu\text{-CO})_3]$, as determined by X-ray crystallography.^[5]

The other $[\text{Cp}_2\text{Mn}_2(\text{CS})_2(\text{CO})]$ structure **21-2T** is a triply bridged triplet, lying 10.8(20.4) kcal/mol above **21-1**. Structure **21-2T** is predicted to be a genuine local minimum by the BP86 method but to have two small imaginary frequencies of $55i$ and $11i\text{ cm}^{-1}$ by the B3LYP method. The bridging carbonyl group in **21-2T** is a semibridging carbonyl group with a short Mn–C distance of 1.802(1.798) Å and a long Mn–C distance of 2.516(2.452) Å. The triply bridged Mn=Mn distance of 2.310(2.287) Å in **21-2T** is about 0.15 Å longer than the triply bridged Mn=Mn dis-

tance in **21-1**. This suggests a formal Mn=Mn double bond in **21-2**, thereby giving each Mn atom the 17-electron configuration for a binuclear triplet.

3.2.4 [$\text{Cp}_2\text{Mn}_2(\text{CS})_2$]

Eight structures were optimized for [$\text{Cp}_2\text{Mn}_2(\text{CS})_2$] (Figures 7 and 8 and Table 5), including four triplet and four singlet structures. The global minimum [$\text{Cp}_2\text{Mn}_2(\text{CS})_2$] structure **20-1T** is found to be a triplet with two normal two-electron donor bridging CS groups (Figure 7 and Table 5). This structure is analogous to the lowest energy structure predicted^[10] for [$\text{Cp}_2\text{Mn}_2(\mu\text{-CO})_2$], except for substitution of two $\mu\text{-CO}$ groups with two $\mu\text{-CS}$ groups. The predicted Mn≡Mn distance of 2.230(2.213) Å is quite close to the previously predicted Mn≡Mn triple bond length of 2.204(2.202) Å in the [$\text{Cp}_2\text{Mn}_2(\text{CO})_2$] global minimum.^[10] This suggests a formal triple bond in **20-1T**, thereby giving each Mn atom the favored 17-electron configuration for a

binuclear triplet. An analogous singlet [$\text{Cp}_2\text{Mn}_2(\text{CS})_2$] structure **20-5** is predicted to be the lowest lying singlet but lies 3.5 kcal/mol (BP86) above **20-1T**. The Mn≡Mn distance in **20-5** is predicted to be 2.119(2.078) Å, which is about 0.11 Å shorter than that in **20-1T**. This is consistent with the formal quadruple bond required to give both Mn atoms in **20-6** the favored 18-electron configuration. An analogous singlet structure of [$\text{Cp}_2\text{Mn}_2(\text{CO})_2$] was found in the previous DFT study of [$\text{Cp}_2\text{Mn}_2(\text{CO})_n$] derivatives,^[10] also with a very short (ca. 2.1 Å) Mn≡Mn distance suggesting a similar formal quadruple bond.

The triplet [$\text{Cp}_2\text{Mn}_2(\text{CS})_2$] structure **20-2T** is predicted to have an SC_2S ligand and an Mn...Mn distance of 3.355(3.157) Å, which is too long for any direct bonding (Figure 7 and Table 5). Structure **20-2T** lies 1.9 kcal/mol above **20-1T** by the BP86 method but a 7.7 kcal/mol below **20-1T** by the B3LYP method. If each manganese atom in **20-2T** receives a single electron from a sulfur atom of the

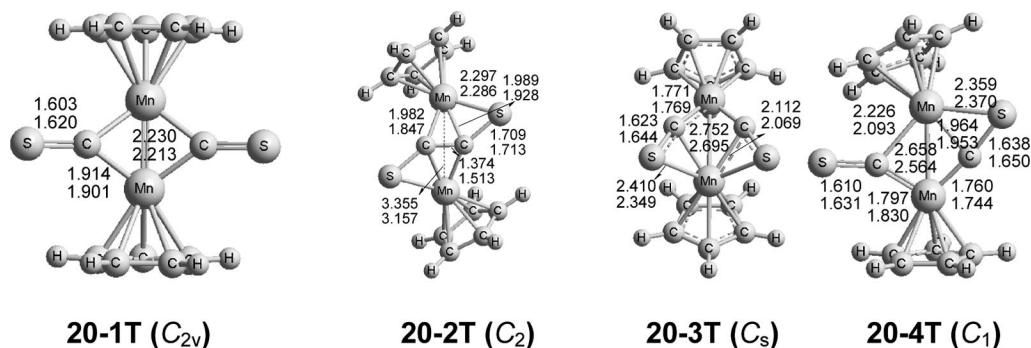


Figure 7. Four optimized triplet [$\text{Cp}_2\text{Mn}_2(\text{CS})_2$] structures.

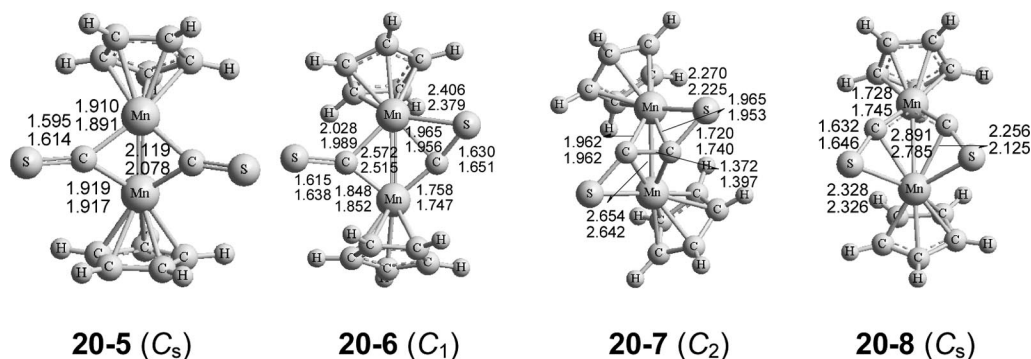


Figure 8. Four optimized singlet [$\text{Cp}_2\text{Mn}_2(\text{CS})_2$] structures.

Table 5. Relative energies (ΔE in kcal/mol), spin expectation values ($\langle S^2 \rangle$), numbers of imaginary vibrational frequencies (N_{img}), and Mn–Mn distances ($R_{\text{Mn–Mn}}$, in Å) for the eight [$\text{Cp}_2\text{Mn}_2(\text{CS})_2$] structures.

| | | 20-1T (C_{2v}) | 20-2T (C_2) | 20-3T (C_s) | 20-4T (C_1) | 20-5 (C_s) | 20-6 (C_1) | 20-7 (C_2) | 20-8 (C_s) |
|-------|-----------------------|---------------------------|------------------------|------------------------|------------------------|-----------------------|-----------------------|-----------------------|-----------------------|
| B3LYP | ΔE | 0.0 | –7.7 | –2.1 | 0.9 | 20.5 | 23.1 | 19.5 | 25.0 |
| | $\langle S^2 \rangle$ | 2.62 | 2.56 | 2.17 | 2.82 | 0.00 | 0.00 | 0.00 | 0.00 |
| | N_{img} | 0 | 0 | 27i | 0 | 0 | 0 | 0 | 0 |
| | $R_{\text{Mn–Mn}}$ | 2.230 | >4.0 | 2.752 | 2.658 | 2.119 | 2.572 | 2.654 | 2.891 |
| BP86 | ΔE | 0.0 | 1.9 | 2.6 | 4.5 | 3.5 | 12.4 | 13.7 | 16.1 |
| | $\langle S^2 \rangle$ | 2.11 | 2.03 | 2.04 | 2.09 | 0.00 | 0.00 | 0.00 | 0.00 |
| | N_{img} | 0 | 0 | 35i | 0 | 0 | 0 | 0 | 31i |
| | $R_{\text{Mn–Mn}}$ | 2.213 | >4.0 | 2.695 | 2.564 | 2.078 | 2.515 | 2.642 | 2.785 |

SC₂S ligand and an additional single electron from each of the carbon atoms, then the SC₂S ligand functions as a three-electron donor to each of the two manganese atoms. This gives each manganese atom in **20-2T** a 15-electron configuration, consistent with a binuclear triplet. A singlet [Cp₂Mn₂(CS)₂] structure **20-7** has a SC₂S group that is bonded to each manganese atom in a similar way as in **20-2T**. However, in the singlet **20-7** the Mn–Mn distance of 2.654(2.642) Å is short enough to correspond to a formal single bond. Since the SC₂S ligand donates three electrons to each manganese atom, both manganese atoms in the singlet **20-7** have a 16-electron configuration. Structure **20-7** is predicted to lie 19.5(13.7) kcal/mol above **20-1T**.

The triplet doubly bridged [Cp₂Mn₂(CS)₂] structure **20-3T** (Figure 7 and Table 5) lies 2.1 kcal/mol below **20-1T** by B3LYP but 2.6 kcal/mol above **20-1T** by BP86 and is predicted to have a small imaginary frequency of 27i(35i) cm⁻¹. The Mn–S distances to the two equivalent bridging CS groups in **20-3T** are short at 2.410(2.349) Å, indicating that both CS groups are four-electron donor η²-μ-CS groups. The Mn–Mn bond length in **20-3T** is predicted to be 2.752(2.695) Å, indicating the Mn–Mn single bond required to give both Mn atoms the 17-electron configuration for a binuclear triplet. The similar singlet [Cp₂Mn₂(CS)₂] structure **20-8** lies 25.0(16.1) kcal/mol above **20-1T**. In **20-8** the Mn–S distances to the equivalent η²-μ-CS groups are 2.328(2.326) Å. The Mn–Mn distance in the singlet **20-8** at 2.891(2.795) Å is similar to that in **20-3T**, again indicating a formal single bond. This gives one Mn atom the favored 18-electron configuration but the other Mn atom only a 16-electron configuration.

The remaining pair of similar [Cp₂Mn₂(CS)₂] structures, namely **20-4T** and **20-6**, both have a four-electron donor CS group and an approximately symmetric bridging CS group (Figures 7, 8 and Table 5). These two structures are reported to lie above **20-1T** by 0.9(4.5) kcal/mol for **20-4T** and by 23.1(12.4) kcal/mol for **20-6**. The Mn=Mn distances predicted to be 2.61 ± 0.04(2.54 ± 0.02) Å correspond to formal double bonds, thereby providing a total of 34 electrons for the two Mn atoms. This gives each manganese atom in the triplet **20-4T** a 17-electron configuration. In the singlet **20-6** one Mn atom has the favored 18-electron configuration but the other Mn atom has only a 16-electron configuration.

3.3 Dissociation and Disproportionation Reactions

Table 6 shows the carbonyl dissociation energies for the reaction [Cp_aMn_a(CS)_a(CO)_n] → [Cp_aMn_a(CS)_a(CO)_{n-1}] + CO. Furthermore these carbonyl dissociation energies are compared with the energies of the corresponding [Cp_aMn_a(CO)_{n+2}] → [Cp_aMn_a(CO)_{n+1}] + CO reactions obtained from a previous theoretical study.^[10] In order to evaluate these energy differences the lowest energy structures of the reactants and products are considered.

Table 6. Bond dissociation energies (kcal/mol) for successive removal of carbonyl groups from [CpMn(CS)(CO)_m], [Cp₂Mn₂(CS)₂(CO)_n], and related compounds.^[10]

| | B3LYP | BP86 |
|--|-------|------|
| [CpMn(CS)(CO) ₂] → [CpMn(CS)(CO)] + CO | 52.2 | 61.9 |
| [CpMn(CS)(CO)] → [CpMn(CS)] + CO | 53.0 | 62.9 |
| [Cp ₂ Mn ₂ (CS) ₂ (CO) ₃] → [Cp ₂ Mn ₂ (CS) ₂ (CO) ₂] + CO | 24.5 | 25.5 |
| [Cp ₂ Mn ₂ (CO) ₅] → [Cp ₂ Mn ₂ (CO) ₄] + CO | 34.1 | 42.4 |
| [Cp ₂ Mn ₂ (CS) ₂ (CO) ₂] → [Cp ₂ Mn ₂ (CS) ₂ (CO)] + CO | 20.9 | 21.1 |
| [Cp ₂ Mn ₂ (CO) ₄] → [Cp ₂ Mn ₂ (CO) ₃] + CO | 16.2 | 15.5 |
| [Cp ₂ Mn ₂ (CS) ₂ (CO)] → [Cp ₂ Mn ₂ (CS) ₂] + CO | 41.5 | 63.7 |
| [Cp ₂ Mn ₂ (CO) ₃] → [Cp ₂ Mn ₂ (CO) ₂] + CO | 46.4 | 67.0 |

The comparison of carbonyl dissociation energies (Table 6) suggests greater stability of [Cp₂Mn₂(CS)₂(CO)₂] relative to the all-carbonyl analogue. This is indicated by a lower carbonyl dissociation energy of [Cp₂Mn₂(CS)₂(CO)₃] to give [Cp₂Mn₂(CS)₂(CO)₂] + CO relative to that of [Cp₂Mn₂(CO)₅] to give [Cp₂Mn₂(CO)₄] + CO; as well as a higher carbonyl dissociation energy of [Cp₂Mn₂(CS)₂(CO)₂] to give [Cp₂Mn₂(CS)₂(CO)] + CO relative to that of [Cp₂Mn₂(CO)₄] to give [Cp₂Mn₂(CO)₃] + CO. This undoubtedly is an effect of the four-electron donor bridging η²-μ-CS group in the lowest energy [Cp₂Mn₂(CS)₂(CO)₂] structure. Thus the lowest energy structure of the corresponding [Cp₂Mn₂(CO)₄] does not have an analogous four-electron donor η²-μ-CO group, but instead only two-electron donor carbonyl groups and a formal Mn=Mn double bond.

Table 7 compares the energies for the disproportionation reactions [2Cp₂Mn₂(CS)₂(CO)_n] → [Cp₂Mn₂(CS)₂(CO)_{n+1}] + [Cp₂Mn₂(CS)₂(CO)_{n-1}] with those of the corresponding reactions [2Cp₂Mn₂(CO)_{n+2}] → [Cp₂Mn₂(CO)_{n+3}] + [Cp₂Mn₂(CO)_{n+1}]. These results indicate that [Cp₂Mn₂(CS)₂(CO)₂], like [Cp₂Mn₂(CO)₄], is thermodynamically unstable with respect to such disproportionation. However, the disproportionation energy of [Cp₂Mn₂(CS)₂(CO)₂] is much lower than that of the corresponding [Cp₂Mn₂(CO)₄]. Like the carbonyl dissociation energies discussed above, the much lower disproportionation energy of [Cp₂Mn₂(CS)₂(CO)₂] relative to [Cp₂Mn₂(CO)₄] may be a consequence of the four-electron donor bridging η²-μ-CS group in the lowest energy structure of [Cp₂Mn₂(CS)₂(CO)₂], but the lack of an analogous η²-μ-CO group in [Cp₂Mn₂(CO)₄]. In contrast to [Cp₂Mn₂(CS)₂(CO)₂] and [Cp₂Mn₂(CO)₄], the analogous compounds [Cp₂Mn₂(CS)₂-

Table 7. Disproportionation energies (in kcal/mol).

| | B3LYP | BP86 |
|---|-------|-------|
| [2Cp ₂ Mn ₂ (CS) ₂ (CO) ₂] → [Cp ₂ Mn ₂ (CS) ₂ (CO) ₃] + [Cp ₂ Mn ₂ (CS) ₂ (CO)] | -3.6 | -4.4 |
| [2Cp ₂ Mn ₂ (CO) ₄] → [Cp ₂ Mn ₂ (CO) ₅] + [Cp ₂ Mn ₂ (CO) ₃] (ref. ^[10]) | -17.9 | -27.0 |
| [2Cp ₂ Mn ₂ (CS) ₂ (CO)] → [Cp ₂ Mn ₂ (CS) ₂ (CO) ₂] + [Cp ₂ Mn ₂ (CS) ₂] | 22.6 | 42.6 |
| [2Cp ₂ Mn ₂ (CO) ₃] → [Cp ₂ Mn ₂ (CO) ₂] + [Cp ₂ Mn ₂ (CO) ₄] (ref. ^[10]) | 30.1 | 51.6 |

(CO)] and $[\text{Cp}_2\text{Mn}_2(\text{CO})_3]$ are both very thermodynamically stable with respect to disproportionation (Table 7).

The energies of the binuclear complexes $[\text{Cp}_2\text{Mn}_2(\text{CS})_2(\text{CO})_n]$ with respect to dissociation into two mononuclear fragments are listed in Table 8. These energies are larger than 40 kcal/mol except for the end-on CE (E = S, O) bridged structures **23-1** and **23-2** for $[\text{Cp}_2\text{Mn}_2(\text{CS})_2(\text{CO})_3]$, which are found to be 16.0(22.4) kcal/mol and 14.3(16.9) kcal/mol, respectively. These dissociation energies are somewhat larger than the corresponding chromium dissociation energies of 9.8(10.1) kcal/mol for analogous (E = S, O) bridged $[\text{Cr}_2(\text{CS})_2(\text{CO})_9]$ structures.^[21] This shows that the $\text{M} \leftarrow \text{E}=\text{C}$ interactions are strengthened from $[(\text{CO})_3\text{Cr}(\text{CS})(\text{CO})]$ to isoelectronic $[\text{CpMn}(\text{CS})(\text{CO})]$, presumably because a Cp ring is a weaker π -acceptor than three carbonyl groups.

Table 8. Energies (units in kcal/mol) and basis set superposition errors (BSSE) for dissociation of the binuclear complexes $[\text{Cp}_2\text{Mn}_2(\text{CS})_2(\text{CO})_n]$ into two mononuclear $[\text{CpMn}(\text{CS})(\text{CO})_x]$ or $[\text{CpMn}(\text{CS})(\text{CO})_{x+1}]$ fragments.

| | B3LYP | | BP86 | |
|--|------------|------|------------|------|
| | ΔE | BSSE | ΔE | BSSE |
| $[\text{Cp}_2\text{Mn}_2(\text{CS})_2(\text{CO})_3]$ (23-1) \rightarrow $[\text{CpMn}(\text{CS})(\text{CO})_2] +$ $[\text{CpMn}(\text{CS})(\text{CO})]$ | 16.0 | 2.8 | 22.4 | 2.6 |
| $[\text{Cp}_2\text{Mn}_2(\text{CS})_2(\text{CO})_3]$ (23-2) \rightarrow $[\text{CpMn}(\text{CS})(\text{CO})_2] +$ $[\text{CpMn}(\text{CS})(\text{CO})]$ | 14.3 | 3.3 | 16.9 | 3.2 |
| $[\text{Cp}_2\text{Mn}_2(\text{CS})_2(\text{CO})_2] \rightarrow$ $2[\text{CpMn}(\text{CS})(\text{CO})]$ | 43.7 | | 58.8 | |
| $[\text{Cp}_2\text{Mn}_2(\text{CS})_2(\text{CO})_2] \rightarrow$ $[\text{CpMn}(\text{CS})(\text{CO})_2] + [\text{CpMn}(\text{CS})]$ | 44.5 | | 59.8 | |
| $[\text{Cp}_2\text{Mn}_2(\text{CS})_2(\text{CO})] \rightarrow$ $[\text{CpMn}(\text{CS})(\text{CO})] + [\text{CpMn}(\text{CS})]$ | 75.8 | | 100.6 | |
| $[\text{Cp}_2\text{Mn}_2(\text{CS})_2] \rightarrow [\text{CpMn}(\text{CS})] +$ $[\text{CpMn}(\text{CS})]$ | 87.3 | | 99.9 | |

4. Discussion

For the coordinately saturated binuclear $[\text{Cp}_2\text{Mn}_2(\text{CS})_2(\text{CO})_3]$ complexes, the structures with four-electron donor “end-on” CE (E = O, S) bridges and no manganese-manganese bond (structures **23-1**, **23-2**, **23-3**, and **23-4** in Figure 3) are energetically preferred over structures with only two-electron donor CO and CS groups and a manganese-manganese bond. In such CE bridges the carbon atom is bonded to one of the manganese atoms through its lone pair and the chalcogen (E) atom is similarly bonded to the other manganese atom through its lone pair. No analogous such structures were found for the carbonyl analogue $[\text{Cp}_2\text{Mn}_2(\text{CO})_5]$ in previous research.^[10] The $[\text{Cp}_2\text{Mn}_2(\text{CS})_2(\text{CO})_3]$ structure **23-1**, in which the bridging group is a thiocarbonyl group, can be derived from the parent mononuclear $[\text{CpMn}(\text{CS})(\text{CO})_2]$ by replacement of one of the carbonyl groups with a $[\text{CpMn}(\text{CS})(\text{CO})_2]$ “ligand,” which bonds to the $[\text{CpMn}(\text{CS})(\text{CO})]$ manganese through its sulfur atom. The Mn–S–C–Mn angle of about 109° predicted for **23-1** is essentially identical to the Cr–S–C–Cr angle of about 110° predicted for the corresponding $(\text{OC})_5\text{CrCS} \rightarrow \text{Cr}(\text{CO})_5$ in earlier work.^[21] Similarly the $[\text{Cp}_2\text{Mn}_2(\text{CS})_2(\text{CO})_3]$ structure **23-2**, in which the bridging group is a carbonyl group, can be derived from the parent mononuclear $[\text{CpMn}(\text{CS})(\text{CO})_2]$ (structure **12-1** in Figure 2) by replacement of one of the carbonyl groups with a $[\text{CpMn}(\text{CO})_3]$ “ligand,” bonded to the $[\text{CpMn}(\text{CO})_2]$ manganese through the oxygen atom. The $[\text{Cp}_2\text{Mn}_2(\text{CS})_2(\text{CO})_3]$ structures **23-1** and **23-2** (Figure 3) are reasonably stable with respect to dissociation into the mononuclear fragments $[\text{CpMn}(\text{CS})_2(\text{CO})] + [\text{CpMn}(\text{CO})_2]$ with typical dissociation energies around ca. 15 kcal/mol. There is thus a distinct possibility that they can be obtained by the photolysis of $[\text{CpMn}(\text{CO})_3/\text{CpMn}(\text{CS})_2(\text{CO})]$ mixtures, at least in low temperature matrices.

The potential energy surface of $[\text{Cp}_2\text{Mn}_2(\text{CS})_2(\text{CO})_2]$ is unusually complicated with 22 structures within 30 kcal/mol of the lowest energy structure by at least one of the two DFT methods. This collection of structures presents a rich cornucopia of possibilities, having singlet and triplet structures with various structural features. These include four-electron bridging $\eta^2\text{-}\mu\text{-CS}$ groups, various combinations of two-electron donor bridging CO and CS groups in doubly bridged structures, and even “end-on” four-electron donor bridging CO or CS groups without manganese-manganese bonds and thus a 16-electron configuration for one of the manganese atoms. The full details of all 22 of the predicted $[\text{Cp}_2\text{Mn}_2(\text{CS})_2(\text{CO})_2]$ structures seem of limited chemical relevance to the chemistry discussed in this paper and may eventually be presented in a more specialized archival journal. This paper presents only four representative $[\text{Cp}_2\text{Mn}_2(\text{CS})_2(\text{CO})_2]$ structures (Figure 5), chosen to illustrate the lowest energy structures representing various structural features. The lowest energy $[\text{Cp}_2\text{Mn}_2(\text{CS})_2(\text{CO})_2]$ structure **22-1** has a four-electron donor bridging $\eta^2\text{-}\mu\text{-CS}$ group and an Mn–Mn distance of about 2.7 Å corresponding to a formal single bond. No analogous $[\text{Cp}_2\text{Mn}_2(\text{CO})_4]$ structures with an analogous four-electron donor bridging $\eta^2\text{-}\mu\text{-CO}$ group were found in previous research.^[10] Instead, the lowest energy $[\text{Cp}_2\text{Mn}_2(\text{CO})_4]$ structure was found to have only two-electron donor carbonyl groups, including two semibridging carbonyl groups, as well as a shorter Mn=Mn distance of about 2.5 Å, indicative of a formal double bond. An analogous structure **22-2** (Figure 5) is also found for $[\text{Cp}_2\text{Mn}_2(\text{CS})_2(\text{CO})_2]$ with an Mn=Mn distance of 2.55 ± 0.01 Å. In structure **22-2** (Figure 5) the bridging groups are thiocarbonyl groups and they are closer to being symmetrical with short M–C(S) distances of about 1.8 Å and long M–C(S) distances of 2.1–2.2 Å. Singlet $[\text{Cp}_2\text{Mn}_2(\text{CS})_2(\text{CO})_2]$ structures, with either one four-electron donor $\eta^2\text{-}\mu\text{-CS}$ group and a formal Mn–Mn single bond or all two-electron donor CO and CS groups, whether bridging or terminal, and a formal Mn=Mn double bond have the favored 18-electron configuration for the manganese atoms.

The $[\text{Cp}_2\text{Mn}_2(\text{CS})_2(\text{CO})_2]$ structures **22-3T** and **22-4T** (Figure 5) are representatives of triplet $[\text{Cp}_2\text{Mn}_2(\text{CS})_2(\text{CO})_2]$ structures. Structure **22-3T** is similar to **22-2** with two two-electron donor bridging thiocarbonyl groups.

However, the Mn–Mn distance in **22-3T** of 2.66 ± 0.03 Å is about 0.1 Å longer than that in **22-2**, consistent with a formal single rather than double bond. This gives each manganese atom in **22-3T** the 17-electron configuration required for a binuclear triplet. The $[\text{Cp}_2\text{Mn}_2(\text{CS})_2(\text{CO})_2]$ structure **22-4T** is an example of an unsaturated structure with an “end-on” four-electron donor CS group and no manganese–manganese bond. The manganese atom bonded to the carbon atom of the bridging CS group in **22-4T** has only a 16-electron configuration, which, in this case, leads to triplet spin multiplicity.

A characteristic of $[\text{Cp}_2\text{Mn}_2(\text{CS})_2(\text{CO})_2]$ is the predicted exothermic disproportionation into $[\text{Cp}_2\text{Mn}_2(\text{CS})_2(\text{CO})_3] + [\text{Cp}_2\text{Mn}_2(\text{CS})_2(\text{CO})]$, with a predicted energy of 4 kcal/mol. However, this disproportionation is significantly less favorable than the corresponding disproportionation of $[\text{Cp}_2\text{Mn}_2(\text{CO})_4]$ into $[\text{Cp}_2\text{Mn}_2(\text{CO})_5] + [\text{Cp}_2\text{Mn}_2(\text{CO})_3]$, which is predicted^[10] to be exothermic by 22 ± 5 kcal/mol. The much lower disproportionation energy of $[\text{Cp}_2\text{Mn}_2(\text{CS})_2(\text{CO})_2]$ relative to $[\text{Cp}_2\text{Mn}_2(\text{CO})_4]$ is probably a consequence of the four-electron donor bridging η^2 - μ -CS group in the former.

The compound $[\text{Cp}_2\text{Mn}_2(\text{CS})_2(\text{CO})]$ has a very simple potential energy surface, particularly when compared with the very complicated potential energy landscape of $[\text{Cp}_2\text{Mn}_2(\text{CS})_2(\text{CO})_2]$. Thus only one singlet and one triplet structure are found for $[\text{Cp}_2\text{Mn}_2(\text{CS})_2(\text{CO})]$ (Figure 6). In both structures all three CE groups (E = O, S) are bridging groups. The singlet $[\text{Cp}_2\text{Mn}_2(\text{CS})_2(\text{CO})]$ structure **21-1** lies 15 ± 5 kcal/mol below the triplet structure **21-2T**. Furthermore, the singlet $[\text{Cp}_2\text{Mn}_2(\text{CS})_2(\text{CO})]$ structure **21-1** is very similar to that of the corresponding pure carbonyl derivative $[\text{Cp}_2\text{Mn}_2(\text{CO})_3]$ by not only having three bridging CE groups but also having a very similar Mn≡Mn distance of about 2.16 Å as compared with the experimental Mn≡Mn distance^[5] of 2.17 Å in $[\text{Cp}_2\text{Mn}_2(\text{CO})_3]$. The very high CO dissociation energy of **21-1** at 53 ± 12 kcal/mol, the highly endothermic disproportionation energy of **21-1** of 32 ± 10 kcal/mol, and the very high energy of 88 ± 13 kcal/mol for the fragmentation $[\text{Cp}_2\text{Mn}_2(\text{CS})_2\text{CO}] \rightarrow [\text{CpMn}(\text{CS})(\text{CO})] + [\text{CpMn}(\text{CS})]$ all predict considerable stability for $[\text{Cp}_2\text{Mn}_2(\text{CS})_2(\text{CO})]$. This suggests $[\text{Cp}_2\text{Mn}_2(\text{CS})_2(\text{CO})]$ as an interesting synthetic objective, possibly by the photolysis of $[\text{CpMn}(\text{CS})(\text{CO})_2]$ analogous to the reported^[4] synthesis of $[\text{Cp}_2\text{Mn}_2(\text{CO})_3]$.

The lowest energy $[\text{Cp}_2\text{Mn}_2(\text{CS})_2]$ structure **20-1T** (Figure 7) is a doubly bridged triplet with a predicted Mn≡Mn distance of 2.22 ± 0.01 Å, which is close to the 2.16 Å Mn≡Mn triple bond length in $[\text{Cp}_2\text{Mn}_2(\mu\text{-CS})_2(\mu\text{-CO})]$ (**21-1** in Figure 6). This suggests a formal triple bond in **20-1T**, thereby giving both manganese atoms the 17-electron configurations for a binuclear triplet. The slightly longer Mn≡Mn distance in **20-1T** relative to the Mn≡Mn distance in **21-1** may relate to the fact that **21-1** has three bridging groups, whereas **20-1T** has only two bridging groups. A singlet $[\text{Cp}_2\text{Mn}_2(\text{CS})_2]$ structure **20-5** (Figure 8) is also found, lying above the triplet structure **20-1T** by 20.5(3.5) kcal/mol.

The Mn≡Mn distance of 2.10 ± 0.02 Å in the singlet **20-5** is about 0.12 Å shorter than that in the triplet **20-1T**. This suggests a formal manganese–manganese quadruple bond in **20-5** thereby leading to the favored 18-electron configuration for a binuclear singlet. No examples of manganese–manganese quadruple bonds are known experimentally. The slightly lower energy of binuclear triplet structures with formal M≡M triple bonds and 17-electron configurations for each metal atom (compared with isomeric binuclear singlet structures with formal M≡M quadruple bonds and 18-electron configurations for each metal atom) is a common feature in the chemistry of unsaturated cyclopentadienylmetal carbonyl derivatives, including not only the analogous $[\text{Cp}_2\text{Mn}_2(\text{CO})_2]$ (ref. 10) but other related compounds such as $[\text{Cp}_2\text{Cr}_2(\text{CO})_3]$ (ref.^[50]) and $\text{Cp}_2\text{V}_2(\text{CO})_4$ (ref.^[51]).

Structures with one or two four-electron donor bridging η^2 - μ -CS groups are also predicted for $[\text{Cp}_2\text{Mn}_2(\text{CS})_2]$. The structures with one four-electron donor η^2 - μ -CS group, namely the triplet **20-4T** (Figure 7) and the singlet **20-6** (Figure 8), have manganese–manganese distances of 2.61 ± 0.05 Å for the triplet and 2.54 ± 0.03 Å for the singlet. Similarly, the $[\text{Cp}_2\text{Mn}_2(\text{CS})_2]$ structures with two four-electron donor η^2 - μ -CS groups, namely the triplet **20-3T** (Figure 7) and singlet **20-8** (Figure 8) have manganese–manganese distances of 2.72 ± 0.3 Å for the triplet and 2.84 ± 0.05 Å for the singlet. The constraints of the four-electron donor η^2 - μ -CS group(s) make it difficult to correlate formal bond order with the manganese–manganese distances in such systems.

The remaining two $[\text{Cp}_2\text{Mn}_2(\text{CS})_2]$ structures, namely the triplet **20-2T** (Figure 7) and the closely related singlet **20-7** (Figure 8) are of interest since the two CS groups have coupled to form an SCCS ligand by forming a new C–C bond with C–C distances of 1.374(1.513) Å in **20-2T** and 1.372(1.397) Å in **20-7**. This SCCS ligand bridges the two manganese atoms as a bridging trihapto ligand in both directions. The Mn⋯Mn distance in the triplet **20-2T** is 3.28 ± 0.08 Å, suggesting no direct interaction. However, the Mn–Mn distance in the corresponding singlet **20-7** of 2.65 ± 0.01 Å is short enough to indicate a formal single bond. The SCCS ligand in **20-2T** and **20-7** can be derived from the double deprotonation of acetylenedithiol, $\text{HSC}\equiv\text{CSH}$. Acetylenedithiol is unknown experimentally and is likely to be too unstable for isolation. However, it has been studied theoretically.^[52] With this interpretation, each sulfur atom of the acetylenedithiolate dianion is bonded to a single manganese atom and donates one electron to that manganese atom, with two lone pairs remaining on each sulfur atom (Figure 9). The acetylene unit is bonded to both manganese atoms, thereby donating two electrons to each manganese atom. Formally the two electrons for one manganese atom come from one of the π components of the $\text{C}\equiv\text{C}$ triple bond and the two electrons for the other manganese atom come from the other π component of the $\text{C}\equiv\text{C}$ triple bond. Thus the acetylenedithiolate unit, considered formally as a neutral ligand bonding in this manner, donates a total of three electrons to each manganese atom, namely one through the sulfur atom and the

other two electrons through one π component of the $\text{C}\equiv\text{C}$ triple bond. In the $[\text{Cp}_2\text{Mn}_2(\text{CS})_2]$ singlet **20-7** with an Mn–Mn single bond, the Mn_2C_2 unit forms a tetrahedron and each manganese atom has a formal 16-electron configuration. The Mn_2C_2 tetrahedron in **20-7** is analogous to the Co_2C_2 tetrahedron found in the well-known [(alkyne)- $\text{Co}_2(\text{CO})_6$] complexes, first synthesized in 1956.^[53–55] In the $[\text{Cp}_2\text{Mn}_2(\text{CS})_2]$ triplet **20-2T** with no Mn–Mn bond, the Mn_2C_2 unit forms a butterfly structure (two triangles sharing an edge) and each manganese atom has a formal 15-electron configuration.

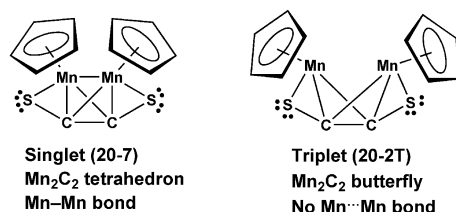


Figure 9. Schematic representation of an acetylenedithiolate ligand bridging two manganese atoms in the singlet $[\text{Cp}_2\text{Mn}_2(\text{CS})_2]$ structure **20-7** and the triplet $[\text{Cp}_2\text{Mn}_2(\text{CS})_2]$ structure **20-2T**, assuming that the (neutral) acetylenedithiolate ligand acts as a three-electron donor to each manganese atom and two lone pairs formally remain on each sulfur atom. If the acetylenedithiolate ligand is a five-electron donor to each manganese atom, then one of the two lone pairs on each sulfur atom is also donated to a manganese atom.

There is also an alternative model for the bonding of the bridging acetylenedithiolate ligand to the two manganese atoms in **20-2T** and **20-7**, if there is additional involvement of one of the two lone pairs on each sulfur atom in the manganese-sulfur bonding (Figure 9). In this case the sulfur atoms each provide three electron donors one of the manganese atoms. This makes the acetylenedithiolate (C_2S_2) ligand a five-electron donor to each metal atom, thereby giving each manganese atom the favored 18-electron configuration in the singlet **20-7** and the typical 17-electron configuration in the binuclear triplet **20-2T**. The alternatives of the bonding of the acetylenedithiolate ligand as a three-electron donor to each metal atom or as a five-electron donor to each metal atom by different involvement of the sulfur lone pairs is not clear from available information from our theoretical studies.

5. Summary

These theoretical explorations of the binuclear cyclopentadienylmanganese carbonyl thiocarbonyls, $[\text{Cp}_2\text{Mn}_2(\text{CS})_2(\text{CO})_n]$ have led to the elucidation of two types of four-electron donor bridging thiocarbonyl ligands. The lowest energy structures of the saturated $[\text{Cp}_2\text{Mn}_2(\text{CS})_2(\text{CO})_3]$ have CS or CO ligands bridging the two manganese atoms by forming a manganese-carbon bond with one manganese atom and a manganese-sulfur bond with the other manganese atom. In such structures the manganese-manganese distances are far too long for any direct metal-metal bonding. The lowest energy structure of $[\text{Cp}_2\text{Mn}_2(\text{CS})_2(\text{CO})_2]$ has a different type of bridging CS group; namely a η^2 - μ -

CS group, which is bonded to one manganese atom through a direct manganese-carbon bond and to the other manganese atom through one of the π -components of the $\text{C}\equiv\text{S}$ triple bond of the thiocarbonyl group. Such a bridging η^2 - μ -CS group is accompanied by a Mn–Mn bond. The still more unsaturated $[\text{Cp}_2\text{Mn}_2(\text{CS})_2(\text{CO})]$ has a triply bridged structure very similar to that of the analogous $[\text{Cp}_2\text{Mn}_2(\text{CO})_3]$, in which the Mn≡Mn distance is short enough for a formal triple bond. The lowest energy structure for the carbonyl-free $[\text{Cp}_2\text{Mn}_2(\text{CS})_2]$ is a triplet, also with a formal Mn≡Mn triple bond. A higher energy singlet $[\text{Cp}_2\text{Mn}_2(\text{CS})_2]$ structure is found with a very short Mn≡Mn distance of about 2.1 Å suggesting the formal quadruple bond required to give each Mn atom the favored 18-electron configuration. Other higher energy singlet and triplet $[\text{Cp}_2\text{Mn}_2(\text{CS})_2]$ structures are found in which the two CS ligands have coupled to form a bridging SCCS ligand, derived from the deprotonation of acetylenedithiol, $\text{HSC}\equiv\text{CSH}$, which is unknown in the free state.

Supporting Information (see also the footnote on the first page of this article): Tables S1–S4: The $\nu(\text{CO})$ and $\nu(\text{CS})$ stretching frequencies and infrared intensities predicted for $[\text{Cp}_2\text{Mn}_2(\text{CS})_2(\text{CO})_3]$ (13 structures), $[\text{Cp}_2\text{Mn}_2(\text{CS})_2(\text{CO})_2]$ (4 structures), $[\text{Cp}_2\text{Mn}_2(\text{CS})_2(\text{CO})]$ (2 structures), and $[\text{Cp}_2\text{Mn}_2(\text{CS})_2]$ (8 structures) using the BP86 method; Tables S5–S34: Theoretical Cartesian coordinates for mononuclear $[\text{CpMn}(\text{CS})(\text{CO})_n]$ ($n = 2, 1, 0$) (3 structures), $[\text{Cp}_2\text{Mn}_2(\text{CS})_2(\text{CO})_3]$ (13 structures), $[\text{Cp}_2\text{Mn}_2(\text{CS})_2(\text{CO})_2]$ (4 structures), $[\text{Cp}_2\text{Mn}_2(\text{CS})_2(\text{CO})]$ (2 structures), and $[\text{Cp}_2\text{Mn}_2(\text{CS})_2]$ (8 isomers) using the B3LYP method; complete Gaussian 03 ref.^[43]

Acknowledgments

We are indebted to the Chinese 111 Project (B07012) and the National Natural Science Foundation of China (20873045 and 20973066) as well as the U. S. National Science Foundation (Grants CHE-0749868 and CHE-0716718) for support of this research.

- [1] E. O. Fischer, R. Jira, *Z. Naturforsch., Teil B* **1954**, 9, 618.
- [2] T. S. Piper, F. A. Cotton, G. Wilkinson, *J. Inorg. Nucl. Chem.* **1955**, 1, 165.
- [3] A. G. Ginzburg, *Usp. Khim.* **1993**, 62, 1098.
- [4] W. A. Herrmann, R. Serrano, J. Weichmann, *J. Organomet. Chem.* **1983**, 246, C57.
- [5] I. Bernal, J. D. Korp, W. A. Hermann, R. Serrano, *Chem. Ber.* **1984**, 117, 434.
- [6] B. S. Creaven, A. J. Dixon, J. M. Kelly, C. Long, M. Poliakoff, *Organometallics* **1987**, 6, 200.
- [7] A. S. Foust, J. K. Hoyano, W. A. G. Graham, *J. Organomet. Chem.* **1971**, 32, 65.
- [8] C. P. Casey, H. Sakaba, P. N. Hazin, D. R. Powell, *J. Am. Chem. Soc.* **1991**, 113, 8165.
- [9] J. K. Hoyano, W. A. G. Graham, *J. Chem. Soc., Chem. Commun.* **1982**, 27.
- [10] X. Zhang, Q. S. Li, Y. M. Xie, R. B. King, H. F. Schaefer, *Organometallics* **2008**, 27, 61.
- [11] B. Xu, Q.-S. Li, Y. Xie, R. B. King, H. F. Schaefer, *Inorg. Chem.* **2008**, 47, 6779.
- [12] I. S. Butler, A. E. J. Fenster, *Organomet. Chem.* **1974**, 66, 161.
- [13] P. V. Yaneff, *Coord. Chem. Rev.* **1977**, 23, 183.
- [14] I. S. Butler, *Acc. Chem. Res.* **1977**, 10, 359.
- [15] P. V. Broadhurst, *Polyhedron* **1985**, 4, 1801.
- [16] W. Petz, *Coord. Chem. Rev.* **2008**, 257, 1689.

- [17] I. S. Butler, A. E. Fenster, *J. Chem. Soc. C* **1970**, 933.
- [18] A. E. Fenster, I. S. Butler, *Inorg. Chem.* **1974**, *13*, 915.
- [19] Z. Zhang, Q. S. Li, Y. Xie, R. B. King, H. F. Schaefer, *Inorg. Chem.* **2009**, *48*, 1974.
- [20] Z. Zhang, Q. S. Li, Y. Xie, R. B. King, H. F. Schaefer, *Inorg. Chem.* **2009**, *48*, 5973.
- [21] Z. Zhang, Q. S. Li, Y. Xie, R. B. King, H. F. Schaefer, *J. Chem. Phys. A* **2009**, *113*, 4672.
- [22] A. W. Ehlers, G. Frenking, *J. Am. Chem. Soc.* **1994**, *116*, 1514.
- [23] B. Delley, M. Wrinn, H. P. Lüthi, *J. Chem. Phys.* **1994**, *100*, 5785.
- [24] J. Li, G. Schreckenbach, T. Ziegler, *J. Am. Chem. Soc.* **1995**, *117*, 486.
- [25] V. Jonas, W. Thiel, *J. Chem. Phys.* **1995**, *102*, 8474.
- [26] T. A. Barckholtz, B. E. Bursten, *J. Am. Chem. Soc.* **1998**, *120*, 1926.
- [27] S. Niu, M. B. Hall, *Chem. Rev.* **2000**, *100*, 353.
- [28] P. Macchi, A. Sironi, *Coord. Chem. Rev.* **2003**, *238*, 383.
- [29] J.-L. Carreon, J. N. Harvey, *Phys. Chem. Chem. Phys.* **2006**, *8*, 93.
- [30] M. Bühl, H. Kabrede, *J. Chem. Theory Comput.* **2006**, *2*, 1282.
- [31] A. D. Becke, *J. Chem. Phys.* **1993**, *98*, 5648.
- [32] C. Lee, W. Yang, R. G. Parr, *Rev. Phys. B* **1988**, *37*, 785.
- [33] A. D. Becke, *Phys. Rev. A* **1988**, *38*, 3098.
- [34] J. P. Perdew, *Phys. Rev. B* **1986**, *33*, 8822.
- [35] See especially F. Furche, J. P. Perdew, *J. Chem. Phys.* **2006**, *124*, 044103.
- [36] H. Y. Wang, Y. Xie, R. B. King, H. F. Schaefer, *J. Am. Chem. Soc.* **2005**, *127*, 11646.
- [37] H. Y. Wang, Y. Xie, R. B. King, H. F. Schaefer, *J. Am. Chem. Soc.* **2006**, *128*, 11376.
- [38] T. H. Dunning, *J. Chem. Phys.* **1970**, *53*, 2823.
- [39] T. H. Dunning, P. J. Hay, *Methods of Electronic Structure Theory* (Eds.: H. F. Schaefer); Plenum: New York, **1977**; pp. 1–27.
- [40] S. Huzinaga, *J. Chem. Phys.* **1965**, *42*, 1293.
- [41] A. J. H. Wachters, *J. Chem. Phys.* **1970**, *52*, 1033.
- [42] D. M. Hood, R. M. Pitzer, H. F. Schaefer, *J. Chem. Phys.* **1979**, *71*, 705.
- [43] M. J. Frisch, et al., *Gaussian 03*, revision C 02, Inc. Gaussian, Wallingford CT, **2004** (see Supporting Information for details).
- [44] B. N. Papas, H. F. Schaefer, *J. Mol. Struct.* **2006**, *768*, 175.
- [45] H. Jacobsen, T. Ziegler, *J. Am. Chem. Soc.* **1996**, *118*, 4631.
- [46] J. M. L. Martin, C. W. Bauschlicher, A. Ricca, *Comput. Phys. Commun.* **2001**, *133*, 189.
- [47] S. Lotz, R. R. Pille, P. H. van Rooyen, *Inorg. Chem.* **1986**, *25*, 3053.
- [48] D. M. Hamilton, W. S. Willis, G. D. Stucky, *J. Am. Chem. Soc.* **1981**, *103*, 4255.
- [49] J. H. Osborne, A. L. Rheingold, W. C. Troglor, *J. Am. Chem. Soc.* **1985**, *107*, 6292.
- [50] X. Zhang, Q.-S. Li, Y. Xie, R. B. King, H. F. Schaefer, *Dalton Trans.* **2008**, 4805.
- [51] Q.-S. Li, X. Zhang, Y. Xie, R. B. King, H. F. Schaefer, *J. Am. Chem. Soc.* **2007**, *129*, 3433.
- [52] Yu. V. Frolov, A. V. Vashchenko, A. G. Mal'kina, B. A. Trofimov, *J. Struct. Chem.* **2009**, *50*, 195.
- [53] H. Greenfield, H. W. Sternberg, R. A. Friedel, J. H. Wotiz, R. Markby, I. Wender, *J. Am. Chem. Soc.* **1956**, *78*, 120.
- [54] R. S. Dickson, P. J. Fraser, *Adv. Organomet. Chem.* **1974**, *12*, 323.
- [55] M. J. Went, *Adv. Organomet. Chem.* **1997**, *41*, 69.

Received: February 11, 2010

Published Online: July 29, 2010

“Piano-Stool” Complexes of Ruthenium(II) Designed with Arenes and *N*-[2-(Arylchalcogeno)ethyl]morpholines: Highly Active Catalysts for the Oxidation of Alcohols with *N*-Methylmorpholine *N*-Oxide, *tert*-Butyl Hydroperoxide and Sodium Periodate and Oxochloride

Pradhum Singh^[a] and Ajai K. Singh^{*[a]}

Keywords: Alcohols / Chalcogens / Homogeneous catalysis / Oxidation / Ruthenium

The reactions of $[(\eta^6\text{-C}_6\text{H}_6)\text{RuCl}(\mu\text{-Cl})_2]$ and $[(\eta^6\text{-}p\text{-cymene})\text{RuCl}(\mu\text{-Cl})_2]$ with *N*-[2-(arylchalcogeno)ethyl]morpholines (L) (aryl = Ph/2-pyridyl for S, Ph for Se, 4-MeOC₆H₄ for Te) and NH₄PF₆ result in “piano-stool” complexes of Ru^{II} of composition $[\text{RuCl}(\eta^6\text{-C}_6\text{H}_6)(\text{L})][\text{PF}_6]$ / $[\text{RuCl}(\eta^6\text{-}p\text{-cymene})(\text{L})][\text{PF}_6]$, which give characteristic ¹H, ¹³C{¹H}, ⁷⁷Se{¹H}, and ¹²⁵Te{¹H} NMR spectra. Some of them have also been characterized by X-ray crystallography [Ru–S, Ru–Se, and Ru–Te bond lengths: 2.3815(12)/2.3742(14), 2.4837(14), and 2.6143(7) Å, respectively]. The cyclic voltammograms show

that all the complexes undergo irreversible oxidation ($E_{1/2} = 0.290\text{--}0.586$ V). All the ruthenium complexes have been explored for their catalytic activity in the oxidation of primary and secondary alcohols with *N*-methylmorpholine *N*-oxide (NMO), *t*BuOOH, NaOCl, and NaIO₄ (TON values upto 9.8×10^4). The efficiency of the catalytic oxidation reaction decreases in the order Te > Se > S. The intermediate species involved in the oxidation reactions appear to incorporate the Ru^{IV}=O group.

Introduction

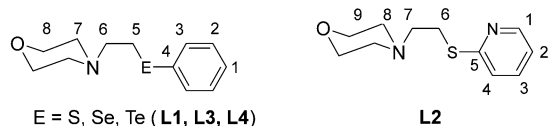
The current interest in “piano-stool” complexes of Ru^{II} having an η^6 -benzene or η^6 -*p*-cymene unit stems from the fact that some of them are known for their diverse catalytic activities. Süss-Fink et al. carried out the hydrogenation of benzene using a cluster with Ru(η^6 -arene) units.^[1] (Arene)-ruthenium complexes with salicyloxazolines are suitable as asymmetric catalysts for Diels–Alder reactions.^[2] The compounds $[\text{Ru}=\text{C}=\text{C}=\text{CR}_2(\text{L})(\text{Cl})(\text{arene})][\text{PF}_6]$ (L = PCy₃, PiPr₃) have been reported by Dixneuf and co-workers to be excellent catalyst precursors for ring-closing olefin metathesis.^[3] The atom-transfer radical polymerization of methyl methacrylate has been catalyzed by $[\text{RuCl}_2(\eta^6\text{-}p\text{-cymene})(\text{PCy}_3)]$.^[4] Dixneuf and co-workers have reported that the in situ generated catalyst from $[\text{RuCl}_2(\eta^6\text{-}p\text{-cymene})]_2$ and a pyrimidinium or benzimidazolium salt in the presence of Cs₂CO₃ selectively promotes the diarylation of 2-pyridylbenzene with aryl bromides.^[5] The acetate-assisted C–H activation of 2-substituted pyridines with $[\text{RuCl}_2(\eta^6\text{-}p\text{-cymene})]_2$ has been reported by Davies and co-workers.^[6] A variety of neutral (carbene)ruthenium complexes,

$[\text{RuCl}_2(\text{carbene})(\text{arene})]$, have been used in the catalytic synthesis of furans.^[7] Kharasch additions are catalyzed by $[\text{RuCl}_2(\eta^6\text{-}p\text{-cymene})(\text{PAR}_3)]$.^[8] Démonceau and co-workers recently reported the exceptional efficacy of $[\text{RuCl}_2(\eta^6\text{-}p\text{-cymene})(\text{PR}_3)]$ complexes as a catalyst precursor for the ring-opening metathesis polymerization of low-strain cyclic olefins.^[9] Chiral cationic (η^6 -arene)(pyridylamino)ruthenium(II) complexes act as enantioselective catalysts in Diels–Alder reactions with good *exolendo* selectivity.^[10] The half-sandwich compounds of Ru^{II} show promising anticancer activity.^[11–15] Thiolate ligand oxygenation is believed to activate cytotoxic half-sandwich $[\text{Ru}(\eta^6\text{-arene})(\text{en})(\text{SR})]^+$ complexes towards DNA-binding.^[16] (arene)Ru^{II} complexes with pyrone-derived ligands are rendered active against cancer cells by the replacement of the coordinated (O,O) donor with the (S,O) donor.^[17] Hartinger and co-workers^[18] have reported that promising cytotoxic effects of water-soluble dinuclear (arene)Ru complexes in human cancer cells can be increased by increasing the spacer length between metal centers. The interaction of $[\text{RuCl}_2(\eta^6\text{-}p\text{-cymene})(\text{pta})]$, reported to be an effective anticancer and antimetastatic agent, with biological nucleophiles, important with respect to the mechanism of action, has been studied.^[19] Organometallic (arene)ruthenium(II) complexes coordinated to maltol-derived ligands have been prepared and their anticancer activity against human tumor cell lines studied.^[20] Therrien and co-workers found that water-soluble (arene)-ruthenium complexes containing pyridinethiolato ligands show cytotoxicity towards ovarian cancer cells.^[21] In vitro

[a] Department of Chemistry, Indian Institute of Technology Delhi, New Delhi 110016, India
Fax: +91-11-26581102
E-mail: aksingh@chemistry.iitd.ac.in
ajai57@hotmail.com

Supporting information for this article is available on the WWW under <http://dx.doi.org/10.1002/ejic.201000319>.

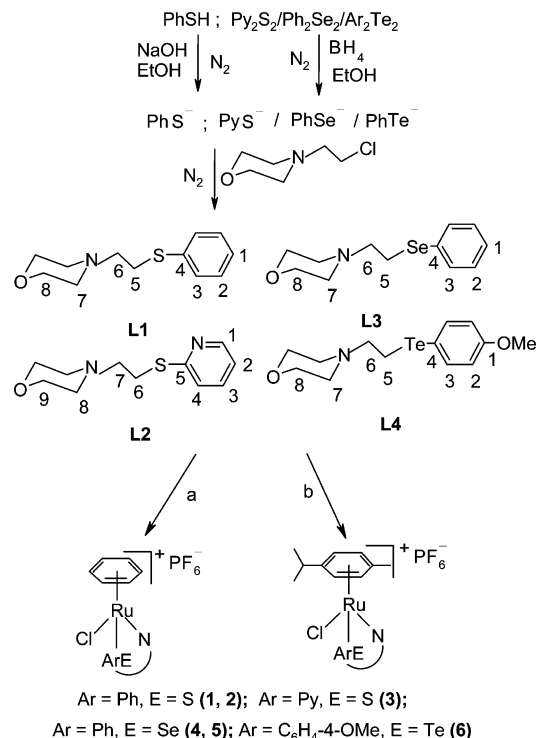
studies by Dyson and co-workers have revealed that the (3,5,6-bicyclopophosphite- α -D-glucufuranoside)(η^6 -*p*-cymene)-dihalogenidoruthenium(II) complex is the most cytotoxic compound for human cancer cell lines.^[22] Because morpholine derivatives are biologically active,^[23–25] it is worthwhile gaining an understanding of the chemistry of half-sandwich compounds that have such ligands. Therefore, the ligands **L1**–**L4** have been designed and their Ru^{II} complexes with the (η^6 -benzene/ η^6 -*p*-cymene) unit synthesized. Their catalytic activity in the oxidation of alcohols with *N*-methylmorpholine *N*-oxide (NMO), *tert*-butyl hydroperoxide (*t*BuOOH), sodium oxychloride (NaOCl), and sodium periodate (NaIO₄) have also been explored. The results of all these investigations are presented in this paper.



Results and Discussion

Scheme 1 summarizes the syntheses of **L1**–**L4** and their “piano-stool”-type ruthenium(II) complexes. **L1** was prepared by a synthetic procedure different to that previously reported; our synthetic procedure is easier and also gives a better yield.^[26] Furthermore, **L1** is also commercially available. Similarly, the procedure described herein for the synthesis of **L4** by using a different workup procedure (diethyl ether/water) resulted in a better yield than that reported previously.^[27,28] The molar conductance values in acetonitrile (see Exp. Sect.) indicates a 1:1 electrolyte nature of the complexes **1**–**6**, which are soluble in CH₃OH, CH₃CN, CH₂Cl₂, and CHCl₃. Their solutions in DMSO show signs of decomposition within a few hours. The complexes **1**, **3**, **4**, and **6** were characterized by X-ray crystallography; crystals suitable for X-ray diffraction could not be grown for **2** or **5**. The ORTEP diagrams of **1**, **3**, **4**, and **6** are given in Figures 1, 2, 3, and 4, respectively. There are inter- and intramolecular Cl \cdots H and F \cdots H interactions [2.630(8)–2.856(2) and 2.308(9)–2.863(9) Å, respectively] in all crystals except for **6** in which intermolecular Cl \cdots H interactions are not observed (see Figures S1–S7 and Table S3 in the Supporting Information). The crystal packing appears to be one of the reasons for these interactions, which are strongest in **1**, in which the chalcogen is sulfur, and weakest in **6**, which has tellurated morpholine as the ligand. The F \cdots H interactions in the case of **4** are shown in Figure 5.

There is a pseudo-octahedral half-sandwich “piano-stool” disposition of ligands around the ruthenium atom in the cations of **1**, **3**, **4**, and **6**. The arene ring occupies one face of the octahedron and Cl and L (**L1**–**L4**) the opposite one. The Ru–S bond length in the cation of **1** is 2.3815(12) Å, somewhat longer than that in **3** [2.3742(14) Å]. Both are within the range 2.3548(15)–2.4156(9) Å in which the Ru–S bond lengths of [(η^6 -C₆H₆)ruthenium(II)Cl(S,N)ligand]⁺, [(η^6 -C₆H₆)ruthenium(II)-



Scheme 1. Synthesis of **L1**–**L4** and their “piano-stool”-type Ru^{II} complexes. (a) [(η^6 -C₆H₆)RuCl(μ-Cl)]₂, NH₄PF₆, MeOH, r.t., 12 h; (b) [(η^6 -*p*-cymene)RuCl(μ-Cl)]₂, NH₄PF₆, MeOH, r.t., 15 h.

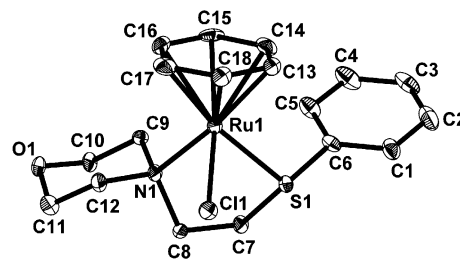


Figure 1. ORTEP diagram of the cation of **1** with ellipsoids at the 50% probability level. Hydrogen atoms and the PF₆[−] anion have been omitted for clarity. Bond lengths [Å]: Ru(1)–S(1) 2.3815(12), Ru(1)–N(1) 2.208(3), Ru(1)–Cl(1) 2.394(12), Ru(1)–C 2.181(4)–2.224(4); bond angles [°]: Cl(1)–Ru(1)–S(1) 81.94(4), N(1)–Ru(1)–S(1) 83.06(9), N(1)–Ru(1)–Cl(1) 85.28(9).

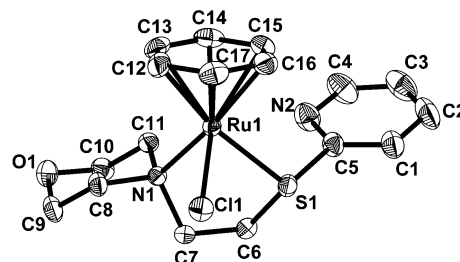


Figure 2. ORTEP diagram of the cation of **3** with ellipsoids at the 30% probability level. Hydrogen atoms and the PF₆[−] anion have been omitted for clarity. Bond lengths [Å]: Ru(1)–S(1) 2.3742(14), Ru(1)–N(1) 2.205(4), Ru(1)–Cl(1) 2.3996(15), Ru(1)–C 2.172(6)–2.196(6); bond angles [°]: Cl(1)–Ru(1)–S(1) 82.26(5), N(1)–Ru(1)–S(1) 82.62(11), N(1)–Ru(1)–Cl(1) 82.32(11).

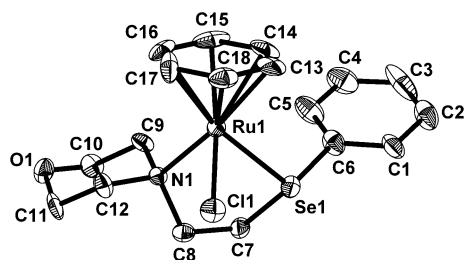


Figure 3. ORTEP diagram of the cation of **4** with ellipsoids at the 30% probability level. Hydrogen atoms and the PF_6^- anion have been omitted for clarity. Bond lengths [Å]: Ru(1)–Se(1) 2.4837(14), Ru(1)–N(1) 2.234(8), Ru(1)–Cl(1) 2.413(3), Ru(1)–C 2.172(13)–2.220(12); bond angles [°]: Cl(1)–Ru(1)–Se(1) 80.57(9), N(1)–Ru(1)–Se(1) 83.50(2), N(1)–Ru(1)–Cl(1) 85.90(2).

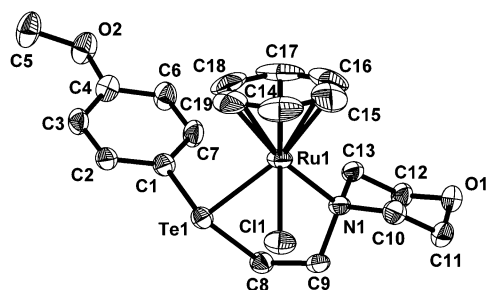


Figure 4. ORTEP diagram of the cation of **6** with ellipsoids at the 30% probability level. Hydrogen atoms and the PF_6^- anion have been omitted for clarity. Bond lengths [Å]: Ru(1)–Te(1) 2.6143(7), Ru(1)–N(1) 2.238(4), Ru(1)–Cl(1) 2.4078(14), Ru(1)–C 2.217(8)–2.217(8); bond angles [°]: Cl(1)–Ru(1)–Te(1) 80.25(4), N(1)–Ru(1)–Te(1) 84.61(10), N(1)–Ru(1)–Cl(1) 86.21(10).

(S,N,Se)ligand] $^+$, $[\text{Cp}^*\text{Ru}(\text{PMe}_3)_2(\text{SC}_6\text{F}_4\text{H})]$, and $[\text{Cp}^*\text{Ru}(\text{NO})(\text{SC}_6\text{F}_4\text{H})_2]$ are reported^[29–31] to fall. Complex **4** is a new example of the little known (η^6 -arene)(seleno ether)ruthenium(II) complex (arene = $\eta^6\text{-C}_6\text{H}_6$ or $\eta^6\text{-}p\text{-cymene}$).^[29,30,32] The Ru–Se bond length of the cation of **4** [2.4837(14) Å] is consistent with the value reported for the half-sandwich complex of Ru^{II} with *N*-[2-(phenylseleno)ethyl]pyrrolidine^[29] [2.4770(5)–2.480(11) Å] and falls within the range 2.4756(10)–2.5240(9) Å reported for the Ru–Se bond lengths in the clusters $[\text{Ru}_3(\mu_3\text{-Se})(\text{CO})_7(\mu_3\text{-CO})(\mu\text{-dppm})]$ and $[\text{Ru}_3(\mu_3\text{-Se})(\mu_3\text{-S})(\text{CO})_7(\mu\text{-dppm})]$.^[33] For the Ru^{IV} complex $[\text{Cp}^*\text{Ru}\{\eta^2\text{-Se}_2\text{P}(\text{iPr})_2\}\{\eta^2\text{-SeP}(\text{iPr})_2\}][\text{PF}_6]$, the Ru–Se bond lengths^[31] are reported to be in the range 2.538(2)–2.590(2) Å, longer than that in the cation of **4** as a result of steric crowding. The Ru–Se bond length found in the dimetallic species $[\text{CpRu}(\text{CO})(\text{C}\equiv\text{CPh})(\mu\text{-Se})\text{ZrCp}_2]$ [2.494(1) Å]^[34] is closer to that in the cation of **4**. In $[\text{Ru}(\eta^5\text{-C}_5\text{Me}_5)(\mu_2\text{-SeR})_3\text{Ru}(\eta^5\text{-C}_5\text{Me}_5)]\text{Cl}$ (R = tolyl), the Ru–Se bond lengths are in the range 2.446(4)–2.466(4) Å^[35] and shorter than that in the cation of **4**, because RSe^- is expected to be bonded more strongly than the seleno ether. In the diselenide-bridged complex $[\text{Ru}(\eta^5\text{-C}_5\text{Me}_5)(\text{PPh}_3)_2]_2(\mu\text{-Se}_2)_2(\text{Otf})_2$, the Ru–Se bond lengths are 2.518(1) and 2.556(1) Å,^[36] respectively, somewhat longer than that in the cation of **4**.

In the cation of complex **6**, ligand **L4** is coordinated to Ru in a bidentate (Te,N) mode, forming a five-membered chelate ring. The Ru–Te bond length [2.6143(7) Å] of the cation of **6** is consistent with earlier reports of 2.619(8) Å for $[\text{RuCl}_2(\eta^6\text{-}p\text{-cymene})\text{L}]$ [L = 2-(4-ethoxyphenyl)telluro-

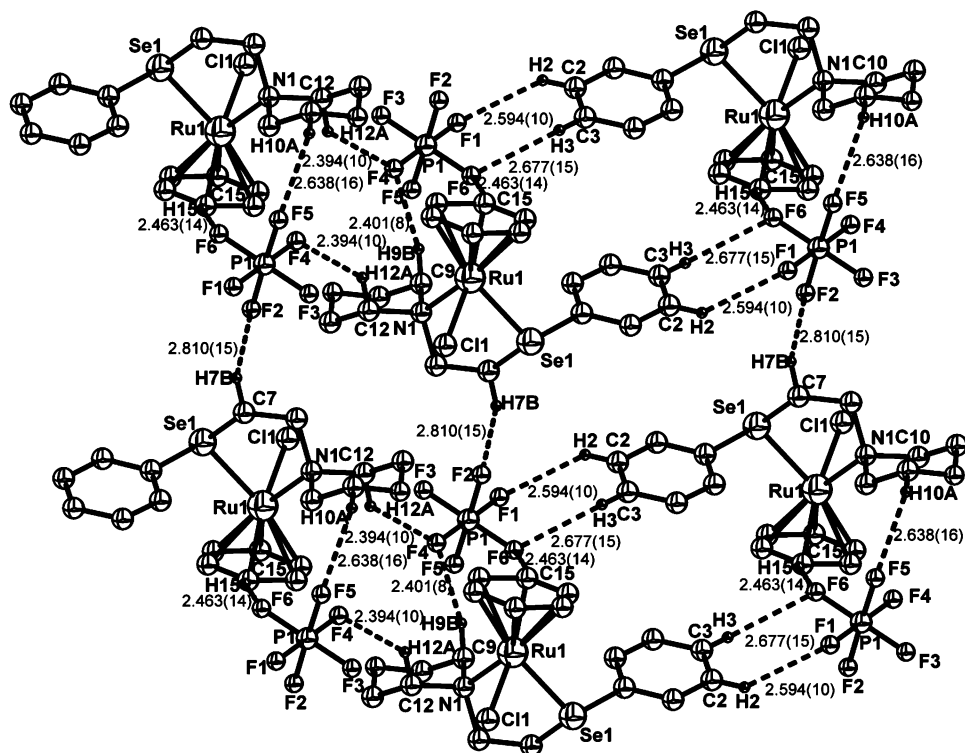


Figure 5. ORTEP diagram showing the P···F···H interactions in **4**. Distances [Å]: P(1)–F(1)···H(2) 2.594(10), P(1)–F(2)···H(7B) 2.810(15), P(1)–F(4)···H(12A) 2.394(10), P(1)–F(5)···H(10A) 2.638(16), P(1)–F(6)···H(15A) 2.463(14).

methyl)tetrahydro-2*H*-pyran]^[37] and shorter than 2.6371(4) Å reported for [RuCl(η⁶-*p*-cymene)(H₂NCH₂CH₂-TeC₆H₄OMe)]Cl·H₂O.^[38] It is also shorter than the reported value 2.6528(9) Å for dichloro(η⁶-*p*-cymene){bis[2-(2-thienyl)ethyl] telluride}ruthenium(II),^[39] 2.651(5) Å for [RuCl₂(η⁶-*p*-cymene){bis[(1,3-dioxan-2-yl)ethyl] telluride}],^[40] and 2.6559(9) Å for [RuCl₂(η⁶-*p*-cymene)(*N*-{2-(4-methoxyphenyl)telluro}ethyl}phthalimide)].^[41] The hybrid organotellurium ligands in all these complexes of Ru^{II}(η⁶-*p*-cymene) bind in a monodentate mode through Te, and this may be responsible to some extent for their longer Ru–Te bonds. The bond angles at the coordinating S, Se, and Te atoms are as expected for near trigonal-pyramidal geometry.

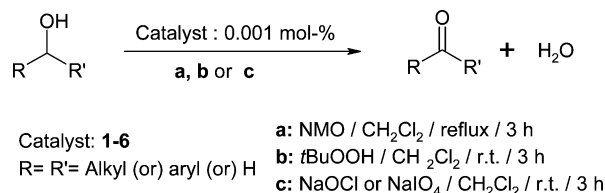
The Ru–C bond lengths of the cations of **1**, **3**, **4**, and **6** [2.159(7)–2.224(4) Å] are consistent with those in earlier reports^[29,30,33,37,39–46] [2.168(5)–2.228(5) Å]. The C–Ru–C bond angles are normal. The Ru–Cl bond lengths (sum of the covalent radii ca. 2.24 Å) of **1** and **3** are 2.394(12) and 2.3996(15) Å, respectively, similar and consistent with the value 2.3914(12) Å reported^[29] for [(η⁶-C₆H₆)ruthenium(II)-Cl(S,N)ligand]⁺. For the cation of **4**, the Ru–Cl bond length [2.413(3) Å] is consistent with those of **1** and **3**. The Ru–Cl bond length of the cation of **6** [2.4078(14) Å] is consistent with those in earlier reports of 2.415(2)/2.422(2) Å for dichloro(η⁶-*p*-cymene){bis[2-(2-thienyl)ethyl] telluride}-ruthenium(II)^[39] and 2.417(2)–2.436(2) Å for [RuCl₂(η⁶-*p*-cymene)L] (L = monodentate Te ligand)^[44–46] and [RuCl{η²-C,N-C₆H₃(CH₂NMe₂)₂-2,6}{η⁶-C₁₀H₁₄}]^[47]. It is somewhat longer than the value 2.308(2) Å reported for [(η⁶-*p*-cymene)RuCl(H₂NCH₂CH₂TeC₆H₄OMe)]Cl·H₂O,^[38] but the difference with the values for **1**, **3**, and **4** are not very significant.

The Ru–N bond lengths (sum of the covalent radii ca. 1.95 Å) of the cations of **1**, **3**, **4**, and **6** are 2.208(3), 2.205(4), 2.234(8), and 2.238(4) Å, respectively. The first two are consistent with each other and with those of the half-sandwich complex of Ru^{II} with *N*-{2-(phenylseleno)ethyl}pyrrolidine [2.190(3)–2.201(5) Å].^[29] The final two values are also consistent with each other, but larger than the first two and those of complexes in several recent literature reports [2.0511(17)–2.163(10) Å].^[33,43] In the half-sandwich complexes of [RuCl(η⁶-*p*-cymene)]^[48–52] with several nitrogen ligands, the Ru–N bond lengths have been reported generally to be between 2.060(5) and 2.156(2) Å, less than those of **1**, **3**, **4**, and **6**. The bond angles at the coordinating N atoms are as expected for near-tetrahedral geometries.

The NMR spectroscopic data for complexes **1–6** are consistent with the structures revealed by single-crystal X-ray diffraction. The signals in the ⁷⁷Se{¹H} NMR spectra of **4** and **5** appear shifted to a higher frequency (by ca. 100 ppm) in comparison with that of free **L3** as Se is coordinated to the ruthenium center. Similarly, in the ¹²⁵Te{¹H} NMR spectrum of **6** the signal appears at a frequency much higher (by ca. 260 ppm) than that of free **L4**. In the ¹H and ¹³C{¹H} NMR spectra of **1–6**, the signals of all the protons and carbon atoms appear at a higher frequency than those of the free ligands, which coordinate to the ruthenium atom in a bidentate mode. However, the magnitude of the shift

to higher frequency is much larger for C5 to C7 (by up to 45 ppm) in the ¹³C{¹H} NMR spectra and for the protons (up to 1 ppm) attached to them. Furthermore, in the ¹H and ¹³C{¹H} NMR spectra of **6**, the signals experience a much larger shift to higher frequency (by ca. 45 and 1.07 ppm, respectively) than those of the other complexes.

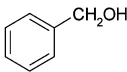
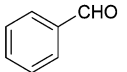
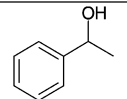
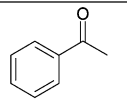
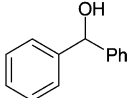
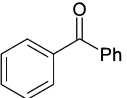
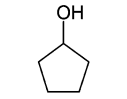
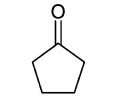
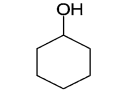
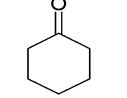
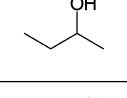
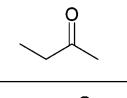
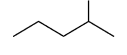
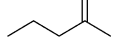
The complexes **1–6** were tested in the catalytic oxidation of primary and secondary alcohols (Scheme 2). The alcohols were oxidized with NaOCl and NaIO₄ at pH = 9–10 because of earlier reports^[53,54] that suggested that this pH range is optimum. A series of blank experiments were carried out under identical conditions (see the Exp. Sect.), which suggests that neither the ruthenium(II) complexes nor the oxidants (NMO, *t*BuOOH, NaOCl, or NaIO₄) alone cause the catalytic oxidation to any significant extent. The cyclic voltammetric experiments performed at 298 K in CH₃CN (0.01 M *n*Bu₄NClO₄ as supporting electrolyte) for **1–6** at a scan rate of 100 mV s^{−1} (anodic sweep) reveal a one-electron irreversible oxidation with *E*_{1/2} values of 0.290–0.586 V (vs. Ag/AgCl; see Table S4 and Figures S8–S13 in the Supporting Information), which is not extreme, implying that both Ru^{II} and Ru^{III} are equally stabilized by the same set of ligands. The narrow range of *E*_{1/2} has previously been reported to be favorable for the catalytic oxidation process;^[55,56] however, no 1:1 relationship has unequivocally been established.



Scheme 2. Oxidation of alcohols catalyzed by **1–6**.

The TON values are given in Table 1 for the oxidation (catalyzed by **1–6**) of various alcohols by four oxidants, namely *N*-methylmorpholine *N*-oxide (NMO), *tert*-butyl hydroperoxide (*t*BuOOH), sodium oxochloride (NaOCl), and sodium periodate (NaIO₄). For all four oxidants **6** appears to be the most efficient of all six Ru species. The benzene derivatives show somewhat better catalytic efficiency than their *p*-cymene counterparts (Table 1). The catalytic efficiency varies with chalcogen ligands in the order Te > Se > S, which is also the order of “softness” of these donor sites. The softer ligand makes easier the formation of Ru^{IV}=O species, which are believed to be the intermediates in the oxidation process on the basis of several observations mentioned below. Undoubtedly, unambiguous determination of the mechanism of these oxidative transformations is not straightforward as the intermediate species are of low stability. On the basis of earlier work^[53,54,57–59] and some of the observations made by us, the mechanism of the catalytic oxidation appears to involve Ru^{IV}=O species that seem to be formed by free radicals (generated by heterolytic cleavage of the oxidants). The addition of AIBN [a free-radical initiator, azobis(isobutyronitrile)] to the oxidation of benzyl alcohol in the presence of **6** (most efficient catalyst)

Table 1. Catalytic oxidation of primary and secondary alcohols by using complexes **1–6** as catalyst.^[a]

| Substrate | Product | | TON (% conversion) | | | | | | |
|--|--|---|-----------------------|--------------------------|--------------------------|--------------------------|--------------------------|--------------------------|--------------------------|
| | | | Blank | 1 | 2 | 3 | 4 | 5 | 6 |
|  |  | a | | 7.8×10 ⁴ (78) | 7.6×10 ⁴ (76) | 8.0×10 ⁴ (80) | 8.2×10 ⁴ (82) | 7.9×10 ⁴ (79) | 8.7×10 ⁴ (87) |
| | | b | Product | 7.5×10 ⁴ (75) | 7.3×10 ⁴ (73) | 7.7×10 ⁴ (77) | 8.0×10 ⁴ (80) | 7.7×10 ⁴ (77) | 8.4×10 ⁴ (84) |
| | | c | not detected | 7.3×10 ⁴ (73) | 7.1×10 ⁴ (71) | 7.6×10 ⁴ (76) | 7.7×10 ⁴ (77) | 7.4×10 ⁴ (74) | 8.2×10 ⁴ (82) |
| | | d | | 7.2×10 ⁴ (72) | 6.8×10 ⁴ (68) | 7.3×10 ⁴ (73) | 7.5×10 ⁴ (75) | 7.3×10 ⁴ (73) | 8.1×10 ⁴ (81) |
|  |  | a | | 9.0×10 ⁴ (90) | 8.5×10 ⁴ (85) | 8.8×10 ⁴ (88) | 9.2×10 ⁴ (92) | 8.5×10 ⁴ (85) | 9.2×10 ⁴ (92) |
| | | b | Product | 8.7×10 ⁴ (87) | 8.4×10 ⁴ (84) | 8.7×10 ⁴ (87) | 9.0×10 ⁴ (90) | 8.3×10 ⁴ (83) | 8.9×10 ⁴ (89) |
| | | c | not detected | 8.6×10 ⁴ (86) | 8.1×10 ⁴ (81) | 8.5×10 ⁴ (85) | 8.7×10 ⁴ (87) | 8.2×10 ⁴ (82) | 8.6×10 ⁴ (86) |
| | | d | | 8.4×10 ⁴ (84) | 8.0×10 ⁴ (80) | 8.3×10 ⁴ (83) | 8.6×10 ⁴ (86) | 8.0×10 ⁴ (80) | 8.4×10 ⁴ (84) |
|  |  | a | | 9.1×10 ⁴ (91) | 8.9×10 ⁴ (89) | 9.0×10 ⁴ (90) | 9.4×10 ⁴ (94) | 9.0×10 ⁴ (90) | 9.5×10 ⁴ (95) |
| | | b | Product | 9.0×10 ⁴ (90) | 8.7×10 ⁴ (87) | 8.9×10 ⁴ (89) | 9.3×10 ⁴ (93) | 8.8×10 ⁴ (88) | 9.3×10 ⁴ (93) |
| | | c | not detected | 8.8×10 ⁴ (88) | 8.6×10 ⁴ (86) | 9.0×10 ⁴ (90) | 9.1×10 ⁴ (91) | 8.5×10 ⁴ (85) | 9.2×10 ⁴ (92) |
| | | d | | 8.5×10 ⁴ (85) | 8.4×10 ⁴ (84) | 8.7×10 ⁴ (87) | 8.9×10 ⁴ (89) | 8.3×10 ⁴ (83) | 9.0×10 ⁴ (90) |
|  |  | a | | 8.8×10 ⁴ (88) | 8.2×10 ⁴ (82) | 8.6×10 ⁴ (86) | 9.0×10 ⁴ (90) | 8.5×10 ⁴ (85) | 9.3×10 ⁴ (93) |
| | | b | Product | 8.6×10 ⁴ (86) | 7.9×10 ⁴ (79) | 8.4×10 ⁴ (84) | 8.9×10 ⁴ (89) | 8.3×10 ⁴ (83) | 9.1×10 ⁴ (91) |
| | | c | not detected | 8.5×10 ⁴ (85) | 7.7×10 ⁴ (77) | 8.3×10 ⁴ (83) | 8.7×10 ⁴ (87) | 8.0×10 ⁴ (80) | 9.0×10 ⁴ (90) |
| | | d | | 8.2×10 ⁴ (82) | 7.4×10 ⁴ (74) | 8.1×10 ⁴ (81) | 8.5×10 ⁴ (85) | 8.1×10 ⁴ (81) | 8.8×10 ⁴ (88) |
|  |  | a | | 9.0×10 ⁴ (90) | 8.7×10 ⁴ (87) | 8.8×10 ⁴ (88) | 9.4×10 ⁴ (94) | 9.1×10 ⁴ (91) | 9.5×10 ⁴ (95) |
| | | b | Product | 8.8×10 ⁴ (88) | 8.4×10 ⁴ (84) | 8.5×10 ⁴ (85) | 9.2×10 ⁴ (92) | 9.0×10 ⁴ (90) | 9.3×10 ⁴ (93) |
| | | c | not detected | 8.9×10 ⁴ (89) | 8.1×10 ⁴ (81) | 8.4×10 ⁴ (84) | 8.9×10 ⁴ (89) | 9.1×10 ⁴ (91) | 9.0×10 ⁴ (90) |
| | | d | | 8.5×10 ⁴ (85) | 7.9×10 ⁴ (79) | 8.2×10 ⁴ (82) | 9.0×10 ⁴ (90) | 8.8×10 ⁴ (88) | 9.1×10 ⁴ (91) |
|  |  | a | | 9.2×10 ⁴ (92) | 9.0×10 ⁴ (90) | 9.2×10 ⁴ (92) | 9.5×10 ⁴ (95) | 9.2×10 ⁴ (92) | 9.6×10 ⁴ (96) |
| | | b | Product | 9.0×10 ⁴ (90) | 8.8×10 ⁴ (88) | 8.9×10 ⁴ (89) | 9.2×10 ⁴ (92) | 9.0×10 ⁴ (90) | 9.5×10 ⁴ (95) |
| | | c | not detected | 8.7×10 ⁴ (87) | 8.5×10 ⁴ (85) | 8.8×10 ⁴ (88) | 9.0×10 ⁴ (90) | 8.8×10 ⁴ (88) | 9.5×10 ⁴ (95) |
| | | d | | 8.6×10 ⁴ (86) | 8.4×10 ⁴ (84) | 8.6×10 ⁴ (86) | 8.8×10 ⁴ (88) | 8.7×10 ⁴ (87) | 9.4×10 ⁴ (94) |
|  |  | a | | 9.3×10 ⁴ (93) | 8.8×10 ⁴ (88) | 9.2×10 ⁴ (92) | 9.6×10 ⁴ (96) | 9.4×10 ⁴ (94) | 9.8×10 ⁴ (98) |
| | | b | Product | 9.2×10 ⁴ (92) | 8.8×10 ⁴ (88) | 9.0×10 ⁴ (90) | 9.5×10 ⁴ (95) | 9.2×10 ⁴ (92) | 9.6×10 ⁴ (96) |
| | | c | not detected | 9.0×10 ⁴ (90) | 8.5×10 ⁴ (85) | 9.1×10 ⁴ (91) | 9.3×10 ⁴ (93) | 9.1×10 ⁴ (91) | 9.3×10 ⁴ (93) |
| | | d | | 8.9×10 ⁴ (89) | 8.1×10 ⁴ (81) | 9.0×10 ⁴ (90) | 9.2×10 ⁴ (92) | 8.8×10 ⁴ (88) | 9.2×10 ⁴ (92) |

[a] Oxidant: a = NMO; b = *t*BuOOH; c = NaIO₄; d = NaOCl; Blank = control experiment in the absence of catalyst.

with any one of the four oxidants under the same reaction conditions resulted in enhanced conversion (86–95%). Further addition of AIBN in the same oxidation reaction in the absence of **6** did not result in any oxidation. In the presence of benzoquinone (a free-radical inhibitor) the conversion was minimal. These observations are consistent with those made by Goldstein and Drago with H₂O₂ and OCl[–] in the oxidation of alkanes.^[59d] On addition of an oxidant to the solutions of complexes **4** and **5**, the signals in the ⁷⁷Se{¹H} NMR spectra are shifted to a higher frequency (by ≥473 ppm). Similarly, in the case of **6** the signal in the ¹²⁵Te{¹H} NMR spectrum shifts to a higher frequency (by ca. 288 ppm) in the presence of an oxidant. The signals in the ⁷⁷Se{¹H} NMR spectrum of **L3** and the ¹²⁵Te{¹H} NMR spectrum of **L4** remain unshifted on addition of any of the four oxidants. Therefore, the ruthenium center is most probably oxidized to Ru^{IV}=O. The UV/Vis spectra on addition of any one of these oxidants to dichloromethane solutions of **1–6** show a new shoulder at 390–394 nm, which is believed^[59,61,64a] to be due to Ru^{IV}=O, the species reported to be responsible for the transfer of the oxygen atom to the alcohol substrates resulting in their catalytic oxidation. The IR spectra of the residues left after evaporating the solvent from the mixtures of any of the oxidants with complexes **1–6** exhibit very strong bands at 845–848 cm^{–1} (ν_{P–F} band at 840–850 cm^{–1} is of medium intensity only), which further supports the formation of the Ru^{IV}=O species^[59a,59b,60–63,64a] responsible for the catalytic oxidation of

alcohols. Moreover, the catalytic activities of the Ru^{IV}=O species towards oxidation reported earlier^[58–60] further strengthens our proposition. The short life-times of the Ru^{IV}=O transient species restricted us from acquiring MS evidence. The ¹H NMR spectra of the ruthenium complexes recorded after the addition of an oxidant are broadened, which indicates the formation of paramagnetic intermediate species.

Conclusions

"Piano-stool" complexes of Ru^{II} of composition [RuCl(η⁶-C₆H₆)(L)][PF₆]/[RuCl(η⁶-*p*-cymene)(L)][PF₆] (**1–6**) have been prepared and characterized. Their catalytic activity in the oxidation of primary and secondary alcohols with *N*-methylmorpholine *N*-oxide (NMO), *t*BuOOH, NaOCl, and NaIO₄ has been investigated. The advantages of **1–6** over recently reported good ruthenium-based catalytic species^[57c,59b,64–68] in the oxidation of alcohols are (i) high efficiency and yield so that smaller quantities are needed, (ii) short reaction times, and (iii) flexibility regarding oxidants. The efficiencies of the catalysts **1–6** in the oxidation of alcohols with any of the oxidants (TON upto 9.8 × 10⁴) are comparable to those of the half-sandwich Ru^{II} complexes containing chalcogenated pyrrolidine, benzotriazole, and Schiff bases with NMO.^[29,30,32]

Experimental Section

General Procedure: Perkin–Elmer 2400 Series II C,H,N analyzer was used for elemental analysis. The ^1H , $^{13}\text{C}\{^1\text{H}\}$, $^{77}\text{Se}\{^1\text{H}\}$, and $^{125}\text{Te}\{^1\text{H}\}$ NMR spectra were recorded with a Bruker Spectrospin DPX-300 NMR spectrometer at 300.13, 75.47, 57.24, and 94.69 MHz, respectively. IR spectra in the range 4000–400 cm^{-1} were recorded with a Nicolet Protège 460 FT-IR spectrometer as KBr pellets. The UV/Vis spectra were recorded with a Perkin–Elmer Lambda BIO-20 model 330 spectrometer. The conductivity measurements were carried out in CH_3CN (conc. ca. 1 mM) by using an ORION conductivity meter, model 162. The catalytic oxidation yields were determined with a NUCON Engineers (New Delhi, India) gas chromatograph (with FID detector), model 5765, equipped with an Alltech (EcTM-1) column of 30 m length, 0.25 mm diameter and having a liquid film thickness of 0.25 μm . The cyclic voltammetry studies were performed with a BAS CV 50W instrument at the University of Delhi (Department of Chemistry). A three-electrode configuration composed of a Pt disk working electrode (3.1 mm^2 area), a Pt wire counter electrode, and an Ag/AgCl reference electrode was used for the measurements. Ferrocene was used as an internal standard ($E_{1/2} = 0.500$ V vs. Ag/AgCl), and all the potentials are expressed with reference to Ag/AgCl. The melting points were measured in an open capillary tube. The ruthenium(II) precursor complexes $[(\eta^6\text{-C}_6\text{H}_6)\text{RuCl}(\mu\text{-Cl})_2]$ and $[(\eta^6\text{-p-cymene})\text{RuCl}(\mu\text{-Cl})_2]$ were prepared according to literature methods.^[69,70]

Synthesis of L1: Thiophenol (0.5 mL, 5.0 mmol) was heated at reflux in dry ethanol (50 mL) under N_2 for 0.5 h. Aqueous NaOH (0.44 g, 11.0 mmol in 5 mL) and 4-(2-chloroethyl)morpholine hydrochloride [0.92 g, 5.0 mmol dissolved in ethanol (20 mL)] were added dropwise successively. After continued heating at reflux for a further 3 h, the reaction mixture was cooled to room temperature and poured into distilled water (100 mL). It was then neutralized with dilute sodium hydroxide and extracted with chloroform (100 mL). The chloroform extract was washed with distilled water (2 \times 50 mL) and dried with anhydrous sodium sulfate. On evaporation of the chloroform in a rotary evaporator, **L1** was obtained as a pale-yellow oil. Yield: 0.87 g, 78%. ^1H NMR (CDCl_3 , 25 $^\circ\text{C}$): $\delta = 2.48\text{--}2.51$ (m, 4 H, 7-H), 2.65 (t, $^3J_{\text{HH}} = 7.5$ Hz, 2 H, 5-H), 3.06 (t, $^3J_{\text{HH}} = 7.5$ Hz, 2 H, 6-H), 3.71–3.76 (m, 4 H, 8-H), 7.17–7.22 (m, 1 H, 1-H), 7.28–7.33 (m, 2 H, 2-H) 7.35–7.38 (m, 2 H, 3-H) ppm. $^{13}\text{C}\{^1\text{H}\}$ NMR (CDCl_3 , 25 $^\circ\text{C}$): $\delta = 30.6$ (C-7), 53.5 (C-5), 58.0 (C-6), 66.8 (C-8), 126.0 (C-1), 128.9 (C-2), 129.1 (C-4), 136.3 (C-3) ppm. IR (KBr): $\tilde{\nu}_{\text{max}} = 3056$ (m, $\nu_{\text{C-H,aromatic}}$), 2957 (s, $\nu_{\text{C-H,aliphatic}}$), 1582 (m, $\nu_{\text{C-C,aromatic}}$), 1207, 1118 (w, $\nu_{\text{C-N}}$), 741 (m, $\nu_{\text{C-H,aromatic}}$) cm^{-1} .

Synthesis of $[\text{RuCl}(\eta^6\text{-C}_6\text{H}_6)(\text{L1})][\text{PF}_6]$ (1**) and $[\text{RuCl}(\eta^6\text{-p-cymene})(\text{L1})][\text{PF}_6]$ (**2**):** Solid $[(\eta^6\text{-C}_6\text{H}_6)\text{RuCl}(\mu\text{-Cl})_2]$ (0.05 g, 0.1 mmol) and **L2** (0.046 g, 0.2 mmol) were allowed to react as described for the synthesis of **1** and **2** to give the yellow microcrystalline solid **3**, which was filtered, washed with cold CH_3OH (10 mL), and dried in vacuo. Single crystals of **3** suitable for X-ray diffraction were obtained similarly to those of **1**. Yield: 0.10 g, 85%. M.p. 173 $^\circ\text{C}$. Mol. cond. (A_M) = 148.8 $\text{Scm}^2\text{mol}^{-1}$. ^1H NMR (CD_3CN , 25 $^\circ\text{C}$): $\delta = 2.26\text{--}2.65$ (m, 4 H, 8-H), 3.11–3.21 (m, 4 H, 7-H), 3.54–3.74 (m, 2 H, 5-H), 3.97–4.34 (m, 2 H, 6-H), 5.63 (s, 6 H, Ru-Ar-H), 7.22–7.44 (m, 1 H, 1-

H + 2-H), 7.67–7.87 (m, 2 H, 3-H) ppm. $^{13}\text{C}\{^1\text{H}\}$ NMR (CD_3CN , 25 $^\circ\text{C}$): $\delta = 30.7$ (C-8), 58.4 (C-7), 62.4 (C-5), 67.2 (C-6), 87.1 (Ru-Ar-C), 129.8 (C-1), 131.5 (C-2), 132.6 (C-3), 134.2 (C-4) ppm. IR (KBr): $\tilde{\nu}_{\text{max}} = 3083$ (m, $\nu_{\text{C-H,aromatic}}$), 2984, 2877 (s, $\nu_{\text{C-H,aliphatic}}$), 1631 (m, $\nu_{\text{C-C,aromatic}}$), 1185, 1114 (w, $\nu_{\text{C-N}}$), 850 (s, $\nu_{\text{P-F}}$), 749 (m, $\nu_{\text{C-H,aromatic}}$) cm^{-1} . $\text{C}_{18}\text{H}_{23}\text{ClINORuS}\cdot\text{PF}_6$ (437.97): calcd. C 37.09, H 3.98, N 2.40; found C 37.00, H 4.05, N 2.49.

2: Yield: 0.10 g, 80%. M.p. 182 $^\circ\text{C}$. Mol. cond. (A_M) = 144.2 $\text{Scm}^2\text{mol}^{-1}$. ^1H NMR (CD_3CN): $\delta = 1.28$ (d, $^3J_{\text{HH}} = 6.6$ Hz, 6 H, CH_3 in *i*Pr), 2.82 (s, 3 H, CH_3 *p* to *i*Pr), 2.86–2.92 (m, 4 H, 8-H), 3.01 (sept, 1 H, CH in *i*Pr), 3.17–3.26 (m, 4 H, 7-H), 3.34–3.37 (m, 2 H, 5-H), 3.89 (m, 2 H, 6-H), 5.28–5.83 (m, 4 H, Ar-H in *p*-cymene), 7.27–7.39 (m, 3 H, 1-H + 2-H), 7.48–7.58 (m, 2 H, 3-H) ppm. $^{13}\text{C}\{^1\text{H}\}$ NMR (CD_3CN , 25 $^\circ\text{C}$): $\delta = 18.9$ (CH_3 *p* to *i*Pr), 22.1, 22.3 (CH_3 in *i*Pr), 31.6 (CH in *i*Pr), 31.8 (C-8), 52.9 (C-7), 56.8 (C-5), 64.4 (C-6), 82.3–106.5 (Ar-C in *p*-cymene), 128.1 (C-1), 130.4 (C-2), 130.6 (C-3), 134.7 (C-4) ppm. IR (KBr): $\tilde{\nu}_{\text{max}} = 3032$ (m, $\nu_{\text{C-H,aromatic}}$), 2973, 2861 (s, $\nu_{\text{C-H,aliphatic}}$), 1630 (m, $\nu_{\text{C-C,aromatic}}$), 1196, 1112 (w, $\nu_{\text{C-N}}$), 840 (s, $\nu_{\text{P-F}}$), 750 (m, $\nu_{\text{C-H,aromatic}}$) cm^{-1} . $\text{C}_{22}\text{H}_{31}\text{ClINORuS}\cdot\text{PF}_6$ (494.08): calcd. C 41.35, H 4.89, N 2.19; found C 41.86, H 4.81, N 2.07.

Synthesis of L2: A solution of 2,2'-dipyridyl disulfide (0.44 g, 2.0 mmol) in ethanol (30 mL) under N_2 was added dropwise to NaBH_4 (0.14 g, 4.0 mmol) dissolved in NaOH (5%, ca. 15 mL) under N_2 until it became colorless due to the formation of PySNa . 4-(2-Chloroethyl)morpholine hydrochloride (0.74 g, 4.0 mmol) dissolved in ethanol (5 mL) was added to this colorless solution with constant stirring. The reaction mixture was further stirred for 3–4 h and poured into ice-cold water (20 mL containing 0.2 g of NaOH). The aqueous phase was extracted with CHCl_3 (5 \times 40 mL). The extract was washed with water (3 \times 50 mL) and dried with anhydrous sodium sulfate. On evaporation of the chloroform under reduced pressure in a rotary evaporator, **L2** was obtained as a yellow oil. Yield: 0.80 g, 80%. ^1H NMR (CDCl_3 , 25 $^\circ\text{C}$): $\delta = 2.52\text{--}2.55$ (m, 4 H, 8-H), 2.69 (t, $^3J_{\text{HH}} = 7.5$ Hz, 2 H, 6-H), 3.34 (t, $^3J_{\text{HH}} = 7.5$ Hz, 2 H, 7-H), 3.69–3.74 (m, 4 H, 9-H), 6.95–6.99 (m, 1 H, 3-H), 7.18 (d, $^3J_{\text{HH}} = 8.1$ Hz, 1 H, 4-H), 7.43–7.49 (m, 1 H, 2-H), 8.42 (d, $^3J_{\text{HH}} = 7.5$ Hz, 1 H, 1-H) ppm. $^{13}\text{C}\{^1\text{H}\}$ NMR (CDCl_3 , 25 $^\circ\text{C}$): $\delta = 26.8$ (C-8), 53.5 (C-6), 58.2 (C-7), 66.9 (C-9), 119.3 (C-3), 122.3 (C-4), 135.8 (C-2), 149.4 (C-1), 158.7 (C-5) ppm. IR (KBr): $\tilde{\nu}_{\text{max}} = 3065$ (m, $\nu_{\text{C-H,aromatic}}$), 2924 (s, $\nu_{\text{C-H,aliphatic}}$), 1575 (m, $\nu_{\text{C-N,aromatic}}$), 1568 (m, $\nu_{\text{C-C,aromatic}}$), 1209, 1114 (w, $\nu_{\text{C-N}}$), 735 (m, $\nu_{\text{C-H,aromatic}}$) cm^{-1} .

Synthesis of $[\text{RuCl}(\eta^6\text{-C}_6\text{H}_6)(\text{L2})][\text{PF}_6]$ (3**):** Solid $[(\eta^6\text{-C}_6\text{H}_6)\text{RuCl}(\mu\text{-Cl})_2]$ (0.05 g, 0.1 mmol) and **L2** (0.046 g, 0.2 mmol) were allowed to react as described for the synthesis of **1** and **2** to give the yellow microcrystalline solid **3**, which was filtered, washed with cold CH_3OH (10 mL), and dried in vacuo. Single crystals of **3** suitable for X-ray diffraction were obtained similarly to those of **1**. Yield: 0.10 g, 85%. M.p. 176.0 $^\circ\text{C}$. Mol. cond. (A_M) = 143.6 $\text{Scm}^2\text{mol}^{-1}$. ^1H NMR (CD_3CN , 25 $^\circ\text{C}$): $\delta = 2.72$ (m, 4 H, 8-H), 2.88–3.32 (m, 2 H, 6-H), 3.52–3.70 (m, 2 H, 7-H), 3.86–4.32 (m, 4 H, 9-H), 5.55 (s, 6 H, Ru-Ar-H), 7.47–7.61 (m, 1 H, 3-H), 7.99 (m, 1 H, 2-H), 8.44 (d, $^3J_{\text{HH}} = 8.1$ Hz, 1 H, 4-H), 8.78 (d, $^3J_{\text{HH}} = 7.5$ Hz, 1 H, 1-H) ppm. $^{13}\text{C}\{^1\text{H}\}$ NMR (CD_3CN , 25 $^\circ\text{C}$): $\delta = 27.4$ (C-8), 54.1 (C-6), 59.4 (C-7), 66.9 (C-9), 87.1 (Ru-Ar-C), 123.3 (C-3), 123.4 (C-4), 137.9 (C-2), 150.2 (C-1), 160.6 (C-5) ppm. IR (KBr): $\tilde{\nu}_{\text{max}} = 3053$ (m, $\nu_{\text{C-H,aromatic}}$), 2968 (s, $\nu_{\text{C-H,aliphatic}}$), 1576 (m, $\nu_{\text{C-N,aromatic}}$), 1571 (m, $\nu_{\text{C-C,aromatic}}$), 1203, 1104 (w, $\nu_{\text{C-N}}$), 842 (s, $\nu_{\text{P-F}}$), 743 (m, $\nu_{\text{C-H,aromatic}}$) cm^{-1} . $\text{C}_{17}\text{H}_{22}\text{ClIN}_2\text{ORuS}\cdot\text{PF}_6$ (438.96): calcd. C 34.97, H 3.80, N 4.80; found C 34.44, H 3.72, N 4.48.

Synthesis of L3: Diphenyl diselenide (0.62 g, 2.0 mmol) was treated with NaBH₄ (0.14 g, 4.0 mmol) as described for the synthesis of L2. The resulting PhSeNa was treated with 4-(2-chloroethyl)morpholine hydrochloride (0.74 g, 4.0 mmol) in a manner similar to that described above for L2 to give L3 as a pale-yellow oil. Yield: 0.86 g, 80%. ¹H NMR (CDCl₃, 25 °C): δ = 2.44–2.46 (m, 4 H, 7-H), 2.68 (t, ³J_{HH} = 7.5 Hz, 2 H, 5-H), 3.02 (t, ³J_{HH} = 7.5 Hz, 2 H, 6-H), 3.66–3.69 (m, 4 H, 8-H), 7.19–7.24 (m, 3 H, 1-H + 2-H), 7.48 (d, ³J_{HH} = 6.6 Hz, 2 H, 3-H) ppm. ¹³C{¹H} NMR (CDCl₃, 25 °C): δ = 24.4 (C-7), 53.1 (C-5), 58.5 (C-6), 66.6 (C-8), 126.6 (C-1), 128.8 (C-2), 130.1 (C-4), 132.2 (C-3) ppm. ⁷⁷Se{¹H} NMR (CDCl₃, 25 °C): δ = 279.5 ppm. IR (KBr): ν_{max} = 3061 (m, ν_{C-H,aromatic}), 2920 (s, ν_{C-H,aliphatic}), 1578 (m, ν_{C-C,aromatic}), 1212, 1117 (w, ν_{C-N}), 738 (m, ν_{C-H,aromatic}) cm⁻¹.

Synthesis of [RuCl(η⁶-C₆H₆)(L3)][PF₆] (4) and [RuCl(η⁶-*p*-cymene)(L3)][PF₆] (5): L3 (0.054 g, 0.2 mmol) was treated with solid [(η⁶-C₆H₆)RuCl(μ-Cl)]₂ (0.05 g, 0.1 mmol) or [(η⁶-*p*-cymene)RuCl(μ-Cl)]₂ (0.06 g, 0.1 mmol) as described for the synthesis of 1 and 2. Solid NH₄PF₆ (0.032 g, 0.2 mmol) was added to the concentrated (to ca. 7 mL) reaction mixture as described above for 1 and 2 to give 4 and 5. Single crystals of 4 were obtained similarly to those of 1.

4: Yield: 0.10 g, 80%. M.p. 181.0 °C. Mol. cond. (*A*_M) = 144.2 Scm²mol⁻¹. ¹H NMR (CD₃CN, 25 °C): δ = 2.62–2.88 (m, 4 H, 8-H), 3.46–3.58 (m, 4 H, 7-H), 3.88–3.96 (m, 2 H, 5-H), 4.25–4.31 (m, 2 H, 6-H), 5.69 (s, 6 H, Ru-Ar-H), 7.61–7.63 (m, 3 H, 1-H + 2-H), 7.82–7.85 (m, 2 H, 3-H) ppm. ¹³C{¹H} NMR (CD₃CN, 25 °C): δ = 32.3 (C-8), 56.2 (C-7), 61.8 (C-5), 64.6 (C-6), 87.4 (Ru-Ar-C), 129.1 (C-1), 130.2 (C-2), 132.1 (C-3), 133.0 (C-4) ppm. ⁷⁷Se{¹H} NMR (CDCl₃, 25 °C): δ = 379.6 ppm. IR (KBr): ν_{max} = 3083 (m, ν_{C-H,aromatic}), 2994, 2877 (s, ν_{C-H,aliphatic}), 1578 (m, ν_{C-C,aromatic}), 1194, 1113 (w, ν_{C-N}), 845 (s, ν_{P-F}), 742 (m, ν_{C-H,aromatic}) cm⁻¹. C₁₈H₂₃ClINORuSe·PF₆ (484.87): calcd. C 34.33, H 3.68, N 2.22; found C 34.03, H 3.60, N 2.28.

5: Yield: 0.11 g, 80%. M.p. 178.0 °C. Mol. cond. (*A*_M) = 140.4 Scm²mol⁻¹. ¹H NMR (CD₃CN, 25 °C): δ = 1.31 (d, ³J_{HH} = 6.6 Hz, 6 H, CH₃ in *i*Pr), 2.25 (s, 3 H, CH₃ *p* to *i*Pr), 2.62–2.67 (m, 4 H, 8-H), 2.90 (sept, 1 H, CH in *i*Pr), 3.02 (m, 4 H, 7-H), 3.28 (m, 2 H, 5-H), 3.91 (m, 2 H, 6-H), 5.31–5.86 (m, 4 H, Ar-H in *p*-cymene), 7.41 (m, 3 H, 1-H + 2-H), 7.66 (m, 2 H, 3-H) ppm. ¹³C{¹H} NMR (CD₃CN, 25 °C): δ = 18.8 (CH₃ *p* to *i*Pr), 22.4, 22.3 (CH₃ in *i*Pr), 31.7 (CH in *i*Pr), 31.9 (C-8), 52.8 (C-7), 57.9 (C-5), 64.5 (C-6), 82.8–106.6 (Ar-C in *p*-cymene), 129.0 (C-1), 130.6 (C-2), 131.9 (C-3), 133.5 (C-4) ppm. ⁷⁷Se{¹H} NMR (CDCl₃, 25 °C): δ = 383.4 ppm. IR (KBr): ν_{max} = 3028 (m, ν_{C-H,aromatic}), 2973, 2858 (s, ν_{C-H,aliphatic}), 1578 (m, ν_{C-C,aromatic}), 1189, 1113 (w, ν_{C-N}), 840 (s, ν_{P-F}), 744 (m, ν_{C-H,aromatic}) cm⁻¹. C₂₂H₃₁ClINORuSe·PF₆ (540.98): calcd. C 38.53, H 4.56, N 2.04; found C 38.33, H 4.50, N 2.07.

Synthesis of L4: Bis(4-methoxyphenyl) ditelluride (0.94 g, 2 mmol) was treated first with NaBH₄ (0.14 g, 4.0 mmol dissolved in 5% NaOH) and thereafter with 4-(2-chloroethyl)morpholine hydrochloride [0.74 g, 4.0 mmol dissolved in ethanol (5 mL)] as described for the synthesis of L2. After workup similar to that for L2, L4 was obtained as a white oil. Yield: 1.12 g, 80%. ¹H NMR (CDCl₃, 25 °C): δ = 2.46–2.49 (m, 4 H, 7-H), 2.78 (t, ³J_{HH} = 7.5 Hz, 2 H, 5-H), 3.04 (t, ³J_{HH} = 7.5 Hz, 2 H, 6-H), 3.68–3.71 (m, 4 H, 8-H), 3.79 (s, 3 H, OCH₃), 6.76 (d, ³J_{HH} = 6.9 Hz, 2 H, 2-H), 7.68 (d, ³J_{HH} = 6.9 Hz, 2 H, 3-H) ppm. ¹³C{¹H} NMR (CDCl₃, 25 °C): δ = 7.8 (C-7), 53.1 (C-5), 55.1 (C-6), 59.3 (C-8), 66.9 (OCH₃), 101.3 (C-1), 115.0 (C-2), 140.7 (C-4), 159.5 (C-3) ppm. ¹²⁵Te{¹H} NMR (CDCl₃, 25 °C): δ = 431.5 ppm. IR (KBr): ν_{max} = 3063 (m,

ν_{C-H,aromatic}), 2918 (s, ν_{C-H,aliphatic}), 1578 (m, ν_{C-C,aromatic}), 1211, 1118 (w, ν_{C-N}) cm⁻¹.

Synthesis of [RuCl(η⁶-C₆H₆)(L4)][PF₆] (6): Solid [(η⁶-C₆H₆)RuCl(μ-Cl)]₂ (0.05 g, 0.1 mmol) and L4 [0.070 g, 0.2 mmol dissolved in CH₃OH (15 mL)] were allowed to react and treated thereafter with solid NH₄PF₆ (0.032 g, 0.2 mmol) as described above for the synthesis of 1 and 2. Complex 6 was isolated, and single crystals suitable for X-ray diffraction were grown by the procedure used for those of 1 and 2. Yield: 0.12 g, 85%. M.p. 186.0 °C. Mol. cond. (*A*_M) = 143.7 Scm²mol⁻¹. ¹H NMR (CD₃CN, 25 °C): δ = 2.98–3.28 (m, 4 H, 8-H), 3.35–3.68 (m, 4 H, 7-H), 3.85 (s, 3 H, OCH₃), 3.97–4.03 (m, 2 H, 5-H), 4.12–4.49 (m, 2 H, 6-H), 5.67 (s, 6 H, Ru-Ar-H), 7.03 (d, ³J_{HH} = 6.9 Hz, 2 H, 2-H), 7.88 (d, ³J_{HH} = 6.9 Hz, 2 H, 3-H) ppm. ¹³C{¹H} NMR (CD₃CN, 25 °C): δ = 30.1 (C-8), 53.3 (C-7), 56.7 (OCH₃), 61.6 (C-5), 65.4 (C-6), 87.2 (Ru-Ar-C), 118.3 (C-1), 130.2 (C-2), 142.2 (C-3), 161.7 (C-4) ppm. ¹²⁵Te{¹H} NMR (CDCl₃, 25 °C): δ = 691.9 ppm. IR (KBr): ν_{max} = 3088 (m, ν_{C-H,aromatic}), 2982, 2878 (s, ν_{C-H,aliphatic}), 1627 (m, ν_{C-C,aromatic}), 1195, 1117 (w, ν_{C-N}), 845 (s, ν_{P-F}), 748 (m, ν_{C-H,aromatic}) cm⁻¹. C₁₉H₂₅ClINO₂RuTe·PF₆ (563.54): calcd. C 32.21, H 3.56, N 1.98; found C 32.11, H 3.50, N 2.06.

X-ray Crystallographic Analysis: The data for the single-crystal structures were collected (at IIT Delhi and IIT Kanpur, India) with a Bruker AXS SMART Apex CCD diffractometer by using Mo-*K*_α (0.71073 Å) radiation. SADABS software was used for absorption correction (if needed) and SHELXTL for space group, structure determination, and refinements.^[71–73] Selected crystal data are given below. Further details of crystal data and structural refinements, bond lengths and angles are available in Tables S1–S3 in the Supporting Information. CCDC-768670 (1), -768671 (3), -768672 (4), and -768673 (6) contain the supplementary crystallographic data for this paper. These data can be obtained free of charge from the Cambridge crystallographic data centre via www.ccdc.cam.ac.uk/data_request.cif.

1: C₁₈H₂₃ClF₆NOPRuS, *M*_r = 582.93, triclinic space group, *P* $\bar{1}$, *a* = 9.825(3), *b* = 10.348(2), *c* = 10.569(3) Å, *α* = 93.753(5), *β* = 96.363(4), *γ* = 101.484(5)°, *V* = 1042.3(5) Å³, *Z* = 2, ρ_{calcd.} = 1.857 gcm⁻³, μ = 1.121 mm⁻¹, -11 ≤ *h* ≤ 11, -12 ≤ *k* ≤ 12, -12 ≤ *l* ≤ 12, *T* = 100(2) K, GOF = 1.098, *R*₁ = 0.0453, *wR*₂ = 0.1268 [*I* > 2σ(*I*)], *R*₁ = 0.0492, *wR*₂ = 0.1356 (all data). Out of 5284 total reflections collected, 3599 (*R*_{int} = 0.0298) were unique.

3: C₁₇H₂₂ClF₆N₂OPRuS, *M*_r = 583.93, triclinic space group, *P* $\bar{1}$, *a* = 9.7965(15), *b* = 10.3459(16), *c* = 10.8061(3) Å, *α* = 93.031(3), *β* = 96.598(2), *γ* = 100.470(3)°, *V* = 1063.4(3) Å³, *Z* = 2, ρ_{calcd.} = 1.824 gcm⁻³, μ = 1.100 mm⁻¹, -11 ≤ *h* ≤ 11, -12 ≤ *k* ≤ 12, -12 ≤ *l* ≤ 12, *T* = 273(2) K, GOF = 1.158, *R*₁ = 0.0525, *wR*₂ = 0.1207 [*I* > 2σ(*I*)], *R*₁ = 0.0558, *wR*₂ = 0.1230 (all data). Out of 10082 total reflections collected, 3760 (*R*_{int} = 0.0307) were unique.

4: C₁₈H₂₃ClF₆NOPRuSe, *M*_r = 629.82, triclinic space group, *P* $\bar{1}$, *a* = 9.889(3), *b* = 10.508(3), *c* = 10.784(3) Å, *α* = 93.107(4), *β* = 96.293(5), *γ* = 101.934(4)°, *V* = 1086.4(5) Å³, *Z* = 2, ρ_{calcd.} = 1.925 gcm⁻³, μ = 2.655 mm⁻¹, -11 ≤ *h* ≤ 11, -12 ≤ *k* ≤ 12, -12 ≤ *l* ≤ 12, *T* = 273(2) K, GOF = 1.076, *R*₁ = 0.0676, *wR*₂ = 0.1414 [*I* > 2σ(*I*)], *R*₁ = 0.1134, *wR*₂ = 0.1580 (all data). Out of 6767 total reflections collected, 3837 (*R*_{int} = 0.0963) were unique.

6: C₁₉H₂₅ClF₆NO₂PRuTe, *M*_r = 708.49, monoclinic space group, *P*2₁/*n*, *a* = 10.4151(17), *b* = 10.9106(17), *c* = 21.007(3) Å, *α* = 90.00, *β* = 96.636(3), *γ* = 90.00°, *V* = 2371.1(6) Å³, *Z* = 4, ρ_{calcd.} = 1.985 gcm⁻³, μ = 2.111 mm⁻¹, -12 ≤ *h* ≤ 12, -12 ≤ *k* ≤ 12, -24 ≤ *l* ≤ 24, *T* = 273(2) K, GOF = 1.044, *R*₁ = 0.0415, *wR*₂ = 0.1092 [*I* > 2σ(*I*)], *R*₁ = 0.0487, *wR*₂ = 0.1136 (all data). Out of

19132 total reflections collected, 4167 ($R_{\text{int}} = 0.0389$) were unique.

Catalytic Oxidation of Alcohols with NMO: The catalytic oxidations of primary alcohols to the corresponding aldehydes and secondary alcohols to ketones with *N*-methylmorpholine *N*-oxide (NMO) and complexes **1–6** were typically carried as follows. A solution of complex **1–6** (0.001 mol-%) in CH_2Cl_2 (20 mL) was mixed with the neat alcohol substrate (1 mmol) and solid NMO (3 mmol). The mixture was heated at reflux for 3 h, and thereafter most of the solvent was evaporated in a rotary evaporator. The residue containing the oxidized product was extracted with petroleum ether (60–80 °C; 20 mL). The catalyst, insoluble in petroleum ether, was recovered almost quantitatively for the next catalytic cycle. The oxidized product present in petroleum ether was analyzed by GC.

Catalytic Oxidation of Alcohols with *t*BuOOH: A mixture complex **1–6** (0.001 mol-%) dissolved in CH_2Cl_2 (20 mL) and neat alcohol substrate (1 mmol) was prepared. *t*BuOOH (4 mmol) was added to the mixture through a dropping funnel over 0.5 h, and the resulting mixture was stirred at room temperature for 3 h. Most of the solvent from the reaction mixture was evaporated in a rotary evaporator to give a semi-solid containing the catalyst and the oxidized alcohol. The mixture was extracted with petroleum ether (60–80 °C; 20 mL). The extract containing the oxidized product was analyzed by GC, and the residue containing the catalyst was preserved in a nearly quantitative amount for the next catalytic cycle.

Catalytic Oxidation of Alcohols with NaOCl and NaIO₄: A solution of the ruthenium complex **1–6** (0.001 mol-%) in CH_2Cl_2 (10 mL) was added to a solution of $\text{NaHCO}_3/\text{Na}_2\text{CO}_3$ (5 mL, 1.0 M, pH = 9.5) buffer. A few drops of aqueous NaOCl/NaIO₄ (0.7 M/1.0 M) were added at 0 °C, and the mixture was stirred vigorously until the organic phase became yellow or orange leaving the aqueous phase colorless. The alcohol (1 mmol) in CH_2Cl_2 (5 mL) was added in one portion to the reaction mixture with stirring. An aqueous solution of 0.7 M NaOCl (5.7 mL)/1.0 M NaIO₄ (4 mL) was added to the reaction mixture dropwise through a dropping funnel over a period of 1 h. The resulting reaction mixture was stirred at room temperature maintaining its pH at ca. 9.5 for 3 h and shaken thereafter with CH_2Cl_2 (30 mL). The organic layer was separated, and most of the solvent was evaporated in a rotary evaporator to give a semi-solid, which was extracted with petroleum ether (60–80 °C; 20 mL). The catalyst left as a solid residue was recovered almost quantitatively for another catalytic cycle. The resulting aldehydes/ketones extracted into petroleum ether were analyzed by GC.

Supporting Information (see footnote on the first page of this article): Crystal data, selected bond lengths and angles, secondary-interaction distances, figures showing secondary interactions, cyclic voltammetric data and diagram of complexes **1–6**.

Acknowledgments

The authors thank the Department of Science and Technology (India) for research project no. SR/S1/IC-23/06 and for partial financial assistance given to establishing the single-crystal X-ray diffraction facility at IIT Delhi, New Delhi (India) under the FIST programme. P. S. thanks the University Grants Commission (India) for the award of a Junior/Senior Research Fellowship.

- [1] G. Süss-Fink, M. Faure, T. R. Ward, *Angew. Chem. Int. Ed.* **2002**, *41*, 99–101.
- [2] A. J. Davenport, D. L. Davies, J. Fawcett, D. R. Russell, *Dalton Trans.* **2004**, 1481–1492.

- [3] A. Fürstner, M. Picquet, C. Bruneau, P. H. Dixneuf, *Chem. Commun.* **1998**, 1315–1316.
- [4] S. Delfosse, Y. Borguet, L. Delaude, A. Demonceau, *Macromol. Rapid Commun.* **2007**, *28*, 492–503.
- [5] I. Özdemir, S. Demir, B. Çetinkaya, C. Gourlaouen, F. Maseras, C. Bruneau, P. H. Dixneuf, *J. Am. Chem. Soc.* **2008**, *130*, 1156–1157.
- [6] Y. Boutadla, O. Al-Duaij, D. L. Davies, G. A. Griffith, K. Singh, *Organometallics* **2009**, *28*, 433–490, and references therein.
- [7] H. Küçükbay, B. Çetinkaya, S. Guesmi, P. H. Dixneuf, *Organometallics* **1996**, *15*, 2434–2439.
- [8] A. Richel, A. Demonceau, A. F. Noels, *Tetrahedron Lett.* **2006**, *47*, 2077–2081.
- [9] D. Jan, L. Delaude, F. Simal, A. Demonceau, A. F. Noels, *J. Organomet. Chem.* **2000**, *606*, 55–64.
- [10] D. Carmona, M. P. Lamata, F. Viguri, R. Rodríguez, F. J. Lahoz, I. T. Dobrinovitch, L. A. Oro, *Dalton Trans.* **2008**, 3328–3338.
- [11] a) G. Süss-Fink, *Dalton Trans.* **2010**, *39*, 1673–1688; b) H. M. Chen, J. A. Parkinson, S. Parsons, R. A. Coxall, R. O. Gould, P. J. Sadler, *J. Am. Chem. Soc.* **2002**, *124*, 3064–3082.
- [12] H. M. Chen, J. A. Parkinson, R. E. Morris, P. J. Sadler, *J. Am. Chem. Soc.* **2003**, *125*, 173–186.
- [13] F. Wang, H. M. Chen, S. Parsons, I. D. H. Ostwald, J. E. Davidson, P. J. Sadler, *Chem. Eur. J.* **2003**, *9*, 5810–5820.
- [14] R. Fernandez, M. Melchart, A. Habtemariam, S. Parsons, P. J. Sadler, *Chem. Eur. J.* **2004**, *10*, 5173–5179.
- [15] Y. K. Yan, M. Melchart, A. Habtemariam, P. J. Sadler, *Chem. Commun.* **2005**, 4764–4776.
- [16] T. Sriskandakumar, H. Petzold, P. C. A. Bruijninx, A. Habtemariam, P. J. Sadler, P. Kennepohl, *J. Am. Chem. Soc.* **2009**, *131*, 13355–13361.
- [17] W. Kandioller, C. G. Hartinger, A. A. Nazarov, M. L. Kuznetsov, R. O. John, C. Bartel, M. A. Jakupc, V. B. Arion, B. K. Keppler, *Organometallics* **2009**, *28*, 4249–4251.
- [18] M. G. Mendoza-Ferri, C. G. Hartinger, R. E. Eichinger, N. Stolyarova, K. Severin, M. A. Jakupc, A. A. Nazarov, B. K. Keppler, *Organometallics* **2008**, *27*, 2405–2407.
- [19] C. G. Hartinger, A. Casini, C. Duhot, Y. O. Tsybin, L. Messori, P. J. Dyson, *J. Inorg. Biochem.* **2008**, *102*, 2136–2141.
- [20] W. Kandioller, C. G. Hartinger, A. A. Nazarov, J. Kasser, R. John, M. A. Jakupc, V. B. Arion, P. J. Dyson, B. K. Keppler, *J. Organomet. Chem.* **2009**, *694*, 922–929.
- [21] M. Gras, B. Therrien, G. Süss-Fink, P. Štěňicka, A. K. Renfrew, P. J. Dyson, *J. Organomet. Chem.* **2008**, *693*, 3419–3424.
- [22] I. Berger, M. Hanif, A. A. Nazarov, C. G. Hartinger, R. O. John, M. L. Kuznetsov, M. Groessl, F. Schmitt, O. Zava, F. Biba, V. B. Arion, M. Galanski, M. A. Jakupc, L. Juillerat-Jeanneret, P. J. Dyson, B. K. Keppler, *Chem. Eur. J.* **2008**, *14*, 9046–9057.
- [23] R. Alexander, A. Balasundaram, M. Batchelor, D. Brookings, K. Crépy, T. Crabbe, M.-F. Deltent, F. Driessens, A. Gill, S. Harris, G. Hutchinson, C. Kulisa, M. Merriman, P. Mistry, T. Parton, J. Turner, I. Whitcombe, S. Wright, *Bioorg. Med. Chem. Lett.* **2008**, *18*, 4316–4320.
- [24] V. Hahn, A. Mikolasch, K. Wende, H. Bartrow, U. Lindequist, F. Schauer, *Biotechnol. Appl. Biochem.* **2009**, *54*, 187–195, and reference therein.
- [25] W. Roel, M. K. S. Vink, E. S. Hans, L. V. D. Floris, H. B. Richard, P. J. T. R. Floris, *Synthesis* **2004**, *5*, 641–662.
- [26] M. H. Kim, R. D. Schuetz, *J. Am. Chem. Soc.* **1952**, *74*, 5102–5104.
- [27] A. K. Singh, J. Sooriyakumar, S. Husebye, K. W. Tornroos, *J. Organomet. Chem.* **2000**, *612*, 46–52.
- [28] A. K. Singh, J. Sooriyakumar, R. J. Butcher, *Inorg. Chim. Acta* **2001**, *312*, 163–169.
- [29] P. Singh, M. Singh, A. K. Singh, *J. Organomet. Chem.* **2009**, *694*, 3872–3880.

- [30] P. Singh, D. Das, M. Singh, A. K. Singh, *Inorg. Chem. Commun.* **2010**, *13*, 223–226.
- [31] Q.-F. Zhang, F. K. M. Cheung, W.-Y. Wong, I. D. Williams, W.-H. Leung, *Organometallics* **2001**, *20*, 3777–3781.
- [32] D. Das, P. Singh, A. K. Singh, *J. Organomet. Chem.* **2010**, *695*, 955–962.
- [33] S. J. Ahmed, M. I. Hyder, S. E. Kabir, M. A. Miah, A. J. Deeming, E. Nordlander, *J. Organomet. Chem.* **2006**, *691*, 309–322.
- [34] Y. Sunada, Y. Hayashi, H. Kawaguchi, K. Tatsumi, *Inorg. Chem.* **2001**, *40*, 7072–7078.
- [35] H. Matsuzaka, T. Ogino, M. Nishio, M. Hidai, Y. Nishibayashi, S. Uemura, *J. Chem. Soc., Chem. Commun.* **1994**, *2*, 223–224.
- [36] J. Amarasekera, E. J. Houser, T. B. Rauchfuss, C. L. Stern, *Inorg. Chem.* **1992**, *31*, 1614–1620.
- [37] A. K. Singh, M. Kadarkaraisamy, M. Mishra, J. Sooriyakumar, J. E. Drake, M. B. Hursthouse, M. E. Light, J. P. Jasinski, *Inorg. Chim. Acta* **2001**, *320*, 133–140.
- [38] R. Kumar, P. A. K. Singh, R. J. Butcher, P. Sharma, R. A. Toscano, *Eur. J. Inorg. Chem.* **2004**, 1107–1114.
- [39] S. Bali, A. K. Singh, P. Sharma, R. A. Toscano, J. E. Drake, M. B. Hursthouse, M. E. Light, *J. Organomet. Chem.* **2004**, *689*, 2346–2353.
- [40] A. K. Singh, J. Sooriyakumar, J. E. Drake, M. B. Hursthouse, M. E. Light, *J. Organomet. Chem.* **2000**, *613*, 244–249.
- [41] A. K. Singh, M. Kadarkaraisamy, G. S. Murthy, J. Srinivas, B. Varghese, R. J. Butcher, *J. Organomet. Chem.* **2000**, *605*, 39–44.
- [42] a) H. Mishra, R. Mukherjee, *J. Organomet. Chem.* **2006**, *691*, 3545–3555; b) H. Mishra, R. Mukherjee, *J. Organomet. Chem.* **2007**, *692*, 3248–3260.
- [43] P. R. Kumar, S. Upreti, A. K. Singh, *Inorg. Chim. Acta* **2008**, *361*, 1426–1436.
- [44] S. Bali, A. K. Singh, J. E. Drake, M. B. Hursthouse, M. E. Light, *J. Organomet. Chem.* **2006**, *691*, 3788–3796.
- [45] A. K. Singh, J. Sooriyakumar, S. Husebye, K. W. Tornroos, *J. Organomet. Chem.* **2000**, *612*, 46–52.
- [46] A. K. Singh, C. V. Amburose, M. Misra, R. J. Butcher, *J. Chem. Res. (S)* **1999**, 716–717.
- [47] P. Steenwinkel, S. L. James, R. A. Gossage, D. M. Grove, H. Kooijman, W. J. J. Smeets, A. L. Spek, G. V. Koten, *Organometallics* **1998**, *17*, 4680–4693.
- [48] T. Bugarcic, A. Habtemariam, R. J. Deeth, F. P. A. Fabbiani, S. Parsons, P. J. Sadler, *Inorg. Chem.* **2009**, *48*, 9444–9453.
- [49] M. L. Soriano, F. A. Jalón, B. R. Manzano, M. Maestro, *Inorg. Chim. Acta* **2009**, *362*, 4486–4492.
- [50] A. Bacchi, P. Pelagatti, C. Pelizzi, D. Rogolino, *J. Organomet. Chem.* **2009**, *694*, 3200–3211.
- [51] A. Singh, N. Singh, D. S. Pandey, *J. Organomet. Chem.* **2002**, *642*, 48–57.
- [52] J. A. Cabeza, I. da Silva, I. del Río, R. A. Gossage, L. Martínez-Méndez, D. Miguel, *J. Organomet. Chem.* **2007**, *692*, 4346–4352.
- [53] L. Gonsalvi, I. W. C. E. Arends, P. Moilanen, R. A. Sheldon, *Adv. Synth. Catal.* **2003**, *345*, 1321–1328.
- [54] L. Gonsalvi, I. W. C. E. Arends, R. A. Sheldon, *Org. Lett.* **2002**, *4*, 1659–1661.
- [55] O. Tutusaus, C. Viñas, R. Núñez, F. Teixidor, A. Demonceau, S. Delfosse, A. F. Noels, I. Mata, E. Molins, *J. Am. Chem. Soc.* **2003**, *125*, 11830–11831.
- [56] L. Delaude, A. Demonceau, A. F. Noels, *Top. Organomet. Chem.* **2004**, *11*, 155–171, and reference therein.
- [57] a) R. S. Drago, *Coord. Chem. Rev.* **1992**, *117*, 185–213; b) T. R. Cundari, R. S. Drago, *Inorg. Chem.* **1990**, *29*, 3904–3907; c) W.-H. Fung, W.-Y. Yu, C.-M. Che, *J. Org. Chem.* **1998**, *63*, 2873–2877, and references therein.
- [58] C.-M. Che, T.-F. Lai, K.-Y. Wong, *Inorg. Chem.* **1987**, *26*, 2289–2299.
- [59] a) V. J. Catalano, R. A. Heck, C. E. Immoos, A. Öhman, M. G. Hill, *Inorg. Chem.* **1998**, *37*, 2150–2157; b) K. N. Kumar, G. Venkatachalam, R. Ramesh, Y. Liu, *Polyhedron* **2008**, *27*, 157–166; c) A. M. El-Hendawy, A. H. Alkubaisi, A. E. Koarashy, M. M. Shanab, *Polyhedron* **1993**, *12*, 2343–2350; d) A. S. Goldstein, R. S. Drago, *J. Chem. Soc., Chem. Commun.* **1991**, 21–22.
- [60] M. M. T. Khan, D. Chatterjee, R. R. Merchant, P. Paul, S. H. R. Abdi, D. Srinivas, M. R. H. Siddiqui, M. A. Moiz, M. M. Bhadbhade, K. Venkatasubramanian, *Inorg. Chem.* **1992**, *31*, 2711–2718.
- [61] W. H. Leung, C. M. Chem, *Inorg. Chem.* **1989**, *28*, 4619–4622.
- [62] M. S. El-Shahawi, A. F. Shoir, *Spectrochim. Acta Part A* **2004**, *60*, 121–127.
- [63] D. Chatterjee, A. Mitra, B. C. Roy, *J. Mol. Catal. A* **2000**, *161*, 17–21.
- [64] a) M. U. Raja, N. Gowri, R. Ramesh, *Polyhedron* **2010**, *29*, 1175–1181; b) Y. Do, S.-B. Ko, I.-C. Hwang, K.-E. Lee, S. W. Lee, J. Park, *Organometallics* **2009**, *28*, 4624–4627.
- [65] W. M. Cheung, H.-Y. Ng, I. D. Williams, W.-H. Leung, *Inorg. Chem.* **2008**, *47*, 4383–4391.
- [66] B. J. Hornstein, D. M. Dattelbaum, J. R. Schoonover, T. J. Meyer, *Inorg. Chem.* **2007**, *46*, 8139–8145.
- [67] H. Mizoguchi, T. Uchida, K. Ishida, T. Katsuki, *Tetrahedron Lett.* **2009**, *50*, 3432–3435.
- [68] S. Ganesamoorthy, K. Shanmugasundaram, R. Karvembu, *Catal. Commun.* **2009**, *10*, 1835–1838.
- [69] R. A. Zelonka, M. C. Baird, *Can. J. Chem.* **1972**, *50*, 3063–3072.
- [70] M. A. Bennet, T. N. Huang, T. W. Matheson, A. K. Smith, *Inorg. Synth.* **1982**, *21*, 74–78.
- [71] G. M. Sheldrick, *Acta Crystallogr., Sect. A* **1990**, *46*, 467–473.
- [72] G. M. Sheldrick, *SHELXL_NT*, Version 6.12, University of Göttingen, **2000**.
- [73] G. M. Sheldrick, *SADABS V2.10*, **2003**.

Received: March 20, 2010

Published Online: July 28, 2010

Synthesis and Electrochemistry of Cyclopentadienyl Ferratricarbollides Substituted by Me and Ph Groups on the Cage Carbon Atoms

Josef Holub,^[a] Mario Bakardjiev,^[a] Bohumil Štíbr,*^[a] Petr Štěpnička,^[b] and Ivana Císařová^[b]

Keywords: Iron / Boron / Carboranes / Cage compounds / Electrochemistry

Neutral tricarbollide tautomers of general formula 7-*t*BuNH-8,9-*R,R'*-*nido*-7,8,9- $C_3B_8H_9$ (**N1**), where *R,R'* = substituents on cage carbon atoms = H, Me, and Ph or their combinations, generated a series of very stable, twelve-vertex ferratricarbollides of general structure [1-Cp-12-*t*BuNH-2,4-*R,R'*-*closo*-1,2,4,12- $FeC_3B_8H_8$] (**2**, Cp = $\eta^5-C_5H_5$; yields 30–35 %) together with the isomeric complexes [1-Cp-10-*t*BuNH-2,4-*R,R'*-*closo*-1,2,4,10- $FeC_3B_8H_8$] (**3**; yields 22–26 %) upon heating with [CpFe(CO)₂]₂ in mesitylene at reflux for 6 h. Individual compounds were isolated and purified by preparative

TLC and characterized by conventional ¹¹B and ¹H NMR spectroscopy combined with two-dimensional [¹¹B-¹H]-COSY and ¹H-¹H-{¹¹B(selective)} NMR spectroscopic techniques). The structures of [1-Cp-12-*t*BuNH-2,4-Me₂-1,2,4,12- $FeC_3B_8H_8$] (**2c**) and [1-Cp-12-*t*BuNH-2-Ph-1,2,4,12- $FeC_3B_8H_9$] (**2d**) were established by single-crystal X-ray diffraction analysis. Electrochemical studies revealed that the Fe^{II}/Fe^{III} redox potentials are primarily affected by the type of the ferratricarbaborane cage and, to a lesser extent, by the Me and Ph substituents residing on the cage carbon atoms.

Introduction

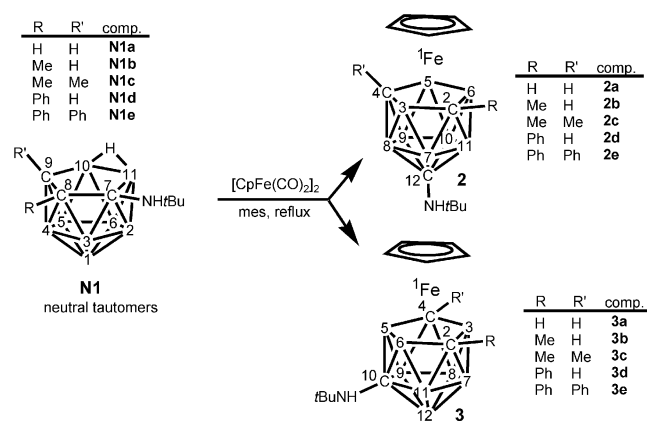
Eleven-vertex *nido*-tricarbaboranes (so-called tricarbollides) were synthesized after 1995 within a collaboration between us and F. Teixidor et al.^[1] as the first representatives of this family of compounds. Later it was found^[2,3] that incorporation of the [CpFe]⁺ fragment (Cp = $\eta^5-C_5H_5$) into the structure of 7-*t*BuNH₂-*nido*-7,8,9- $C_3B_8H_9$ (**Z1a**), using [CpFe(CO)₂]₂ or [CpFe(C₆H₆)]⁺ as the CpFe⁺ source, is associated with an extensive rearrangement of cluster carbon atoms to generate the isomeric *closo* cyclopentadienyl ferratricarbollides [1-Cp-12-*t*BuNH-*closo*-1,2,4,12- $FeC_3B_8H_{10}$] (**2a**) and [1-Cp-10-*t*BuNH-*closo*-1,2,4,10- $FeC_3B_8H_{10}$] (**3a**), which contain a substituted amine group in the *para* and *meta* positions with respect to the iron centre. Just recently, we have synthesized a series of carbon-substituted 7-*t*BuNH-8,9-*R,R'*-*nido*-7,8,9- $C_3B_8H_9$ compounds (neutral tautomers **N1**) (where *R/R'* = H, Me, and Ph or their combinations),^[4] which now allowed us to synthesize a series of Me- and Ph-substituted ferratricarbollides of types **2** and **3**, which are the subject of this paper. Discussed are also the NMR spectroscopic consequences of

the substitution together with electrochemical properties of these compounds, namely the trends in the Fe^{II}/Fe^{III} redox potentials in relation to the skeletal shape and type of substitution.

Results and Discussion

Syntheses

Upon heating with [CpFe(CO)₂]₂ in mesitylene at reflux for 6 h, the recently prepared^[4] neutral tricarbollide tautomers of general formula 7-*t*BuNH-8,9-*R,R'*-*nido*-7,8,9- $C_3B_8H_9$ (**N1**) (*R/R'* = Me/H, Ph/H, Me/Me, or Ph/Ph;

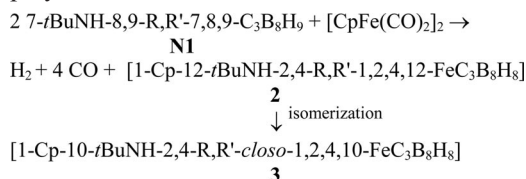


Scheme 1. The complexation of the **N1** tautomers by incorporation of the [CpFe] fragment. C: C (if substituted) or CH; other numbered vertices: BH; mes: mesitylene.

[a] Institute of Inorganic Chemistry, Academy of Sciences of the Czech Republic, 250 68 Řež, Czech Republic
Fax: +420-220940157
E-mail: stibr@iic.cas.cz

[b] Department of Inorganic Chemistry, Faculty of Science, Charles University in Prague, Hlavova 2030, 12840 Prague, Czech Republic

Scheme 1) afforded a series of very stable, twelve-vertex ferratricarbollides [1-Cp-12-*t*BuNH-2,4-R,R'-*closo*-1,2,4,12-FeC₃B₈H₈] (**2**; yields 30–35%) together with the isomeric complexes [1-Cp-10-*t*BuNH-2,4-R,R'-*closo*-1,2,4,10-FeC₃B₈H₈] (**3**; yields 22–26%) (Scheme 1). The complexes of structure **3** are evidently formed by thermal isomerization of compounds **2** under the reaction conditions employed.^[2b]



Compounds **2** and **3** could be readily separated as orange bands by preparative TLC on a silica gel substrate and were both isolated as orange crystalline materials upon crystallization by slow concentration of hexane solutions at approximately 0 °C.

NMR Spectroscopy

Graphical comparison of the ¹H and ¹¹B NMR chemical shifts, assigned on the basis of [¹¹B-¹¹B]-COSY^[5] and ¹H-¹¹B(selective)}^[6] NMR spectroscopic experiments (see Figures 1 and 2), indicates that the spectra of the 2,4-R₂-disubstituted (R = Me or Ph) complexes of types **2** and **3** show gross similarities with those of the unsubstituted analogues **2a** and **3a**,^[2] because of the preservation of the symmetry plane. In contrast, the monosubstituted (2-R) complexes display eight different BH resonances due to the absence of higher symmetry.

Comparisons of the changes in Δδ(¹¹B), defined as Δδ = δ(¹¹B)_{subst} – δ_{unsubst}, in individual cage positions implies that the Me and Ph substituents remarkably affect the magnetic properties of the individual cluster vertices. For the monosubstituted compounds in both series **2** and **3**, it is readily seen that the β positions are mostly deshielded, while antipodal (A) positions are shielded, which is generally observed for all boron cluster compounds.^[7] Similar deshielding at β positions is observed also for the disubstituted compounds, though, in this case, the β-effect is combined with the A-effect at the B9,11 sites, which leads mostly to deshielding.

Structural Studies

The solid-state structures of **2c** and **2d** were determined by X-ray diffraction analysis. PLATON^[8] plots of the molecular structures are presented in Figures 3 and 4, respectively, together with selected distances and angles.

Comparisons of the corresponding C–B and B–B intracuster bond lengths in **2c** and **2d** with those of the unsubstituted complexes **2a** and **3a** reveal only minor differences, which could be attributed to an unhindered rotation of the unsubstituted cage rather than to an electronic influence of the Me and Ph substituents.^[2] Likewise, the geometric parameters of **2c** and **2d** are very similar.

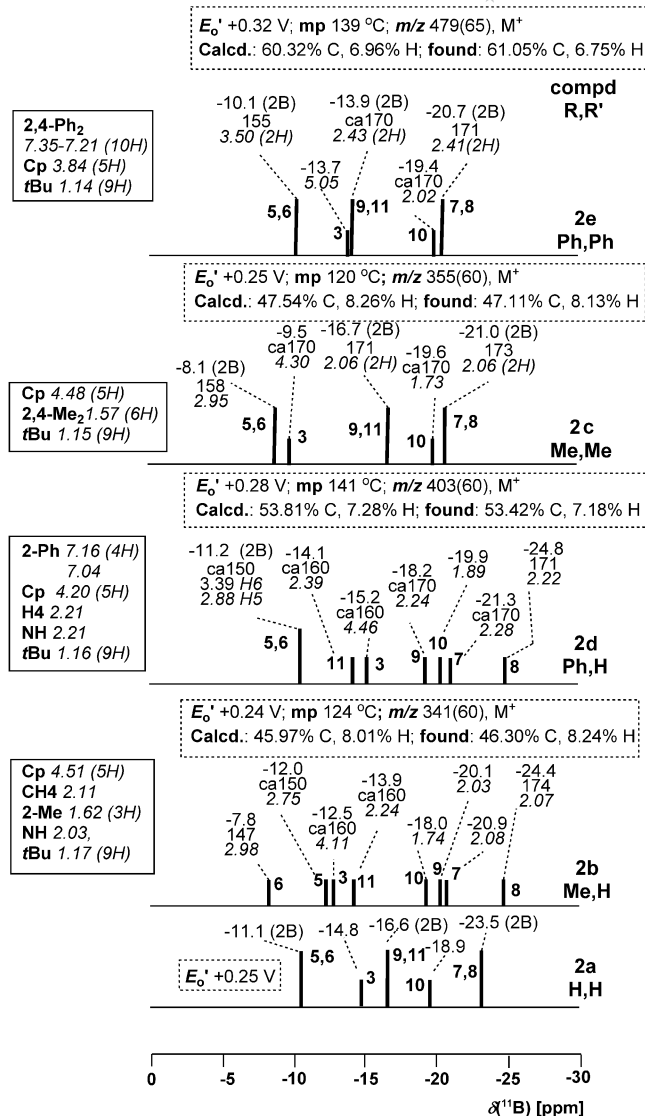


Figure 1. Graphical representation of experimental data for complexes of type **2** based on stick-type comparison of relative intensities in the ¹¹B NMR spectra. Included are numerical values for individual cluster BH vertices [ordered as δ(¹¹B), ¹J(BH)/Hz (where readable) and δ(¹H) (in italics), indicated are intensities other than 1]. Data for the unsubstituted **2a** from ref.^[2] are included for comparison. In full frames there are additional δ(¹H) data (in italics). Other experimental data (*E*^o, melting point, *m/z*, and elemental analysis) are listed in dotted frames within each diagram.

The Fe–Cp (ring centroid) distances are generally shorter than the corresponding Fe–C₂B₃ (ring centroid) bond vectors. The observed differences, 0.271 and 0.258 Å for **2c** and **2d**, respectively, are similar to those found in all Cp–Fe–borane complexes deposited with the Cambridge Structure Database.^[9] Furthermore, the planes defined by the Cp ring carbon atoms and the C₂B₃ atoms forming the upper rim of the tricarbollide part in **2c** and **2d** are parallel, virtually unaffected by the substituents as evidenced by the associated dihedral angles of 0.60(15)° and 1.57(9)° for **2c** and **2d**, respectively. Consequently, the dihedral angles of the phenyl plane in **2d** to the previously defined planes are practically equal, 12.74(9)° to Cp and 13.89(7)° for the Cp and C₂B₃

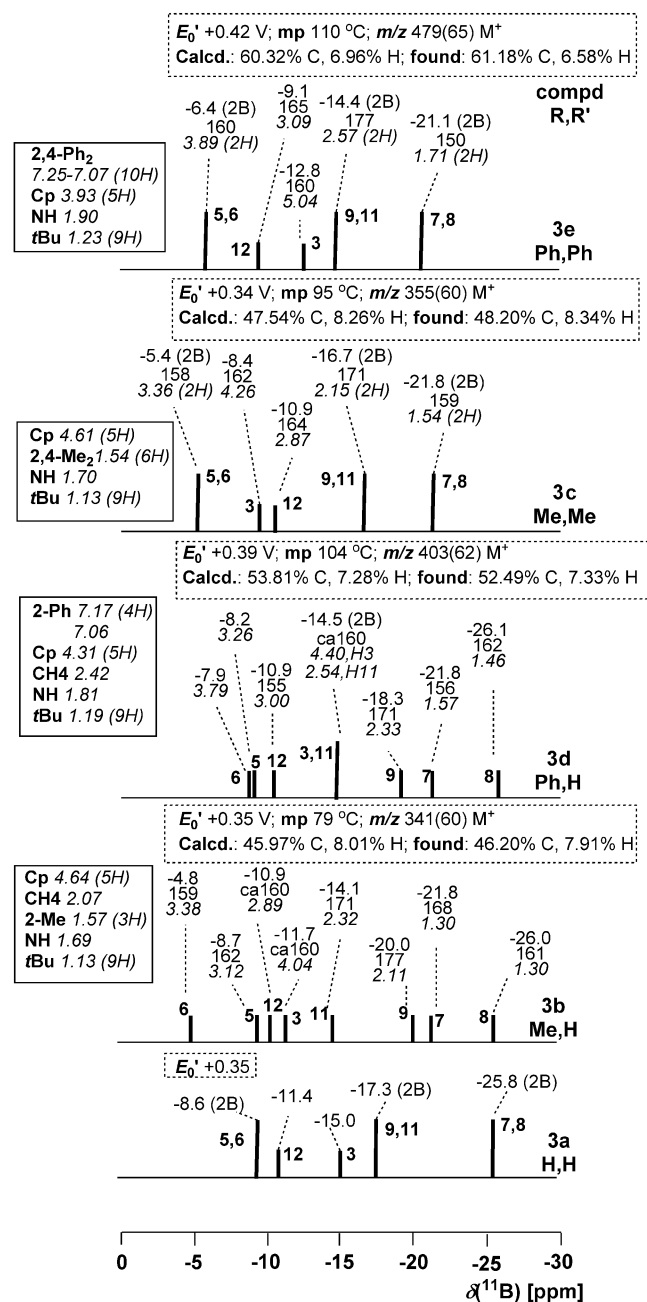


Figure 2. Graphical representation of experimental data of the cage-isomeric complexes of type 3. Data for unsubstituted **3a** are taken from ref.^[2] For other comments, see the caption of Figure 1.

ring planes. In the crystals of **2c** and **2d**, no significant intermolecular interactions that could aid the crystal packing were detected. However, the lack of hydrogen bonds generated by the >N–H moiety can be accounted for by steric hindrance of the attached *tert*-butyl moiety.

Electrochemistry

The electrochemical behaviour of the ferratricarbaborane complexes **2** and **3** has been studied by cyclic (CV) and difference pulse (DPP) voltammetry at a platinum disc elec-

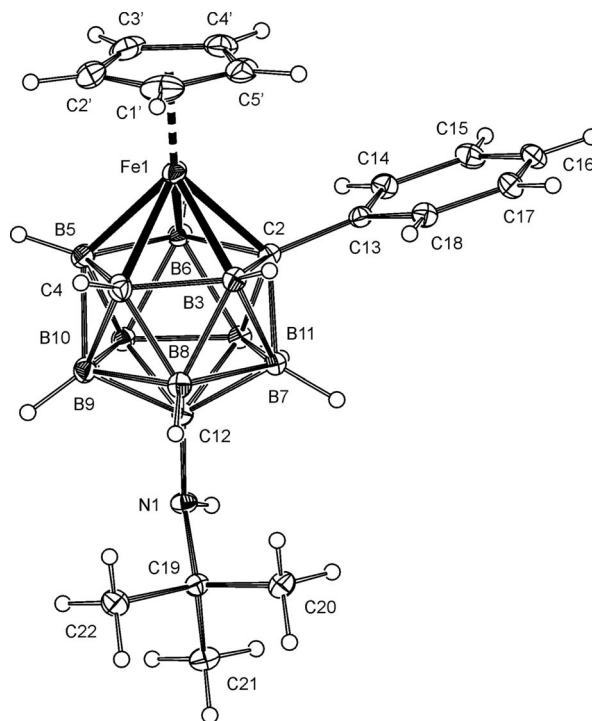


Figure 3. PLATON representation of the crystal and molecular structure of [1-Cp-12-*tert*-BuNH-2-Ph-*closo*-1,2,4,12-FeC₃B₈H₉] (**2d**). The displacement ellipsoids are drawn at the 30% probability level. Selected bond lengths [Å] and angles [°]: Fe1–Cp (ring centroid) 1.679, Fe1–C2B3 (ring centroid) 1.408, Fe1–C2 2.047(2), Fe1–B3 2.011(2), Fe1–C4 2.0480(19), Fe1–B5 2.058(3), Fe1–B6 2.054(3), C–C (Cp ring) 1.398(3)–1.425(3), C2–C13 1.524(3), C2–B3 1.729(3), C2–B6 1.721(3), B3–C4 1.740(3), C4–B5 1.724(3), C4–C14 1.531(3), B5–B6 1.801(4), C12–N1 1.442(3), C2–Fe1–B3 50.42(9), B3–Fe1–C4 50.77(9), C4–Fe1–B5 49.66(9), B5–Fe1–B6 51.95 (11), B3–C2–B6 111.23(15), C2–B3–C4 104.74(15), B3–C4–B5 111.47(16), C4–B5–B6 105.40 (16), B5–B6–C2 106.47(15).

trode in dichloromethane solutions containing 0.1 M Bu₄N[PF₆] as the supporting electrolyte.

In the accessible potential range, all compounds displayed single, well-defined, chemically reversible redox changes. These redox processes are all diffusion-controlled in which i_{pa} is proportional to $[\text{scan rate}]^{1/2}$ at the scan rates 0.1–1 V s^{−1} (i_{pa} is the anodic peak current in CV) and corresponds to a one-electron exchange, as evidenced by comparison of the CV and DPP peak currents with those of ferrocene at the same concentration. Individual redox potentials relative to the ferrocene/ferrocenium reference are presented in Figures 1 and 2.^[10]

The observed redox processes can be attributed to the Fe^{II}/Fe^{III} couple. Their redox potentials are more positive than that of the related complex [1-Cp-1,2,3-FeC₂B₉H₁₁] (−0.08 V vs. SCE in 1:1 acetone/water)^[11] and change with the substitution pattern. First, the redox potentials of the isomers **2** and **3**, namely for the isomeric pairs **2a/3a**, **2b/3b** (Figure 5), **2c/3c**, **2d/3d** and **2e/3e**, differ uniformly by approximately 100 mV, compounds **3** of each pair being more difficult to oxidize. Second, the oxidation potentials of the hydrogen- and methyl-substituted metallaboranes are

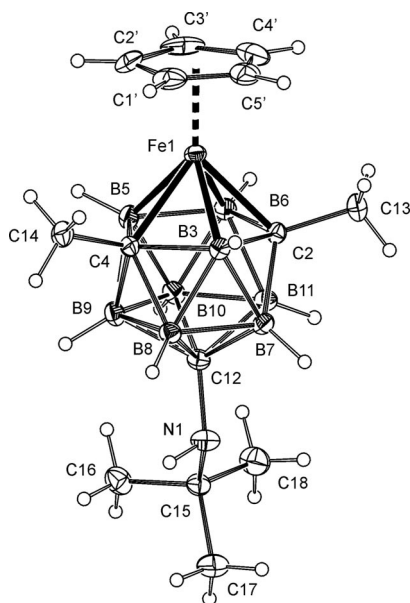


Figure 4. PLATON representation of the crystal and molecular structure of [1-Cp-12-*tert*-BuNH-8,9-Me₂-closo-1,2,4,12-FeC₃B₈H₈] (**2c**). The displacement ellipsoids are drawn at the 30% probability level. Selected bond lengths [Å] and angles [°]: Fe1–Cp (ring centroid) 1.673, Fe1–C2B3 (ring centroid) 1.415, Fe1–C2 2.0455(13), Fe1–B3 2.0262(16), Fe1–C4 2.0495(15), Fe1–B5 2.0463(16), Fe1–B6 2.0577(15), C–C (Cp ring) 1.398(3)–1.425(3), C2–C13 1.5098(18), C2–B3 1.733(2), C2–B6 1.7340(19), B3–C4 1.732(2), C4–B5 1.707(2), B5–B6 1.781(2), C12–N1 1.4268(17), C2–Fe1–B3 50.38(6), B3–Fe1–C4 50.29(6), C4–Fe1–B5 49.26(6), B5–Fe1–B6 51.43(6), B3–C2–B6 111.38(10), C2–B3–C4 104.14(10), B3–C4–B5 111.71(11), C4–B5–B6 106.65(11), B5–B6–C2 105.49(10).

lower than those of their phenylated analogues. This leads to the following sequence of the oxidation potentials (cf. Figures 1 and 2): H/H \approx H/Me \approx Me/Me < Ph/H < Ph/Ph

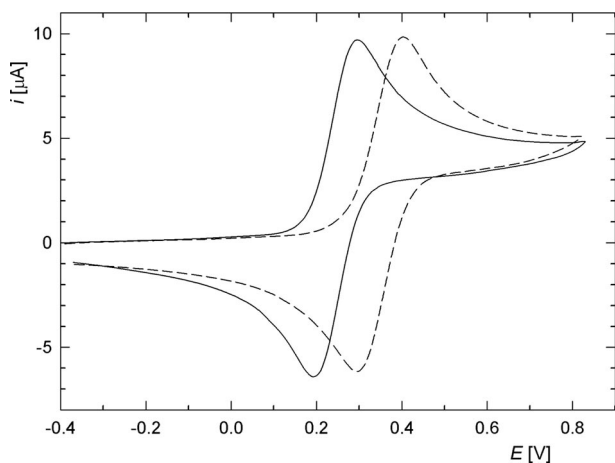


Figure 5. Cyclic voltammograms of the isomeric boranes **2b** (solid line) and **3b** (dashed line) as recorded at a platinum disc electrode and at a scan rate of 0.1 V s^{−1} in dichloromethane. The potential scale is referenced to the ferrocene/ferrocenium couple.

(combinations of R substituents at 2,4-cage positions), which roughly corresponds to the electronic nature of these substituents.^[12]

Conclusions

We have shown that the insertion of the {CpFe} fragment into the pentagonal open face of the C-substituted *nido* 7-*tert*-BuNH-8,9-R,R'-7,8,9-C₃B₈H₉ compounds by high-temperature reactions with [CpFe(CO)₂]₂ proceeds in the same manner as that of the parent unsubstituted compound **N1** to afford two series of the cage-isomeric *closo* complexes: [1-Cp-12-*tert*-BuNH-2,4-R,R'-1,2,4,12-FeC₃B₈H₈] (**2**) and [1-Cp-10-*tert*-BuNH-2,4-R,R'-1,2,4,10-FeC₃B₈H₈] (**3**). Two representatives from the former series were characterized by single-crystal X-ray crystallography. Also studied were effects of the Me and Ph substituents on NMR spectroscopic behaviour and the Fe^{II}/Fe^{III} redox potentials of individual compounds. Electrochemical studies revealed that the redox changes are primarily affected by the type of the ferratricarbaborane cage and, to a lesser extent, by the organic substituents residing on the cage carbon atoms. Further work associated with developments of iron carborane chemistry is underway in our laboratories.

Experimental Section

Materials and Methods: All reactions were carried out by using standard vacuum or inert-atmosphere techniques as described by Shriver.^[13] Other operations, such as column LC or preparative TLC, were carried out in air. The starting tricarbollide compounds **N1** were prepared according to the recently reported procedure.^[3] Dichloromethane and hexane (Fluka) were dried with CaH₂ and freshly distilled before use. Other chemicals were of reagent or analytical grade and were used as purchased. NMR spectroscopic and mass spectrometric instrumentation and techniques were essentially the same as those in other recent publications from our laboratories.^[14] Electrochemical measurements were carried out with a computer-controlled multipurpose potentiostat μAUTOLAB III (Eco Chemie, Netherlands) at room temperature equipped with a standard Metrohm three-electrode cell with a rotating platinum disc electrode (AUTOLAB RDE, 3 mm diameter) as the working electrode, a platinum sheet auxiliary electrode and a saturated calomel reference electrode (SCE), which was separated from the analyzed solution by a salt bridge. The analyzed compounds were dissolved in dichloromethane (Fluka, absolute, declared H₂O content \leq 0.005%) to give a solution containing approximately 5×10^{-4} M analyte and 0.1 M Bu₄N[PF₆] (Fluka, purissimum for electrochemistry) as the supporting electrolyte. The solutions were deaerated with argon before the measurement and then kept under an argon blanket. The redox potentials (see Figures 1 and 2) are given relative to the ferrocene/ferrocenium reference.

Synthesis of Complexes [1-Cp-12-*tert*-BuNH-2,4-R,R'-1,2,4,12-FeC₃B₈H₈] (type **2) and [1-Cp-10-*tert*-BuNH-2,4-R,R'-1,2,4,10-FeC₃B₈H₈] (type **3**):** Compounds of type **N1** (**N1a**–**N1e**, reaction scale: 1.0 mmol) were heated with [CpFe(CO)₂]₂ (177 mg, 0.5 mmol) in mesitylene (10 mL) at reflux for 8 h. The bulk of the solvent was evaporated at reduced pressure, and the resulting mixtures were separated by threefold preparative TLC on silica gel

plates using 40% CH₂Cl₂ in hexane to develop two orange bands. The front fractions ($R_f = 0.50\text{--}0.60$) contained compounds of type **2**, whereas the second fractions ($R_f = 0.30\text{--}0.50$) contained compounds of type **3**. Individual complexes were isolated by extraction with CH₂Cl₂, followed by evaporation and vacuum sublimation at approximately 200 °C (bath) as orange, air-stable compounds in yields in the range 30–35% for compounds **2** and 22–26% for compounds **3**. The compounds can be crystallized by a slow concentration of their hexane solutions at low temperatures (around 0 °C). Characterization data for individual complexes of types **2** and **3** are given in Figures 1 and 2.

X-ray Crystallography

Crystallographic Data for 2c: C₁₄H₂₉B₈FeN, $M = 353.71$, orange plates, $0.45 \times 0.18 \times 0.10 \text{ mm}^3$, orthorhombic, space group $P2_12_12_1$ (no. 19), $a = 8.4298(2) \text{ \AA}$, $b = 8.82270(10) \text{ \AA}$, $c = 24.8092(4) \text{ \AA}$; $V = 1845.15(6) \text{ \AA}^3$, $Z = 4$, $D_{\text{calc}} = 1.273 \text{ g mL}^{-1}$. Full-set diffraction data ($\pm h \pm k \pm l$) were recorded at 150(2) K with a Nonius Kappa CCD diffractometer by using graphite-monochromatized Mo- K_α radiation ($\lambda = 0.71073 \text{ \AA}$); absorption was neglected ($\mu = 0.81 \text{ mm}^{-1}$). A total of 22868 diffractions were measured ($\theta_{\text{max}} = 27.5^\circ$), of which 4215 were unique ($R_{\text{int}} = 4.2\%$), and 3933 were observed according to the $I > 2\sigma(I)$ criterion.

The structure was solved by direct methods (SIR97^[15]) and refined by a full-matrix least-squares procedure based on F^2 (SHELXL97^[16]). All non-hydrogen atoms were refined with anisotropic displacement parameters. The hydrogen atoms were refined isotropically except those in the cyclopentadienyl and methyl moieties, which were placed in their idealized positions and refined as riding atoms, $U_{\text{iso}}(\text{H})$ being assigned to a multiple of U_{eq} of their bonding atom. The refinement converged ($\Delta/\sigma_{\text{max}} = 0.001$, 258 parameters) to $R = 3.3\%$ for the observed diffractions and to $wR = 8.0\%$, GOF = 1.06 for all diffractions. The final difference map displayed no peaks of chemical significance ($\Delta\rho_{\text{max}} = 0.51$, $\Delta\rho_{\text{min}} = -0.25 \text{ e \AA}^{-3}$).

Crystallographic Data for 2d: C₁₈H₂₉B₈FeN, $M = 401.75$, orange prisms, $0.25 \times 0.18 \times 0.15 \text{ mm}^3$, monoclinic, space group $P2_1/c$ (no. 14), $a = 12.6881(2) \text{ \AA}$, $b = 10.1177(2) \text{ \AA}$, $c = 16.1934(2) \text{ \AA}$, $\beta = 96.5326(11)^\circ$; $V = 2065.32(6) \text{ \AA}^3$, $Z = 4$, $D_{\text{calc}} = 1.292 \text{ g mL}^{-1}$. The diffraction data were collected with a Nonius Kappa CCD diffractometer [$\lambda = 0.71073 \text{ \AA}$, $T = 150(2) \text{ K}$; absorption was neglected, $\mu = 0.73 \text{ mm}^{-1}$]. A total of 31844 diffractions was collected ($\pm h \pm k \pm l$, $\theta_{\text{max}} = 27.5^\circ$), of which 4729 were unique ($R_{\text{int}} = 3.2\%$), and 4130 were observed according to the $I > 2\sigma(I)$ criterion.

The structure solution and refinement was carried out as described above (SIR97 and SHELXL97). All heavy atoms were refined with anisotropic displacement parameters, while the hydrogen atoms were refined isotropically except those in the cyclopentadienyl and methyl moieties, which were placed in their calculated positions and refined as riding atoms. The refinement converged ($\Delta/\sigma_{\text{max}} = 0.001$, 296 parameters) to $R = 2.9\%$ for the observed diffractions and to $wR = 7.4\%$, GOF = 1.06 for all diffractions. The final difference map showed no peaks of chemical significance ($\Delta\rho_{\text{max}} = 0.27$, $\Delta\rho_{\text{min}} = -0.31 \text{ e \AA}^{-3}$).

CCDC-754560 (for **2c**) and -754561 (for **2d**) contain the supplementary crystallographic data for this paper. These data can be obtained free of charge from The Cambridge Crystallographic Data Centre via www.ccdc.cam.ac.uk/data_request/cif.

Acknowledgments

The work was financially supported by the Ministry of Education of the Czech Republic (project nos. LC 523 and MSM 0021620857).

- [1] See, for example: a) B. Štíbr, J. Holub, F. Teixidor, C. Viñas, *J. Chem. Soc., Chem. Commun.* **1995**, 795; b) B. Štíbr, J. Holub, I. Císařová, F. Teixidor, C. Viñas, J. Fusek, Z. Plzák, *Inorg. Chem.* **1996**, 35, 3635; c) J. Holub, B. Štíbr, D. Hnyk, J. Fusek, I. Císařová, F. Teixidor, C. Viñas, Z. Plzák, P. v. R. Schleyer, *J. Am. Chem. Soc.* **1997**, 119, 7750.
- [2] a) J. Holub, B. Grüner, I. Císařová, J. Fusek, Z. Plzák, F. Teixidor, C. Viñas, B. Štíbr, *Inorg. Chem.* **1999**, 38, 2775; b) B. Grüner, A. Lehtonen, R. Kivekäs, R. Sillanpää, J. Holub, F. Teixidor, C. Viñas, B. Štíbr, *Inorg. Chem.* **2000**, 39, 2577.
- [3] J. Holub, B. Grüner, D. S. Perekalin, D. G. Golovanov, K. A. Lyssenko, P. V. Petrovskii, A. R. Kudinov, B. Štíbr, *Inorg. Chem.* **2005**, 44, 1655.
- [4] M. Bakardjiev, J. Holub, B. Štíbr, I. Císařová, *Dalton Trans.* **2010**, 39, 4186.
- [5] See, for example: a) J. D. Kennedy in *Multinuclear NMR* (Ed.: J. Mason), Plenum Press, New York, **1987**, p. 221; b) W. C. Hutton, T. L. Venable, R. N. Grimes, *J. Am. Chem. Soc.* **1984**, 106, 29; c) J. Schraml, J. M. Bellama, *Two-Dimensional NMR Spectroscopy*, Wiley, New York, **1982**, and references therein.
- [6] X. L. R. Fontaine, J. D. Kennedy, *J. Chem. Soc., Dalton Trans.* **1987**, 1573.
- [7] S. Heřmánek, *Chem. Rev.* **1992**, 92, 325, and references therein.
- [8] A. L. Spek, *J. Appl. Crystallogr.* **2003**, 36, 7.
- [9] A search of the Cambridge Structural Database (version 5.30 of November 2008 with updates of November 2008, and February, May and September 2009) resulted in 15 hits with only one duplicity. The reference codes are as follows: BEMTES, BORREF, CYPCFE/CYPCFE01, HATHUG, MUJHEE, NEJGEP, NEJGIT, UMUKES, VIGQUX, VIGTOU, WUPCUF, YAWWOJ, YOLPIY, ZEKQEL.
- [10] The formal redox potentials, E° , were determined as $E^\circ = 0.5(E_{\text{pa}} + E_{\text{pc}})$, where E_{pa} and E_{pc} are the anodic and cathodic peak potentials in cyclic voltammetry, respectively.
- [11] M. F. Hawthorne, D. C. Young, T. D. Andrews, D. V. Howe, R. L. Pilling, A. D. Pitts, M. Reintjes, L. F. Warren Jr., P. A. Wegner, *J. Am. Chem. Soc.* **1968**, 90, 879.
- [12] C. Hansch, A. Leo, R. W. Taft, *Chem. Rev.* **1991**, 91, 65.
- [13] D. F. Shriver, M. A. Drezdon, *Manipulation of Air Sensitive Compounds*, 2nd ed., Wiley, New York, **1986**.
- [14] M. Bakardjiev, J. Holub, D. Hnyk, B. Štíbr, *Chem. Eur. J.* **2008**, 14, 6529.
- [15] A. Altomare, M. C. Burla, M. Camalli, G. L. Cascarano, C. Giacovazzo, A. Guagliardi, A. G. G. Moliterni, G. Polidori, R. Spagna, *J. Appl. Crystallogr.* **1999**, 32, 115.
- [16] G. M. Sheldrick, *SHELXL97, Program for Crystal Structure Refinement from Diffraction Data*, University of Göttingen, Germany, **1997**.

Received: February 23, 2010

Published Online: July 29, 2010

Mono-, Bi-, Tri- and Tetranuclear Palladium(II), Copper(I), and Gold(I) Complexes of Morpholine- and *N*-Methylpiperazine-Functionalized Cyclodiphosph(III)azans, *cis*-[(*t*BuN- μ)₂(PNC₄H₈X)₂] (X = O, NMe)

Maravanji S. Balakrishna,^{*[a]} Devarajan Suresh,^[a] and Joel T. Mague^[b]

Keywords: Heterometallic complexes / Cyclodiphosphazanes / Palladium / Copper / Gold

Bis(amido)cyclodiphosphazanes, *cis*-[(*t*BuN- μ)₂(PNC₄H₈O)₂] (**2**) and *cis*-[(*t*BuN- μ)₂(PNC₄H₈NMe)₂] (**3**) were synthesized by treating the corresponding amines with *cis*-[ClP(*t*BuN- μ)₂-PCl] (**1**). The stoichiometric reactions of **2** or **3** with elemental sulfur and selenium afforded the bis-chalcogenides, *cis*-[(*t*BuN- μ)₂(P(E)NC₄H₈X)₂] (X = O, E = S; **4**, X = NMe, E = S; **5**, X = O, E = Se; **6**, X = O, E = Se; **7**). The reactions of **2** or **3** with [PdCl₂(SMe₂)₂] produced exclusively the mononuclear *trans*-[PdCl₂{(*t*BuN- μ)₂(PNC₄H₈X)₂}₂] (X = O; **8**, X = NMe; **9**), whereas the reactions with [Pd(μ -Cl)(η^3 -C₃H₅)₂] afforded the bimetallic complexes [(PdCl(η^3 -C₃H₅))₂[(*t*BuN- μ)₂(PNC₄H₈X)₂]] (X = O; **10**, X = NMe; **11**) in good yield. Treatment of

2 or **3** with [AuCl(SMe₂)] in 1:1 and 1:2 molar ratios yielded the mono- and binuclear complexes, [(AuCl(*t*BuN- μ)₂(PNC₄H₈O)₂)] (X = O; **12**, X = NMe; **13**), [(AuCl)₂{(*t*BuN- μ)₂(PNC₄H₈O)₂}] (X = O; **14**, X = NMe; **15**), respectively. The Pd^{II} (**8**) and Au^I (**12**) complexes were used as metallo-ligands to prepare homo- and heterometallic complexes, *trans*-[PdCl₂{(*t*BuN- μ)₂(PNC₄H₈O)₂}₂][Pd(η^3 -C₃H₅)Cl]₂] (**16**), *trans*-[PdCl₂{(*t*BuN- μ)₂(PNC₄H₈O)₂}₂](AuCl)₂] (**17**), and [Cu(CH₃CN)(μ -Cl)₂Cu(CH₃CN)]{(*t*BuN- μ)₂(PNC₄H₈O)₂}(AuI)₂] (**18**). The crystal structures of **2**, **4**, **7–9**, **14**, **15**, and **18** were established by single-crystal X-ray diffraction studies.

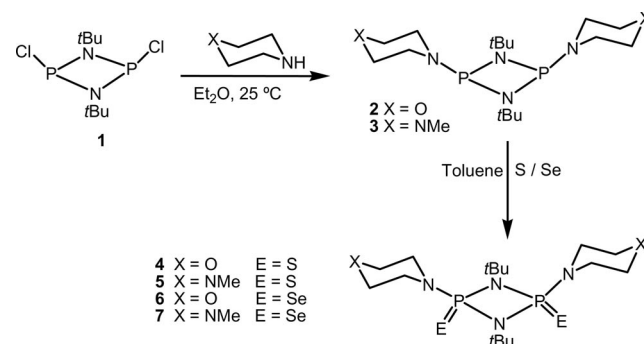
Introduction

Cyclodiphosphazanes constitute the major class of P–N compounds having alternate phosphorus and nitrogen atoms in their four-membered cyclic skeletons.^[1] Recently, we explored the transition-metal chemistry of cyclodiphosphazanes containing several hemilabile functionalities. Slight variations in the phosphorus substituents brought significant changes in their binding properties and resulted in novel complexes with totally different and interesting structural features, especially with Group 11 metals.^[2] As an extension of our^[3] interest and for others^[4] with an interest in cyclodiphosphazane ligand systems, we report in this paper some transition-metal complexes of cyclodiphosphazanes appended with morpholine and *N*-methylpiperazine functionalities.

Results and Discussion

The reactions of *cis*-[(*t*BuN- μ)₂PCl]₂ (**1**) with four equivalents of morpholine or *N*-methyl piperazine in diethyl ether afforded the corresponding bis(amido)cyclodiphosphazane derivatives *cis*-[(*t*BuN- μ)₂(PNC₄H₈O)₂] (**2**) and *cis*-[(*t*BuN-

μ)₂(PNC₄H₈NMe)₂] (**3**) in good yield (Scheme 1). The ligands **2** and **3** are colorless crystalline solids and are moderately stable towards air and moisture both in the solid state and in solution. The ³¹P NMR spectra of **2** and **3** show single resonances at δ = 92.8 and 91.4 ppm, respectively. The high field chemical shifts confirm the *cis* conformation with respect to the phosphorus substituents.^[1d,5] The ¹H NMR spectrum of ligand **2** shows a triplet at δ = 3.52 ppm (*J*_{HH} = 9.2 Hz) for the OCH₂ protons and the NCH₂ protons appeared as a broad signal at δ = 3.15 ppm. The two different sets of NCH₂ protons of **3** resonate as singlets at δ = 3.12 and 2.37 ppm, whereas the NCH₃ protons appear as a sharp singlet at δ = 2.21 ppm. The molecular structure of **2** was confirmed by a single-crystal X-ray diffraction study.



Scheme 1. Synthesis and derivatization of bis(amido)cyclodiphosphazanes **2** and **3**.

[a] Phosphorus Laboratory, Department of Chemistry, Indian Institute of Technology, Bombay, Mumbai 400 076, India
Fax: +91-22-2576-7152
E-mail: krishna@chem.iitb.ac.in

[b] Department of Chemistry, Tulane University, New Orleans, LA 70118, USA

The bis(amido)cyclodiphosphazanes **2** and **3** react smoothly with elemental sulfur or selenium to give the corresponding 2,4-dichalcogen-substituted cyclodiphosph(V)-azanes, *cis*-[(*t*BuN- μ)₂(P(E)NC₄H₈X)₂] (**4**–**7**) in good yield. The bis(sulfide) derivatives *cis*-[(*t*BuN- μ)₂(P(S)NC₄H₈X)₂] (**4**, X = O; **5**, X = NMe) appear as sharp singlets at δ = 46.7 and 46.6 ppm in their phosphorus-31 NMR spectra. The ³¹P NMR spectra of *cis*-[(*t*BuN- μ)₂(P(Se)NC₄H₈X)₂] (**6**, X = O; **7**, X = NMe) consist of sharp singlets at δ = 39.2 and 40.2 ppm, respectively, superimposed on which are two approximate doublets (92:8 as per NMR intensity) corresponding to the ⁷⁷Se satellites arising from the [(NC₄H₈X)-P(Se)(μ -N*t*Bu)P(⁷⁷Se)(NC₄H₈X)] isotopomer. The satellite pattern is strictly the AA' portion of an AA'X spin system [A, A' = ³¹P; X = ⁷⁷Se (*I* = 1/2, 7.6% abundance)] as a result of magnetic nonequivalence of the phosphorus atoms. From the satellite spectra one obtains ¹J_{PSe}(AX) couplings of 893 and 917 Hz, respectively, for **6** and **7** and similarly ²J_{PP}(AA') couplings of 28.9 and 27.8 Hz, respectively, which are comparable with literature values for related compounds.^[6] The ¹H NMR spectra and microanalyses of the compounds **4**–**7** are consistent with the proposed structures. Further, the molecular structures of **4** and **7** were confirmed by single-crystal X-ray diffraction studies.

Palladium(II) Complexes

The reactions of **2** or **3** with *cis*-[PdCl₂(COD)] or *trans*-[PdCl₂(SMe₂)₂] afforded exclusively the mononuclear *trans*-[PdCl₂{(*t*BuN- μ)₂(PNC₄H₈X)₂}] (**8**, X = O; **9**, X = NMe) complexes irrespective of the stoichiometry of the reactants and the reaction conditions. In contrast, the treatment of [Pd(μ -Cl)(η^3 -C₃H₅)]₂ with ligands **2** or **3** in 1:1 molar ratio afforded the binuclear complexes [{PdCl(η^3 -C₃H₅)}₂(*t*BuN- μ)₂(PNC₄H₈X)₂] (**10**, X = O; **11**, X = NMe), where the cyclodiphosphazanes are coordinated in a bridged bidentate fashion (Scheme 2).

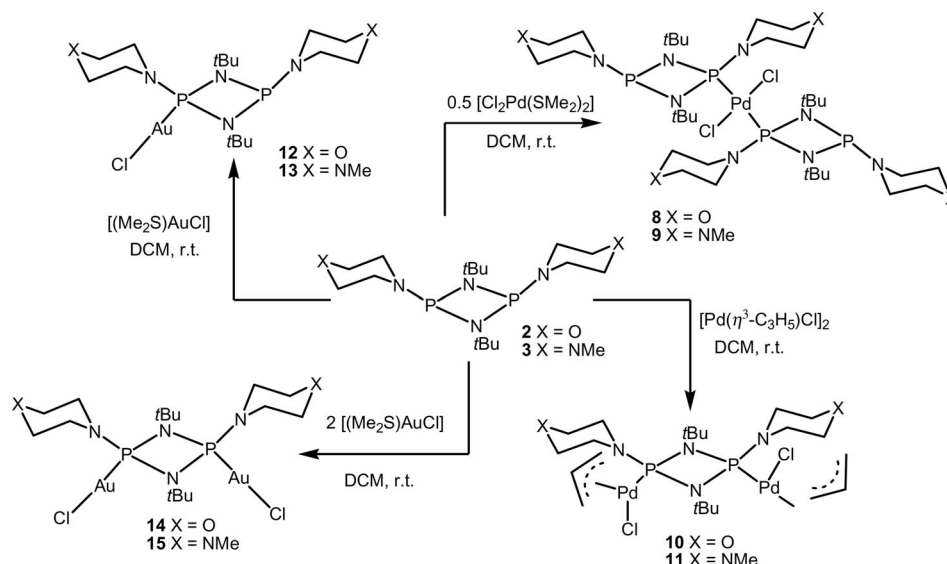
The ³¹P NMR spectra of complexes **8** and **9** show two single resonances at δ = 98.3 and 97.8 ppm for the uncoordinated phosphorus centers, whereas the coordinated phosphorus centers appear as singlets at δ = 70.6 and 70.2 ppm, with the coordination shifts of 22.6 and 21.2 ppm, respectively. The uncoordinated phosphorus centers **8** and **9** show downfield shifts of 5.5 and 6.4 ppm, respectively, in their ³¹P NMR spectrum. The ¹H NMR spectra of **8** and **9** show unresolved multiplets for the morpholine and *N*-methylpiperazine protons in the region of 3.89–2.76 ppm. The ³¹P NMR spectra of binuclear palladium complexes **10** and **11** show singlets at δ = 94.3 and 93.8 ppm, respectively. The molecular structures of *trans*-[PdCl₂{(*t*BuN- μ)₂(PNC₄H₈O)₂}] (**8**) and *trans*-[PdCl₂{(*t*BuN- μ)₂(PNC₄H₈NMe)₂}] (**9**) were determined by single-crystal X-ray diffraction studies.

Gold(I) Complexes

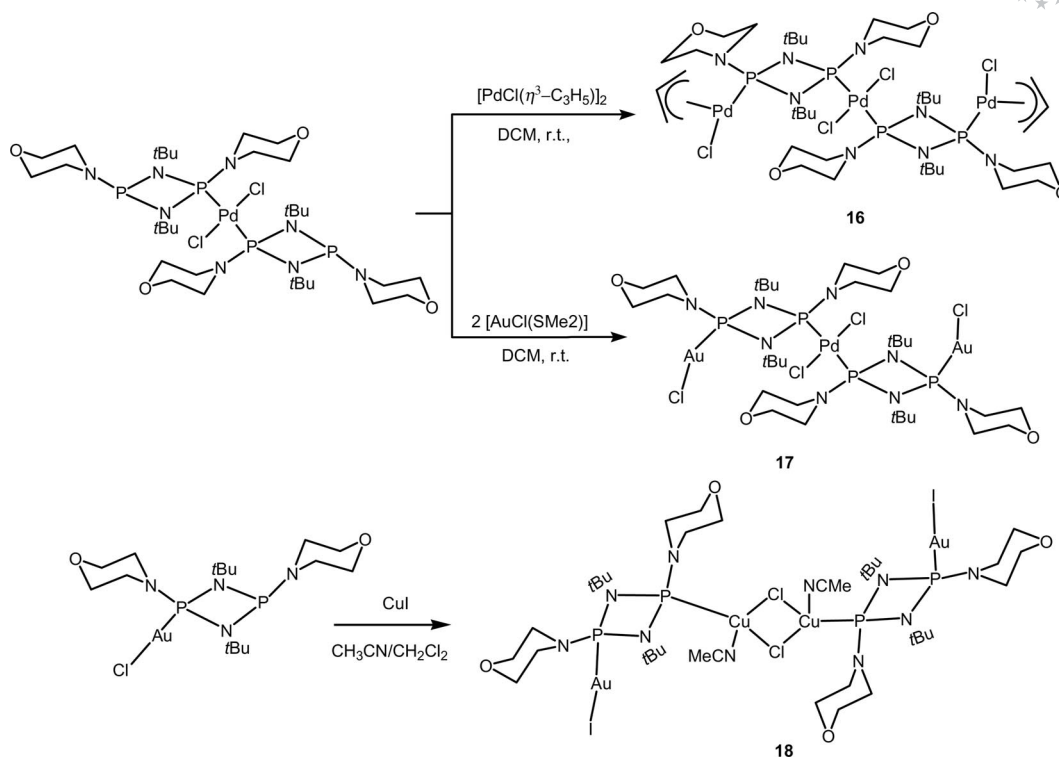
Slow addition of [AuCl(SMe₂)] to ligands **2** or **3** in 1:1 molar ratio afforded the mononuclear gold(I) complexes [AuCl{(*t*BuN- μ)₂(PNC₄H₈X)₂}] (**12**, X = O; **13**, X = NMe) in good yield. The ³¹P NMR spectra of complexes **12** and **13** show singlets at δ = 87.1 and 86.4 ppm for the uncoordinated phosphorus centers, whereas the chemical shifts due to the coordinated phosphorus centers appear as singlets at δ = 71.6 and 70.2 ppm, respectively. Similar reactions in 1:2 molar ratio produce the binuclear complexes [{AuCl₂}₂{(*t*BuN- μ)₂(PNC₄H₈X)₂}] (**14**, X = O; **15**, X = NMe) (Scheme 2). The ³¹P NMR spectra of **14** and **15** show single resonances at δ = 76.8 and 76.9 ppm, respectively. The ¹H NMR spectra and elemental analyses data of **12**–**15** are consistent with the proposed structures. The molecular structures of **14** and **15** were further confirmed by single-crystal X-ray diffraction studies.

Homo- and Heterometallic Complexes of **8** and **12**

The coordination modes of cyclodiphosphazane (monodentate or bridging bidentate) ligands **2** and **3** can be al-



Scheme 2. Synthesis of Pd^{II} and Au^I complexes of ligands **2** and **3**.



Scheme 3. Homo- and heterometallic complexes of metalloligands **8** and **12**.

tered by choosing the appropriate metal precursors and their stoichiometry.^[2b] Since the metal complexes such as Pd^{II} (**8**) and Au^{I} (**12**) containing cyclodiphosphazane bound in a monodentate fashion can act as metalloligands due to the presence of uncoordinated phosphorus atoms, they can be conveniently used to construct homo- or heterometallic complexes and high nuclearity clusters.

The 1:1 reaction of $[\text{Pd}(\mu\text{-Cl})(\eta^3\text{-C}_3\text{H}_5)]_2$ with metalloligand **8** gave the reddish yellow trinuclear ($\text{Pd}/2\text{Pd}'$) complex $\text{trans}[\text{PdCl}_2\{(t\text{BuN-}\mu)_2(\text{PNC}_4\text{H}_8\text{O})_2\}_2(\text{Pd}(\eta^3\text{-C}_3\text{H}_5)\text{Cl})_2]$ (**16**) in good yield. The ^{31}P NMR spectrum of **16** shows two singlets at $\delta = 94.3$ and 57.1 ppm, respectively for the $\text{Pd}'\text{-P}$ and Pd-P centers. Treatment of two equivalents of $[\text{AuCl}(\text{SMe}_2)]$ with **8** in dichloromethane afforded hetero trinuclear ($\text{Pd}/2\text{Au}$) $\text{trans}[\text{PdCl}_2\{(t\text{BuN-}\mu)_2(\text{PNC}_4\text{H}_8\text{O})_2\}_2(\text{AuCl})_2]$ (**17**) as a yellow crystalline solid. The ^{31}P NMR spectrum of trimetallic complex **17** shows a sharp singlet at $\delta = 87.1$ ppm for gold-bound phosphorus centers and a singlet at $\delta = 71.7$ ppm for the palladium-bound phosphorus centers. The reaction of mononuclear gold(I) complex **12** with CuI in 1:1 molar ratio resulted in the formation of a tetranuclear bimetallic $2\text{Cu}^{\text{I}}/2\text{Au}^{\text{I}}$ complex $[(\text{Cu}(\mu\text{-Cl})_2\text{Cu})(\text{CH}_3\text{CN})_2\{(t\text{BuN-}\mu)_2(\text{PNC}_4\text{H}_8\text{O})_2\}_2(\text{AuI})_2]$ (**18**) as shown in Scheme 3. The ^{31}P NMR spectrum of tetranuclear complex **18** shows a broad singlet at $\delta = 86.8$ ppm and a sharp singlet at $\delta = 68.3$ ppm, respectively for the copper- and gold-bound phosphorus centers. The ^1H NMR spectra and elemental analyses data of heterometallic complexes **16–18** are consistent with the proposed structures. Further, the molecular structure of **18** was confirmed by a single-crystal X-ray diffraction study. The X-ray crystal structure of **18**

reveals the presence of Au-I bonds instead of Au-Cl bonds. This clearly indicates that halide exchange has occurred although it is not quite complete as the X-ray analysis shows the bridging position between the copper atoms to be 90% chloride and 10% iodide. We suggest that halide exchange occurs first between **12** and CuI to form the Au-I derivative with simultaneous formation of CuCl which later reacts with the uncoordinated phosphorus center to afford the tetranuclear complex **18**. Similar halogen exchange between CuI and platinum metal halide complexes was observed in our previous studies.^[2a,2b]

Molecular Structures of Compounds **2**, **4**, **7–9**, **14**, **15**, and **18**

Perspective views of the molecular structures of **2**, **4**, **7–9**, **14**, **15**, and **18** along with the atom labeling schemes are shown in Figures 1, 2, 3, 4, 5, 6, 7, and 8. The crystallographic data and details of the structural determinations are given in Tables 1 and 2 and selected bond lengths and angles are listed in Tables 3, 4, 5, 6, 7, 8, 9, and 10.

The colorless crystals of **2** suitable for single-crystal X-ray diffraction study were obtained by keeping the toluene solution at -25°C for a day.

Ligand **2** possesses crystallographically imposed centrosymmetry so that the asymmetric unit consists of one half molecule. The amido $[\text{-NC}_4\text{H}_8\text{O}]$ groups present on the P_2N_2 ring have the thermodynamically stable chair conformation. The rigid four-membered P_2N_2 ring is folded along the $\text{N1}\cdots\text{N1}'$ axis such that the dihedral angle between the

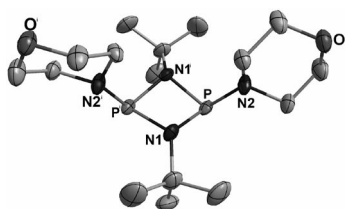


Figure 1. The molecular structure of **2**. All hydrogen atoms were omitted for clarity. Thermal ellipsoids are drawn at the 50% probability level.

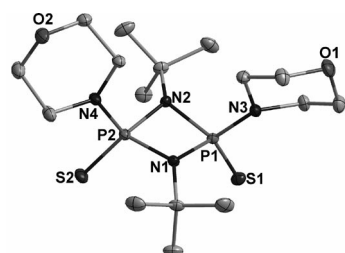


Figure 2. The molecular structure of **4**. All hydrogen atoms were omitted for clarity. Thermal ellipsoids are drawn at the 50% probability level.

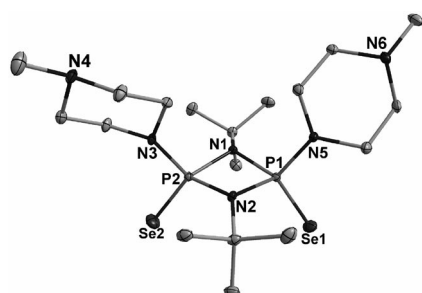


Figure 3. The molecular structure of **7**. All hydrogen atoms were omitted for clarity. Thermal ellipsoids are drawn at the 50% probability level.

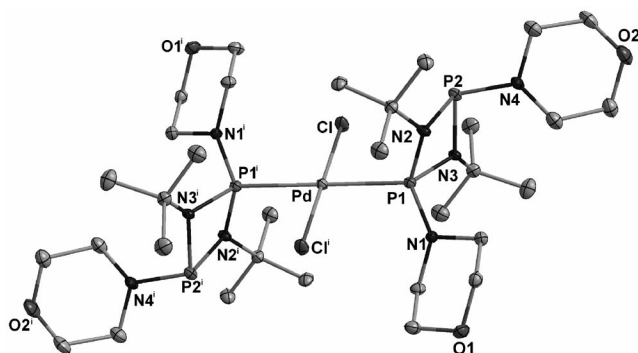


Figure 4. The molecular structure of **8**. All hydrogen atoms were omitted for clarity. Thermal ellipsoids are drawn at the 50% probability level.

PN1N1' and P'N1N1' planes is 25.6(3)°. The phosphorus atoms are in distorted pyramidal geometry being attached to two $-NtBu$ moieties and one amido $[-N(CH_2)_4O]$ group. The *endo* P–N1 bond length is 1.724(3) Å which is close to the range of P–N single bond lengths found previously

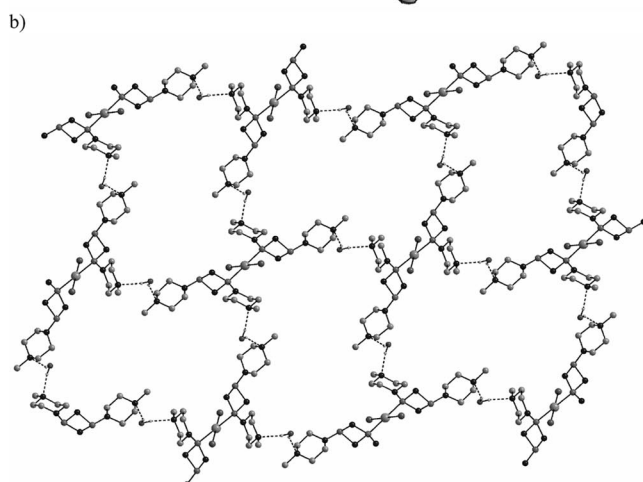
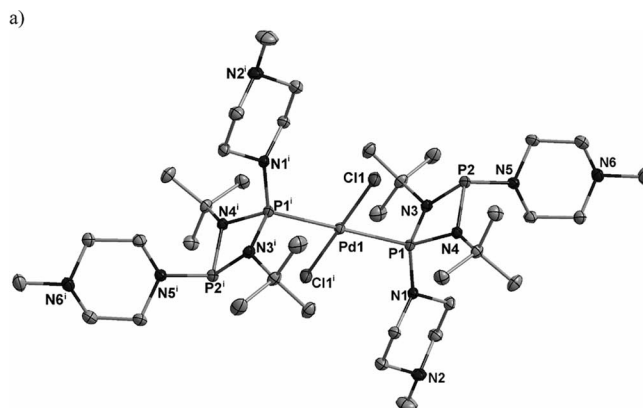


Figure 5. a) The molecular structure of **9**. All hydrogen atoms and lattice water molecules were omitted for clarity. Thermal ellipsoids are drawn at the 50% probability level. b) Ball-and-stick model showing the two-dimensional sheet structure of **9** in the crystal lattice due to the presence of intermolecular hydrogen bonding with the lattice water.

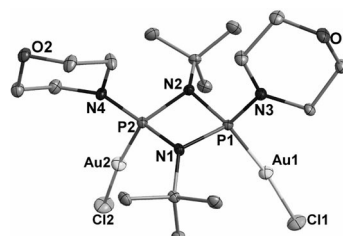


Figure 6. The molecular structure of **14**. All hydrogen atoms were omitted for clarity. Thermal ellipsoids are drawn at the 50% probability level.

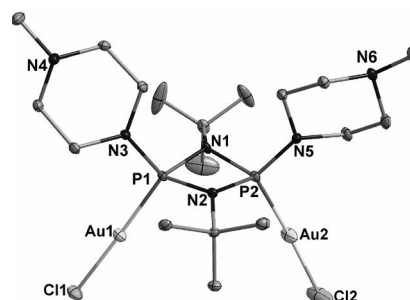


Figure 7. The molecular structure of **15**. All hydrogen atoms and lattice acetonitrile were omitted for clarity. Thermal ellipsoids are drawn at the 50% probability level.

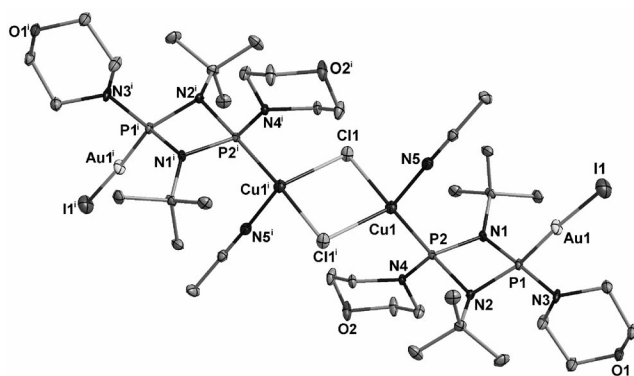


Figure 8. The molecular structure of **18**. All hydrogen atoms and lattice acetonitrile were omitted for clarity. Thermal ellipsoids are drawn at the 50% probability level.

(1.75–1.80 Å). By contrast, the *exo* P–N2 distance is significantly shorter at 1.662(3) Å. This is close to the average of P–N single bond (1.75–1.80 Å) and P–N double bond (1.47–1.55 Å) distances, indicating the involvement of the lone pair of electrons on the nitrogen atom in p_{π} – d_{π} or $N_{\text{pr}}\text{--}P_{\sigma^*}$ bonding.^[1d,5] The C–O bond lengths (Table 3) appear to be slightly different. There are no significant C–H \cdots O intermolecular interactions.

The bis(sulfide) **4** crystallizes without crystallographically imposed symmetry. The folding of the cyclodiphosphazane ring along the N1 \cdots N2 axis is less than that in **2** with the dihedral angle between the P1N1N2 and P2N1N2 planes being 19.4(1)°. The sulfur atom and the *exo*-cyclic amido substituents on the phosphorus centers are present in the *cis* configuration. The ring nitrogen atoms adopt near planar geometry with the sum of the bond angles around nitrogen atoms being 354.31°(N1) and

354.23°(N2). The *exo*- and *endo*-cyclic P–N bond lengths are 1.6447(12) Å (P1–N3) and 1.6869(12) Å (P1–N1), respectively. The P=S bond lengths [P1–S1, 1.9302(4) Å and P2–S2, 1.9387(5) Å] are nearly the same and are comparable with those in other related compounds such as *cis*-[(*t*BuN- μ)₂(P(S)N(H)Ph)₂] (**2**) [P–S, 1.9264(9) Å] and {*cis*-[S=P(μ -N*t*Bu)]₂[μ (–OCH₂CMe₂CH₂O–)]₂} [P–S 1.912(2)–1.923(2) Å].^[7] There are two C–H \cdots S contacts which are somewhat shorter than the sum of the van der Waals radii (3.00 Å),^[8] viz. C7–H7b \cdots S1 (at 0.5 – *x*, 1.5 – *y*, –*z*): 2.97 Å, 161°; C9–H9b–S2 (at –*x*, 0.5 + *y*, 0.5 – *z*): 2.86 Å, 138°. A survey of structures reported in the Cambridge Crystallographic Database which contain the {P=S} moiety shows that about 55 have intermolecular C–H \cdots S contacts less than 2.90 Å although in only one case^[9] was this feature commented on and there appears as yet to be no consideration whether this interaction should be considered as a weak C–H \cdots S hydrogen bond.

The X-ray quality crystals of **7** were grown by keeping the toluene solution overnight at –25 °C. The bis(selenide) **7**, in which the asymmetric unit contains two independent molecules, is quite similar to the structure of **4** although the folding of the P₂N₂ rings along the N \cdots N axes is slightly less [15.9(1)° and 15.5(1)° for molecules 1 and 2, respectively]. There is also a small twist in the orientations of the exocyclic substituents on each ring as evidenced by a dihedral angle of 6.4(1)° between the Se1P1N5 and Se2P2N3 planes in molecule 1 and of 4.3(1)° between the Se3P3N9 and Se4P4N11 planes in molecule 2. The two independent molecules differ relatively little in their other metrical parameters except that the *N*-methylpyrazine groups built on N5 and N11 have opposite chair conformations. The P=Se distances fall in the narrow range 2.0885(7)–2.0934(7) Å. While the other bond parameters follow the same pattern

Table 1. Crystallographic data for **2**, **4**, and **7–9**.

| | 2 | 4 | 7 | 8 | 9 |
|--|--|---|---|---|---|
| Formula | C ₁₆ H ₃₄ N ₄ O ₂ P ₂ | C ₁₆ H ₃₄ N ₄ O ₂ P ₂ S ₂ | C ₁₈ H ₄₀ N ₆ P ₂ Se ₂ | C ₃₂ H ₆₈ Cl ₂ N ₈ O ₄ P ₄ Pd | C ₃₆ H ₈₀ Cl ₂ N ₁₂ P ₄ Pd·2H ₂ O |
| <i>F</i> _w | 376.41 | 440.55 | 560.42 | 930.14 | 1018.33 |
| Crystal system | orthorhombic | orthorhombic | orthorhombic | triclinic | monoclinic |
| Space group | <i>Pbcn</i> (No. 60) | <i>P2₁2₁2₁</i> (No. 19) | <i>Aba2</i> (No. 41) | <i>P</i> $\bar{1}$ (No. 2) | <i>P2₁/n</i> (No. 14) |
| <i>a</i> [Å] | 16.858(3) | 10.3997(7) | 44.534(3) | 9.7985(9) | 10.3512(4) |
| <i>b</i> [Å] | 7.319(10) | 14.5038(9) | 15.071(1) | 10.0093(9) | 23.0698(9) |
| <i>c</i> [Å] | 17.205(3) | 14.6807(9) | 15.024(1) | 12.482(1) | 11.5075(4) |
| α [°] | 90 | 90 | 90 | 93.244(1) | 90 |
| β [°] | 90 | 90 | 90 | 101.068(1) | 114.067(1) |
| γ [°] | 90 | 90 | 90 | 116.401(1) | 90 |
| <i>V</i> [Å ³] | 2122.8(6) | 2214.4(2) | 10083.7(12) | 1061.99(16) | 2509.11(16) |
| <i>Z</i> | 4 | 4 | 16 | 1 | 2 |
| $\rho_{\text{calcd.}}$ [g cm ^{–3}] | 1.178 | 1.321 | 1.477 | 1.454 | 1.348 |
| μ (Mo- <i>K</i> α) [mm ^{–1}] | 0.220 | 0.403 | 3.077 | 0.758 | 0.647 |
| <i>F</i> (000) | 816 | 944 | 4608 | 488 | 1080 |
| Crystal size [mm] | 0.17 × 0.20 × 0.22 | 0.15 × 0.20 × 0.24 | 0.12 × 0.13 × 0.22 | 0.07 × 0.15 × 0.28 | 0.10 × 0.17 × 0.24 |
| <i>T</i> [K] | 100 | 100 | 100 | 100 | 100 |
| 2 θ range [°] | 2.4, 28.4 | 2.4, 28.3 | 1.8, 28.3 | 1.7, 28.3 | 2.1, 28.3 |
| Total reflections | 17165 | 39382 | 44440 | 15061 | 43795 |
| Independent reflections | 2606 [<i>R</i> _(int) = 0.043] | 5499 [<i>R</i> _(int) = 0.041] | 11953 [<i>R</i> _(int) = 0.037] | 15061 [<i>R</i> _(int) = 0.0372] | 6207 [<i>R</i> _(int) = 0.038] |
| <i>R</i> ₁ ^[a] | 0.0661 | 0.0263 | 0.0285 | 0.0372 | 0.0268 |
| <i>wR</i> ₂ ^[b] | 0.2150 | 0.0662 | 0.0620 | 0.0809 | 0.0671 |
| GOF [<i>F</i> ²] | 1.131 | 1.092 | 1.031 | 0.951 | 1.054 |

[a] $R = \Sigma ||F_o| - |F_c|| / \Sigma |F_o|$. [b] $wR_2 = \{ \Sigma w(F_o^2 - F_c^2)^2 / \Sigma w(F_o^2)^2 \}^{1/2}$; $w = 1 / [\sigma^2(F_o^2) + (xP)^2]$.

Table 2. Crystallographic data for **14**, **15**, and **18**.

| | 14 | 15 | 18 |
|---|--|---|---|
| Formula | C ₁₆ H ₃₄ Au ₂ Cl ₂ N ₄ O ₂ P ₂ | C ₁₈ H ₄₀ Au ₂ Cl ₂ N ₆ P ₂ ·CH ₃ CN | C ₃₆ H ₇₂ Au ₂ Cl ₂ Cu ₂ I ₂ N ₁₀ O ₄ P ₄ ·2H ₂ O |
| <i>F</i> _w | 841.24 | 908.39 | 1716.68 |
| Crystal system | monoclinic | orthorhombic | triclinic |
| Space group | <i>P</i> 2 ₁ / <i>n</i> (No. 14) | <i>Pbca</i> (No. 61) | <i>P</i> 1̄ (No. 2) |
| <i>a</i> [Å] | 10.332(1) | 16.897(12) | 9.0919(3) |
| <i>b</i> [Å] | 15.857(2) | 16.444(12) | 10.2931(4) |
| <i>c</i> [Å] | 14.979(2) | 21.753(2) | 16.2912(6) |
| <i>α</i> [°] | 90 | 90 | 75.381(1) |
| <i>β</i> [°] | 94.215(2) | 90 | 80.925(1) |
| <i>γ</i> [°] | 90 | 90 | 75.997(1) |
| <i>V</i> [Å ³] | 2447.4(5) | 6044(6) | 1423.79(9) |
| <i>Z</i> | 4 | 8 | 1 |
| <i>ρ</i> _{calcd.} [g cm ^{−3}] | 2.283 | 1.997 | 2.025 |
| <i>μ</i> (Mo- <i>K</i> _α) [mm ^{−1}] | 12.344 | 10.002 | 7.211 |
| <i>F</i> (000) | 1584 | 3472 | 836 |
| Crystal size [mm] | 0.14 × 0.15 × 0.15 | 0.09 × 0.17 × 0.20 | 0.14 × 0.20 × 0.22 |
| <i>T</i> [K] | 102 | 100 | 100 |
| 2 θ range [°] | 2.3, 28.5 | 2.4, 28.3 | 2.1, 28.8 |
| Total reflections | 42048 | 27822 | 25423 |
| Independent reflections | 6129 [<i>R</i> _{int} = 0.058] | 7522 [<i>R</i> _{int} = 0.044] | 7195 [<i>R</i> _{int} = 0.025] |
| <i>R</i> ₁ ^[a] | 0.0351 | 0.0251 | 0.0194 |
| <i>wR</i> ₂ ^[b] | 0.0958 | 0.0562 | 0.0489 |
| GOF [<i>F</i> ²] | 1.044 | 1.050 | 1.086 |

[a] $R = \Sigma ||F_o| - |F_c|| / \Sigma |F_o|$. [b] $wR_2 = \{[\Sigma w(F_o^2 - F_c^2)^2] / \Sigma w(F_o^2)^2\}^{1/2}$; $w = 1/[\sigma^2(F_o^2) + (xP)^2]$.

Table 3. Selected bond lengths [Å] and bond angles [°] for **2**.

| Bond lengths | [Å] | Bond angles | [°] |
|--------------|----------|-----------------------|------------|
| P–N1 | 1.724(3) | N1–P–N2 | 108.61(13) |
| P–N2 | 1.662(3) | N1–P–N1 ⁱ | 79.99(11) |
| O–C3 | 1.409(4) | N1 ⁱ –P–N2 | 107.24(12) |
| O–C4 | 1.432(7) | C3–O–C4 | 110.7(3) |
| N1–C1 | 1.481(4) | P–N1–C1 | 123.4(2) |
| N2–C2 | 1.489(6) | P–N2–C2 | 116.6(2) |
| | | P–N2–C5 | 126.1(3) |

Table 4. Selected bond lengths [Å] and bond angles [°] for **4**.

| Bond lengths | [Å] | Bond angles | [°] |
|--------------|------------|-------------|------------|
| S1–P1 | 1.9302(4) | S1–P1–P2 | 120.66(2) |
| S2–P2 | 1.9387(5) | S1–P1–N1 | 120.29(4) |
| P1–N1 | 1.6869(12) | S1–P1–N2 | 117.75(4) |
| P1–N2 | 1.7102(12) | S1–P1–N3 | 112.16(4) |
| P2–N1 | 1.7013(12) | P2–P1–N1 | 42.72(4) |
| P2–N2 | 1.6796(12) | P2–P1–N3 | 127.17(4) |
| P2–N4 | 1.6484(13) | N2–P1–N3 | 112.47(6) |
| O1–C10 | 1.422(2) | C10–O1–C11 | 109.36(12) |
| N1–C1 | 1.4925(19) | C14–O2–C15 | 108.84(12) |

as for **4**. The most significant intermolecular interaction is a weak C–H···N hydrogen bond [C35–H35B···N10 (at 1 – *x*, 1 – *y*, *z*): 2.69 Å, 159°].

The mononuclear *trans*-palladium(II) complex **8** has crystallographically imposed centrosymmetry with the two P₂N₂ rings arranged in *trans* orientations with respect to the uncoordinated phosphorus centers. The geometry around the palladium metal center is distorted square planar with the corners occupied by two phosphorus atoms from the cyclodiphosphazane ligands and two chlorine

Table 5. Selected bond lengths [Å] and bond angles [°] for **7**.

| Bond lengths | [Å] | Bond angles | [°] |
|--------------|------------|-------------|------------|
| Se1–P1 | 2.0892(7) | Se1–P1–N1 | 120.68(8) |
| Se2–P2 | 2.0934(7) | Se1–P1–N2 | 117.16(8) |
| P1–N2 | 1.712(2) | Se1–P1–N5 | 111.42(8) |
| P1–N1 | 1.679(2) | N1–P1–N2 | 83.27(10) |
| P1–N5 | 1.647(2) | N1–P1–N5 | 108.55(11) |
| P2–N2 | 1.686(2) | N2–P1–N5 | 112.96(11) |
| P2–N1 | 1.715(2) | N1–P2–N2 | 82.97(10) |
| P2–N3 | 1.6414(19) | N1–P2–N3 | 113.33(11) |
| N6–C18 | 1.460(4) | N2–P2–N3 | 108.59(11) |
| N4–C10 | 1.462(4) | C15–N6–C16 | 109.2(2) |
| | | C15–N6–C18 | 110.0(2) |
| | | C10–N4–C11 | 109.2(2) |
| | | C10–N4–C13 | 109.0(2) |

Table 6. Selected bond lengths [Å] and bond angles [°] for **8**.

| Bond lengths | [Å] | Bond angles | [°] |
|--------------|------------|------------------------|------------|
| Pd–Cl | 2.3013(5) | Cl–Pd–P1 | 92.58(2) |
| Pd–P1 | 2.3440(5) | Cl–Pd–Cl ⁱ | 180.00 |
| P1–N1 | 1.6537(16) | Cl ⁱ –Pd–P1 | 87.42(2) |
| P1–N2 | 1.6784(18) | P1–Pd–P1 ⁱ | 180.00 |
| P1–N3 | 1.6972(15) | Pd–P1–N1 | 114.66(6) |
| P2–N2 | 1.7677(15) | Pd–P1–N2 | 111.19(5) |
| P2–N3 | 1.7291(18) | Pd–P1–N3 | 121.98(5) |
| P2–N4 | 1.6832(16) | N1–P1–N2 | 109.14(8) |
| O1–C2 | 1.431(3) | N2–P1–N3 | 82.86(8) |
| | | C2–O1–C3 | 110.48(14) |
| | | C13–O2–C14 | 110.03(15) |

atoms. The *cis* angles around the palladium metal center are 92.58(2)° (P1–Pd–Cl) and 87.42(2)° (P1ⁱ–Pd–Cl). The Pd–P1 bond length of 2.3440(5) Å is comparable to that in the aminophosphane complex *trans*-[PdCl₂–

Table 7. Selected bond lengths [Å] and bond angles [°] for **9**.

| Bond lengths | [Å] | Bond angles | [°] |
|--------------|------------|--------------------------|------------|
| Pd1–Cl1 | 2.3182(4) | Cl1–Pd1–P1 | 93.30(1) |
| P1–N1 | 1.6610(13) | Cl1–Pd1–P1 ⁱ | 86.70(1) |
| P1–N3 | 1.6860(15) | Cl1–Pd1–Cl1 ⁱ | 180.00 |
| P1–N4 | 1.6913(13) | Pd1–P1–N1 | 114.22(5) |
| P2–N3 | 1.7650(14) | Pd1–P1–N4 | 123.03(5) |
| P2–N4 | 1.7357(14) | Pd1–P1–N3 | 110.66(5) |
| P2–N5 | 1.6784(15) | N1–P1–N3 | 110.40(7) |
| N6–C18 | 1.461(2) | N3–P1–N4 | 82.62(7) |
| N2–C5 | 1.463(2) | C15–N6–C16 | 109.46(14) |
| | | C15–N6–C18 | 110.57(14) |
| | | C2–N2–C5 | 109.75(15) |
| | | C3–N2–C5 | 110.56(14) |

Table 8. Selected bond lengths [Å] and bond angles [°] for **14**.

| Bond lengths | [Å] | Bond angles | [°] |
|--------------|------------|-------------|------------|
| Au1–Cl1 | 2.2933(15) | Cl1–Au1–P1 | 174.29(5) |
| Au1–P1 | 2.2253(13) | Cl2–Au2–P2 | 173.70(6) |
| Au2–Cl2 | 2.2761(15) | Au1–P1–N1 | 113.28(16) |
| Au2–P2 | 2.2139(14) | Au1–P1–N2 | 118.85(17) |
| P1–N1 | 1.709(4) | Au1–P1–N3 | 114.46(18) |
| P1–N2 | 1.694(5) | N1–P1–N2 | 82.8(2) |
| P1–N3 | 1.638(5) | Au2–P2–N1 | 115.87(16) |
| O1–C10 | 1.427(8) | Au2–P2–N2 | 114.97(17) |
| O1–C11 | 1.422(8) | Au2–P2–N4 | 114.81(19) |
| | | N1–P2–N2 | 83.0(2) |
| | | N1–P2–N4 | 111.4(2) |
| | | N2–P2–N4 | 113.0(3) |

Table 9. Selected bond lengths [Å] and bond angles [°] for **15**.

| Bond lengths | [Å] | Bond angles | [°] |
|--------------|------------|-------------|------------|
| Au1–Cl1 | 2.2864(19) | Cl1–Au1–P1 | 178.46(4) |
| Au1–P1 | 2.2224(18) | Cl2–Au2–P2 | 177.37(4) |
| Au2–Cl2 | 2.285(2) | Au1–P1–N1 | 119.59(10) |
| Au2–P2 | 2.2216(19) | Au1–P1–N2 | 117.41(10) |
| P1–N1 | 1.686(3) | Au1–P1–N3 | 110.23(11) |
| P1–N2 | 1.704(3) | Au2–P2–N1 | 116.91(10) |
| P1–N3 | 1.632(3) | Au2–P2–N2 | 117.73(10) |
| N1–C1 | 1.496(5) | Au2–P2–N5 | 112.40(12) |
| N3–C9 | 1.472(4) | | |

Table 10. Selected bond lengths [Å] and bond angles [°] for **18**.

| Bond lengths | [Å] | Bond angles | [°] |
|--------------|-----------|--------------------------|-----------|
| Au1–I1 | 2.5633(2) | I1–Au1–P1 | 176.31(2) |
| Au1–P1 | 2.2486(6) | Cl1–Cu1–P2 | 115.99(7) |
| Cu1–Cl1 | 2.389(3) | Cl1–Cu1–Cl1 ⁱ | 94.42(9) |
| Cu1–N5 | 2.009(2) | P2–Cu1–N5 | 116.25(7) |
| Cu1–P2 | 2.1981(7) | Cl1–Cu1–N5 | 112.82(9) |
| P1–N2 | 1.688(2) | Cl1 ⁱ –Cu1–P2 | 111.86(6) |
| P1–N3 | 1.650(2) | Au1–P1–N2 | 117.29(8) |
| P1–N1 | 1.690(2) | Au1–P1–N1 | 121.68(8) |
| P2–N2 | 1.743(2) | | |

(Ph₂PNHCH₂CH₂OCH₃)₂] [2.3304(12) Å]^[10] but is slightly longer than that observed in *trans*-[PdCl₂[(*t*BuNP(OC₆H₄OMe-*o*))₂]] [Pd–P is 2.299(1) Å] indicating a

greater sigma donor character of the bis(amido) cyclodiphosphazane ligand. The extent of folding of the P₂N₂ ring is 21.4(1)°.

Complex **9** has a structure very similar to that of **8** and also has crystallographically imposed centrosymmetry. The patterns of bond lengths and bond angles in **9** are similar to those in **8** while the folding of the P₂N₂ ring is somewhat greater at 23.1(1)°. The interesting feature in the molecular structure of **9** is the presence of intermolecular hydrogen bonding between the hydrogen atoms of the lattice water molecules and the nitrogen atoms of the *N*-methyl piperazine moieties. The hydrogen bond parameters are H1O⋯N2 2.23 Å, O1–H1O⋯N2 171° and H2O⋯N6 2.20 Å, O1–H2O⋯N6 144°. The presence of these intermolecular hydrogen bonding interactions leads to the formation of an extended two-dimensional sheet structure in the crystal lattice as shown in part b of Figure 5. In addition the lattice water is involved in a C–H⋯O hydrogen bond within the asymmetric unit (C12–H12b⋯O1: 2.59 Å, 158°).

Crystals of **14** suitable for X-ray diffraction study were grown by slow evaporation of a mixture of dichloromethane and petroleum ether at room temperature. The two univalent gold atoms are in nearly linear coordination with P1–Au1–Cl1 and P2–Au2–Cl2 bond angles of 174.29(5)° and 173.70(6)°, respectively. These moieties are less linear than in the complex (PPh₃)AuCl (P–Au–Cl 179.63°). The Au–P bond lengths in **14** differ slightly [Au1–P1, 2.2253(13) Å and Au2–P2, 2.2139(14) Å] as do the Au–Cl bond lengths [Au1–Cl1, 2.2933(14) Å and Au2–Cl2, 2.2761(15) Å]. The folding of the P₂N₂ ring amounts to 18.6(3)° and there are two notable intermolecular hydrogen bonds involving C–H units. These are C12–H12b⋯O2 (at 1.5 – x, –0.5 + y, 1.5 – z) with H⋯O 2.42 Å and C–H⋯O 175° and C4–H4c⋯Cl2 (at –0.5 + x, 0.5 – y, –0.5 + z) with H⋯Cl 2.82 Å and C–H⋯Cl 148°. The two gold atoms are separated by 4.473 Å indicating the absence of a gold–gold interaction.

In complex **15**, the P–Au–Cl units are significantly more linear [P1–Au1–Cl1 178.46(4)° and P2–Au2–Cl2 177.37(4)°] than is the case in complex **14** but the folding of the P₂N₂ ring is essentially the same [18.2(2)°]. The other bond lengths and bond angles of **15** are similar to those of **14** and there is an intermolecular C–H⋯N hydrogen bond [C8–H8a⋯N6 (at 1.5 – x, 0.5 + y, z) with H⋯N 2.56 Å and C–H⋯N 167°].

The X-ray quality crystals of **18** were grown from a 1:1 solution of CH₂Cl₂/CH₃CN (1:1) at room temperature. The tetranuclear complex **18** has crystallographically imposed centrosymmetry with the cyclodiphosphazane bridging the gold(I) and copper(I) metal centers in a *cis* fashion. The P₂N₂ ring present in the tetranuclear complex **18** is folded along the N1⋯N2 axis by 21.2(2)°. The planarity of the Cu₂X₂ unit is a consequence of the centrosymmetry.

The unique gold center is nearly linear [I1–Au1–P1 176.31(2)°] whereas the copper atoms exist in a distorted tetrahedral environment being coordinated by two bridging chloride ions, one phosphorus atom and a nitrogen atom from acetonitrile. The bond angles around Cu1 vary from 94.42(9)° (Cl1–Cu1–Cl1ⁱ) to 116.25(7)° (P2–Cu1–N5). The

distance between the two copper centers in the dimeric unit is 3.271 Å which is longer than the sum of the van der Waal radii^[8] thus suggesting no metallophilic interactions. The Cu1–P2 and Cu1–N5 bond lengths are 2.1981(7) and 2.009(2) Å which are comparable to that of other copper(I) complexes containing cyclodiphosphazane ligands. The Au1–P1 bond length in **18** is 2.2486(6) Å, which is longer than the same found in the binuclear gold complex **14** [Au–P 2.2252(14) Å], and is likely due to a stronger bonding between gold and iodide than between gold and chloride. As with **9**, the lattice water in the crystal of **18** holds the main molecules together via OH⋯Cl and OH⋯O hydrogen bonds but here the result is one-dimensional ribbons parallel to the *ab* plane [O3–H3oa⋯Cl1 (at 1 + *x*, *y*, *z*): H⋯Cl 2.47 Å; O–H⋯Cl 148° and O3–H3ob⋯O2 (at 1 + *x*, 1 + *y*, *z*): H⋯O 2.12 Å; O–H⋯O 139°].

Conclusions

Two new bis(amino)cyclodiphosphazanes containing morpholine and *N*-methyl piperazine substituents have been synthesized and structurally characterized. The coordination chemical shifts are negative in all complexes. Interestingly, the sulfide derivative **4** shows two C–H⋯S contacts which are somewhat shorter than the sum of the van der Waals radii (3.00 Å). Although similar observations were made in 55 molecules containing the P=S moiety, no studies have looked into these weak C–H⋯S hydrogen-bond interactions. The bis(amino)cyclodiphosphazane ligands showed flexible coordination behavior with the palladium(II) and gold(I) metal precursors which led to the isolation of both mono- and binuclear complexes containing cyclodiphosphazane moieties. The mononuclear palladium(II) and gold(I) complexes were utilized to construct homo- and hetero tri- and tetranuclear complexes containing Pd^{II}/2Pd^{II}, Pd^{II}/2Au^I, and 2Au^I/2Cu^I metal centers. Utilization of these metal complexes as catalysts in various organic transformations and also to involve the coordination of donor atoms present in the side arm to form catalytic precursors is an area of active interest in our laboratory.

Experimental Section

General Procedures: All experimental manipulations were carried out under a dry nitrogen or argon atmosphere, using standard Schlenk techniques unless otherwise stated. Solvents were dried and distilled prior to use by conventional methods. CuI was purchased from Aldrich and used without further purification. The precursors [CIP(μ-N*t*Bu)]₂,^[11] [PdCl₂(SMe₂)₂],^[12] [Pd(μ-Cl)(η³-C₃H₅)₂],^[13] and [AuCl(SMe₂)]₂^[14] were prepared according to the published procedures.

Spectroscopy: The ¹H and ³¹P{¹H} NMR (δ in ppm) spectra were obtained with a Varian VXR 400 spectrometer operating at frequencies of 400 and 162 MHz, respectively. Tetramethylsilane and 85% H₃PO₄ were used as internal and external standards for ¹H and ³¹P{¹H} NMR, respectively. Positive shifts lie downfield of the standard in all cases. Microanalyses were carried out with a Carlo-Erba Model 1106 elemental analyzer. Electro-spray ionization (EI)

mass spectrometry experiments were carried out with a Waters Q-ToF micro-YA-105 instrument. Melting points of all compounds were determined with Veego melting point apparatus and were uncorrected. GC analyses were performed with a Perkin–Elmer Clarus 500 GC fitted with a flame-ionization detector (FID) and packed column.

Synthesis of *cis*-[(*t*BuN-μ)₂(PNC₄H₈O)₂] (2**):** A solution of morpholine (2.41 g, 27.64 mmol) in diethyl ether (15 mL) was added dropwise to a stirring solution of [CIP(μ-N*t*Bu)]₂ (1.90 g, 6.91 mmol) in ethyl ether (30 mL) at 0 °C over the course of 15 min. The reaction mixture was allowed to attain room temperature and stirring was continued for 16 h. The hydrochloride salts were filtered off, the solvent was removed under reduced pressure, and the white residue was dissolved in toluene and stored at –25 °C for a day to give **2** as a colorless crystalline compound; yield 90% (2.34 g, 6.22 mmol); m.p. 138–140 °C. C₁₆H₃₄N₄O₂P₂ (376.42): calcd. C 51.05, H 9.10, N 14.88; found C 51.25, H 9.15, N 14.75%. ¹H NMR (400 MHz, CDCl₃): δ = 3.59 (t, *J*_{HH} = 9.2 Hz, 8 H, CH₂), 3.15 (br. s, 8 H, CH₂), 1.24 (s, 18 H, *t*Bu) ppm. ³¹P{¹H} NMR (161.8 MHz, CDCl₃): δ = 92.8 (s) ppm.

Synthesis of *cis*-[(*t*BuN-μ)₂(PNC₄H₈NMe)₂] (3**):** A solution of *N*-methyl piperazine (2.04 g, 20.35 mmol) in diethyl ether (15 mL) was added dropwise to a stirring solution of [CIP(μ-N*t*Bu)]₂ (1.40 g, 5.09 mmol) in ethyl ether (30 mL) at 0 °C over the course of 10 min. The reaction mixture was allowed to attain room temperature and the stirring was continued for a further 20 h. The hydrochloride salts formed were filtered through frit containing celite. All the volatiles were removed under vacuum leaving an oily liquid, which was dissolved in acetonitrile and kept at –25 °C for 10 h to give **3** as a colorless crystalline compound; yield 83% (1.70 g, 4.23 mmol); m.p. 92–94 °C. C₁₈H₄₀N₆P₂ (402.50): calcd. C 53.71, H 10.01, N 20.88; found C 53.62, H 9.82, N 20.53%. ¹H NMR (400 MHz, CDCl₃): δ = 3.12 (br. s, 16 H, CH₂), 2.21 (s, 6 H, *N*Me), 1.14 (s, 18 H, *t*Bu) ppm. ³¹P{¹H} NMR (161.8 MHz, CDCl₃): δ = 91.4 (s) ppm.

Synthesis of *cis*-[(*t*BuN-μ)₂(P(S)NC₄H₈O)₂] (4**):** A mixture of **2** (0.102 g, 0.26 mmol) and elemental sulfur (0.017 g, 0.53 mmol) in toluene (10 mL) was heated under reflux for 16 h. The reaction mixture was allowed to cool to room temperature and all the volatiles were removed under vacuum. The residue was extracted with dichloromethane, layered with petroleum ether (3 mL), and stored at room temperature to give **4** as a colorless crystalline solid; yield 92% (0.11 g, 0.25 mmol); m.p. 198–200 °C. C₁₆H₃₄N₄O₂P₂S₂ (440.54): calcd. C 43.62, H 7.78, N 12.71, S 14.55; found C 43.59, H 7.65, N 12.55, S 14.63%. ¹H NMR (400 MHz, CDCl₃): δ = 3.68 (t, *J*_{HH} = 9.2 Hz, 8 H, CH₂), 3.46 (br. s, 8 H, CH₂), 1.52 (s, 18 H, *t*Bu) ppm. ³¹P{¹H} NMR (161.8 MHz, CDCl₃): δ = 46.7 (s) ppm.

Synthesis of *cis*-[(*t*BuN-μ)₂(P(S)NC₄H₈NMe)₂] (5**):** This was synthesized by a procedure similar to that of **4**, using **3** (0.102 g, 0.25 mmol) and elemental sulfur (0.015 g, 0.50 mmol); yield 88% (0.102 g, 0.22 mmol); m.p. 184–186 °C. C₁₈H₄₀N₆P₂S₂ (466.62): calcd. C 46.33, H 8.64, N 18.01, S 13.74; found C 46.45, H 8.82, N 18.23, S 13.65%. ¹H NMR (400 MHz, CDCl₃): δ = 3.54 (8 H, br. s, CH₂), 2.39 (br. s, CH₂, 8 H), 2.31 (s, 6 H, *N*Me), 1.54 (s, 18 H, *t*Bu) ppm. ³¹P{¹H} NMR (161.8 MHz, CDCl₃): δ = 46.6 (s) ppm.

Synthesis of *cis*-[(*t*BuN-μ)₂(P(Se)NC₄H₈O)₂] (6**):** This was synthesized by a procedure similar to that of **4**, using **2** (0.039 mg, 0.104 mmol) and elemental selenium powder (0.016 mg, 0.207 mmol); yield 90% (0.050 g, 0.093 mmol); m.p. 254–256 °C. C₁₆H₃₄N₄O₂P₂Se₂ (534.34): calcd. C 35.96, H 6.41, N 10.48; found C 35.85, H 6.62, N 10.23. ¹H NMR (400 MHz, CDCl₃): δ = 3.67

(t, $J_{\text{HH}} = 9.2$ Hz, 8 H, CH_2), 3.51 (br. s, 8 H, CH_2), 1.56 (s, 18 H, $t\text{Bu}$) ppm. $^{31}\text{P}\{^1\text{H}\}$ NMR (161.8 MHz, CDCl_3): $\delta = 39.2$ (s, $^1J_{\text{PSe}} = 893$, $^2J_{\text{PP}} = 28.9$ Hz) ppm.

Synthesis of *cis*-[($t\text{BuN}-\mu$) $_2(\text{P}(\text{S})\text{NC}_4\text{H}_8\text{NMe})_2$] (7): This was synthesized by a procedure similar to that of **4**, using **3** (0.143 mg, 0.35 mmol) and elemental selenium powder (0.562 mg, 0.71 mmol); yield 85% (0.169 g, 0.30 mmol); m.p. 216–218 °C. $\text{C}_{18}\text{H}_{40}\text{N}_6\text{P}_2\text{Se}_2$ (560.42): calcd. C 38.57, H 7.19, N 14.99; found C 38.39, H 7.20, N 15.15%. ^1H NMR (400 MHz, CDCl_3): $\delta = 3.44$ (br. s, 8 H, CH_2), 2.29 (br. s, CH_2 , 8 H), 2.11 (s, 6 H, NMe), 1.44 (s, 18 H, $t\text{Bu}$) ppm. $^{31}\text{P}\{^1\text{H}\}$ NMR (161.8 MHz, CDCl_3): $\delta = 40.2$ (s, $^1J_{\text{PSe}} = 917$, $^2J_{\text{PP}} = 27.8$ Hz) ppm.

Synthesis of *trans*-[$\text{PdCl}_2\{(\text{tBuN}-\mu)_2(\text{PNC}_4\text{H}_8\text{O})_2\}_2$] (8): A dichloromethane solution (5 mL) of $[\text{PdCl}_2(\text{SMe}_2)_2]$ (0.022 g, 0.073 mmol) was added dropwise to **2** (0.055 g, 0.15 mmol) in dichloromethane (5 mL) at room temperature. The reaction mixture was stirred for 6 h and then concentrated to 5 mL, layered with petroleum ether (2 mL) and placed at -25 °C for 18 h to afford compound **8** as a yellow crystalline solid; yield 82% (0.055 g, 0.060 mmol); m.p. 160–162 °C (dec.). $\text{C}_{32}\text{H}_{68}\text{Cl}_2\text{N}_8\text{O}_4\text{P}_4\text{Pd}$ (930.14): calcd. C 41.32, H 7.37, N 12.04; found C 41.44, H 7.41, N 12.15%. ^1H NMR (400 MHz, CDCl_3): $\delta = 3.98$ – 3.11 (m, 32 H, CH_2), 1.56 (s, 36 H, $t\text{Bu}$) ppm. $^{31}\text{P}\{^1\text{H}\}$ NMR (161.8 MHz, CDCl_3): $\delta = 98.3$ (s), 70.6 (s, Pd-P) ppm.

Synthesis of *trans*-[$\text{PdCl}_2\{(\text{tBuN}-\mu)_2(\text{PNC}_4\text{H}_8\text{NMe})_2\}_2$] (9): This was synthesized by a procedure similar to that of **8**, using **3** (0.055 g, 0.137 mmol) and $[\text{PdCl}_2(\text{SMe}_2)_2]$ (0.021 g, 0.068 mmol); yield 77% (0.052 g, 0.053 mmol); m.p. 164–166 °C (dec.). $\text{C}_{36}\text{H}_{80}\text{Cl}_2\text{N}_{12}\text{P}_4\text{Pd}$ (982.31): calcd. C 44.01, H 8.28, N 17.11; found C 44.12, H 8.30, N 17.15%. ^1H NMR (400 MHz, CDCl_3): $\delta = 3.89$ – 3.22 (m, 32 H, CH_2), 2.30 (s, 6 H, NMe), 2.28 (s, 6 H, NMe), 1.51 (s, 36 H, $t\text{Bu}$) ppm. $^{31}\text{P}\{^1\text{H}\}$ NMR (161.8 MHz, CDCl_3): $\delta = 97.8$ (s), 70.2 (s, Pd-P) ppm. MS (EI): m/z (%) = 983.4 [M – Cl].

Synthesis of [$\text{PdCl}(\eta^3\text{-C}_3\text{H}_5)_2\{(\text{tBuN}-\mu)_2(\text{PNC}_4\text{H}_8\text{O})_2\}$] (10): A pale yellow solution of $[\text{Pd}(\mu\text{-Cl})(\eta^3\text{-C}_3\text{H}_5)_2]$ (0.035 g, 0.096 mmol) in dichloromethane (5 mL) was added to a solution of **2** (0.036 g, 0.096 mmol) in dichloromethane (8 mL) at room temperature. The reaction mixture was stirred for 4 h. The clear yellow solution was concentrated and layered with petroleum ether to obtain **10** as a yellow crystalline solid; yield 86% (0.061 g, 0.081 mmol); m.p. 140–142 °C (dec.). $\text{C}_{22}\text{H}_{44}\text{Cl}_2\text{N}_4\text{O}_2\text{P}_2\text{Pd}_2$ (742.27): calcd. C 35.59, H 5.97, N 7.55; found C 35.41, H 5.95, N 7.38%. ^1H NMR (400 MHz, CDCl_3): $\delta = 5.59$ (br. s, 6 H, CH_2), 4.76 (br. s, 4 H, CH), 3.74 (br. s, 8 H, CH_2), 3.47 (br. s, 8 H, CH_2), 1.57 (s, 18 H, $t\text{Bu}$) ppm. $^{31}\text{P}\{^1\text{H}\}$ NMR (161.8 MHz, CDCl_3): $\delta = 94.3$ (s) ppm.

Synthesis of [$\text{PdCl}(\eta^3\text{-C}_3\text{H}_5)_2\{(\text{tBuN}-\mu)_2(\text{PNC}_4\text{H}_8\text{NMe})_2\}$] (11): This was synthesized by a procedure similar to that of **10**, using **3** (0.036 g, 0.089 mmol) and $[\text{Pd}(\mu\text{-Cl})(\eta^3\text{-C}_3\text{H}_5)_2]$ (0.033 g, 0.089 mmol); yield 90% (0.068 g, 0.081 mmol); m.p. 156–158 °C (dec.). $\text{C}_{24}\text{H}_{50}\text{Cl}_2\text{N}_6\text{P}_2\text{Pd}_2$ (768.35): calcd. C 37.51, H 6.55, N 10.93; found C 37.21, H 6.49, N 10.69%. ^1H NMR (400 MHz, CDCl_3): $\delta = 5.63$ (br. s, 6 H, CH_2), 4.73 (br. s, CH , 4 H), 3.74 (br. s, 8 H, CH_2), 3.47 (br. s, 8 H, CH_2), 2.3 (s, 6 H, NMe), 1.42 (s, 18 H, $t\text{Bu}$) ppm. $^{31}\text{P}\{^1\text{H}\}$ NMR (161.8 MHz, CDCl_3): $\delta = 93.8$ (s) ppm. MS (EI): m/z (%) = 733.4 [M – Cl].

Synthesis of [$\text{AuCl}(\text{tBuN}-\mu)_2(\text{PNC}_4\text{H}_8\text{O})_2$] (12): To a solution of **2** (0.026 g, 0.068 mmol) in dichloromethane (4 mL) was added a solution of $[\text{AuCl}(\text{SMe}_2)]$ (0.020 g, 0.068 mmol) in dichloromethane (8 mL) at room temperature. The reaction mixture was stirred under dark for 4 h. The clear solution was concentrated and layered with petroleum ether to obtain **12** as a colorless solid; yield 85%

(0.035 g, 0.058 mmol); m.p. 212–216 °C (dec.). $\text{C}_{16}\text{H}_{34}\text{AuClN}_4\text{O}_2\text{P}_2$ (608.84): calcd. C 31.56, H 5.63, N 9.20; found C 31.47, H 5.69, N 9.36%. ^1H NMR (400 MHz, CDCl_3): $\delta = 3.87$ – 3.08 (m, 16 H, CH_2), 1.42 (s, 18 H, $t\text{Bu}$) ppm. $^{31}\text{P}\{^1\text{H}\}$ NMR (161.8 MHz, CDCl_3): $\delta = 87.1$ (s), 71.6 (s, Au-P) ppm. MS (EI): m/z (%) = 573.2 (M – Cl).

Synthesis of [$\text{AuCl}(\text{tBuN}-\mu)_2(\text{PNC}_4\text{H}_8\text{NMe})_2$] (13): This was synthesized by a procedure similar to that of **12**, using **3** (0.027 g, 0.068 mmol) and $[\text{AuCl}(\text{SMe}_2)]$ (0.020 g, 0.068 mmol); yield 77% (0.033 g, 0.052 mmol); m.p. 194–196 °C (dec.). $\text{C}_{18}\text{H}_{40}\text{AuClN}_6\text{P}_2$ (634.92): calcd. C 34.05, H 6.35, N 13.24; found C 34.12, H 6.27, N 13.18%. ^1H NMR (400 MHz, CDCl_3): $\delta = 3.68$ – 3.25 (m, 16 H, CH_2), 2.27 (s, 3 H, NMe), 2.24 (s, 3 H, NMe), 1.32 (s, 18 H, $t\text{Bu}$) ppm. $^{31}\text{P}\{^1\text{H}\}$ NMR (161.8 MHz, CDCl_3): $\delta = 86.4$ (s), 70.2 (s, Au-P) ppm.

Synthesis of [$\text{AuCl}_2\{(\text{tBuN}-\mu)_2(\text{PNC}_4\text{H}_8\text{O})_2\}$] (14): This was synthesized by a procedure similar to that of **12**, using **2** (0.022 g, 0.059 mmol) and $[\text{AuCl}(\text{SMe}_2)]$ (0.035 g, 0.119 mmol); yield 92% (0.046 g, 0.054 mmol); m.p. 168–170 °C (dec.). $\text{C}_{16}\text{H}_{34}\text{Au}_2\text{Cl}_2\text{N}_4\text{O}_2\text{P}_2$ (841.26): calcd. C 22.84, H 4.07, N 6.66; found C 22.69, H 4.18, N 6.52%. ^1H NMR (400 MHz, CDCl_3): $\delta = 3.69$ (br. s, 8 H, CH_2), 3.67 (br. s, 8 H, CH_2), 1.58 (s, 18 H, $t\text{Bu}$) ppm. $^{31}\text{P}\{^1\text{H}\}$ NMR (161.8 MHz, CDCl_3): $\delta = 76.7$ (s, Au-P) ppm. MS (EI): m/z (%) = 805.8 (M – Cl).

Synthesis of [$\text{AuCl}_2\{(\text{tBuN}-\mu)_2(\text{PNC}_4\text{H}_8\text{NMe})_2\}$] (15): This was synthesized by a procedure similar to that of **12**, using **3** (0.024 g, 0.059 mmol) and $[\text{AuCl}(\text{SMe}_2)]$ (0.035 g, 0.119 mmol); yield 88% (0.046 g, 0.053 mmol); m.p. 156–158 °C (dec.). $\text{C}_{18}\text{H}_{40}\text{Au}_2\text{Cl}_2\text{N}_6\text{P}_2$ (867.34): calcd. C 24.92, H 4.65, N 9.69; found C 24.86, H 4.69, N 9.85%. ^1H NMR (400 MHz, CDCl_3): $\delta = 3.51$ (s, 8 H, CH_2), 3.49 (b, 8 H, CH_2), 2.40 (s, 6 H, NMe), 1.56 (s, 18 H, $t\text{Bu}$) ppm. $^{31}\text{P}\{^1\text{H}\}$ NMR (161.8 MHz, CDCl_3): $\delta = 76.9$ (s) ppm.

Synthesis of *trans*-[$\text{PdCl}_2\{(\text{tBuN}-\mu)_2(\text{PNC}_4\text{H}_8\text{O})_2\}_2(\text{Pd}(\eta^3\text{-C}_3\text{H}_5)\text{-Cl})_2$] (16): To a solution of **8** (0.040 g, 0.043 mmol) in dichloromethane (10 mL) was added dropwise $[\text{Pd}(\mu\text{-Cl})(\eta^3\text{-C}_3\text{H}_5)_2]$ (0.016 g, 0.043 mmol) in dichloromethane (5 mL) over the course of 3 min. The reaction mixture was stirred well at room temperature for 8 h. The clear solution was concentrated and layered with petroleum ether to afford **16** as a reddish yellow crystalline solid; yield 76% (0.042 g, 0.033 mmol); m.p. 152–154 °C (dec.). $\text{C}_{38}\text{H}_{78}\text{Cl}_4\text{N}_8\text{O}_4\text{P}_4\text{Pd}_3$ (1295.99): calcd. C 35.21, H 6.06, N 8.64; found C 35.06, H 6.25, N 8.79%. ^1H NMR (400 MHz, CDCl_3): $\delta = 5.59$ (br. s, 6 H, CH_2), 4.76 (br. s, 4 H, CH), 3.74– 3.26 (m, 32 H, CH_2), 1.78 (s, 36 H, $t\text{Bu}$) ppm. $^{31}\text{P}\{^1\text{H}\}$ NMR (161.8 MHz, CDCl_3): $\delta = 94.3$ (s, Pd'-P), 57.1 (s, Pd-P) ppm.

Synthesis of *trans*-[$\text{PdCl}_2\{(\text{tBuN}-\mu)_2(\text{PNC}_4\text{H}_8\text{O})_2\}_2(\text{AuCl})_2$] (17): A dichloromethane solution (5 mL) of $[\text{AuCl}(\text{SMe}_2)]$ (0.015 g, 0.053 mmol) was added dropwise to **8** (0.025 g, 0.026 mmol) in dichloromethane (10 mL). The stirring was continued for a further 6 h at room temperature. A deep yellow solution was concentrated and layered with acetonitrile to obtain **17** as a yellow crystalline solid; yield 70% (0.026 g, 0.018 mmol); m.p. 190–192 °C (dec.). $\text{C}_{32}\text{H}_{68}\text{Au}_2\text{Cl}_4\text{N}_8\text{O}_4\text{P}_4\text{Pd}$ (1394.98): calcd. C 27.55, H 4.91, N 8.03; found C 27.38, H 4.83, N 7.89%. ^1H NMR (400 MHz, CDCl_3): $\delta = 3.78$ – 3.25 (m, 32 H, CH_2), 1.66 (s, 36 H, $t\text{Bu}$) ppm. $^{31}\text{P}\{^1\text{H}\}$ NMR (161.8 MHz, CDCl_3): $\delta = 87.1$ (s, Au-P), 71.7 (s, Pd-P) ppm.

Synthesis of [$(\text{Cu}(\mu\text{-Cl})\text{Cu})(\text{CH}_3\text{CN})_2\{(\text{tBuN}-\mu)_2(\text{PNC}_4\text{H}_8\text{O})_2\}_2(\text{AuI})_2$] (18): To a solution of **12** (0.040 g, 0.066 mmol) in dichloromethane (5 mL) was added dropwise CuI (0.013 g, 0.067 mmol) in acetonitrile (5 mL) over the course of 2 min. The reaction mixture was stirred well at room temperature for 4 h. The clear solution

was concentrated and kept at room temperature for 2 d to afford **18** as a colorless crystalline compound; yield 66% (0.037 g, 0.044 mmol); m.p. 212–216 °C (dec.). $C_{36}H_{72}Au_2Cl_2Cu_2I_2N_{10}O_4P_4$ (1678.66): calcd. C 25.75, H 4.32, N 8.34; found C 25.78, H 4.35, N 8.49%. 1H NMR (400 MHz, $CDCl_3$): δ = 3.82–3.56 (m, 32 H, CH_2), 2.04 (s, 6 H, CH_3), 1.57 (s, 36 H, tBu) ppm. $^{31}P\{^1H\}$ NMR (161.8 MHz, $CDCl_3$): δ = 86.8, (br. s, Cu-P), 68.3 (s, Au-P) ppm.

X-ray Crystallography: A crystal of each of the compounds **2**, **4**, **7–9**, **14**, **15**, and **18** suitable for X-ray crystal analysis was mounted in a CryolooptTM with a drop of paratone oil and placed in the cold nitrogen stream of the KryoflexTM attachment of the Bruker APEX CCD diffractometer. Full spheres of data were collected using 606 scans in ω (0.3° per scan) at ϕ = 0, 120, and 240° (**2**, **7**, **8**) or a combination of three sets of 400 scans in ω (0.5° per scan) at ϕ = 0, 90, and 180° plus two sets of 800 scans in ϕ (0.45° per scan) at ω = –30 and 210° (**4**, **9**, **14**, **15**, **18**), all under the control of the SMART^[15] (**2**, **4**, **7**, **8**) and APEX2^[16] (**9**, **14**, **15**, **18**) software packages. For **8** and **15**, inspection of reciprocal lattice displays of selected reflections taken from the full data sets gave definite evidence for twinning. Processing of these reflection sets with CELL_NOW^[17] showed that the crystal of **8** was twinned by a 180° rotation about c^* while **15** was twinned by a 180° rotation about a . The raw data were reduced to F^2 values using the SAINT software^[18] and global refinements of unit cell parameters using 3206–9976 reflections chosen from the full data sets were performed. Multiple measurements of equivalent reflections provided the basis for empirical absorption corrections as well as corrections for any crystal deterioration during the data collection (SADABS^[19] for all but **8** and **15** where TWINABS^[20] was used). All the structures were solved by direct methods, except for **8**, **9**, and **18** where Patterson methods were employed, and refined by full-matrix least-squares procedures using the SHELXTL program package.^[21] Hydrogen atoms were placed in calculated positions and included as riding contributions with isotropic displacement parameters tied to those of the attached non-hydrogen atoms. Pertinent crystallographic data and other experimental details are summarized in Tables 1 and 2.

CCDC No. 761309–761316 (for compounds **2**, **4**, **7–9**, **14**, **15**, and **18**) contain the supplementary crystallographic data for this paper. These data can be obtained free of charge from the Cambridge Crystallographic Data Centre via www.ccd.cam.ac.uk/data_request/cif.

Acknowledgments

We are grateful to the Department of Science and Technology (DST), New Delhi, for financial support of this research through grant SR/S1/IC-02/007. We also thank the Department of Chemistry Instrumentation Facilities, Bombay, for spectral and analytical data and J. T. M. thanks the Louisiana Board of Regents for purchase of the CCD diffractometer and the Chemistry Department of Tulane University for support of the X-ray laboratory.

- [1] a) M. S. Balakrishna, D. Eisler, T. Chivers, *Chem. Soc. Rev.* **2007**, *36*, 650–664; b) G. G. Briand, T. Chivers, M. Krahn, *Coord. Chem. Rev.* **2002**, *233–234*, 237–254; c) L. Stahl, *Coord. Chem. Rev.* **2000**, *210*, 203–250; d) M. S. Balakrishna, V. S. Reddy, S. S. Krishnamurthy, J. F. Nixon, J. C. T. R. B. S. Laurent, *Coord. Chem. Rev.* **1994**, *129*, 1–90.

- [2] a) P. Chandrasekaran, J. T. Mague, R. Venkateswaran, M. S. Balakrishna, *Eur. J. Inorg. Chem.* **2007**, 4988–4997; b) P. Chandrasekaran, J. T. Mague, M. S. Balakrishna, *Inorg. Chem.* **2005**, *44*, 7925–7932; c) P. Chandrasekaran, J. T. Mague, M. S. Balakrishna, *Polyhedron* **2008**, *27*, 80–86; d) D. Suresh, M. S. Balakrishna, J. T. Mague, *Dalton Trans.* **2008**, 3272–3274.
- [3] a) M. S. Balakrishna, R. Venkateswaran, J. T. Mague, *Inorg. Chem.* **2009**, *48*, 1398–1406; b) P. Chandrasekaran, J. T. Mague, M. S. Balakrishna, *Dalton Trans.* **2009**, 5478–5486; c) D. Suresh, M. S. Balakrishna, K. Rathinasamy, D. Panda, S. M. Mobin, *Dalton Trans.* **2008**, 2812–2814; d) P. Chandrasekaran, J. T. Mague, M. S. Balakrishna, *Inorg. Chem.* **2006**, *45*, 5893–5897; e) P. Chandrasekaran, J. T. Mague, M. S. Balakrishna, *Inorg. Chem.* **2006**, *45*, 6678–6683; f) P. Chandrasekaran, J. T. Mague, M. S. Balakrishna, *Organometallics* **2005**, *24*, 3780–3783; g) D. Suresh, M. S. Balakrishna, J. T. Mague, *Tetrahedron Lett.* **2007**, *48*, 2283–2285; h) P. Chandrasekaran, J. T. Mague, M. S. Balakrishna, *Tetrahedron Lett.* **2007**, *48*, 5227–5229; i) M. S. Balakrishna, P. Chandrasekaran, R. Venkateswaran, *J. Organomet. Chem.* **2007**, *692*, 2642–2648; j) M. S. Balakrishna, *J. Organomet. Chem.* **2010**, *695*, 925–936.
- [4] a) R. Rama Suresh, K. C. Kumara Swamy, *Tetrahedron Lett.* **2009**, *50*, 6004–6007; b) K. C. Kumara Swamy, N. N. Bhuvan Kumar, E. Balaraman, K. V. P. Pavan Kumar, *Chem. Rev.* **2009**, *109*, 2551–2651; c) N. N. Bhuvan Kumar, K. C. Kumara Swamy, *Tetrahedron Lett.* **2008**, *49*, 7135–7137; d) S. González-Calera, D. J. Eisler, J. V. Morey, M. McPartlin, S. Singh, D. S. Wright, *Angew. Chem. Int. Ed.* **2008**, *47*, 1111–1114; e) P. Kommana, K. C. Kumara Swamy, *Inorg. Chem.* **2000**, *39*, 4384–4385; f) G. R. Lief, D. F. Moser, L. Stahl, R. J. Staples, *J. Organomet. Chem.* **2004**, *689*, 1110–1121; g) P. Kommana, K. V. P. Pavan Kumar, K. C. Kumara Swamy, *Ind. J. Chem. A* **2003**, *42*, 2371–2375; h) E. L. Doyle, L. Riera, D. S. Wright, *Eur. J. Inorg. Chem.* **2003**, 3279–3289.
- [5] R. Keat, *Top. Curr. Chem.* **1982**, *102*, 89–116.
- [6] I. J. Colquhoun, H. Christina, E. McFarlane, W. McFarlane, J. A. Nash, R. Keat, D. S. Rycroft, D. G. Thompson, *Org. Magn. Reson.* **1979**, *12*, 473–475.
- [7] P. Kommana, K. C. Kumara Swamy, *Inorg. Chem.* **2000**, *39*, 4384–4385.
- [8] A. Bondi, *J. Phys. Chem.* **1964**, *68*, 441–451.
- [9] J. Fischer, M. Schürmann, M. Mehring, U. Zachwieja, K. Jurkschat, *Organometallics* **2006**, *25*, 2886–1893.
- [10] A. D. Burrows, M. F. Mahon, M. T. Palmer, *J. Chem. Soc., Dalton Trans.* **2000**, 1669–1677.
- [11] A. Bashall, E. L. Doyle, C. Tubb, S. J. Kidd, M. McPartlin, A. D. Woods, D. S. Wright, *Chem. Commun.* **2001**, 2542.
- [12] P. K. Byers, A. J. Canty, H. Jin, D. Kruis, B. A. Markies, J. Boersma, G. van Koten, G. S. Hill, M. J. Irwin, L. M. Rendina, R. J. Puddephatt, *Inorg. Synth.* **1998**, *32*, 162.
- [13] Y. Tatsuno, T. Yoshida, S. Otsuka, *Inorg. Synth.* **1990**, *28*, 342–343.
- [14] M. Brandys, M. C. Jennings, R. J. Puddephatt, *J. Chem. Soc., Dalton Trans.* **2000**, 4601–4606.
- [15] SMART, version 5.625, Bruker-AXS, Madison, WI, **2000**.
- [16] APEX2, version 2.1.0, Bruker-AXS, Madison, WI, **2006**.
- [17] G. W. Sheldrick, CELL_NOW, University of Göttingen, Germany, **2002**, **2005**.
- [18] SAINT, versions 7.03 and 7.34A, Bruker AXS, Madison, WI, **2004**, **2006**.
- [19] G. W. Sheldrick, SADABS, versions 2.05 and 2007/2, University of Göttingen, Germany, **2002**, **2007**.
- [20] G. W. Sheldrick, TWINABS, University of Göttingen, Germany, **2002**, **2007**.
- [21] SHELXTL, version 6.10, Bruker-AXS, Madison, WI, **2000**.

Received: March 17, 2010
Published Online: July 23, 2010